Spring 4-5-2018

Microtextural Studies of Feldspar in Ordinary Chondrites

Jonathan A. Lewis
University of New Mexico

Jonathan Alan Lewis

Candidate

Earth and Planetary Sciences

Department

This dissertation is approved, and it is acceptable in quality and form for publication:

Approved by the Dissertation Committee:

Dr. Rhian H. Jones, Co-chairperson

Dr. Adrian J. Brearley, Co-chairperson

Dr. Francis M. McCubbin

Dr. Tobias P. Fischer

Dr. Conel M. O'D. Alexander

MICROTEXTURAL STUDIES OF FELDSPAR IN ORDINARY CHONDRITES

by

JONATHAN A. LEWIS

B.S., Earth and Planetary Sciences, University of New Mexico, 2013

DISSERTATION

Submitted in Partial Fulfillment of the
Requirements for the Degree of

Doctor of Philosophy
Earth and Planetary Sciences

The University of New Mexico
Albuquerque, New Mexico

May, 2018

for my family
without whom I would not be here at all

ACKNOWLEDGMENTS

First and foremost, I must thank Rhian Jones for her time, patience, and dedication over these last few years. Without her guidance, I would not have been able to make it this far. I am indebted to Adrian Brearley for many helpful conversations concerning the perils of chondrites, feldspar, and electron microscopy. I am grateful to Mousumi Roy for being my second project advisor and I would like to thank my committee: Francis McCubbin, Tobias Fischer, and Conel Alexander, for thought-provoking discussions.

I am grateful to the Department of Earth and Planetary Sciences at the University of New Mexico for being my home, and especially to Cindy, Paula, Faith, and Mabel, without whom no one would ever graduate. I am thankful for the financial support from the Kelley-Silver Foundation, New Mexico Space Grant Consortium, NASA, and the Department of Earth and Planetary Sciences. I especially want to acknowledge the NASA Cosmochemistry program for funding this project. I want to thank the Institute of Meteoritics for liberal use of their thin section collection, Mike Spilde for his guidance on the Probe and SEM, and Elena Dobrică for her expert assistance with the FIB and TEM.

I am also grateful to the School of Earth and Environmental Sciences at the University of Manchester for sponsoring my visit and want to thank those who made me feel at home during those delightfully damp months: Jamie Gilmour, Torsten Henkel, Ian Lyon, Katy Joy, John Pernet-Fisher, Sarah Crowther, Patricia Clay, Romain Tartèse, Katie Moore, and Serafina Garcea and, of course: Alex, Nat, Dayl, and Mark. I also want to thank Natasha Almeida and Martin Lee for useful conversations.

I could not have made it through without the help and support of my friends in and out of the department: Alison, Elena, Kathleen, Laura, Marika, Poorna, and Sheri. I would like to thank the denizens of Chondrite Club and the highly exclusive Petrology Reading Group, for broadening my horizons. I also want to acknowledge the roll of the Perpetually Unnamed Adventuring Group in doubling my understanding of sharks.

I need to thank my family for their support despite not knowing quite what I do, especially my parents Paul and Nancy, grandparents Eugene and Eulalia and, I suppose, Kachina. I am saddened that Eulalia did not make it to see me finish as she was always so excited about my geological studies. I particularly want to thank Cara for her enduring support and patience in my pursuit of things not related to Pluto. I also want to acknowledge the support of my New York family: Ira, Celia, and Dave.

Lastly, I am indebted to Juno in her role as dissertation support cat, and for letting me know when it is time to play. I would also like to show my appreciation for the furry company of Kitty Kitty, Olive, Watson, Juliette, Garvaghy, Hamilton, and Oscar.

MICROTEXTURAL STUDIES OF FELDSPAR IN ORDINARY CHONDRITES

by

JONATHAN A. LEWIS

B.S., Earth and Planetary Sciences, University of New Mexico, 2013
Ph.D., Earth and Planetary Sciences, University of New Mexico, 2018

ABSTRACT

Ordinary chondrites contain an important record of events that took place during the earliest period of solar system evolution. These include primary processes, such as chondrule formation, and secondary processes, those that affected asteroids after accretion and modified primary components. Secondary processes include aqueous alteration, thermal metamorphism, and shock effects from impact events. Secondary minerals can provide insight into the chemical and physical conditions that affected their parent asteroids. Feldspar is known to be a secondary mineral that crystallized during thermal metamorphism. The goal of this work is to use the formation and evolution of feldspar to elucidate the conditions of secondary processing on the ordinary chondrite parent asteroids. I show the common occurrence of primary feldspar in chondrules and reveal ubiquitous evidence for widespread metasomatism recorded by feldspar, which has not been fully recognized previously.

Chapter 1 provides an overview of the effects of metamorphism in the L group of ordinary chondrites, as observed in feldspar as well as secondary phosphate minerals. I show that metamorphism of secondary minerals is similar in H, L, and LL groups of

ordinary chondrites. Chapter 2 presents a study of the minimally metamorphosed ordinary chondrite Semarkona. I show that primary igneous plagioclase, with a wide range of compositions, is present within chondrules. Chapter 3 then follows the formation and alteration of feldspar in chondrules through the metamorphic sequence. I observe abundant evidence for metasomatism in feldspar, particularly in altered calcic plagioclase, crystallized secondary albite, and exsolved of K-feldspar from primary and secondary albite. I present a three-stage model of metasomatism involving prograde hydrous alteration, dehydration near peak metamorphism, and late-stage infiltration of anhydrous fluids. In Chapter 4, I examine fine-scale exsolution lamellae of K-feldspar in albite to determine cooling rates. I find fast cooling rates at high temperatures and discuss implications for thermal histories of ordinary chondrite parent bodies. Chapter 5 explores the development of porosity in chondrules. I show that pores in chondrules are the result of dissolution of feldspar and mesostasis glass, and that their existence facilitated fluid flow and chemical transport between chondrules and surrounding matrix.

TABLE OF CONTENTS

LIST OF FIGURES

LIST OF TABLES

PREFACE

This dissertation is composed of five chapters and three appendices. Each chapter is written as a separate, independent manuscript with its own introduction, methods, results, discussion, and references. As such, a degree of repetition between the chapters is unavoidable. The chapters were also written over a period of time so some refer to conference abstracts that are now full manuscripts. Each chapter has at least one coauthor whose contributions will be discussed below. The vast majority of the analytical work was done myself and I will be the first author on the resulting publications.

Chapter 1 describes the mineralogy of phosphates and feldspar in L chondrites. It extends work on phosphates in H (Jones et al., 2016) and LL (Jones et al., 2014) chondrites and feldspar in H and LL chondrites (Kovach and Jones, 2010). Most of the phosphate data was obtained for my undergraduate senior thesis and presented at the 2013 Lunar and Planetary Science Conference (Lewis and Jones, 2013). Some of the feldspar data was obtained by Jane Gallegos for her undergraduate senior thesis and presented at the 2011 Annual Meeting of the Meteoritical Society (Gallegos and Jones, 2011). I acquired the remaining data, provided the synthesis and interpretation, and wrote the final manuscript. Rhian Jones contributed significantly to interpretation of the data and editing of the manuscript. This chapter is published in *Meteoritics & Planetary Science* as Lewis and Jones (2016).

Chapter 2 presents a detailed description of the feldspar mineralogy within chondrules of the LL3.00 chondrite Semarkona. All the data was acquired by myself, some of which was presented at the 2014 Annual Meeting of the Meteoritical Society (Lewis and Jones, 2014a) and the 2015 Lunar and Planetary Science Conference (Lewis

and Jones, 2015b). Rhian Jones contributed significantly to interpretation of the data and editing of the manuscript. This chapter has been submitted for publication to *Meteoritics & Planetary Science* and is cited as Lewis and Jones (in review).

Chapter 3 follows the alteration and equilibration of plagioclase in ordinary chondrites. It extends the work of Chapters 1 and 2 as well as Kovach and Jones (2010) and Jones and Brearley (2010). All data was acquired myself and presented, in various parts, at Lunar and Planetary Science Conferences in 2014, 2016, and 2018 (Lewis and Jones, 2014b, 2018; Lewis et al., 2016) and at Annual Meetings of the Meteoritical Society in 2014, 2015, and 2016 (Lewis and Jones, 2014a, 2015a, 2016a). Rhian Jones and Adrian Brearley contributed to interpretation of the data and Rhian Jones helped with the editing of the chapter. It will be submitted for publication to *Geochimica et Cosmochimica Acta* and is cited as Lewis et al. (in preparation).

Chapter 4 uses K-feldspar exsolution textures to estimate cooling rates in ordinary chondrites. It builds on the work developed in the first three chapters as well as Kovach and Jones (2010) and Jones and Brearley (2011). I acquired all the data, some of which was presented at the 2015 Annual Meeting of the Meteoritical Society (Lewis and Jones, 2015a) and the 2016 Lunar and Planetary Science Conference (Lewis et al., 2016). Rhian Jones and Adrian Brearley contributed to interpretation of the data and Rhian Jones helped with the editing of the chapter. It will be submitted for publication to *Geochimica et Cosmochimica Acta* and is cited as Lewis et al. (in preparation).

Chapter 5 takes a close look at porosity in chondrules using X-ray tomography. I acquired the X-ray tomography data with help from the staff of the Manchester X-ray Imaging Facility at the University of Manchester. The rest of the data I acquired myself

using electron beam facilities at the Department of Earth and Planetary Sciences, University of New Mexico. Part of the data was presented at the 2017 Lunar and Planetary Science Conference (Lewis et al., 2017). Rhian Jones contributed significantly to interpretation of the data and editing of the manuscript. Serafina Garcea provided guidance concerning the processing and interpretation of the tomography data, and contributed to editing of the manuscript. This chapter was submitted for publication to *Geochimica et Cosmochimica Acta* and is cited (Lewis et al., in review).

Appendix 1 consists of the individual EPMA analyses for data acquired in Chapters 1-3. Appendix 2 illustrates the methodology used in Chapters 2 and 5 for calculating density-corrected bulk chemical compositions from quantitative EPMA maps. Appendix 3 is a compilation of standardized radiogenic of age data for chondrites using various radioisotope systems and was produced as the final project for the Radiogenic Isotope Geochemistry class in the spring of 2015. These data were used to create the probability density plots in Chapter 4 and provided general guidance concerning early solar system chronology for the entire dissertation.

References

Gallegos J. and Jones R. H. (2011) Equilibration of feldspar in petrologic type 4-6 L and LL chondrites: Metamorphic conditions on chondrite parent bodies. *74th Annual Meeting of the Meteoritical Society*, Abstract #5433.

Jones R. H. and Brearley A. J. (2011) Exsolution in feldspar in the Tuxtuac (LL5) chondrite: A new perspective on cooling rates for metamorphosed chondrites. *74th Annual Meeting of the Meteoritical Society*, Abstract #5475.

Jones R. H. and Brearley A. J. (2010) Late-stage fluids on the LL chondrite parent body: Evidence from feldspar in the LL4 chondrites Bo Xian and Bjurböle. *41st Lunar and Planetary Science Conference*, Abstract #2133.

Jones R. H., McCubbin F. M., Dreeland L., Guan Y., Burger P. V. and Shearer C. K. (2014) Phosphate minerals in LL chondrites: A record of the action of fluids

during metamorphism on ordinary chondrite parent bodies. *Geochimica et Cosmochimica Acta* **132**, 120–140.

Jones R. H., McCubbin F. M. and Guan Y. (2016) Phosphate minerals in the H group of ordinary chondrites, and fluid activity recorded by apatite heterogeneity in the Zag H3-6 regolith breccia. *American Mineralogist* **101**, 2452–2467.

Kovach H. A. and Jones R. H. (2010) Feldspar in type 4–6 ordinary chondrites: Metamorphic processing on the H and LL chondrite parent bodies. *Meteoritics & Planetary Science* **45**, 246–264.

Lewis J. A. and Jones R. H. (2018) Evidence from secondary minerals for three stages of metasomatism during thermal metamorphism in ordinary chondrites. *49th Lunar and Planetary Science Conference*, Abstract #1254.

Lewis J. A. and Jones R. H. (2016a) Feldspar in the L4 chondrite Saratov: The history and timing of metasomatism. *79th Annual Meeting of the Meteoritical Society*, Abstract #6121.

Lewis J. A. and Jones R. H. (2014a) Microtextural study of feldspar in petrologic type 3 LL ordinary chondrites: A record of parent body metasomatism. *77th Annual Meeting of the Meteoritical Society*, Abstract #5176.

Lewis J. A. and Jones R. H. (2015a) Microtextural study of feldspar in petrologic type 4 ordinary chondrites: Contrasting records of parent body metasomatism. *78th Annual Meeting of the Meteoritical Society*, Abstract #5119.

Lewis J. A. and Jones R. H. (2014b) Nephelinization and metasomatism in the ordinary chondrite Parnallee (LL3.6). *45th Lunar and Planetary Science Conference*, Abstract #1661.

Lewis J. A. and Jones R. H. (2016b) Phosphate and feldspar mineralogy of equilibrated L chondrites: The record of metasomatism during metamorphism in ordinary chondrite parent bodies. *Meteoritics & Planetary Science* **51**, 1886–1913.

Lewis J. A. and Jones R. H. (2013) Phosphate mineralogy of petrologic type 4-6 L ordinary chondrites. *44th Lunar and Planetary Science Conference*, Abstract #2722.

Lewis J. A. and Jones R. H. (2015b) Primary feldspar in Semarkona (LL3.00) chondrules. *46th Lunar and Planetary Science Conference*, Abstract #2067.

Lewis J. A. and Jones R. H. (in review) Primary feldspar in the Semarkona LL3.00 chondrite: Constraints on chondrule formation and secondary alteration. *Meteoritics & Planetary Science*.

Lewis J. A., Jones R. H. and Brearley A. J. (2016) Alkali feldspar exsolution in ordinary chondrites: Alkali metasomatism, metamorphism, and cooling rates. *47th Lunar and Planetary Science Conference,* Abstract #2559.

Lewis J. A., Jones R. H. and Brearley A. J. (in preparation) K-feldspar exsolution in ordinary chondrites: Evidence for late stage fluids and rapid cooling.

Lewis J. A., Jones R. H. and Brearley A. J. (in preparation) Plagioclase alteration and equilibration in ordinary chondrites: Evidence for three stages of metasomatism during thermal metamorphism.

Lewis J. A., Jones R. H. and Garcea S. C. (in review) Chondrule porosity in the L4 chondrite Saratov: Dissolution, chemical transport, and fluid flow. *Geochimica et Cosmochimica Acta*.

Lewis J. A., Jones R. H. and Garcea S. C. (2017) Chondrule porosity in the L4 chondrite Saratov: Mesostasis dissolution and chemical transport. *48th Lunar and Planetary Science Conference,* Abstract #2108.

CHAPTER 1

Phosphate and feldspar mineralogy of equilibrated L chondrites: The record of metasomatism during metamorphism in ordinary chondrite parent bodies

In collaboration with:
Rhian H. Jones

Citation:
Lewis, J. A. and Jones, R. H. (2016) Phosphate and feldspar mineralogy of equilibrated L chondrites: The record of metasomatism during metamorphism in ordinary chondrite parent bodies. *Meteoritics & Planetary Science*, **51**, 1886–1913.

Abstract

In ordinary chondrites (OCs), phosphates and feldspar are secondary minerals known to be products of parent body metamorphism. Both minerals provide evidence that metasomatic fluids played a role during metamorphism. We studied the petrology and chemistry of phosphates and feldspar in petrologic type 4-6 L chondrites, to examine the role of metasomatic fluids, and to compare metamorphic conditions across all three OC groups. Apatite in L chondrites is Cl-rich, similar to H chondrites, whereas apatite in LL chondrites has lower Cl/F ratios. Merrillite has similar compositions among the three chondrite groups. Feldspar in L chondrites shows a similar equilibration trend to LL chondrites, from a wide range of plagioclase compositions in petrologic type 4 to a homogeneous albitic composition in type 6. This contrasts with H chondrites which have homogeneous albitic plagioclase in petrologic types 4-6. Alkali- and halogen-rich and likely hydrous metasomatic fluids acted during prograde metamorphism on OC parent bodies, resulting in albitization reactions and development of phosphate minerals. Fluid compositions transitioned to a more anhydrous, Cl-rich composition after the asteroid

began to cool. Differences in secondary minerals between H chondrites and L, LL chondrites can be explained by differences in fluid abundance, duration, or timing of fluid release. Phosphate minerals in the regolith breccia, Kendleton, show lithology-dependent apatite compositions. Bulk Cl/F ratios for OCs inferred from apatite compositions are higher than measured bulk chondrite values, suggesting that bulk F abundances are overestimated and that bulk Cl/F ratios in OCs are similar to CI.

1. Introduction

Ordinary chondrites (OCs) show a sequence of equilibration of both textural and chemical characteristics. These changes are described by petrologic types 3-6 and are generally accepted to represent progressive degrees of metamorphism which occurred within 65 million years after accretion (Van Schmus and Wood 1967; Huss et al. 2006). Textural changes include recrystallization of the matrix, crystallization of chondrule mesostasis, blurring of the chondrule-matrix texture, and growth of secondary phases. Olivine and pyroxene show a wide range of compositions in type 3. Due to differences in the Mg-Fe interdiffusion rate for olivine and pyroxene, equilibration in olivine occurs by petrologic type 4 followed by pyroxene which is equilibrated by type 5.

The metamorphic environment on OC parent bodies is only poorly constrained and peak temperatures are only roughly defined. Peak temperatures for petrologic type 3 are not thought to exceed 500 ºC, types 4-5 range from 500-800 ºC, and type 6 from 800 ºC to the onset of melting at ~1000 ºC (Scott and Krot 2014). Additionally, although the presence of fluids has been inferred from mineralogical observations, the importance of fluids and their role during metamorphism is still poorly understood. Low petrologic type chondrites show evidence for the action of fluids from the presence of phyllosilicates

(Alexander et al. 1989), carbide-magnetite assemblages (Krot et al. 1997), sulfide-magnetite assemblages (Huss 1979), and bleached chondrules (Grossman et al. 2000). Increases in Fe oxidation (McSween and Labotka 1993) and possible mixing of O-isotope reservoirs (Bridges et al. 1999) are indication of fluid activity in the higher petrologic types.

Secondary minerals that occur as a result of thermal metamorphism can be used to understand the environment in which they form and evolve. Specifically, phosphate and feldspar minerals can preserve a record of any fluids present, and feldspar microstructures are a sensitive indicator of thermal history. Two phosphate minerals are present in petrologic type 4-6 ordinary chondrites: apatite ($Ca_5(PO_4)_3X$, where X represents monovalent anions, typically Cl^-, F^- or OH^-) and merrillite ($Na_2(Mg,Fe^{2+})_2Ca_{18}(PO_4)_{14}$) (Brearley and Jones 1998). In the traditional view of metamorphism, phosphates are considered to form in a solid-state oxidation reaction, with P derived from its primary occurrence in Fe,Ni metal (Ahrens 1970; Jones et al. 2014). Feldspar is typically albitic in composition and generally is considered to form from the crystallization of chondrule mesostasis by petrologic type 4, with progressive coarsening to type 6 (Van Schmus and Wood 1967).

Previous studies of LL and H chondrites reveal histories involving fluid interactions, for both phosphates (Jones and McCubbin 2012; Jones et al. 2014) and feldspar (Kovach and Jones 2010). Jones et al. (2014) showed that apatite in LL chondrites has high Cl/F ratios and H_2O abundances less than 100 ppm. Due to the lack of apatite equilibration with increasing petrologic type they argue for the presence of a dry, Cl-rich fluid acting after peak metamorphism. Apatite in H chondrites was found to

be similar, although with slightly higher Cl/F ratios than LL chondrites (Jones and McCubbin 2012). Kovach and Jones (2010) showed that a wide range of plagioclase feldspar compositions is present in petrologic type 4 LL chondrites which equilibrate to an albitic composition (~An_{12}) by petrologic type 6. LL chondrites also show evidence for alkali metasomatism where interaction with Na- and K-bearing fluids result in albitization reactions, and uptake of K in feldspar that later exsolves. In contrast, Kovach and Jones (2010) showed that H chondrites have homogeneous plagioclase compositions in types 4-6, indicating that equilibration occurred in petrologic type 3, i.e., at lower peak temperatures than in the LL chondrites. Currently, it is not clear how the L chondrites compare with the H and LL chondrites, and whether they show similarities to either of these groups. In this study, we extend these previous findings to examine the behavior of phosphates and feldspar in L chondrites, in order to compare the metamorphic and metasomatic histories of all three ordinary chondrite groups and to assess similarities and differences among the ordinary chondrite parent bodies.

2. Samples and analytical methods

We studied both phosphates and feldspar in three equilibrated ordinary chondrites: Santa Barbara (L4), Elenovka (L5), and Bruderheim (L6) (Fig. 1.1a-c). We also analyzed phosphates in the regolith breccia Kendleton (L3-5) (Fig. 1.1d-f) and feldspar in Kramer Creek (L4) and Roy 1933 (L5) (Table 1.1). Kramer Creek and Roy 1933 are finds with low degrees of terrestrial weathering, W3 and W2 respectively, which we determined using the method of Wlotzka (1993). The other four chondrites are falls and were chosen in order to minimize the effects of terrestrial weathering. Low to moderate shock stages have been reported for Kramer Creek (S2), Roy 1933 (S3),

Table 1.1. Sample list.

	Thin section	Petrologic type	Shock stage	Weathering
Santa Barbara	UNM 120	L4	S2	Fall
Kramer Creek	UNM 82	L4	S2	W3
Elenovka	UNM 246E	L5	S3	Fall
Roy 1933	UNM 31	L5	S3	W2
Bruderheim	UNM 53	L6	S4	Fall
Kendleton, *regolith breccia*				Fall
L3 clast	UNM 710A	L3	S3	
L4 host	UNM 713	L4	S3	
L5 clast	UNM 714A	L5	S2	

Elenovka (S3) and Bruderheim (S4) (Stöffler et al. 1991; Rubin 2004). Santa Barbara was also determined to have a low shock stage (S2) during the course of this study according to the method described by Stöffler et al. (1991). Kendleton is a regolith breccia with an L4 chondritic host, clasts of L3 and L5 material, areas of shock darkening, and shock melt veins (Ehlmann et al. 1988). Despite these shock features, the material we studied only has low to moderate reported shock stages of ~S3 for the L3 clast and L4 host and ~S2 for the L5 clast (Ehlmann et al. 1988; Rubin 2004).

Phosphate and feldspar grains were located in each thin section using optical microscopy, and scanning electron microscopy (SEM). We used a JEOL 5800LV SEM and a FEI Quanta 3D field emission gun SEM for backscattered electron (BSE) imaging and energy-dispersive spectroscopic (EDS) analysis. Quantitative wavelength-dispersive spectroscopic (WDS) analysis was conducted on a JEOL 8200 electron probe microanalyzer (EPMA) with a 15 kV accelerating voltage and 20 nA beam current. Phosphates were analyzed with a 5 μm spot using the following standards: Taylor apatite (Ca, P, F), Taylor olivine (Mg, Fe), sodalite (Cl, Na), Y-phosphate (Y), and Ce-phosphate (Ce). We also used a second apatite standard, FM020, for Ca and P (McCubbin et al.

2012). We used the live chart recorder to monitor F and Cl count rates during the analyses to ensure migration was not occurring, particularly in F (Stormer et al. 1993; McCubbin et al. 2010) and F was analyzed using the LDE crystal spectrometer. Feldspar grains were analyzed with a 2-10 μm beam diameter using the following Taylor standards: albite (Si, Al, Na), orthoclase (Al, K), diopside (Ca, Si), olivine (Fe, Mg), and chromite (Cr).

Phosphate abundances and distribution maps were generated from combined WDS/EDS element maps for each thin section using the electron microprobe (Fig. 1.1). Maps were obtained over a 10 mm x 10 mm area for Santa Barbara, Elenovka, and Bruderheim, a 5 mm x 15 mm area for the Kendleton L4 host, a 5 mm x 5 mm area for the L3 clast, and a 5 mm x 10 mm area for the L5 clast. The maps were generated with a step size of 10 μm/px with a 20 ms dwell time per pixel and a 10 μm wide electron beam. We determined modal abundances by pixel counting in Adobe Photoshop. The total phosphate abundance was calculated by counting pixels containing both P and Ca above a 25% threshold. Apatite abundance was then calculated by counting phosphate pixels with Cl above a 10% threshold and merrillite was determined by difference. Volume percentages were calculated as an area since no fabric was noted on any of the samples. Uncertainty in phosphate abundances are estimated to be ±0.1% by volume, absolute. This uncertainty is estimated by varying the thresholding parameters by ±10% and is consistent with the uncertainty estimated for phosphate abundances in LL chondrites by Jones et al. (2014) using a similar thresholding technique.

Phosphate distribution maps were also used to determine maximum and average grain sizes for apatite and merrillite using particle analysis in ImageJ. Individual grain

sizes were taken to be the maximum dimension (width or height) produced by the particle analysis. Maximum grain sizes measured in this manner are very close to sizes of the largest grains measured in BSE images. For example, the large merrillite grain in Kendleton's L5 clast (Fig. 1.4e) is approximately 400 μm x 650 μm in size and the particle analysis yields a grain size of 620 μm. However, since the phosphate map resolution is 10 μm/px, average grain sizes are inevitably biased by grains greater than or equal to 10 μm. Maximum grain sizes are likely much more accurate than the averages.

3. Results

3.1. Phosphates

3.1.1. Abundances and distribution

Phosphate abundances and grain sizes are summarized in Table 1.2 and illustrated in Figure 1.1. Apatite and merrillite appear to have a homogeneous and random distribution throughout the mapped areas of Elenovka and Bruderheim. Santa Barbara has an increase in phosphate abundance and average size from the lower left to the upper right of the thin section (Fig. 1.1a). This change in texture does not appear to correspond with any obvious differences in thin section texture. Total phosphate volume percentages are 0.4%, 0.7%, and 0.5% for Santa Barbara, Elenovka, and Bruderheim respectively. Merrillite is more common than apatite in Elenovka and Bruderheim, but in Santa Barbara phosphates are approximately equal in abundance (49% apatite to 51% merrillite). Average apatite grain sizes are larger than merrillite by nearly a factor of 2 though size distributions for both phosphates are very broad and dominated by small grains. Average grain sizes in Santa Barbara, Elenovka, and Bruderheim are 58 μm, 62 μm, and 55 μm for apatite and 30 μm, 35 μm, and 31 μm for merrillite respectively.

Table 1.2. Phosphate abundances and grain sizes.

	Volume %			Phosphate %		Max grain size (μm)		Mean grain size (μm)			
	Total	Apatite	Merrillite	Apatite	Merrillite	Apatite	Merrillite	Apatite	*1σ*	Merrillite	*1σ*
Santa Barbara (L4)	0.4	0.2	0.2	49	51	230	290	58	*51*	30	*36*
Elenovka (L5)	0.7	0.2	0.5	30	70	390	490	62	*82*	35	*71*
Bruderheim (L6)	0.5	0.1	0.4	26	74	400	390	55	*70*	31	*53*
Kendleton, *regolith breccia*											
L3 clast	0.2	0.1	0.1	46	54	160	80	39	*43*	20	*16*
L4 host	0.3	0.0	0.3	3	97	60	280	28	*15*	40	*31*
L5 clast	0.7	0.3	0.4	37	63	290	620	42	*50*	45	*94*

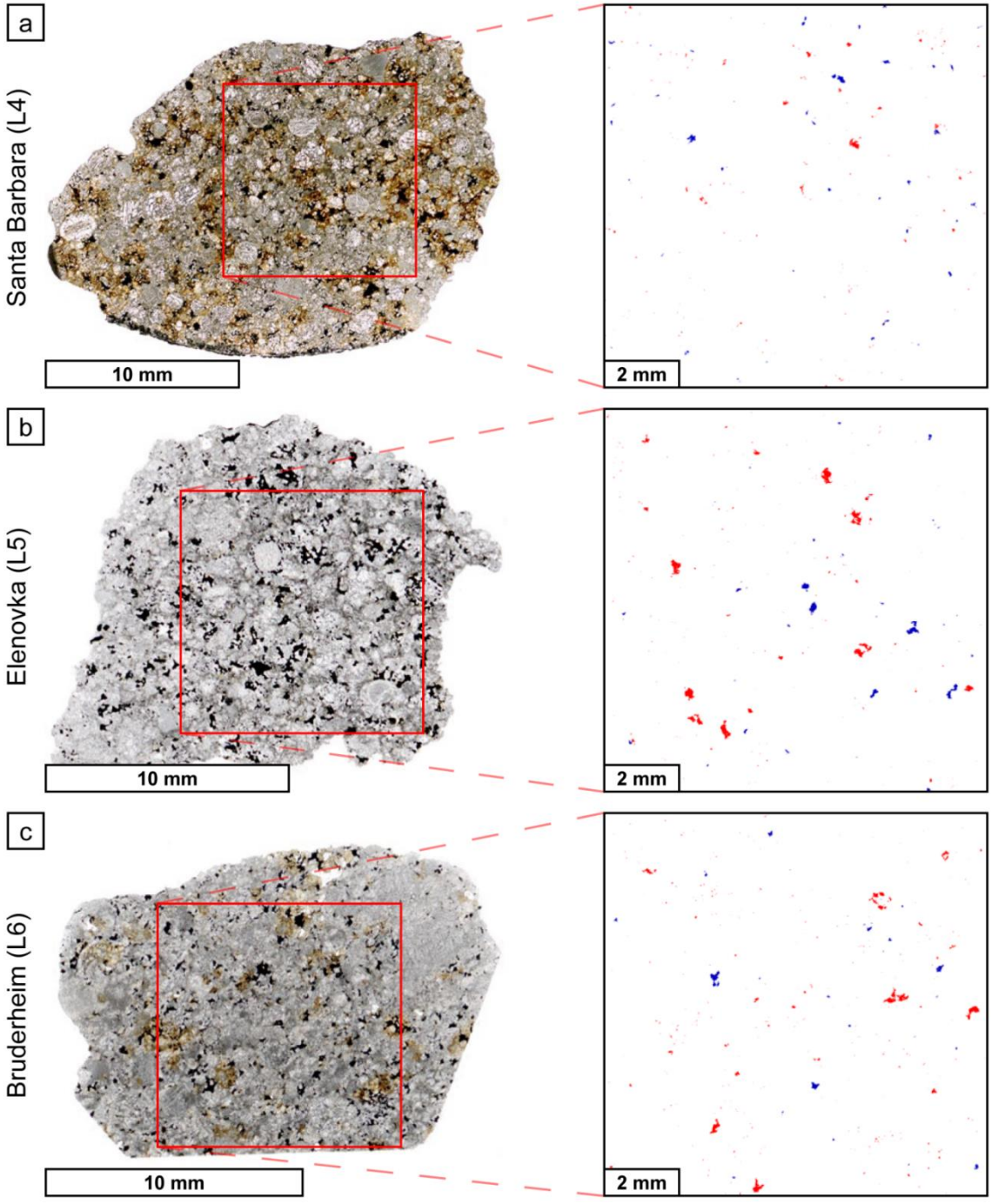

Figure 1.1. Thin sections of samples studied: images on the left are flat-bed optical scans of (a) Santa Barbara (L4), (b) Elenovka (L5), (c) Bruderheim (L6). Maps on the right show the distribution of merrillite (red) and apatite (blue) in selected regions of each thin section. Phosphate distributions were generated using WDS element maps, see text for details.

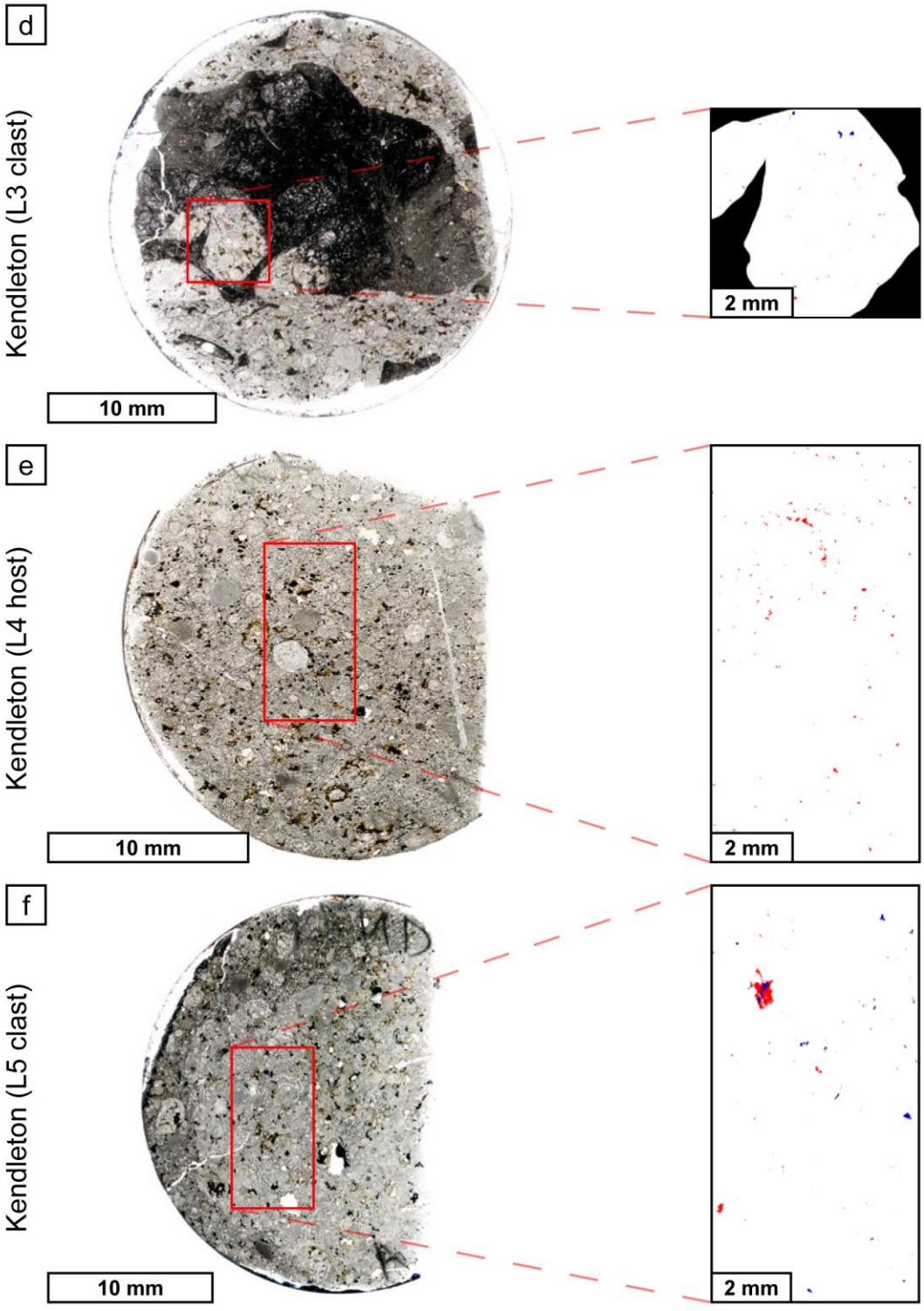

Figure 1.1. *(Continued)*. Thin sections of samples studied: images on the left are flat-bed optical scans the L regolith breccia Kendleton's (d) L3 clast, (e) L4 host, (f) L5 clast. Maps on the right show the distribution of merrillite (red) and apatite (blue) in selected regions of each thin section. Phosphate distributions were generated using WDS element maps, see text for details.

The largest merrillite grains are 10-30% larger than the largest apatite grains. Maximum grain sizes for Santa Barbara, Elenovka, and Bruderheim are 230 μm, 390 μm, and 400 μm for apatite and 290 μm, 490 μm, and 390 μm for merrillite respectively.

In the regolith breccia Kendleton we focused on an L3 clast ~5 mm in diameter present within an impact melt vein (Fig. 1.1d), the L4 host (Fig. 1.1e) which comprises ~80% of the material (Ehlmann et al. 1988), and an L5 clast ~20 mm in diameter (Fig. 1.1f). Kendleton also has a largely homogeneous and random distribution of phosphates in the mapped areas. However, the L5 clast is dominated by a single large (approximately 400 μm x 650 μm) apatite-bearing merrillite grain (Fig. 1.1f). This is the largest grain we observed in any sample and its presence skews the phosphate abundance and grain size distribution for this clast. The L3 clast and L4 host have comparatively low phosphate abundances of 0.2% and 0.3% respectively while the L5 clast has a much larger phosphate abundance of 0.7%. Apatite abundances in Kendleton's L3 and L5 clasts are similar to the other samples, 46% and 37% of the total phosphate respectively. However, the L4 host has an extremely low apatite abundance of 3% of the total phosphate. Apatite grain size is also small in the L4 host with an average size of 28 μm and the largest grain only 60 μm, whereas merrillite has a larger average and maximum grain size of 40 μm and 280 μm respectively. The L3 clast has larger average and maximum grain sizes for apatite (39 μm and 160 μm respectively) than merrillite (20 μm and 80 μm respectively) though the counting statistics are poor because of the small size of the clast. The L5 clast on the other hand has a larger average and maximum grain size for merrillite (45 μm and 620 μm respectively) than apatite (42 μm and 290 μm respectively) due to the single large grain of merrillite.

Although the low abundance of apatite in the Kendleton L4 host does somewhat reflect its sparse distribution (Fig. 1.1d), our abundance value may be exaggerated by a known bias in our method of calculating abundances. The defocused, 10 μm beam integrates signal over the full 10 μm area, causing smaller grains to get lost in the signal of larger or more numerous grains. The phosphate minerals in the L4 host are generally quite small so may be subject to this analytical effect. Additionally, Cl has a relatively weak signal compared to P and Ca. The Cl signal also has a large amount of noise due to small amounts of Cl present in the epoxy used to mount the thin section. As a result, small-scale intergrowths of apatite and merrillite, also common in the L4 host, may be recognized primarily as merrillite. As the phosphate grains grow in size and compositional distinction, as seen in Elenovka and Bruderheim, this bias is significantly reduced.

3.1.2. Petrography

Santa Barbara (L4)

Small grains of apatite are highly fractured (Fig. 1.2a,b) while larger grains are typically much smoother. In general, merrillite is less fractured than apatite (Fig. 1.3a,b). Neither phosphate mineral has a preferred silicate association and both occur adjacent to olivine, pyroxene, and feldspar (Fig. 1.2a,b, 1.3a,b). Both merrillite and apatite commonly contain silicate inclusions which are predominantly olivine and feldspar (e.g., Fig. 1.3a) and only rarely pyroxene. Both apatite and merrillite also occur commonly in association with large grains of Fe,Ni metal, sulfides, and chromite (e.g., Fig. 1.3b). The two phosphates do not occur together with the exception of a single 100 μm grain in which apatite and merrillite are intergrown (Fig. 1.2b).

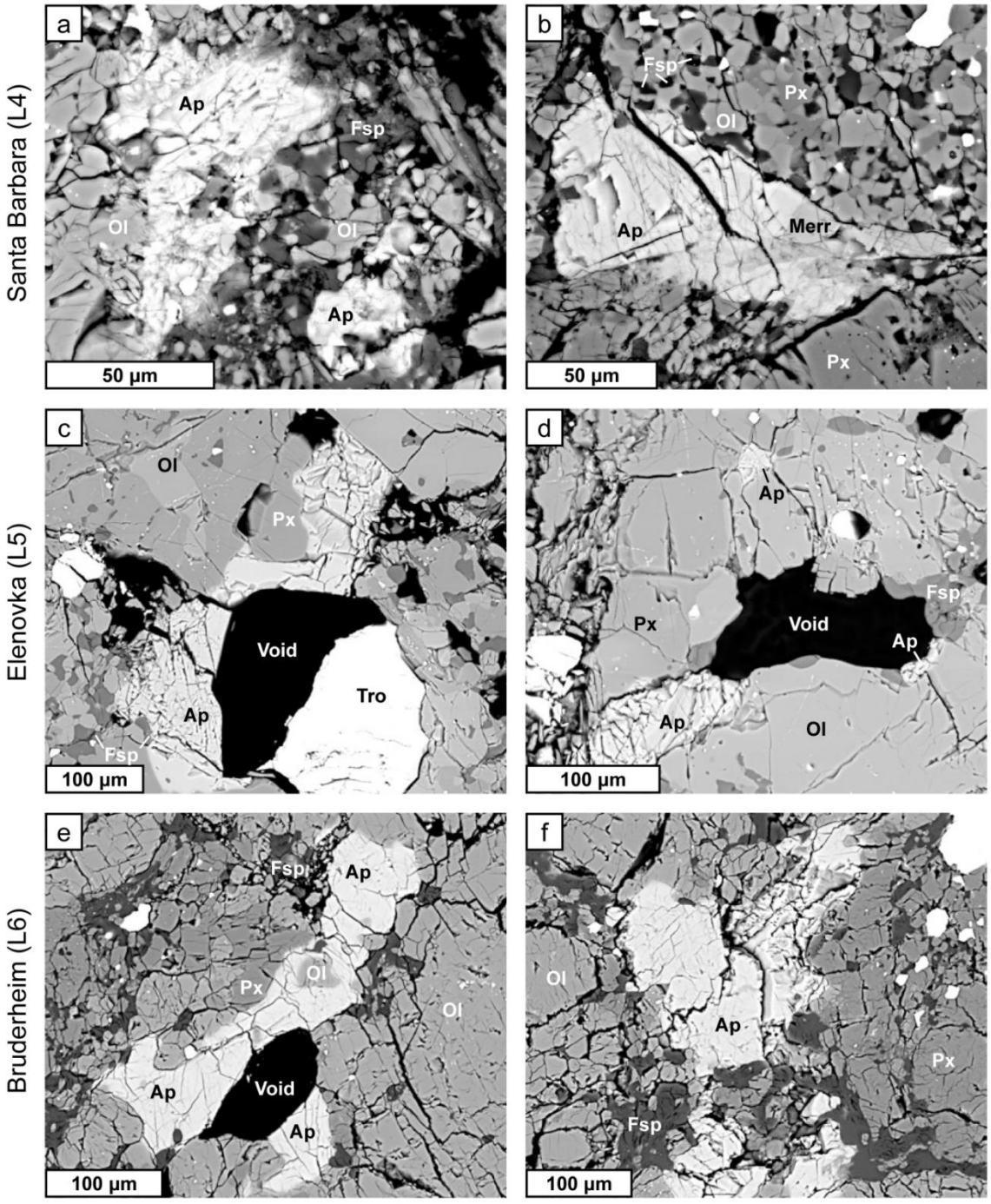

Figure 1.2. BSE images of apatite in L chondrites. (a,b) Santa Barbara (L4) illustrating (a) fine-grained apatite (Ap) and feldspar (Fsp) with olivine (Ol) and (b) an apatite and merrillite (Merr) intergrowth with olivine and low-Ca pyroxene (Px). (c,d) Elenovka (L5) illustrating apatite occurring adjacent to voids, in association with troilite (Tro), olivine, pyroxene, and feldspar. (e,f) Bruderheim (L6) illustrating (e) apatite adjacent to a void with an olivine inclusion and adjacent feldspar, pyroxene, and olivine and (f) large apatite grain occurring with feldspar, olivine, and pyroxene.

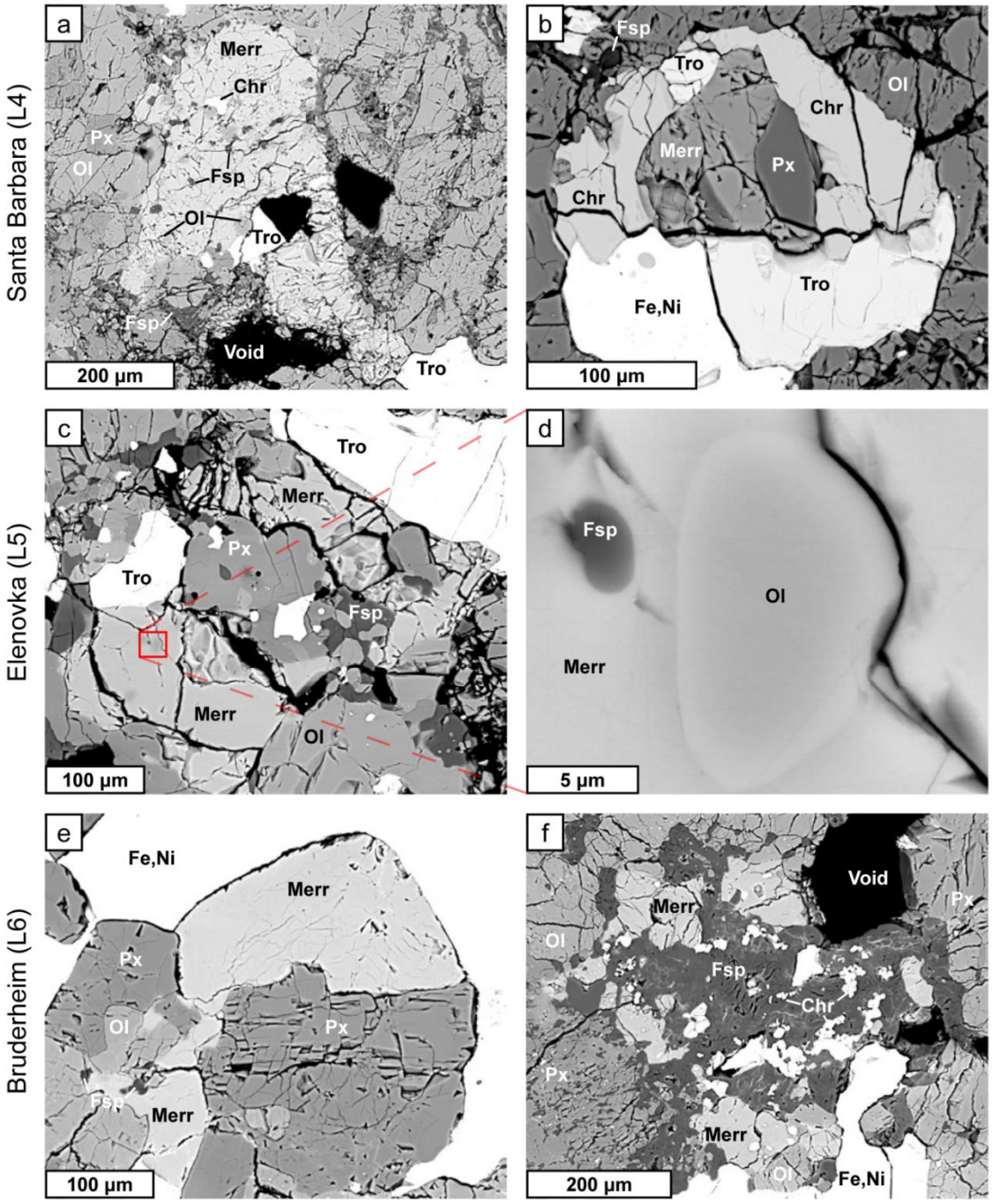

Figure 1.3. BSE images of merrillite in L chondrites. (a,b) Santa Barbara (L4) illustrating (a) large merrillite (Merr) grain with inclusions of olivine (Ol), feldspar (Fsp), chromite (Chr), and troilite (Tro), adjacent to olivine, pyroxene (Px), feldspar and a void and (b) merrillite and pyroxene enclosed by Fe,Ni metal (Fe,Ni), chromite and troilite. (c,d) Elenovka (L5) illustrating (c) merrillite adjacent to troilite, pyroxene, olivine, and feldspar and blown up portion (d) showing inclusions of feldspar and olivine. (e,f) Bruderheim (L6) illustrating (e) merrillite adjacent to Fe,Ni metal, olivine, pyroxene, and minor feldspar and (f) merrillite associated with chromite-plagioclase assemblage.

Elenovka (L5)

Fracturing is pervasive in apatite (Fig. 1.2c,d) but much less common in merrillite (Fig. 1.3c). Apatite is commonly found adjacent to or surrounding voids (Fig. 1.2c,d). It is not clear if these voids are original or the result of sample preparation in which grains of apatite (or grains adjacent to apatite, such as Fe,Ni metal) are preferentially lost during the polishing process. Merrillite occurs frequently adjacent to Fe,Ni metal and sulfides (Fig. 1.3c), though like Santa Barbara, there is no preferential association with a single silicate phase. Olivine, pyroxene, and small grains of feldspar occur adjacent to both apatite and merrillite. Inclusions in merrillite are almost exclusively olivine and feldspar. Figure 1.3d shows two such inclusions: a 10 μm olivine inclusion and a 2 μm feldspar inclusion.

Bruderheim (L6)

Apatite is only lightly to moderately fractured (Fig. 1.2e,f). Fig. 1.2f illustrates possible crystallographic control to the fractures. Merrillite is generally smooth (Fig. 1.3e). Apatite is commonly found near voids (Fig. 1.2e) and merrillite occurs in contact with Fe,Ni metal (Fig. 1.3e) and sulfides. Olivine, pyroxene, and feldspar are common minerals in association with the phosphates. Olivine and feldspar are other common inclusions in both merrillite and apatite (Fig. 1.2e, 1.3f). In the assemblage illustrated in Fig. 1.3f, feldspar surrounds merrillite and also contains abundant, fine-grained chromite. Chromite inclusions are also present within the merrillite.

Kendleton (L3 clast)

Apatite and merrillite occur in association with recrystallized feldspathic mesostasis within chondrules (Fig. 1.4a) and outside chondrules in association with fine-

grained matrix. Merrillite is also commonly associated with Fe,Ni metal (Table 1.2, Fig. 1.4b). Figure 1.4b shows multiple merrillite inclusions within Fe,Ni metal where merrillite is surrounded by Ni-rich halos. Ni-enrichment may have occurred during merrillite grain growth during which Fe was removed from the metal and incorporated into the phosphate. This particular metal grain is located close to the impact melt vein and may have been influenced by the vein's formation.

Kendleton (L4 host)

Phosphates in Kendleton's L4 host differ substantially from Santa Barbara, Elenovka, and Bruderheim. Merrillite dominates the phosphates, accounting for 97% (Table 1.2). Unlike L4 Santa Barbara (Figs. 1.2a,b and 1.3a,b), merrillite and apatite in the Kendleton L4 material commonly occur together, with a texture suggesting apatite is replacing the merrillite (Fig. 1.4c). Both apatite and merrillite are only moderately fractured. Apatite also commonly occurs as small grains in the matrix or along cracks (Fig. 1.4d). Individual merrillite grains tend to be small and can occur in chains of small, interconnected grains or as inclusions within Fe,Ni metal, similar to the inclusions seen in the L3 clast (Fig. 1.4b).

Kendleton (L5 clast)

The large phosphate assemblage in the L5 clast consists of a large merrillite grain with intergrown apatite. The merrillite has numerous feldspar and olivine inclusions but few pyroxene inclusions. Apatite and merrillite also occur together in other grains (e.g., Fig. 1.4f) with textures intermediate to the replacement texture seen in the L4 host (Fig. 1.4c) and the intergrowth seen in Santa Barbara (Fig. 1.2d).

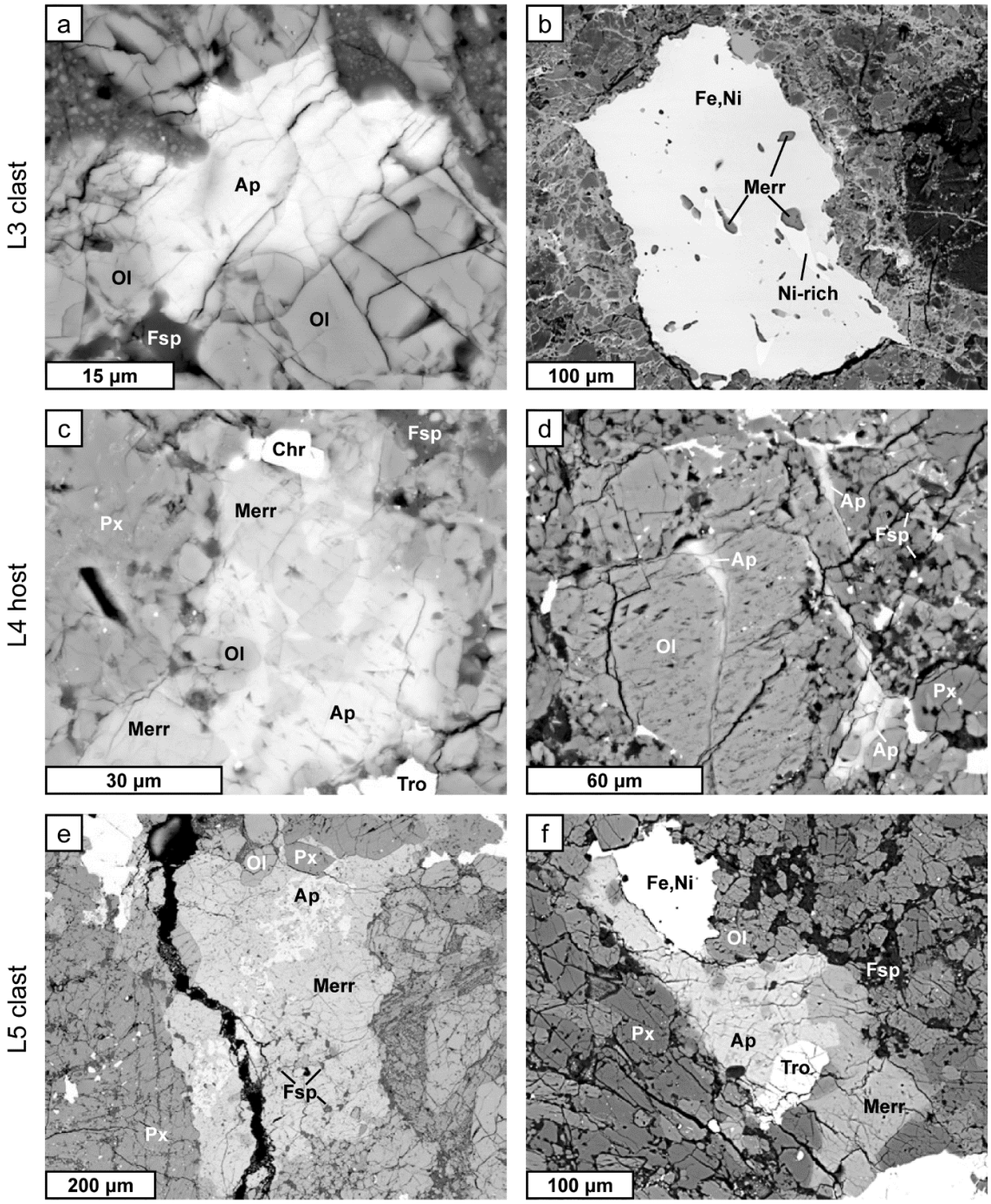

Figure 1.4. BSE images of apatite and merrillite in the L regolith breccia Kendleton. (a,b) L3 clast illustrating (a) small apatite (Ap) grain in olivine (Ol) with minor feldspar (Fsp) and (b) merrillite (Merr) inclusions in Fe,Ni metal (Fe,Ni): merrillite is surrounded by Ni-rich halos. (c,d) L4 host material illustrating (c) apatite and merrillite intergrowth with adjacent pyroxene (Px), feldspar, and troilite (Tro) and (d) vein-filling apatite in and around olivine grain. (e,f) L5 clast illustrating (e) large apatite-merrillite intergrowth with inclusions of feldspar and (f) apatite-merrillite intergrowth with adjacent Fe,Ni metal, troilite, olivine, pyroxene, and feldspar.

3.1.3. Compositions

Average apatite compositions in each chondrite are summarized in Table 1.3 and individual analyses are presented in Appendix 1. The apatite formula was calculated with 13 anions. OH values were calculated by difference assuming the X-site anions summed to unity, and were not added to the formula totals. Apatite is generally chlorine rich with average atomic Cl/F ratios of 6.6, 6.1, and 5.0 for Santa Barbara, Elenovka, and Bruderheim respectively. Kendleton's L3 and L5 clasts have similar atomic Cl/F ratios of 5.5 and 4.7 respectively. However, apatite in Kendleton's L4 host has a much higher F content (1.1 wt%) than the other chondrites (0.4-0.6 wt%), and a significantly lower atomic Cl/F ratio of 1.9. Figure 1.5 illustrates the anion distribution in apatite. The third apex of the apatite ternary (after Cl and F) is typically reserved for OH. However, Jones et al. (2014) measured apatite H_2O abundance in type 4-6 LL chondrites using SIMS

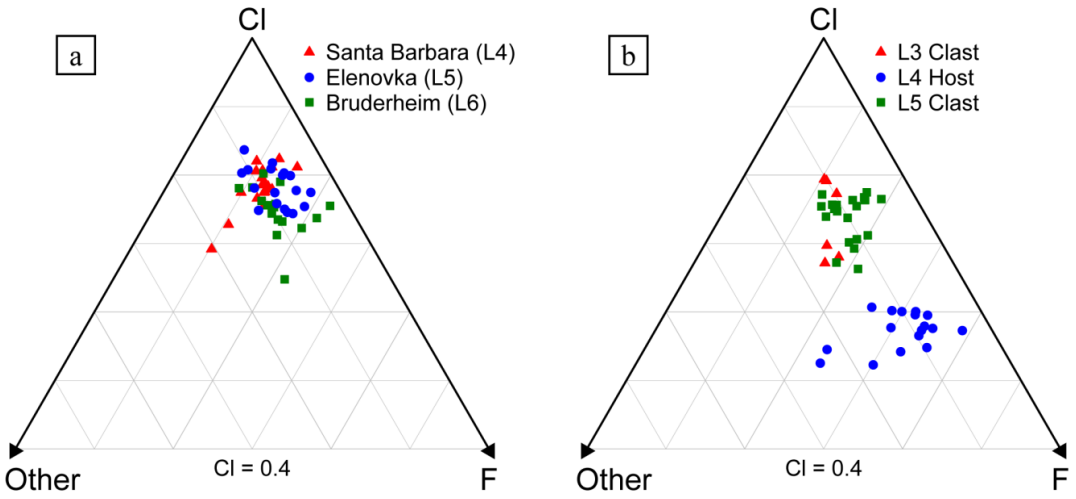

Figure 1.5. Atomic Cl-F-Other anion ternaries from EPMA analysis of apatite in (a) non-brecciated L chondrites and (b) the L regolith breccia Kendleton. Each point represents a single analysis. The ternaries are truncated at Cl = 0.4. The non-brecciated chondrites have similar Cl-rich compositions. Kendleton has lithology-dependent apatite compositions where the L4 host shows significant F-enrichment over the L3 and L5 clasts which are similar to the non-brecciated L chondrites.

Table 1.3. Average apatite compositions.

	Santa Barbara		Elenovka		Bruderheim		Kendleton					
	L4	*1σ*	L5	*1σ*	L6	*1σ*	L3 clast	*1σ*	L4 host	*1σ*	L5 clast	*1σ*
CaO	52.6	*0.6*	53.3	*0.3*	53.4	*0.3*	54.0	*1.1*	53.0	*0.7*	53.7	*0.8*
MgO	0.05	*0.06*	n.d.		0.04	*0.02*	0.04	*0.02*	0.18	*0.16*	0.02	*0.02*
FeO	0.84	*0.54*	0.24	*0.13*	0.31	*0.11*	0.26	*0.17*	0.55	*0.41*	0.27	*0.18*
Na_2O	0.37	*0.03*	0.39	*0.02*	0.37	*0.03*	0.39	*0.02*	0.38	*0.10*	0.41	*0.02*
P_2O_5	40.5	*0.5*	40.8	*0.3*	40.8	*0.2*	40.8	*0.6*	41.0	*0.4*	41.0	*0.4*
Y_2O_3	n.d.		n.d.		n.d.		n.d.		n.d.		n.d.	
Ce_2O_3	n.d.		n.d.		0.05	*0.02*	n.d.		n.d.		n.d.	
F	0.43	*0.05*	0.51	*0.13*	0.58	*0.14*	0.52	*0.12*	1.14	*0.15*	0.60	*0.10*
Cl	5.29	*0.22*	5.32	*0.19*	5.09	*0.23*	5.02	*0.33*	3.91	*0.19*	5.05	*0.19*
-O = (F+Cl)	1.38	*0.06*	1.28	*0.03*	1.39	*0.04*	1.35	*0.03*	1.36	*0.08*	1.39	*0.03*
Total	98.8	*1.0*	99.2	*0.7*	99.2	*0.4*	99.7	*1.4*	98.8	*0.7*	99.7	*0.9*
formula based on 13 anions												
Ca	4.92	*0.03*	4.95	*0.02*	4.96	*0.02*	4.99	*0.03*	4.91	*0.05*	4.96	*0.03*
Mg	0.01	*0.01*	n.d.		0.00	*0.00*	0.00	*0.00*	0.02	*0.02*	0.00	*0.00*
Fe	0.06	*0.04*	0.02	*0.01*	0.02	*0.01*	0.02	*0.01*	0.04	*0.03*	0.02	*0.01*
Na	0.06	*0.01*	0.07	*0.00*	0.06	*0.00*	0.07	*0.00*	0.06	*0.02*	0.07	*0.00*
P	2.99	*0.01*	3.00	*0.01*	2.99	*0.01*	2.98	*0.01*	3.00	*0.01*	2.99	*0.01*
Y	n.d.		n.d.		n.d.		n.d.		n.d.		n.d.	
Ce	n.d.		n.d.		0.00	*0.00*	n.d.		n.d.		n.d.	
F	0.12	*0.01*	0.14	*0.03*	0.16	*0.04*	0.14	*0.03*	0.31	*0.04*	0.16	*0.03*
Cl	0.78	*0.03*	0.78	*0.03*	0.75	*0.04*	0.73	*0.06*	0.57	*0.03*	0.74	*0.03*
Other[1]	0.10	*0.04*	0.08	*0.02*	0.09	*0.03*	0.13	*0.03*	0.12	*0.05*	0.10	*0.03*
Total	8.94	*0.04*	8.96	*0.02*	8.95	*0.03*	8.94	*0.03*	8.92	*0.06*	8.94	*0.02*
Cl/F[2]	6.64	*0.85*	6.08	*2.10*	5.03	*1.52*	5.54	*1.69*	1.87	*0.27*	4.70	*0.99*
Cl#[3]	86.8	*1.4*	84.9	*3.6*	82.5	*4.1*	83.9	*4.0*	64.8	*3.2*	82.0	*3.1*
n[4]	18		18		16		6		17		20	

n.d. = not detected (detection limits: 0.02 wt% for MgO, 0.04 wt% for Y_2O_3, 0.05 wt% for Ce_2O_3)

[1] missing component calculated by difference: Other = 1-(Cl+F), not included in the total

[2] atomic ratio

[3] Cl# = Cl/(Cl+F)x100, atomic

[4] n = number of analyses

Table 1.4. Average merrillite compositions.

	Santa Barbara		Elenovka		Bruderheim		Kendleton					
	L4	*1σ*	L5	*1σ*	L6	*1σ*	L3 clast	*1σ*	L4 host	*1σ*	L5 clast	*1σ*
CaO	46.3	*0.7*	46.5	*0.4*	46.6	*0.1*	46.4	*0.1*	46.1	*0.3*	46.6	*0.2*
MgO	3.44	*0.09*	3.47	*0.15*	3.46	*0.04*	3.50	*0.04*	3.48	*0.04*	3.58	*0.05*
FeO	1.05	*0.66*	0.56	*0.18*	0.57	*0.24*	0.45	*0.10*	0.74	*0.37*	0.58	*0.29*
Na_2O	2.57	*0.22*	2.66	*0.12*	2.67	*0.03*	2.83	*0.02*	2.63	*0.05*	2.83	*0.05*
P_2O_5	45.6	*0.6*	45.5	*0.4*	45.6	*0.2*	45.8	*0.4*	45.6	*0.2*	45.8	*0.2*
Y_2O_3	0.04	*0.02*	n.d.		0.04	*0.02*	0.04	*0.03*	n.d.		n.d.	
Ce_2O_3	n.d.		n.d.		0.05	*0.02*	n.d.		n.d.		n.d.	
Total	99.0	*0.9*	98.8	*0.6*	98.9	*0.4*	99.0	*0.6*	98.7	*0.5*	99.5	*0.3*
					formula based on 56 oxygens							
Ca	18.0	*0.1*	18.1	*0.1*	18.1	*0.1*	18.0	*0.1*	17.9	*0.1*	18.0	*0.1*
Mg	1.86	*0.05*	1.87	*0.09*	1.87	*0.02*	1.88	*0.03*	1.88	*0.02*	1.92	*0.03*
Fe	0.32	*0.20*	0.17	*0.05*	0.17	*0.07*	0.14	*0.03*	0.22	*0.11*	0.18	*0.09*
Na	1.80	*0.15*	1.87	*0.08*	1.88	*0.02*	1.98	*0.01*	1.85	*0.04*	1.98	*0.03*
P	14.0	*0.1*	14.0	*0.0*	14.0	*0.0*	14.0	*0.0*	14.0	*0.0*	14.0	*0.0*
Y	0.01	*0.00*	n.d.		0.01	*0.00*	0.01	*0.01*	n.d.		n.d.	
Ce	n.d.		n.d.		0.01	*0.00*	n.d.		n.d.		n.d.	
Total	35.9	*0.1*	36.0	*0.1*	36.0	*0.0*	36.0	*0.0*	35.9	*0.1*	36.0	*0.1*
Mg#[1]	86.0	*7.4*	91.7	*2.2*	91.6	*3.1*	93.3	*1.4*	89.6	*4.6*	91.8	*3.5*
n[2]	22		12		15		6		14		23	

n.d. = not detected (detection limits: 0.04 wt% for Y_2O_3, 0.05 wt% for Ce_2O_3)

[1] Mg# = Mg/(Mg+Fe)x100, atomic

[2] n = number of analyses

analysis and found the values to be extremely low, less than 100 ppm. The balance of the X anion site remains unidentified and so we label the third apex "other."

Apatite compositions in Santa Barbara, Elenovka, and Bruderheim show considerable overlap with a mean atomic Cl/F ratio of 5.9 for all the analyses in these three meteorites. Although there is a slight correlation between the mean Cl/F ratio and petrologic type, it is not clear that this is due to changes that occur during metamorphism. Applying a t-test to the three mean Cl/F ratios only reveals a significant difference between Santa Barbara and Bruderheim. Additionally, there is no evidence for progressive compositional equilibration with petrologic type.

Average compositions of merrillite in each chondrite are summarized in Table 1.4 and Figure 1.6 and individual analyses are presented in Appendix 1: the merrillite formula is calculated assuming 56 oxygens. The resulting formulae are close to ideal with little deviation. Santa Barbara has an average Mg# (Mg/(Mg+Fe)x100) of 85 and a much larger spread in values than Elenovka or Bruderheim which both have an average Mg# of 92. The average Mg# of the L3 clast is 93 and with little spread, although this could be due to the small number of analyses. Similar to Santa Barbara, Kendleton's L4 host has a significant spread and Mg# of 90. Like the other high petrologic types Elenovka and Bruderheim, the average Mg# of Kendleton's L5 clast is 92 with a small spread. Figure 1.6 also shows merrillite distributions for H (Jones and McCubbin 2012) and LL (Jones et al. 2014) chondrites of petrologic types 4, 5 and 6 for comparison with the L data, discussed below.

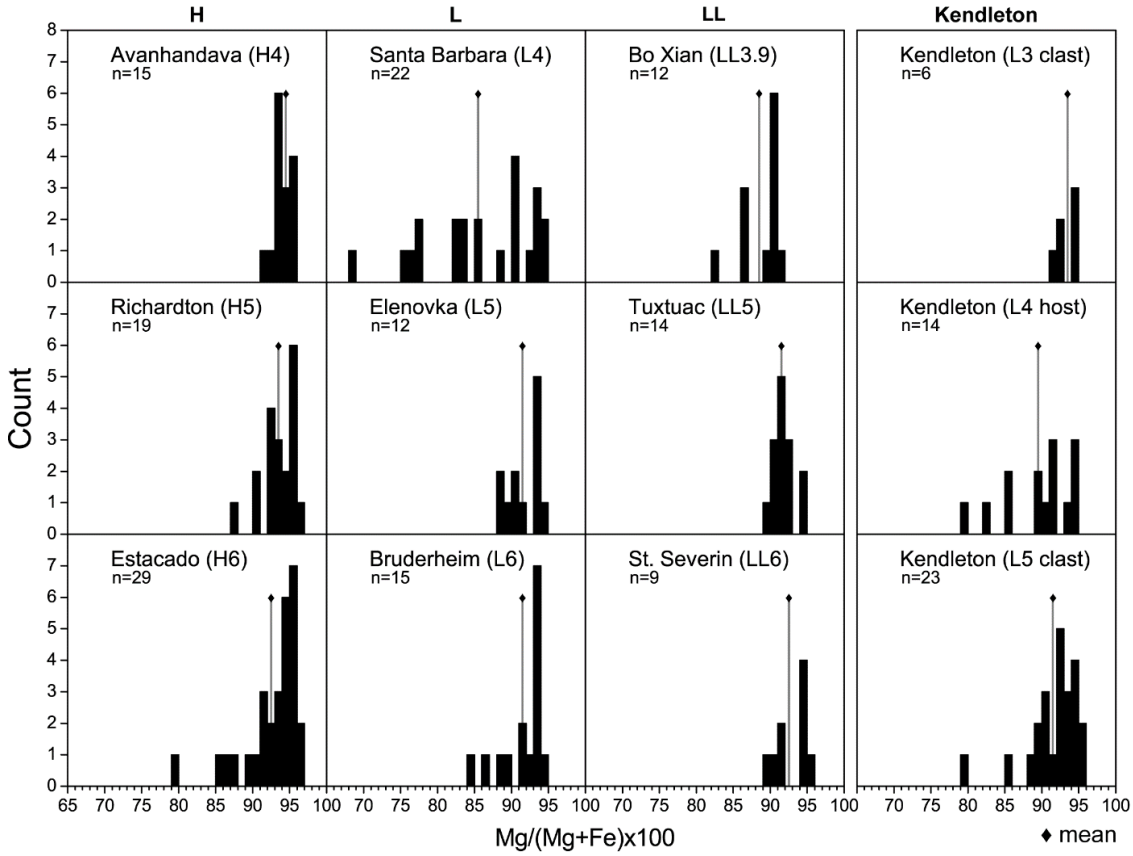

Figure 1.6. Histograms of atomic Mg# (Mg/(Mg+Fe)x100) from individual EPMA analyses of merrillite in H, L, LL OCs and the L regolith breccia Kendleton. Mg# is binned into 1% bins and the diamond and thin line show the sample mean.

3.2. Feldspar

In this study, we focused on feldspar within chondrules, which is largely formed from the devitrification of chondrule mesostasis and should share a similar history of development throughout the chondrite. We do not consider feldspar found within the chondrite matrix, because limiting our observations to chondrule-hosted feldspar allows for a direct comparison with the similar study conducted on H and LL chondrites by Kovach and Jones (2010).

3.2.1. Petrography

Santa Barbara (L4)

Feldspar in Santa Barbara chondrules is typically present interstitial to the olivine and pyroxene phenocrysts. It has an irregular, space-filling morphology and appears to represent recrystallized mesostasis (Fig. 1.7a). Most feldspar grains are <20 μm in size although some range up to 100 μm. The majority of the feldspar grains have inclusions of micron-sized clinopyroxene and abundant micron and submicron inclusions of oxides (typically chromite) and sulfides (Fig. 1.7b). Micropores are also abundant. Anorthitic feldspar is commonly observed being replaced by albitic feldspar, particularly around grain boundaries (Fig. 1.7b). In these instances, the albite is smooth and largely inclusion free while the anorthite contains numerous oxides and micropores. In other chondrules, all feldspar is albitic. Regions of smooth albite occasionally contain fine-scale K-feldspar exsolution lamellae (Fig. 1.7d).

Kramer Creek (L4)

Like L4 Santa Barbara, feldspar in Kramer Creek is typically irregular in shape and intergrown with elongate grains of pyroxene and olivine. Micron-sized oxides are present in many feldspar grains but are not as abundant as in Santa Barbara. Porosity is common in both anorthitic and albitic feldspar. Anorthitic feldspar is commonly replaced by albite along grain boundaries (Fig. 1.7f) in a similar manner to, but less extensively than, Santa Barbara (Fig. 1.7b). Generally, feldspar grains are small (<30 μm), but they can range up to 100 μm. Terrestrial weathering does not appear to have affected the feldspar texture.

Elenovka (L5)

In Elenovka, smooth, inclusion-free albitic feldspar is common. Grain sizes vary within chondrules but are generally larger than Santa Barbara and Kramer Creek, >30 μm with some >100 μm. Individual feldspar grains vary from subhedral to irregular and are space-filling in morphology (Fig. 1.7g). Unlike in Santa Barbara and Kramer Creek, we did not observe feldspar grains that are porous in texture nor did they contain many fine-grained oxide inclusions. In a few chondrules, feldspar is included within irregular grains of pyroxene, where it is assumed to be recrystallized mesostasis. Some grains show minor exsolution of K-feldspar in albitic host grains (Fig. 1.7h).

Roy 1933 (L5)

Feldspar in Roy 1933 varies in size but is generally similar to Elenovka. Individual feldspar grain textures vary from anhedral to subhedral and many have irregular morphologies. A few feldspar grains are porous in texture, or contain fine-grained oxide/sulfide inclusions. In many chondrules, feldspar is intergrown with elongate grains of olivine, and is assumed to be recrystallized mesostasis. Like L5 Elenovka (Fig. 1.7h), rare exsolution of K-feldspar is present in host grains of albitic feldspar (Fig. 1.7j).

Bruderheim (L6)

Bruderheim contains very few well-defined relict chondrules, and chondrule/matrix boundaries are not very distinct. However, it was possible to identify individual feldspar grains in relict chondrules (Fig. 1.7k) with a range of sizes slightly greater than in the type 5 chondrites. Most are >30 μm and they can be larger than 150 μm. Some grains contain a few fine-grained chromite and sulfide inclusions.

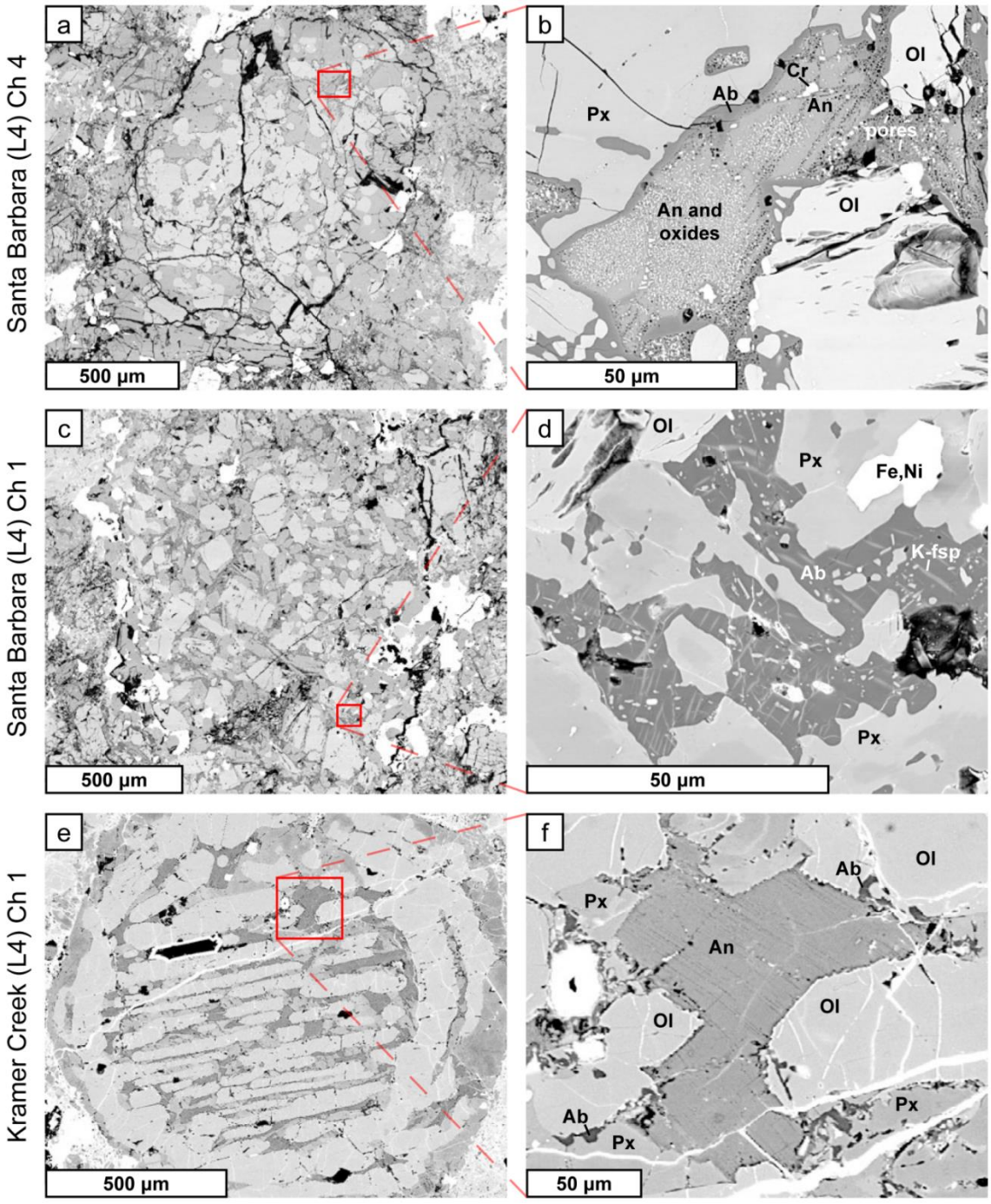

Figure 1.7. BSE images of occurrences of feldspar within relict chondrules in L chondrites. (a-d) Santa Barbara (L4) illustrating (a) POP chondrule with (b) anorthitic plagioclase (An) containing submicron oxides and micropores, surrounded by albitic (Ab) rims; (c) POP chondrule with (d) albitic plagioclase showing K-feldspar exsolution. (e,f) Kramer Creek (L4) illustrating (e) BO chondrule containing (f) anorthitic plagioclase with dissolution lamellae and minor albite along the rims.

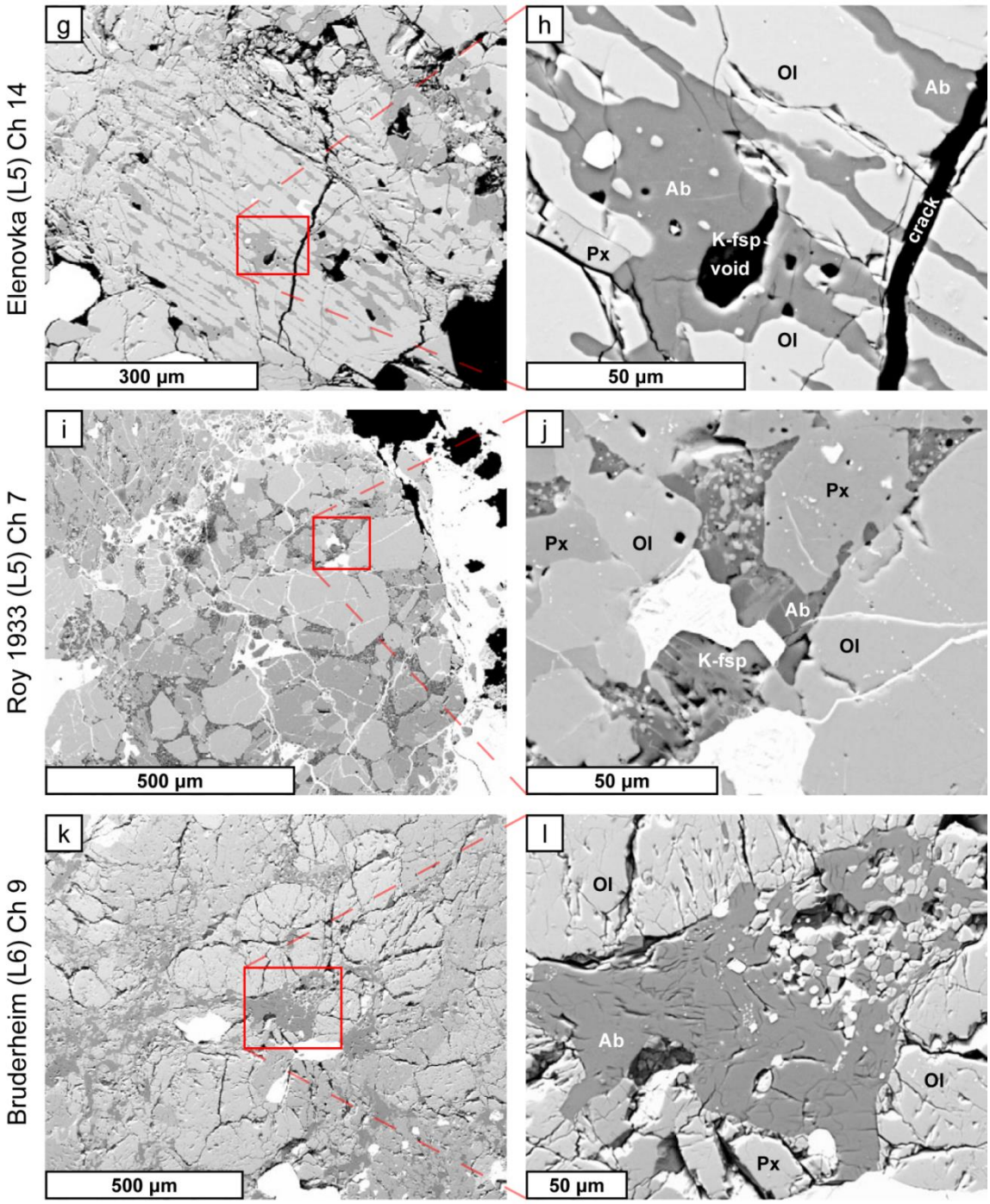

Figure 1.7 *(Continued)*. BSE images of occurrences of feldspar within relict chondrules in L chondrites. (g,h) Elenovka (L5) illustrating (g) relict BO chondrule containing (h) albitic plagioclase with minor K-feldspar exsolution that occurs both within the grain and around the rim of a void. (i,j) Roy 1933 (L5) illustrating (i) relict POP chondrule with (j) albitic plagioclase and K-feldspar exsolution. (k,l) Bruderheim (L6) illustrating (k) relict POP chondrule with (l) typical uniform albitic plagioclase.

Individual grain textures vary from anhedral to subhedral, and include many feldspar grains with irregular morphologies. Similar to type 5, feldspar grains are intergrown with elongate grains of pyroxene and irregular grains of olivine, but in Bruderheim, the grains in these areas are larger and more abundant (Fig. 1.7l). We observed no K-feldspar.

3.2.2. Compositions

Average feldspar compositions are summarized in Table 1.5 and individual point analyses are tabulated in Appendix 1 and illustrated on feldspar ternary diagrams in Fig. 1.8 and tabulated in Appendix 1. The L4 chondrites Santa Barbara and Kramer Creek (Fig. 1.8a,b) show a wide range of plagioclase compositions, An_{82}-An_4 and An_{88}-An_2 respectively. Each chondrule typically has a limited range of compositions, although those with albitization reactions (e.g., Santa Barbara chondrule 4, shown in Fig. 1.7b) show both An-rich and Ab-rich components. Kramer Creek has the widest range of plagioclase compositions and the lowest Or component which does not exceed Or_3. Santa Barbara feldspar has a larger range of K contents, up to Or_{23}. High K contents are measured in grains that show fine-scale K-feldspar exsolution, and represent analyses that overlap albitic and K-feldspar compositions within those grains.

The L5 chondrites Elenovka and Roy 1933 show a much more restricted range in plagioclase compositions, An_{12}-An_8 and An_{17}-An_4 respectively, compared to the L4 chondrites. Both have grains that show K-feldspar exsolution, although only the grains in Roy 1933 chondrule 7 (Fig. 1.7j) are large enough for individual microprobe analysis: these have Or content up to Or_{65}. The highest Or content measured in Elenovka was only Or_{13} which represents the bulk composition of the grain, due to the fine-scale nature of

Table 1.5. Average feldspar compositions.

	Santa Barbara		Kramer Creek		Elenovka		Roy 1933		Bruderheim	
	L4	*1σ*	L4	*1σ*	L5	*1σ*	L5	*1σ*	L6	*1σ*
SiO_2	62.0	*6.5*	54.2	*9.4*	66.2	0.4	65.5	*1.0*	66.0	*0.5*
Al_2O_3	23.3	*4.1*	28.6	*6.6*	21.2	0.2	21.0	*0.6*	21.3	*0.3*
Cr_2O_3	0.30	*0.63*	0.21	*0.27*	n.d.		n.d.		n.d.	
FeO	1.03	*0.72*	0.55	*0.30*	0.46	0.14	0.42	*0.26*	0.52	*0.16*
MgO	0.16	*0.24*	0.04	*0.03*	0.04	0.16	0.05	*0.08*	n.d.	
CaO	4.38	*4.79*	10.7	*7.5*	2.15	0.14	2.09	*0.61*	2.19	*0.10*
Na_2O	8.75	*2.66*	5.48	*4.32*	10.00	0.16	9.58	*1.50*	9.80	*0.36*
K_2O	1.03	*0.99*	0.14	*0.15*	1.04	0.20	1.38	*2.32*	1.00	*0.16*
Total	100.9	*0.9*	99.9	*0.5*	101.1	0.6	100.1	*0.7*	100.9	*0.6*
				formula based on 8 oxygens						
Si	2.74	*0.25*	2.45	*0.37*	2.90	*0.01*	2.89	*0.03*	2.89	*0.01*
Al	1.22	*0.24*	1.53	*0.38*	1.09	*0.01*	1.10	*0.03*	1.10	*0.01*
Cr	0.01	*0.02*	0.01	*0.01*	n.d.		n.d.		n.d.	
Fe	0.04	*0.03*	0.02	*0.01*	0.02	*0.01*	0.02	*0.01*	0.02	*0.01*
Mg	0.01	*0.02*	0.00	*0.00*	0.00	*0.01*	0.00	*0.01*	n.d.	
Ca	0.21	*0.24*	0.53	*0.37*	0.10	*0.01*	0.10	*0.03*	0.10	*0.00*
Na	0.75	*0.22*	0.47	*0.37*	0.85	*0.01*	0.82	*0.13*	0.83	*0.03*
K	0.06	*0.06*	0.01	*0.01*	0.06	*0.01*	0.08	*0.14*	0.06	*0.01*
Total	5.04	*0.02*	5.02	*0.01*	5.01	*0.01*	5.01	*0.01*	5.00	*0.02*
An	20.9	*23.6*	52.2	*37.0*	10.0	*0.6*	9.9	*2.9*	10.4	*0.6*
Ab	73.4	*21.5*	47.0	*36.2*	84.2	*1.2*	82.1	*12.5*	84.0	*1.1*
Or	5.7	*5.5*	0.8	*0.8*	5.8	*1.1*	7.9	*13.6*	5.6	*1.0*
n[1]	43		41		81		38		25	

n.d. = not detected (detection limits: 0.07 wt% for Cr_2O_3, 0.02 wt% for MgO)

[1] n = number of analyses

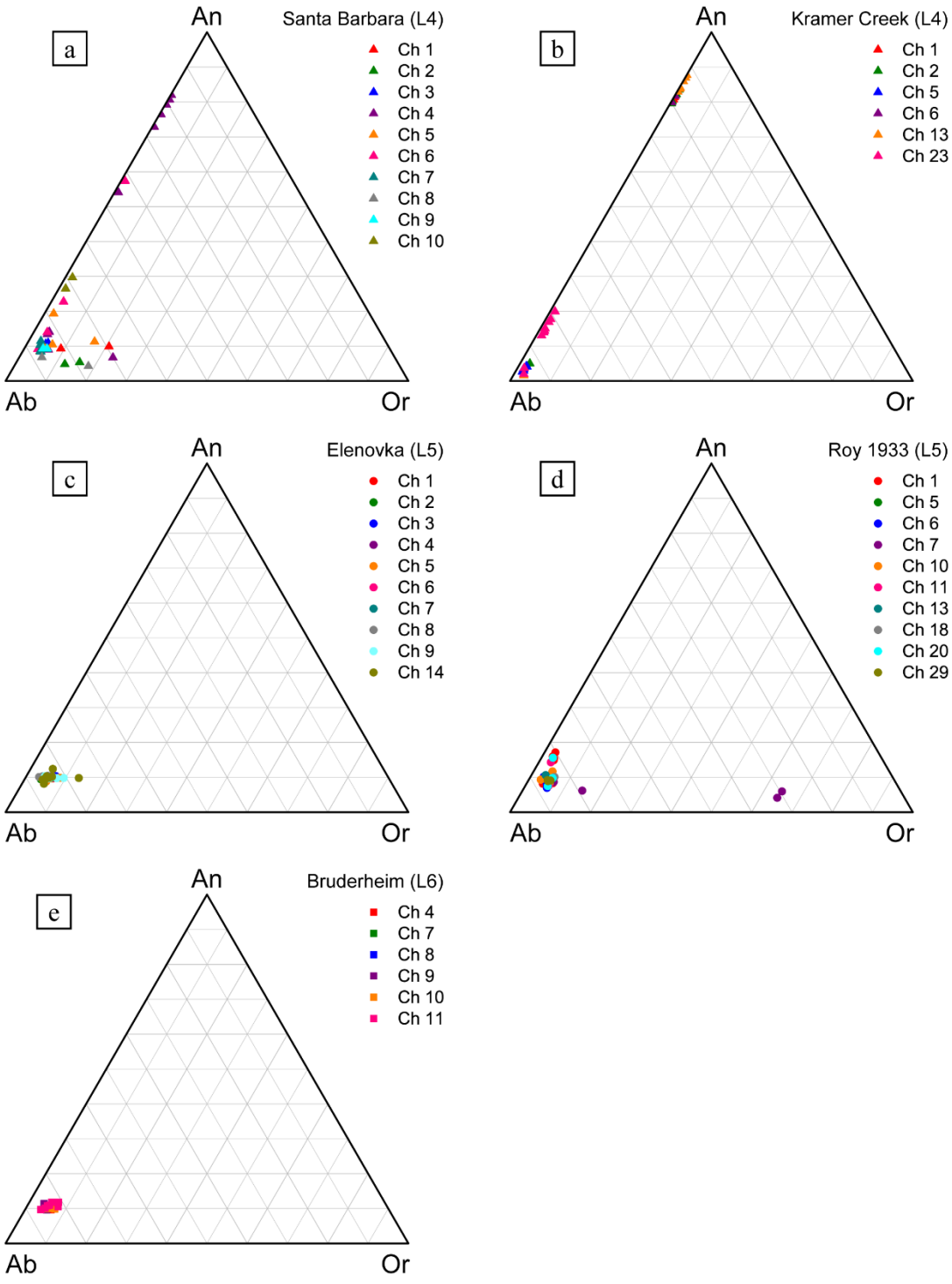

Figure 1.8. Feldspar compositions in L ordinary chondrites from EPMA analysis: (a) Santa Barbara (L4), (b) Kramer Creek (L4), Elenovka (L5), (d) Roy 1033 (L5), and (e) Bruderheim (L6). Each point represents a single analysis and each color represents a single chondrule.

the exsolution lamellae. Feldspar in the L6 Bruderheim is fully equilibrated with an average composition of $An_{10}Ab_{84}Or_6$ and very little variation.

4. Discussion

Thermal metamorphism is one of the most important processes that affected the evolution of ordinary chondritic asteroids. Although there is some evidence for metasomatizing fluids on OC parent bodies, the extent of fluid interactions is poorly described. Because the presence of fluids can strongly affect the metamorphic environment, characterizing these fluids is essential for a complete understanding of chondrite metamorphism. In addition, characterizing volatile species present within chondritic asteroids provides important information about the volatile composition of the solar nebula from which the Earth and other terrestrial planets were formed.

Phosphates and feldspar are secondary minerals that form in response to thermal metamorphism of ordinary chondrites. These minerals can be used as tools for understanding the composition of fluids that are present during their formation and evolution. Specifically, the X anion site in apatite records information about the relative abundance of the halogens Cl and F in addition to OH, an indicator of the presence of water. Feldspar contains information about the relative abundance of the alkali elements Na and K, which are readily transported in aqueous fluids, and can contain microtextures that indicate the presence of aqueous fluids.

In the discussion below, we compare our study on phosphates and feldspar in L chondrites to previous studies on these minerals in H and LL chondrites (Kovach and Jones 2010; Jones and McCubbin 2012; Jones et al. 2014). We examine the similarities and differences in secondary mineralogy between the three ordinary chondrite groups to

further understand the metamorphic history of each group. We compare the phosphate mineralogy of brecciated and non-brecciated chondrites which gives insight into the mineralogical effects imparted by impact processing. We discuss the overall mechanisms and timing for the formation of secondary minerals and the evidence for the presence of fluids during metamorphism. Finally, we use apatite to estimate the bulk halogen abundances in ordinary chondrites and compare these to measured bulk values from the literature as a means to assess uncertainties on halogen abundances.

4.1. Comparison of secondary phosphates and feldspar in H, L, and LL ordinary chondrites

Since phosphate and feldspar are both secondary phases, chemical and textural changes in these minerals through the metamorphic sequence inform us about the process and conditions of equilibration. A comparison of the different OC groups provides insight into the processes common to all three OC parent bodies as well as the individual characteristics of each parent body.

4.1.1. Phosphates

There are many similarities in phosphate mineralogy between the L chondrites described above and the H and LL chondrites described by Jones and McCubbin (2012) and Jones et al. (2014). We can make the following generalizations, although the observations have been made on a limited number of chondrites (3 LL chondrites, 3 L chondrites, 4 H chondrites). Phosphates in all three ordinary chondrite groups show a small increase in phosphate abundance with increasing petrologic type, particularly between type 4 (0.4% volume) and types 5, 6 (0.5% volume), when averaged across phosphate abundances of individual H, L and LL chondrites. Although this increase is

close to the error of 0.1% volume, it is consistent across all OC groups and appears to be meaningful. Maximum grain sizes range between 100 μm and 400 μm for both apatite and merrillite, and merrillite is typically larger than apatite. Maximum grain sizes in L and LL chondrites generally increase with increasing petrologic type, but H chondrite phosphates are more uniform in maximum grain size across all petrologic types. Overall, phosphate minerals in all three OC groups appear to have developed under similar conditions.

Because P is originally hosted in metal in unequilibrated chondrites (e.g., Zanda et al. 1994), we might expect to observe an increase in abundance of phosphate minerals, consistent with increasing metal content from LL to L to H chondrites. However, phosphate abundance does not appear to show any correlation with metal content: our mean total phosphate abundances (% volume) in the different groups are 0.47 for H, 0.54 for L, 0.46 for LL. In fact, this observation is consistent with bulk chondrite P abundances: while bulk chondrites show a 540% increase in metal content from LL to H chondrites (2.5 wt% to 16 wt%: Lodders and Fegley 1998), the corresponding bulk P contents show a much smaller increase of 32% (910 ppm to 1200 ppm: Lodders and Fegley 1998). This relatively small difference in bulk P abundances between the different OC groups means that in our studies it is likely that any systematic differences between the groups are below the precision of our abundance calculation method. The lack of correlation between phosphate (or bulk P) abundance and metal abundance is probably attributable to the fact that chondrule mesostasis is also an important source of P for formation of phosphates in ordinary chondrites (Jones et al. 2014).

The petrological occurrences of phosphate minerals are also similar among the three OC groups. Individual grains of apatite and merrillite occur throughout the chondrite matrix of all studied unbrecciated H and L (Fig. 1.1a-c) chondrites as well as types 5 and 6 LL chondrites. Individual grains of apatite are rare in the L/LL4 Bjurböle and absent from the LL3.9 Bo Xian, but apatite is commonly present in association with merrillite in both chondrites. Apatite/merrillite intergrowth and reaction textures were reported for LL3.9, L/LL4, LL6, H4, and H5 chondrites but we did not observe similar textures in the unbrecciated L chondrites, with the exception of a single intergrowth grain in the L4 Santa Barbara (Fig. 1.2b). Jones et al. (2014) argued that these textures are the result of incomplete coupled dissolution-reprecipitation reactions, which suggests that in low petrologic type L chondrites, any similar reactions that may have occurred have gone to completion. This would indicate that halogen-bearing fluids were more common in low petrologic type L chondrites than in H or LL. In general, apatite/merrillite reactions are less common in higher petrologic types. In an onion shell model, the higher petrologic type OCs are sourced deeper, and thus may have been exposed to a larger volume of halogen-bearing fluid, as well as being at a higher temperature, allowing for the replacement reaction to go to completion.

In all three groups, apatite and merrillite typically have no preferred silicate association but they are commonly associated with Fe,Ni metals, sulfides, and chromite (Fig. 1.2c, 1.3a-c,e-f) and are found adjacent to voids (Fig. 1.2c-e, 1.3a,f). Both minerals occasionally contain silicate inclusions, typically olivine and feldspar but rarely pyroxene (Fig. 1.2e-f, 1.3a,c-d). In LL3.9 and L/LL4 chondrites, merrillite is observed as small, rounded inclusions in Fe,Ni metal grains but such inclusions were not observed in

unbrecciated type 4 L or H chondrites. Since these inclusions most likely migrate out of the metal during textural equilibration in higher petrologic types (5 and 6), our interpretation of their absence in type 4 L and H chondrites is that the type 4 chondrites we studied experienced higher temperatures than the LL3.9 and L/LL4 chondrites from Jones et al. (2014).

In the L6 chondrite, Bruderheim we observed merrillite in association with some chromite-plagioclase assemblages (Fig. 1.3f). There is a similar association of apatite and merrillite with chromite-plagioclase assemblages in the LL6 Saint Séverin (Jones et al. 2014). Chromite-plagioclase assemblages are thought to be indicators of shock (Rubin 2003) and their presence is consistent with the moderately high shock stage assigned to Bruderheim (S4; Stöffler et al. 1991) and the complex shock history of Saint Séverin (Ashworth et al. 1977; Ashworth 1980; Leroux et al. 1996). Jones et al. (2014) proposed that since phosphates are readily incorporated into partial chondritic melts (Feldstein et al. 2001), impact-generated melts include a phosphate component which then crystallized back out of the melt as an igneous mineral. In the example in Bruderheim, there is no apparent compositional difference between merrillite associated with the chromite-plagioclase assemblage and other merrillite in the rock: hence, equilibration of the whole rock likely occurred after formation of the chromite-plagioclase assemblage. However, if shock does play a role in phosphate formation, Pb-Pb ages based on apatite may not only record metamorphism, but also post-metamorphic shock events (Jones et al. 2014). The fracturing noted in the phosphates, particularly in apatite (Fig. 1.2a-d), may also be due to the effects of shock. Alternatively, fractures could be related to initial growth of the phosphate grains as fine-grained aggregates. The aggregates then experienced textural

equilibration during thermal metamorphism because there is a decrease in the abundance of fractures with increasing petrologic type.

In all three OC groups, apatite compositions are similar in that they are all Cl-rich and all show a similar degree of compositional heterogeneity. However, each group has a distinct field on the apatite anion ternary. Figure 1.9 compares apatite anion compositions between the three ordinary chondrite groups: points represent single analyses and fields enclose all analyses reported for all samples within the group. In general, there is a trend of increasing "other" component (0.05, 0.09, and 0.17 mean atom % anion) from H to L to LL chondrites, although L chondrite apatites overlap considerably with both H and LL fields. Figure 1.10 shows relative halogen compositions plotted as Cl/(Cl+F)x100 (hereafter Cl#) for each chondrite, with error bars representing 1σ and group averages signified by red vertical lines. Average apatite compositions for H and L chondrites are similar (Cl# = 84.9 and 84.7, atomic Cl/F = 6.5 and 5.9 respectively) although there is much more scatter for individual chondrites in the H group compared with the L chondrites. LL chondrites are more F rich with average Cl# = 76.1 and atomic Cl/F = 3.2. The single L/LL chondrite Bjurböle has an average apatite composition (Cl# = 83.9, atomic Cl/F = 5.6) closer to L and H chondrites than LL chondrites.

Slight differences in Cl/F ratios among individual meteorites within each chondrite group appear to reflect differences in fluid chemistry. These differences are independent of petrologic type in H and LL chondrites but L chondrites do show a slight trend towards decreasing atomic Cl/F with increasing petrologic type. It is not apparent whether the L trend is process-related or purely coincidental. Given that F is more volatile than Cl, and if Cl/F ratios are controlled by temperature, we would expect a trend

toward more Cl-rich compositions with increasing degree of metamorphism and not the observed trend toward more F-rich compositions. In addition, because the L trend is not reproduced in the H or LL chondrites, it is more likely that differences in fluid chemistry between the petrologic types are due to the local environments rather than metamorphic history. Overall, the similarity in apatite compositions between the three groups implies the same process is forming apatite on all three parent bodies, but with minor differences in the fluid chemistry that controls apatite composition, as discussed in more detail below.

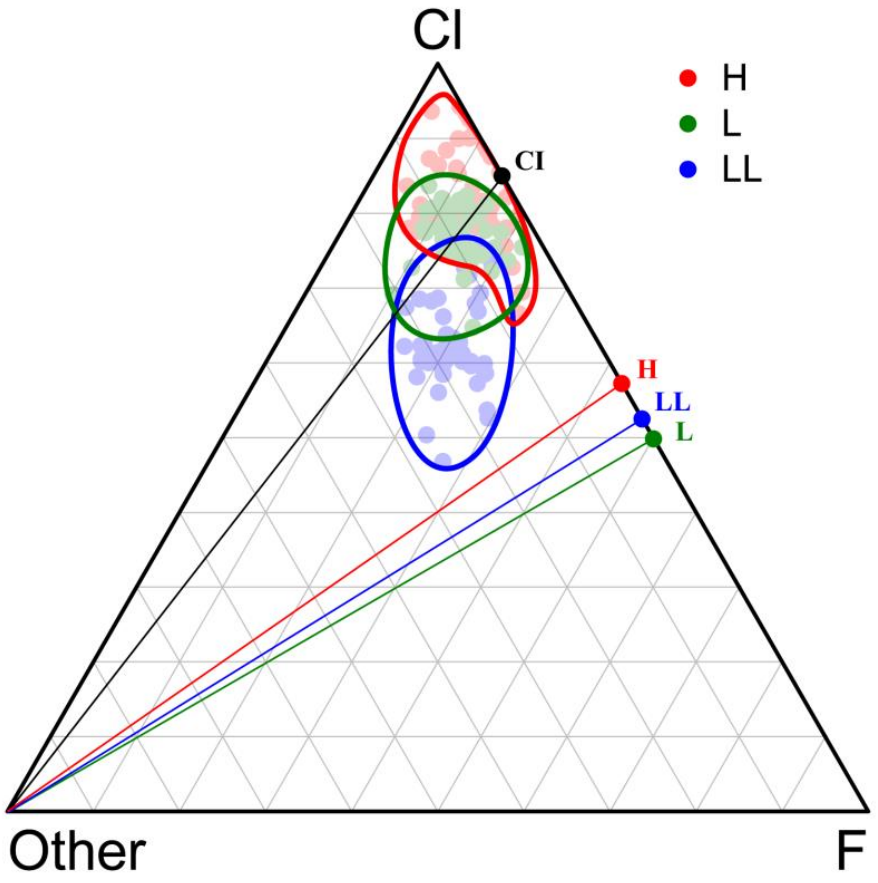

Figure 1.9. Apatite atomic Cl-F-Other anion ternary diagram, for H (red), L (green), and LL (blue) OCs. Each point represents a single analysis and each field encloses all the analyses in that group. Bulk chondrite Cl/F ratios from Wasson and Kallemeyn (1988) for OCs and CI chondrites are illustrated as tie-lines from the Cl-F ternary join to the Other apex.

Merrillite compositions are also similar among the three OC groups. Figure 1.6 shows histograms of merrillite Mg# for H (Jones and McCubbin 2012), L (this work), and LL (Jones et al. 2014) chondrites as well as the brecciated chondrite, Kendleton. All merrillite is magnesian with mean Mg# between 86 and 94 for all groups and petrologic types. H chondrites have a slightly higher average Mg# (93) than L (90) and LL (91) chondrites which is consistent with the more reduced nature, and higher Mg# in olivine and pyroxene, for H chondrites. The average Mg# for merrillite is higher than the average Mg# for olivine and low-Ca pyroxene (olivine Mg#: ~82, 76, 71 for H, L, LL; low-Ca pyroxene Mg#: ~84, 80, 76 for H, L, LL; Brearley and Jones 1998).

Within the L and LL chondrites, merrillite Mg# is lower in type 4 than in types 5 and 6 (Fig. 1.6). In addition, the L chondrites show an increase in degree of compositional equilibration with increasing petrologic type (Fig. 1.6), a trend that is possibly present but not as clear in the data for LL chondrites. In contrast, H chondrite merrillite has approximately the same Mg# through the petrologic sequence and no trend of increasing compositional equilibration with petrologic type. The differences in merrillite equilibration between the H chondrites and L and LL chondrites are also reflected in the feldspar equilibration history, as discussed below.

4.1.2. Feldspar

Feldspar within chondrules in L chondrites shows textural and compositional changes with increasing petrologic type that we interpret as progressive equilibration in response to metamorphism. Average grain size increases from types 4 to 6. Fine-grained oxide inclusions and micropores are common in anorthitic and albitic plagioclase in type 4, rare in type 5, and absent in type 6. Albite replaces anorthite along grain boundaries in

petrologic type 4. Fine-scale K-feldspar exsolution from albitic plagioclase is present in types 4 and 5 but absent in type 6. There is a wide range of plagioclase compositions, An_{88}-An_{2}, in the L4 chondrites Santa Barbara and Kramer Creek and we measured K content up to Or_{23} in Santa Barbara. Plagioclase compositions are considerably more restricted in the L5 chondrites Elenovka and Roy 1933 with a maximum range of An_{17}-An_{4} but K contents range up to Or_{65} for coarse K-feldspar regions in Roy 1933. Type 6 Bruderheim is fully equilibrated with a plagioclase composition of An_{10} and a K-feldspar content of Or_{6}.

Characteristics of feldspar in types 4-6 L chondrites described above are very similar to feldspar within chondrules of type 4-6 LL chondrites reported by Kovach and Jones (2010). In the LLs, grain sizes increase from types 4 to 6 and albitic rims around anorthite cores are present in type 4 but absent in types 5 and 6. The fine-grained oxides (Fig. 1.7b) and micropores (Fig. 1.7b,d,f) we observe in L chondrite feldspar were not reported in the LL chondrites. However, the Kovach and Jones (2010) study focused on clear areas of plagioclase, and areas with complex microtextures were avoided. K-feldspar exsolution from albite was only reported for type 5 LL chondrites. Type 6 LL chondrites contain largely uniform regions of albitic plagioclase.

Feldspar compositions in L and LL chondrites are also similar: LL chondrites show compositional progressive equilibration with increasing petrologic type, from a wide range in L/LL4 Bjurböle (An_{85} to An_{5}), to a much more restricted range in LL5 and LL6 (~An_{10}) (Kovach and Jones 2010). The LL6 Saint Séverin has a slightly larger compositional variation in An and Or than the L6 Bruderheim. Kovach and Jones (2010) proposed that the relative heterogeneity of feldspar compositions in Saint Séverin

compared to other type 6 chondrites was due to elemental redistribution during pre- and sin-metamorphic shock (Ashworth et al. 1977; Ashworth 1980; Leroux et al. 1996) and incomplete annealing during metamorphism (Rubin 2004).

In contrast to L and LL chondrites, feldspar in petrologic type 4-6 H chondrites has a single albitic plagioclase composition, ~$An_{12}Or_6$ (Kovach and Jones 2010) although Rubin (1992) showed that variable plagioclase compositions (up to An_{28}) can occur in equilibrated H chondrites due to the effects of shock. Grain size does increase with increasing petrologic type in the H chondrites but anorthitic plagioclase was not observed by Kovach and Jones (2010). K-feldspar exsolution also was not observed by Kovach and Jones (2010), but we have since shown that it is present (Lewis et al. 2016). Since the difference between petrologic types 3 and 4 is based on the degree of olivine equilibration, we would assume that type 4 chondrites from the three groups reached similar peak temperatures for similar durations. Hence, there must be a factor other than peak temperature that controls the differences in feldspar properties between H chondrites and L, LL chondrites. Below we discuss the possibility that the differences are caused by a difference in timing of fluid activity, fluid composition, and/or fluid abundances during the early stages of metamorphism.

4.2. Phosphates in regolith breccias

In contrast to unbrecciated chondrites of all ordinary chondrite groups, the regolith breccia Kendleton has a heterogeneous, lithology-dependent distribution of apatite compositions (Fig. 1.5b, 1.10, Table 1.3). The L3 and L5 clasts have apatite compositions similar to each other (Cl# = 83.9 and 82.0, atomic Cl/F = 4.7 and 4.5, respectively) and similar to those of the unbrecciated L chondrites (Cl# = 84.7, Cl/F =

5.9), but apatite in the L4 host material is significantly more F-rich (Cl# = 64.8, Cl/F = 1.9, Fig. 1.10). In contrast, merrillite compositions in Kendleton are fairly homogeneous and show no significant differences among the three lithologies: they are similar to unbrecciated L chondrites (Fig. 1.6).

Texturally, the Kendleton L3 clast contains small, round merrillite inclusions within Fe,Ni metal, similar to LL3.9 and L/LL4 chondrites (Jones et al. 2014). The L3 clast has a lower phosphate abundance than the other L chondrites but this measurement may not be very accurate due to the small size of the clast (Fig. 1.1d, Table 1.2). The L4 host material contains roughly the same phosphate abundance as the unbrecciated L4 Santa Barbara, but it has a high proportion of merrillite (97%) compared to approximately equal amounts of apatite and merrillite in Santa Barbara (Fig. 1.1e, Table 1.2). The L5 clast contains roughly equivalent abundances and proportions of phosphates to the unbrecciated L5 Elenovka (Table 1.2). Apatite-merrillite intergrowth textures are common in Kendleton's L4 host (Fig. 1.4c) and L5 clast (Fig. 1.4e-f) but we did not observe these textures in unbrecciated type 4 and 5 L chondrites with the exception of the single grain in Santa Barbara (Fig. 1.2b). However, these intergrowth textures are present in LL3.9, L/LL4, LL6, H4, and H5 chondrites studied by Jones et al. (2014) and Jones and McCubbin (2012).

A difference in apatite compositions between lithologies is also observed in the H regolith breccia, Zag (Jones et al. 2011). Apatite in the type 4 lithology and one type 6 clast of Zag have Cl-rich compositions similar to unbrecciated H chondrites, but apatite in a second type 6 lithology is considerably more variable and extends from Cl-rich to F-rich compositions.

Based on the observations from these two meteorites, it appears that relatively F-rich apatite might be a common feature of surficial material on ordinary chondritic asteroids. There are several possible explanations for how this could occur. For Kendleton, we need a mechanism that results in lower abundance of apatite relative to merrillite in the L4 lithology, along with a more F-rich apatite composition. Since apatite in all the unbrecciated chondrites is Cl-rich, we assume that we need a process that results in F enrichment in the L4 lithology, rather than F depletion in the other material. Fluorine could have been introduced during impact processing on the asteroid surface. Impact melt veins are common in Kendleton (e.g., Fig. 1.1d) and the release of volatiles, including the particularly volatile F, through the regolith from impact melt veins and pools could have reacted with existing Cl-rich apatite in order to produce the more F-rich compositions we observe.

It is also possible that F could have an exogenous origin, from a volatile-rich impactor. For Zag and the H5 breccia Monahans, evidence for an external volatile source comes from halite and sylvite that have been shown to be of non-OC origin (Yurimoto et al. 2010). The presence of carbonaceous chondrite material within Zag is also consistent with a volatile-rich impactor (Zolensky et al. 2003). However, the source of the F in such a volatile-rich impactor is difficult to ascertain. For a carbonaceous impactor, the host phase for F in carbonaceous chondrites is not known (Brearley and Jones 2018). It is possible that F could be contained within amorphous phases in the matrix that would easily be released into the surrounding material, even with mild impact-induced heating.

The small phosphate grain sizes and low abundance of apatite in the Kendleton L4 lithology may also be related to impact processing. An impact could have disrupted

the L4 material during metamorphism, after merrillite formed but before fluids could alter a significant amount of the merrillite to apatite (e.g., Fig. 1.4c). The impact could have fragmented the phosphates into small grains (Fig. 1.1e) and imparted the F-bearing component recorded in the apatite, while possibly forming additional apatite in the vein-filling morphology (Fig. 1.4d).

If F-rich apatite is related to an impact process, we need to consider why this only affected certain lithologies. One possibility is that the affected lithologies were substantially more permeable during F infiltration (e.g., unconsolidated regolith) and thus preferentially altered over the less permeable lithologies. However, this model does not seem likely because there is no evidence for more F-rich apatite at the clast edges as we would expect for a single impact event releasing F through the material. A more plausible model is that the F-rich lithology was close to the source of F, e.g., at the surface of the asteroid, and that the unaltered lithologies were incorporated later during excavation by subsequent impact events. This would be consistent with a rubble-pile model for the parent asteroid. The mixed shock stages of the three lithologies may be further evidence of multiple impact events. Mixed shock stages within a regolith breccia are not uncommon (Rubin 2004) though it is possible that the lower shock stage reported for the Kendleton L5 could be attributed to post-shock annealing. It is also possible that some of the apatite crystallized from an F-rich impact melt. However, apatite textures in the L4 host (Fig. 1.4c,d) are more consistent with alteration by fluids, i.e., they show replacement and vein-filling textures. Clearly regolith breccias have experienced complex chemical processing in addition to mechanical processing.

4.3. Formation and evolution of secondary minerals: Mechanisms, timing, and the role of fluids

Metamorphism in ordinary chondrites has long been considered to be a solid-state process whereby progressive textural and compositional equilibration occur in a closed system as a response to increasing temperature (Huss et al. 2006). There is general agreement that the source of heating was the decay of short-lived radioisotopes during the first few million years of the solar system, shortly after the asteroids accreted (McSween et al. 2002). Heating may also have resulted from impacts (Rubin 2004). However, as previously discussed, there are only rough constraints on the overall metamorphic environment: peak temperatures are poorly constrained and the role of metasomatic fluids, which may represent an open system, is not understood. We can address some of these unknowns by considering the metamorphic environments from which secondary minerals form in the three ordinary chondrite groups.

The general model for formation of phosphate minerals and feldspar is that merrillite forms by the reaction of metal-derived P with olivine, pyroxene, chondrule mesostasis, and matrix material (Ahrens 1970; Jones et al. 2014), apatite forms from reactions and further equilibration within this mineral assemblage, and fine-grained albitic plagioclase crystallizes out of chondrule mesostasis (Van Schmus and Wood 1967). All mineral grains coarsen and experience progressive chemical and textural equilibration with increasing extent of thermal processing. We compare our observations of phosphate and feldspar development through the petrologic sequence to the general model of thermal metamorphism, in order to interpret the mechanisms and relative timing

of their formation, and discuss the evidence from each of these minerals for the presence, composition, and timing of fluids during the metamorphic process.

Jones et al. (2014) trace the chemical origin of phosphate minerals in LL chondrites in detail and propose both solid-state and fluid-based formation mechanisms. They suggest that in lower petrologic types (≤ type 4), merrillite forms via a solid-state reaction with oxidized P (from Fe,Ni metal), and fine-grained apatite-merrillite assemblages form via fluid reactions with merrillite and/or silicate minerals. Rubin and Grossman (1985) reported chlorapatite rims around several Fe,Ni metal grains in the LL3.2 Krymka, which indicates the phosphate formation process occurs early in the metamorphic process. In higher petrologic types (types 5 and 6), apatite can form either via an interface-coupled dissolution-reprecipitation reaction between existent merrillite and a halogen-bearing fluid, or by direct precipitation from a fluid. Thermal metamorphism also accounts for the general increase in grain size with increasing petrologic type.

The lack of compositional equilibration in apatite that would be expected for a metamorphic origin is explained by Jones et al. (2014) as overprinting by a late-stage reaction with dry, Cl-rich fluids. Each chondrite has its own individual mean apatite composition so that fluid compositions appear to be fairly localized within a single parent body. Similarly, the heterogeneity within each chondrite group indicates a low fluid-rock ratio. Since phosphate minerals share similar properties in the H, L, and LL groups, as discussed above, we consider the processes governing phosphate formation to be similar between the three ordinary chondrite groups so that the mechanisms described above for LL chondrites are also valid for H and L chondrites.

At first glance, the initial formation of feldspar from chondrule mesostasis is a more straightforward process. Chondrule mesostasis is typically feldspathic in composition (Scott and Krot 2014), so thermal metamorphism should lead to the crystallization of mesostasis as feldspar. This view is supported by the fact that there is a wide range of plagioclase compositions (~An_{85}-An_5) in the chondrules of type 4 L (this study) and LL (Kovach and Jones 2010) chondrites and each chondrule has an average plagioclase composition that is distinct and likely related to the original composition of the mesostasis. The diversity in plagioclase compositions shows that crystallization of mesostasis must have occurred before diffusional equilibration across the chondrite could have taken place. In addition, primary igneous plagioclase present within the chondrule mesostasis, such as that identified in the LL3.0 Semarkona (Lewis and Jones 2015), may aid the nucleation of secondary plagioclase during the crystallization process.

Metamorphic equilibration of plagioclase to albitic compositions with increasing petrologic type in L and LL chondrites is not only a solid state process. We propose that chemical equilibration of feldspar is a metasomatic process involving a hydrous, alkali-bearing fluid. In types 4 and 5, anorthitic plagioclase shows a range of alteration features indicative of the action of water, including the replacement by albite (albitization) along grain boundaries and the presence of micropores. Albitization is an interface-coupled dissolution-reprecipitation reaction that is common in terrestrial water-rock interactions with alkali-bearing fluids (Putnis 2009). Development of porosity indicates the dissolution of anorthitic plagioclase by an aqueous fluid and is commonly associated with the albitization reaction (Engvik et al. 2008; Hövelmann et al. 2010).

Hövelmann et al. (2010) conducted albitization experiments on crystals of labradorite (An_{60}) and oligoclase (An_{23}) and showed that the reaction is very rapid. They were able to produce albitic rims on the plagioclase grain up to 50 μm across in less than two weeks in a sodium silicate solution at 600 °C and 2 kbars. At the experimental conditions the fluid had a pH of 9 and enough was added to theoretically convert all the plagioclase to albite. Grains of anorthitic plagioclase in type 4 L and LL chondrites are typically much smaller than 50 μm but have rims only ~1-3 μm in width (e.g., Fig. 1.7b) indicating that the albitization reaction did not go to completion. However, the predominantly albitic composition of petrologic types 5-6 L and LL and types 4-6 H chondrites show that the reaction has gone to completion under these metamorphic conditions. There could be a number of reasons for the differences in the extent of these reactions, including variability in temperature, pressure, composition, duration, and/or the availability of the metasomatizing fluids (i.e., water-rock ratio).

The most obvious difference between the petrologic types is temperature. The peak temperature range attributed to type 4-5 chondrites (500-800 °C) encompasses the temperature at which the experiments of Hövelmann et al. (2010) were conducted, 600 °C. Because there is not a well-defined division between peak temperatures in types 4 and 5, it is impractical to ascribe specific temperature dependent effects to these two types. However, even if type 4 L and LL chondrites only saw the lower end of that temperature range during metasomatism, we would expect more extensive albitization if all other conditions were equivalent to the above experimental setup (high pressure, pH, and water-rock ratio). Types 6 OCs have seen temperatures above 800 °C, which would presumably cause the reaction to proceed faster and thus to completion.

Unlike temperature, pressure seems unlikely to have a significant effect in determining differences between petrologic types and OC groups. In the onion shell model, type 6 material should experience slightly higher pressures than type 4 material though the differences are not likely to be significant. The interior pressure of chondritic asteroids is much lower (10s-100s of bars) than the experimental pressure (2 kbars) used by Hövelmann et al. (2010). However, pressure could have an important effect on fluid composition relative to the experimental study. Converting anorthite to albite depends on the availability of Na and Si in solution. While Na is highly soluble, limits in Si solubility may restrict the rate at which the reaction will proceed. Silicon solubility increases with increasing temperature, pressure, and pH (Alexander et al. 1954; Morey et al. 1964; Fournier and Rowe 1977). At high temperature and pH, silica solubility is very sensitive to pressure, so the low pressure asteroidal environment may cause the rate of the albitization reaction to be limited by the amount of Si available in solution (Fournier and Rowe 1977). Similarly, silica solubility may be controlled by pH and/or temperature effects. Overall, the differences in silica solubility between the asteroidal environment and experimental conditions may significantly reduce the rate at which chondritic albitization occurred.

Fluid availability and the duration of fluid-bearing episodes also control the degree of albitization. Lower amounts of fluid (i.e., low water-rock ratio) in type 4 and 5 L and LL chondrites could cause lower degrees of albitization whereas higher amount of fluid in H chondrites and type 6 L and LL chondrites would allow the reaction to proceed to completion. Alternatively, a similar effect could be produced by a limited duration of fluid activity coupled with a low reaction rate due to low silica solubility. If one assumes

the same amount of fluid was present in ordinary chondrites of all petrologic types (e.g., derived locally from ices incorporated into the matrix), an onion-shell asteroid would experience longer durations of metasomatism (and at higher temperatures) with increasing petrologic type. Given a slow rate of albitization, only the longest duration of metasomatism (type 6) would result in a complete replacement of anorthitic plagioclase. However, this does not address the difference between type 4 H chondrites and L, LL chondrites for which another factor, such as fluid composition, must be invoked.

In addition to Na, increased K content within albitized regions in type 4 and 5 chondrites implies the metasomatizing fluid is also K-bearing. Potassium was clearly incorporated into the feldspar during the metamorphic processes and exsolved as K-feldspar during cooling (e.g., Figs. 1.7d,h,j). Both Na and K are incorporated into the feldspar structure at a high temperature where the solvus covers a small compositional range. As the temperature decreases, the solvus widens and the two feldspars unmix to produce cryptoantiperthite (Jones and Brearley 2011; Lewis et al. 2016). Replacement reactions such as this are common in alkali feldspars in hydrothermal systems on Earth (Parsons and Lee 2009). The presence of K-feldspar exsolution near voids (Fig. 1.7h) shows that fluids flowed through the chondrules using inherent porosity. However, the amount of K present within the fluid appears to be limited because K content in the plagioclase (as seen by K-feldspar exsolution) is not typically uniform from chondrule to chondrule or even within a single chondrule (Fig. 1.7h,j). We did not observe K-feldspar exsolution in type 6 L and H chondrites: this could be the result of lower K abundances in the fluid, although Or contents of albitic feldspar in type 6 chondrites are comparable to those in type 5. Orville (1963) showed that the Na/K ratio of a fluid in equilibrium with

alkali feldspar decreases with increasing temperature independent of feldspar composition. The higher temperature of type 6 OCs could increase K solubility in the fluid and decrease the amount of K incorporated into feldspar. The absence of exsolution could also indicate a more rapid cooling rate for the type 6 material, which would be inconsistent with an onion-shell model.

The above arguments assume that metasomatizing fluids were acting during peak metamorphism within each of the petrologic types. However, thermal modeling of an onion shell asteroid (e.g., Harrison and Grimm 2010) shows that peak temperatures for each petrologic type are not coincident: there is a time interval of millions of years between the peak temperature of type 4 (earlier) and type 6 (later). An alternative model for feldspar formation is that the fluid causing the albitization reactions was derived from a deep source (not the local environment) and was delivered relatively late in the thermal evolution of the parent body, e.g., near peak metamorphism of type 6. In this case, the lower petrologic types would have cooled down during retrograde metamorphism and the albitization reaction would proceed slower at these lower temperatures. Such a model could also explain the difference in equilibration between type 4 H (more albitized) and L, LL (less albitized) chondrites. An earlier release of metasomatizing fluids (e.g., near peak metamorphism of type 4 material) would allow the reaction to occur at a higher temperature, and proceed to completion, in types 4-6.

In order to fully understand the metasomatic/metamorphic environment, we must reconcile observations on phosphate and feldspar minerals. Our generalized model is as follows. First, plagioclase crystallizes from chondrule mesostasis during the onset of metamorphism at roughly the same time that merrillite forms from the oxidation of

metal-derived phosphorus. These are thought to be solid-state processes although fluid assistance is not necessarily ruled out. Also, there may be some primary feldspar in chondrules. Alteration of Ca-bearing feldspar to albite, and alteration of merrillite to apatite, requires a hydrous brine to facilitate the interface-coupled dissolution-reprecipitation reactions. However, the increasing degree of albitization with increasing petrologic type is not reflected in a change in the apatite/merrillite ratio which actually decreases slightly with increasing petrologic type, owing largely to an increase in merrillite abundance. It appears that the conditions that allowed for the conversion of merrillite to apatite were limited in duration and predominantly occurred within lower petrologic types. In higher petrologic types, merrillite abundances continued to increase, consistent with the presence of an alkali-bearing fluid. During retrograde metamorphism, K-feldspar exsolved from the albite and a dry, Cl-rich fluid overprinted the apatite compositions but did not affect plagioclase compositions.

The composition of the fluid that alters anorthite to alkali feldspar and merrillite to apatite has been characterized above as a hydrous brine containing the alkali elements Na and K and the halogens Cl and F. The fluid also contains Si inferred by the alteration of anorthite to albite. We can show the feldspar alteration by the following simplified equation where anorthite and low-Ca pyroxene react with a siliceous brine to form alkali feldspar, Ca-rich pyroxene, oxides (spinel in this case), with release of $CaCl_2$ back into the fluid:

$$2CaAl_2Si_2O_8 + Mg_2Si_2O_6 + 2SiO_2(aq) + 2NaCl(aq) \rightarrow$$
$$2NaAlSi_3O_8 + CaMgSi_2O_6 + MgAl_2O_4 + CaCl_2(aq).$$

While we do not see direct evidence for the consumption of low-Ca pyroxene, we do see areas of albitized anorthite with accessory oxides and Ca-rich pyroxene. However, it is

likely that chondrule mesostasis, and not low-Ca pyroxene, provides the important cations for the replacement reaction to proceed. Potassium can follow Na into the alkali feldspar. The resultant $CaCl_2(aq)$ can react with merrillite to form apatite according to the following simplified equation:

$$3Ca_9NaMg(PO_4)_7 + 8CaCl_2(aq) \rightarrow 7Ca_5(PO_4)_3Cl + 3NaCl(aq) + 3MgCl_2(aq).$$

In this case, the resultant NaCl can feed back into the anorthite alteration reaction. Fluorine can follow Cl into apatite. However, the apatite reaction represented here does not take into account the late-stage, dry, Cl-rich fluid that may have overprinted the apatite composition. Apatite forming from a hydrous reaction should have a significant OH component in addition to the Cl/F ratio of the fluid from which it formed.

Overall, evidence is mounting that fluids were present during thermal metamorphism and that a simple picture of solid-state recrystallization alone is not sufficient. The presence of fluids in equilibrated ordinary chondrites has been inferred previously from studies of modal mineralogy (McSween and Labotka 1993; Dunn et al. 2010a,b) and oxygen isotopes (Bridges et al. 1999; Li et al. 2000; Rubin 2005). McSween and Labotka (1993) suggested that the observed increase in FeO and decrease in Fe metal with progressive metamorphism could be caused by small amounts of water vapor. Similar observations were made by Dunn et al. (2010b) using modal mineralogy determined by XRD. Rubin (2005) proposed that water could be derived from dehydration of phyllosilicates during metamorphism and could be responsible for the trend of decreasing $\delta^{17}O$ and $\delta^{18}O$ with increasing petrologic type observed by Clayton et al. (1991). Li et al. (2000) showed that plagioclase and glass separates from the LL3.9 chondrite Bo Xian had higher $\delta^{17}O$ and $\delta^{18}O$ than olivine and pyroxene and suggested

this was due to interaction with ^{16}O-poor hydrous fluid. Our studies of phosphates and feldspar show that interface-coupled dissolution-reprecipitation reactions in a hydrous halogen- and alkali-bearing fluid were at least partially responsible for changes in mineralogy, and the equilibration of plagioclase appears to be driven almost entirely by fluid processes. Late-stage anhydrous, Cl-rich fluids were proposed by Jones et al. (2014) to have overprinted apatite compositions during retrograde metamorphism.

4.4. Cl and F abundances in ordinary chondrites

It is important to know bulk halogen abundances in chondrites because they are used to estimate the halogen compositions of the Earth and other terrestrial planets (McDonough and Sun 1995). However, these values are not well constrained in chondrites (Brearley and Jones 2018) and elemental abundance compilations such as those of Wasson and Kallemeyn (1988) and Lodders and Fegley (1998) provide widely varying values based on limited data. L chondrites have particularly large uncertainties with Wasson and Kallemeyn (1988) reporting 76 ppm and 41 ppm for bulk Cl and F respectively (atomic Cl/F = 1.0) in contrast to 270 ppm and 100 ppm for Cl and F (atomic Cl/F = 1.4) from Lodders and Fegley (1998). Brearley and Jones (2016) provide a review of the studies from which these compiled values were obtained and conclude that the halogen abundances of Wasson and Kallemeyn (1988) are likely more representative of the limited data but should still be treated with caution.

A number of halogen-bearing phases occur in unequilibrated ordinary chondrites, including sodalite, scapolite, and smectite, in addition to apatite (Brearley and Jones 2018). Most of these phases are not stable at high temperatures and only apatite is present in chondrites that have undergone significant degrees of thermal metamorphism. Because

of this, apatite is likely the major host of Cl and F in equilibrated (petrologic type 4-6) ordinary chondrites and we can use the abundances of Cl and F measured in apatite to understand the bulk halogen characteristics of ordinary chondrites. In Figure 1.9, we compare bulk Cl/F ratios for H, L, LL, and CI chondrites from Wasson and Kallemeyn (1988) with apatite compositions of the three ordinary chondrite groups. Apatite Cl/F ratios in ordinary chondrites are significantly higher than the bulk chondrite values of Wasson and Kallemeyn (1988). In fact, ordinary chondrite apatite actually shows CI-like Cl/F ratios, with quite a lot of scatter, and the Cl/F ratio in L chondrite apatite (atomic Cl/F = 5.9) is very close to the CI ratio (atomic Cl/F = 5.7). Figure 1.10 further illustrates this point by showing bulk Cl/F ratios (expressed as Cl#) for ordinary and CI chondrites. The figure also illustrates the differences between the compilations of Wasson and Kallemeyn (1988) and Lodders and Fegley (1998). There are two possible explanations for the differences between apatite and bulk chondrite Cl/F ratios: either there are other F-bearing phases in equilibrated ordinary chondrites that have not been recognized, or the available bulk chondrite values are incorrect, with underestimated Cl and/or overestimated F abundances, as discussed by Jones et al. (2014).

We can obtain an independent estimate of bulk chondrite Cl and F abundances from our measurements of apatite abundances and compositions. For the L chondrites, apatite has average Cl and F abundances of 5.2 wt% and 0.5 wt%, respectively (Table 1.3). Using the calculated average volume abundance of 0.17% for apatite (Table 1.2), the bulk Cl and F abundances due to the presence of apatite are roughly 91 ppm and 9 ppm, respectively (not taking into account densities). These bulk values drop to 86 ppm and 8 ppm for Cl and F, respectively, if the calculation includes the mineral density for

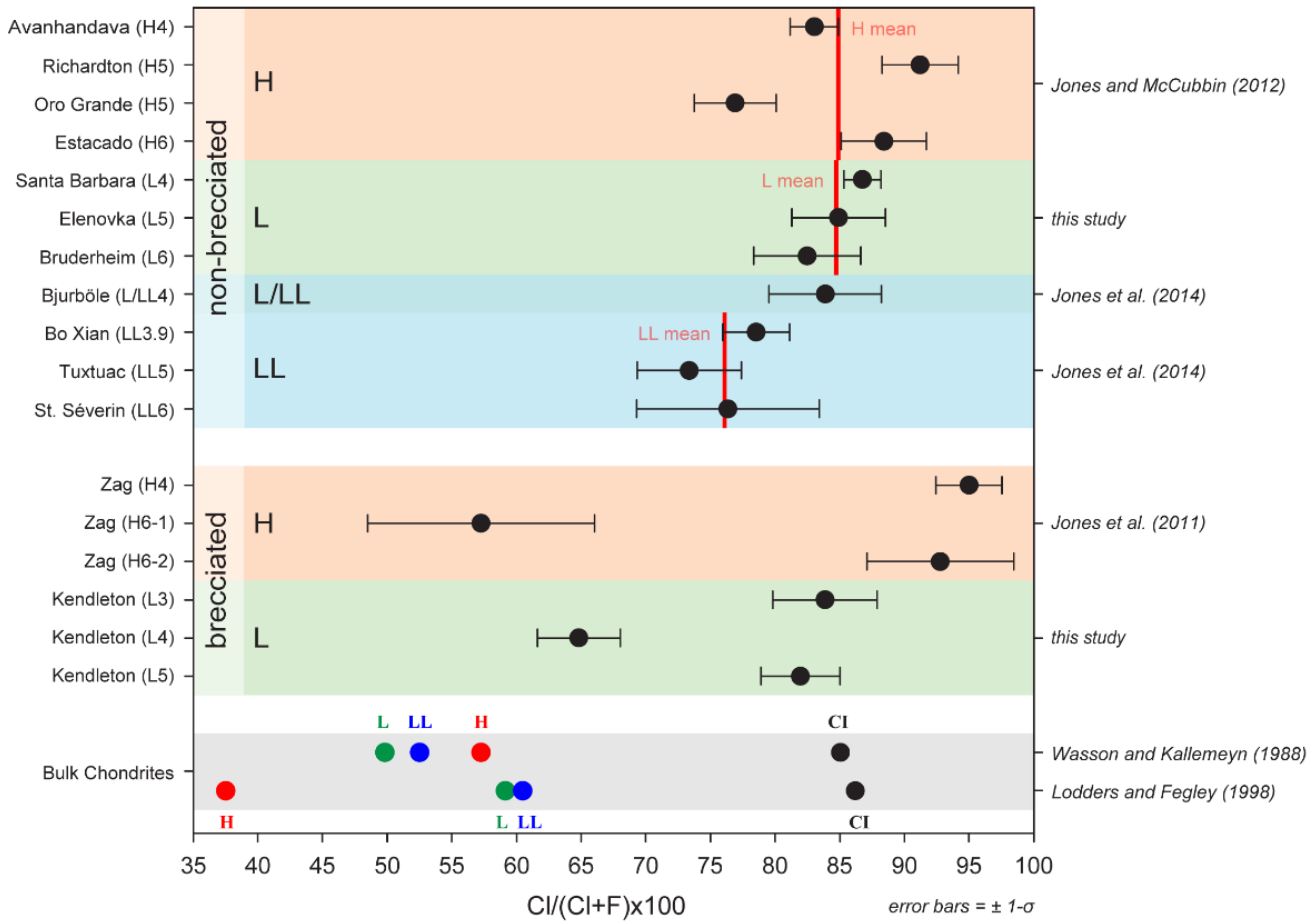

Figure 1.10. Mean Cl# (atomic Cl/(Cl+F)x100) for individual non-brecciated and brecciated OCs. Data are from the following sources: H chondrites, Jones and McCubbin (2012); L chondrites, this study; LL chondrites, Jones et al. (2014); Zag H4-6 breccia, Jones et al. (2011). Error bars represent ± 1σ. Bulk Cl# values for OCs and CI chondrites from Wasson and Kallemeyn (1988) and Lodders and Fegley (1998) are shown for comparison.

chlorapatite (Bideaux et al. 2000) and the bulk density of L chondrites (Consolmagno et al. 2008). In comparison, the bulk L chondrite Cl abundance given by Wasson and Kallemeyn (1988) is very similar, 76 ppm. This is consistent with apatite being the major host for Cl. However, the bulk value for F given by Wasson and Kallemeyn (1988) is 41 ppm, about 5 times greater than the F abundance accounted for by apatite alone. A similar discrepancy was shown for the LL chondrites (Jones et al. 2014) in that apatite is clearly the major carrier of Cl, but F in apatite only accounts for ~10% of the reported bulk value. Other workers have also reported discrepancies between apatite abundance and bulk F content (e.g., Reed 1964; Van Schmus and Ribbe 1969).

While bulk chlorine contents of the different chondrite groups are well established, reported bulk fluorine contents have large uncertainties (Brearley and Jones 2018). Although it is possible that F is present in other phases, as suggested by Reed (1964), it is unlikely that silicates would be able to retain significant F at the low pressures of OC parent bodies. We consider it more likely that the reported halogen abundances of bulk ordinary chondrites have overestimated F abundances, and that the CI-like Cl/F ratio recorded in apatite is more representative of bulk OC values. If OCs have a CI-like Cl/F ratio then perhaps all chondrites formed with a solar Cl/F ratio that indicates a roughly uniform distribution of Cl/F in early planetesimals.

5. Summary and conclusions

We conducted a detailed study of phosphate and feldspar in equilibrated L ordinary chondrites in order to understand the metamorphic and metasomatic environment on the L parent body and compare it to previous studies of H and LL chondrites. Apatite abundances and compositions in L chondrites are Cl-rich and similar

on average to H chondrites; both are similar to LL chondrites, but apatite in LL chondrites has a lower Cl/F ratio. Merrillite abundances and compositions are similar among the three chondrite groups and show a trend of compositional equilibration with metamorphism. Feldspar in L chondrites shows an equilibration trend from a wide range of plagioclase compositions in petrologic type 4 to a homogeneous albitic composition in type 6. This is very similar to the feldspar equilibration trend in LL chondrites, and different from H chondrites, in which plagioclase is homogeneous and albitic in petrologic types 4-6. Metasomatic fluids acted during metamorphic heating on the OC parent bodies. The fluids were alkali- and halogen-rich and likely hydrous during prograde metamorphism, transitioning to a more anhydrous, Cl-rich composition after the asteroid began to cool. The differences in secondary minerals (largely plagioclase equilibration) between H and L, LL chondrites can be explained by differences in fluid abundance/duration or the timing of deep-sourced fluid release. Regolith breccias have lithology-dependent apatite compositions, some with more F-rich apatite compositions than unbrecciated chondrites, possibly due to F-rich degassing from impact melts or an F-rich impactor. Bulk Cl/F ratios for ordinary chondrites inferred from apatite compositions are inconsistent with measured bulk chondrite halogen values. We suggest that this is because F abundances in bulk ordinary chondrites are overestimated, and that bulk Cl/F ratios of ordinary chondrites are actually close to CI chondrite, i.e., that they are unfractionated from solar values.

Acknowledgements

We would like to thank A. Rubin and M. Kimura for helpful reviews, Adrian Brearley and Francis McCubbin for useful conversations, and Mike Spilde for his help

with the microprobe. We also thank Jane Gallegos who conducted analytical work on feldspar. Electron microprobe and SEM work was carried out in the Electron Microbeam Analysis Facility, Department of Earth and Planetary Sciences and Institute of Meteoritics, University of New Mexico. J. Lewis acknowledges support from the Kelley-Silver Foundation, University of New Mexico. The work was partially funded by NASA grant NNX12AH61G (P.I. R. Jones).

References

Ahrens L. H. 1970. The composition of stony meteorites (VIII) observations on fractionation between the L and H chondrites. *Earth and Planetary Science Letters* 9:345–347.

Alexander C. M. O'D., Barber D. J., and Hutchison R. 1989. The microstructure of Semarkona and Bishunpur. *Geochimica et Cosmochimica Acta* 53:3045–3057.

Alexander G. B., Heston W., and Iler R. K. 1954. The solubility of amorphous silica in water. *The Journal of Physical Chemistry* 58:453–455.

Ashworth J. R. 1980. Chondrite thermal histories: Clues from electron microscopy of orthopyroxene. *Earth and Planetary Science Letters* 46:167–177.

Ashworth J. R., Barber D. J., Brown G. M., and Smith J. V. 1977. Electron microscopy of some stony meteorites. *Philosophical Transactions of the Royal Society of London A: Mathematical, Physical and Engineering Sciences* 286:493–506.

Bideaux R. A., Bladh K. W., and Monte M. C. 2000. *Handbook of Mineralogy: Arsenates, Phosphates, Vanadates*, edited by Anthony J. W. Mineral Data Publishing. p. 111.

Brearley A. J. and Jones R. H. 1998. Chondritic meteorites. In *Planetary Materials*, edited by Papike J. J. Reviews in Mineralogy and Geochemistry, vol. 36. Chantilly, Virginia: The Mineralogical Society of America. pp. 3.1–3.398.

Brearley A. J. and Jones R. H. 2018. Halogens in chondritic meteorites. In *Halogens*, edited by Harlov D. Springer.

Bridges J. C., Franchi I. A., Sexton A. S., and Pillinger C. T. 1999. Mineralogical controls on the oxygen isotopic compositions of UOCs. *Geochimica et Cosmochimica Acta* 63:945–951.

Clayton R. N., Mayeda T. K., Goswami J. ., and Olsen E. J. 1991. Oxygen isotope studies of ordinary chondrites. *Geochimica et Cosmochimica Acta* 55:2317–2337.

Consolmagno G. J., Britt D. T., and Macke R. J. 2008. The significance of meteorite density and porosity. *Chemie der Erde* 68:1–29.

Dunn T. L., Cressey G., McSween H. Y., and McCoy T. J. 2010a. Analysis of ordinary chondrites using powder X-ray diffraction: 1. Modal mineral abundances. *Meteoritics & Planetary Science* 45:123–134.

Dunn T. L., McSween Jr. H. Y., McCoy T. J., and Cressey G. 2010b. Analysis of ordinary chondrites using powder X-ray diffraction: 2. Applications to ordinary chondrite parent-body processes. *Meteoritics & Planetary Science* 45:135–156.

Ehlmann A. J., Scott E. R. D., Keil K., Mayeda T. K., Clayton R. N., Weber H. W., and Schultz L. 1988. Origin of fragmental and regolith meteorite breccias: Evidence from the Kendleton L chondrite breccia. In *Lunar and Planetary Science Conference Proceedings*, edited by Ryder G. pp. 545–554.

Engvik A. K., Putnis A., Fitz Gerald J. D., and Austrheim H. 2008. Albitization of granitic rocks: The mechanism of replacement of oligoclase by albite. *The Canadian Mineralogist* 46:1401–1415.

Feldstein S. N., Jones R. H., and Papike J. J. 2001. Disequilibrium partial melting experiments on the Leedey L6 chondrite: Textural controls on melting processes. *Meteoritics & Planetary Science* 36:1421–1441.

Fournier R. O. and Rowe J. J. 1977. Solubility of amorphous silica in water at high temperatures and high pressure. *American Mineralogist* 62:1052–1056.

Grossman J. N., Alexander C. M. O'D., Wang J., and Brearley A. J. 2000. Bleached chondrules: Evidence for widespread aqueous processes on the parent asteroids of ordinary chondrites. *Meteoritics & Planetary Science* 35:467–486.

Harrison K. P. and Grimm R. E. 2010. Thermal constraints on the early history of the H-chondrite parent body reconsidered. *Geochimica et Cosmochimica Acta* 74:5410–5423.

Hövelmann J., Putnis A., Geisler T., Schmidt B., and Golla-Schindler U. 2010. The replacement of plagioclase feldspars by albite: Observations from hydrothermal experiments. *Contributions to Mineralogy and Petrology* 159:43–59.

Huss G. R. 1979. The matrix of unequilibrated ordinary chondrites: Implications for the origin and subsequent history of chondrites. Master's thesis, University of New Mexico, Albuquerque, New Mexico, USA.

Huss G. R., Rubin A. E., and Grossman J. N. 2006. Thermal metamorphism in chondrites. In *Meteorites and the Early Solar System II*, edited by Lauretta D. S., and McSween Jr. H. Y. Tucson, AZ: The University of Arizona Press. pp. 567–586.

Jones R. H. and Brearley A. J. 2011. Exsolution in feldspar in the Tuxtuac (LL5) chondrite: A new perspective on cooling rates for metamorphosed chondrites. (abstract #5475) 74th Annual Meeting of the Meteoritical Society.

Jones R. H. and McCubbin F. M. 2012. Phosphate mineralogy and the bulk chlorine/fluorine ratio of ordinary chondrites. (abstract #2029) 43rd Lunar and Planetary Science Conference.

Jones R. H., McCubbin F. M., Dreeland L., Guan Y., Burger P. V., and Shearer C. K. 2014. Phosphate minerals in LL chondrites: A record of the action of fluids during metamorphism on ordinary chondrite parent bodies. *Geochimica et Cosmochimica Acta* 132:120–140.

Jones R. H., McCubbin F. M., and Guan Y. 2011. Phosphate mineralogy and the role of fluids in the Zag H chondrite. (abstract #2435) 42nd Lunar and Planetary Science Conference.

Kovach H. A. and Jones R. H. 2010. Feldspar in type 4–6 ordinary chondrites: Metamorphic processing on the H and LL chondrite parent bodies. *Meteoritics & Planetary Science* 45:246–264.

Krot A. N., Zolensky M. E., Wasson J. T., Scott E. R. D., Keil K., and Ohsumi K. 1997. Carbide-magnetite assemblages in type-3 ordinary chondrites. *Geochimica et Cosmochimica Acta* 61:219–237.

Leroux H., Doukhan J.-C., and Guyot F. 1996. An analytical electron microscopy (AEM) investigation of opaque inclusions in some type 6 ordinary chondrites. *Meteoritics & Planetary Science* 31:767–776.

Lewis J. A. and Jones R. H. 2015. Primary feldspar in Semarkona (LL3.00) chondrules. (abstract #2067) 46th Lunar and Planetary Science Conference.

Lewis J. A., Jones R. H., and Brearley A. J. 2016. Alkali feldspar exsolution in ordinary chondrites: Alkali metasomatism, metamorphism, and cooling rates. (abstract #2559) 47th Lunar and Planetary Science Conference.

Li C., Bridges J. C., Hutchison R., Franchi I. A., Sexton A. S., Ouyang Z., and Pillinger C. T. 2000. Bo Xian (LL3.9): Oxygen-isotopic and mineralogical characterisation of separated chondrules. *Meteoritics & Planetary Science* 35:561–568.

Lodders K. and Fegley B. 1998. *The Planetary Scientist's Companion*, New York: Oxford University Press.

McCubbin F. M., Hauri E. H., Elardo S. M., Vander Kaaden K. E., Wang J., and Shearer C. K. 2012. Hydrous melting of the martian mantle produced both depleted and enriched shergottites. *Geology* 40:683–686.

McCubbin F. M., Steele A., Nekvasil H., Schnieders A., Rose T., Fries M., Carpenter P. K., and Jolliff B. L. 2010. Detection of structurally bound hydroxyl in fluorapatite from Apollo Mare basalt 15058,128 using TOF-SIMS. *American Mineralogist* 95:1141–1150.

McDonough W. F. and Sun S. -s. 1995. The composition of the Earth. *Chemical Evolution of the Mantle* 120:223–253.

McSween H. Y., Ghosh A., Grimm R. E., Wilson L., and Young E. D. 2002. Thermal evolution models of asteroids. In *Asteroids III*, edited by Bottke W. F., Cellino A., Paolicchi P., and Binzel R. P. Tucson, AZ: The University of Arizona Press. pp. 559–571.

McSween H. Y. and Labotka T. C. 1993. Oxidation during metamorphism of the ordinary chondrites. *Geochimica et Cosmochimica Acta* 57:1105–1114.

Morey G. W., Fournier R. O., and Rowe J. J. 1964. The solubility of amorphous silica at 25 °C. *Journal of Geophysical Research* 69:1995–2002.

Orville P. M. 1963. Alkali ion exchange between vapor and feldspar phases. *American Journal of Science* 261:201–237.

Parsons I. and Lee M. R. 2009. Mutual replacement reactions in alkali feldspars I: microtextures and mechanisms. *Contributions to Mineralogy and Petrology* 157:641–661.

Putnis A. 2009. Mineral replacement reactions. In *Thermodynamics and Kinetics of Water-Rock Interaction*. Reviews in Mineralogy and Geochemistry, vol. 70. Chantilly, Virginia: The Mineralogical Society of America. pp. 87–124.

Reed G. W. 1964. Fluorine in stone meteorites. *Geochimica et Cosmochimica Acta* 28:1729–1743.

Rubin A. E. 1992. A shock-metamorphic model for silicate darkening and compositionally variable plagioclase in CK and ordinary chondrites. *Geochimica et Cosmochimica Acta* 56:1705–1714.

Rubin A. E. 2003. Chromite-plagioclase assemblages as a new shock indicator; implications for the shock and thermal histories of ordinary chondrites. *Geochimica et Cosmochimica Acta* 67:2695–2709.

Rubin A. E. 2004. Postshock annealing and postannealing shock in equilibrated ordinary chondrites: Implications for the thermal and shock histories of chondritic asteroids. *Geochimica et Cosmochimica Acta* 68:673–689.

Rubin A. E. 2005. Relationships among intrinsic properties of ordinary chondrites: Oxidation state, bulk chemistry, oxygen-isotopic composition, petrologic type, and chondrule size. *Geochimica et Cosmochimica Acta* 69:4907–4918.

Rubin A. E. and Grossman J. N. 1985. Phosphate-sulfide assemblages and Al/Ca ratios in type-3 chondrites. *Meteoritics* 20:479–489.

Scott E. R. D. and Krot A. N. 2014. Chondrites and their components. In *Treatise on Geochemistry (Second Edition), Volume 1: Meteorites and Cosmochemical Processes*, edited by Davis A. M. Elsevier, Oxford. pp. 65–137.

Stöffler D., Keil K., and Edward R.D S. 1991. Shock metamorphism of ordinary chondrites. *Geochimica et Cosmochimica Acta* 55:3845–3867.

Stormer J. C., Pierson M. L., and Tacker R. C. 1993. Variation of F and Cl X-ray intensity due to anisotropic diffusion in apatite during electron microprobe analysis. *American Mineralogist* 78:641–648.

Van Schmus W. R. and Ribbe P. H. 1969. Composition of phosphate minerals in ordinary chondrites. *Geochimica et Cosmochimica Acta* 33:637–640.

Van Schmus W. R. and Wood J. A. 1967. A chemical-petrologic classification for the chondritic meteorites. *Geochimica et Cosmochimica Acta* 31:747–765.

Wasson J. T. and Kallemeyn G. W. 1988. Compositions of chondrites. *Philosophical Transactions of the Royal Society of London A: Mathematical, Physical and Engineering Sciences* 325:535–544.

Wlotzka F. 1993. A weathering scale for the ordinary chondrites. *Meteoritics* 28:460.

Yurimoto H., Itoh S., Zolensky M. E., Kusakabe M., and Karen A. 2010. Isotopic compositions of fluid inclusions in halites from ordinary chondrites. *Meteoritics and Planetary Science Supplement* 73:5178.

Zanda B., Bourot-Denise M., Perron C., and Hewins R. H. 1994. Origin and metamorphic redistribution of silicon, chromium, and phosphorus in the metal of chondrites. *Science* 265:1846–1849.

Zolensky M. E., Clayton R. N., Mayeda T., Chokai J., and Norton O. R. 2003. Carbonaceous chondrite clasts in the halite-bearing H5 chondrite Zag. *Meteoritics and Planetary Science Supplement* 38:5216.

CHAPTER 2

Primary feldspar in the Semarkona LL3.00 chondrite: Constraints on chondrule formation and secondary alteration

In collaboration with:
Rhian H. Jones

Submitted for publication to:
Meteoritics & Planetary Science

Abstract

Feldspar in ordinary chondrites (OCs) is often associated with thermal metamorphism, as a secondary mineral that forms from the crystallization of matrix and chondrule mesostasis. However, studies of feldspar in equilibrated OCs show that there is a range of plagioclase compositions within chondrules, some of which may be primary products of chondrule crystallization. It is important to recognize primary feldspar within chondrules because it can be used to help understand the secondary effects of thermal metamorphism and aqueous alteration. The presence of primary feldspar also provides important petrologic constraints on chondrule formation. We undertook a careful study of Semarkona (LL3.00) and observed feldspar in 18% of chondrules. The feldspar is plagioclase covering a wide range of compositions (An_2-An_{99}) with little K-feldspar component ($<Or_3$). We show that plagioclase is a primary igneous phase, based on grain morphology and compositions consistent with growth from a melt having the bulk compositions of the host chondrules. Based on experimental studies, the presence of plagioclase suggests chondrules cooled slowly, on the order 1 ºC/hour at temperatures close to the solidus. We also observed several secondary features consistent with the aqueous alteration. These features include zoning of Na and Ca in plagioclase,

heterogeneity in plagioclase compositions in altered chondrules, development of porosity from the dissolution of chondrule glass, and alteration of glass to phyllosilicates. Alteration of major Al-bearing phases, like plagioclase and glass, has important implications for interpretations of ages derived from Al-Mg dating of chondrules, if they have been affected by secondary processes.

1. Introduction

Feldspar in ordinary chondrites (OCs) is commonly considered to be a secondary phase that forms during thermal metamorphism (e.g., Huss et al. 2006). As chondrule mesostasis glass, often feldspathic in composition, and chondrite matrix recrystallize, plagioclase and other phases develop in what has historically been treated as a solid-state, temperature-dependent process (Huss et al. 2006). The classification scheme of Van Schmus and Wood (1967), used to differentiate degrees of thermal metamorphism, describes the crystallization of chondrule mesostasis into albite as an important feature of the effect of thermal metamorphism. According to this classification scheme, fine-grained albite crystallizes by petrologic type 4 and then undergoes textural equilibration through types 5 and 6, ultimately resulting in grains of albite >50 μm in size (Huss et al. 2006; Van Schmus and Wood 1967).

However, recent studies of feldspar in equilibrated OCs (Kovach and Jones 2010; Lewis and Jones 2016) show that the general model of Van Schmus and Wood (1967) does not fully describe the feldspar equilibration process or the range in compositions and textures found in OC feldspar. Plagioclase is not solely albitic in composition and a wide range of plagioclase compositions (An_2-An_{88}) is present in relict chondrules in type 4 L and LL chondrites (Kovach and Jones 2010; Lewis and Jones 2016). Only in type 6

chondrites is feldspar equilibrated chemically, in addition to texturally, to an albitic composition of ~An_{11}.

The wide range of feldspar compositions within chondrules in type 4 L and LL chondrites is plausibly derived from variable initial mesostasis compositions. However, chondrules may also contain primary igneous plagioclase, with a range of compositions that could reflect the compositions of plagioclase observed in type 4 OCs. Primary, igneous anorthitic feldspar has been described in Type I chondrules in OCs but it is not well characterized, unlike similar occurrences in carbonaceous chondrites (CCs) (Brearley and Jones 1998; Wick and Jones 2012). Aluminum-rich chondrules in OCs also contain primary anorthite that is useful for age dating using Al-Mg systematics (e.g., Huss et al. 2001). Although Type II chondrules in OCs are rich in Na and K, albitic plagioclase or alkali feldspar is not generally observed (Jones 1990). Grossman and Brearley (2005) noted that crystalline albite is present within Semarkona, but did not indicate whether it is primary or secondary in origin.

To understand how secondary plagioclase develops during metamorphism, it is essential to know the abundance and composition of primary plagioclase. The mineralogical and chemical changes that affect chondrule mesostasis during thermal metamorphism depend on the composition and initial crystallinity of the mesostasis, in addition to temperature and available fluids. The presence of primary feldspar can influence the subsequent crystallization of the mesostasis glass by providing surfaces on which secondary plagioclase can nucleate. Plagioclase is also affected by alkali metasomatism, so secondary effects recorded in primary plagioclase can provide an indicator of the presence of fluids in type 3 chondrites. Plagioclase alteration can affect

Al-Mg systematics resulting in low precision isochrons or ages that are difficult to interpret. In addition to its importance in terms of interpreting metamorphism, understanding the origin and development of primary feldspar can help constrain chondrule cooling rates, an important parameter in chondrule formation models (Connolly and Jones 2016).

We have investigated the presence and characteristics of primary igneous plagioclase within chondrules of the LL3.00 chondrite Semarkona. Semarkona is the least thermally metamorphosed OC fall with a maximum metamorphic temperature estimated to be less than 260 °C (Alexander et al. 1989). It is the ideal sample in which to investigate primary chondrule minerals because chondrule mesostasis glass has not undergone crystallization (Huss et al. 2006). The mineralogy and petrology of Semarkona chondrules were studied extensively by Jones and Scott (1989) and Jones (1990, 1994, 1996), but primary igneous plagioclase was not recognized in those studies. Marked improvements in SEM technology has enabled higher resolution investigations into chondrule mineralogy and allowed for studies on phases too small to be fully characterized in earlier studies. We show that primary igneous plagioclase is abundant in Semarkona chondrules and that careful observations of plagioclase are important for interpreting the effects of metamorphism, alteration, and the results of Al-Mg isotope systematics.

2. Samples and analytical methods

For this study, we examined a single thin section of Semarkona from the Institute of Meteoritics Collection at the University of New Mexico, UNM 549. Feldspar was identified using backscattered electron (BSE) imaging and energy-dispersive

spectroscopic (EDS) analysis on an FEI Quanta 3D Field Emission Gun Scanning Electron Microscope (FEG-SEM) at the University of New Mexico. High contrast BSE images were captured at 10 kV and 16 nA. Cathodoluminescence (CL) images were acquired at the Williamson Research Centre, University of Manchester using a CITL Cold Cathode CL 8200 MK3 with optical stage operated at 15-20 kV and 300-400 μA.

Quantitative wavelength-dispersive spectroscopic (WDS) analysis was performed on a JEOL 8200 Electron Probe Microanalyzer (EPMA) at the University of New Mexico operated at 10-15 kV and 10 nA with a focused beam. The low accelerating voltage was used to minimize the interaction volume when analyzing small feldspar grains. We used the following standards: Taylor olivine (Mg, Fe), Taylor albite (Na, K), Taylor orthoclase (K, Al, Si), and a doped diopside (Ca, Cr, Mn). We used time dependent intensity corrections on Na using the Probe for EPMA software to compensate for the effects of Na migration in Na-bearing plagioclase during focused-beam analysis.

We determined bulk silicate compositions for four chondrules, based on quantitative WDS maps obtained using EPMA. 300x300 pixel maps were acquired in two passes using an 80 ms/px dwell time and a 1-3 μm spot size. This provided coverage between 300x300 μm and 900x900 μm, depending on the size of the chondrule. The resulting intensity maps were processed using mean atomic number (MAN) background corrections to produce quantitative oxide maps. MAN curves were generated using the following Taylor standards: olivine, albite, orthoclase, chromite, spessartine, MgO, hematite, and nickel and additional standards: doped diopside, labradorite, and sodalite. Chondrules were masked in Adobe Photoshop and the bulk silicate compositions of the chondrules were calculated. We used a custom MATLAB script to identify the chondrule

pixels in which analytical sums lie between 90% and 110%. In addition, pixels with SiO_2 content less than 20% were omitted to eliminate Fe-Ni metal and sulfides. Densities were determined for each pixel based on assigned mineral phase and the bulk silicate composition of each chondrule was calculated as the mean density-weighted composition of accepted pixels. A detailed description of this process is presented in Appendix 2.

A section from Ch 28 was prepared using a focused ion beam (FIB) on the FEI Quanta 3D Dual-beam FEG-SEM/FIB with a final polish conducted at 5 kV to reduce surface amorphization. The section was imaged at the University of New Mexico using a JEOL 2010F Scanning Transmission Electron Microscope (STEM) operated at 200 kV in scanning mode using a high-angle annular dark-field (HAADF) detector. An EDS map was obtained over a 2.4 μm x 1.8 μm region using an Oxford Instruments AZtec EDS system equipped with an Oxford X-Max^N 80T SDD EDS detector.

3. Results

Fig. 2.1 shows a BSE map of thin section UNM 549 in which feldspar-bearing chondrules are outlined in white. Chondrules referred to in the text, figures, and tables are labeled in Fig. 2.1 by chondrule number. Eighteen percent of chondrules were found to contain primary igneous feldspar that exhibit a range of sizes and textures described below.

3.1. Petrography

Examples of chondrules that contain near-endmember albite and anorthite (Ch3 and Ch36, respectively) are illustrated in Fig. 2.2. Ch3 (Fig. 2.2a) is a Type II (FeO-rich) porphyritic olivine pyroxene (POP) chondrule. It is dominated by a single large (450 μm) olivine grain in addition to smaller grains of olivine (up to 150 μm) and low-Ca pyroxene

(up to 75 μm). The olivine grains show normal igneous zoning and the low-Ca pyroxene grains have oscillatory zoning (Fig. 2.2b). Calcium-rich pyroxene is present around the perimeters of the low-Ca pyroxene grains. The albite has a composition of An_2 and is present predominantly along the chondrule perimeter in bunches of thin, 1-8 μm wide, laths (Fig. 2.2b) up to 60 μm in length within the chondrule glass. Some of these laths are curved and have convex terminations indicating rapid growth. Albite luminesces bright blue in the CL image (Fig. 2.2b, inset), but the glass does not luminesce significantly making albite easy to recognize via CL in this, and other, albite-bearing chondrules. Along the chondrule edge, in contact with the matrix, mesostasis glass is partially altered to phyllosilicates and the albite laths are zoned subparallel to the regions of alteration (Fig. 2.2c).

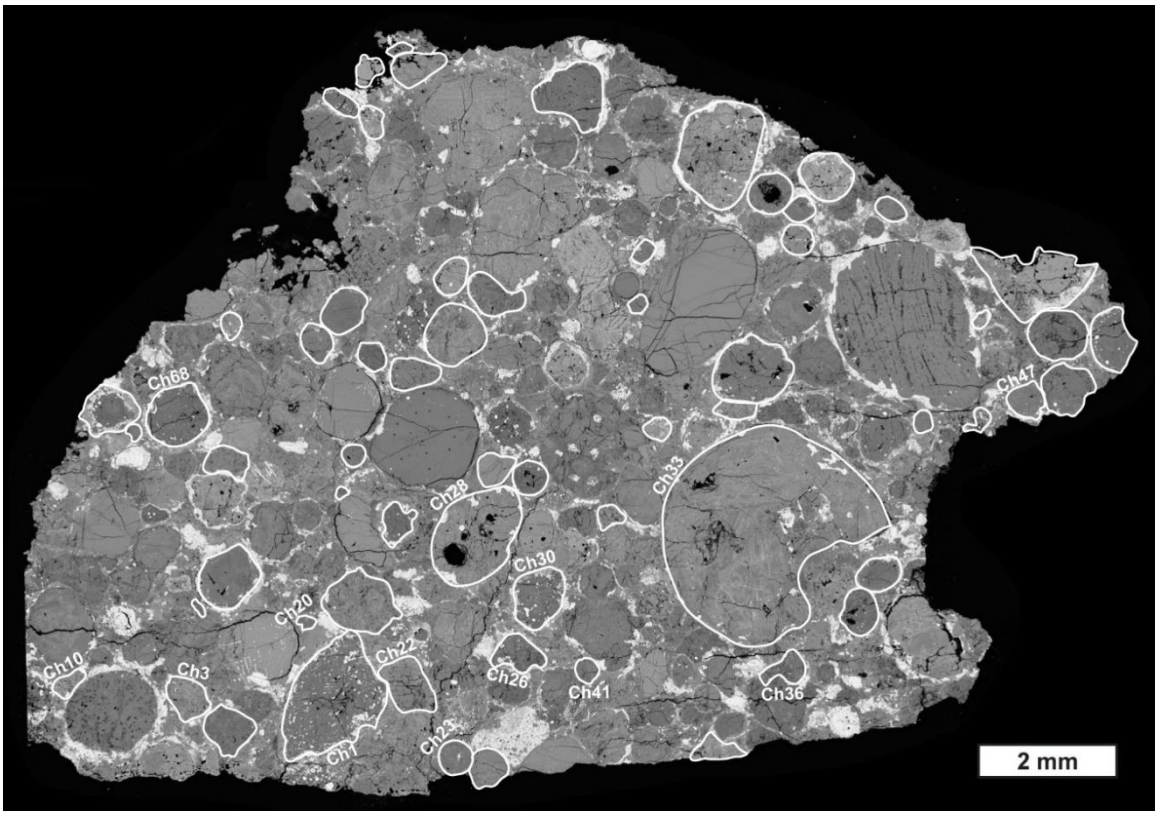

Figure 2.1. BSE mosaic of Semarkona thin section UNM 549. Plagioclase-bearing chondrules are circled in white. Numbered chondrules are referenced in the text, figures, and tables.

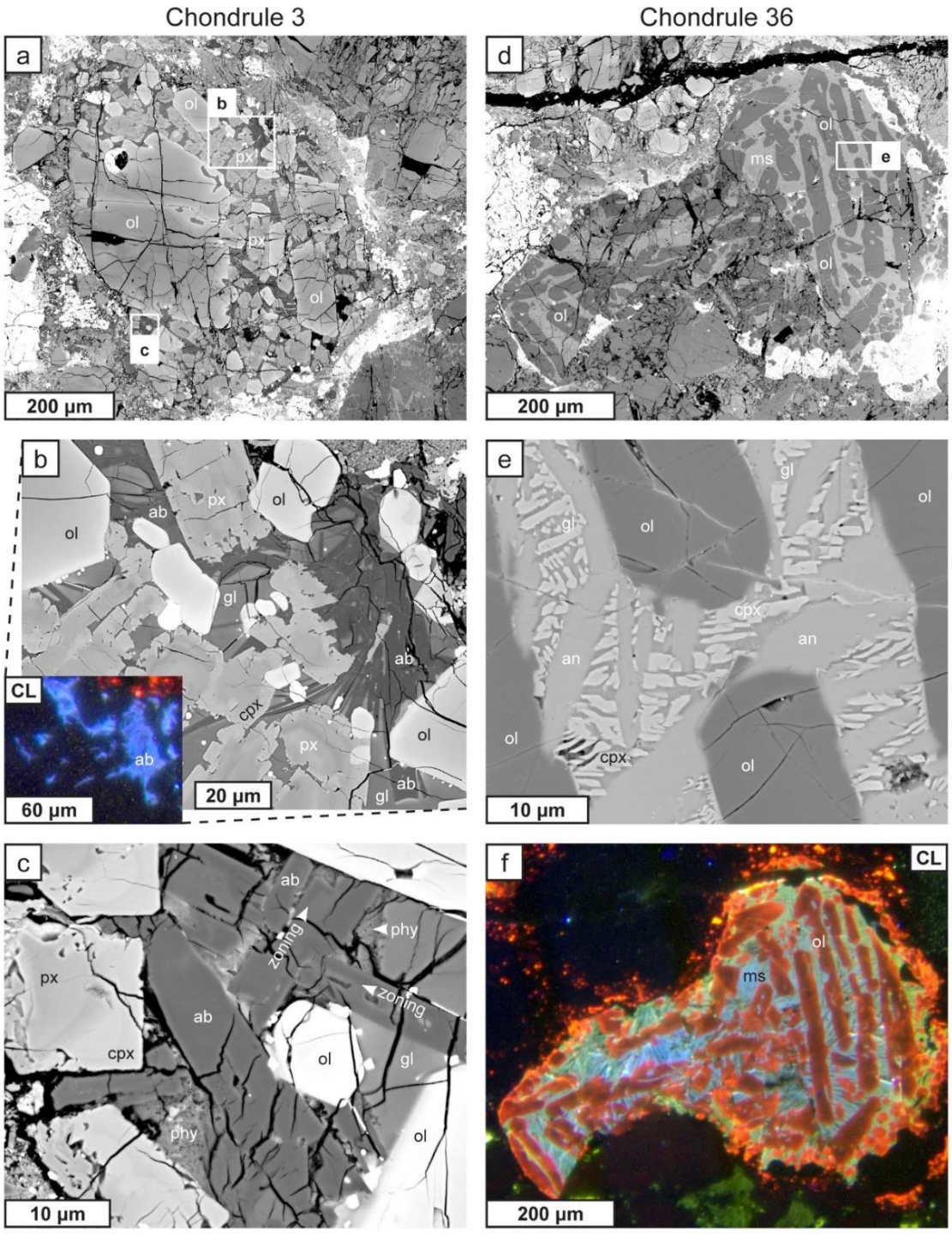

Figure 2.2. Examples of albite- and anorthite-bearing chondrules with end-member plagioclase compositions. (a,b) BSE images of Ch3, a Type I POP chondrule with laths of albite (ab, An_2) in mesostasis glass (gl) between grains of olivine (ol), low-Ca pyroxene (px), and Ca-rich pyroxene (cpx). Inset in (b) shows CL image of same region illustrating the bright blue luminescence of albite laths. (c) Region of Ch3 along the rim in which the albite laths are zoned and some of the glass is replaced by phyllosilicates (phy). *(Caption continues on the following page).*

Figure 2.2. *(Caption continued from the previous page).* (d,e) BSE images of Ch36, an FeO-poor BO chondrule with light grey mesostasis (ms) and laths of anorthite (an, An_{99}) between the olivine bars. Ca-rich pyroxene and glass occur interstitial to the anorthite. (f) CL image of the entire chondrule in which the anorthite luminesces light blue and the glass luminesces pale yellow in the center and bright yellow along the rim.

Ch36 (Fig. 2.2d) is an FeO-poor barred olivine (BO) chondrule that has 10-30 μm wide bars of forsteritic olivine. The chondrule has extensive fracturing, particularly in the central region, and appears to have been crushed. Between the olivine bars are abundant 1-6 μm wide laths of anorthite (An_{99}, Fig. 2.2e). Interstitial to the anorthite laths are small (~1 μm) clinopyroxene quench crystallites and minor remnant glass. The glass is largely intact but is replaced by voids in a few places throughout the chondrule. A CL image of Ch36 (Fig. 2.2f) shows the plagioclase luminescing light blue. Olivine bars luminesce red and are zoned, with the brightest parts toward the exterior of the grains. The mesostasis glass luminesces bright yellow along the chondrule rim and pale yellow toward the interior.

Representative BSE images of chondrules that contain plagioclase with intermediate compositions are shown in Fig. 3. Ch28 (Fig. 2.3a) is a Type II POP chondrule with olivine grains up to 150 μm long and low-Ca pyroxene grains up to 250 μm long. Like in Ch3, the olivine and low-Ca pyroxene grains in Ch28 are zoned and Ca-rich pyroxene is found along the perimeter of the olivine and low-Ca pyroxene grains. Several large voids (up to 370 μm in diameter) are present in the chondrule interior. Albitic plagioclase (Fig. 3b) is present as 1-6 μm wide laths interstitial to the olivine and pyroxene grains throughout the chondrule and is zoned with a range of compositions from An_3 to An_{19}. Pores and porous phyllosilicates are present within, and between, the plagioclase laths.

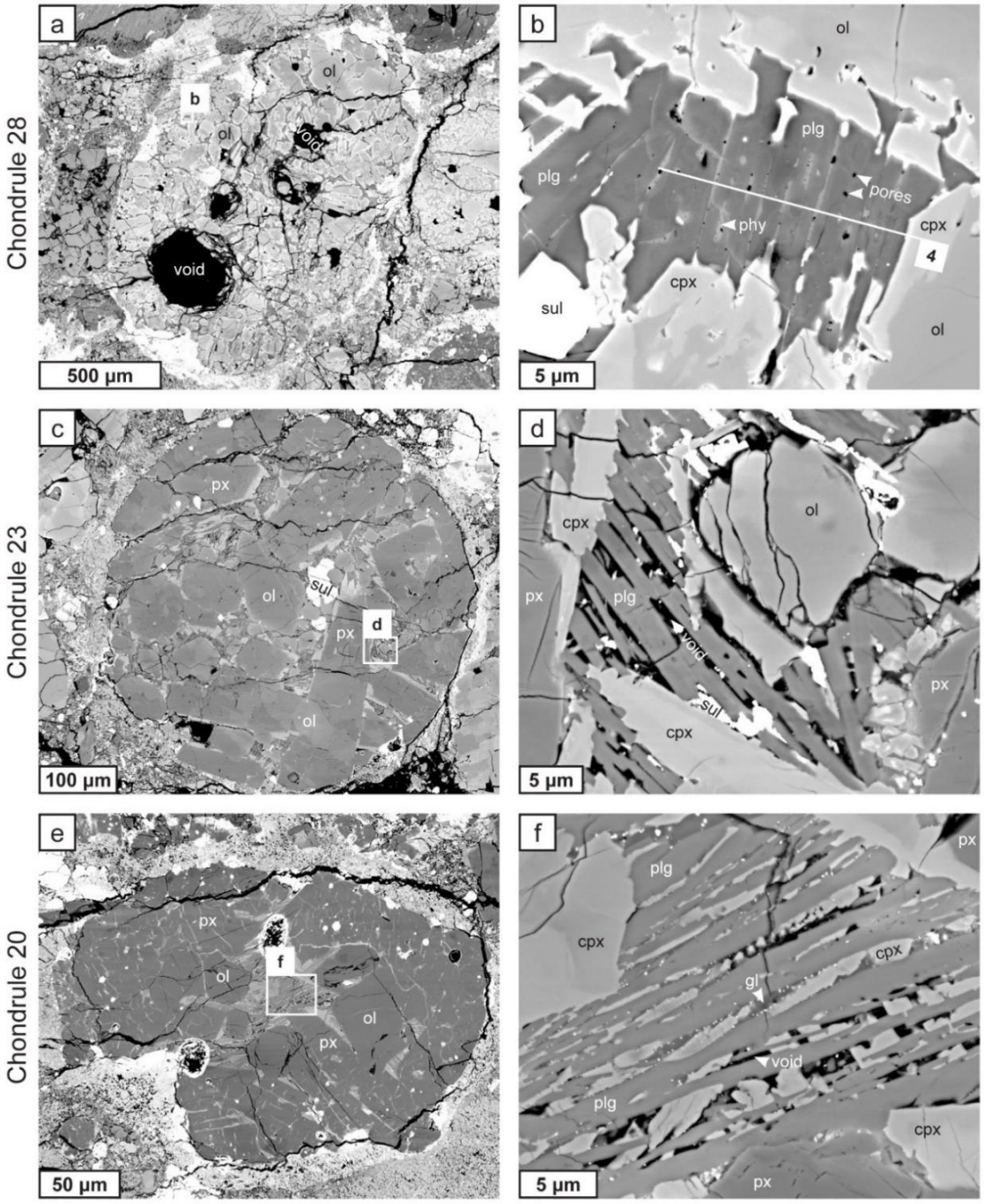

Figure 2.3. Examples of chondrules with plagioclase of intermediate composition. Ch28 (a,b) is a Type II POP chondrule with large voids. Plagioclase (plg, An_{10}) in this chondrule is present as laths interstitial to grains olivine (ol), Ca-rich pyroxene (cpx), and minor sulfides (sul). The plagioclase is zoned and pores and phyllosilicates are present between the plagioclase laths. The white line shows the region from which a FIB section was made (see Fig. 2.4). Ch23 (c,d) is a Type I POP chondrule with plagioclase (An_{37}) interstitial to olivine, low-Ca pyroxene (px), and Ca-rich pyroxene. The mesostasis glass has been completely leached out and is replaced with voids. *(Caption continues on the following page).*

Figure 2.3. *(Caption continued from the previous page).* Ch20 (e,f) is a Type I POP chondrule with plagioclase (An_{66}) interstitial to low-Ca pyroxene and some Ca-rich pyroxene. Smaller grains of Ca-rich pyroxene and glass are present in between the plagioclase laths as well as some areas of leached mesostasis glass that are replaced with void space.

A FIB section (Fig. 2.4a) was extracted from Ch28 (white line in Fig. 2.3b) to further investigate the plagioclase zoning seen in the BSE image (Fig. 2.3b). Plagioclase laths in the HAADF STEM image (Fig. 2.4b) show zoning parallel to the grain boundaries. This zoning is visible in the Ca EDS map (Fig. 2.4c) that shows that Ca is moderately enriched in the core but heterogeneously distributed from core to rim within individual laths. The outer ~100 nm of the laths are Ca-poor and a narrow region of Ca-enrichment is present between the core and Ca-poor rim. Between the plagioclase laths, adjacent to the Ca-poor zones, are porous phyllosilicates. Vertical lineations in Fig. 2.4a, also seen in Fig. 2.4b inclined to the right, are a curtaining artefact produced during sample preparation.

Ch23 (Fig. 2.3c) is a Type I (FeO-poor) POP chondrule containing large low-Ca pyroxene grains up to 250 μm long and smaller (up to 150 μm long), zoned olivine grains. Interstitial to the major grains are 1-2 μm wide laths of intermediate plagioclase (An_{37}, Fig. 2.3d), up to 30 μm long. The plagioclase laths are zoned like those in Ch28 and much of the mesostasis interstitial to the plagioclase laths appears to have been dissolved away as it is now void space. Ca-rich pyroxene is found along the perimeter of the low-Ca pyroxene grains with plagioclase largely interstitial to it. However, the terminations of the plagioclase laths slightly embay into the Ca-rich pyroxene.

Ch20 (Fig. 2.3e) is also a Type I POP chondrule with 30-70 μm olivine grains clustered near the interior and pyroxene grains up to 120 μm long near the chondrule exterior. Plagioclase is located at the center of the chondrule and occurs as 1-3 μm wide

laths, up to 60 μm long, with a composition of An_{66} (Fig. 2.3f). Ca-rich pyroxene is present both interstitial to the plagioclase laths and along the low-Ca pyroxene perimeters. Like Ch23, some of the mesostasis glass appears to have been dissolved away, leaving voids interstitial to the plagioclase and Ca-rich pyroxene grains.

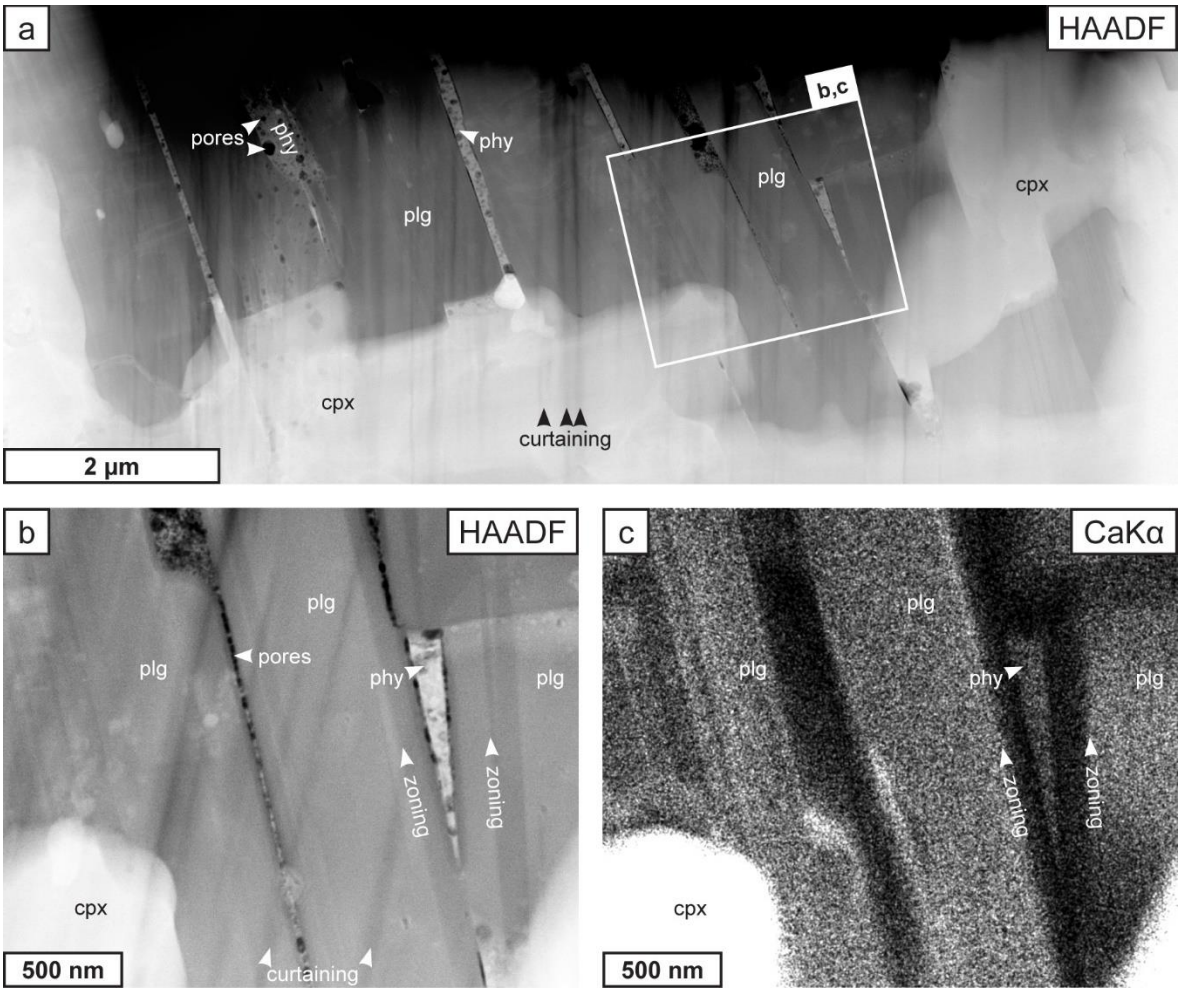

Figure 2.4. FIB section from Ch28 (see Fig. 2.3b). (a) HAADF image showing plagioclase (plg), Ca-rich pyroxene (cpx), and porous phyllosilicates (phy) interstitial to the plagioclase laths. Vertical banding is curtaining, a sample preparation artefact. (b) Close-up of selected area in (a) illustrating zoning in the plagioclase laths and the relationship of zoning to grain boundaries, pores, and phyllosilicates. (c) Ca Kα EDS image of the same region as (b) which illustrates the loss, and heterogeneous zoning, of Ca in the altered plagioclase.

3.2. Feldspar compositions

EPMA data for feldspar measured in 14 chondrules are presented in Fig. 2.5, average compositions for individual chondrules are given in Table 2.1, and individual analyses are tabulated in Appendix 1. Feldspar compositions span the full range along the Ab-An plagioclase join, from An_2 to An_{100}. The K_2O contents are minor but increases slightly with decreasing An content to a maximum of Or_2 in Ch3 (An_2). No K-feldspar was observed in any of the chondrules. The compositional range of plagioclase within each chondrule varies considerably from chondrule to chondrule. In the truncated ternary diagram in Fig. 2.5, each spot represents an individual analysis. On the scale to the left, we illustrate the range in anorthite content by plotting the average plagioclase composition for each chondrule with error bars representing one standard deviation of the mean.

Greater compositional ranges are correlated with secondary features such as dissolved mesostasis glass and the presence of phyllosilicates (e.g., Ch28: Figs. 2.3b and 2.4 and Ch23: Fig. 2.3d). Ch3 also has phyllosilicates and dissolved mesostasis glass (Fig. 2.2c) but a low standard deviation in its An content because only a few of the plagioclase grains in contact with the matrix have undergone alteration. Ch10 has the greatest standard deviation because only 3 points are included in the calculation and there is a 15 mol % spread between the highest and lowest values (An_{21}-An_{36}). The lowest An value measured in Ch10 is associated with the region of greatest alteration.

Cr_2O_3 and MnO contents of plagioclase in all chondrules are low, typically less than 0.1 wt.% each, and there is no correlation with anorthite content. The FeO and MgO contents of the plagioclase vary greatly from chondrule to chondrule as well as within

each chondrule but can be of significant abundance (up to 4.5 wt.% total in individual analyses). It is not clear whether these elements are incorporated into plagioclase or not, and if they are incorporated, how they are substituting into the crystal structure. The high abundances of these elements do not correlate significantly with An content as would be expected if they were directly substituting for Ca, and the system is too reducing for Fe to be trivalent and substitute for Al. However, the Mg# (Mg/(Mg+Fe)) of the plagioclase does correlate with An content, for example atomic Mg# = 24 and 95 for An_2 and An_{99}, respectively, suggesting that the compositions were determined during crystallization. FeO and MgO (up to 3 and 1.2 wt.%, respectively) are commonly reported in meteoritic plagioclase over a range of compositions, summarized by Smith and Brown (1988), so the presence of these cations in our measurements is not unusual. The crystallization conditions may be such that the incorporation of FeO and MgO into plagioclase represents a disequilibrium feature of rapid plagioclase growth.

However, Smith and Brown (1988) caution the over interpretation of feldspar EPMA data without careful consideration of the analytical conditions. Secondary fluorescence can be a major issue, particularly in Fe-rich samples. It is also possible that some of the FeO and MgO content comes from analytical overlap of adjacent phases such as Ca-rich pyroxene, metals, and sulfides. Despite using low accelerating voltages (10-15 kV) during EPMA analysis to reduce the analytical interaction volume, the small size of the plagioclase laths (~1-5 μm wide) means some overlap with other mesostasis phases is difficult to avoid. Hence, we cannot be sure that the analyses are not influenced by analytical artefacts. However, TEM EDS estimated up to 0.5 wt.% FeO and 0.2 wt.% MgO in Ch28 zoned plagioclase (Fig. 2.4), values in the range of those measured by

EPMA for Ch28. This suggests that at least some of the FeO and MgO measured by EMPA resides in plagioclase.

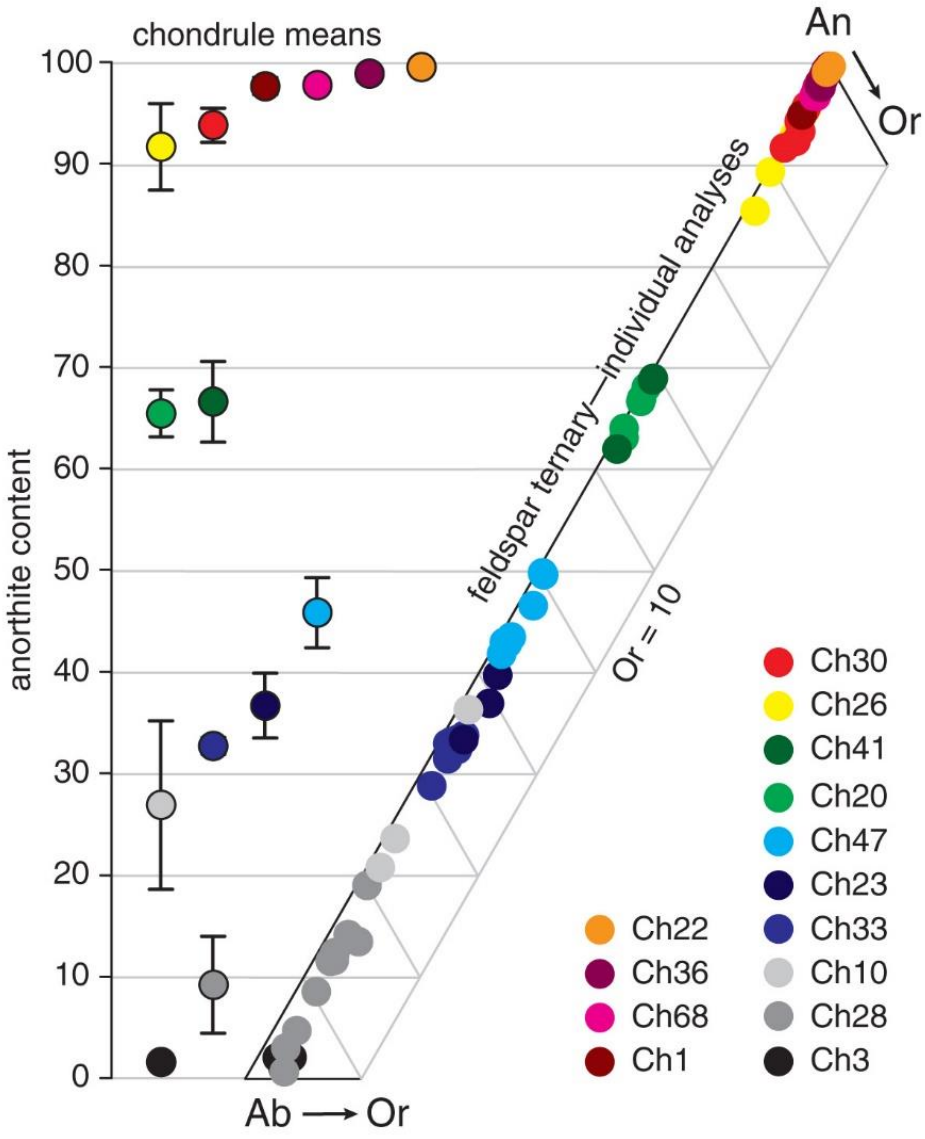

Figure 2.5. Compositions of plagioclase measured by EPMA. The range of measured plagioclase compositions in Semarkona chondrules is illustrated on the left. Each point represents the mean plagioclase composition in each chondrule. Error bars represent 1 standard deviation of the mean and the points are offset horizontally for ease of viewing. Individual analyses are plotted on a feldspar ternary on the right. The ternary is truncated at Or_{10} and the colors in the ternary correspond to those for the chondrule means on the left-hand side of the diagram.

Table 2.1. Average feldspar compositions.

	Chondrule 3		Chondrule 28		Chondrule 10		Chondrule 33		Chondrule 23		Chondrule 47		Chondrule 20	
	wt. %	*1σ*	wt. %	*1σ*	wt. %	*1σ*	wt. %	*1σ*	wt. %	*1σ*	wt. %	*1σ*	wt. %	*1σ*
SiO_2	69.4	*0.9*	65.8	*2.1*	62.2	*2.5*	60.4	*0.7*	61.7	*1.2*	57.2	*1.1*	53.1	*0.9*
Al_2O_3	18.3	*0.6*	20.4	*0.8*	20.4	*1.8*	23.0	*1.1*	22.4	*0.6*	26.2	*1.1*	27.6	*1.0*
Cr_2O_3	0.01	*0.01*	0.02	*0.01*	0.04	*0.02*	0.02	*0.01*	0.08	*0.05*	0.04	*0.04*	0.05	*0.03*
FeO	1.29	*0.55*	1.33	*0.74*	2.13	*0.15*	1.92	*1.08*	1.34	*0.20*	0.58	*0.24*	0.50	*0.27*
MnO	0.04	*0.02*	0.04	*0.02*	0.03	*0.01*	0.06	*0.04*	0.18	*0.07*	0.07	*0.06*	0.14	*0.04*
MgO	0.23	*0.06*	0.31	*0.40*	1.07	*0.06*	0.33	*0.32*	1.42	*0.71*	0.51	*0.13*	1.31	*0.49*
CaO	0.41	*0.17*	2.15	*1.15*	5.71	*1.59*	6.61	*0.35*	7.03	*0.82*	9.50	*0.82*	13.2	*0.7*
Na_2O	11.3	*0.6*	10.3	*0.7*	8.50	*1.20*	7.50	*0.29*	6.48	*0.40*	6.09	*0.36*	3.73	*0.24*
K_2O	0.43	*0.10*	0.34	*0.11*	0.19	*0.03*	0.26	*0.06*	0.33	*0.04*	0.15	*0.04*	0.08	*0.03*
Total	101.4	*1.5*	100.8	*0.9*	100.2	*1.1*	100.2	*0.7*	101.0	*0.7*	100.3	*0.8*	99.7	*1.0*
						formula based on 8 oxygens								
Si	3.01	*0.01*	2.89	*0.06*	2.79	*0.09*	2.71	*0.02*	2.73	*0.05*	2.57	*0.05*	2.42	*0.04*
Al	0.94	*0.02*	1.06	*0.05*	1.08	*0.10*	1.22	*0.05*	1.17	*0.03*	1.38	*0.05*	1.48	*0.05*
Cr	0.00	*0.00*	0.00	*0.00*	0.00	*0.00*	0.00	*0.00*	0.00	*0.00*	0.00	*0.00*	0.00	*0.00*
Fe	0.05	*0.02*	0.05	*0.03*	0.08	*0.01*	0.07	*0.04*	0.05	*0.01*	0.02	*0.01*	0.02	*0.01*
Mn	0.00	*0.00*	0.00	*0.00*	0.00	*0.00*	0.00	*0.00*	0.01	*0.00*	0.00	*0.00*	0.01	*0.00*
Mg	0.01	*0.00*	0.02	*0.03*	0.07	*0.01*	0.02	*0.02*	0.09	*0.05*	0.03	*0.01*	0.09	*0.03*
Ca	0.02	*0.01*	0.10	*0.05*	0.27	*0.08*	0.32	*0.02*	0.33	*0.04*	0.46	*0.04*	0.64	*0.03*
Na	0.95	*0.03*	0.88	*0.05*	0.74	*0.11*	0.65	*0.02*	0.56	*0.04*	0.53	*0.03*	0.33	*0.02*
K	0.02	*0.01*	0.02	*0.01*	0.01	*0.00*	0.01	*0.00*	0.02	*0.00*	0.01	*0.00*	0.00	*0.00*
Total	5.01	*0.02*	5.03	*0.02*	5.05	*0.03*	5.01	*0.02*	4.97	*0.04*	5.01	*0.01*	5.00	*0.01*
An	1.9	*0.8*	10.1	*5.4*	26.9	*8.3*	32.3	*1.6*	36.7	*3.2*	45.9	*3.5*	65.8	*2.1*
Ab	95.7	*0.7*	88.0	*5.1*	72.0	*8.2*	66.2	*1.6*	61.2	*3.1*	53.3	*3.3*	33.7	*2.0*
Or	2.4	*0.6*	1.9	*0.6*	1.0	*0.1*	1.5	*0.4*	2.1	*0.4*	0.9	*0.3*	0.5	*0.2*
n[1]	4		11		3		8		3		8		5	

[1] n = number of analyses

Table 2.1. *(Continued)*. Average feldspar compositions.

	Chondrule 41		Chondrule 26		Chondrule 30		Chondrule 1		Chondrule 68		Chondrule 36		Chondrule 22	
	wt. %	*1σ*	wt. %	*1σ*	wt. %	*1σ*	wt. %	*1σ*	wt. %	*1σ*	wt. %	*1σ*	wt. %	*1σ*
SiO_2	52.6	*1.3*	46.2	*1.1*	48.8	*0.8*	49.9	*0.6*	44.3	*1.1*	48.3	*0.7*	44.8	*0.6*
Al_2O_3	28.5	*1.0*	32.6	*2.2*	30.4	*1.5*	30.9	*0.8*	34.0	*1.9*	30.0	*1.3*	35.5	*0.6*
Cr_2O_3	0.04	*0.02*	0.03	*0.02*	0.06	*0.03*	0.03	*0.03*	0.05	*0.06*	0.02	*0.02*	0.02	*0.02*
FeO	1.03	*0.59*	0.90	*0.92*	0.49	*0.25*	0.43	*0.20*	0.17	*0.14*	0.20	*0.15*	1.03	*0.19*
MnO	0.10	*0.06*	0.06	*0.04*	0.05	*0.05*	0.02	*0.02*	0.03	*0.03*	0.01	*0.01*	0.03	*0.02*
MgO	0.99	*0.37*	1.64	*1.17*	1.83	*1.08*	1.82	*0.68*	1.20	*1.26*	2.19	*0.37*	0.73	*0.20*
CaO	13.3	*1.0*	17.8	*1.3*	17.6	*0.5*	18.3	*0.3*	19.5	*0.4*	19.4	*0.3*	19.8	*0.2*
Na_2O	3.61	*0.36*	0.84	*0.42*	0.60	*0.17*	0.22	*0.09*	0.22	*0.07*	0.10	*0.07*	0.04	*0.03*
K_2O	0.09	*0.03*	0.07	*0.04*	0.07	*0.06*	0.03	*0.01*	0.04	*0.02*	0.03	*0.02*	0.04	*0.01*
Total	100.2	*0.9*	100.2	*1.3*	99.9	*0.8*	101.7	*0.7*	99.4	*0.6*	100.3	*0.7*	102.1	*0.3*
						formula based on 8 oxygens								
Si	2.39	*0.05*	2.13	*0.05*	2.24	*0.04*	2.25	*0.02*	2.06	*0.05*	2.22	*0.04*	2.04	*0.03*
Al	1.53	*0.05*	1.77	*0.10*	1.65	*0.07*	1.64	*0.04*	1.87	*0.11*	1.62	*0.06*	1.91	*0.03*
Cr	0.00	*0.00*	0.00	*0.00*	0.00	*0.00*	0.00	*0.00*	0.00	*0.00*	0.00	*0.00*	0.00	*0.00*
Fe	0.04	*0.02*	0.03	*0.04*	0.02	*0.01*	0.02	*0.01*	0.01	*0.01*	0.01	*0.01*	0.04	*0.01*
Mn	0.00	*0.00*	0.00	*0.00*	0.00	*0.00*	0.00	*0.00*	0.00	*0.00*	0.00	*0.00*	0.00	*0.00*
Mg	0.07	*0.03*	0.11	*0.08*	0.13	*0.07*	0.12	*0.05*	0.08	*0.09*	0.15	*0.03*	0.05	*0.01*
Ca	0.65	*0.05*	0.88	*0.05*	0.86	*0.02*	0.89	*0.01*	0.97	*0.02*	0.96	*0.01*	0.97	*0.01*
Na	0.32	*0.03*	0.08	*0.04*	0.05	*0.02*	0.02	*0.01*	0.02	*0.01*	0.01	*0.01*	0.00	*0.00*
K	0.01	*0.00*	0.00	*0.00*	0.00	*0.00*	0.00	*0.00*	0.00	*0.00*	0.00	*0.00*	0.00	*0.00*
Total	5.00	*0.02*	5.02	*0.02*	4.96	*0.03*	4.94	*0.02*	5.02	*0.02*	4.97	*0.01*	5.01	*0.01*
An	66.6	*4.0*	91.7	*4.3*	93.8	*1.7*	97.7	*0.8*	97.8	*0.8*	98.9	*0.7*	99.5	*0.2*
Ab	32.8	*3.8*	7.9	*4.1*	5.7	*1.5*	2.1	*0.8*	2.0	*0.7*	1.0	*0.6*	0.3	*0.3*
Or	0.6	*0.2*	0.4	*0.3*	0.4	*0.4*	0.2	*0.1*	0.2	*0.1*	0.2	*0.1*	0.2	*0.0*
n[1]	3		5		6		16		7		15		4	

[1] n = number of analyses

3.3. Bulk chondrule composition and modal mineralogy

Bulk silicate compositions of selected chondrules measured using quantitative EPMA maps are tabulated in Table 2.2. The oxide maps used to determine the bulk compositions are illustrated in Fig. 2.6. The data show a clear trend of increasing An content in plagioclase with increasing bulk Mg#. With increasing An contents in the plagioclase, the bulk chondrule Na/Al ratio decreases (1.1-0.1) but the Ca/Al ratio remains constant across the four chondrules (1.4-1.5). K_2O is enriched in the type II chondrule Ch3 (0.13 wt.%) relative to the other three chondrules which have relatively constant, and low, K_2O abundances (0.07-0.08 wt.%). Bulk Cr_2O_3 is depleted in the BO chondrule Ch36 (0.25 wt.%) relative to the other three chondrules that are similar in Cr_2O_3 content (0.63-0.71 wt.%).

The modal silicate mineralogy of the chondrules (Table 2.2) was estimated from the EPMA maps which and are illustrated as mineral maps in Fig. 2.6. Ch3 is a POP chondrule dominated by olivine (63%) and containing approximately equal amounts of low-Ca pyroxene and Ca-rich pyroxene (13% and 14%, respectively), and 10% mesostasis. The measured mesostasis abundance includes plagioclase, glass, and small amounts of Ca-rich pyroxene. Ch23 and Ch20 are similar with 27% and 19% olivine, 57% and 66% low-Ca pyroxene, similar amounts of Ca-rich pyroxene (7%), and 9% and 8% mesostasis, respectively. The BO chondrule Ch36 consists of 66% olivine and 32% mesostasis. The 2% that was measured as Ca-rich pyroxene represents large grains while most of the Ca-rich pyroxene is ~1 μm in size (Fig. 2.2e) and is included in the reported mesostasis abundance.

Table 2.2. Bulk silicate compositions of selected chondrules.

	Ch3 Type II	Ch23 Type I	Ch20 Type I	Ch36 BO
SiO_2	45.4	52.1	53.9	43.4
Al_2O_3	2.08	2.44	2.50	6.93
Cr_2O_3	0.63	0.78	0.71	0.25
FeO	16.3	5.31	3.43	1.76
MgO	32.7	36.7	37.1	41.7
CaO	1.58	1.99	1.91	5.65
Na_2O	1.21	0.59	0.40	0.28
K_2O	0.13	0.08	0.07	0.07
Total	100.0	100.0	100.0	100.0
Mg#[1]	66.8	87.4	91.5	95.9
Mg#[2]	78.2	92.5	95.1	97.7
Na/Al[3]	1.1	0.5	0.3	0.1
Ca/Al[3]	1.4	1.5	1.4	1.5
An[4]	1.9	36.7	65.8	98.9
Liquidus[5]	1672 °C	1688 °C	1685 °C	1744 °C
	Modal mineral abundances[6]			
Olivine	63%	27%	19%	66%
Low-Ca pyx	13%	57%	66%	0%
Ca-pyx	14%	7%	7%	2%
Mesostasis[7]	10%	9%	8%	32%

[1] Mg# = Mg/(Mg+Fe)x100, wt. % oxide
[2] Mg# = Mg/(Mg+Fe)x100, atomic
[3] atomic
[4] average plagioclase composition, from Table 2.1
[5] estimated using Rhyolite-MELTS
[6] estimated from EPMA maps (see Fig. 2.6)
[7] includes glass, plagioclase, and minor Ca-rich pyroxene

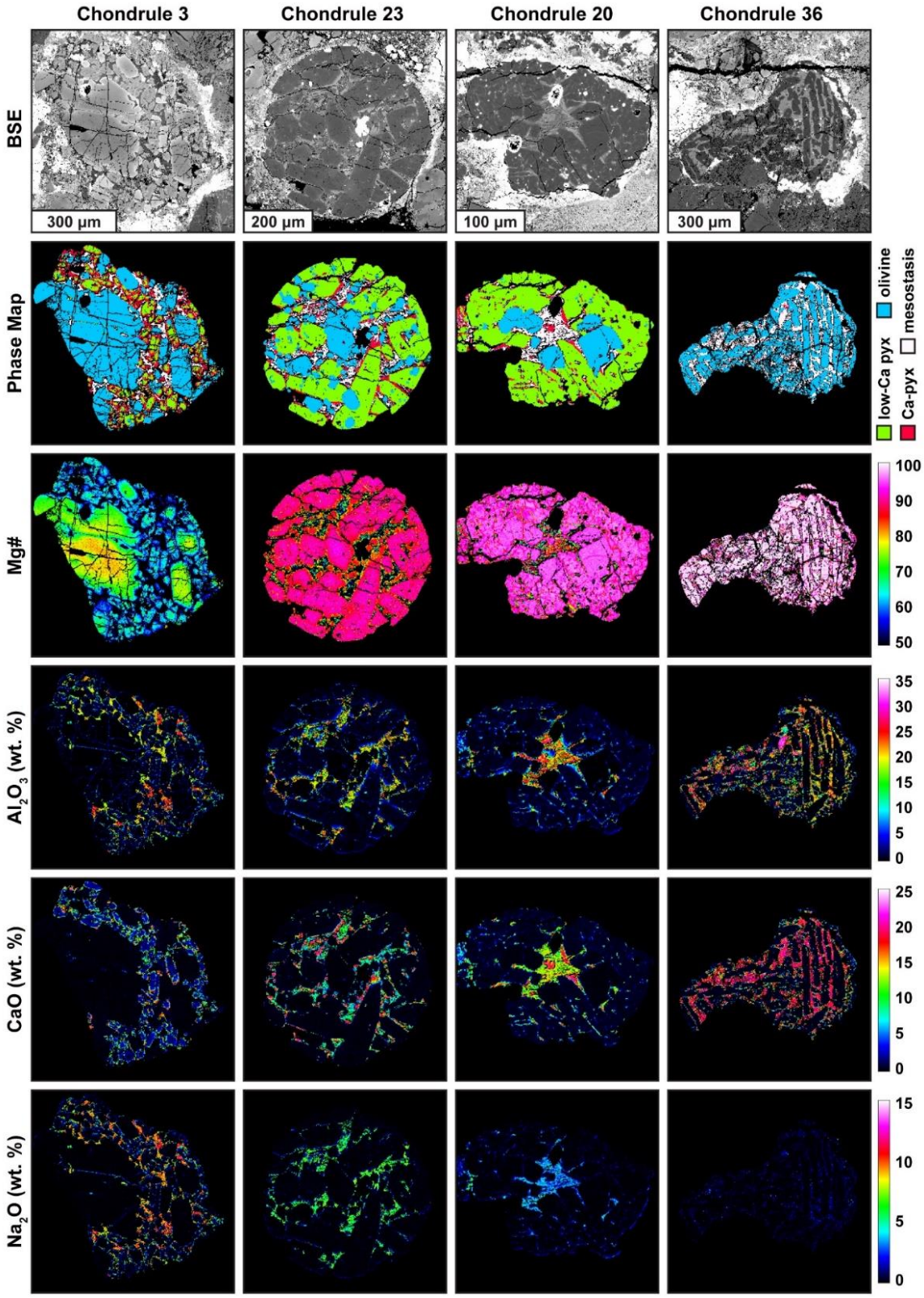
Chondrule 3
Chondrule 23
Chondrule 20
Chondrule 36
BSE
300 µm
200 µm
100 µm
300 µm
Phase Map
olivine
mesostasis
low-Ca pyx
Ca-pyx
Mg#
100
90
80
70
60
50
Al2O3 (wt. %)
35
30
25
20
15
10
5
0
CaO (wt. %)
25
20
15
10
5
0
Na2O (wt. %)
15
10
5
0

Figure 2.6. *(On previous page).* Data from EPMA maps of Ch3, Ch23, Ch20, and Ch36, used to determine bulk chondrule compositions. The anorthite content of primary plagioclase in these chondrules increases from left (An_2) to right (An_{99}). The first row shows BSE images for each chondrule. The second row shows phase maps highlighting the dominant phases of olivine (blue), low-Ca pyroxene (green), Ca-rich pyroxene (red), and mesostasis (white). Here, mesostasis consists of glass, plagioclase, and minor Ca-rich pyroxene. The third row shows atomic Mg# maps illustrating the increase in Mg# from left to right. Rows 4, 5, and 6 show quantitative wt. % oxide maps of Al_2O_3, CaO, and Na_2O, respectively.

4. Discussion

Primary chondrule minerals contain important information about physical and chemical conditions present in the solar nebula during chondrule formation. They can provide information about the timing of the chondrule forming event through relative radiogenic chronometers (e.g., Al-Mg dating), and about cooling rates through petrologic studies. Characterizing primary minerals is also important for revealing the effects of secondary processes. Because these processes alter the chemistry and mineralogy of chondrules, well characterized primary minerals are important for interpreting the effects of thermal metamorphism and metasomatism.

While the presence of primary plagioclase has been noted in OC chondrules before (e.g., Grossman and Brearley 2005; Huss et al. 2001; Russell et al. 2000), its petrography and relation to bulk chondrule composition have not been studied in detail. In the discussion that follows, we will show that primary plagioclase nucleated and grew as a primary igneous phase during chondrule cooling, discuss the conditions under which it formed, and consider the implications for chondrule formation including cooling rates and nebular environment. We will also show how secondary features in plagioclase indicate parent body alteration and discuss why an accurate chondrule chronology depends on detailed investigations of chondrule mineralogy.

4.1. Primary igneous plagioclase

Although plagioclase is not thought of as a common primary mineral in OC chondrules, we show that it is relatively abundant. Brearley and Jones (1998) did not mention plagioclase in their review of chondrules in type 3 OC. However, anorthite has been noted in Al-rich OC chondrules (Huss et al. 2001; Russell et al. 2000), used largely for Al-Mg chronology, and crystalline albite was seen in a Semarkona chondrule (Grossman and Brearley 2005). It is important first to show that the plagioclase within these chondrules is a primary igneous phase, so that we can use it to understand chondrule formation and the nebular environment in which chondrules were formed.

4.1.1. Feldspar as an igneous phase

Mineral textures can be used to illustrate the igneous nature of plagioclase in Semarkona chondrules. The plagioclase grains we observe are smooth laths, regardless of their composition (Figs. 2.2b,c,e, 2.3b,d,f), consistent with an igneous origin. In contrast, plagioclase that crystallizes from devitrified mesostasis glass is extremely fine grained in the lower petrologic types and does not display a lath-like morphology (Huss et al. 2006). The morphology of plagioclase in Ch3 (Fig. 2.2b) is similar to fan spherulites, indicating rapid growth with high degrees of undercooling (Corrigan 1982; Lofgren 1974). Albitic laths such as these are common in the outer portions of albite-bearing chondrules. An external nucleation agent such as nebular dust impinging on the outside of the chondrule could have helped the plagioclase to nucleate and, combined with undercooling, grow rapidly as the textures indicate. In a similar manner, Connolly and Hewins (1995) were able to experimentally reproduce a variety of chondrule textures by puffing dust onto the surface of molten chondrule droplets to induce nucleation. Although these experiments

did not produce plagioclase, it is a reasonable mechanism for producing the albite textures we observe here.

Another way to assess whether the plagioclase in Semarkona chondrules is a primary phase is to look at the bulk compositions of the chondrules in which it is found. A relationship between plagioclase composition and bulk chondrule composition is expected for growth of plagioclase from the melt. As discussed above, the anorthite content in chondrule plagioclase is directly related to the bulk composition of the chondrule: increasing atomic Mg# from 78 to 98 in the bulk chondrule corresponds to average plagioclase compositions varying from An_2 to An_{99}, an increase in bulk chondrule abundances of refractory elements Al and Ca, and a decrease in the volatile element Na (Table 2.2). Because the Ca/Al ratio is constant across the four measured chondrules, the composition of the plagioclase seems tied to the bulk Na abundance and Na/Al ratio, which in turn is inversely correlated with Mg#, as has been shown previously Grossman and Wasson (1983).

We can use bulk chondrule and plagioclase compositions to provide upper limits on the temperatures at which the plagioclase formed. However, as we discuss further below, plagioclase and mesostasis glass in some of these chondrules have been affected by aqueous alteration, although the major phases (olivine and pyroxene) appear unaffected. Because plagioclase and mesostasis glass are rich in Na, Ca, Al, and Si, these elements are likely to differ slightly in the bulk silicate composition we measured when compared to the fresh, unaltered chondrule. For this discussion, we assume that the measured bulk silicate compositions are the original igneous compositions.

We used the thermodynamic model rhyolite-MELTS (Ghiorso and Gualda 2015; Gualda et al. 2012) to model the equilibrium crystallization of the bulk compositions listed in Table 2.2. We used rhyolite-MELTS instead of the classic MELTS package because of the increased computational stability added to rhyolite-MELTS. The calibration for low-SiO_2 compositions, relevant to the bulk composition of Semarkona chondrules, is the same for the two programs. Chondrule compositions were cooled from the calculated liquidus temperature (Table 2.2), in 1 °C increments, at a constant 1 bar pressure, and kept at a constant fO_2 along the IW buffer.

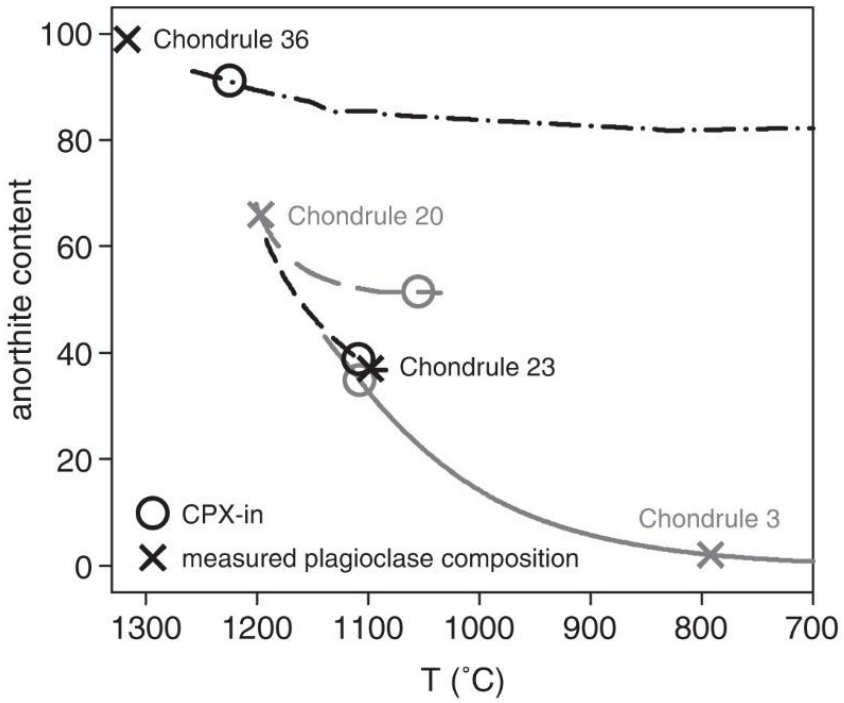

Figure 2.7. Results of equilibrium crystallization of chondrule bulk compositions in rhyolite-MELTS. Lines illustrate equilibrium plagioclase compositions with decreasing temperature (increasing crystallization). The average plagioclase composition measured in each chondrule is marked with a cross at the corresponding temperature. The plagioclase composition for Ch36 (An_{99}) is not on the plagioclase crystallization line, so the crystallization temperature of anorthite in the Fo-Di-An system (1317 °C) is plotted instead. Circles mark the temperatures at which Ca-rich pyroxene becomes stable. See text for details.

The results are illustrated in Fig. 2.7. Lines show the equilibrium plagioclase composition predicted to crystallize for each bulk chondrule composition. Crosses indicate measured plagioclase composition and corresponding equilibrium crystallization temperature. For Ch36, the cross is not on the line because the measured anorthite composition (An_{99}) was not produced during the modeled plagioclase crystallization: this will be discussed below. Circles indicate the point at which clinopyroxene becomes stable. For each chondrule, the range of plagioclase compositions predicted to crystallize from the bulk composition is close to the measured plagioclase composition from those chondrules: more anorthitic chondrules (Ch36 and Ch20) have plagioclase compositions closer to the first composition to crystallize whereas the more albitic chondrules (Ch23 and Ch3) are closer to the final compositions to crystallize.

Rhyolite-MELTS simulates batch crystallization under equilibrium conditions but the rapid cooling experienced by chondrules means that equilibrium conditions were unlikely during crystallization. In fact, due to the extremely slow rate of Si-Al interdiffusion, it is unlikely that any feldspar truly grows under equilibrium conditions (Brown and Parsons 1994). However, using rhyolite-MELTS to look at the equilibrium plagioclase compositions is instructive to understand the expected plagioclase compositions and to provide upper limits for formation temperatures. These temperatures are 1197, 1098, and 792 °C for Ch20, Ch23, and Ch3 respectively.

The measured plagioclase composition in Ch36 has a greater anorthite content (An_{99}) than the most anorthitic composition from the rhyolite-MELTS model (An_{93}). This puts a lower limit on the plagioclase crystallization temperature for this composition of >1260 °C, the temperature at which rhyolite-MELTS predicts that plagioclase would start

to form. We can also consider this chondrule within the ternary Fo-Di-An system in order to provide a better constraint on the upper limit of the plagioclase crystallization temperature. Forsterite, diopside, and anorthite are the three major phases present within this chondrule and their compositions are close to the Mg-free and Na-free endmembers of the system. We projected the bulk composition measured for Ch36 onto the Fo-Di-An ternary resulting in a relative composition of 70, 8, and 22 wt.% Fo, Di, and An, respectively, and close to the measured modal mineral abundances (Table 2.2). Under equilibrium crystallization conditions, the melt composition, which begins in the Fo primary field, intersects the Fo-An join around 1317 °C (Osborn and Tait 1952), consistent with the rhyolite-MELTS estimate of >1260 °C. The temperature of 1317 °C is used to indicate the plagioclase crystallization temperature for Ch36 on Fig. 2.7.

Figure 2.7 also shows the expected relative timing of plagioclase and Ca-rich pyroxene during equilibrium crystallization. Textures showing the relative timing of plagioclase and Ca-rich pyroxene crystallization are a further indicator that plagioclase is primary. Calcium-rich pyroxene is often one of the last silicate phases to crystallize in chondrules and it nucleates off the existing phenocrysts of olivine and low-Ca pyroxene (e.g., red in the phase maps in Fig. 2.6). The temperature at which Ca-rich pyroxene becomes stable is relatively insensitive to bulk composition (1055-1225 °C, Fig. 2.7). Because the crystallization temperature of plagioclase is strongly dependent on its composition, we would expect albitic plagioclase to crystallize after Ca-rich pyroxene and anorthitic plagioclase to crystallize before Ca-rich pyroxene but after low-Ca pyroxene. Ch3, Ch28, and Ch23 have albitic plagioclase compositions and the plagioclase is interstitial to the Ca-rich pyroxene growth (Figs. 2.2b,c, 2.3b,d). Ch20,

with an intermediate plagioclase composition (An_{66}), has plagioclase intergrown with Ca-rich pyroxene (Fig. 2.3f): Ca-rich pyroxene appears to have nucleated first but continued to grow during plagioclase crystallization. Ch36 has an anorthitic plagioclase composition (An_{99}) and Ca-rich pyroxene is present between plagioclase laths (Fig. 2.2e). Hence, despite the undercooling discussed above, our observations are broadly consistent with the equilibrium model.

Overall, the plagioclase textures, the dependence of plagioclase composition on bulk chondrule composition, the similarity of measured and modeled plagioclase compositions, and the relative crystallization of plagioclase and Ca-rich pyroxene provide evidence that the plagioclase in these chondrules is a primary igneous phase. Rhyolite-MELTS predicts a wide range in the equilibrium crystallization temperatures, 792-1317 °C. These are considered upper limits because of the effects of undercooling. The presence of primary plagioclase in chondrules has implications for chondrule formation that will be explored in the following section.

4.1.2. Implications for chondrule formation and chondrule forming conditions in the solar nebula

Chondrules are the most abundant constituent of the most common type of meteorite in our collections. Understanding chondrule formation is vital for understanding what appears to be a ubiquitous process (or set of processes) in the solar nebula (Connolly and Jones 2016). However, the myriad of petrologic and experimental constraints provided by chondrule chemistry and mineralogy have not yet stemmed the proliferation of chondrule formation models (Connolly and Desch 2004; Connolly and Jones 2016). Because plagioclase crystallizes at a lower temperature than the dominant

minerals found in chondrules, olivine and low-Ca pyroxene, and because most constraints are based on observations of those minerals, plagioclase can help put further constraints on the physical conditions and nebular environment in which chondrules formed.

We observe a wide range of plagioclase compositions (An_{37}-An_{100}) in FeO-poor chondrules. Plagioclase has not previously been recognized in Type I porphyritic chondrules in OCs (Brearley and Jones 1998) but it has been noted as a common phase in Al-rich OC chondrules (Huss et al. 2001; Russell et al. 2000). Plagioclase in Al-rich chondrules has a range of compositions (An_{70}-An_{100}) and is commonly $\geq An_{90}$ (Huss et al. 2001). Aluminum-rich chondrules have a close affinity to calcium-aluminum-rich inclusions that are anorthite-bearing. Anorthite has also been described in Type I chondrules in various CCs (Brearley and Jones 1998). Approximately 10% of Type I chondrules in CO chondrites contain anorthite (Jones 1997; Wick and Jones 2012). Type I chondrules are the dominant chondrule type in CO chondrites consisting of ~85% of all chondrules compared to only ~20% of OC chondrules (Jones 2012). The implications of anorthite-bearing Type I chondrules in CO chondrites were explored experimentally by Wick and Jones (2012). They melted a Type I chondrule-like composition at 1500-1600 °C and cooled the chondrules in stages at rates between 1 °C and 25 °C per hour. They found that only the slowest cooling rate (1 °C/hour in the final cooling stage from 1000-800 °C) could nucleate anorthitic plagioclase. All experiments with faster cooling rates produced glass instead of crystalline plagioclase.

We observed Na-rich plagioclase (An_{2}-An_{32}) in FeO-rich chondrules in Semarkona, which has not been widely recognize before (Brearley and Jones 1998; Jones 1990). This is not surprising due to the fine scale of the plagioclase laths observed in the

chondrules of this study (e.g., Fig. 2.2b). Grossman and Brearley (2005) identified crystalline albite in Semarkona chondrules through TEM analysis. The recent availability of high resolution field emission SEMs has allowed for more detailed petrologic studies of chondrules revealing mineral phases and textures overlooked in previous studies.

The presence of plagioclase in Type II chondrules can also provide constraints on chondrule cooling rates. Rocha and Jones (2012) used the inferred absence of plagioclase in Type IIA OC chondrules to experimentally constrain cooling rates in these chondrules. Using a relatively rapid constant cooling rate, 30 °C/hour, they reproduced plagioclase-free Type IIA textures. However, by reducing the final cooling rate to 1 °C/hour (950-900 °C) they crystallized plagioclase, but only in a Type IIAB-like texture. This plagioclase had a composition of An_{97}, closer to the composition expected in the Type I chondrules, which is the result of Na loss during the experiment. Because of the low Na content, these experiments are not perfectly analogous to the albite-bearing Type II chondrules we observe in Semarkona. Nucleation of alkali feldspar in anhydrous crystallization experiments is extremely difficult (Smith and Brown 1988). However, the presence of albite growing from the chondrule exterior suggests that it might have been nucleated by dust impinging on the chondrule exterior after the melt was cooled below the equilibrium crystallization temperature.

The presence of volatile elements, such as Na and K, in chondrules is a conundrum for chondrule forming scenarios. These elements should have rapidly diffused out of molten chondrules at the high temperatures and low ambient nebular pressure thought to be present during their formation (Yu and Hewins 1998) and then they could have recondensed back onto the chondrule during cooling (Grossman et al.

2002; Lewis et al. 1993). However, measurements of Na zoning in olivine are consistent with growth from a melt with constant Na (Alexander et al. 2008) suggesting Na retention even during the relatively slow cooling rates necessary to nucleate plagioclase. Models show that Na can be retained within the chondrules if the chondrule forming region had a dust to gas ratio much greater than solar (Ebel and Grossman 2000) resulting in a high partial pressure of Na (Hewins et al. 2005). The presence of albite in chondrules supports the model of a Na-enriched atmosphere in the chondrule forming region allowing for Na to be retained within the chondrules.

4.2. Secondary alteration of chondrule glass and feldspar

Semarkona has undergone a moderate degree of aqueous alteration. Evidence for this includes the presence of phyllosilicates in the matrix (Alexander et al. 1989; Hutchison et al. 1987), carbonates (Alexander et al. 2015), carbide-magnetite assemblages (Krot et al. 1997), sulfide-magnetite assemblages (Huss 1979), bleached chondrules (Grossman et al. 2000), and zoned chondrules (Grossman et al. 2002). Our observations of the dissolution of mesostasis glass, and the presence of phyllosilicates in chondrules, are similar to what has been described before (Grossman et al. 2000; Alexander et al. 1989; Hutchison et al. 1987), but we have extended the previous observations to a larger variety of chondrules. Furthermore, our observations of the alteration of primary igneous feldspar add to the arguments for fluid activity. Understanding whether feldspar grains are pristine or altered has important implications for early solar system chronology as determined by Al-Mg systematics.

4.2.1. Evidence for the presence of fluids in chondrule glass

Nearly all the plagioclase-bearing chondrules we examined show at least some porosity between plagioclase laths that we interpret as the dissolution of chondrule mesostasis glass by an aqueous fluid. The chondrules in Fig. 2.3 (Ch28, Ch23, and Ch20) show extensive dissolution of glass while Ch3 and Ch36 in Fig. 2.2 have smaller patches of dissolved glass, typically along the chondrule perimeter (e.g., Fig. 2.2e). Large pores (>50 μm in diameter) are also present in several chondrules (e.g., Ch28) and are easily visible as black spots within chondrules on the thin section BSE map (Fig. 2.1). Ch28 has very large pores (up to 370 μm in diameter, Fig. 2.3a) although it is not clear if the large pores are inherent to the sample or a product of the sample preparation process (i.e., plucked metal grains). The FIB section of the zoned albite in Ch28 (Fig. 2.4a) shows pores between plagioclase laths as small as 20 nm.

Grossman et al. (2000) conducted a detailed study of bleached chondrules in Semarkona: these are fine-grained, cryptocrystalline and radiating pyroxene chondrules that have zones of dissolved mesostasis along their outer edges. They showed that these chondrules were affected by a parent body alteration process that preferentially dissolved the mesostasis without affecting the adjacent pyroxene. They noted that the mesostasis in porphyritic chondrules did not appear to be affected by the alteration process in the same way as the fine-grained chondrules and attributed this to either differences in mesostasis compositions or grain sizes between the various chondrule types.

The glass in cryptocrystalline and radiating pyroxene chondrules contains a high percentage of normative albite, whereas the glass in Type I chondrules is anorthitic and in Type II chondrules is rich in normative quartz (Grossman et al. 2000). However, we have

shown that all the porphyritic chondrules we studied have varying amounts of dissolved mesostasis glass, some quite extensive (e.g., Ch23, Fig. 2.3d). This implies that mesostasis composition cannot be the sole determining factor for glass dissolution. Grossman et al. (2000) also pointed out that uniformly fine-grained chondrules contain more grain boundaries than the relatively coarse-grained porphyritic chondrules and thus more avenues for fluid to flow into and out of the chondrules from the matrix. In porphyritic chondrules, radial bleaching zones, like those seen in uniformly fine-grained chondrules, are less likely to occur due to considerations of surface area from heterogeneous distributions of grain sizes in regions of mesostasis.

Phyllosilicates have been identified in Semarkona matrix and, like the bleached chondrules, imply alteration of primary phases by an aqueous fluid (Alexander et al. 1989; Hutchison et al. 1987). Grossman et al. (2000) showed that bleached chondrules contain phyllosilicates that are compositionally distinct from those found in the matrix, and argued that they formed by the alteration of chondrule glass in the same event that dissolved some of the mesostasis glass. We observe phyllosilicates in place of mesostasis glass in Ch28 (Figs. 2.3b, 2.4a) and Ch26 and in very minor amounts in Ch3 (Fig. 2.2c) that likely formed in a similar way. In these chondrules, the mesostasis glass between feldspar laths has both been dissolved, resulting in pores, and replaced by phyllosilicates (Fig. 2.4a).

Dobrică and Brearley (2016) investigated a fine-grained matrix inclusion in a Semarkona POP chondrule. They showed porosity associated with glass altered to phyllosilicates, like what we describe above. Clearly this mode of fluid alteration was widespread in Semarkona and resulted in the alteration of a range of chondrule types (and

matrix), not just fine-grained, bleached chondrules. Grossman et al. (2000) noted that bleached chondrules are present in nearly all petrologic types and suggested that all OCs underwent fluid alteration of this sort before the onset of thermal metamorphism. It would be reasonable to extend this model to porphyritic chondrules as well.

4.2.2. Secondary alteration of primary plagioclase

Feldspar is nearly homogeneous in chondrules that either do not show the mesostasis alteration described above, or are minimally altered e.g., Ch3 and Ch36, Table 2.1, Fig. 2.5. However, chondrules with extensively dissolved mesostasis glass or presence of phyllosilicates show much more variation in their feldspar compositions. This variation in chondrule-wide plagioclase compositions is illustrated in Fig. 2.5. The vertical error bars represent one standard deviation about the mean An content measured for each chondrule and can be over 5 mol. % An. Variation is also seen within individual plagioclase laths that are present adjacent to regions of alteration. Plagioclase in Ch28 (Fig. 2.3b,4) and Ch23 (Fig. 2.3d) is irregularly zoned subparallel to the regions of dissolved chondrule mesostasis glass and, in the case of Ch28, glass alteration to phyllosilicates.

A FIB section (Fig. 2.4a) was prepared of a zoned plagioclase region in Ch28 (white line in Fig. 2.3b) to explore the zoning in more detail. A HAADF image of a representative area is shown in Fig. 2.4b and the corresponding EDS Ca Kα map is shown in Fig. 2.5c. Zoning is observed in Al, Na, and Ca but Ca shows the most heterogeneity and is likely responsible for the zoned appearance of the plagioclase grains in the BSE image (Fig. 2.3b). Calcium is variably zoned and predominantly absent from

the outer 100-150 nm of the ~650 nm wide laths. There also appear to be enrichments of Ca on the border of the low-Ca outer zone as well as in the phyllosilicates themselves.

A similar zoning profile (Ca-rich core, Na-rich rim) is expected from normal igneous zoning, but several features are inconsistent with an igneous origin for the zoning in these grains. First, the Ca zoning shows considerable variation along the long axis of the grain and is not symmetric about the core (Fig. 2.5b). Second, the degree of Ca zoning appears to reflect proximity to areas of dissolved mesostasis glass or phyllosilicate growth. Third, plagioclase in chondrules from which the glass has not been dissolved does not show similar compositional zoning or widespread heterogeneity. Fourth, Ch3 has dominantly homogeneous albite (Fig. 2.2b), but zoned albite is only seen in regions of alteration (Fig. 2.2c). Clearly, plagioclase zoning in these chondrules is due to secondary processes and is not attributable to primary igneous growth.

Closely related to our observations of Ca-zoning in altered primary plagioclase, calcic plagioclase is replaced by more sodic compositions as the result of Na-metasomatism during metamorphism in higher petrologic type chondrites. In petrologic types 4 and 5, anorthitic plagioclase is affected by albitization, creating rims of nearly pure albite (Kovach and Jones 2010; Jones and Brearley 2010; Lewis and Jones 2016). Progressive metamorphism equilibrates plagioclase compositions to a uniform ~An_{11} by petrologic type 6 (Kovach and Jones 2010; Van Schmus and Wood 1967). The presence of alteration in Semarkona plagioclase grains possibly represents the first step in the feldspar equilibration process that was experienced in varying amounts by all ordinary chondrites.

4.2.3. Characteristics of the fluid environment

The alteration of mesostasis glass and primary plagioclase in Semarkona chondrules strongly argues for open system behavior between chondrules and the matrix and the transport of material into and out of chondrules by an aqueous fluid. The characteristics of this process are described at length by Grossman et al. (2000, 2002) in their studies of bleached and zoned chondrules and our observations generally agree with their conclusions. The bleaching process, removal of chondrule glass, results in depletions of Na, K, Sr, Si, and Al from the outer regions of the affected chondrules. The hydration and alteration of the remaining glass to phyllosilicates is associated with the introduction of Fe, Ni, halogens, and water (Grossman et al. 2000). This process has also been documented in the H/L3.6 Tieschitz (e.g., Hutchison et al. 1998).

Complementary to the bleached chondrules, chondrule mesostases in many low-FeO chondrules display concentric chemical zoning with enrichments in Na, K, other moderately volatile elements, and water and depletions in Ca, Cr, and Ti (Grossman et al. 2002). We observe a similar pattern in the homogeneous anorthite-bearing BO chondrule Ch36 in which the CL image shows zoning of mesostasis glass from pale yellow in the center to bright yellow along the rim (Fig. 2.2f), a signature of Na enrichment in the rim noted by Grossman et al. (2002). The transfer of these elements by an aqueous fluid did not result in the devitrification of the chondrule glass nor the extensive leaching seen in bleached chondrules (Grossman et al. 2002).

Water in chondrites is commonly assumed to be derived from ices present during accretion. The ices melt and water flows though the permeable matrix and along grain boundaries in order to redistribute a variety of water soluble elements. However, the

conditions of glass and plagioclase alteration were not severe enough to affect olivine or pyroxene. Grossman et al. (2000) argued that the alteration temperature may have been less than 100 °C based on similarities to CC alteration assemblages. This is less than the maximum temperature of 260 °C estimated by Alexander et al. (1989) based on the stability of the phyllosilicates found in the matrix. The dissolution of Si from the mesostasis glass implies a high pH (Alexander et al. 1954) and is consistent with the presence of calcite in Semarkona (Alexander et al. 2015). Incomplete and inconsistent alteration between chondrules, even of similar chemical compositions, implies a low water-rock ratio, the effects of which may be exaggerated by limited chondrule permeability.

Overall, the degree of aqueous alteration observed in Semarkona chondrules is not consistent between chondrules, from grain to grain within a chondrule, or within individual mineral grains. Limited fluid availability, variation in fluid permeability of the matrix and chondrules, and the wide variety of chondrule mesostasis compositions, some of which were more easily altered than others, likely gave rise to the complex pattern of alteration we now see.

4.2.4. Implication for Al-Mg dating of Semarkona chondrules and solar system chronology

High resolution chronology using short-lived radioactive isotopes is a powerful tool for understanding the relative order of events during a very important time in the history of the early solar system. The Al-Mg system is used for dating chondrules because they contain significant amounts of Al. Bulk chondrule compositions typically contain 1-5 wt.% Al_2O_3 but can be >10 wt.% Al_2O_3 in Al-rich chondrules (Brearley and

Jones 1998). Mesostasis glass and plagioclase are major hosts of Al in chondrules although minor amounts are also present in clinopyroxene and spinel. As shown above, chondrule mesostasis glass in a significant number of Semarkona chondrules shows evidence of being dissolved and/or altered to phyllosilicates. Plagioclase also shows evidence for alteration through Na-Ca and Al-Si. Therefore, it is important to evaluate what effects alteration may have had on measured Al-Mg ages.

Chondrules within Semarkona have been dated using Al-Mg systematics by a number of workers (Hutcheon and Hutchison 1989; Kita et al. 2000; Mishra and Goswami 2014; Mishra et al. 2010; Mostefaoui et al. 2002; Rudraswami et al. 2008; Russell et al. 1997; Villeneuve et al. 2009). These studies report ages that range between 0.76 Ma and 3.07 Ma after CAI formation, a span of 2.3 million years. The wide range of ages has been explained as the period during which chondrules were formed. However, the reported errors in many of the Semarkona measurements are broad (0.5-1 Ma) implying that the isochrons were defined through considerable scatter.

Since we observe ubiquitous aqueous alteration of Al-bearing phases in Semarkona it is conceivable that the Al-Mg systematics have been inconsistently disturbed by secondary processes on Semarkona's parent asteroid. This disturbance would generate large errors in the measured isochrons or may have reset the Al-Mg system in some chondrules altogether, yielding younger ages. Thus, the reported chondrule formation ages in Semarkona may record a combination of secondary aqueous alteration and primary chondrule formation. In support of this argument, aqueous alteration in carbonaceous chondrites, measured by Mn-Cr dating of carbonates (Fujiya et al. 2012, 2013; Hoppe et al. 2007; Jilly et al. 2014; Lee et al. 2012; de Leuw et al. 2009;

Petitat et al. 2011), overlaps the formation period for Semarkona chondrules (between 0.4 Ma and 6.2 Ma after CAIs). However, it is important to note that the history of low temperature secondary processes on the ordinary and carbonaceous chondrite parent bodies are not necessarily identical.

These conclusions reinforce the need for high-resolution petrographic studies of chondritic materials prior to utilizing high precision analytical techniques on what is only assumed to be unaltered nebular material. Careful consideration needs to be made of the state of the major, and possibly minor, phases relevant to the technique. For Al-Mg, dissolution of chondrule mesostasis glass, alteration of primary plagioclase, formation of secondary minerals, like phyllosilicates, and zoning of volatile elements like Na within the chondrule glass would be reason to suspect a compromised system. For example, Mostefaoui et al. (2002) found a correlation between younger Al-Mg age and increasing bulk Na, Mn, and Cr abundances relative to Mg. These are elements shown by Grossman et al. (2002) to be zoned in Semarkona chondrules, the result of aqueous alteration.

5. Summary and conclusions

We conducted a detailed study of plagioclase in Semarkona chondrules to characterize this mineral as a primary igneous phase and to understand how it might be affected by secondary processes such as aqueous alteration and thermal metamorphism. We found plagioclase with a wide range of compositions (An_2-An_{99}) was present within 18% of the chondrules in the thin section we studied. The plagioclase grains have lath-like morphologies consistent with growth from a melt. Plagioclase compositions are also directly related to the bulk composition of the chondrule: plagioclase in FeO-poor chondrules is more Ca-rich, and plagioclase in FeO-rich chondrules is more Na-rich.

Experimental investigations into plagioclase growth in chondrules indicate plagioclase-bearing chondrules cooled extremely slowly as they approach the solidus (1 ºC/hour for anorthitic plagioclase), so these slow cooling rates apparently apply to a high proportion of OC chondrules.

The aqueous alteration that is known to affect Semarkona mineralogy has also altered the texture and composition of primary plagioclase in many chondrules. This has led to zoning of Na and Ca in plagioclase grains and a general spread in the plagioclase compositions within altered chondrules. These effects are seen in association with the development of porosity from the dissolution of chondrule mesostasis glass and the alteration of glass to phyllosilicates. These features have been observed previously in bleached and zoned chondrules in Semarkona and imply a low temperature, high pH fluid at a low water-rock ratio (Alexander et al. 1954; Grossman et al. 2000, 2002). The pervasive nature of alteration calls into question the reliability of Al-Mg systematics for understanding the chronology of chondrule formation, in cases where chondrules have undergone alteration of mesostasis glass and plagioclase.

Acknowledgements

We would like to thank Mike Spilde for his help with the microprobe, Elena Dobrică for her assistance with TEM sample preparation, and Adrian Brearley for useful discussions. Work was carried out at the Electron Microbeam Analysis Facility, Department of Earth and Planetary Sciences and Institute of Meteoritics, University of New Mexico and at the Williamson Research Centre, University of Manchester. J. Lewis acknowledges support from the Kelley-Silver Foundation, University of New Mexico, the New Mexico Space Grant Consortium, and is grateful to the University of Manchester for

sponsoring his visit to the School of Earth and Environmental Sciences. The work was partially funded by NASA grant NNX12AH61G (P.I. R. Jones).

References

Alexander G. B., Heston W., and Iler R. K. 1954. The solubility of amorphous silica in water. *The Journal of Physical Chemistry* 58:453–455.

Alexander C. M. O'D., Barber D. J., and Hutchison R. 1989. The microstructure of Semarkona and Bishunpur. *Geochimica et Cosmochimica Acta* 53:3045–3057.

Alexander C. M. O'D., Grossman J. N., Ebel D. S., and Ciesla F. J. 2008. The formation conditions of chondrules and chondrites. *Science* 320:1617–1619.

Alexander C. M. O'D., Bowden R., Fogel M. L., and Howard K. T. 2015. Carbonate abundances and isotopic compositions in chondrites. *Meteoritics & Planetary Science* 50:810–833.

Brearley A. J. and Jones R. H. 1998. Chondritic meteorites. In *Planetary Materials*, edited by Papike J. J. pp. 3.1–3.398.

Brown W. L. and Parsons I. 1994. Feldspars in igneous rocks. In *Feldspars and Their Reactions*, edited by Parsons I. Dordrecht: Springer Netherlands. pp. 449–499.

Connolly H. C. and Hewins R. H. 1995. Chondrules as products of dust collisions with totally molten droplets within a dust-rich nebular environment: An experimental investigation. *Geochimica et Cosmochimica Acta* 59:3231–3246.

Connolly H. C. and Desch S. J. 2004. On the origin of the "kleine Kügelchen" called Chondrules. *Chemie der Erde - Geochemistry* 64:95–125.

Connolly H. C. and Jones R. H. 2016. Chondrules: The canonical and noncanonical views. *Journal of Geophysical Research: Planets* 121:1885–1899.

Corrigan G. 1982. The crystal morphology of plagioclase feldspar produced during isothermal supercooling and constant rate cooling experiments. *Mineralogical Magazine* 46:433–439.

Dobrică E. and Brearley A. J. 2016. Selective dissolution of plagioclase in Semarkona: Low-temperature fluid-solid interactions (abstract #6228). 79th Annual Meeting of the Meteoritical Society.

Ebel D. S. and Grossman L. 2000. Condensation in dust-enriched systems. *Geochimica et Cosmochimica Acta* 64:339–366.

Fujiya W., Sugiura N., Hotta H., Ichimura K., and Sano Y. 2012. Evidence for the late formation of hydrous asteroids from young meteoritic carbonates. *Nature Communications* 3:627.

Fujiya W., Sugiura N., Sano Y., and Hiyagon H. 2013. Mn–Cr ages of dolomites in CI chondrites and the Tagish Lake ungrouped carbonaceous chondrite. *Earth and Planetary Science Letters* 362:130–142.

Ghiorso M. S. and Gualda G. A. R. 2015. An H_2O–CO_2 mixed fluid saturation model compatible with rhyolite-MELTS. *Contributions to Mineralogy and Petrology* 169:53.

Grossman J. N. and Wasson J. T. 1983. The compositions of chondrules in unequilibrated chondrites: An evaluation of models for the formation of chondrules and their precursor materials. In *Chondrules and their Origins*, edited by King E. A. pp. 88–121.

Grossman J. N., Alexander C. M. O'D., Wang J., and Brearley A. J. 2000. Bleached chondrules: Evidence for widespread aqueous processes on the parent asteroids of ordinary chondrites. *Meteoritics & Planetary Science* 35:467–486.

Grossman J. N., Alexander C. M. O., Wang J., and Brearley A. J. 2002. Zoned chondrules in Semarkona: Evidence for high- and low-temperature processing. *Meteoritics & Planetary Science* 37:49–73.

Grossman J. N. and Brearley A. J. 2005. The onset of metamorphism in ordinary and carbonaceous chondrites. *Meteoritics & Planetary Science* 40:87–122.

Gualda G. A. R., Ghiorso M. S., Lemons R. V., and Carley T. L. 2012. Rhyolite-MELTS: a modified calibration of MELTS optimized for silica-rich, fluid-bearing magmatic systems. *Journal of Petrology* 53:875–890.

Hewins R. H., Connolly H. C. Lofgren, G. E., Jr., and Libourel G. 2005. Experimental constraints on chondrule formation. In *Chondrites and the Protoplanetary Disk*, edited by Krot A. N., Scott E. R. D., and Reipurth B. pp. 286–316.

Hoppe P., MacDougall D., and Lugmair G. W. 2007. High spatial resolution ion microprobe measurements refine chronology of carbonate formation in Orgueil. *Meteoritics & Planetary Science* 42:1309–1320.

Huss G. R. 1979. The matrix of unequilibrated ordinary chondrites: Implications for the origin and subsequent history of chondrites. Master's thesis, Albuquerque: University of New Mexico.

Huss G. R., MacPherson G. J., Wasserburg G. J., Russell S. S., and Srinivasan G. 2001. Aluminum-26 in calcium-aluminum-rich inclusions and chondrules from unequilibrated ordinary chondrites. *Meteoritics & Planetary Science* 36:975–997.

Huss G. R., Rubin A. E., and Grossman J. N. 2006. Thermal metamorphism in chondrites. In *Meteorites and the Early Solar System II*, edited by Lauretta D. S., and McSween Jr. H. Y. Tucson, AZ: The University of Arizona Press. pp. 567–586.

Hutcheon I. D. and Hutchison R. 1989. Evidence from the Semarkona ordinary chondrite for 26Al heating of small planets. *Nature* 337:238–241.

Hutchison R., Alexander C. M. O'D., and Barber D. J. 1987. The Semarkona meteorite: First recorded occurrence of smectite in an ordinary chondrite, and its implications. *Geochimica et Cosmochimica Acta* 51:1875–1882.

Hutchison R., Alexander C. M. O'D., and Bridges J. C. 1998. Elemental redistribution in Tieschitz and the origin of white matrix. *Meteoritics & Planetary Science* 33:1169–1179.

Jilly C. E., Huss G. R., Krot A. N., Nagashima K., Yin Q.-Z., and Sugiura N. 2014. $^{53}Mn/^{53}Cr$ dating of aqueously formed carbonates in the CM2 lithology of the Sutter's Mill carbonaceous chondrite. *Meteoritics & Planetary Science* 49:2104–2117.

Jones R. H. 1990. Petrology and mineralogy of Type II, FeO-rich chondrules in Semarkona (LL3.0): Origin by closed-system fractional crystallization, with evidence for supercooling. *Geochimica et Cosmochimica Acta* 54:1785–1802.

Jones R. H. 1994. Petrology of FeO-poor, porphyritic pyroxene chondrules in the Semarkona chondrite. *Geochimica et Cosmochimica Acta* 58:5325–5340.

Jones R. H. 1996. FeO-rich, porphyritic pyroxene chondrules in unequilibrated ordinary chondrites. *Geochimica et Cosmochimica Acta* 60:3115–3138.

Jones R. H. 1997. Ubiquitous anorthitic plagioclase in type I chondrules in CO3 chondrites: Implications for chondrule formation and parent body metamorphism (abstract #5240). 60th Annual Meeting of the Meteoritical Society.

Jones R. H. and Brearley A. J. 2010. Late-stage fluids on the LL chondrite parent body: Evidence from feldspar in the LL4 chondrites Bo Xian and Bjurböle (abstract #2133). 41st Lunar and Planetary Science Conference.

Jones R. H. 2012. Petrographic constraints on the diversity of chondrule reservoirs in the protoplanetary disk. *Meteoritics & Planetary Science* 47:1176–1190.

Kita N. T., Nagahara H., Togashi S., and Morishita Y. 2000. A short duration of chondrule formation in the solar nebula: evidence from ^{26}Al in Semarkona ferromagnesian chondrules. *Geochimica et Cosmochimica Acta* 64:3913–3922.

Kovach H. A. and Jones R. H. 2010. Feldspar in type 4–6 ordinary chondrites: Metamorphic processing on the H and LL chondrite parent bodies. *Meteoritics & Planetary Science* 45:246–264.

Krot A. N., Zolensky M. E., Wasson J. T., Scott E. R. D., Keil K., and Ohsumi K. 1997. Carbide-magnetite assemblages in type-3 ordinary chondrites. *Geochimica et Cosmochimica Acta* 61:219–237.

Lee M. R., Lindgren P., Sofe M. R., Alexander C. M. O'D., and Wang J. 2012. Extended chronologies of aqueous alteration in the CM2 carbonaceous chondrites: Evidence from carbonates in Queen Alexandra Range 93005. *Geochimica et Cosmochimica Acta* 92:148–169.

de Leuw S., Rubin A. E., Schmitt A. K., and Wasson J. T. 2009. ^{53}Mn–^{53}Cr systematics of carbonates in CM chondrites: Implications for the timing and duration of aqueous alteration. *Geochimica et Cosmochimica Acta* 73:7433–7442.

Lewis R. D., Lofgren G. E., Franzen H. F., and Windom K. E. 1993. The effect of Na vapor on the Na content of chondrules. *Meteoritics* 28:622–628.

Lewis J. A. and Jones R. H. 2016. Phosphate and feldspar mineralogy of equilibrated L chondrites: The record of metasomatism during metamorphism in ordinary chondrite parent bodies. *Meteoritics & Planetary Science* 51:1886–1913.

Lofgren G. 1974. An experimental study of plagioclase crystal morphology: Isothermal crystallization. *American Journal of Science* 274:243–273.

Mishra R. K., Goswami J. N., Tachibana S., Huss G. R., and Rudraswami N. G. 2010. ^{60}Fe and ^{26}Al in chondrules from unequilibrated chondrites: Implications for early solar system processes. *The Astrophysical Journal Letters* 714:L217.

Mishra R. K. and Goswami J. N. 2014. Fe–Ni and Al–Mg isotope records in UOC chondrules: Plausible stellar source of ^{60}Fe and other short-lived nuclides in the early Solar System. *Geochimica et Cosmochimica Acta* 132:440–457.

Mostefaoui S., Kita N. T., Togashi S., Tachibana S., Nagahara H., and Morishita Y. 2002. The relative formation ages of ferromagnesian chondrules inferred from their initial aluminum-26/aluminum-27 ratios. *Meteoritics & Planetary Science* 37:421–438.

Osborn E. F. and Tait D. B. 1952. The system diopside-forsterite-anorthite. *American Journal of Science* 38:413–433.

Petitat M., Marrocchi Y., McKeegan K. D., Mostefaoui S., Meibom A., Zolensky M. E., and Gounelle M. 2011. ^{53}Mn-^{53}Cr ages of Kaidun carbonates. *Meteoritics & Planetary Science* 46:275–283.

Rocha S. E. and Jones R. H. 2012. An experimental study of the conditions of type II chondrule formation in ordinary chondrites (abstract #2595). 43rd Lunar and Planetary Science Conference.

Rudraswami N. G., Goswami J. N., Chattopadhyay B., Sengupta S. K., and Thapliyal A. P. 2008. ^{26}Al records in chondrules from unequilibrated ordinary chondrites: II. Duration of chondrule formation and parent body thermal metamorphism. *Earth and Planetary Science Letters* 274:93–102.

Russell S. S., Huss G. R., MacPherson G. J., and Wasserburg G. J. 1997. Early and late chondrule formation: New constraints for solar nebula chronology from ^{26}Al/^{27}Al in unequilibrated ordinary chondrites (abstract #1468). 28th Lunar and Planetary Science Conference.

Russell S. S., MacPherson G. J., Leshin L. A., and McKeegan K. D. 2000. ^{16}O enrichments in aluminum-rich chondrules from ordinary chondrites. *Earth and Planetary Science Letters* 184:57–74.

Smith J. V. and Brown W. L. 1988. *Feldspar Minerals: Volume 1 Crystal Structures, Physical, Chemical, and Microtextural Properties*, Springer Berlin Heidelberg.

Van Schmus W. R., and Wood J. A. 1967. A chemical-petrologic classification for the chondritic meteorites. *Geochimica et Cosmochimica Acta* 31:747–765.

Villeneuve J., Chaussidon M., and Libourel G. 2009. Homogeneous distribution of ^{26}Al in the solar system from the Mg isotopic composition of chondrules. *Science* 325:985–988.

Wick M. J. and Jones R. H. 2012. Formation conditions of plagioclase-bearing type I chondrules in CO chondrites: A study of natural samples and experimental analogs. *Geochimica et Cosmochimica Acta* 98:140–159.

Yu Y. and Hewins R. H. 1998. Transient heating and chondrule formation: Evidence from sodium loss in flash heating simulation experiments. *Geochimica et Cosmochimica Acta* 62:159–172.

CHAPTER 3

Plagioclase alteration and equilibration in ordinary chondrites: Evidence for three stages of metasomatism during thermal metamorphism

In collaboration with:
Rhian H. Jones
Adrian J. Brearley

To be submitted for publication to:
Geochimica et Cosmochimica Acta

Abstract

Feldspar in ordinary chondrites (OCs) is present in chondrules as a primary, igneous phase, and as a secondary phase that results from crystallization of chondrule mesostasis glass during thermal metamorphism. Studies of plagioclase feldspar equilibration, in petrologic types 4-6, have revealed textural features that indicate metasomatism during thermal metamorphism, such as albitization. However, because plagioclase development and alteration in type 3 OCs remains poorly characterized, the role of fluids in the development of secondary minerals, particularly during the early stages of metamorphism remains ambiguous. In order to further understand the chemical and physical conditions present during thermal metamorphism in OCs, we conducted a study of feldspar microtextures focusing on alteration and equilibration, within chondrules, from OCs representing the full metamorphic sequence (types 3-6).

We found that primary calcic plagioclase alters to sodalite, scapolite, and nepheline in petrologic types 3.2-3.9, and to albite in types 3.6-5. Plagioclase also develops alteration features such as zoning, micropores, and alteration lamellae in types 3-4. Albitic plagioclase is present in minor amounts as a primary phase, forms from the crystallization of chondrule mesostasis glass (types 3.2-3.9), and forms through the

albitization reaction in calcic plagioclase (types 3.6-5). K-feldspar occurs in albite in types 3.6-6 as fine-scale exsolution lamellae and as larger patches. Plagioclase has a maximum An content of An_{99} in type 3.2, and An_{84-87} in types 3.4-3.9. Maximum An content in the type 4 OCs we measured range from An_{85} to An_{50}. We argue that alteration and equilibration of feldspar is a metasomatic process facilitated by hydrous fluids at high pH and low water/rock ratios during thermal metamorphism. At low temperatures, calcic plagioclase alters to sodalite/scapolite in fluids with a low Na/Cl ratio, and nepheline in fluids with high Na/Cl. Albitization occurs at higher temperatures due to the increased solubility of Si. The Or content of the plagioclase also increases with temperature.

We combine these observations into an overall three-stage model of metasomatism during thermal metamorphism in OCs. Stage 1 involves hydrous alteration during prograde metamorphism resulting in the majority of the alteration and equilibration features we observe in plagioclase. During stage 2, dehydration occurs close to peak metamorphism. Stage 3 then involves infiltration of anhydrous, alkali- and halogen-bearing fluids during retrograde metamorphism in short duration, high temperature bursts. Overall, we show that metasomatism is present throughout the metamorphic sequence in OCs with important consequences for short-lived radioisotope chronometers, such as Al-Mg and I-Xe, that rely on the integrity of sensitive phases such as plagioclase and feldspathic mesostasis glass.

1. Introduction

Secondary processes, those that take place on the planetesimals after they accreted, result in a myriad of chemical and physical changes to the primary material.

These processes include low-temperature aqueous alteration from the action of water, thermal metamorphism resulting from the decay of radioactive species such as ^{26}Al, and a variety of shock effects from impact events. Ordinary chondrites (OCs) have long been known to have experienced varying degrees of thermal metamorphism resulting in progressive chemical and textural equilibration (Sorby, 1877). The classification scheme developed by Van Schmus and Wood (1967) describes thermal metamorphism in terms of petrologic types ranging from types 3 to 6. Chondrites assigned type 3 show little or no evidence for the effects of thermal metamorphism whereas chondrites assigned type 6 are fully equilibrated, both texturally and compositionally.

The petrologic classification scheme for type 3 chondrites was extended by Sears et al. (1980) to include the subdivisions 3.0-3.9 where type 3.0 is the least metamorphosed. These subdivisions were created in recognition of the fact that petrologic type 3 chondrites represent a wide range of thermal metamorphic temperatures that were not fully described by the original classification scheme. Grossman and Brearley (2005) further subdivided the least thermally metamorphosed OCs to include 3.00-3.15 because of the importance of deciphering primary nebular components and processes from the effects of parent body thermal metamorphism.

Although the classification scheme for thermal metamorphism is based on petrographic indicators, attempts have been made at assigning metamorphic temperatures to the various stages in the petrologic sequence. The maximum temperature for type 3.00-3.15 is estimated to be <260 °C based on the presence of phyllosilicates (Alexander et al., 1989) in Semarkona (LL3.00) and Bishunpur (LL3.15), but the peak temperature could be much lower. Type 3 material has a range of peak temperatures up to a maximum

estimated to be between 600ºC and 700ºC (Huss et al., 2006). Metamorphic temperatures for Types 4-6 OCs are poorly constrained but generally estimated to be between 500ºC and 800ºC for types 4 and 5 and between 800ºC and 1000ºC for type 6 (Scott and Krot, 2014). Melting of chondritic compositions is estimated to begin between 950ºC and 1000ºC (Huss et al., 2006).

Thermal metamorphism was historically considered to be separate from aqueous alteration, a parent body processes found predominantly in carbonaceous chondrites. Aqueous alteration is now known to have affected low petrologic type OCs resulting in a variety of features. These features include the presence of phyllosilicates (Hutchison et al., 1987; Alexander et al., 1989; Dobrică and Brearley, 2014), carbonates (Alexander et al., 2015), magnetite-sulfide assemblages (Huss, 1979), carbide-magnetite assemblages (Krot et al., 1997), bleached chondrules (Grossman et al., 2000), and chondrules zoned in alkalis (Grossman et al., 2002). The presence of fluids has also been inferred by increased oxidation of Fe through the petrologic sequence, up to petrologic type 6 (McSween and Labotka, 1993; Dunn et al., 2010).

A useful way of understanding the effects of thermal metamorphism, and the presence of fluids during heating, is through the study of the secondary minerals that are produced during these processes. Plagioclase feldspar is a common secondary mineral in OCs that forms from the crystallization of chondrule mesostasis glass and fine-grained matrix. Feldspar has been used to characterize the textural equilibration that occurs during metamorphism. The typical textural equilibration sequence states that fine-grained albite (<2 μm in size) forms by petrologic type 4 and coarsens through type 5 (2-10 μm) until type 6 in which plagioclase grains reach 50 μm in size and are easily seen using

optical microscopy (Van Schmus and Wood, 1967; Van Schmus and Ribbe, 1968; Huss et al., 2006).

However, in detail, the development of plagioclase during OC metamorphism is much more complex. We have shown that primary igneous plagioclase with a range of compositions from An_{2}-An_{99} is present in OC chondrules in the least metamorphosed OC Semarkona (LL3.00) (Lewis and Jones, in review). In type 4 L and LL chondrites, anorthitic plagioclase is still present, up to An_{88} in composition (Kovach and Jones, 2010; Lewis and Jones, 2016). By petrologic type 6, plagioclase has equilibrated to an albitic composition of $An_{10\text{-}12}$, confirming early measurements (Van Schmus and Wood, 1967; Van Schmus and Ribbe, 1968). However, the plagioclase measured by Kovach and Jones (2010) in types 4-6 H chondrites all had equilibrated compositions of ~An_{12}.

In addition to compositional equilibration in plagioclase, the studies of Kovach and Jones (2010), Jones and Brearley (2010, 2011), and Lewis and Jones (2016) describe textural features that indicate plagioclase equilibration was not simply a solid state diffusional process, but was mediated by the presence of an alkali-rich fluid. These features were found predominantly in anorthitic plagioclase and include albitization along grain boundaries, alteration lamellae, K-feldspar exsolution from albite, and the presence of micropores and oxides in the cores of equilibrated plagioclase grains. These studies suggested that the differences in plagioclase alteration between the H chondrites and L and LL chondrites can be attributed to differences in fluid duration, timing, and/or availability. Fluid alteration of secondary minerals in equilibrated OCs has also been inferred by the characteristics of chlorapatite, particularly in replacement reactions with merrillite (Jones et al., 2014; Jones et al., 2016; Lewis and Jones, 2016).

Lewis and Jones (in review) show that some primary igneous plagioclase in chondrules in the unequilibrated LL3.00 chondrite Semarkona was also affected by aqueous alteration. This alteration is in the form of Ca-Na zoning in plagioclase laths and is found in regions where the mesostasis glass was either dissolved or replaced by phyllosilicates. Compositional zoning in the primary plagioclase laths is different from the albitization reaction seen in the equilibrated OC feldspar, indicating differences in the fluid environment that are likely driven by temperature. Plagioclase is compositionally and texturally homogeneous in Semarkona chondrules where the mesostasis glass appears unaltered.

The evolution and alteration of plagioclase in the type 3 metamorphic sequence has not previously been studied in detail. Anorthitic plagioclase has been described in Al-rich chondrules in a range of type 3 chondrites in studies concerned with Al-Mg chronology and $^{26}Al/^{27}Al$ distribution (Huss et al., 2001). Plagioclase alteration via replacement by nepheline has been noted in Sharps (H3.4) and Chainpur (LL3.4) by Russell et al. (2000). The presence of nepheline, sodalite, and scapolite was also observed in Chainpur and Parnallee (LL3.6) by Bridges et al. (1997) but was interpreted as igneous phases that had crystallized from a melt. However, feldspathoids have not been identified in Semarkona chondrules. Because Semarkona has undergone lower temperature thermal metamorphism than Chainpur or Parnallee, these phases are expected to be present if they were a primary chondrule phase. Thus, it is likely that feldspathoids are secondary phases that formed from the alteration of plagioclase as suggested by Alexander et al. (1987) and Russell et al. (2000).

Understanding the sequence of feldspar equilibration and alteration in ordinary chondrites is important for characterizing the chemical and physical environment that OCs experienced during thermal metamorphism. The changing fluid and thermal environment can be tracked by understanding how plagioclase changes through the type 3 sequence from unaltered, and minimally altered, primary igneous plagioclase in type 3.0, through the alteration of primary plagioclase and formation of fine-grained secondary plagioclase in type 4, to full textural and chemical equilibration to albite in type 6. From feldspar, we can gain insight into which chemical species are mobile, where they are sourced, and the fluid conditions necessary to form the secondary minerals we observe. Alteration of feldspar and feldspathic mesostasis glass also has important implications for the integrity of the short-lived radioisotope systems that rely on these phases, such as Al-Mg and I-Xe.

We have conducted a detailed study of feldspar textures and compositions through the petrologic sequence (types 3-6) in H, L and LL OCs, to further constrain the conditions and the fluid processes acting during thermal metamorphism. We chose a suite of OCs (Table 3.1) to help answer several questions posed by the current work. We selected LL chondrites from petrologic types 3.1-6 to follow feldspar development from the primary igneous plagioclase observed in chondrules from LL3.00 (Lewis and Jones, in review) through to the homogeneous secondary albite observed in LL6 (Kovach and Jones, 2010). In particular, we aim to understand the evolution of plagioclase compositions through the type 3 sequence and to place the observations of alteration to nepheline, sodalite, and scapolite described above into context with albitization observed in type 4 and 5 (Kovach and Jones, 2010; Lewis and Jones, 2016). This is possible in LL

chondrites because they are well represented throughout the petrologic sequence, especially in subtypes 3.0-3.9.

We also characterized type 4 L and H chondrites (Table 3.1) to further explore the microtextural complexity of feldspar in type 4 OCs. Of specific interest were microtextural features that might inform the observed compositional difference between the type 4 H chondrites and the type 4 L and LL chondrites (Kovach and Jones, 2010; Lewis and Jones, 2016). In addition, we included the H3.8 Dhajala to further understand whether there are fundamental differences between the feldspar evolution in the H chondrites and other OC groups. In all cases, we only studied feldspar within chondrules because chondrule mineralogy is simpler and relatively coarse-grained when compared to chondrite matrix, particularly in type 3 OCs. This is in keeping with previous studies of OC plagioclase (Lewis and Jones, in review; Kovach and Jones, 2010; Lewis and Jones, 2016) and allows us to track changes to primary igneous feldspar as well as the development of secondary feldspar from the crystallization of chondrule mesostasis glass. Because this study focuses on plagioclase alteration and evolution, observations of K-feldspar will be noted, within the context of plagioclase alteration and equilibration, but a more extensive discussion of K-feldspar exsolution is presented in Lewis et al. (In preparation).

2. Methods

For this study we examined 11 OC thin sections from the Institute of Meteoritics Meteorite Collection at the University of New Mexico (Table 3.1): Bishunpur (LL3.15, UNM 1038), Chainpur (LL3.4, UNM 1041), Parnallee (LL3.6, UNM 1018), Dhajala (H3.8, UNM 301), Bo Xian (LL3.9, UNM 265), Bjurböle (L/LL4, UNM 117), Saratov

(L4, UNM 1145), Santa Barbara (L4, TUNM 120), Avanhandava (H4, UNM 88), Tuxtuac (LL5, UNM 627), and Sulagiri (LL6, UNM 1160). To avoid terrestrial alteration of chondrite mineralogy, we only selected meteorite falls. We also chose samples that were unshocked or weakly shocked. Feldspar is known to be highly susceptible to the effects of shock metamorphism. In the shock classification scheme of Stöffler et al. (1991), plagioclase becomes partially isotropic in shock stage S4 and is converted to maskelynite in S5. The samples we chose were assigned shock stages S1-S3 by various studies as summarized in Table 3.1.

Table 3.1. Samples studied.

	Thin section	Petrologic type	Shock stage
LL chondrites			
Bishunpur	UNM 1038	LL3.15	S2[R99,G05]
Chainpur	UNM 1041	LL3.4	S1[S91,R99,G05]
Parnallee	UNM 1018	LL3.6	S3[G05]
Bo Xian	UNM 265	LL3.9	S2[L00], S3[R94]
Bjurböle	UNM 117	L/LL4	S1[S91,R94,R04,G05]
Tuxtuac	UNM 627	LL5	S2[R94,R04,G05]
Sulagiri	UNM 1160	LL6	S2[W09]
L4 chondrites			
Saratov	UNM 1145	L4	S2[R94,R04,G05], S3[F04]
Santa Barbara	UNM 120	L4	S2[LJ16]
H3.8-4 chondrites			
Dhajala	UNM 301	H3.8	S1[S91,S14]
Avanhandava	UNM 88	H4	S1[S14], S2[S91,R94,R04]

[S91] (Stöffler et al., 1991), [R94] (Rubin, 1994), [R99] (Rubin, 1999),
[L00] (Li et al., 2000), [R04] (Rubin, 2004), [F04] (Friedrich et al., 2004),
[G05] (Gattacceca et al., 2005), [W09] (Weisberg et al., 2009),
[S14] (Scott et al., 2014), [LJ16] (Lewis and Jones, 2016)

Feldspar, feldspathoids, and other phases were identified using backscattered electron (BSE) imaging and energy-dispersive spectroscopic (EDS) X-ray analysis on an FEI Quanta 3D scanning electron microscope equipped with a field emission gun (FEG-SEM) at the University of New Mexico. High contrast BSE images with high spatial resolution were needed to successfully image fine-scale feldspar textures. To accomplish

this, we typically used SEM beam conditions of 10 kV and 16 nA. Quantitative wavelength-dispersive spectroscopic (WDS) X-ray analysis of feldspar in type 3 and 4 OCs was performed on a JEOL 8200 Electron Probe Microanalyzer (EPMA) at the University of New Mexico operated at 10-15 kV and 10 nA with a focused beam. The low accelerating voltage was used to minimize the interaction volume when analyzing small feldspar grains. We used the following standards: Taylor olivine (Mg, Fe), Taylor albite (Na, K), Taylor orthoclase (K, Al, Si), and a doped diopside (Ca, Cr, Mn). We used time dependent intensity corrections on Na using the Probe for EPMA software to compensate for the effects of Na migration in Na-bearing plagioclase during focused-beam analysis. Despite the care taken during EPMA analysis, fragile mineralogy, small grain sizes, and abundant inclusions necessitated relaxed restrictions on oxide and cation totals.

3. Results

3.1. Petrography

In each thin section, we identified chondrules that exhibited alteration features in primary and/or secondary plagioclase. While not all chondrules appeared to be altered, our focus on alteration is aimed at providing an overall picture of the metasomatic conditions present during thermal metamorphism. Because the nature and extent of alteration is strongly correlated with petrologic type, the samples will be discussed in order of increasing petrologic type and subtype. BSE images of plagioclase alteration, and their host chondrules, are presented in Figs. 3.1-3.11. EPMA analysis of select chondrules are tabulated in Table 3.2 and discussed in more detail in section 3.2. Individual EPMA analyses are tabulated in Appendix 1.

Bishunpur (LL3.15)

Plagioclase alteration is not common in Bishunpur chondrules but leached mesostasis glass is more pervasive. Fig. 3.1 illustrates two chondrules, one in which anorthite is being altered to sodalite (Fig. 3.1a-c) and one in which mesostasis glass, interstitial to plagioclase laths, is being leached (Fig. 3.1d-e). Chondrule 7 (Fig. 3.1a) is a porphyritic olivine and pyroxene (POP) chondrule fragment that has 10-20 μm wide regions of anorthitic plagioclase (An_{97-100}) and 5-10 μm grains of Ca-rich pyroxene interstitial to the major phenocrysts (Fig. 3.1b). Small (~1 μm), rounded silica grains occur as inclusions in the plagioclase. These are likely primary igneous features and do not appear to be associated with alteration (Fig. 3.1c). Most of the material interstitial to plagioclase and pyroxene is sodalite with irregular, but sharp, alteration boundaries. Sodalite has numerous cracks and irregularly-shaped pores (Fig. 3.1c). Armalcolite, $(Mg,Fe)Ti_2O_5$, identified using EDS, is present along the plagioclase-scapolite alteration interface as grains ~1 μm in size.

Chondrule 1 (Fig. 3.1d), is also a POP chondrule and has 0.5-2.5 μm wide laths of plagioclase (An_{48-51}) interstitial to olivine phenocrysts and intergrown with Ca-rich pyroxene (Fig. 3.1e). The plagioclase appears to be unaltered but the mesostasis glass, interstitial to the plagioclase laths and Ca-rich pyroxene grains, has been leached out in some areas and is now void space. The development of porosity is an important feature that facilitates fluid flow during and alteration, particularly in higher petrologic types (Lewis et al., in review).

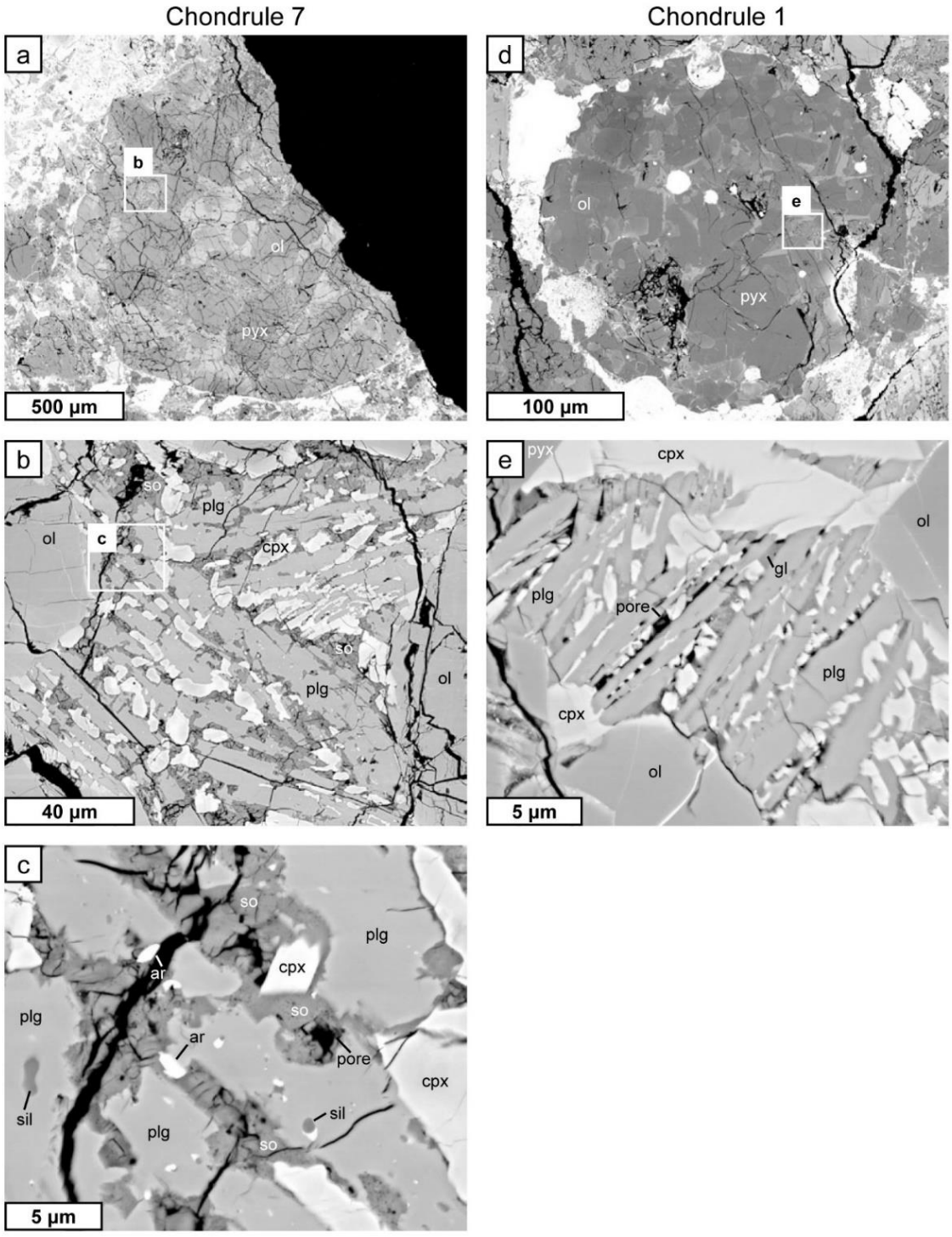

Figure 3.1. BSE images showing alteration in two feldspar-bearing chondrules in Bishunpur (LL3.15). (a-c) Chondrule 7 (a), a 1.5 mm diameter porphyritic olivine and pyroxene (POP) chondrule fragment on the thin section edge. (b) Close-up of Ca-rich pyroxene (cpx) and anorthite (plg, An_{97-100}) that has undergone alteration to sodalite (so), interstitial to olivine (ol) phenocrysts. *(Caption continues on the following page).*

Figure 3.1. *(Caption continued from the previous page).* (c) Close-up of anorthite alteration to sodalite showing irregular alteration front and ~1 μm grains of armalcolite (ar) at the alteration interface. Sodalite contains numerous, irregularly-shaped pores and elongate cracks. Anorthite contains small (~1 μm), rounded grains of silica (sil). (d-e) Chondrule 1 (d), a 0.26 mm diameter POP chondrule. (e) Close-up of Ca-rich pyroxene grains and 0.5-2.5 μm wide laths of plagioclase (An_{48-51}) interstitial to olivine phenocrysts. Mesostasis glass (gl) is interstitial to the plagioclase laths in some regions and appears to have been leached out in other regions, producing pores.

Chainpur (LL3.4)

Plagioclase in Chainpur has two modes of alteration: replacement and zoning. Alteration affects calcic plagioclase whereas zoning affects porous chondrules with sodic and intermediate plagioclase. These modes are illustrated with two chondrules in Fig. 3.2. Chondrule 16 (Fig. 3.2a) is a porphyritic olivine (PO) chondrule in which plagioclase (An_{83-86}) is present between the olivine phenocrysts along with Ca-rich pyroxene. Plagioclase is altered to porous scapolite near boundaries Ca-rich pyroxene grains (Fig. 3.2b), like chondrule 7 in Bishunpur (Fig. 3.1c), but also contains pseudomorphic alteration to nepheline through the plagioclase cores (Fig. 3.2c). Nepheline alteration appears to be roughly crystallographically controlled with some regions containing parallel lamellae. The altered region is close to the chondrule edge and more nepheline replacement is observed closer to the border with the matrix. Plagioclase is not present in the chondrule interior but mesostasis glass has experienced extensive leaching. Silica grains, like those in Bishunpur (Fig. 3.1c), are observed in calcic plagioclase in some Chainpur chondrules. However, in areas of alteration, these silica grains have rims of Fe-bearing Ca-rich pyroxene.

Chondrule 18 (Fig. 3.2d) is a POP chondrule with 50-100 μm diameter pores throughout the chondrule interior and a ~50 μm thick, porous, fine-grained igneous rim composed largely of FeO-rich olivine. Plagioclase laths (An_{36-41}), 1-2.5 μm wide, are

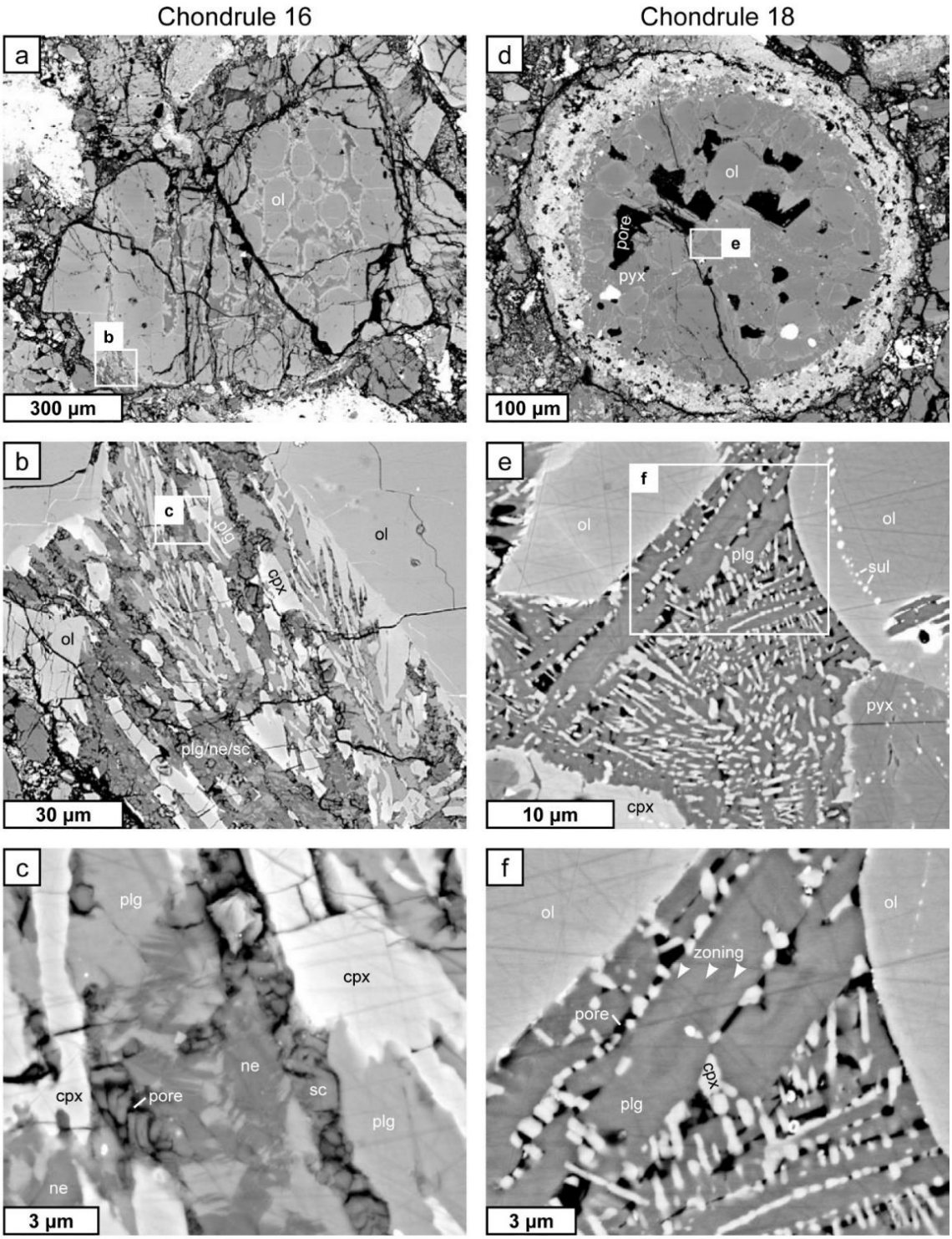

Figure 3.2. BSE images showing alteration in two feldspar-bearing chondrules in Chainpur (LL3.4). (a-c) Chondrule 16 (a), a 1 mm diameter porphyritic olivine (PO) chondrule. (b) Close-up of region near the chondrule edge, interstitial to olivine (ol) phenocrysts, showing Ca-rich pyroxene (cpx) and plagioclase (plg, An_{83-86}) alteration to scapolite (sc) and nepheline (ne). *(Caption continues on the following page).*

Figure 3.2. *(Caption continued from the previous page).* (c) Close-up of plagioclase alteration, illustrating porous scapolite bounding regions of plagioclase altered to nepheline. Nepheline replacement is lamellar in a few places indicating a minor degree of crystallographic control. (d-f) Chondrule 18 (d), a 0.5 mm diameter, porphyritic olivine and pyroxene (POP) chondrule with large (50-100 μm) pores in the chondrule interior and a porous, fine-grained rim 40-60 μm thick. (e) Close-up of region interstitial to olivine and low-Ca pyroxene (pyx) phenocrysts with 1-2.5 μm wide laths of plagioclase (An_{36-41}) and grains of Ca-rich pyroxene. (f) Close-up of plagioclase laths illustrating roughly concentric zoning and a porous intergranular region.

present between the large olivine and pyroxene grains (Fig. 3.2e). Interstitial to the plagioclase laths are μm-sized grains of Ca-rich pyroxene and pores where the mesostasis glass has been leached (Fig. 3.2f). Zoning in the plagioclase laths is roughly concentric and occurs uniformly throughout chondrule 18. This is similar to the plagioclase zoning in some Semarkona chondrules where the mesostasis glass was leached out or replaced by phyllosilicates (Lewis and Jones, in review).

Parnallee (LL3.6)

Plagioclase alteration textures are more pervasive in Parnallee and can be observed in many chondrules. The style of alteration varies, depending on the plagioclase composition. Three representative chondrules are shown in Fig. 3.3. Chondrule 3 (Fig. 3.3a) is a POP chondrule in which a 40 μm wide region of plagioclase (An_{74-85}) is altered to sodalite and nepheline (Fig. 3.3b) and resembles the texture observed in Chainpur chondrule 16 (Fig. 3.2c). Nepheline lamellae protruding into the plagioclase are more abundant in in Parnallee than in Chainpur. In some chondrules in Parnallee, plagioclase has been completely replaced by nepheline with minor sodalite/scapolite. In chondrule 3, μm-sized, rounded silica grains are present in the nepheline, like those seen in anorthite in Bishunpur chondrule 7 (Fig. 3.1c), but they have rims of Fe-bearing Ca-rich pyroxene like those noted in Chainpur.

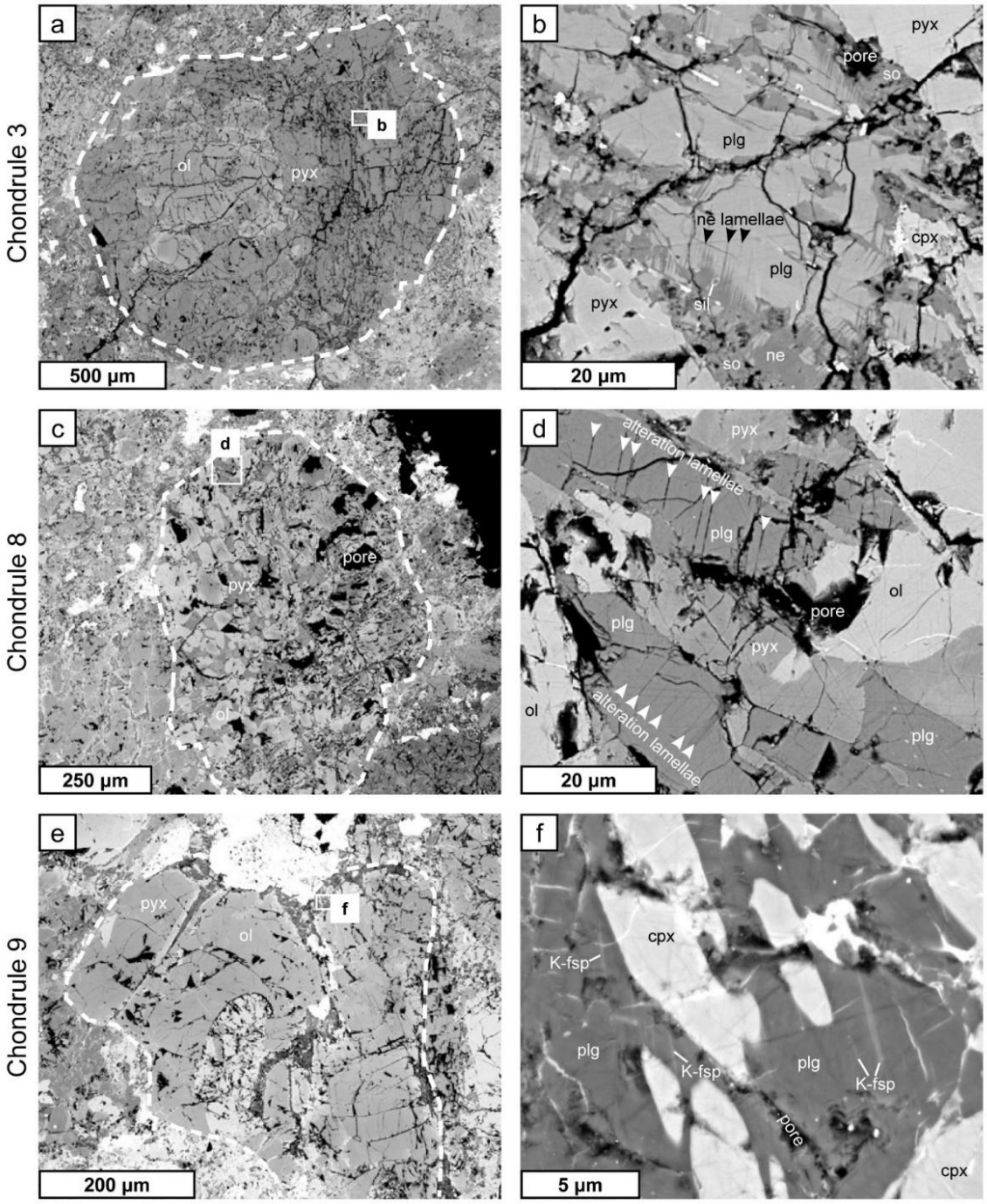

Figure 3.3. BSE images showing alteration in three feldspar-bearing chondrules in Parnallee (LL3.6), outlined with white dashed lines. (a-b) Chondrule 3 (a), a 1.6 mm diameter porphyritic olivine and pyroxene (POP) chondrule. (b) Close-up of region interstitial to pyroxene (pyx) phenocrysts in which plagioclase (plg, An_{74-85}) is being altered to nepheline (ne) and sodalite (so). Alteration to nepheline is largely expressed through lamellae in the plagioclase. Regions of alteration to sodalite are porous and are concentrated along the pyroxene boundaries and some cracks. Ca-rich pyroxene (cpx) is present as are small (~1 µm diameter) silica (sil) grains with Fe-bearing Ca-rich pyroxene rims. *(Caption continues on the following page).*

Figure 3.3. *(Caption continued from the previous page).* (c-d) Chondrule 8 (c), a 0.9 mm POP chondrule, with large (20-100 μm) pores. (d) Close-up of region interstitial to olivine (ol) and pyroxene phenocrysts in which plagioclase (An_{76-80}) contains numerous, 0.1-0.2 μm, crystallographically-controlled, alteration lamellae. (e-f) Chondrule 9 (e), an irregularly shaped, 0.5 mm diameter POP chondrule. (f) Close-up of region with Na-rich plagioclase (An_{1-14}) and grains of Ca-rich pyroxene. Plagioclase is moderately porous and has 0.1-0.3 μm exsolution lamellae of K-feldspar (K-fsp).

Chondrule 8 (Fig. 3.3c) is also a POP chondrule and has abundant, large (20-100 μm) pores throughout the chondrule. Plagioclase laths (An_{76-80}) are 5-20 μm wide and contain numerous, 0.1-0.2 μm wide, crystallographically-controlled, alteration lamellae (Fig. 3.3d). The lamellae are roughly perpendicular to the long axis of the laths and are irregularly spaced. Similar lamellae observed by Jones and Brearley (2010) in Bjurböle (L/LL4) and Bo Xian (LL3.9) were composed of silica, faceted voids, and euhedral chromite.

Chondrule 9 (Fig. 3.3e) is a POP chondrule in which albitic plagioclase (An_{1-14}) is present with grains of Ca-rich pyroxene between the major phenocrysts (Fig. 3.3f). Plagioclase has μm-sized pores and 0.1-0.3 μm wide exsolution lamellae of K-feldspar. K-feldspar lamellae are not evenly spaced, evenly distributed, nor consistently sized. We did not observe K-feldspar exsolution in the lower petrologic type LL chondrites we studied: Semarkona (LL3.00: Lewis and Jones, in review), Bishunpur (LL3.15), and Chainpur (LL3.4).

Dhajala (H3.8)

Plagioclase in Dhajala chondrules has numerous alteration features including alteration lamellae, albitization, zoning, and K-feldspar exsolution. This is illustrated by three chondrules in Fig. 3.4. Chondrule 2 (Fig. 3.4a) is a PO chondrule with plagioclase (An_{76-80}), interstitial to the olivine and pyroxene phenocrysts. Plagioclase has alteration

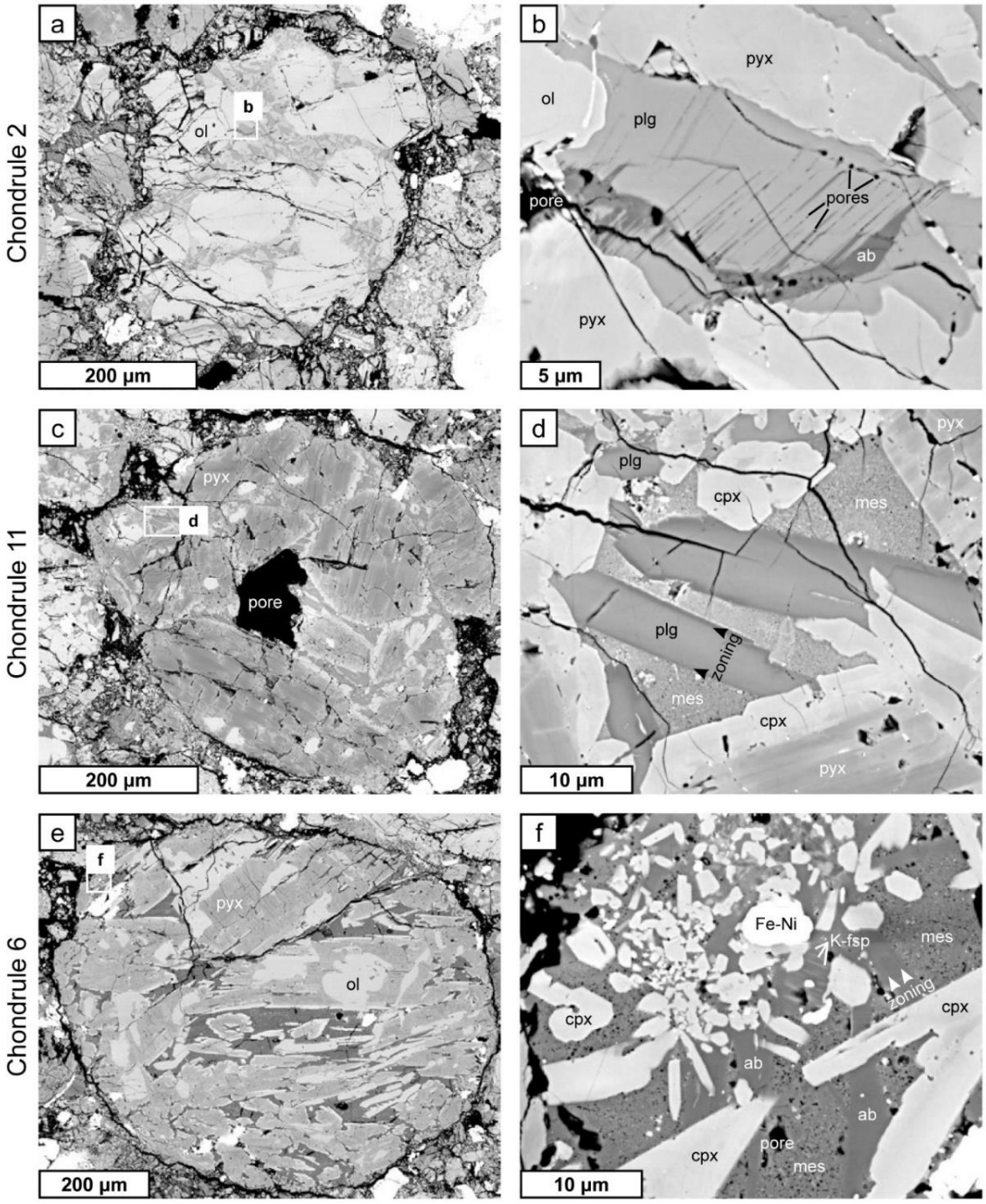

Figure 3.4. BSE images showing alteration in three feldspar-bearing chondrules in Dhajala (H3.8). (a-b) Chondrule 2 (a), a 0.5 mm diameter porphyritic olivine (PO) chondrule. (b) Close-up of region interstitial to pyroxene (pyx) and olivine (ol) phenocrysts in which plagioclase (plg, An_{76-80}) is being altered to albite along alteration lamellae. Alteration is accompanied by µm and sub-µm pores. (c-d) Chondrule 11 (c), a 0.5 mm diameter porphyritic pyroxene (PP) chondrule with a large (120 µm) pore in the center. *(Caption continues on the following page).*

Figure 3.4. *(Caption continued from the previous page).* (d) Close-up of region interstitial to pyroxene phenocrysts with Ca-rich pyroxene (cpx) grains and 3-7 μm wide plagioclase (An_{30-52}) laths are present in fine-grained, crystallized mesostasis glass (mes). Plagioclase is zoned with Ca-rich cores and Na-rich rims. (e-f) Chondrule 6 (e), a 0.8 mm diameter porphyritic olivine and pyroxene (POP) chondrule. (f) Close-up of region near chondrule edge, interstitial to pyroxene phenocrysts in which 1-4 μm wide albite (ab) laths, Ca-rich pyroxene grains, and Fe-Ni metal are present in fine-grained, porous, crystallized mesostasis glass. Some plagioclase laths have sub-μm K-feldspar (K-fsp) exsolution lamellae and some are compositionally zoned.

lamellae like those observed in Parnallee but in this case, plagioclase is being altered to albite along some of the lamellae (Fig. 3.4b). Albitization also occurs along μm-sized pores and adjacent to the grain boundary with pyroxene. The altered region has numerous μm and sub-μm pores but the albitization is largely pseudomorphic, like that of the nepheline replacement in Chainpur (Fig. 3.2c) and Parnallee (Fig. 3.3b).

Chondrule 11 (Fig. 3.4c) is a porphyritic pyroxene (PP) chondrule with a large (120 μm) pore in the center. Plagioclase (An_{30-52}) laths, 3-7 μm wide, are present in fine-grained, crystallized mesostasis glass (Fig. 3.4d). The plagioclase laths are zoned with Ca-rich cores and narrow, Na-rich rims. The zoning of these laths is different from the zoning in Chainpur (Fig. 3.2f) in two ways. First, zoning is strongly controlled by the lath morphology and does not have a complex profile like the laths in Chainpur. Second, the zoning in Chainpur is associated with dissolution of mesostasis glass whereas the zoning in Dhajala appears to be the result of alkali exchange with the crystallizing mesostasis glass, during metamorphism, which is still present in chondrule 11. The orientation of plagioclase laths with respect to the thin section surface may also result in different apparent zoning profiles.

Chondrule 6 (Fig. 3.4e) is a POP chondrule with 1-4 μm wide albite laths, Ca-rich pyroxene grains, and Fe-Ni metal in fine-grained, porous, crystallized mesostasis glass along the chondrule edge (Fig. 3.4f). The crystallized mesostasis glass is largely albite

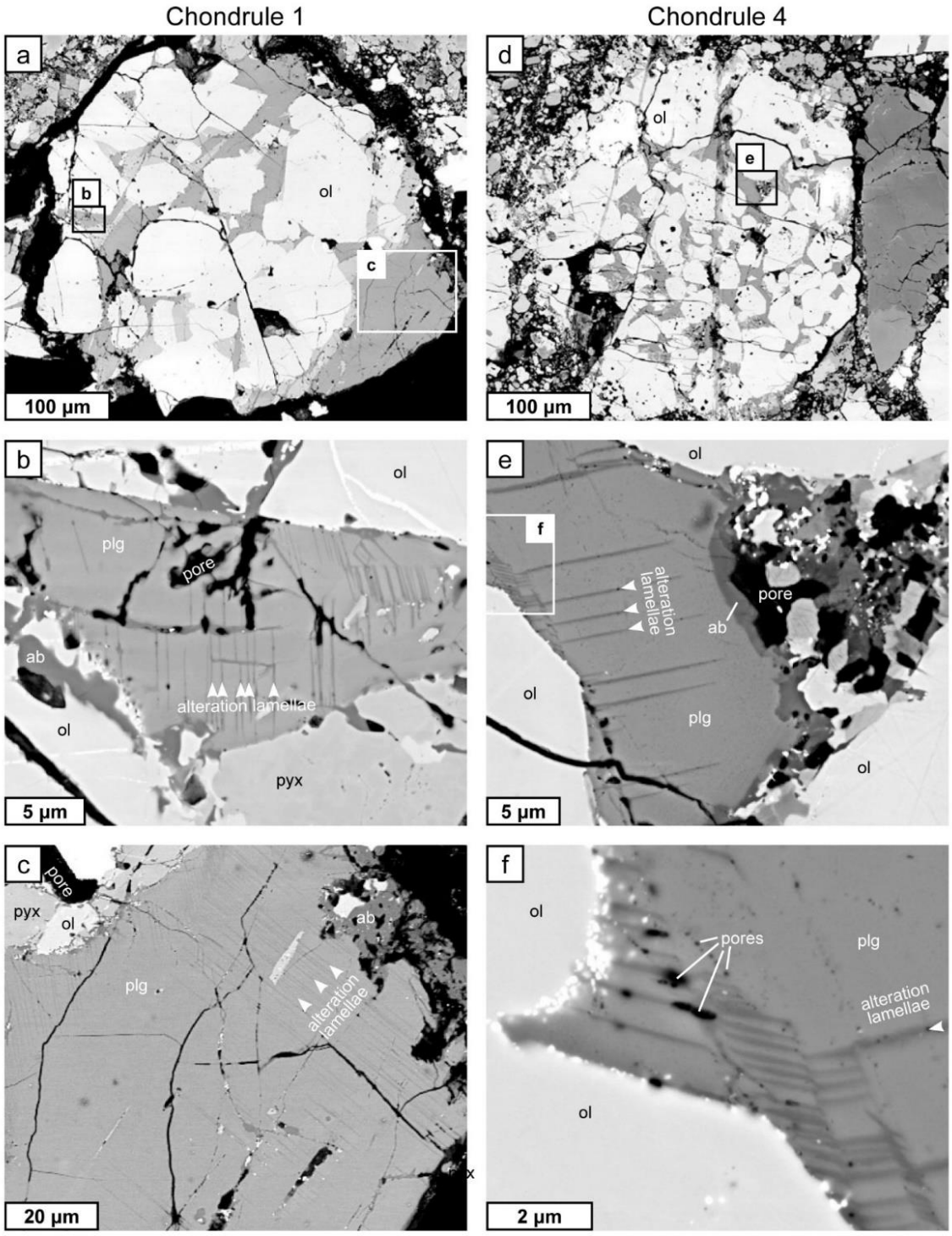

Figure 3.5. BSE images showing alteration in two feldspar-bearing chondrules in Bo Xian (LL3.9). (a-c) Chondrule 1 (a), a 0.4 mm diameter porphyritic olivine (PO) chondrule. (b) Close-up of region interstitial to olivine (ol) and pyroxene (pyx) phenocrysts in which plagioclase (plg, An_{75-80}) is being altered to albite (ab) along grain boundaries. Alteration is accompanied by alteration lamellae and µm to sub-µm pores. *(Caption continues on the following page).*

Figure 3.5. *(Caption continued from the previous page).* (c) Close-up of a large (200 μm long) region of plagioclase near chondrule edge with a high concentration of sub-μm alteration lamellae. Albitization is present along the chondrule edge with an irregular, porous border with the plagioclase. (d-f) Chondrule 4 (d), a 0.4 mm PO chondrule. (e) Close-up of region interstitial to olivine phenocrysts in which plagioclase (An_{73-84}) is being altered to albite near porous region. Plagioclase also contains alteration lamellae and sub-μm pores. (f) Close-up of altered region illustrating alteration lamellae and porosity associated with the lamellae. Very small pores are also found throughout the plagioclase.

and consistent through the whole chondrule. These laths are similar to those described as primary igneous albite in Semarkona chondrules (Lewis and Jones, in review) and like those observed in Semarkona, only present on the chondrule edge. Some laths have sub-μm K-feldspar (K-fsp) exsolution lamellae perpendicular to the long axis of the grain. Complex zoning, subparallel to the grain morphology, is also present in some albite laths and is closer in appearance to the complex zoning in the Chainpur grains (Fig. 3.2f) than the zoning in Dhajala chondrule 11.

Bo Xian (LL3.9)

Alteration of calcic plagioclase in Bo Xian is similar to the albitization observed in Dhajala chondrule 2 (Fig. 3.4b) and is shown in two chondrules in Fig. 3.5. Chondrule 1 (Fig. 3.5a) is a PO chondrule in which plagioclase (An_{75-80}) is being altered to albite along grain boundaries (Fig. 3.5b). Alteration is accompanied by crystallographically oriented alteration lamellae in the interior of the grain, and μm to sub-μm pores. Like Dhajala, alteration lamellae may be albite, related to the albitization reaction at the edge of the grain. Toward the edge of the chondrule (Fig. 3.5c), plagioclase contains a high concentration of sub-μm, crystallographically-oriented alteration lamellae. Albite is also present on the chondrule edge where it has an irregular, porous border with the calcic plagioclase.

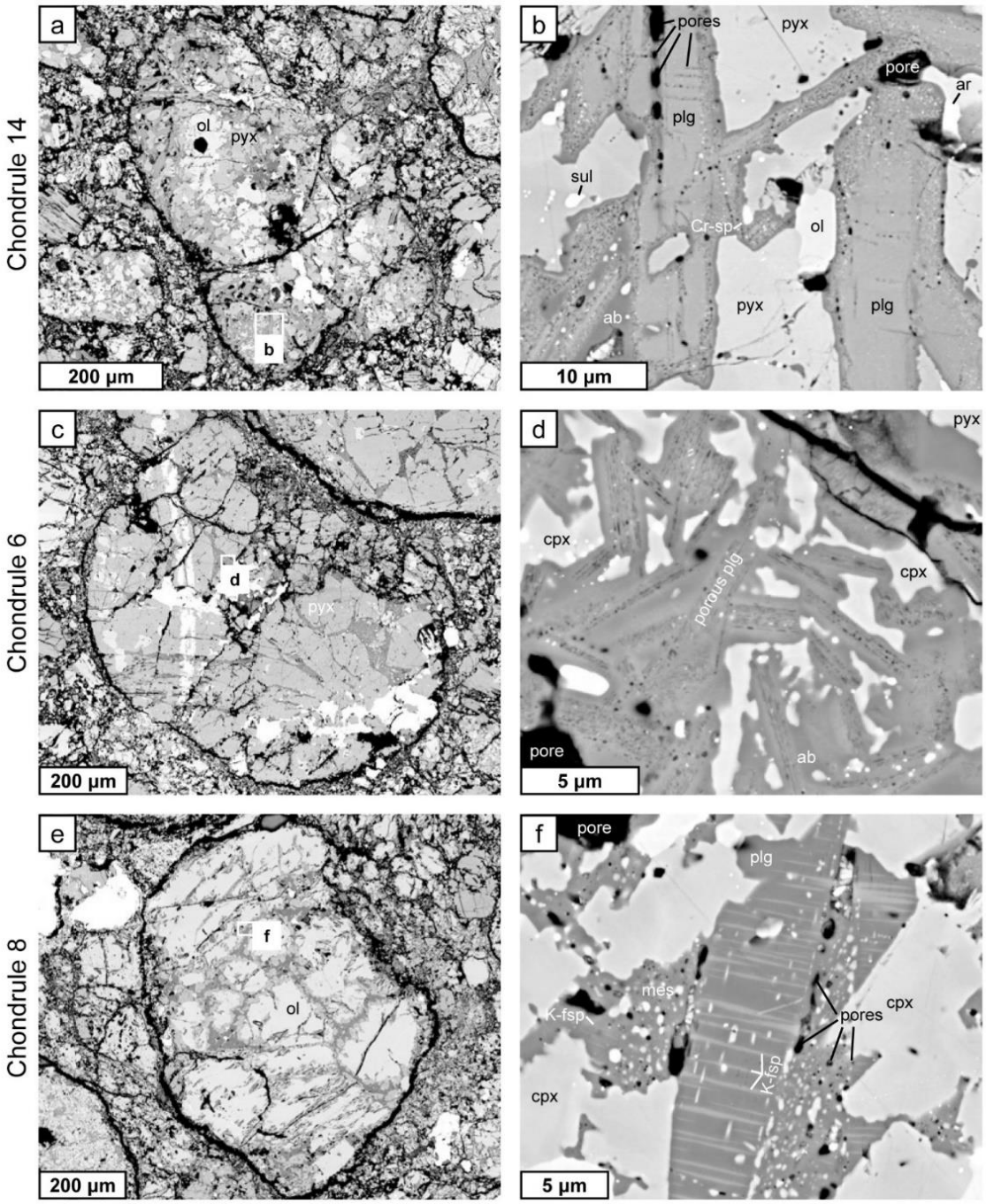

Figure 3.6. BSE images showing alteration in three relict feldspar-bearing chondrules in Bjurböle (L/LL4). (a-b) Chondrule 14 (a), a 0.6 mm diameter porphyritic olivine and pyroxene (POP) chondrule. (b) Close-up of region interstitial to olivine (ol) and pyroxene (pyx) phenocrysts in which plagioclase (plg, An_{66-81}) laths are being altered to albite (ab, An_{5-7}) along grain boundaries. Pores are concentrated along the alteration boundaries. Small (µm-sized) sulfides (sul), Cr-spinel (Cr-sp), and armalcolite (ar) are present as well as abundant sub-µm oxides and sulfides throughout the altered region. (c-d) Chondrule 6 (c), a 1 mm diameter porphyritic pyroxene (PP) chondrule. *(Caption continues on the following page).*

Figure 3.6. *(Caption continued from the previous page).* (d) Close-up of region interstitial to pyroxene phenocrysts in which plagioclase (plg) laths, between Ca-rich pyroxene (cpx) grains, are being altered to albite along grain boundaries. Plagioclase has developed extensive sub-μm porosity in the cores of the laths. (e-f) Chondrule 8 (e), a 0.8 mm diameter porphyritic olivine (PO) chondrule. (f) Close-up of region interstitial to olivine phenocrysts in which 4-6 μm wide albite (An_{2-5}) laths, with sub-μm K-feldspar (K-fsp) exsolution lamellae, are present in crystallized mesostasis glass (mes), between larger Ca-rich pyroxene grains. The crystallized mesostasis glass is fine-grained, porous, and the albite component also contains fine-scale K-feldspar exsolution lamellae.

Chondrule 4 (Fig. 3.5d) is a PO chondrule with plagioclase (An_{73-84}) that is being altered to albite near porous regions (Fig. 3.5e). Plagioclase also contains crystallographically oriented alteration lamellae and sub-μm pores. A close-up image of the plagioclase in this region reveals ~0.5 μm size pores along the alteration lamellae and much smaller pores throughout the calcic plagioclase, resulting in a spongy texture (Fig. 3.5f). These features, particularly the alteration lamellae, were also described in Bo Xian by Jones and Brearley (2010). They also noted the presence of fine-scale nepheline lamellae in calcic plagioclase.

Bjurböle (L/LL4)

Plagioclase in type 4 OCs has the most complex alteration features out of all the petrologic types in the chondrites we studied. These features are pervasive throughout the chondrules. They are effectively more developed versions of the alteration features observed in the type 3.8-3.9 chondrites. Jones and Brearley (2010) noted alteration lamellae and albitization in Bjurböle, in addition to the alteration features we will describe.

Relict chondrules in Bjurböle are illustrated in Fig. 3.6. Chondrule 14 (Fig. 3.6a) is a POP chondrule with plagioclase (An_{66-81}) laths altered to albite (An_{5-7}) along grain boundaries, with sub-μm pores concentrated along the alteration boundaries (Fig. 3.6b).

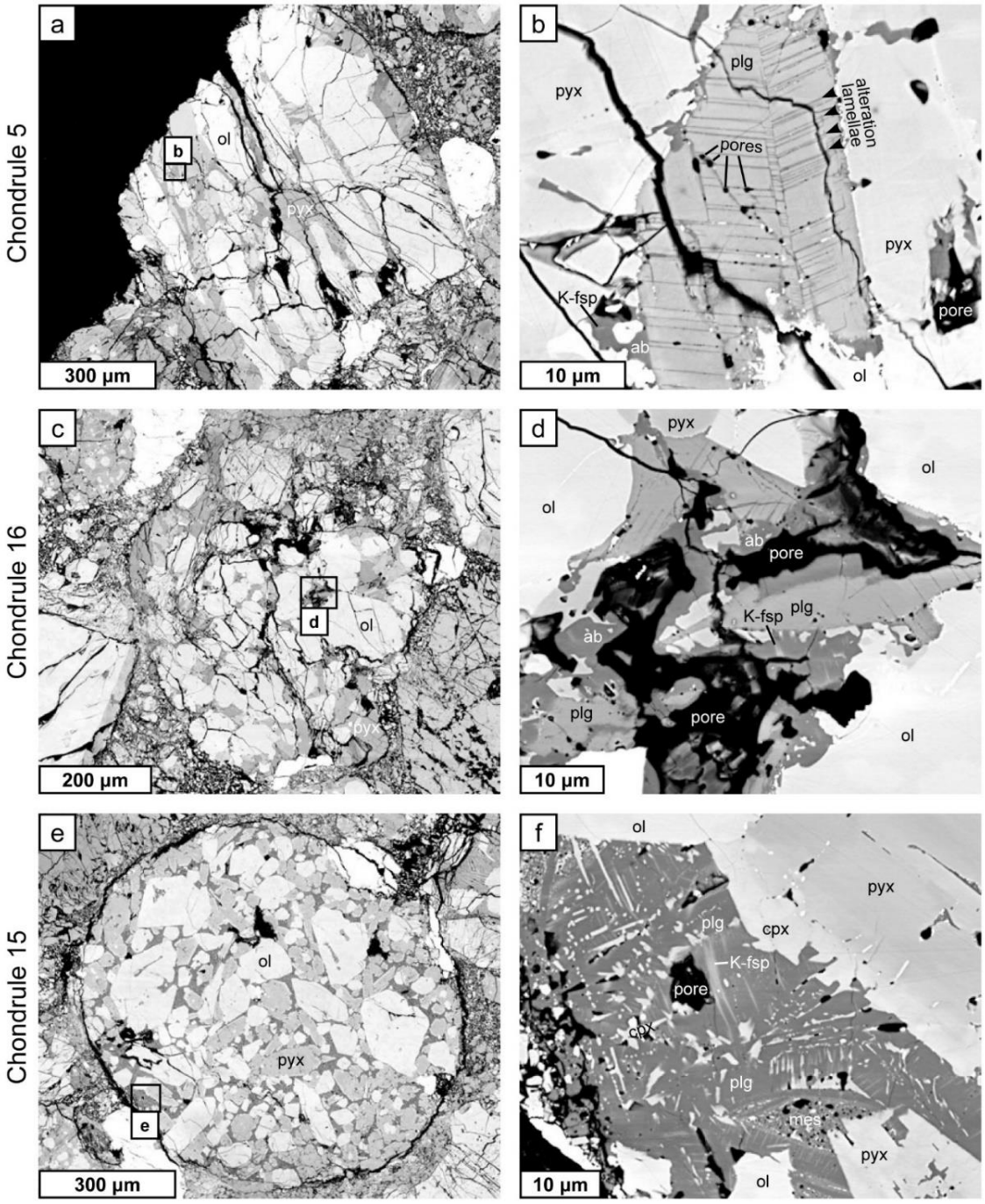

Figure 3.7. BSE images showing alteration in three relict feldspar-bearing chondrules in Saratov (L4). (a-b) Chondrule 5 (a), a 1 mm diameter porphyritic olivine and pyroxene (POP) chondrule on the edge of the thin section. (b) Close-up of region interstitial to pyroxene (pyx) and olivine (ol) phenocrysts showing plagioclase (plg, An_{73-84}) laths with alteration lamellae and sub-µm pores. Plagioclase laths are being altered to albite (ab) along grain boundaries and fine-scale K-feldspar (K-fsp) exsolution is present within the albite. (c-d) Chondrule 16 (c), a 0.7 mm diameter POP chondrule. *(Caption continues on the following page).*

Figure 3.7. *(Caption continued from the previous page).* (d) Close-up of highly porous region interstitial to olivine and pyroxene phenocrysts showing calcic plagioclase with extensive albitization along the pore boundaries. Plagioclase has some alteration lamellae and sub-μm pores. Albite has some fine-scale K-feldspar exsolution. (e-f) Chondrule 15 (e), a 0.8 mm diameter POP chondrule. (f) Close-up of region near chondrule edge, interstitial to olivine and pyroxene phenocrysts showing 1-4 μm wide albite (An_{1-11}) laths, μm-sized Ca-rich pyroxene (cpx), and crystallized mesostasis glass (mes). Albite has fine-scale K-feldspar exsolution which coarsens near the larger pores.

Small (μm-sized) grains of Cr-spinel and armalcolite are present in the alteration regions, as well as abundant sub-μm oxides and sulfides. Chondrule 6 (Fig. 3.6c), a PP chondrule, also has plagioclase laths with albite along grain boundaries but the plagioclase has developed extensive sub-μm porosity in the cores of more calcic laths, parallel to the long axis (Fig. 3.6d). Plagioclase is zoned in Na and Ca in ~1 μm-wide regions from the albite to the edge of the porous calcic plagioclase cores.

Chondrule 8 (Fig. 3.6e), a PO chondrule, that contains two generations of plagioclase. Primary albite (An_{2-5}) occurs as 4-6 μm wide laths, with sub-μm K-feldspar exsolution lamellae that are more abundant than the exsolution texture described in Dhajala (Fig. 3.4f). The albite laths occur within crystallized mesostasis glass that consists mostly of fine-grained secondary albite in addition to Ca-rich pyroxene and sub-μm pores. The crystallized glass in Bjurböle is coarser-grained than the crystallized glass observed in Dhajala (Figs. 3.4f). The albite component of the crystallized glass also contains fine-scale K-feldspar exsolution lamellae.

Saratov (L4)

Plagioclase alteration in Saratov (Fig. 3.7) is pervasive and like the alteration in Bjurböle. Chondrule 5 (Fig. 3.7a) is a relict POP chondrule on the edge of the thin section. Plagioclase (An_{73-84}) laths have sub-μm, crystallographically controlled alteration lamellae, some of which contain pores (Fig. 3.7b). Albite is present along grain

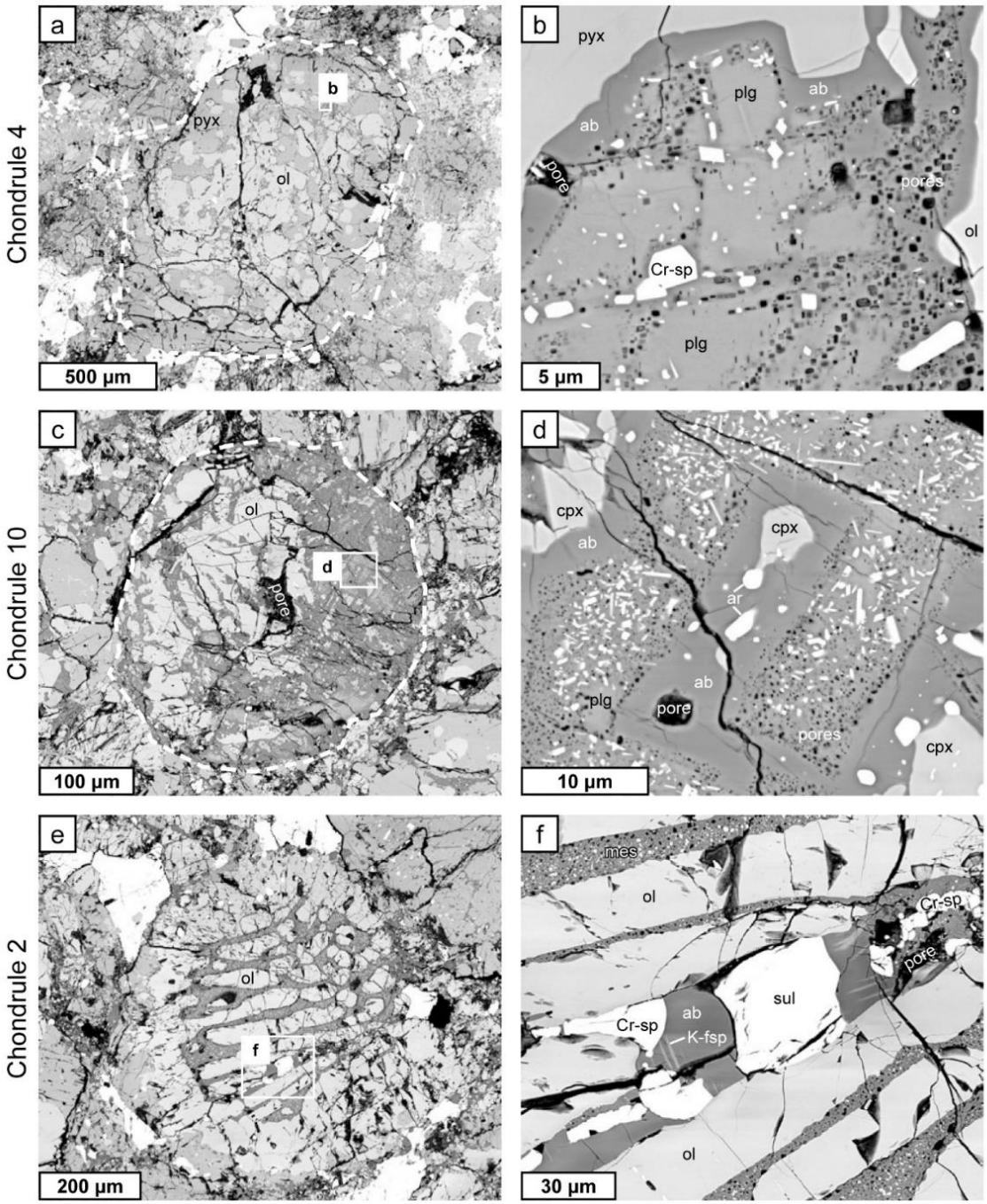

Figure 3.8. BSE images showing alteration in three relict feldspar-bearing chondrules in Santa Barbara (L4). (a-b) Chondrule 4 (a), a 1.6 mm diameter porphyritic olivine and pyroxene (POP) chondrule, outlined with a white dashed line. (b) Close-up of region interstitial to pyroxene (pyx) and olivine (ol) phenocrysts showing calcic plagioclase (plg) altered to albite (ab) along the phenocryst grain boundaries. Cr-spinel (Cr-sp) is present within the albitized regions and faceted pores are abundant. (c-d) Chondrule 10 (c), a 0.35 mm diameter porphyritic olivine (PO) chondrule, outlined with a white dashed line. Olivine phenocrysts are abundant only in one half of the chondrule and plagioclase dominates the other half. *(Caption continues on the following page).*

Figure 3.8. *(Caption continued from the previous page).* (d) Close-up of plagioclase-dominated region with Ca-rich pyroxene (cpx) grains within areas of smooth albite. 2-3 μm sized grains of armalcolite (ar) are also present in the albite. Porous plagioclase is more calcic than the albitized regions and contains abundant, euhedral oxides. (e-f) Chondrule 2 (e), a 0.7 mm diameter barred olivine (BO) chondrule. (f) Close-up of region interstitial to olivine bars which contains crystallized mesostasis glass (mes) and smooth regions of albite with 0.5-1 μm wide K-feldspar exsolution lamellae near cracks and pores. Albite is accompanied by a large sulfide (sul) grain and Cr-spinel grains.

boundaries with the olivine and pyroxene phenocrysts. Fine-scale K-feldspar exsolution is observed within the albite. Chondrule 16 (Fig. 3.7c), is also a relict POP chondrule but plagioclase has fewer alteration lamellae than chondrule 5 (Fig. 3.7d). Albitization is extensive in a highly porous region, adjacent to the pores, and along grain boundaries with the olivine phenocrysts. Sub-μm pores are also present along the albitization boundaries and the albite has some fine-scale K-feldspar exsolution lamellae.

A region near the edge of chondrule 15 (Fig. 3.7e), a relict POP chondrule, contains albite (An_{1-11}) laths, μm-sized Ca-rich pyroxene grains, and porous, crystallized mesostasis glass (Fig. 3.7f). The albite laths here are similar in appearance to the primary albite in Dhajala chondrule 6 (Fig. 3.4f) and, to a lesser extent, Bjurböle chondrule 8 (Fig. 3.6f). The laths contain abundant, fine-scale K-feldspar exsolution lamellae. The lamellae are perpendicular to the long axis of the albite laths, and parallel/sub-parallel to the small Ca-rich pyroxene grains. The lamellae are also coarser near large pores and the pores along albite grain boundaries.

Santa Barbara (L4)

Plagioclase alteration in Santa Barbara is different from that in Saratov and Bjurböle as illustrated in three relict chondrules in Fig. 3.8. Feldspar composition for these chondrules are reported in Lewis and Jones (2016). Chondrule 4 (Fig. 3.8a) is a POP chondrule in which calcic plagioclase (An_{73-82}) is being altered to albite (An_{7-9})

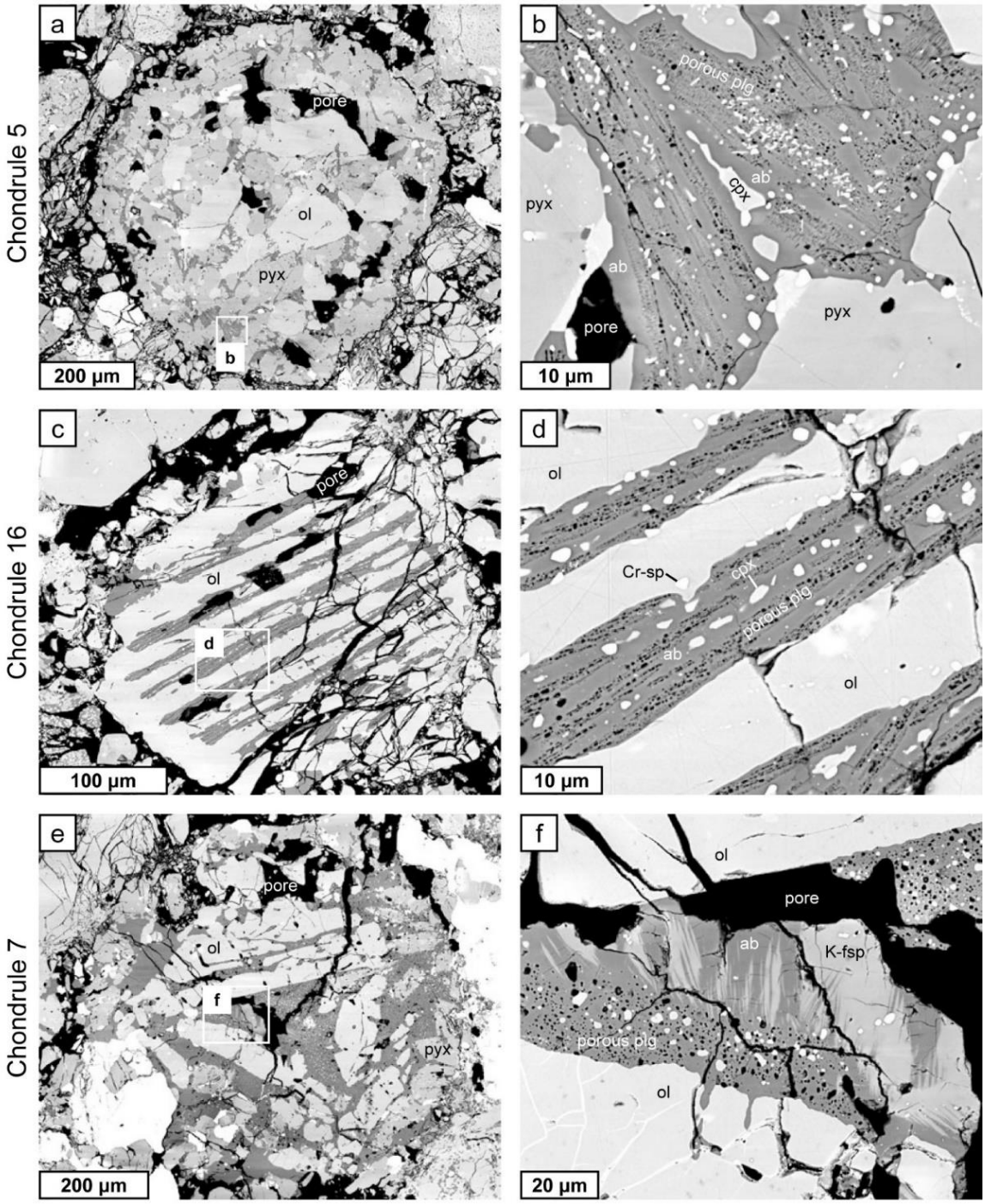

Figure 3.9. BSE images showing alteration in three relict feldspar-bearing chondrules in Avanhandava (H4). (a-b) Chondrule 5 (a), a 0.8 mm diameter porphyritic olivine and pyroxene (POP) chondrule with many 50 µm diameter pores. (b) Close-up of region interstitial to pyroxene (pyx) phenocrysts with Ca-rich pyroxene (cpx) and plagioclase (plg, An_{11-50}) laths altered to albite (ab) along grain boundaries. Plagioclase lath interiors are highly porous with abundant, euhedral oxides. (c-d) Chondrule 16 (c), a 0.3 mm diameter barred olivine (BO) chondrule with large (30 µm diameter) pores between the olivine bars. *(Caption continues on the following page).*

Figure 3.9. *(Caption continued from the previous page).* (d) Close-up of region interstitial to olivine (ol) bars with albitic plagioclase alternating regions of smooth and porous textures. Smooth regions have μm-sized grains of Ca-rich pyroxene. Porous regions are reminiscent of plagioclase laths. Few oxides are present. (e-f) Chondrule 7 (e), a 0.7 mm diameter POP chondrule. (f) Close-up of porous region, interstitial to olivine phenocrysts, with smooth albitic plagioclase (An_{6-12}) and a large patch K-feldspar (K-fsp, Or_{84}). Plagioclase outside the smooth region is porous and contains μm-sized grains of Ca-rich pyroxene.

along grain boundaries with the olivine and pyroxene phenocrysts (Fig. 3.8b). While this is somewhat like previously described albitization reactions, alteration in this chondrule differs in that it is accompanied by abundant faceted pores and euhedral Cr-spinel. Chondrule 10 (Fig. 3.8c), a PO chondrule, is similar but the alteration reaction appears to have gone further to completion (Fig. 3.8d). Albite rims are wider in chondrule 10, and their formation is possibly crystallographically controlled as some have a square morphology. Porosity and euhedral oxides are more abundant, and the calcic plagioclase (a maximum of An_{27-30}) is almost completely removed. The albite also contains μm-sized grains of armalcolite.

Chondrule 2 (Fig. 3.8e) is a barred olivine (BO) chondrule. Interstitial to olivine bars there are separate regions of porous, crystallized mesostasis glass and smooth albite (An_{5-9}) with sulfides and Cr-spinel. Albite contains 0.5-1 μm wide K-feldspar exsolution lamellae near cracks and pores. The albite here differs from Saratov chondrule 15 (Fig. 3.7f), Bjurböle chondrule 8 (Fig. 3.6f), and Dhajala chondrule 6 (Fig. 3.4f) in that it does not have lath-like morphology. Smooth albite only exists in this one region of the chondrule: the rest of the area between the olivine bars consists of porous albite consistent with crystallized mesostasis glass.

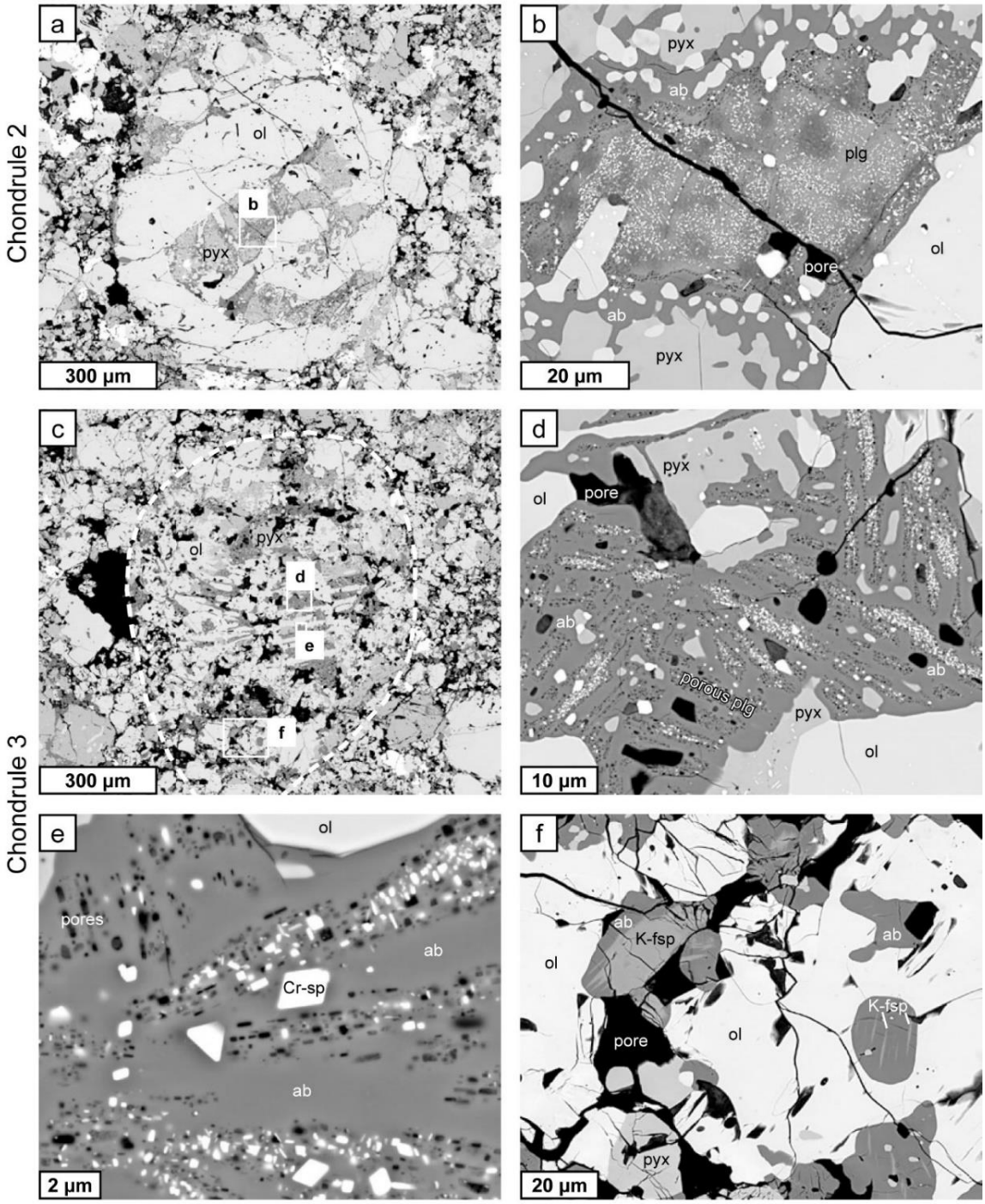

Figure 3.10. BSE images showing alteration in two relict feldspar-bearing chondrules in Tuxtuac (LL5). (a-b) Chondrule 2 (a), a 0.8 mm diameter porphyritic olivine and pyroxene (POP) chondrule. (b) Close-up of region interstitial to olivine (ol) and pyroxene (pyx) phenocrysts in which calcic plagioclase (plg) is altered to albite (ab) along grain boundaries. The plagioclase interior contains abundant, euhedral oxides and the border between the interior and albitized rims is highly porous. *(Caption continues on the following page).*

Figure 3.10. *(Caption continued from the previous page).* (c-f) Chondrule 3 (c), a 0.8 mm diameter POP chondrule. (d-f) Close-up images of plagioclase-bearing regions interstitial to olivine and pyroxene phenocrysts. (d) Plagioclase laths altered to albite along grain boundaries with porous, oxide-bearing cores. Numerous larger (3-5 μm diameter) pores are present, many in close association with albitized rims. (e) Plagioclase laths altered to albite, like (d). Sub-μm, euhedral Cr-spinel (Cr-sp) and pores are abundant in the plagioclase cores. Lighter-colored plagioclase in porous regions is higher in calcium. (f) Porous region in which smooth albite shows fine and coarse K-feldspar (K-fsp) exsolution lamellae.

Avanhandava (H4)

Plagioclase alteration in Avanhandava is more like Santa Barbara than Saratov or Bjurböle. Alteration has gone further to completion than the other type 4s, including Santa Barbara, and very little calcic plagioclase remains. This was also noted by Kovach and Jones (2010). We describe three relict chondrules in Fig. 3.9, all of which have considerable large-scale internal porosity. Chondrule 5 (Fig. 3.9a) is a POP chondrule with many 50 μm diameter pores in the outer third of the chondrule. Plagioclase laths (An_{11-50}) are altered to albite along grain boundaries with lath interiors that are highly porous and contain abundant, euhedral oxides (Fig. 3.9b). This texture is similar to, but more advanced than, Bjurböle chondrule 6 (Fig. 3.6d).

Chondrule 16 (Fig. 3.9c) is a BO chondrule with 30 μm diameter pores between the olivine bars. Albitic plagioclase is present in alternating regions of smooth and porous textures (Fig. 3.9d). Smooth regions have μm-sized grains of Ca-rich pyroxene. Porous regions indicate the presence of altered plagioclase laths. Few oxides are present. This BO chondrule appears to be an altered form of the anorthite-bearing BO chondrule in Semarkona described by Lewis and Jones (in review).

Chondrule 7 (Fig. 3.9e) is a POP chondrule with a region of smooth albitic plagioclase (An_{6-12}) and an extensive K-feldspar patch ($\sim Or_{84}$) adjacent to a large porous region (Fig. 3.9f). Plagioclase outside the smooth feldspar region contains μm to sub-μm

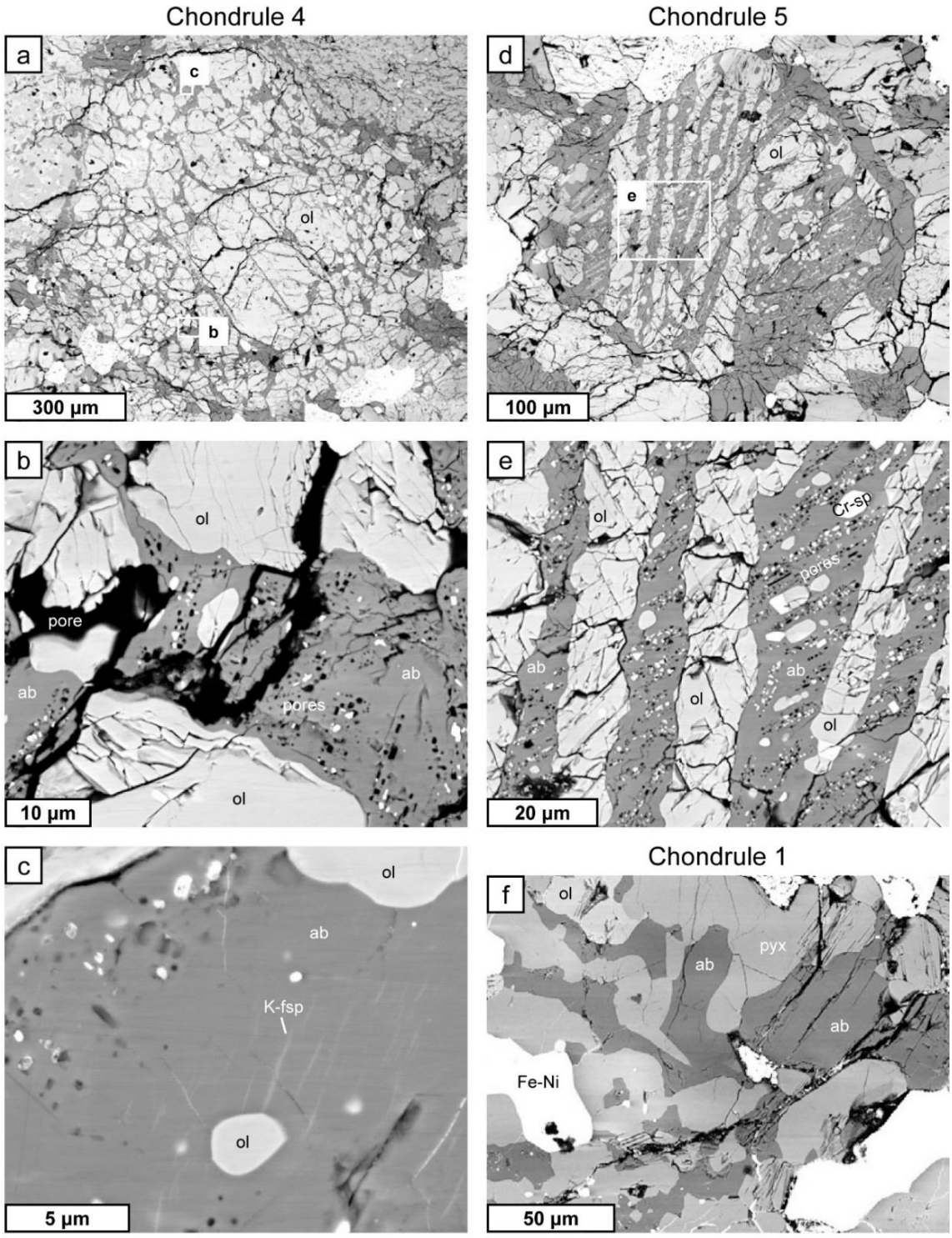

Figure 3.11. BSE images three relict feldspar-bearing chondrules in Sulagiri (LL6). (a-c) Chondrule 4 (a), a 1 mm diameter porphyritic olivine (PO) chondrule. (b-c) Close-up images of regions interstitial to olivine (ol) phenocrysts in which plagioclase is completely equilibrated to albite (ab) and contains subhedral pores and oxides. (c) Sub-µm K-feldspar (K-fsp) exsolution lamellae in a region of smooth albite. *(Caption continues on the following page).*

Figure 3.11. *(Caption continued from the previous page).* (d-e) Chondrule 5 (d), a 0.4 mm diameter barred olivine (BO) chondrule. (e) Close-up of region between the olivine bars that has equilibrated to albite. Pores and some euhedral oxides, mostly Cr-spinel (Cr-sp), highlight the cores of relict calcic plagioclase laths. (f) Close-up of region in chondrule 1 illustrating the typical appearance of equilibrated plagioclase in Sulagiri as smooth regions of albite >50 μm in size.

pores and μm-sized grains of Ca-rich pyroxene. Potassium-rich feldspar is abundant in many chondrules in Avanhandava in a range of textures from scattered, individual K-feldspar exsolution lamellae to coherent regions of crypto-antiperthite 100s of μm in size. A more detailed description of K-feldspar exsolution in Avanhandava is presented in Lewis et al. (In preparation).

Tuxtuac (LL5)

Plagioclase in Tuxtuac is like Santa Barbara and Avanhandava. Chondrule 2 (Fig. 3.10a) is a relict POP chondrule in which calcic plagioclase is altered to albite along grain boundaries (Fig. 3.10b). The plagioclase interior contains abundant, euhedral oxides and sub-μm pores, much like Santa Barbara chondrules 4 and 10 (Figs. 3.8b,d). Chondrule 3 (Fig. 3.10c) is a extensively recrystallized POP chondrule where plagioclase laths are altered to albite along grain boundaries with porous, oxide-bearing cores (Fig. 3.10d), similar to Avanhandava chondrules 5 and 16 (Figs. 3.9b,d). Numerous larger (3-5 μm diameter) pores are present, many in close association with albitized rims. Sub-μm, euhedral Cr-spinel and faceted pores are abundant in the plagioclase cores (Fig. 3.10e). In another region of chondrule 3, smooth albite contains fine-scale K-feldspar exsolution lamellae and a 20 μm K-feldspar patch in association with extensive porosity (Fig. 3.10f).

Sulagiri (LL6)

Plagioclase alteration in Sulagiri is like alteration in Tuxtuac and Avanhandava. Chondrule 4 (Fig. 3.11a), a relict PO chondrule, contains plagioclase that is completely

altered to albite but with some subhedral pores and oxides (Fig. 3.11b). Sub-μm K-feldspar exsolution lamellae are present in a region of smooth albite (Fig. 3.11c). Chondrule 5 (Fig. 3.11d), a relict BO chondrule, contains plagioclase that is altered to albite (Fig. 3.11e), much like BO chondrule 16 in Avanhandava (Fig. 3.9d). Pores and some euhedral to subhedral oxides, mostly Cr-spinel, mark the cores of the relict calcic plagioclase laths. While we focused on alteration textures in this study, it is important to note that most plagioclase in Sulagiri is present in large (>50 μm), smooth regions, such as the ones illustrated in Fig. 3.11f, from chondrule 1. Textural equilibration to smooth plagioclase appears to be the product of thermal metamorphism whereas the albitization reaction described above is responsible for the majority of the chemical transition to albite. Compositional equilibration in large, smooth regions of plagioclase were the focus of the OC feldspar studies by Kovach and Jones (2010) and Lewis and Jones (2016).

3.2. Feldspar compositions

Calcic feldspar was measured in type 3 OCs using EPMA to determine how An contents change from those measured previously in the unequilibrated Semarkona OC (Lewis and Jones, in review) through to the equilibrated OCs (Kovach and Jones, 2010; Lewis and Jones, 2016). EPMA data for type 3 OCs are tabulated in Table 3.2 and plotted in feldspar ternaries in Fig. 3.12. Plagioclase in some Bishunpur chondrules contains near-end-member anorthite (An_{99} in chondrule 7). However, Chainpur, Parnallee, Dhajala, and Bo Xian have a lower maximum An content in their plagioclase, between An_{84} and An_{87}. Orthoclase content is generally low, less than Or_1. Additional analyses of K-feldspar in Parnallee albite (chondrules 2 and 9), yielded higher Or contents, up to Or_{10}, because the electron beam overlapped fine-scale K-feldspar exsolution lamellae

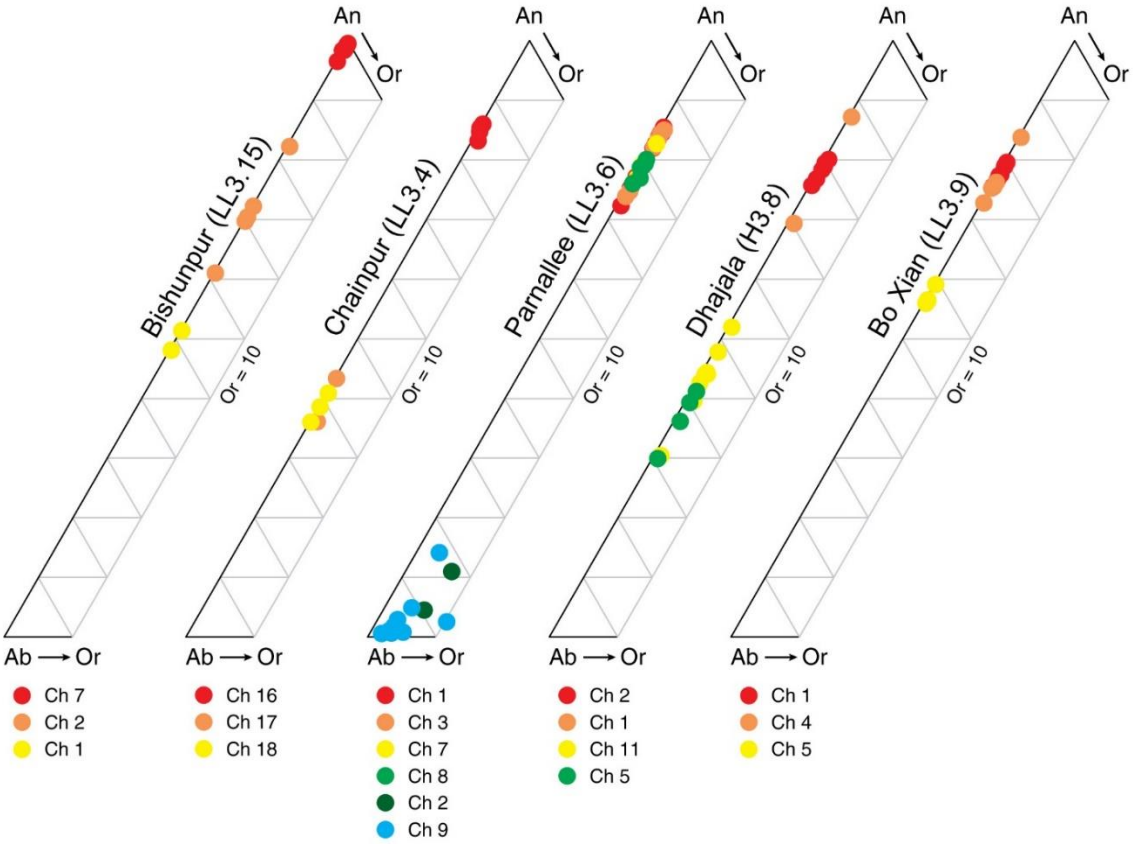

Figure 3.12. Feldspar compositions in type 3 OCs, obtained with EPMA. Each point is a single analysis, and each color is an individual chondrule. All feldspar ternary plots are truncated at Or_{10}. Albitic plagioclase is present in all chondrites analyzed but quantitative compositional data were obtained for only the most Ca-rich plagioclase, to understand the equilibration process. The albitic analyses in Parnallee are from regions containing K-feldspar exsolution. While the plagioclase compositions within each chondrite, taken together, is large, the range of plagioclase compositions within each chondrule is limited.

(e.g., Fig. 3.3f). Each chondrule within a chondrite has a limited range of plagioclase compositions, consistent with observations in previous studies (Lewis and Jones, in review; Kovach and Jones, 2010; Lewis and Jones, 2016).

Feldspars of all compositions were measured in type 4 OC chondrules and are given in Table 3.2 and illustrated in Fig. 3.13. Plagioclase in Bjurböle and Saratov has a maximum An content of ~An_{85}, consistent with the maximum An content of calcic plagioclase in subtypes 3.4-3.9, $An_{84\text{-}87}$. Avanhandava has a much reduced maximum An

Table 3.2. Average feldspar compositions for selected chondrules.

	Bishunpur (LL3.15)						Chainpur (LL3.4)					
	Chondrule 7		Chondrule 2		Chondrule 1		Chondrule 16		Chondrule 17		Chondrule 18	
	wt. %	*1σ*	wt. %	*1σ*	wt. %	*1σ*	wt. %	*1σ*	wt. %	*1σ*	wt. %	*1σ*
SiO_2	43.5	*1.1*	50.0	*1.1*	55.6	*0.4*	46.5	*1.6*	62.0	*3.6*	60.6	*0.7*
Al_2O_3	36.3	*0.7*	28.7	*1.0*	27.0	*0.1*	35.2	*0.9*	23.9	*3.1*	26.7	*1.2*
Cr_2O_3	<0.07	*0.05*	0.14	*0.11*	0.11	*0.03*	<0.07	*0.06*	<0.07	*0.07*	<0.07	*0.00*
FeO	0.55	*0.23*	0.64	*0.19*	0.71	*0.18*	0.68	*0.10*	0.90	*0.32*	0.91	*0.28*
MnO	<0.08	*0.05*	<0.08	*0.07*	<0.08	*0.09*	<0.08	*0.05*	0.23	*0.11*	<0.08	*0.00*
MgO	0.33	*0.13*	1.40	*0.73*	1.08	*0.15*	0.10	*0.04*	1.26	*1.03*	0.81	*0.91*
CaO	20.4	*0.4*	14.5	*0.9*	11.0	*0.5*	17.1	*0.9*	8.4	*0.4*	8.9	*0.5*
Na_2O	0.11	*0.10*	3.69	*0.66*	6.11	*0.28*	1.65	*0.07*	7.03	*1.11*	7.80	*0.39*
K_2O	0.04	*0.01*	0.03	*0.01*	0.05	*0.01*	0.07	*0.06*	0.12	*0.12*	0.05	*0.01*
Total[1]	101.2	*1.0*	99.2	*0.9*	101.7	*0.5*	101.4	*1.8*	103.9	*2.9*	105.7	*0.3*
	formula based on 8 oxygens											
Si	2.00	*0.04*	2.32	*0.04*	2.48	*0.01*	2.11	*0.05*	2.68	*0.09*	2.59	*0.02*
Al	1.97	*0.04*	1.57	*0.04*	1.42	*0.00*	1.89	*0.06*	1.22	*0.19*	1.34	*0.06*
Cr	0.00	*0.00*	0.01	*0.00*	0.00	*0.00*	0.00	*0.00*	0.00	*0.00*	0.00	*0.00*
Fe	0.02	*0.01*	0.02	*0.01*	0.03	*0.01*	0.03	*0.00*	0.03	*0.01*	0.03	*0.01*
Mn	0.00	*0.00*	0.00	*0.00*	0.00	*0.00*	0.00	*0.00*	0.01	*0.00*	0.00	*0.00*
Mg	0.02	*0.01*	0.10	*0.05*	0.07	*0.01*	0.01	*0.00*	0.08	*0.06*	0.05	*0.06*
Ca	1.00	*0.02*	0.72	*0.05*	0.53	*0.03*	0.83	*0.04*	0.39	*0.03*	0.40	*0.02*
Na	0.01	*0.01*	0.33	*0.06*	0.53	*0.02*	0.15	*0.01*	0.59	*0.08*	0.65	*0.03*
K	0.00	*0.00*	0.00	*0.00*	0.00	*0.00*	0.00	*0.00*	0.01	*0.01*	0.00	*0.00*
Total	5.02	*0.02*	5.06	*0.00*	5.07	*0.00*	5.02	*0.02*	5.01	*0.04*	5.07	*0.03*
An	98.8	*0.8*	68.3	*5.0*	49.7	*2.3*	84.8	*1.2*	39.7	*5.1*	38.5	*2.4*
Ab	0.9	*0.9*	31.5	*5.0*	50.0	*2.2*	14.8	*0.9*	59.7	*4.5*	61.3	*2.5*
Or	0.2	*0.1*	0.2	*0.0*	0.2	*0.1*	0.4	*0.4*	0.7	*0.6*	0.2	*0.1*
n[2]	12		4		2		4		2		3	

[1] measurements below detection limit not included in totals

[2] n = number of analyses

Table 3.2. *(Continued).* Average feldspar compositions for selected chondrules.

	Parnallee (LL3.6)								Dhajala (H3.8)							
	Chondrule 1		Chondrule 3		Chondrule 8		Chondrule 9		Chondrule 2		Chondrule 1		Chondrule 11		Chondrule 5	
	wt. %	*1σ*	wt. %	*1σ*	wt. %	*1σ*	wt. %	*1σ*	wt. %	*1σ*	wt. %	*1σ*	wt. %	*1σ*	wt. %	*1σ*
SiO_2	46.1	*0.6*	45.8	*1.2*	47.1	*0.3*	68.9	*1.7*	49.8	*0.3*	49.1	*2.8*	60.4	*2.5*	61.8	*1.7*
Al_2O_3	35.8	*0.4*	35.2	*0.2*	33.5	*0.3*	18.5	*1.0*	34.1	*0.3*	34.0	*1.8*	27.1	*2.0*	26.8	*0.8*
Cr_2O_3	<0.03	*0.01*	<0.03	*0.03*	<0.03	*0.02*	<0.03	*0.04*	<0.07	*0.05*	<0.07	*0.00*	<0.07	*0.05*	<0.07	*0.08*
FeO	0.76	*0.40*	0.28	*0.11*	0.33	*0.07*	1.04	*0.73*	0.34	*0.14*	0.24	*0.13*	0.48	*0.29*	0.65	*0.12*
MnO	<0.03	*0.02*	<0.03	*0.02*	<0.03	*0.00*	<0.03	*0.02*	<0.09	*0.05*	<0.09	*0.00*	<0.09	*0.11*	<0.09	*0.00*
MgO	0.12	*0.08*	0.24	*0.14*	0.34	*0.23*	0.55	*0.53*	0.05	*0.02*	0.22	*0.06*	0.63	*0.95*	0.18	*0.16*
CaO	16.9	*0.8*	17.0	*0.6*	16.3	*0.3*	0.7	*0.9*	16.8	*0.4*	17.0	*2.1*	9.6	*1.3*	8.6	*1.0*
Na_2O	2.11	*0.52*	2.22	*0.64*	2.40	*0.17*	10.93	*0.74*	2.53	*0.19*	2.57	*1.56*	6.95	*0.84*	8.11	*0.78*
K_2O	0.09	*0.02*	0.10	*0.02*	0.11	*0.04*	0.71	*0.42*	0.09	*0.02*	0.12	*0.07*	0.16	*0.05*	0.17	*0.02*
Total[1]	101.8	*0.6*	100.9	*0.8*	100.1	*0.5*	101.3	*1.6*	103.7	*0.3*	103.2	*0.8*	105.5	*1.2*	106.3	*0.7*
	formula based on 8 oxygens															
Si	2.09	*0.01*	2.09	*0.03*	2.17	*0.01*	3.00	*0.02*	2.20	*0.02*	2.19	*0.10*	2.58	*0.07*	2.62	*0.05*
Al	1.91	*0.01*	1.90	*0.03*	1.81	*0.01*	0.95	*0.04*	1.78	*0.02*	1.79	*0.11*	1.37	*0.11*	1.34	*0.05*
Cr	0.00	*0.00*	0.00	*0.00*	0.00	*0.00*	0.00	*0.00*	0.00	*0.00*	0.00	*0.00*	0.00	*0.00*	0.00	*0.00*
Fe	0.03	*0.02*	0.01	*0.00*	0.01	*0.00*	0.04	*0.03*	0.01	*0.01*	0.01	*0.00*	0.02	*0.01*	0.02	*0.00*
Mn	0.00	*0.00*	0.00	*0.00*	0.00	*0.00*	0.00	*0.00*	0.00	*0.00*	0.00	*0.00*	0.00	*0.00*	0.00	*0.00*
Mg	0.01	*0.01*	0.02	*0.01*	0.02	*0.02*	0.04	*0.04*	0.00	*0.00*	0.01	*0.00*	0.04	*0.06*	0.01	*0.01*
Ca	0.82	*0.04*	0.84	*0.04*	0.80	*0.01*	0.03	*0.04*	0.80	*0.02*	0.81	*0.11*	0.44	*0.07*	0.39	*0.05*
Na	0.19	*0.04*	0.20	*0.06*	0.21	*0.02*	0.92	*0.05*	0.22	*0.02*	0.22	*0.13*	0.57	*0.06*	0.67	*0.06*
K	0.01	*0.00*	0.01	*0.00*	0.01	*0.00*	0.04	*0.02*	0.00	*0.00*	0.01	*0.00*	0.01	*0.00*	0.01	*0.00*
Total	5.05	*0.02*	5.06	*0.02*	5.04	*0.01*	5.01	*0.02*	5.02	*0.00*	5.04	*0.02*	5.03	*0.01*	5.05	*0.01*
An	81.2	*4.3*	80.6	*5.0*	78.5	*1.5*	3.2	*4.3*	78.2	*1.7*	78.2	*12.6*	43.1	*6.3*	36.6	*4.9*
Ab	18.3	*4.2*	18.9	*4.9*	20.9	*1.4*	92.8	*5.0*	21.3	*1.7*	21.1	*12.2*	56.1	*6.1*	62.5	*4.9*
Or	0.5	*0.1*	0.6	*0.1*	0.6	*0.2*	4.0	*2.5*	0.5	*0.1*	0.6	*0.4*	0.8	*0.2*	0.9	*0.1*
n[2]	13		6		7		9		6		2		8		4	

[1] measurements below detection limit not included in totals

[2] n = number of analyses

Table 3.2. *(Continued).* Average feldspar compositions for selected chondrules.

	Bo Xian (LL3.9)						Bjurböle (L/LL4)							
	Chondrule 1		Chondrule 4		Chondrule 5		Chondrule 15		Chondrule 14		Chondrule 6		Chondrule 8	
	wt. %	*1σ*	wt. %	*1σ*	wt. %	*1σ*	wt. %	*1σ*	wt. %	*1σ*	wt. %	*1σ*	wt. %	*1σ*
SiO_2	47.2	*0.4*	46.6	*0.9*	51.9	*0.3*	50.9	*1.5*	55.0	*9.1*	59.0	*3.5*	69.6	*1.5*
Al_2O_3	34.6	*0.3*	34.3	*0.6*	31.0	*0.4*	33.4	*1.0*	29.1	*6.8*	28.1	*2.4*	20.0	*0.3*
Cr_2O_3	<0.08	*0.04*	<0.08	*0.00*	<0.08	*0.00*	0.08	*0.07*	0.33	*0.58*	0.15	*0.03*	<0.06	*0.05*
FeO	0.36	*0.24*	0.76	*0.05*	0.79	*0.07*	0.79	*0.10*	1.15	*1.21*	0.60	*0.14*	0.56	*0.26*
MnO	<0.08	*0.04*	<0.08	*0.00*	<0.08	*0.00*	<0.07	*0.06*	<0.07	*0.00*	<0.07	*0.00*	<0.07	*0.03*
MgO	<0.02	*0.02*	<0.02	*0.02*	0.02	*0.04*	0.06	*0.02*	0.14	*0.14*	0.25	*0.21*	0.47	*0.31*
CaO	16.8	*0.3*	16.9	*0.7*	12.9	*0.4*	15.5	*1.1*	10.8	*7.6*	9.5	*2.5*	0.8	*0.2*
Na_2O	2.63	*0.18*	2.80	*0.53*	5.33	*0.16*	3.20	*0.66*	5.51	*4.23*	6.95	*1.37*	10.49	*0.49*
K_2O	0.07	*0.01*	0.07	*0.02*	0.07	*0.02*	0.14	*0.03*	0.27	*0.26*	0.17	*0.04*	2.29	*0.80*
Total[1]	101.7	*0.6*	101.5	*0.4*	101.9	*0.2*	104.1	*0.3*	102.3	*1.2*	104.7	*0.2*	104.2	*1.7*
	formula based on 8 oxygens													
Si	2.14	*0.01*	2.13	*0.03*	2.33	*0.02*	2.24	*0.06*	2.44	*0.36*	2.54	*0.13*	2.96	*0.02*
Al	1.85	*0.01*	1.85	*0.04*	1.64	*0.02*	1.73	*0.06*	1.53	*0.38*	1.43	*0.13*	1.00	*0.01*
Cr	0.00	*0.00*	0.00	*0.00*	0.00	*0.00*	0.00	*0.00*	0.01	*0.02*	0.01	*0.00*	0.00	*0.00*
Fe	0.01	*0.01*	0.03	*0.00*	0.03	*0.00*	0.03	*0.00*	0.04	*0.05*	0.02	*0.01*	0.02	*0.01*
Mn	0.00	*0.00*	0.00	*0.00*	0.00	*0.00*	0.00	*0.00*	0.00	*0.00*	0.00	*0.00*	0.00	*0.00*
Mg	0.00	*0.00*	0.00	*0.00*	0.00	*0.00*	0.00	*0.00*	0.01	*0.01*	0.02	*0.01*	0.03	*0.02*
Ca	0.81	*0.01*	0.83	*0.04*	0.62	*0.02*	0.73	*0.05*	0.52	*0.36*	0.44	*0.12*	0.04	*0.01*
Na	0.23	*0.02*	0.25	*0.05*	0.46	*0.01*	0.27	*0.06*	0.47	*0.35*	0.58	*0.11*	0.87	*0.04*
K	0.00	*0.00*	0.00	*0.00*	0.00	*0.00*	0.01	*0.00*	0.02	*0.01*	0.01	*0.00*	0.12	*0.04*
Total	5.05	*0.01*	5.08	*0.02*	5.09	*0.01*	5.03	*0.00*	5.03	*0.02*	5.04	*0.00*	5.04	*0.01*
An	77.6	*1.4*	76.7	*4.2*	56.9	*1.4*	72.3	*5.5*	51.8	*36.2*	42.7	*11.3*	3.5	*0.9*
Ab	22.0	*1.4*	22.9	*4.1*	42.7	*1.4*	26.9	*5.3*	46.7	*34.8*	56.4	*11.1*	84.4	*3.9*
Or	0.4	*0.1*	0.4	*0.1*	0.4	*0.1*	0.7	*0.1*	1.5	*1.4*	0.9	*0.2*	12.1	*4.1*
n[2]	8		5		4		3		6		3		8	

[1] measurements below detection limit not included in totals

[2] n = number of analyses

Table 3.2. *(Continued).* Average feldspar compositions for selected chondrules.

	Saratov (L4)								Avanhandava (H4)							
	Chondrule 5		Chondrule 8		Chondrule 10		Chondrule 15		Chondrule 4		Chondrule 5		Chondrule 2		Chondrule 7	
	wt. %	*1σ*	wt. %	*1σ*	wt. %	*1σ*	wt. %	*1σ*	wt. %	*1σ*	wt. %	*1σ*	wt. %	*1σ*	wt. %	*1σ*
SiO_2	48.7	*0.4*	50.0	*0.5*	63.6	*2.6*	70.4	*1.4*	63.2	*2.1*	62.6	*6.0*	68.2	*1.7*	66.1	*1.0*
Al_2O_3	35.1	*0.6*	32.5	*0.7*	23.4	*2.0*	18.7	*1.3*	25.7	*0.8*	25.0	*3.6*	21.3	*1.3*	21.8	*1.0*
Cr_2O_3	<0.07	*0.04*	0.17	*0.09*	0.23	*0.28*	<0.07	*0.07*	<0.07	*0.00*	0.09	*0.15*	<0.07	*0.00*	<0.07	*0.00*
FeO	0.52	*0.13*	0.94	*0.16*	1.19	*0.42*	0.85	*0.31*	0.43	*0.10*	0.34	*0.07*	0.32	*0.15*	0.30	*0.15*
MnO	<0.08	*0.00*	<0.08	*0.00*	<0.08	*0.05*	<0.08	*0.07*	<0.08	*0.00*	<0.08	*0.00*	<0.08	*0.00*	<0.08	*0.00*
MgO	<0.02	*0.02*	0.07	*0.03*	1.36	*0.87*	1.05	*1.04*	0.04	*0.03*	0.03	*0.02*	0.28	*0.58*	<0.02	*0.03*
CaO	17.4	*0.5*	15.5	*0.4*	7.4	*1.8*	1.4	*1.2*	6.4	*0.9*	5.5	*4.5*	2.2	*1.2*	1.8	*0.8*
Na_2O	2.50	*0.57*	3.53	*0.11*	8.13	*1.06*	11.30	*0.84*	8.17	*1.02*	8.37	*2.29*	7.11	*4.28*	7.76	*4.45*
K_2O	0.11	*0.03*	0.16	*0.07*	0.25	*0.09*	0.51	*0.11*	0.44	*0.04*	0.70	*0.46*	5.36	*6.56*	4.14	*6.44*
Total[1]	104.3	*1.0*	102.9	*0.7*	105.6	*1.4*	104.3	*0.9*	104.3	*1.5*	102.6	*0.4*	104.8	*1.7*	101.9	*1.3*
	formula based on 8 oxygens															
Si	2.15	*0.02*	2.24	*0.03*	2.71	*0.08*	2.98	*0.02*	2.70	*0.05*	2.71	*0.22*	2.91	*0.04*	2.89	*0.03*
Al	1.83	*0.02*	1.72	*0.03*	1.17	*0.11*	0.93	*0.05*	1.29	*0.06*	1.28	*0.21*	1.07	*0.05*	1.12	*0.02*
Cr	0.00	*0.00*	0.01	*0.00*	0.01	*0.01*	0.00	*0.00*	0.00	*0.00*	0.00	*0.01*	0.00	*0.00*	0.00	*0.00*
Fe	0.02	*0.00*	0.04	*0.01*	0.04	*0.02*	0.03	*0.01*	0.02	*0.00*	0.01	*0.00*	0.01	*0.01*	0.01	*0.01*
Mn	0.00	*0.00*	0.00	*0.00*	0.00	*0.00*	0.00	*0.00*	0.00	*0.00*	0.00	*0.00*	0.00	*0.00*	0.00	*0.00*
Mg	0.00	*0.00*	0.00	*0.00*	0.09	*0.05*	0.07	*0.07*	0.00	*0.00*	0.00	*0.00*	0.02	*0.04*	0.00	*0.00*
Ca	0.83	*0.03*	0.74	*0.02*	0.34	*0.09*	0.07	*0.05*	0.29	*0.04*	0.26	*0.21*	0.10	*0.05*	0.08	*0.03*
Na	0.21	*0.05*	0.31	*0.01*	0.67	*0.09*	0.93	*0.06*	0.68	*0.07*	0.70	*0.18*	0.58	*0.35*	0.65	*0.37*
K	0.01	*0.00*	0.01	*0.00*	0.01	*0.01*	0.03	*0.01*	0.02	*0.00*	0.04	*0.03*	0.30	*0.37*	0.24	*0.37*
Total	5.05	*0.03*	5.06	*0.02*	5.04	*0.05*	5.03	*0.02*	5.00	*0.03*	5.01	*0.01*	4.99	*0.03*	4.99	*0.02*
An	79.0	*4.1*	70.1	*1.0*	33.1	*7.6*	6.4	*5.2*	29.5	*5.3*	25.8	*21.1*	10.1	*5.2*	8.5	*3.4*
Ab	20.4	*4.1*	29.0	*1.0*	65.6	*7.2*	90.9	*5.8*	68.1	*5.3*	70.4	*18.7*	58.8	*34.8*	66.5	*37.8*
Or	0.6	*0.2*	0.9	*0.3*	1.4	*0.6*	2.7	*0.6*	2.4	*0.1*	3.9	*2.6*	31.2	*38.7*	25.0	*39.7*
n[2]	5		4		6		4		6		3		12		4	

[1] measurements below detection limit not included in totals

[2] n = number of analyses

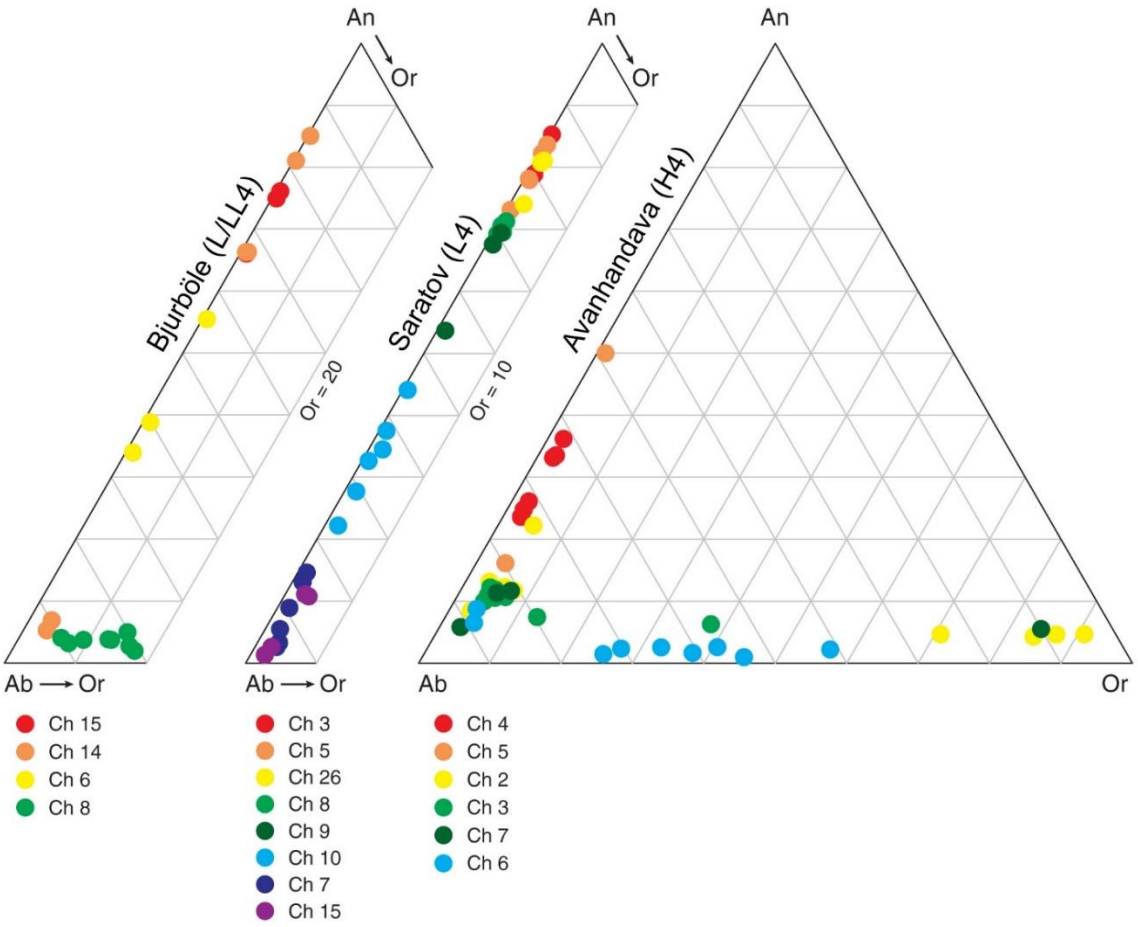

Figure 3.13. Feldspar compositions in type 4 OCs, obtained with EPMA. Each point is a single analysis, and each color is an individual chondrule. Feldspar ternary plots are truncated at Or_{20} for Bjurböle and Or_{10} for Saratov. Analyses with a significant Or component represent overlap between plagioclase and K-feldspar exsolution lamellae. In Bjurböle, K-feldspar exsolution in chondrule 8 were too fine-scale (Fig. 3.6f) to yield significant Or content in the analyses. Exsolution in Avanhandava is much coarser (e.g., Fig. 3.9f) and yields more Or-rich compositions. In Saratov, no K-feldspar was present in the analyses. Maximum An content is An_{85} in Saratov and Bjurböle and An_{50} in Avanhandava. Like the type 3 OCs (Fig. 3.12), the range of plagioclase compositions is limited within each chondrule, except for Bjurböle chondrule 14. In this chondrule, partial albitization (Fig. 3.6b) has produced a bimodal distribution.

content of An_{50}: this composition was measured in a remnant calcic plagioclase core in chondrule 5 (Figs. 3.9a,b). Some analyses for Bjurböle plagioclase overlap K-feldspar exsolution lamellae (chondrule 8, Fig. 3.6f). Avanhandava has extensive K-feldspar exsolution (e.g., Fig. 3.9f), shown by analyses that are albitic as well as those with high

Or content (Fig. 3.13, chondrules 2, 3, 7, and 6). While Saratov has some observed K-feldspar exsolution (e.g., Figs. 3.7d,f), no EPMA analyses significantly overlapped these lamellae. Like the type 3 OCs, plagioclase compositions for type 4 OCs are limited within each chondrule, except for Bjurböle chondrule 14 in which albitization (Fig. 3.6b) has produced a bimodal distribution.

4. Discussion

The overall goal of this study is to understand the metamorphic conditions, specifically the record of fluids, as indicated by feldspar. As we discussed in the introduction, alteration effects have previously been observed in OC feldspar but systematic studies have not been conducted. Previous studies invoke a variety of models to describe observations in ordinary and carbonaceous chondrites that are similar to the observations we present here. These models include the formation of nepheline, sodalite, and/or scapolite during chondrule crystallization (Bridges et al., 1997), formation or alteration in the solar nebula by infiltration of Na- and Cl-rich gasses (Bridges et al., 1997; Kimura and Ikeda, 1998), or alteration on the parent asteroid by hydrous (Alexander et al., 1987; Krot et al., 1998a; Russell et al., 2000) or anhydrous fluids (Kimura and Ikeda, 1998).

Overall, we consider these different models using the observations we present here and conclude that that plagioclase alteration and equilibration in OCs is a parent body, metasomatic process, facilitated by aqueous fluids during thermal metamorphism. Through our observations, we aim to establish an overall framework for understanding changes in feldspar textures and compositions through the petrologic sequence and to tie

this framework to an overall model of metasomatism during thermal metamorphism in ordinary chondrites.

In the discussion that follows, we will summarize our observations into a model of plagioclase alteration and discuss how well this model applies to H, L, and LL OCs. We will then compare our observations to other studies of ordinary and carbonaceous chondrites, discuss the evidence that indicates plagioclase alteration and equilibration is a fluid-driven, parent-body process, and place constraints on the physical and chemical environment through the changing modes of plagioclase alteration. We will frame the interpretations drawn from our observations into an overall, three-stage model of metasomatism during thermal metamorphism on OC parent bodies. Finally, we will discuss the implications for plagioclase alteration on the interpretation of chronology derived from short-lived radioisotope systematics, particularly Al-Mg and I-Xe.

4.1. A model for alteration and equilibration of plagioclase

A summary of our observations of plagioclase alteration and equilibration is presented in Fig. 3.14. Our previous observations of chondrules in Semarkona (Lewis and Jones, in review) showed the presence of primary igneous plagioclase with a wide range of compositions. Calcic plagioclase, which commonly occurs in MgO-rich chondrules, is lost as alteration proceeds, so its absence is an indicator of alteration. We observe primary anorthitic plagioclase in types 3 and 4 with features indicating various degrees of alteration. In types 5 and 6, highly altered calcic plagioclase is present only as relict cores. The green wedge in Fig. 3.14 shows this process. Note that the wedge increases slightly in width from 3.0 to 3.6 because some anorthite may be crystallizing from mesostasis glass.

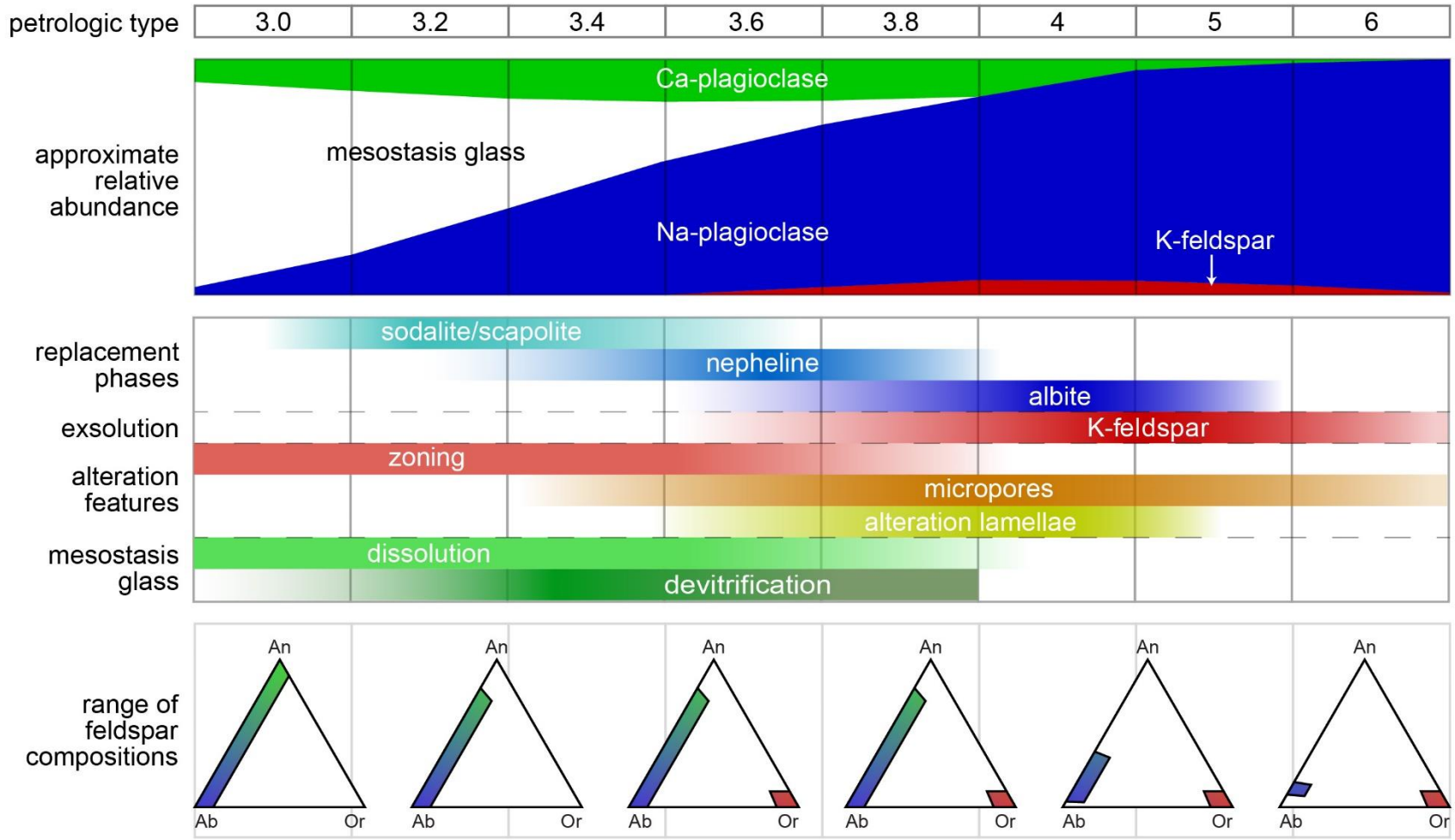

Figure 3.14. Summary of plagioclase alteration and equilibration observations. See section 4.1 for details.

Alteration of calcic plagioclase to sodalite/scapolite, nepheline, and albite are shown by the cyan, light blue, and dark blue bars in Fig. 3.14, respectively. Sodalite/scapolite alteration is seen in types 3.2-3.6, nepheline in types 3.4-3.9, and albite in types 3.6-5. In calcic plagioclase, micropores are observed in types 3.4-6 (orange bar) and alteration lamellae (yellow bar) are observed in types 3.6-5. Primary igneous plagioclase of a range of compositions shows zoning (light red bar) in areas of mesostasis dissolution (light green bar) in types 3.0-3.8.

Primary sodic plagioclase is also present in Semarkona, typically in FeO-rich chondrules (Lewis and Jones, in review) and while primary laths of albite are observed through petrologic types 3 and 4, the majority of albite in chondrules is produced through the devitrification of chondrule mesostasis glass (dark green bar). From type 3.0 to 3.9, mesostasis glass crystallizes into a fine-grained assemblage of albitic plagioclase, Ca-rich pyroxene, and oxides. This process is illustrated in Fig. 3.14 by the blue wedge expanding at the expense of mesostasis glass (white) through the type 3 sequence. Additional albite forms from albitization of calcic plagioclase (dark blue bar) starting around petrologic subtype 3.6 and proceeding through type 5. In type 6, nearly all plagioclase is albitic.

The evolution of plagioclase compositions to albite is also described in the schematic feldspar ternary diagrams at the bottom of Fig. 3.14. Plagioclase in chondrules has a wide range of compositions in type 3.0 (Lewis and Jones, in review), but the maximum An-content is reduced to ~An_{85} through the type 3 sequence. Between types 4 and 6, the plagioclase composition further equilibrates to a single composition of ~An_{11} (Kovach and Jones, 2010; Lewis and Jones, 2016) with the majority of the equilibration

occurring in the type 4s. Compositional equilibration of plagioclase is achieved largely through albitization, an interface-coupled dissolution-reprecipitation reaction in the presence of an alkali-bearing hydrothermal fluid.

Fine-scale K-feldspar exsolution lamellae and patches, represented by the small red wedge and red bar, are present in types 3.6-6 but are most abundant in petrologic types 4 and 5. The lowest petrologic type observations of K-feldspar exsolution lamellae in albite (red bar) are the same as the earliest observations of the albitization reaction (blue bar). However, K-feldspar is not only present in albitized regions, but also occurs in laths of primary albite and in fine-grained, secondary albite. In addition, K-feldspar exsolution, and especially larger patches, are commonly observed adjacent to voids. Potassium-rich feldspar in OCs is discussed in more detail by Lewis et al. (In preparation).

The model of plagioclase alteration and equilibration we describe here is drawn from observations in H, L, and LL OCs, and we propose that it is applicable to all three OC groups. However, Kovach and Jones (2010) argued that plagioclase equilibration in H chondrites differs from the LL chondrites. They came to this conclusion because their measurements of plagioclase compositions in H4-6 chondrites yielded a single equilibrated plagioclase composition of ~An_{12}, whereas in the LL chondrites, they measured a range of plagioclase compositions in the type 4 sample that narrowed progressively through types 5 and 6. Lewis and Jones (2016) showed that plagioclase equilibration trend in equilibrated L chondrites closely matches the Kovach and Jones (2010) trend for the LL chondrites.

Our observations in this study show that the H4 chondrite Avanhandava, the same H4 chondrite used in the Kovach and Jones (2010) study, contains a wider range of plagioclase compositions (up to An_{50}, Fig. 3.13) than previously reported. This is due, in part, to the focus of the Kovach and Jones (2010) study on large, smooth regions of plagioclase that are more equilibrated than the porous regions containing relict anorthitic plagioclase with higher Ca content (e.g., Fig. 3.9b). Telus et al. (2014) measured plagioclase compositions in four H4 chondrites and found plagioclase up to $An_{80\text{-}90}$ in Ste. Marguerite and Forest Vale, but only up to $An_{25\text{-}30}$ in Beaver Creek and Sena, suggesting varying degrees of equilibration within the type 4s. Along these lines, we can describe Avanhandava as a "high" type 4 that has seen more progressive equilibration than other type 4 OCs. This will be discussed in more detail in section 4.3. Furthermore, the H3.8 Dhajala has similar plagioclase composition and alteration features to LL chondrites of similar petrologic type and argues strongly against differences in plagioclase equilibration between the H chondrites and the L and LL chondrites.

Overall, we argue that the alteration and equilibration of plagioclase in OCs, summarized in Fig. 3.14, can be applied to all OC groups, and can provide important insights into the chemical and physical conditions experienced by their parent asteroids during thermal metamorphism. There is a clear progression of alteration modes from replacement of calcic plagioclase by sodalite/scapolite in subtypes 3.2-3.6, nephelinization in subtypes 3.4-3.9, to albitization in types 3.6-5. In the sections that follow, we will compare our model of alteration and equilibration to observations from other studies to help constrain the conditions experienced during secondary processing

and to further understand the role of fluids during thermal metamorphism on the OC parent bodies.

4.2. Origin of sodalite, scapolite, and nepheline in ordinary and carbonaceous chondrites

We observe scapolite ($Na_4Al_3Si_9O_{24}Cl$) and the feldspathoids sodalite ($Na_8Al_6Si_6O_{24}Cl_2$) and nepheline ($NaAlSiO_4$) as the products of plagioclase alteration in type 3 OCs. Alteration to these phases has previously been observed in OCs and in the CV and CO groups of carbonaceous chondrites (CCs). Although CCs are not considered to have undergone the same secondary history as OCs, it is helpful to compare different occurrences of plagioclase alteration to understand what conditions the different chondrite groups had in common. In addition to the alteration of plagioclase in chondrules, the focus of this work, previous studies have shown evidence for alteration of related aluminosilicate phases, such as anorthite normative mesostasis glass and melilite, in a variety of chondrite components including igneous clasts, refractory inclusions, dark inclusions, and matrix. To explain the presence of the sodalite, scapolite, and nepheline observed in OC as well as CV and CO groups, a variety of nebular and parent body mechanisms has been invoked. These mechanisms include igneous crystallization during chondrule formation, anhydrous nebular alteration prior to accretion, and both hydrous and anhydrous parent body alteration. We now assess the origin of sodalite, scapolite, and nepheline in OC and CC chondrules, and other chondrite components, with respect to these different models and the observations we present above.

4.2.1. Ordinary chondrites

We identified sodalite in Bishunpur (LL3.15, Fig. 3.1c) and Parnallee (LL3.6, Fig. 3.3b) and scapolite in Chainpur (LL3.4, Fig. 3.2c) but it is evident from other studies (Alexander et al., 1987; Hutchison et al., 1994; Bridges et al., 1995, 1997) that both minerals are present in all three chondrites. Alexander et al. (1987) described scapolite in a granular clast in Bishunpur (LL3.15) and attributed its presence to Cl-metasomatism after accretion. They argued that because phosphates do not form until higher petrologic types (i.e., greater degrees of metamorphism), a Cl-rich fluid would preferentially alter plagioclase instead of going into the formation of apatite. This model fits well with our observations and will be discussed in more detail in section 4.2.3.

Sodalite, scapolite, and nepheline were described in Chainpur (LL3.4) and Parnallee (LL3.6) by Bridges et al. (1995, 1997) and Hutchison et al. (1994). They found these phases in chondrule mesostasis glass and in the plagioclase of a barred olivine chondrule (Hutchison et al., 1994; Bridges et al., 1997). Hutchison et al. (1994) discussed the possibility that these phases could be the product of parent body metasomatism, but concluded that elevated REE abundances in nepheline indicated that it crystallized from residual melt. Bridges et al. (1997) invoked several mechanisms to explain their observations. For some Chainpur chondrules, they argued for prolonged, metastable crystallization of Ca-rich pyroxene producing silica-undersaturated residual melts that ultimately result in the crystallization of feldspathoids. In one Chainpur chondrule, where silica undersaturation is not expected because of the presence of large olivine phenocrysts, they argued that an influx of Na and Cl during crystallization is necessary to explain the intimate intergrowth of feldspathoids, plagioclase, and pyroxene. However,

for Parnallee chondrules, Bridges et al. (1997) suggest nepheline and sodalite/scapolite formed from minor amounts of residual melt after plagioclase crystallization.

Bridges et al. (1995) also described a large (3 mm) igneous clast in Parnallee containing 88% plagioclase and 12% Cl-bearing nepheline. They argued that the clast had carbonaceous chondrite affinities, due to its O-isotope composition, and link it to the ureilite group of achondrites. To explain the presence of nepheline, they invoked an influx of Na and Cl during crystallization on the parent body. However, our observations of Parnallee suggest that nephelinization was pervasive and the process affected both chondrules and igneous clasts.

A study conducted by Russell et al. (2000), looking at the oxygen isotope composition of Al-rich OC chondrules, described nepheline replacing calcic plagioclase in chondrules from Chainpur and Sharps (H3.4). They observed that nephelinization was pervasive in the Sharps chondrule, replacing most of the plagioclase laths, while Chainpur chondrules only contained nepheline as thin lamellae. Although they did not suggest a model for nepheline formation, nebular or parent body, they did refer to it as an alteration feature, suggesting that they did not believe it was an igneous feature. Russell et al. (2000) also measured the oxygen isotope composition of a nepheline-bearing region in the Sharps chondrule and found that it was indistinguishable from the spinel phenocrysts that comprise the majority of the chondrule. Russell et al. (2000) did not discuss the possibility of parent body alteration but we would expect mixing of the oxygen isotope composition of the anorthite and the interacting fluid if nepheline formed via this mechanism. Because we infer nepheline formation to be a parent-body process, the similar oxygen isotopic composition of nepheline to the phenocrysts implies either

that there was not significant isotopic exchange during alteration (e.g., low water/rock ratio) or that the altering fluid was ^{16}O-rich like the chondrule phenocrysts. We suggest the former possibility is more likely because the oxygen isotopic composition of equilibrated OCs, which have undergone significant plagioclase alteration via albitization, is ^{16}O-poor (Clayton, 2003).

4.2.2. Carbonaceous chondrites

The feldspathoids sodalite and nepheline have been described in a variety of CV and CO carbonaceous chondrites, in which they are widely considered to have formed via metasomatic reactions (Brearley and Krot, 2013). Feldspathoids are commonly observed in CV chondrites as alteration phases in a variety of components including refractory inclusions (Fagan et al., 2007), chondrules (Ikeda and Kimura, 1995; Kimura and Ikeda, 1995, 1996, 1997, 1998; Krot et al., 1998a,b, 2000; Wasserburg et al., 2011), matrix (Ikeda and Kimura, 1995; Matsumoto et al., 2014), and dark inclusions (Ikeda and Kimura, 1995; Krot et al., 1998a,b, 2000). Sodalite and nepheline typically replace Ca-rich phases such as melilite, Ca-plagioclase, and anorthite-normative chondrule mesostasis glass.

Weisberg et al. (1997) and Krot et al. (1998a,b) showed that oxidized CV3 chondrites can be split into two subgroups based on their alteration features that suggest parent-body alteration under differing conditions. The Allende-like group ($CV3_{oxA}$) contains the feldspathoid alteration features whereas the Bali-like group ($CV3_{oxB}$) contains phyllosilicates and not feldspathoids. Krot et al. (1998a,b) suggest that the difference between the two subgroups is related to temperature and that the $CV3_{oxB}$ group was exposed to lower temperature aqueous alteration (<300 °C) than the $CV3_{oxA}$ group.

There is also a range in alteration features in the reduced group of CV3 chondrites ($CV3_{red}$). Some $CV3_{red}$ chondrites contain sodalite and nepheline (e.g., Efremovka and Vigarano: Kimura and Ikeda, 1996, 1997), but only rare nepheline lamellae are present in others (e.g., Leoville: Kimura and Ikeda, 1997).

Some authors have argued that alteration to feldspathoids in CV chondrites is the product of anhydrous alteration from Na- and Cl-rich gases, either in the solar nebula or on the parent asteroid (Ikeda and Kimura, 1995, 1996; Kimura and Ikeda, 1995, 1997, 1998). However, Krot et al. (1998a,b) proposed a hydrous, parent body origin citing several observations. First, the alteration of Ca-bearing phases in $CV3_{oxA}$ chondrules did not change the bulk abundance of Ca in this subgroup relative to the $CV3_{oxB}$ subgroup suggesting closed-system behavior of Ca. Second, the bulk Na content is similar between the two subgroups but the carrier phase of Na differs based on alteration conditions. In the $CV3_{oxB}$, alteration is to Na-phlogopite and saponite whereas in the $CV3_{oxA}$ nepheline and sodalite are the alteration phases. Third, the $CV3_{oxB}$ subgroup clearly experienced aqueous alteration due to the presence of phyllosilicates illustrating that water was available on the CV parent body.

Bonal et al. (2006) conducted a Raman study of the maturity of organic matter in the matrix of CV3 chondrites to determine their metamorphic history in comparison to unequilibrated OCs. They suggested that Allende experienced metamorphic temperatures equivalent to petrologic type 3.7 in OCs. The fact that they estimate the feldspathoid-bearing Allende to have had a similar thermal history to Parnallee (LL3.6) is consistent with our observations. Bonal et al. (2006) also set petrologic types for the $CV3_{red}$ group chondrites Leoville, Efremovka, and Vigarano, in order of increasing metamorphism, to

between petrologic types 3.1 and 3.4 on the OC scale. Again, this is consistent with our observations of the presence of feldspathoids petrologic subtype from Bishunpur (LL3.15) to Chainpur (LL3.4).

CO3 carbonaceous chondrites have been formally divided into petrologic subtypes, 3.0-3.7, based on similar metamorphic characteristics to OC chondrites of the same petrologic subtypes (Scott and Jones, 1990; Sears et al., 1991). Like CV3 chondrites, CO3 chondrites contain nepheline, and minor sodalite, as alteration phases in CAIs (Tomeoka et al., 1992; Kojima et al., 1995; Russell et al., 1998; Wasson et al., 2001; Itoh et al., 2004), chondrules (Jones, 1997; Tomeoka and Itoh, 2004; Wick and Jones, 2012), and dark inclusions (Itoh and Tomeoka, 2003). In particular, a study by Tomeoka and Itoh (2004) described nepheline, occurring in lamellae, as a plagioclase alteration phase in type I CO chondrules. Nepheline alteration occurs in petrologic subtypes 3.2-3.7 in increasing abundance with increasing subtype. This is very similar to the feldspathoid alteration we observe in type 3 OCs. However, the presence of sodalite, common in CV chondrites, was rare in the CO3 chondrites they studied. Further, scapolite is not observed in CV or CO chondrites and is currently an alteration feature observed solely in OCs.

Tomeoka and Itoh (2004) suggested that nephelinization of plagioclase in CO chondrules, and likely CAIs and dark inclusions, is a parent body process in which Na-rich fluids alter plagioclase to hydrated nepheline. Then, during further thermal metamorphism, the hydrated nepheline dehydrates to the nepheline that is now observed. In addition, Itoh et al. (2004) measured the oxygen isotopic composition of altered and unaltered regions from a CAI in Kainsaz (CO3.2). They found the altered regions to be

depleted in ^{16}O compared to the unaltered regions, suggesting isotopic exchange with an altering ^{16}O-poor fluid.

4.2.3. Alteration to sodalite, scapolite, and nepheline

Overall, the presence of feldspathoids in CCs has been recognized as an indicator of aqueous alteration for some time, whereas for OCs, there is no common consensus on the mechanism for what appear to be similar mineral reactions. In reduced and Allende-like oxidized CV3 chondrites ($CV3_{red}$ and $CV3_{oxA}$), feldspathoids form through the alteration of Ca-bearing phases like melilite and Ca-plagioclase in petrologic subtypes equivalent to 3.1-3.7. In CO3 chondrites, nepheline is the dominant alteration phase, present as lamellae in Ca-plagioclase, and occurring in petrologic subtypes 3.2-3.7. We have shown that alteration to scapolite and feldspathoids in OCs follows a similar trend, occurring in types 3.1-3.9, initially as replacement by sodalite/scapolite but then transitioning to nepheline between 3.4 and 3.6.

The transition from sodalite/scapolite alteration to nepheline, in OCs, could either be the result of increasing temperature or changes in chemical environment. We suggest the latter process is dominant because a similar shift in alteration mode from sodalite to nepheline is not observed in the CV chondrites over the equivalent range in petrologic subtypes. As such, a rising Na/Cl ratio of the fluid with increasing petrologic subtype is a likely source of the shift in alteration modes. The OCs, unlike CV chondrites, contain another major Cl-bearing mineral, apatite, which forms either from reactions of the phosphate merrillite with Cl-rich fluids, or from direct precipitation from a fluid (Jones et al., 2014, 2016; Lewis and Jones, 2016). An increasing abundance of apatite throughout the petrologic type 3 sequence could provide a sink for Cl, raise the Na/Cl ratio of the

fluid, and shift the plagioclase alteration mode from sodalite/scapolite to nepheline. This process was also suggested by Alexander et al. (1987) to explain the presence of scapolite in Bishunpur (LL3.15).

The difference between scapolite and sodalite alteration is less clear as they both have the same molar Na/Cl ratio of 4, and both are observed in subtypes 3.2-3.6. Sodalite is a feldspathoid, like nepheline, that forms in silica undersaturated conditions. Sodalite and nepheline have Si/Al ratios of 1 whereas scapolite has a Si/Al ratio of 3, the same as albite. Because, as we will discuss in the next section, albitization requires higher temperatures with higher SiO_2 solubility than nephelinization, we would not expect scapolite to form in the lower petrologic type 3 subtypes. One possibility is that scapolite forms in regions within chondrules that contain Si-rich mesostasis glass whereas sodalite forms from relatively Si-poor anorthitic plagioclase. Another possibility is that scapolite forms from the breakdown of Cl-bearing smectite during moderate degrees of thermal metamorphism. Chlorine-bearing smectite is identified as an alteration feature in Semarkona (LL3.00) and Bishunpur (LL3.15) by Alexander et al. (1989). However, in this model, the presence of both smectite and scapolite in Bishunpur is difficult to reconcile.

Nephelinization of plagioclase and melilite was explored experimentally by Ichimura et al. (2017) to understand the alteration conditions of phases, including plagioclase, in CV and CO chondrites as well as in OCs. Following the procedure of Nomura and Miyamoto (1998), they produced nepheline through a two-part process: alteration of plagioclase to Na-zeolites followed by dehydration to nepheline. In detail, they heated powdered plagioclase (An_{48}) to 200 °C in NaOH solutions of pH 12.8 and

13.9 for 168 hours (1 week). They used a water to rock ratio of 46.7. Under these conditions, plagioclase altered to the Na-zeolites analcime ($Na_2Al_2Si_4O_{12}•2H_2O$) and fabriesite ($Na_3Al_3Si_3O_{12}•2H_2O$) with little of the original plagioclase remaining. All characterization was determined by X-ray powder diffraction.

The dehydration portion of the study was executed on samples prepared separately from the alteration samples with the aim of understanding the rate and temperature regime under which the zeolites dehydrated to nepheline. Fabriesite was transformed to nepheline in two ways: isothermal heating at 600-650 °C for 24 hours or progressive heating at 5 °C/min to carnegieite at 692 °C before converting to nepheline at 828 °C. Analcime only converted to nepheline when heated isothermally at 800 °C for 24 hours. However, they argue that dehydration could take place at much lower temperatures over the much longer time scales experienced by asteroids undergoing thermal metamorphism.

In SEM images, the analcime aggregates (which were expected to be the precursors of the dehydration reaction into nepheline) contain blocky cores of remnant plagioclase. This texture is significantly different from the smooth and lamellar textures of nepheline alteration that we observe (e.g., Fig. 3.3b) and that have been reported in other studies (Russell et al., 2000; Tomeoka and Itoh, 2004; Wick and Jones, 2012). The texture in chondrites is crystallographically controlled, arguing against a hydration/dehydration mechanism involving zeolites. Because of these textural differences, we consider that there is likely another mechanism of nepheline alteration in OCs and COs that involves direct replacement of plagioclase with nepheline. Although the general temperature regimes of Ichimura et al. (2017) fit the expected characteristics

of plagioclase alteration in types 3.1-3.9, the resulting textural differences present an important problem that needs to be resolved. One possibility, as suggested by Tomeoka and Itoh (2004), is alteration in a hydrous, Na-rich fluid produces hydrated nepheline that later dehydrates during thermal metamorphism.

The model of nepheline and sodalite/scapolite crystallizing during chondrule formation, either by silica undersaturation or by Na and Cl infiltration (Bridges et al., 1997), has several problems. First, plagioclase-bearing chondrules in the minimally metamorphosed OC Semarkona (LL3.00) do not contain nepheline, sodalite, or scapolite (Lewis and Jones, in review) as would be expected if these phases were formed, even if rarely, during chondrule crystallization. Second, the limited range of petrologic types in which nepheline is found in OCs, 3.4-3.6, indicates that formation of nepheline is related to thermal metamorphism, and not to nebular processes. Third, Gilmour et al. (2000) measured I-Xe ages for the nepheline-bearing chondrule and clast from Parnallee described by Bridges et al. (1995, 1997) and Hutchison et al. (1994) and showed that it is ~7 Myr younger than the chondrules that did not contain observable nepheline. These ages are well within the realm of parent body processing and strongly argue against a nebular origin.

4.3. Albitization, oxides, and exsolution

We have shown that plagioclase undergoes reactions that result in albitization, the extent of which is related to the degree of metamorphism (Figs. 3.4-3.11, 3.14). Albitization of anorthitic plagioclase along grain boundaries has previously been described by Kovach and Jones (2010), Jones and Brearley (2010), and Lewis and Jones (2016) in type 4 OCs. Alteration lamellae in anorthitic plagioclase were described by

Jones and Brearley (2010) and Lewis and Jones (2016). TEM investigations showed that alteration lamellae in Bjurböle (L/LL4) consist of silica with sub-μm faceted voids and chromite (Jones and Brearley, 2010). In these studies, albitization, formation of alteration lamellae, and development of porosity have been attributed to secondary alteration by an aqueous fluid (metasomatism) during thermal metamorphism.

Unlike the transition of plagioclase alteration reaction from sodalite/scapolite to nepheline, a process we suggest results from an increase in Na/Cl ratio of the fluid, the transition from nephelinization to albitization is likely dependent on temperature. The albitization reaction in OCs is discussed in some detail by Lewis and Jones (2016) using the experimental results of Hövelmann et al. (2010). In these experiments, plagioclase (An_{60} and An_{23}) was reacted with a sodium silicate solution of pH 9 at 600 °C and 2 kbar. At these conditions, 50 μm rims of albite were produced on the plagioclase grains in less than 2 weeks. These length scales are comparable to the size of most plagioclase grains in type 6 OCs, and much larger than the albitized rims we show in types 3.9-4 (Figs. 3.5b,e, 3.6a, 3.7b,d, 3.8b,d). Like the formation of zeolites in the Ichimura et al. (2017) experiments, this is very rapid considering the $>10^6$ year timescale (Huss et al., 2006) expected for OC metamorphism, demonstrating the reaction was restricted, particularly in types 3.8-4.

Lewis and Jones (2016) argue that the albitization reaction was limited by the solubility of Si in the altering fluid. Because Si solubility increases with increasing temperature, pressure, and pH, the most likely explanation is that changes of temperature cause both the shift from nephelinization to albitization and the progressive degree of

albitization observed in petrologic types 4-6. The alteration of anorthite to nepheline does not require mobilization of Si, only the introduction of Na and removal of Ca:

$$CaAl_2Si_2O_8 + Na_2O(aq) \rightarrow 2NaAlSiO_4 + CaO(aq),$$

while the alteration of anorthite to albite requires mobility of Si and Al in addition to Na and Ca:

$$2CaAl_2Si_2O_8 + 2SiO_2\textit{(aq)} + Na_2O\textit{(aq)} \rightarrow 2NaAlSi_3O_8 + 2CaO\textit{(aq)} + Al_2O_3\textit{(aq)}.$$

In a more realistic example, the following reaction shows two minerals found in type I chondrules, anorthite and enstatite, reacting with an aqueous brine containing Si, Na, and Cl to produce an assemblage of albite, diopside, and spinel, common products of alteration:

$$2CaAl_2Si_2O_8 + Mg_2Si_2O_6 + 2SiO_2(aq) + 2NaCl(aq) \rightarrow 2NaAlSi_3O_8 + CaMgSi_2O_6 + MgAl_2O_4 + CaCl_2(aq).$$

In this case, the rate of reaction also depends on the availability of Si in solution and Al goes into forming spinel. Furthermore, the Cl in this reaction provides charge balance and the resulting $CaCl_2$ can react with merrillite to form chlorapatite as discussed in Lewis and Jones (2016).

The presence of spinel as a reaction product is important because we observe spinel, typically Cr-spinel, as well as other oxides, in regions of albitization. Albitization is an interface-coupled dissolution-reprecipitation reaction in which the surface of the anorthite is broken down and the new surface of albite is formed pseudomorphically (e.g., Putnis, 2009). In anorthitic plagioclase, particularly when formed at high temperature, Fe and Mg can substitute for Ca, and Cr and Ti can substitute for Al and Si, respectively. Because these metals are not compatible in low-temperature albite, the albitization process results in the formation of the μm to sub-μm, euhedral oxides we observe,

including Cr-spinel (Fig. 3.6b, 3.8b), armalcolite (Fig. 3.8d), and chromite (Jones and Brearley, 2010). In fact, μm and sub-μm oxides are extremely common in regions of pervasive albitization (Fig. 3.6b, 3.8b,d, 3.9b,d, 3.10b,d,e, 3.11e). This process is also observed in terrestrial examples of albitization in which hematite precipitates at the reaction boundary resulting in a distinctive red hue on the outcrop scale (Engvik et al., 2008).

Potassium-rich feldspar has previously been described in equilibrated OC chondrules (Kovach and Jones, 2010; Jones and Brearley, 2011; Lewis and Jones, 2016), in the LL5 chondrite Chelyabinsk (Taylor et al., 2014), and in samples returned from the asteroid Itokawa by the Hayabusa mission (Nakamura et al., 2011; Nakamura et al., 2014). Itokawa is an S-type asteroid and the material returned is similar to LL chondrites with grains bearing metamorphic features indicating petrologic types 4-6 (Nakamura et al., 2011). In all cases, K-feldspar is present in albite as fine-scale exsolution lamellae (e.g., Fig. 3.8f) or as larger patches (e.g., Fig. 3.9f). Most K-feldspar is associated with pores (e.g., 3.7d,f, 3.8f, 3.9f) implying transport of K through the pore network and preferential incorporation into albite along pore boundaries. The heterogeneous distribution of K-feldspar in albite suggests incorporation of K postdates albitization.

Jones and Brearley (2011) discuss that fine-scale exsolution lamellae indicate relatively rapid cooling, ~1 °C per 10 years, of the host material through the exsolution interval (600-500 °C). This contrasts with the slow, metallographic cooling rates, ~1 °C per 10^4-10^6 years, measured for many chondrites through the similar temperature range. Jones and Brearley (2011) were not able to explain the discrepancy in cooling rates. We discuss K-feldspar exsolution in more detail in Lewis et al. (In preparation). Here, we

focus on the mechanism of K incorporation into albite, and the temperatures that can be obtained from the Or content of plagioclase from the feldspar solvus.

The plagioclase composition can provide an estimate of the temperature at which it equilibrated due to the increased solubility of K within the plagioclase structure with increasing temperature (Nekvasil, 1994). While type 3 OCs do not have a significant Or component (Fig. 3.12), plagioclase in the type 4 OCs we measured does (Fig. 3.13). Although there is some scatter in the data due to analytical overlap of partially albitized plagioclase and fine-scale K-feldspar exsolution lamellae, there is a clear trend of increasing Or with increasing Ab along the plagioclase side of the feldspar ternary. The Or content differs between the type 4 OCs, indicating different temperatures of incorporation. For example, Saratov has a lower Or content for chondrules near the Ab apex than Avanhandava does (Fig. 3.13), implying that Avanhandava incorporated K at a higher temperature than Saratov.

In Fig. 3.15, we show plagioclase compositions for type 4 to 6 OCs from this study (Fig. 3.13) and from Lewis and Jones (2016), in relation to plagioclase solvi for various temperatures at 1 bar, generated by SOLVCALC (Wen and Nekvasil, 1994). We used the ternary feldspar model of Elkins and Grove (1990) that is calibrated by hydrous experiments conducted at 1-3 kbar between 700 °C and 900 °C. The type 4 chondrites are ordered by increasing Or content in the plagioclase to show the progressive increase in equilibration temperature. The lowest temperature inferred from the plagioclase in the type 4 OCs we are considering is from Kramer Creek and Saratov, both of which plot along the 400 °C solvus. Bjurböle plots around 450 °C when considering the more Na-rich compositions that are not affected by analytical overlap of K-feldspar exsolution.

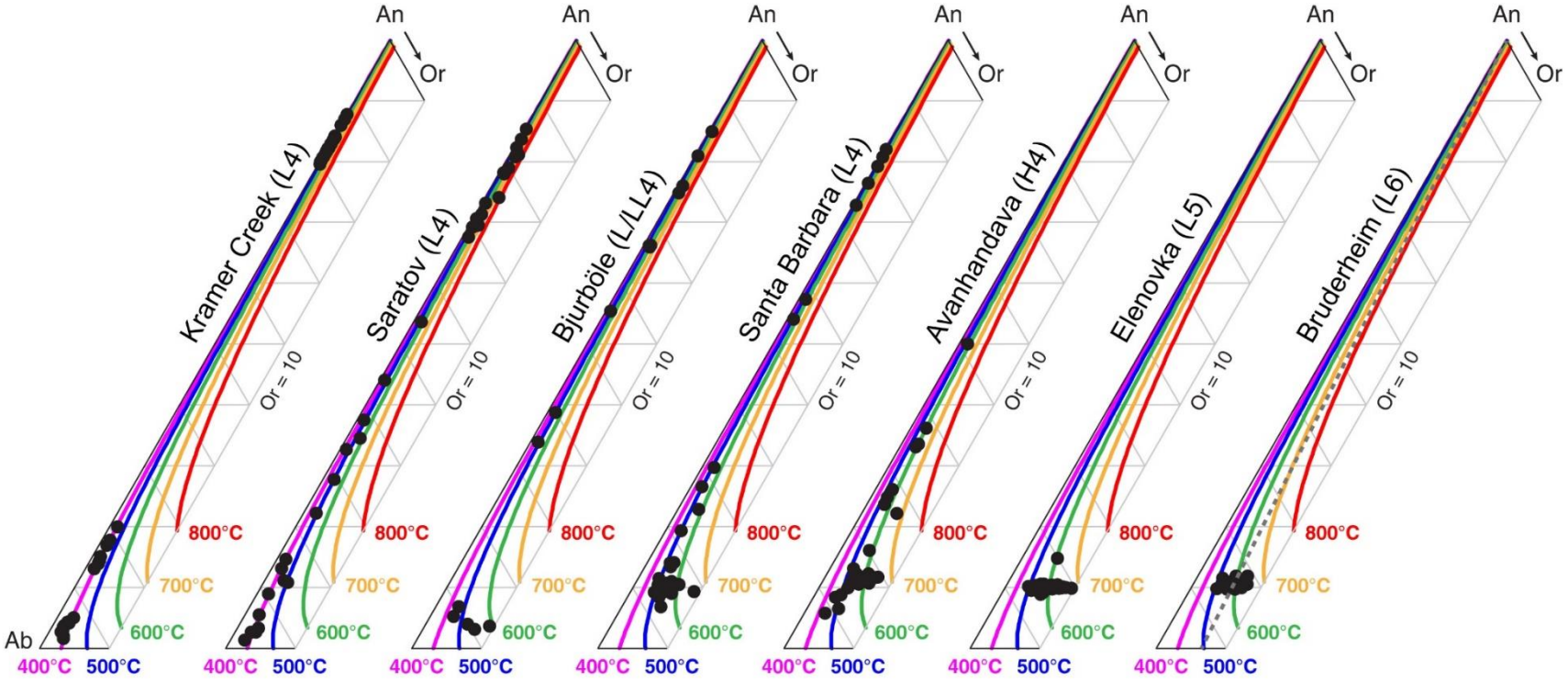

Figure 3.15. Plagioclase compositions in petrologic type 4-6 OCs plotted on feldspar solvi, illustrating an increase in equilibration temperature with petrologic type. Data for Kramer Creek, Santa Barbara, Elenovka, and Bruderheim are from (Lewis and Jones, 2016). Feldspar ternary diagrams are truncated at Or=10. Colored lines indicate plagioclase solvi for various temperatures generated by SOLVCALC (Wen and Nekvasil, 1994), at 1 bar, using the ternary feldspar model of (Elkins and Grove, 1990). Gray dashed line plotted over the Bruderheim data represents the average bulk OC Na/K ratio from Wasson and Kallemeyn (1988).

Santa Barbara and Avanhandava plot close to 500 °C and 550 °C, respectively. Elenovka and Bruderheim, types 5 and 6, both plot near the 600 °C solvus. Equilibration at the 600 °C solvus likely occurs because the Na/K ratio of the plagioclase reaches the Na/K ratio of the bulk chondrite (average atomic OC Na/K=14.5: Wasson and Kallemeyn, 1988). This is illustrated by the gray dashed line plotted over the Bruderheim data in Fig. 3.15. There is also some scatter in the data as analyses of albitic plagioclase include overlap from K-feldspar exsolution lamellae and remnant Ca-plagioclase. However, in general, the analyses follow the solvi remarkably well considering that they were measured in multiple chondrules that contain a wide range of alteration features.

The temperatures inferred from the plagioclase compositions are at the low end of the range of peak metamorphic temperatures generally estimated for types 4 and 5, 500-800 °C, and far below the peak metamorphic temperature range for type 6, 800-1000 °C (Scott and Krot, 2014). Because the plagioclase solvus model is calibrated between 700 °C and 900 °C (Elkins and Grove, 1990), the resultant solvi are most accurate in this range and suffer from extrapolation errors at lower temperatures. However, we argue that the temperatures recorded in the plagioclase compositions of type 4 OCs are in fact metasomatic temperatures, the temperatures at which the plagioclase was altered. If the fluid altering plagioclase had a Na/K ratio similar to that of the bulk OCs (equivalent to $Or_{6.5}$), then the temperature at which albitization occurred will dictate the Or content in the plagioclase until it reached a temperature where the plagioclase composition would have been in equilibrium with the fluid composition. In this case, equilibrium is at 600 °C, and represents the highest temperature that can be recorded by plagioclase. The metasomatic temperatures we estimate for the types 4-5, 400-550 °C, are significantly

lower than the peak metamorphic temperatures, 500-800 °C, which implies plagioclase alteration ended before peak metamorphism, possibly due to dehydration. Dehydration prior to peak metamorphism is consistent with observations of partial albitization in the type 4 (Figs. 3.6b, 3.7d, 3.8b) and 5 (Fig. 3.10b) OCs.

The metasomatic temperature of 600 °C, as a lower bound for type 6 OCs, is consistent with temperature estimates from plagioclase disorder (Nakamura and Motomura, 1999). Nakamura and Motomura (1999) used Si-Al disorder in plagioclase to measure metamorphic temperatures in type 6 OCs and found a temperature range of 725-820 °C, based on maximum disorder measured in each sample. This temperature range is 100-200 °C lower than those reported for pyroxene thermometry (865-945 °C: Slater-Reynolds and McSween, 2005). Slater-Reynolds and McSween (2005) argue that the difference in plagioclase and two-pyroxene thermometry is because plagioclase was fully crystallized prior to peak metamorphism.

The sequence of increasing metasomatic temperatures inferred for the type 4 OCs is also consistent with their range of alteration features. For example, Saratov plagioclase contains alteration lamellae (Fig. 3.7b) which are absent in Santa Barbara (Fig. 3.8) and Avanhandava (Fig. 3.9). This progression in metasomatic temperatures (i.e., Or component in albite) could potentially be used to create a metasomatic petrologic scale to subdivide type 4 OCs. In this scale, Kramer Creek and Saratov would be a "low" type 4s (<450 °C), Bjurböle would be a "medium" type 4 (450-500 °C), and Santa Barbara and Avanhandava would be "high" type 4s (500-550 °C). Although more work would need to be done to confirm and calibrate these subdivisions, there may be utility in such a scale.

For example, “low” type 4s may retain isotopic and mineralogical heterogeneities that are lost in the “high” type 4s.

Similarly, the metasomatic temperatures also appear to provide a division between type 4 (<600 °C) and type 5 (~600 °C). Unlike the types 3-4 division which is marked by the compositional equilibration of olivine, the current division between the type 4 and 5 OCs is hazy. Huss et al. (2001) summarizes the 4-5 division as having the loss of recognizable matrix and matrix CL, minor to moderate chondrule textural equilibration, and increased grain sizes of secondary feldspar (2 μm to 2-10 μm) and Ca-rich pyroxene (<1 μm to 2-5 μm). While more analyses are needed to confirm the type 4-5 division we observe in plagioclase Or content, having a quantitative measure of equilibration, like that for olivine, would be useful for the classification of equilibrated OCs.

4.4. Three-stage model of metasomatism during metamorphism in ordinary chondrites

Thermal metamorphism on chondrite parent bodies is generally accepted to have been the result of heating from the decay of short-lived radioisotopes, largely ^{26}Al, during the first few million years after solar system formation (McSween et al., 2002). However, heating may have also been the result of impacts (Rubin, 2004), or a combination of the two sources. As we have shown above, feldspar undergoes a variety of chemical and textural changes during thermal metamorphism that are attributable to the presence of fluids. Fluid activity is also shown to be important for the formation and composition of apatite (Jones et al., 2014, 2016; Lewis and Jones, 2016). In order to account for the alteration and equilibration of feldspar, and the development and composition of apatite,

we have developed an overall model of chemical alteration, i.e., metasomatism, during thermal metamorphism in OCs.

This model consists of three general stages: hydrous alteration during prograde metamorphism, dehydration close to peak metamorphic temperatures, and infiltration of anhydrous fluids during retrograde metamorphism. The three stages are indicated schematically in Fig. 3.16a on the time-temperature plot describing onion-shell thermal metamorphism of an H-chondrite-like asteroid from Harrison and Grimm (2010). Harrison and Grimm (2010) used peak metamorphic temperatures for petrologic types 3, 4-5, and 6 of 675 °C, 865 °C, and 1000 °C, respectively, from studies that used two-pyroxene and olivine-spinel thermometry (Slater-Reynolds and McSween, 2005; Wlotzka, 2005; Kessel et al., 2007). Thermal modeling predicts that accretion of the H chondrite parent body occurs ~2 Myr after CAI formation (McSween et al., 2002) and Harrison and Grimm (2010) use an accretion age of 2.2 Myr after CAIs (blue band in Fig. 3.16a). While the onion-shell model is not a required basis for our chemical alteration model, and the onion-shell model is probably an over-simplification (Scott et al., 2014), its simplicity is useful for the discussion that follows.

4.4.1. Stage 1: Aqueous alteration during prograde thermal metamorphism

During prograde metamorphism, heating occurs relatively rapidly. In Fig. 3.16a, time on the x-axis is presented as a log scale illustrating that heating to peak temperatures only takes a few Myr, whereas cooling takes tens of Myr. We contend that most of the observed plagioclase alteration features occurred during this initial heating interval. Ices that accrete along with the matrix, metals, sulfides, and chondrules, melt and allow for short-range (cm-scale) transport of soluble cations and anions between chondrite

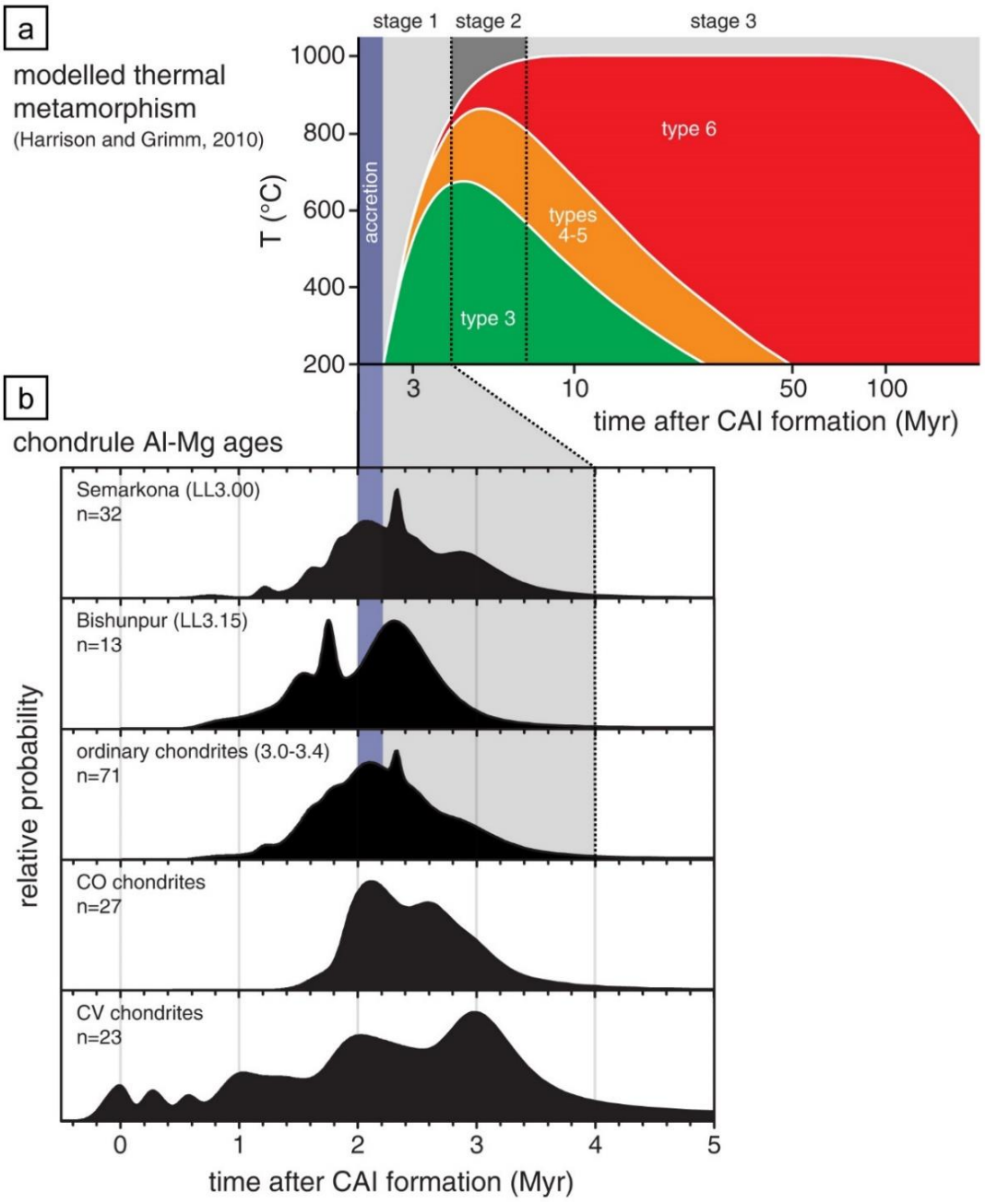

Figure 3.16. Diagrams illustrating thermal metamorphism and measured chondrule ages during first 100 Myr after CAI formation. (a) Three stages of metasomatism indicated on a time-temperature diagram for OC thermal metamorphism model from Harrison and Grimm (2010). Petrologic type ranges are indicated in each color, peak metamorphic temperatures for petrologic types 3, 4-5, and 6 of 675, 865, and 1000 °C, respectively. Blue band illustrates estimated accretion time at ~2 Myr after CAIs (McSween et al., 2002). The thermal model of Harrison and Grimm (2010) is optimized to accretion at 2.2 Myr after CAIs. (b) Probability density plots for measured Al-Mg ages of chondrules in Semarkona, Bishunpur, type 3.0-3.4 OCs (including Semarkona and Bishunpur), CO chondrites, and CV chondrites. Blue band marks expected accretion time and gray band is our estimated timescale for stage 1 metasomatism. Plot data and corresponding references are in Appendix 3.

components. This initially resulted in the dissolution of chondrule mesostasis glass, which increases chondrule porosity allowing for further fluid infiltration and alteration of chondrule mineralogy (Lewis et al., in review). Because of the low matrix abundance in OCs (Scott and Krot, 2014), and the inner solar system origin of OC material, the amount of water derived from accreted ices is presumably significantly lower than for carbonaceous chondrites. This is consistent with the lower overall aqueous alteration of petrologic type 3 OCs compared with their carbonaceous counterparts (Brearley, 2006).

The composition of the accreted ices could be water ice (H_2O) or HCl clathrates ($HCl•3H_2O$) or a mixture of the two. Zolotov and Mironenko (2007) suggested that the incorporation of clathrates could be a viable mechanism for Cl incorporation into chondrites. Williams et al. (2015) suggest that variability in Cl-isotope compositions among OCs could be due to variable degrees of incorporation of HCl clathrates during accretion. Melting of the clathrates would initially produce a low-pH fluid that could dissolve, in part, chondrule mesostasis glass and plagioclase. The pH of the fluid is expected to rise rapidly at low water to rock ratios due to the dissolution of plagioclase and feldspathic mesostasis glass (Blum and Stillings, 1995). Similarly, thermodynamic calculations for CI chondrites indicate that a high Na^+ content in aqueous fluids corresponds to high pH at low water to rock ratios (Zolotov, 2012).

The high pH fluid leads to the formation of phyllosilicates in subtypes 3.0-3.2 (Alexander et al., 1989). At higher temperatures, calcic plagioclase and mesostasis glass are replaced by feldspathoids (subtypes 3.1-3.9). The type of feldspathoid is dictated by the Na/Cl ratio of the fluid which in turn is dictated by the development of phosphates (Alexander et al., 1987). Phosphorous from Fe,Ni metal starts oxidizing at low degrees of

thermal metamorphism to form merrillite. Apatite then forms in a reaction between merrillite and halogen-bearing fluids or by direct precipitation from the fluid (Jones et al., 2014). Chlorapatite rims around metal grains are reported as early as type 3.2 (Rubin and Grossman, 1985). We suggest that the availability of merrillite to react with a Cl-fluid increases between types 3.2 and 3.6, causing the Na/Cl ratio to increase, and ultimately resulting in the observed shift in sodalite/scapolite alteration (types 3.1-3.6) to nepheline (types 3.4-3.9). Whether the alteration of plagioclase to nepheline occurs via alteration to zeolites (Ichimura et al., 2017), via hydrated nepheline (Tomeoka and Itoh, 2004), or some other process is still unknown. However, if either of the first two options are correct, the pre-nepheline phase requires later dehydration (Stage 2).

Starting at about petrologic type 3.6, replacement of calcic plagioclase by albite becomes the major mode of replacement alteration. Albitization, an interface-coupled dissolution-reprecipitation reaction (Putnis, 2009) that also occurs in a basic (pH ~ 12), hydrous environment at temperatures higher than were inferred from the production of feldspathoids (Hövelmann et al., 2010; Ichimura et al., 2017). Fluids facilitate the introduction of Na and Si and removal of Ca and Al. During this process, Fe, Mg, Cr, and Ti that are present in trace amounts in the Ca-plagioclase structure, are removed and form oxides nearby, typically Cr-spinel, chromite, and armalcolite (Engvik et al., 2008). In lower petrologic types, albitization is limited to μm-size rims near grain boundaries and in regions of high porosity, but the degree of albitization increases with petrologic type, and it has gone to completion by type 6 (Kovach and Jones, 2010; Lewis and Jones, 2016). Due to the low water-rock ratio expected for these reactions in OC material,

discussed above, we suggest that the degree of completion of the reaction is strongly correlated with the temperature and not an increase in water-rock ratio.

4.4.2. Stage 2: Dehydration through peak metamorphism

We suggest that due to limited fluid availability and increasing metamorphic temperatures, OC material undergoes dehydration through and after peak metamorphism. Only in the lowest petrologic types, 3.0-3.2, do hydrated minerals (phyllosilicates) survive peak metamorphism (Alexander et al., 1989). Any zeolite minerals or hydrated nepheline formed by alteration of calcic plagioclase would undergo dehydration to nepheline as temperatures increase. This process likely occurs at moderate temperatures (400-600 ºC) over the million-year time scale expected for this stage (Ichimura et al., 2017). Textural equilibration of secondary albitic plagioclase, formed by albitization of plagioclase, or by crystallization of chondrule mesostasis glass, also occurs through peak metamorphism, especially in higher petrologic types where temperatures >800 ºC persist for several million years (Fig. 3.16a).

4.4.3. Stage 3: Infiltration of anhydrous fluids during retrograde metamorphism

The existence of late-stage fluids has been inferred from observations in feldspar and phosphates. Fine-scale, K-feldspar exsolution in albite is found preferentially adjacent to pores suggesting incorporation of K into albite via fluid flow through the pore network. If K was incorporated during the initial albitization reaction, then we would expect the K to homogenize due to the rapid nature of Na-K interdiffusion in alkali feldspars at metamorphic temperatures and timescales (Cherniak, 2010). The diffusion length over 1 Myr at 600 ºC is ~250 μm (Brady and Yund, 1983), longer than most feldspar patches in type 6 OCs (Kovach and Jones, 2010; Lewis and Jones, 2016). In

addition, the fine-scale nature of much of the exsolution textures implies cooling rates that are orders of magnitude faster than metallographic cooling rates (Lewis et al., In preparation; Jones and Brearley, 2011). If K was incorporated into plagioclase during initial crystallization, or alteration, the exsolution lamellae should develop over millions of years and be much coarser (Jones and Brearley, 2011).

As discussed above, the phosphates apatite and merrillite also form during stage 1 through interactions with a fluid. However, apatite compositions in OCs are anhydrous (<100 ppm H_2O: Jones et al., 2014) with no trend of increasing homogeneity with increasing petrologic type, as would be expected if apatite compositions were set prior to peak metamorphism (Lewis and Jones, 2016). Furthermore, like K-feldspar, apatite is frequently observed adjacent to pores implying a relationship between apatite formation and fluid flow through the pore network (Lewis and Jones, 2016).

To explain these observations, we suggest that OCs experienced high-temperature, short duration bursts of fluid activity. A possible source for such fluids is degassing of partial melts in the asteroid core (Jones et al., 2014), in which case a burst might be possible if there was a buildup of overpressure that was released periodically. An alternative is that fluids were released following impacts. We suggest that either of these scenarios could have resulted in infiltration of an anhydrous, halogen- and alkali-bearing fluid through the OC parent body, utilizing the pore networks developed in Stage 1. During infiltration, K was incorporated into albite adjacent to the pores through which the fluid moved. The prevalence of K-feldspar exsolution near pores can be attributed to limited K diffusion into albite due to short burst durations. If the temperatures achieved are higher than the ambient temperature of the surrounding material, cooling would occur

relatively quickly, perhaps on timescales of days to years that are likely necessary to produce the fine-scale K-feldspar exsolution textures (Jones and Brearley, 2011). Similarly, Cl, and F, were incorporated into apatite during these high energy events.

4.5. Implications for short-lived radioisotope chronometers

Primary plagioclase, and chondrule mesostasis glass from which secondary plagioclase crystallizes, are important carrier phases for short-lived radioisotope systems that are used for producing a chronology of the early solar system. Aluminum, key to Al-Mg chronology, is hosted primarily in plagioclase and mesostasis glass. Alteration of these phases can result in Mg loss and disturbance of the Al-Mg system. Kita et al. (2000) argued that chondrules in OCs greater than petrologic subtype 3.3 suffered from parent body processing because they had younger Al-Mg ages than less thermally-metamorphosed OCs. Based on our observations, we concur strongly with that assessment, and further argue that ages obtained from OCs of subtypes <3.3 might also be compromised by alteration.

This point is illustrated in Fig. 3.16b through a set of probability density plots generated from Al-Mg ages of chondrules from low petrologic type OCs as well as CO and CV chondrites, for comparison. The data from which these plots were generated, and their corresponding references, are in in appendix 3. The top two plots show the probability distribution for chondrule ages in Semarkona (LL3.00) and Bishunpur (LL3.15). These plots are aligned with the 2-2.2 Myr accretion blue band from Fig. 3.16a, and show that accretion is estimated to occur near the midpoint of the chondrule age distributions. The gray band represents the period we estimated for Stage 1 metasomatism, during which most of the plagioclase alteration occurs. A significant

portion of the probability density occurs between 2 and 4 Myr after CAIs and may be due to resetting during parent body alteration.

The middle plot in Fig. 3.16b is generated from 71 Al-Mg ages from 12 different OCs, including Semarkona and Bishunpur. The probability distribution is like Semarkona and Bishunpur with a peak at 2.1 Myr after CAIs and a significant distribution between 2 and 4 Myr during expected Stage 1 metasomatism. The distribution of Al-Mg ages for CO chondrules is close to the distribution seen in OCs. However, the CO distribution is made entirely with data from chondrules in the CO3.05 Y-81020, so may not be representative of the whole CO group. The CV chondrite distribution is composed of Allende ($CV3_{oxA}$) and Efremovka (CV_{red}) chondrules and has a much broader range of Al-Mg ages. The oldest ages cluster around CAI formation (0 Myr) but there is significant distribution though 4 Myr after CAIs. As we discussed above, CO and CV chondrites have many of the same alteration feature as OCs in the Al-rich phases important for Al-Mg chronology.

Another consideration for the quality of Al-Mg ages is that diffusion of Mg has been shown to be significantly faster in albite than anorthite (Van Orman et al., 2014). For example, a 20 μm diameter albite sphere at 600ºC will experience diffusive loss of 50% of its ^{26}Mg, representing one half-life, in 6 years. The same loss in an anorthite sphere will take 17 kyr. At 500ºC, 50% diffusive loss is 1 kyr and 3 Myr for albite and anorthite, respectively. Furthermore, the Al-Mg closure temperature of albite is 100-150 ºC lower than anorthite (Van Orman et al., 2014). So, in addition to the disturbance expected for Al-Mg chondrule formation ages due to secondary alteration, albitized rims, or fine-grained albite could suffer significant diffusion of ^{26}Mg out of the mineral

structure. Although porous regions are typically avoided during SIMS analysis, the fine-scale nature of some of these features means that careful assessment of chondrule mineralogy and microtextures are vital for a reliable, and interpretable, chronology using easily disturbed, short-lived radioisotope systematics.

Unlike Al, the host phase for I, key to I-Xe chronology, is not fully known. However, it is a highly incompatible element and thus is likely to have concentrated in the residual chondrule melt. Dissolution of chondrule mesostasis glass is associated with the alteration of primary plagioclase (Lewis and Jones, in review) and the formation of secondary plagioclase (Lewis et al., in review). Gilmour et al. (2000) used I-Xe systematics to date a range of OC chondrules and clasts, including one of the Parnallee chondrules from Bridges et al. (1997) and the feldspar-nepheline clast described by Bridges et al. (1995) that we referred to above (see Section 4.2.1). They found ages of 7.50±0.98 Myr and 7.04±0.15 Myr after the Bjurböle standard, respectively. The two ages are within error of each other, and several million years younger than the other Parnallee clasts and chondrules measured, which were within error of the Bjurböle standard.

While Gilmour et al. (2000) discussed the possibility that the late chondrule age could be due to plagioclase alteration, they did not discuss this possibility for the feldspar-nepheline clast, despite the similarity of their I-Xe ages, and the similarity in their apparent alteration histories. Our observations are entirely consistent with secondary nepheline formation, and the young ages measured for the nepheline-bearing chondrule and clast may correspond to dehydration of hydrated nepheline during Stage 2 metasomatism. Swindle et al. (1991) used I-Xe to measure chondrule ages in Chainpur

(3.4) and found ages spanning 50 Myr, which corresponds the time period for Stage 3 metasomatism. While they attributed the range in ages to shock resetting events, the high-temperature, short-duration bursts resulting from internal degassing may also be a possibility.

5. Summary and conclusions

We conducted a study of feldspar alteration and equilibration in chondrules through the petrologic sequence, to further characterize the chemical and physical conditions present during thermal metamorphism in ordinary chondrites. We found that primary calcic plagioclase alters to sodalite/scapolite in petrologic types 3.2-3.6, nepheline in types 3.4-3.9, and albite in types 3.6-5. Calcic plagioclase also develops micropores in types >3.4 and alteration lamellae in types 3.6-5. Plagioclase is zoned in some type 3 chondrules and zoning is correlated with dissolution of chondrule mesostasis glass through the type 3s. Albitic plagioclase is present in minor amounts as a primary phase and forms as a secondary phase by the crystallization of chondrule mesostasis glass through the type 3 sequence. Albite also forms through the albitization reaction with calcic plagioclase. K-feldspar occurs in albite in types 3.6-6 as fine-scale lamellae and in larger patches, and both are often associated with the porosity. Plagioclase in Bishunpur (LL3.15) has a maximum An content of An_{99} and types 3.4-3.9 have maximum An contents of An_{84-87}. The type 4 OCs have max An contents of An_{85} for Bjurböle (L/LL4) and Saratov (L4) and An_{50} for Avanhandava (H4).

We argue that alteration and equilibration of plagioclase in OCs is mediated by hydrous fluids during the early stages of thermal metamorphism. The mode of alteration depends on fluid chemistry, temperature, and pH. The pH of the fluid is initially low,

resulting in the dissolution of chondrule mesostasis glass that opens chondrules up to further alteration. pH then increases due to interactions with feldspar and plagioclase alteration occurs in high pH fluids. At low temperatures, calcic plagioclase alters to sodalite/scapolite in fluids with low Na/Cl ratios. Alteration transitions to nepheline as apatite forms causing the Na/Cl ratio of the fluid to drop. The increased Si solubility that comes with higher temperatures transitions the alteration mode to albite. The degree of albitization is correlated with temperature and we suggest that all reactions occur at low water/rock ratios. The Or content of the plagioclase also increases with temperature and may have potential as a method for determining metamorphic subtypes within petrologic type 4 OCs.

We combined these observations into an overall model of metasomatism during thermal metamorphism in ordinary chondrites. The model consists of three general stages. First, hydrous alteration occurs during prograde metamorphism producing a majority of the alteration features we observe in plagioclase. Second, dehydration occurs close to peak metamorphic temperatures, driving off water, and dehydrating hydrous minerals that formed during the first stage. Third, infiltration of anhydrous, alkali- and halogen-bearing fluids during retrograde metamorphism occurs in short duration, high temperature bursts that incorporate K into albite and reset apatite compositions. These three stages of metasomatism have the potential to disturb or reset short-lived radioisotope chronometers, such as Al-Mg and I-Xe, that rely on the integrity of sensitive phases like plagioclase and feldspathic mesostasis glass.

Acknowledgements

We would like to thank Mike Spilde for his help with the microprobe. Thin sections were provided by the Institute of Meteoritics and analytical work was carried out at the Electron Microbeam Analysis Facility, Department of Earth and Planetary Sciences and Institute of Meteoritics, University of New Mexico. J. Lewis acknowledges support from the Kelley-Silver Foundation, University of New Mexico and the New Mexico Space Grant Consortium. The work was partially funded by NASA grant NNX12AH61G (P.I. R. Jones).

References

Alexander C. M. O'D., Hutchison R., Graham A. L. and Yabuli H. (1987) Discovery of scapolite in the Bishunpur (LL3) chondritic meteorite. *Mineralogical Magazine* **51**, 733–735.

Alexander C. M. O'D., Barber D. J. and Hutchison R. (1989) The microstructure of Semarkona and Bishunpur. *Geochimica et Cosmochimica Acta* **53**, 3045–3057.

Alexander C. M. O'D., Bowden R., Fogel M. L. and Howard K. T. (2015) Carbonate abundances and isotopic compositions in chondrites. *Meteoritics & Planetary Science* **50**, 810–833.

Blum A. E. and Stillings L. L. (1995) Feldspar dissolution kinetics. In *Chemical Weathering of Silicate Minerals* (eds. White A. F. and Brantley S. L.) Reviews in Mineralogy and Geochemistry, vol. 31. pp. 291–352.

Bonal L., Quirico E., Bourot-Denise M. and Montagnac G. (2006) Determination of the petrologic type of CV3 chondrites by Raman spectroscopy of included organic matter. *Geochimica et Cosmochimica Acta* **70**, 1849–1863.

Brady J. B. and Yund R. A. (1983) Interdiffusion of K and Na in alkali feldspars: Homogenization experiments. *American Mineralogist* **68**, 106–111.

Brearley A. J. (2006) The action of water. In *Meteorites and the Early Solar System II* (eds. D. S. Lauretta and H. Y. McSween). The University of Arizona Press, Tucson, AZ. pp. 587–624.

Brearley A. J. and Krot A. N. (2013) Metasomatism in the early solar system: The record from chondritic meteorites. In *Metasomatism and the Chemical Transformation of Rock: The Role of Fluids in Terrestrial and Extraterrestrial Processes* Springer Berlin Heidelberg, Berlin, Heidelberg. pp. 659–789.

Bridges J. C., Alexander C. M. O'D., Hutchison R., Franchi I. A. and Pillinger C. T. (1997) Sodium-, chlorine-rich mesostases in Chainpur (LL3) and Parnallee (LL3) chondrules. *Meteoritics & Planetary Science* **32**, 555–565.

Bridges J. C., Hutchison R., Franchi I. A., Alexander C. M. O'D. and Pillinger C. T. (1995) A feldspar-nepheline achondrite clast in Parnallee. *Antarctic Meteorite Research* **8**, 195.

Cherniak D. J. (2010) Cation diffusion in feldspars. In *Diffusion in Minerals and Melts* (eds. Zhang Y. and Cherniak D. J.) Reviews in Mineralogy and Geochemistry, vol. 72. pp. 691–733.

Clayton R. N. (2003) Oxygen isotopes in meteorites. In *Treatise on Geochemistry, Volume 1: Meteorites, Comets, and Planets* (ed. Davis A. M.). Pergamon, Oxford. pp. 129–142.

Dobrică E. and Brearley A. J. (2014) Widespread hydrothermal alteration minerals in the fine-grained matrices of the Tieschitz unequilibrated ordinary chondrite. *Meteoritics & Planetary Science* **49**, 1323–1349.

Dunn T. L., Cressey G., McSween H. Y. and McCoy T. J. (2010) Analysis of ordinary chondrites using powder X-ray diffraction: 1. Modal mineral abundances. *Meteoritics & Planetary Science* **45**, 123–134.

Elkins L. T. and Grove T. L. (1990) Ternary feldspar experiments and thermodynamic models. *American Mineralogist* **75**, 544–559.

Engvik A. K., Putnis A., Fitz Gerald J. D. and Austrheim H. (2008) Albitization of granitic rocks: The mechanism of replacement of oligoclase by albite. *The Canadian Mineralogist* **46**, 1401–1415.

Fagan T. J., Guan Y. and MacPherson G. J. (2007) Al-Mg isotopic evidence for episodic alteration of Ca-Al-rich inclusions from Allende. *Meteoritics & Planetary Science* **42**, 1221–1240.

Friedrich J. M., Bridges J. C., Wang M.-S. and Lipschutz M. E. (2004) Chemical studies of L chondrites. VI: variations with petrographic type and shock-loading among equilibrated falls. *Geochimica et Cosmochimica Acta* **68**, 2889–2904.

Gattacceca J., Rochette P., Denise M., Consolmagno G. and Folco L. (2005) An impact origin for the foliation of chondrites. *Earth and Planetary Science Letters* **234**, 351–368.

Gilmour J. D., Whitby J. A., Turner G., Bridges J. C. and Hutchison R. (2000) The iodine-xenon system in clasts and chondrules from ordinary chondrites: Implications for early solar system chronology. *Meteoritics & Planetary Science* **35**, 445–455.

Grossman J. N., Alexander C. M. O'D., Wang J. and Brearley A. J. (2000) Bleached chondrules: Evidence for widespread aqueous processes on the parent asteroids of ordinary chondrites. *Meteoritics & Planetary Science* **35**, 467–486.

Grossman J. N., Alexander C. M. O'D., Wang J. and Brearley A. J. (2002) Zoned chondrules in Semarkona: Evidence for high- and low-temperature processing. *Meteoritics & Planetary Science* **37**, 49–73.

Grossman J. N. and Brearley A. J. (2005) The onset of metamorphism in ordinary and carbonaceous chondrites. *Meteoritics & Planetary Science* **40**, 87–122.

Harrison K. P. and Grimm R. E. (2010) Thermal constraints on the early history of the H-chondrite parent body reconsidered. *Geochimica et Cosmochimica Acta* **74**, 5410–5423.

Hövelmann J., Putnis A., Geisler T., Schmidt B. and Golla-Schindler U. (2010) The replacement of plagioclase feldspars by albite: Observations from hydrothermal experiments. *Contributions to Mineralogy and Petrology* **159**, 43–59.

Huss G. R. (1979) The matrix of unequilibrated ordinary chondrites: Implications for the origin and subsequent history of chondrites. Master's thesis, University of New Mexico.

Huss G. R., MacPherson G. J., Wasserburg G. J., Russell S. S. and Srinivasan G. (2001) Aluminum-26 in calcium-aluminum-rich inclusions and chondrules from unequilibrated ordinary chondrites. *Meteoritics & Planetary Science* **36**, 975–997.

Huss G. R., Rubin A. E. and Grossman J. N. (2006) Thermal metamorphism in chondrites. In *Meteorites and the Early Solar System II* (eds. D. S. Lauretta and H. Y. McSween Jr.). The University of Arizona Press, Tucson, AZ. pp. 567–586.

Hutchison R., Alexander C. M. O'D. and Barber D. J. (1987) The Semarkona meteorite: First recorded occurrence of smectite in an ordinary chondrite, and its implications. *Geochimica et Cosmochimica Acta* **51**, 1875–1882.

Hutchison R., Alexander C. M. O'D. and Bridges J. C. (1994) Chlorine metasomatism and elemental redistribution in unequilibrated ordinary chondrites. *Meteoritics* **29**, 476–477.

Ichimura S., Seto Y. and Tomeoka K. (2017) Nepheline formation in chondrite parent bodies: Verification through experiments. *Geochimica et Cosmochimica Acta* **210**, 114–131.

Ikeda Y. and Kimura M. (1995) Anhydrous alteration of Allende chondrules in the solar nebula I: Description and alteration of chondrules with known oxygen isotopic compositions. *Antarctic Meteorite Research* **8**, 97.

Ikeda Y. and Kimura M. (1996) Anhydrous alteration of Allende chondrules in the solar nebula III: Alkali-zoned chondrules and heating experiments for anhydrous alteration. *Antarctic Meteorite Research* **9**, 51.

Itoh D. and Tomeoka K. (2003) Dark inclusions in CO3 chondrites: New indicators of parent-body processes. *Geochimica et Cosmochimica Acta* **67**, 153–169.

Itoh S., Kojima H. and Yurimoto H. (2004) Petrography and oxygen isotopic compositions in refractory inclusions from CO chondrites. *Geochimica et Cosmochimica Acta* **68**, 183–194.

Jones R. H. (1997) Alteration of plagioclase-rich chondrules in CO3 chondrites: Evidence for late-stage sodium and iron metasomatism in a nebular environment. In *Parent-Body and Nebular Modification of Chondritic Materials* (eds. M. E. Zolensky, A. N. Krot, and E. R. D. Scott). p. 30.

Jones R. H. and Brearley A. J. (2011) Exsolution in feldspar in the Tuxtuac (LL5) chondrite: A new perspective on cooling rates for metamorphosed chondrites. *74th Annual Meeting of the Meteoritical Society*, Abstract #5475.

Jones R. H. and Brearley A. J. (2010) Late-stage fluids on the LL chondrite parent body: Evidence from feldspar in the LL4 chondrites Bo Xian and Bjurböle. *41st Lunar and Planetary Science Conference*, Abstract #2133.

Jones R. H., McCubbin F. M., Dreeland L., Guan Y., Burger P. V. and Shearer C. K. (2014) Phosphate minerals in LL chondrites: A record of the action of fluids during metamorphism on ordinary chondrite parent bodies. *Geochimica et Cosmochimica Acta* **132**, 120–140.

Jones R. H., McCubbin F. M. and Guan Y. (2016) Phosphate minerals in the H group of ordinary chondrites, and fluid activity recorded by apatite heterogeneity in the Zag H3-6 regolith breccia. *American Mineralogist* **101**, 2452–2467.

Kessel R., Beckett J. R. and Stolper E. M. (2007) The thermal history of equilibrated ordinary chondrites and the relationship between textural maturity and temperature. *Geochimica et Cosmochimica Acta* **71**, 1855–1881.

Kimura M. and Ikeda Y. (1995) Anhydrous alteration of Allende chondrules in the solar nebula II: Alkali-Ca exchange reactions and formation of nepheline, sodalite and Ca-rich phases in chondrules. *Antarctic Meteorite Research* **8**, 123.

Kimura M. and Ikeda Y. (1997) Comparative study of anhydrous alteration of chondrules in reduced and oxidized CV chondrites. *Antarctic Meteorite Research* **10**, 191.

Kimura M. and Ikeda Y. (1996) Comparative study on alteration processes of chondrules in oxidized and reduced CV chondrites. *Meteoritics & Planetary Science Supplement* **31**, A70-A71.

Kimura M. and Ikeda Y. (1998) Hydrous and anhydrous alterations of chondrules in Kaba and Mokoia CV chondrites. *Meteoritics & Planetary Science* **33**, 1139–1146.

Kita N. T., Nagahara H., Togashi S. and Morishita Y. (2000) A short duration of chondrule formation in the solar nebula: Evidence from ^{26}Al in Semarkona ferromagnesian chondrules. *Geochimica et Cosmochimica Acta* **64**, 3913–3922.

Kojima T., Yada S. and Tomeoka K. (1995) Ca-Al-rich inclusions in three Antarctic CO3 chondrites, Yamato-81020 Yamato-82050 and Yamato-790992: Record of low temperature alteration. *Antarctic Meteorite Research* **8**, 79.

Kovach H. A. and Jones R. H. (2010) Feldspar in type 4–6 ordinary chondrites: Metamorphic processing on the H and LL chondrite parent bodies. *Meteoritics & Planetary Science* **45**, 246–264.

Krot A. N., Petaev M. I., Scott E. R. D., Choi B.-G., Zolensky M. E. and Keil K. (1998a) Progressive alteration in CV3 chondrites: More evidence for asteroidal alteration. *Meteoritics & Planetary Science* **33**, 1065–1085.

Krot A. N., Petaev M. I., Zolensky M. E., Keil K., Scott E. R. D. and Nakamura K. (1998b) Secondary calcium-iron-rich minerals in the Bali-like and Allende-like oxidized CV3 chondrites and Allende dark inclusions. *Meteoritics & Planetary Science* **33**, 623–645.

Krot A. N., Petaev M., Meibom A. and Keil K. (2000) In situ growth of Ca-rich rims around Allende dark inclusions. *Geochemistry International* **38**, 351–368.

Krot A. N., Zolensky M. E., Wasson J. T., Scott E. R. D., Keil K. and Ohsumi K. (1997) Carbide-magnetite assemblages in type-3 ordinary chondrites. *Geochimica et Cosmochimica Acta* **61**, 219–237.

Lewis J. A. and Jones R. H. (2016) Phosphate and feldspar mineralogy of equilibrated L chondrites: The record of metasomatism during metamorphism in ordinary chondrite parent bodies. *Meteoritics & Planetary Science* **51**, 1886–1913.

Lewis J. A. and Jones R. H. (in review) Primary feldspar in the Semarkona LL3.00 chondrite: Constraints on chondrule formation and secondary alteration. *Meteoritics & Planetary Science*.

Lewis J. A., Jones R. H. and Brearley A. J. (in preparation) K-feldspar exsolution in ordinary chondrites: Evidence for late stage fluids and rapid cooling.

Lewis J. A., Jones R. H. and Garcea S. C. (in review) Chondrule porosity in the L4 chondrite Saratov: Dissolution, chemical transport, and fluid flow. *Geochimica et Cosmochimica Acta*.

Li C., Bridges J. C., Hutchison R., Franchi I. A., Sexton A. S., Ouyang Z. and Pillinger C. T. (2000) Bo Xian (LL3.9): Oxygen-isotopic and mineralogical characterisation of separated chondrules. *Meteoritics & Planetary Science* **35**, 561–568.

Matsumoto M., Tomeoka K., Seto Y., Miyake A. and Sugita M. (2014) Nepheline and sodalite in the matrix of the Ningqiang carbonaceous chondrite: Implications for formation through parent-body processes. *Geochimica et Cosmochimica Acta* **126**, 441–454.

McSween H. Y., Ghosh A., Grimm R. E., Wilson L. and Young E. D. (2002) Thermal evolution models of asteroids. In *Asteroids III* (eds. W. F. Bottke, A. Cellino, P. Paolicchi, and R. P. Binzel). The University of Arizona Press, Tucson, AZ. pp. 559–571.

McSween H. Y. and Labotka T. C. (1993) Oxidation during metamorphism of the ordinary chondrites. *Geochimica et Cosmochimica Acta* **57**, 1105–1114.

Nakamura T., Nakato A., Ishida H., Wakita S., Noguchi T., Zolensky M. E., Tanaka M., Kimura M., Tshuchiyama A., Ogami T., Hashimoto T., Konno M., Uesugi M., Yada T., Shirai K., Fujimura A., Okazaki R., Sandford S. A., Ishibashi Y., Abe M., Okada T., Ueno M. and Kawaguchi J. (2014) Mineral chemistry of MUSES-C Regio inferred from analysis of dust particles collected from the first- and second-touchdown sites on asteroid Itokawa. *Meteoritics & Planetary Science* **49**, 215–227.

Nakamura T., Noguchi T., Tanaka M., Zolensky M. E., Kimura M., Tsuchiyama A., Nakato A., Ogami T., Ishida H., Uesugi M., Yada T., Shirai K., Fujimura A., Okazaki R., Sandford S. A., Ishibashi Y., Abe M., Okada T., Ueno M., Mukai T., Yoshikawa M. and Kawaguchi J. (2011) Itokawa dust particles: A direct link between S-Type asteroids and ordinary chondrites. *Science* **333**, 1113–1116.

Nakamura Y. and Motomura Y. (1999) Sodic plagioclase thermometry of type 6 ordinary chondrites: Implications for the thermal histories of parent bodies. *Meteoritics & Planetary Science* **34**, 763–772.

Nekvasil H. (1994) Ternary feldspar/melt equilibria: A review. In *Feldspars and Their Reactions* (ed. I. Parsons). Springer Netherlands, Dordrecht. pp. 195–219.

Nomura K. and Miyamoto M. (1998) Hydrothermal experiments on alteration of Ca-Al-rich inclusions (CAIs) in carbonaceous chondrites: Implication for aqueous alteration in parent asteroids. *Geochimica et Cosmochimica Acta* **62**, 3575–3588.

Putnis A. (2009) Mineral replacement reactions. In *Thermodynamics and Kinetics of Water-Rock Interaction* (eds. Oelkers E. H. and Schott J.). Reviews in Mineralogy and Geochemistry, vol. 70. pp. 87–124.

Rubin A. E. (1999) Formation of large metal nodules in ordinary chondrites. *Journal of Geophysical Research: Planets* **104**, 30799–30804.

Rubin A. E. (1994) Metallic copper in ordinary chondrites. *Meteoritics* **29**, 93–98.

Rubin A. E. (2004) Postshock annealing and postannealing shock in equilibrated ordinary chondrites: Implications for the thermal and shock histories of chondritic asteroids. *Geochimica et Cosmochimica Acta* **68**, 673–689.

Rubin A. E. and Grossman J. N. (1985) Phosphate-sulfide assemblages and Al/Ca ratios in type-3 chondrites. *Meteoritics* **20**, 479–489.

Russell S. S., Huss G. R., Fahey A. J., Greenwood R. C., Hutchison R. and Wasserburg G. J. (1998) An isotopic and petrologic study of calcium-aluminum-rich inclusions from CO3 meteorites. *Geochimica et Cosmochimica Acta* **62**, 689–714.

Russell S. S., MacPherson G. J., Leshin L. A. and McKeegan K. D. (2000) ^{16}O enrichments in aluminum-rich chondrules from ordinary chondrites. *Earth and Planetary Science Letters* **184**, 57–74.

Scott E. R. D. and Jones R. H. (1990) Disentangling nebular and asteroidal features of c03 carbonaceous chondrite meteorites. *Geochimica et Cosmochimica Acta* **54**, 2485–2502.

Scott E. R. D. and Krot A. N. (2014) Chondrites and their components. In *Treatise on Geochemistry (Second Edition), Volume 1: Meteorites and Cosmochemical Processes* (ed. Davis A. M.). Elsevier, Oxford. pp. 65–137.

Scott E. R. D., Krot T. V., Goldstein J. I. and Wakita S. (2014) Thermal and impact history of the H chondrite parent asteroid during metamorphism: Constraints from metallic Fe–Ni. *Geochimica et Cosmochimica Acta* **136**, 13–37.

Sears D. W. G., Batchelor J. D., Lu J. and Keck B. D. (1991) Metamorphism of CO and CO-like chondrites and comparisons with type 3 ordinary chondrites. *Antarctic Meteorite Research* **4**, 319.

Sears D. W., Grossman J. N., Melcher C. L., Ross L. M. and Mills A. A. (1980) Measuring metamorphic history of unequilibrated ordinary chondrites. *Nature* **287**, 791–795.

Slater-Reynolds V. and McSween H. Y. (2005) Peak metamorphic temperatures in type 6 ordinary chondrites: An evaluation of pyroxene and plagioclase geothermometry. *Meteoritics & Planetary Science* **40**, 745–754.

Sorby H. C. (1877) On the structure and origin of meteorites. *Nature* **15**, 495–498.

Stöffler D., Keil K. and Edward R.D S. (1991) Shock metamorphism of ordinary chondrites. *Geochimica et Cosmochimica Acta* **55**, 3845–3867.

Swindle T. D., Caffee M. W., Hohenberg C. M., Lindstrom M. M. and Taylor G. J. (1991) Iodine-xenon studies of petrographically and chemically characterized Chainpur chondrules. *Geochimica et Cosmochimica Acta* **55**, 861–880.

Taylor L. A., Liu Y., Guan Y., Day J. M. D., Ma C., Hiroi T., Corder C. A., Assayag N., Rumble D., Cartigny P., Chen Y., Hand K. P., Pieters C. M., Eiler J. M., Pokhilenko N. P. and Podgornykh N. M. (2014) Metamorphism in the Chelyabinsk meteorite. *45th Lunar and Planetary Science Conference,* Abstract #2346.

Telus M., Huss G. R., Nagashima K. and Ogliore R. C. (2014) Revisiting Al-26-Mg-26 systematics of plagioclase in H4 chondrites. *Meteoritics & Planetary Science* **49**, 929–945.

Tomeoka K. and Itoh D. (2004) Sodium-metasomatism in chondrules in CO3 chondrites: Relationship to parent body thermal metamorphism. *Meteoritics & Planetary Science* **39**, 1359–1373.

Tomeoka K., Nomura K. and Takeda H. (1992) Na-bearing Ca-Al-rich inclusions in the Yamato-791717 CO carbonaceous chondrite. *Meteoritics* **27**, 136–143.

Van Orman J. A., Cherniak D. J. and Kita N. T. (2014) Magnesium diffusion in plagioclase: Dependence on composition, and implications for thermal resetting of the 26Al–26Mg early solar system chronometer. *Earth and Planetary Science Letters* **385**, 79–88.

Van Schmus W. R. and Ribbe P. H. (1968) The composition and structural state of feldspar from chondritic meteorites. *Geochimica et Cosmochimica Acta* **32**, 1327–1342.

Van Schmus W. R. and Wood J. A. (1967) A chemical-petrologic classification for the chondritic meteorites. *Geochimica et Cosmochimica Acta* **31**, 747–765.

Wasserburg G. J., Hutcheon I. D., Aléon J., Ramon E. C., Krot A. N., Nagashima K. and Brearley A. J. (2011) Extremely Na- and Cl-rich chondrule from the CV3 carbonaceous chondrite Allende. *Geochimica et Cosmochimica Acta* **75**, 4752–4770.

Wasson J. T. and Kallemeyn G. W. (1988) Compositions of chondrites. *Philosophical Transactions of the Royal Society of London A: Mathematical, Physical and Engineering Sciences* **325**, 535–544.

Wasson J. T., Yurimoto H. and Russell S. S. (2001) ^{16}O-rich melilite in CO3.0 chondrites: Possible formation of common, ^{16}O-poor melilite by aqueous alteration. *Geochimica et Cosmochimica Acta* **65**, 4539–4549.

Weisberg M. K., Prinz M., Clayton R. N. and Mayeda T. K. (1997) CV3 chondrites: Three subgroups, not two. *Meteoritics and Planetary Science Supplement* **32**, A138.

Weisberg M. K., Smith C., Benedix G., Herd C. D. K., Righter K., Haack H., Yamaguchi A., Aoudjehane H. C. and Grossman J. N. (2009) The meteoritical bulletin, no. 96, September 2009. *Meteoritics & Planetary Science* **44**, 1355–1397.

Wen S. and Nekvasil H. (1994) SOLVCALC: An interactive graphics program package for calculating the ternary feldspar solvus and for two-feldspar geothermometry. *Computers & Geosciences* **20**, 1025–1040.

Wick M. J. and Jones R. H. (2012) Formation conditions of plagioclase-bearing type I chondrules in CO chondrites: A study of natural samples and experimental analogs. *Geochimica et Cosmochimica Acta* **98**, 140–159.

Williams J. T., Sharp Z. D., Lewis J. A., Shearer C. K., McCubbin F. M. and Agee C. B. (2015) Using chlorine isotopes to track the composition of ice incorporated into chondrite parent bodies. *78th Annual Meeting of the Meteoritical Society*, Abstract #5309.

Wlotzka F. (2005) Cr spinel and chromite as petrogenetic indicators in ordinary chondrites: Equilibration temperatures of petrologic types 3.7 to 6. *Meteoritics & Planetary Science* **40**, 1673–1702.

Zolotov M. Y. (2012) Aqueous fluid composition in CI chondritic materials: Chemical equilibrium assessments in closed systems. *Icarus* **220**, 713–729.

Zolotov M. Y. and Mironenko M. V. (2007) Hydrogen chloride as a source of acid fluids in parent bodies of chondrites. *38th Lunar and Planetary Science Conference*, Abstract #2340.

CHAPTER 4

K-feldspar exsolution in ordinary chondrites: Evidence for rapid cooling at high temperatures in all ordinary chondrite groups

In collaboration with:
Rhian H. Jones
Adrian J. Brearley

To be submitted for publication to:
Geochimica et Cosmochimica Acta

Abstract

Thermal metamorphism in ordinary chondrites (OCs) is thought to have occurred through the radioactive decay of ^{26}Al in an onion-shell-like structure. During retrograde metamorphism, the onion-shell model predicts slower cooling rates with increasing petrologic type. However, cooling rates determined by pyroxene diffusion and metallographic methods are inconsistent with onion-shell-like cooling. These inconsistencies have led to a model of asteroid disruption and reaccretion into a rubble pile, after peak metamorphism. Potassium-feldspar exsolution in albite, in a perthite texture, has been noted in OCs and can be used as another method for determining cooling rates. We conducted a survey of K-feldspar occurrences and textures, within chondrules, in petrologic type 3.6-6 H, L, and LL OCs. Potassium-feldspar is present as a secondary feature, in primary and secondary albite, as fine-scale exsolution lamellae, 0.1-1.5 μm wide, as well as in larger patches up to 50 μm in size. Exsolution is present in all OC groups and is most common in petrologic type 4.

In the H4 chondrite Avanhandava, we estimated the cooling rate from perthite to be 1 °C per 1-4 months over a temperature interval of 670-765 °C. Peristerite is also present in Avanhandava for which we estimated a cooling rate of 1 °C in 10^3-10^4 years

from 570-540 °C. In general, the fast, high temperature cooling rate determined by perthite is similar to cooling rates determined by pyroxene diffusion. The peristerite cooling rate is closer to the slow, lower temperature metallographic cooling rates. Because K-feldspar exsolution is present in similar fine-scale lamellae in all OC groups, we suggest that all OC parent bodies experienced the same cooling history at high temperatures. These results lead us to question predications of OC asteroid cooling from both onion-shell and rubble-pile models.

1. Introduction

Ordinary chondrites (OCs) have undergone varying degrees of thermal metamorphism resulting in a myriad of chemical, textural, and mineralogical changes (Huss et al., 2006). These changes include compositional and textural equilibration of olivine and pyroxene, recrystallization of matrix and chondrule mesostasis, and the formation of secondary minerals, including feldspar and phosphates. The petrologic classification scheme is used to describe the extent of thermal metamorphism experienced by OCs (Van Schmus and Wood, 1967). In this scheme, OCs assigned petrologic type 3 have been minimally affected by heating whereas those assigned petrologic type 6 are considered fully equilibrated, both compositionally and texturally. Two general models are used to describe observations connected to asteroid thermal metamorphism: the onion-shell model and the rubble-pile model.

The onion-shell model, the name first adopted by Pellas and Storzer (1981), describes an internally heated asteroid that cools by radiative transfer from the surface and by conduction through the asteroid interior. The heating mechanism for asteroids is generally accepted to be the radioactive decay of energetic, short-lived radionuclides,

largely ^{26}Al (McSween et al., 2002; Huss et al., 2006). Heating from impact events may have also been a contributing factor (Rubin, 2004). In the onion-shell scenario, heating is rapid and results in extensive thermal metamorphism in the interior of the asteroid, corresponding to petrologic type 6. Partial melting at the core may also occur (e.g., Elkins-Tanton et al., 2011). Out from the highly metamorphosed central region, onion-like shells of material experience less heating progressively closer to the cold, radiative surface. This results in petrologic types 5, 4, and 3 with type 3 being the least metamorphosed closest to the asteroid surface.

While the onion-shell model works well in describing the observed petrographic indicators of thermal metamorphism, the detailed model predictions do not completely match the meteorite record. For example, the models have not been able to match the relative abundances of the different petrologic types contained in the meteorite record (McSween et al., 2002). This discrepancy has been ascribed to a bias in sample delivery to the Earth's surface (e.g., Akridge et al., 1998).

The biggest challenge to the onion-shell model has come from measurements of cooling rates. Onion-shell-like cooling predicts decreasing cooling rates with increasing petrologic type (Pellas and Storzer, 1981). However, Scott et al. (2014) show that in H chondrites, there is a range of metallographic cooling rates (~1 °C per 10^5-10^6 years) for most samples of all petrologic types and that these cooling rates are not correlated with petrologic type. Further, Ganguly et al. (2013, 2016) show that cooling rates determined through considerations of diffusion in pyroxene, between 750-875 °C, are significantly faster (~1 °C per $10^{0.5}$-10^2 years) than those obtained by metallographic methods at lower temperature (500 °C).

To account for a lack of correlation between metallographic cooling rate and petrologic type, Scott and Rajan (1981) proposed a rubble-pile model in which OC asteroids may have initially evolved in an onion-shell-like manner but were ultimately disrupted by collisions, randomly reassembled, and then cooled in a way that did not correspond with their petrologic type. A rubble-pile model is also favored by Scott et al. (2014) and Ganguly et al. (2013, 2016). To explain the 3-4 orders-of-magnitude difference in cooling rates between the metallographic and pyroxene-based measurements, Ganguly et al. (2013, 2016) suggest that the rapid cooling rates determined by pyroxene diffusion reflect cooling from high temperatures, soon after excavation of material by an impactor, near peak metamorphism. Slower metallographic cooling rates then record cooling through lower temperatures long after the asteroid reassembled.

Alkali feldspar exsolution textures can also be used to measure cooling rates to further elucidate models of asteroid evolution. Potassium-feldspar has been noted previously in OCs (Lewis et al., in preparation; Lewis et al., in review; Kovach and Jones, 2010; Jones and Brearley, 2011; Taylor et al., 2014; Lewis and Jones, 2016) and by Nakamura et al. (2011) in a plagioclase-bearing particle returned from the asteroid Itokawa by the Hayabusa mission. Jones and Brearley (2011) argued that the fine-scale nature of exsolution lamellae in the LL5 chondrite Tuxtuac suggested rapid cooling rates. They estimated cooling rates from feldspar exsolution to be orders of magnitude faster (~1 °C per 100 years) than metallographic cooling rates, even though the two systems record cooling through a similar temperature range, 500-600 °C. While the cooling rate determined for K-feldspar exsolution in Tuxtuac is generally in line with cooling rates

determined through pyroxene diffusion, the estimated exsolution interval is considerably lower in temperature than the modelled pyroxene diffusion temperatures.

In our study of OC plagioclase alteration and evolution (Lewis et al., in preparation), we showed that K-feldspar in chondrule albite occurs in nearly all OC samples in petrologic types ≥3.6, with the greatest abundance in petrologic type 4. Potassium-feldspar is present in two forms: fine-scale exsolution lamellae and larger K-feldspar patches. We argued that incorporation of K into albite occurred after peak metamorphism by mobilization of anhydrous fluids in short-duration, high-temperature events. This model was inferred from both the presence of fine-scale exsolution lamellae indicating rapid cooling, and the presence of K-feldspar preferentially near porous regions (Lewis et al., in review), suggesting the movement of K through the pore network.

In this study, we conduct a more thorough examination of K-feldspar in chondrules from H, L, and LL chondrites in petrologic types 3.6-6, and quantify the cooling rate inferred from the fine-scale exsolution lamellae in the H4 chondrite Avanhandava. We compare that cooling rate to the cooling rates measured using other methods and discuss the connection between the thermochemical observations of OC parent body evolution and the onion-shell and rubble-pile models.

2. Methods

This study uses the same samples and analytical conditions as described in Lewis et al. (in preparation), which will be summarized here. We examined 11 OC thin sections from the Institute of Meteoritics Collection at the University of New Mexico (Table 4.1): Bishunpur (LL3.15, UNM 1038), Chainpur (LL3.4, UNM 1041), Parnallee (LL3.6, UNM

1018), Dhajala (H3.8, UNM 301), Bo Xian (LL3.9, UNM 265), Bjurböle (L/LL4, UNM 117), Saratov (L4, UNM 1145), Santa Barbara (L4, UNM 120), Avanhandava (H4, UNM 88), Tuxtuac (LL5, UNM 627), and Sulagiri (LL6, UNM 1160). K-feldspar was identified in chondrules using backscattered electron (BSE) imaging and energy-dispersive spectroscopic (EDS) X-ray analysis on an FEI Quanta 3D Scanning Electron Microscope equipped with a Field Emission Gun (FEG-SEM) at the University of New Mexico. High-contrast BSE images were captured at 10 kV and 16 nA. Quantitative X-ray chemical analysis was performed using an Electron Probe Microanalyzer (EPMA) is reported in Lewis et al. (in preparation).

Transmission electron microscope (TEM) sections from Avanhandava chondrule 6 and Bjurböle chondrule 8 were prepared using the focused ion beam (FIB) on the FEI Quanta 3D Dual-beam FEG-SEM/FIB, with a final polish conducted at 5 kV to reduce surface amorphization. The sections were imaged at the University of New Mexico using a JOEL 2010 TEM for bright field (BF) images and a JEOL 2010F Scanning TEM (STEM) operated at 200 kV in scanning mode using a high-angle annular dark-field (HAADF) detector for dark field (DF) images.

Table 4.1. Samples studied.

	thin section	petrologic type	shock stage	K-feldspar exsolution
Bishunpur	UNM 1038	LL3.15	S2[R99,G05]	*not observed*
Chainpur	UNM 1041	LL3.4	S1[S91,R99,G05]	*not observed*
Parnallee	UNM 1018	LL3.6	S3[G05]	rare
Dhajala	UNM 301	H3.8	S1[S91,S14]	rare
Bo Xian	UNM 265	LL3.9	S2[L00], S3[R94]	*not observed*
Bjurböle	UNM 117	L/LL4	S1[S91,R94,R04,G05]	common
Saratov	UNM 1145	L4	S2[R94,R04,G05], S3[F04]	common
Santa Barbara	UNM 120	L4	S2[LJ16]	common
Avanhandava	UNM 88	H4	S1[S14], S2[S91,R94,R04]	common
Tuxtuac	UNM 627	LL5	S2[R94,R04,G05]	uncommon
Sulagiri	UNM 1160	LL6	S2[W09]	uncommon

[S91] Stöffler et al. (1991), [R94] Rubin (1994), [R99] Rubin (1999), [L00] Li et al. (2000), [R04] Rubin (2004), [F04] Friedrich et al. (2004), [G05] Gattacceca et al. (2005), [W09] Weisberg et al. (2009), [S14] Scott et al. (2014), [LJ16] Lewis and Jones (2016)

3. Results

We searched for K-feldspar within chondrules in keeping with previous studies of OC feldspar (Lewis et al., in preparation; Lewis and Jones, in review; Kovach and Jones, 2010; Lewis and Jones, 2016). As we described in Lewis et al. (in preparation), K-feldspar in chondrules occurs as fine-scale exsolution lamellae in albite, or as larger patches in albite. Both forms commonly occur in association with pores. While we describe both forms here, we will focus on the fine-scale exsolution lamellae in our discussion on cooling rates.

3.1. Petrologic type 3

In the petrologic type 3 OCs we studied (Table 4.1), we observed rare, fine-scale K-feldspar exsolution textures in chondrules in Parnallee (LL3.6) and Dhajala (H3.8). We did not observe K-feldspar in chondrules in Bishunpur (LL3.15), Chainpur (LL3.4), or Bo Xian (LL3.9). Although we did not observe K-feldspar in Bo Xian, its scarcity in Parnallee and Dhajala could make it difficult to locate in type 3 OCs in general, despite the fact that albite is common (Lewis et al., in preparation). We also did not observe K-feldspar in primary-albite-bearing chondrules in the LL3.00 chondrite Semarkona (Lewis and Jones, in review).

In Parnallee, K-feldspar exsolution was not observed in many chondrules and was only found in a few regions near chondrule edges. Figure 4.1a-c shows two occurrences in adjacent chondrules. In chondrule 10 (Fig. 4.1a), K-feldspar is present as 0.2-0.7 μm wide, irregular filaments (Fig. 4.1b) in an albite host, close to the edge of the chondrule. It is also present at the interface with an adjacent chondrule as 1-3 μm wide patches in albite (Fig. 4.1c). An example of isolated K-feldspar lamellae in another Parnallee

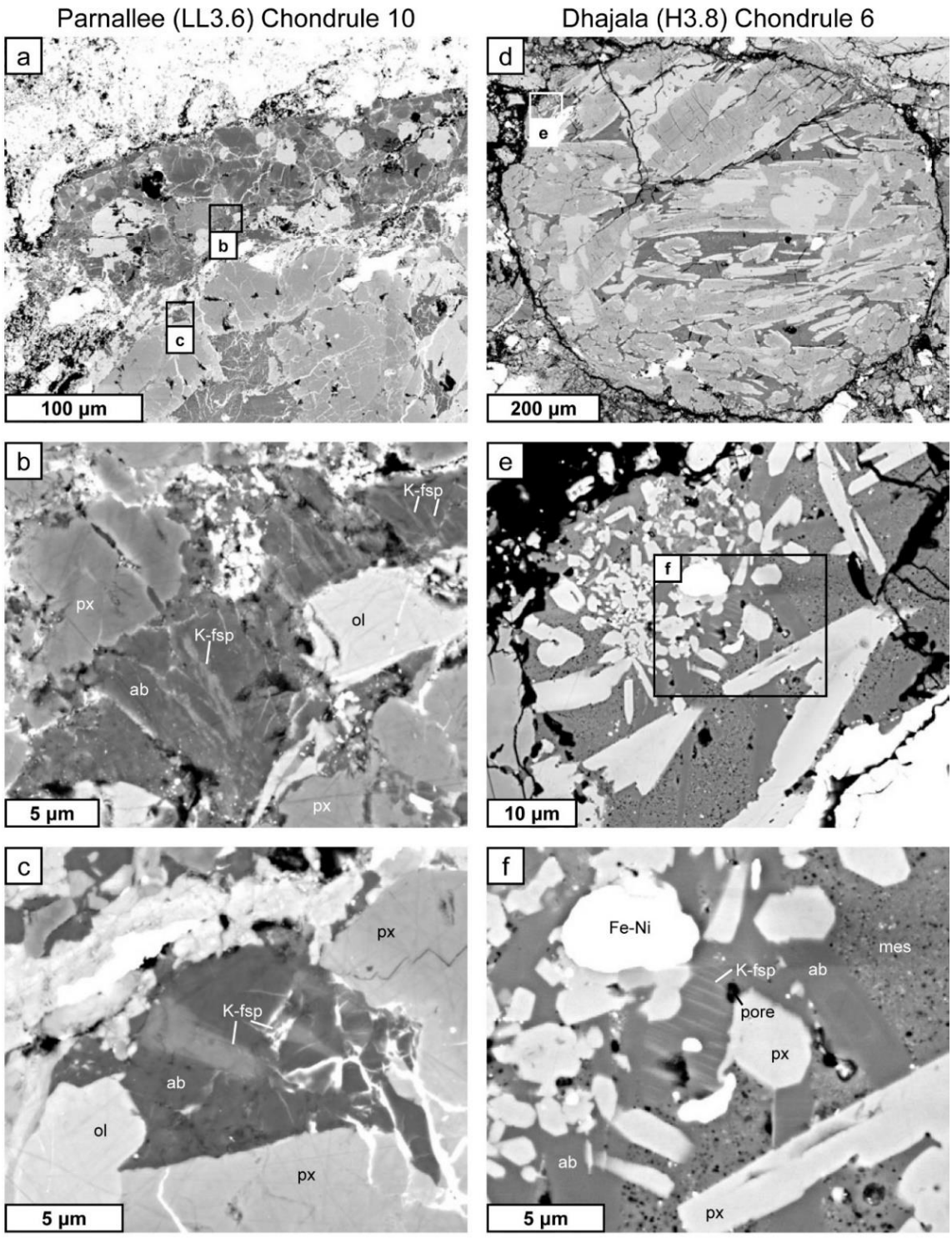

Figure 4.1. BSE images of K-feldspar in Parnallee (LL3.6) and Dhajala (H3.8) chondrules. Parnallee chondrule 10 (a) is an elongated porphyritic olivine (ol) and pyroxene (px) (POP) chondrule. K-feldspar (K-fsp) is present within the chondrule (b) and at the border with the adjacent chondrule (c). Within the chondrule (b), K-feldspar is present as filaments, 0.2-0.7 µm wide, within an albite (ab) host. *(Caption continues on the following page).*

Figure 4.1. *(Caption continued from the previous page).* Along the chondrule border (c), K-feldspar is present as 1-3 μm wide patches within albite. Dhajala chondrule 6 (d) is a POP chondrule with a patch of primary albite (e) along the chondrule edge. In one albite lath (f), very fine scale, 0.1-0.3 μm wide, K-feldspar exsolution lamellae are present near μm-scale pores. The albite laths exist with grains of pyroxene and Fe-Ni metal in fine-grained, crystallized mesostasis glass (mes).

chondrule is shown in Fig. 3.3f of Lewis et al. (in preparation). K-feldspar exsolution is also rare in Dhajala (Fig. 4.1d-f), mainly occurring as fine-scale lamellae in primary albite laths adjacent to pores. This lath morphology is exemplified in chondrule 6 (Fig. 4.1d), that has a patch of primary albite near the chondrule edge (Fig. 4.1e). Within one of the albite laths (Fig. 4.1f), fine-scale, 0.1-0.3 μm wide K-feldspar exsolution lamellae are present adjacent to pores and the porous, fine-grained crystallized mesostasis glass.

3.2. Petrologic type 4

K-feldspar exsolution is abundant in petrologic type 4 OC chondrules (Figs. 4.2-4.5). In the L4 chondrites Santa Barbara and Saratov, K-feldspar is commonly observed within both primary and secondary albite throughout many chondrules, as exemplified by the two porphyritic olivine and pyroxene (POP) chondrules shown in Fig. 4.2. K-feldspar is present in Santa Barbara chondrule 1 (Fig. 4.2a) as 0.2-0.7 μm wide exsolution lamellae in large regions of smooth albite (Fig. 4.2b,c). Unlike the type 3 chondrites (Fig. 4.1), exsolution lamellae are not observed preferentially adjacent to pores or near the chondrule edge (Fig. 4.2b,c). In Saratov chondrule 4 (Fig. 4.2d), K-feldspar exsolution is clearly visible in patches of primary albite close to the chondrule edge (Figs. 4.2e,f). In parts of Fig. 4.2e, K-feldspar exsolution lamellae lie at a low angle to the polished thin section surface, resulting in diffuse lamellae boundaries and making it difficult to measure lamellae widths. This is not the case in Fig. 4.2f where lamellae are generally 0.1-0.4 μm wide. There is also one 7 μm wide region of K-feldspar adjacent to an

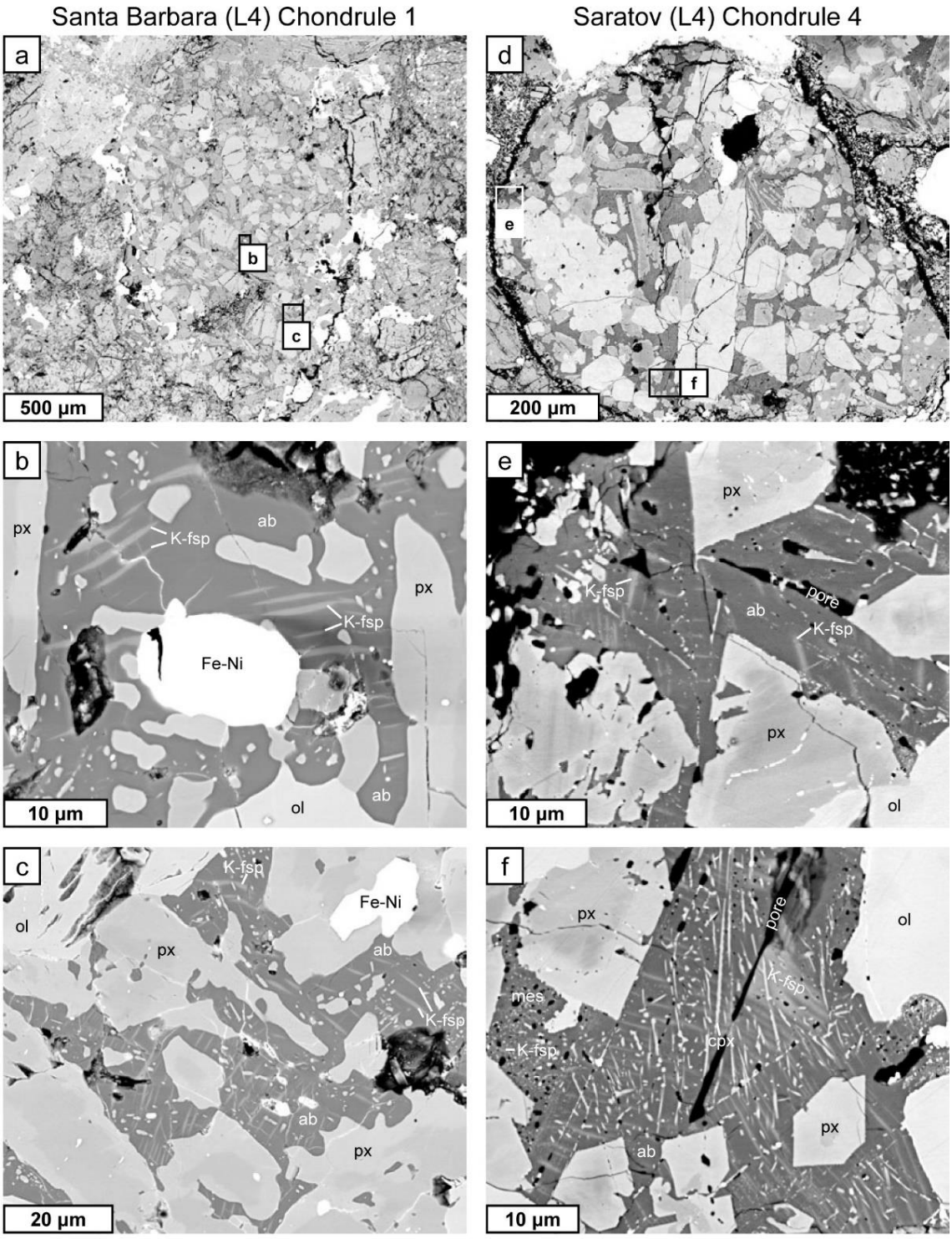

Figure 4.2. BSE images of K-feldspar in the L4 chondrites Santa Barbara and Saratov. Santa Barbara chondrule 1 (a) is a porphyritic olivine (ol) and pyroxene (px) (POP) chondrule. K-feldspar (K-fsp) is present throughout the chondrule as 0.2-0.7 µm wide exsolution lamellae in albite (b). In this chondrule, exsolution lamellae are not found preferentially adjacent to pores (c). *(Caption continues on the following page).*

Figure 4.2. *(Caption continued from the previous page).* Saratov chondrule 4 (d) is a POP chondrule with several patches of primary albite close to the chondrule edge (e,f). K-feldspar exsolution from the primary albite in (e) is at a low angle to the polished thin section surface, resulting in diffuse lamellae boundaries. Exsolution in (f) is mostly in 0.1-0.4 μm wide lamellae, but there is one 7 μm wide region of K-feldspar adjacent to an elongated pore. Exsolution is also present in the fine-grained, crystallized mesostasis glass (mes). Elongated Ca-rich pyroxene (cpx) crystallites are also present in the primary albite laths.

elongated pore. In addition to exsolution in primary albite laths of chondrule 4, lamellae are also present in the fine-grained, crystallized mesostasis glass. Acicular Ca-rich pyroxene crystallites are also present in the albite laths and are not to be confused with the exsolution lamellae.

In Bjurböle (L/LL4), exsolution is common. Figure 4.3 shows an example of a typical chondrule in which K-feldspar exsolution is present throughout. Chondrule 8 is a POP chondrule (Fig. 4.3a) with K-feldspar exsolution from both smooth primary albite and secondary, fine-grained albite throughout (Figs. 3b,c). Figure 4.3b shows a 70 μm long lath of primary albite surrounded by fine-grained crystallized mesostasis glass. The lath has 0.2-0.4 μm wide exsolution lamellae, regularly spaced, normal to the long axis of the grain. Exsolution lamellae of similar widths are also present in the albite component of the crystallized mesostasis glass (Fig. 4.3b). In another region of chondrule 8 (Fig. 4.3c), K-feldspar exsolution lamellae vary in width from 0.2-1.6 μm. The widest patches of K-feldspar are adjacent to grain boundaries and Fe-Ni metal and may be composed of multiple lamellae. A FIB section extracted from the primary feldspar lath in Fig. 4.3b (black line) is examined in a HAADF TEM image in Fig. 4.3d. The HAADF image shows sub-μm K-feldspar lamellae perpendicular to the long axis of the host albite grain, sub-μm inclusions of Ca-rich pyroxene, and pores up to 1 μm in size. The crystallized

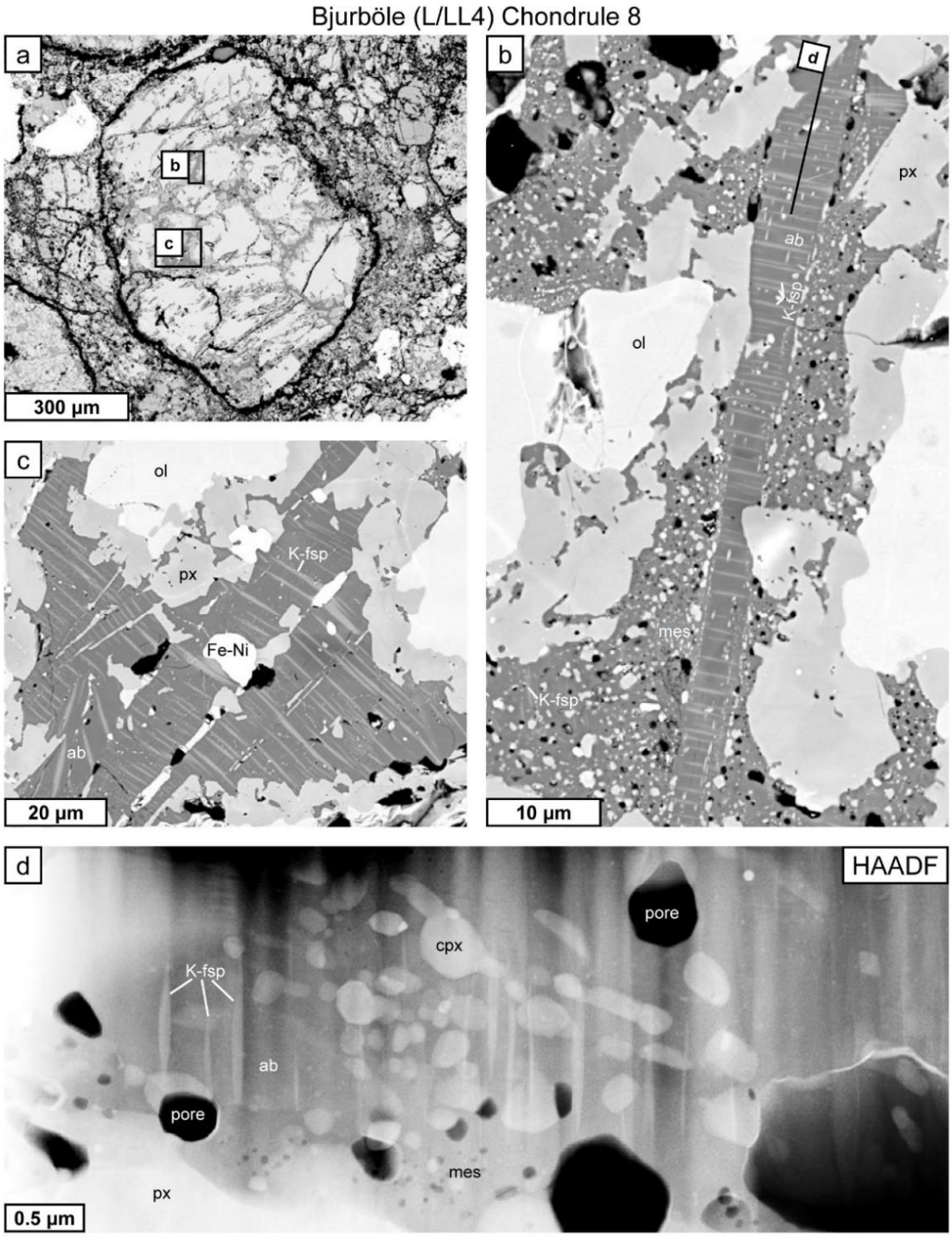

Figure 4.3. BSE SEM images (a-c) and a HAADF TEM image (d) showing albite with K-feldspar exsolution in Bjurböle (L/LL4) POP chondrule 8. K-feldspar (K-fsp) exsolution from primary and secondary albite (ab) occurs throughout the chondrule. The 70 µm long lath of primary albite in the center of (b) has 0.2-0.4 µm wide exsolution lamellae, regularly spaced, normal to the long axis of the grain. Exsolution lamellae of a similar size range are also present in the albite component of the crystallized mesostasis glass (mes, Fig. 4.3b). *(Caption continues on the following page).*

Figure 4.3. *(Caption continued from the previous page).* K-feldspar lamellae in (c) vary in width from 0.2-1.6 μm with the widest lamellae observed adjacent to grain boundaries and Fe-Ni metal. The black line in (b) indicates the location of a FIB section extracted for TEM imaging, shown in (d). The HAADF image (d) illustrates the relationship between the sub-μm K-feldspar lamellae, Ca-rich pyroxene (cpx) inclusions, pores, and the host albite lath. Porous crystallized mesostasis glass is present under the albite lath.

mesostasis glass observed in the FIB section occurred beneath the albite lath in the SEM image of Fig. 4.1b. It contains abundant, fine-scale (<0.1 μm) pores.

In Avanhandava (H4) exsolution is very common and Fig. 4.4 illustrates a particularly dramatic example. Chondrule 6, a porphyritic pyroxene (PP) chondrule (Fig. 4a), has K-feldspar exsolution within large, smooth regions of albite throughout the chondrule. In a region near the chondrule center (Fig. 4.4b), exsolution lamellae are extremely abundant and are evenly distributed through many, randomly oriented -subdomains (Fig. 4.4c-e). K-feldspar lamellae within this region vary from 0.2-1.5 μm in width. Some wider lamellae have linear fractures through the lamella center and fractures are present in albite, between lamellae, inclined 72-75° to the length of the K-feldspar lamellae (Fig. 4.4c). Both sets of fractures may be the result of coherency strain between the lamellae and the albite host. The bulk composition of a region in Fig. 4.5d, measured using EPMA with a 5 μm diameter, defocused beam (dashed circle), is $An_{2.5}Ab_{64.8}Or_{32.7}$ (Lewis et al. [in preparation], Appendix 1: Table A1.26, analysis #72).

A FIB section was extracted from the region illustrated in Fig. 4.4e (black line) for further analysis by TEM (Fig. 4.5). A HAADF STEM image shows the K-feldspar exsolution lamellae and albite host (Fig. 4.5a). Exsolution lamellae range in width from 160-310 nm with an average wavelength of 650 nm. The average wavelength was determined by measuring the distance across multiple lamellae, edge to edge, perpendicular to the lamellae axes, midway up the section, and then dividing by the

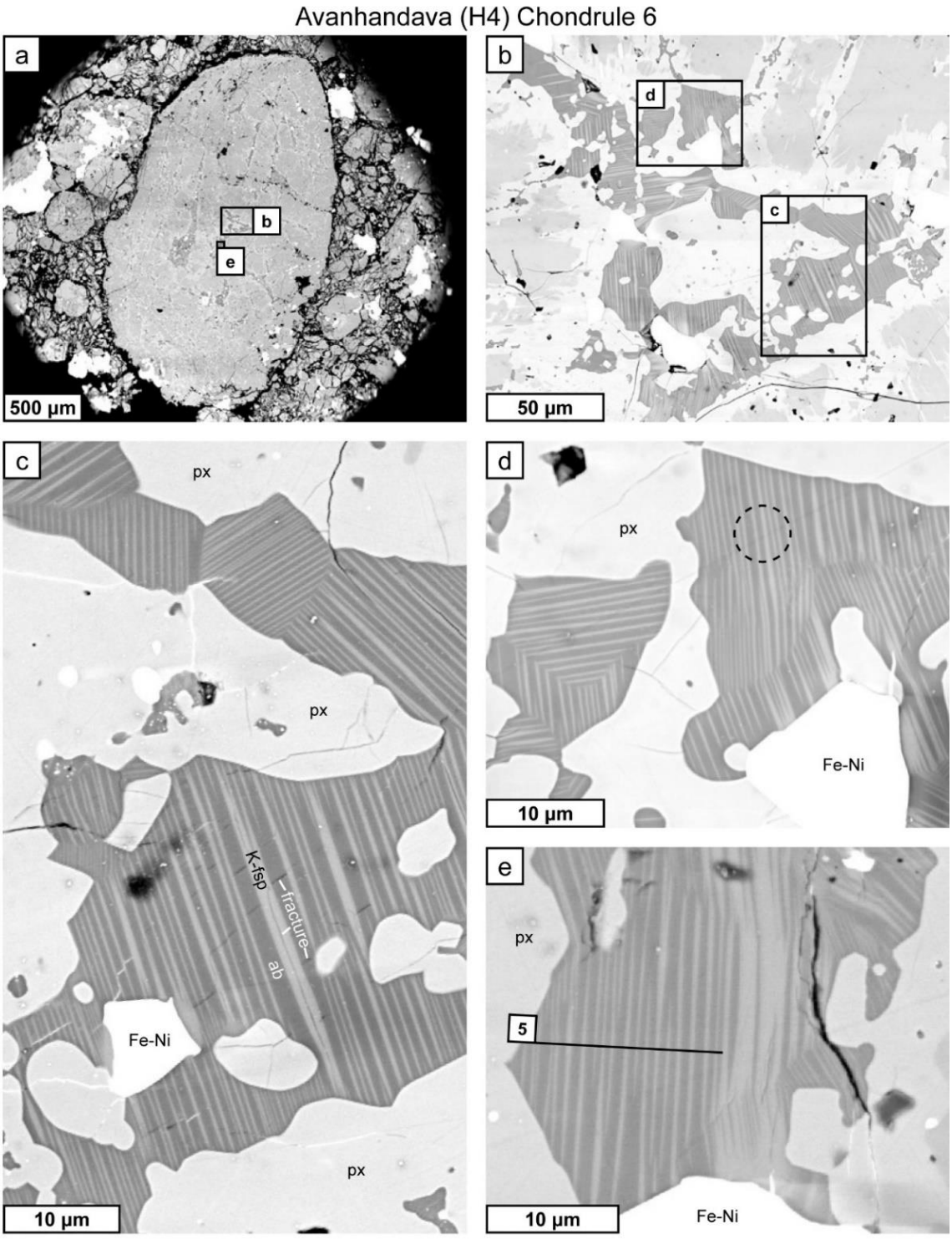

Figure 4.4. BSE images of albite with K-feldspar exsolution in Avanhandava (H4) PP chondrule 6. K-feldspar (K-fsp) exsolution from albite (ab) occurs throughout the chondrule. In a region near the chondrule center (b), exsolution lamellae are extremely abundant and are evenly distributed through many, randomly oriented subdomains (c,d). *(Caption continues on the following page).*

Figure 4.4. *(Caption continued from the previous page).* K-feldspar lamellae in (c) vary in width from 0.2-1.5 μm. Some wider lamellae have linear fractures through the lamellae center and fractures are present in albite, between lamellae, inclined 72-75°. (d) A region near (c) with regular lamellae in which a 5 μm diameter EPMA analysis (dashed circle) was performed to estimate the bulk feldspar composition. (e) A region near (c) from which a FIB section was extracted (black line) and imaged using TEM (Fig. 4.5).

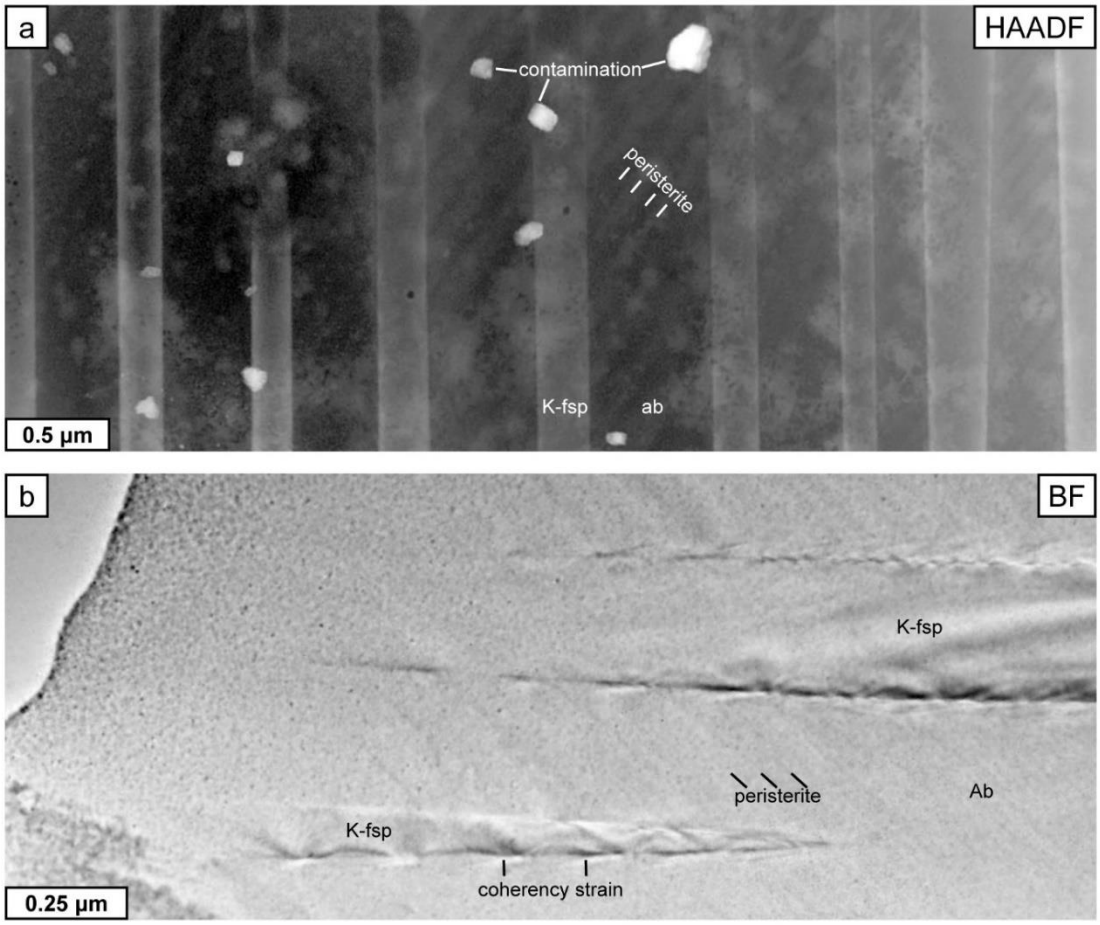

Figure 4.5. TEM images of a FIB section extracted from Avanhandava (H4) chondrule 6 (black line in Fig. 4.4e). (a) HAADF TEM image showing K-feldspar exsolution lamellae (K-fsp) and albite (ab) host. Exsolution lamellae range in width from 160-310 nm with an average wavelength of 650 nm. A peristerite intergrowth is visible in the albite region with wavelengths from 90-160 nm. Light spots are Cu surface contamination. (b) BF TEM image illustrating coherency strain between the K-feldspar exsolution lamellae and the albite host. Peristerite intergrowth is also visible in this image.

number of lamellae. Within the albite host, alternating bands of Ca-rich and Na-rich albite are present in what we are describing as peristerite. Peristerite is a subsolidus exsolution texture formed through NaSi-CaAl exchange in Na-rich plagioclase. The peristerite in Fig. 4.5a has wavelengths from 90-160 nm when measured in the albite host. The peristerite intergrowth is also visible in this image ~44° to the K-feldspar exsolution lamellae. Light spots on the HAADF image are Cu surface contamination from the sputtering process. A BF TEM image (Fig. 4.5b) illustrates coherency strain between the K-feldspar exsolution lamellae and the albite host.

3.3. Petrologic types 5 and 6

K-feldspar is also present in relict chondrules in the petrologic types 5 and 6 chondrites Tuxtuac (LL5) and Sulagiri (LL6), but in lower abundance than we observed in the type 4 OCs. In Tuxtuac chondrule 3, a relict POP chondrule (Fig. 4.6a), K-feldspar is present throughout as discrete lamellae in albite (0.2-0.7 μm wide, Fig. 4.6b) as well as in larger patches (20-30 μm in size, Fig. 4.6b,c) adjacent to large pores. Kovach and Jones (2010) show a similar texture in a Tuxtuac chondrule (their Fig. 4.7a). Additional examples of exsolution in L5 chondrites are shown in Lewis and Jones (2016) (Figs. 1.7g-j). In Sulagiri chondrule 6, a relict PP chondrule (Fig. 4.6d), K-feldspar is present in patches (Fig. 4.6e) and in lamellae 0.1-0.7 μm wide (Fig. 4.6f). Unlike in Tuxtuac, the K-feldspar patch in Sulagiri is irregular in shape and not specifically adjacent to large pores in the plane of the thin section, but it is present within a network of fractures.

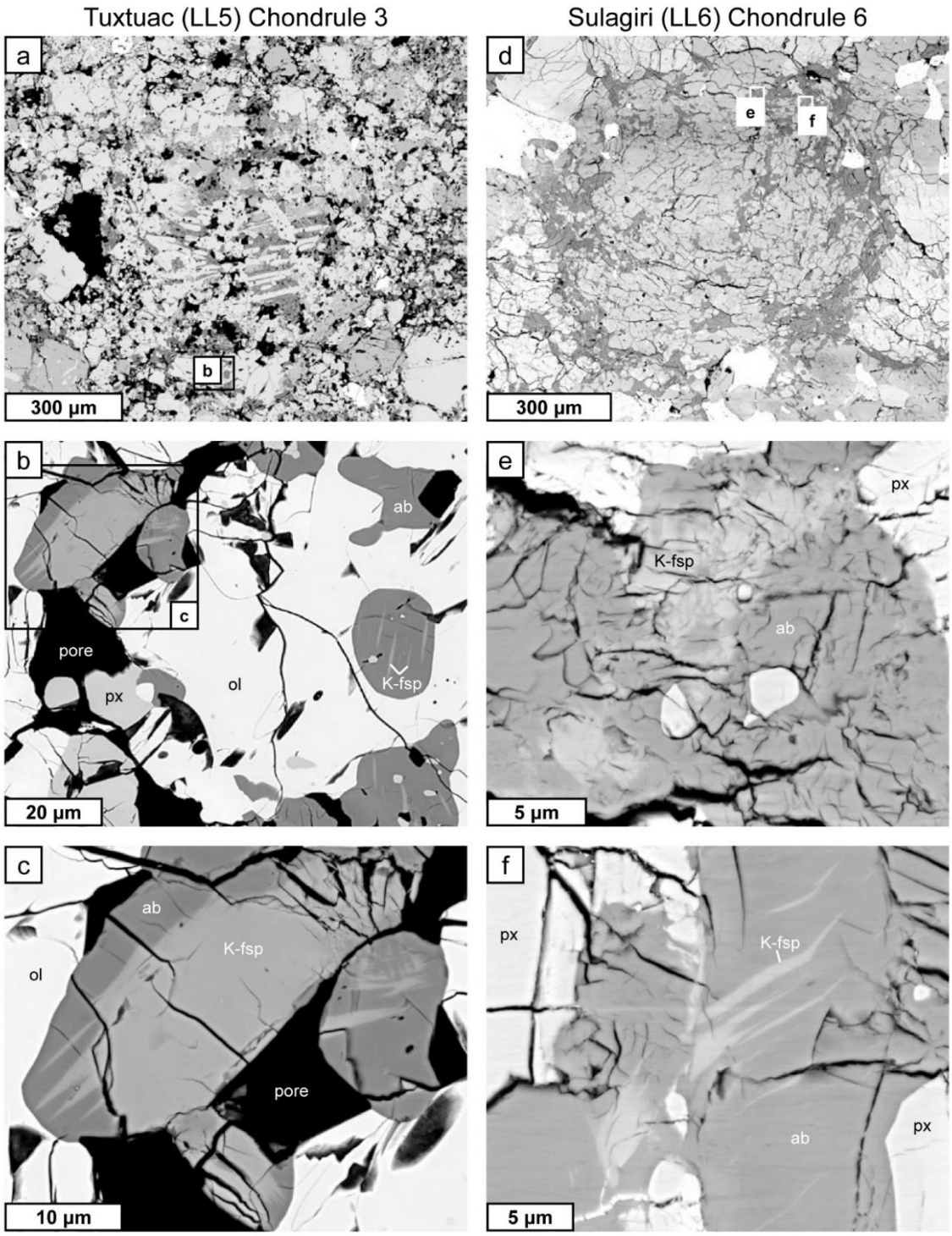

Figure 4.6. BSE images of K-feldspar in Tuxtuac (LL5) and Sulagiri (LL6) relict chondrules. Tuxtuac chondrule 3 is a relict porphyritic olivine (ol) and pyroxene (px) chondrule (a). K-feldspar (K-fsp) occurs throughout as discrete lamellae (0.2-0.7 µm wide) in an albite (ab) host (b) and in larger patches, 10s of µm in size (c). Sulagiri chondrule 6 is a relict porphyritic pyroxene chondrule (d) in which K-feldspar is present as irregular patches (e) and in lamellae 0.1-0.7 µm wide (f).

4. Discussion

The goal of this study is to understand the abundance and textures of K-feldspar in all OC petrologic types and groups, and to use the fine-scale exsolution microstructures we observe to provide an independent measure of OC cooling rates. We observed K-feldspar in most OCs of petrologic types 3.6-6. The occurrence of K-feldspar has been described in a few studies previously (Lewis et al., in preparation; Kovach and Jones, 2010; Nakamura et al., 2011; Jones and Brearley, 2011; Taylor et al., 2014; Lewis and Jones, 2016) but in general it has not been widely reported. Previous studies of OCs likely overlooked K-feldspar because of the extremely fine-scale nature of the exsolution lamellae and the high contrast needed to image exsolution using BSE imaging.

K-feldspar is most common in type 4, less common in types 5 and 6, and rare in type 3 (Table 4.1). K-feldspar is observed in two general textures: fine-scale lamellae, typically 0.1-1.5 μm wide, and larger irregular patches (up to 50 μm: Fig. 3.9f, Lewis et al. [in preparation]). Intergrowths of K-feldspar and albite are generally referred to as *perthite* but perthite can also refer to albite exsolution from K-feldspar (Parsons, 2010). Exsolution textures involving K-feldspar lamellae in an albite host are referred to as *antiperthite*. Fine-scale exsolution textures that are too small to be visible under an optical microscope earn the prefix: *crypto*. Thus, the fine-scale exsolution texture we observe is termed *cryptoantiperthite* (Parsons, 2010). However, for the sake of brevity, we will refer to this texture simply as *perthite* in the following discussion. While the K-feldspar patches may have initially formed by the same mechanism of K incorporation as the perthite, patches only seem to have been affected by exsolution along some boundaries (e.g., Fig. 4.6c).

In the discussion that follows, we look at the general implications of K-feldspar exsolution in OCs, estimate a cooling rate from a region of perthite in Avanhandava, and compare that result to the cooling rates measured using other techniques. We then discuss the general implications of K-feldspar exsolution on models of OC asteroid evolution.

4.1. K-feldspar exsolution in OCs: General implications for metamorphism

In low petrologic type OCs (petrologic types 3.00-3.15), the full range of plagioclase compositions from An_2 to An_{99}, with low Or content ($<Or_3$), is present within chondrules as primary, igneous feldspar (Lewis et al., in preparation; Lewis and Jones, in review). With increasing petrologic type, albitic plagioclase crystallizes from chondrule mesostasis glass and anorthitic plagioclase compositions become progressively albitized (Lewis et al., in preparation). Hence, albite can be either primary or secondary. K-feldspar, which is observed in OCs of petrologic types 3.6-6, is present only as a secondary phase, in primary and secondary albite, and most commonly as an exsolution texture. In general, exsolution textures form when the alkali feldspar falls below the solvus temperature for that bulk composition and the feldspar separates into a Na-rich component and a K-rich component. The wavelength of the lamellae that form depend on the temperature at which unmixing occurs, and the cooling rate. A more detailed interpretation of exsolution microstructures and compositions is discussed below (section 4.2).

In Lewis et al. (in preparation), we argue that incorporation of K occurred after peak metamorphism in high temperature, short duration events, such as internal jetting or external impact events. If K was incorporated prior to peak metamorphism, during, for example, the albitization reaction that is responsible for equilibration of anorthitic

plagioclase to albitic compositions, we would expect a homogeneous distribution of K-feldspar throughout the chondrules due to the relatively rapid nature of Na-K diffusion at metamorphic temperatures. While some chondrules do show a moderately homogenous distribution of K-feldspar (e.g., Santa Barbara chondrule 1 and Avanhandava chondrule 7), most do not.

Another important observation is the fact that K-feldspar is often observed either adjacent to pores or in highly porous regions (e.g., Figs. 4.1f, 4.2f, 4.3b,c). This relationship could be coincidental in that the frequent occurrence of K-feldspar adjacent to pores in type 4 OCs is related to the fact that type 4 OCs are also the most porous of the petrologic types (Macke, 2010). However, the common occurrence of large K-feldspar patches (e.g., Fig. 4.6c) and wide lamellae (e.g., Figs. 4.1f, 4.2f, 4.3b,c) adjacent to pores indicates the relationship between K-feldspar and porosity is process related and not coincidental. More importantly, it implies that K is incorporated into albitic plagioclase in a process that utilizes the pore network, e.g., fluid migration. Furthermore, Lewis et al. (in review) show K-enrichment in two large chondrules in Saratov correlates with the large-scale porosity. In one chondrule, K is concentrated in K-feldspar exsolution lamellae but in the other chondrule K is present in merrihueite, a silica alteration phase. The presence of both K-feldspar and merrihueite argue for general, late-stage introduction of K into the chondrules.

In the type 4 OCs we studied, Santa Barbara and Avanhandava have somewhat more uniform distributions of K-feldspar exsolution in chondrules (Figs. 4.2c, 4.4c) than those observed in Saratov or Bjurböle chondrules (Figs. 4.2f, 4.3b). We also observe a variety of differences between the two groups in terms of texture and composition. In

Saratov and Bjurböle regions of primary albite occur within fine-grained secondary albite from crystallized chondrule mesostasis glass. Texturally, they could be considered "low" type 4s, chondrites that experienced lower degrees of thermal metamorphism than "high" type 4s. Also, Saratov and Bjurböle have plagioclase Or contents that are in equilibrium with plagioclase solvi of 400-500 °C (Lewis et al., in preparation). In contrast, large, smooth regions of albite are present in Santa Barbara and Avanhandava that could be considered "high" type 4s. Santa Barbara and Avanhandava also have plagioclase compositions with Or content in equilibrium with solvi of 500-600 °C (Lewis et al., in preparation), higher than Saratov and Bjurböle.

The general model we have from these observations is that K was mobilized in an anhydrous fluid during late stage thermal metamorphism, incorporated into albitic plagioclase at high temperature through previously developed porosity, and then K-feldspar exsolved during cooling (Lewis et al., in preparation). Because we observe similar textures in all OC groups, we suggest that this process is common in all OC parent bodies. This has implications for models of parent body evolution that will be discussed further below (section 4.3).

4.2. Cooling rates determined from exsolution in alkali feldspar

In the OCs we studied, feldspar compositions are typically Na-rich so that during unmixing, the Ab-rich component is more abundant than the Or-rich component. This results in exsolution of K-feldspar lamellae within an albite host. Alkali feldspar exsolution has been studied extensively in terrestrial systems and has been the subject of numerous experimental investigations (e.g., Yund, 1974; Sipling and Yund, 1976; Yund and Davidson, 1978; Brown and Parsons, 1984; Liu and Yund, 1992; Carpenter, 1994;

Nekvasil, 1994; Abart et al., 2009; Parsons and Lee, 2009; Parsons and Fitz Gerald, 2011). As a result, the characteristics of alkali feldspar exsolution textures can be used to understand the environment in which they form. In general, as the system cools the alkali feldspar passes below the coherent solvus and unmixes into Ab- and Or-rich components (Yund, 1974). The rate of diffusion decreases rapidly with temperature, so that the final texture resulting from coherent exsolution is strongly dependent on both the temperature at which nucleation begins and the cooling rate (Abart et al., 2009). This relationship is useful for determining cooling rates using basic observations of alkali feldspar exsolution.

However, like any natural system, a few caveats exist that limit the precision of the cooling rates we are attempting to calculate. First, alkali feldspar exsolution rates were originally calibrated experimentally using Ca-free alkali feldspar and were intended to be used in analogous systems (Yund and Davidson, 1978). Second, the cooling rate dependence on exsolution texture requires that exsolution maintains coherency because post-exsolution coarsening can occur via mechanisms that release strain energy, such as in hydrothermal settings (e.g., Parsons and Lee, 2009). Third, the exsolution texture used to determine a cooling rate needs to have a reasonably consistent range of wavelengths (Parsons and Fitz Gerald, 2011). This means that random, or isolated, exsolution lamellae (e.g., Fig. 4.2b) or K-feldspar patches (e.g., Fig. 4.6c) are not useful for determining cooling rates. Finally, because of the time constraints of experimental studies, exsolution time scales extrapolated to very long durations can only be used as order-of-magnitude references.

It is with these caveats in mind that we chose Avanhandava chondrule 6 (Fig. 4.4) to further investigate alkali feldspar cooling rates recorded by perthite. Anorthite contents of alkali feldspar compositions in this chondrule are generally low, but non-zero (average of $An_{3.2}$: Lewis et al., [in preparation], Appendix 1: Table A1.26). We discuss the implications of the non-zero An content below. Exsolution is coherent in this chondrule, which is illustrated by the coherency strain between the exsolution lamellae and the host in Fig. 4.5b. The exsolution lamellae in this chondrule are remarkably regular in terms of lamellae width and exsolution wavelength (the average distance between lamellae). Also, Avanhandava is an H4 chondrite and H chondrites have been the subject of previous cooling rate studies (e.g., Ganguly et al., 2013; Scott et al., 2014) to which we can compare our results. Further, a metallographic cooling rate for Avanhandava was determined at 500 °C to be 20 °C/Myr by Scott et al. (2014).

4.2.1. Exsolution temperature

We employed two different methods to determine the temperature at which K-feldspar exsolution began (i.e., the solvus temperature). The first method involved normalizing the bulk feldspar composition into alkali feldspar components and finding the corresponding temperature for the coherent solvus. The bulk composition we used is $An_{2.5}Ab_{64.8}Or_{32.7}$ (Lewis et al. [in preparation], Appendix 1: Table A1.26, analysis #72), which was measured using EPMA with a defocused, 5 μm beam in a region of evenly spaced exsolution lamellae (Fig. 4.4d). Normalizing the composition into Ca-free components results in a composition of $Ab_{66}Or_{34}$. Figure 4.7 illustrates the subsolidus phase relations along the Or-Ab join for alkali feldspar from Parsons and Lee (2009). Parsons and Lee (2009) constructed these solvi using the experimental studies of Brown

and Parsons (1984) and Yund (1974), in order to describe layered syenites from the Klokken intrusion in South Greenland. Because coherency strain restricts unmixing until lower temperatures, the coherent solvus is below the strain-free solvus (Fig. 4.7). Since we have shown that the alkali feldspar in question is strain-controlled (Fig. 4.5a), we can determine the exsolution temperature using the coherent solvus. For our projected composition, Or_{34}, the solvus temperature is 700 °C, near the solvus maximum.

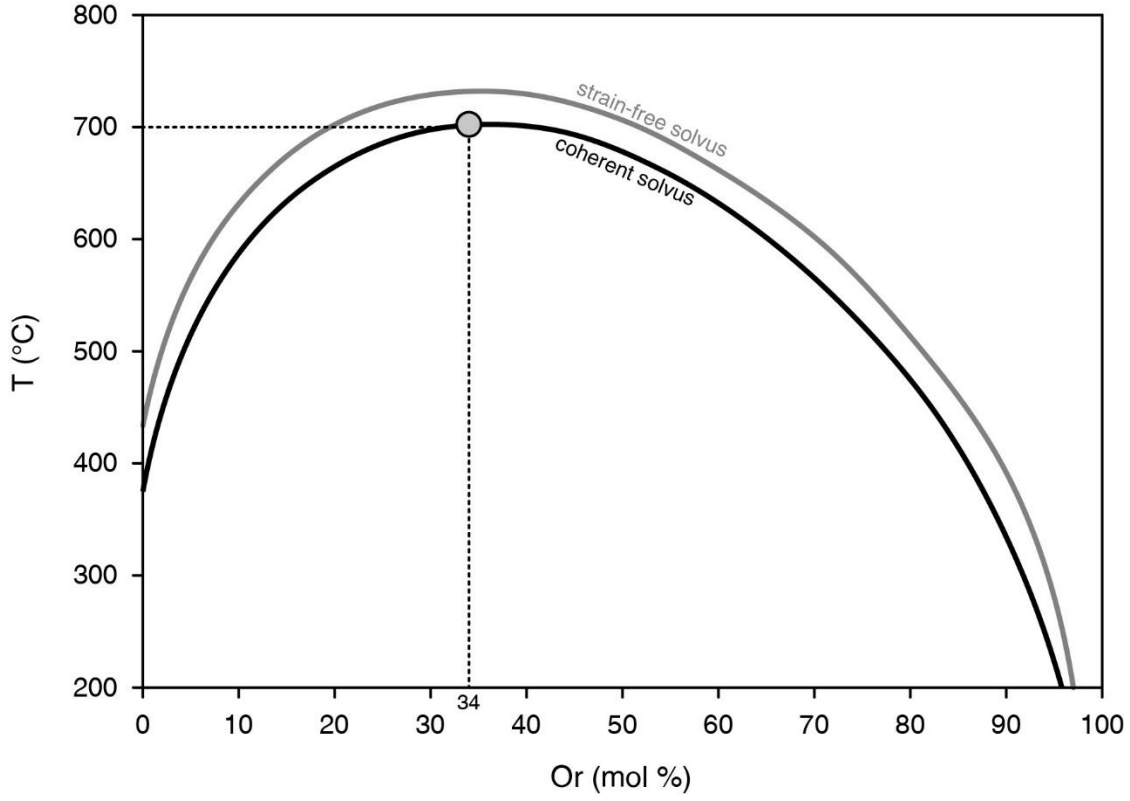

Figure 4.7. Alkali feldspar subsolidus T-composition plot after Parsons and Lee (2009). Coherent solvus from Yund (1974) and strain-free solvus from Brown and Parsons (1984). The solvus temperature, 700 °C, is shown for the average composition measured for the Avanhandava grain shown in Fig. 4.4d ($An_{2.5}Ab_{64.8}Or_{32.7}$) normalized to a Ca-free, alkali feldspar (Or_{34}).

It is important to note that the exsolution lamellae we observe may have formed via spinodal decomposition and not via nucleation and growth. However, the coarsening kinetics of the two processes are the same because they depend on the Na-K interdiffusion rate that is independent of the growth mechanism. In addition, the position of the coherent spinodal at the bulk composition of interest is likely within a few degrees of the coherent solvus (Sipling and Yund, 1976). Thus, as argued by Yund and Davidson (1978), the coarsening timescale will not be significantly influenced by exsolution mechanism.

The second method we used to determine the solvus temperature was by employing the SOLVCALC software (Wen and Nekvasil, 1994) with the calibration of Elkins and Grove (1990) and a pressure of 1 bar. In Fig. 4.8, we plot all the EPMA measurements (gray points) from Avanhandava chondrule 6 from Lewis et al. (in preparation) (Appendix 1: Table A1.26) onto a feldspar ternary diagram. The point outlined in black is the bulk composition that we are working with, $An_{2.5}Ab_{64.8}Or_{32.7}$ measured from the region indicated in Fig. 4.4d. Most of the Or-rich (Or>20) points plot between the 700 °C and 800 °C solvi despite their range in compositions. The two points to the far left of the solvi are from Ab-rich regions without exsolution. The outlined point best matches a solvus temperature of 765 °C.

As expected, the ternary solvus temperature is 65 °C higher than the Ca-free solvus temperature (e.g., Parsons and Lee, 2009). The errors associated with these temperatures are likely large but difficult to quantify. The temperature produced by the Ca-free alkali feldspar solvus depends on the degree of Si-Al disorder of the alkali feldspar at the time of exsolution and can vary up to 150 °C (Sipling and Yund, 1976).

We used the solvus of Yund (1974) for ordered feldspar because it has been successful in describing the cooling history of samples with similar microstructures (Parsons and Lee, 2009). The Elkins and Grove (1990) ternary feldspar calibration was produced using experiments conducted between 700 °C and 900 °C. So, the modelled solvi are most accurate in this range (Nekvasil, 1994) and we can neglect errors due to extrapolation. Elkins and Grove (1990) compared their model with experimental data from other sources and could reproduce the experimental temperatures with a typical error of ±20 °C. For the discussion that follows, we will adopt both the solvus temperatures we calculated, 765 °C and 700 °C, as upper and lower bounds.

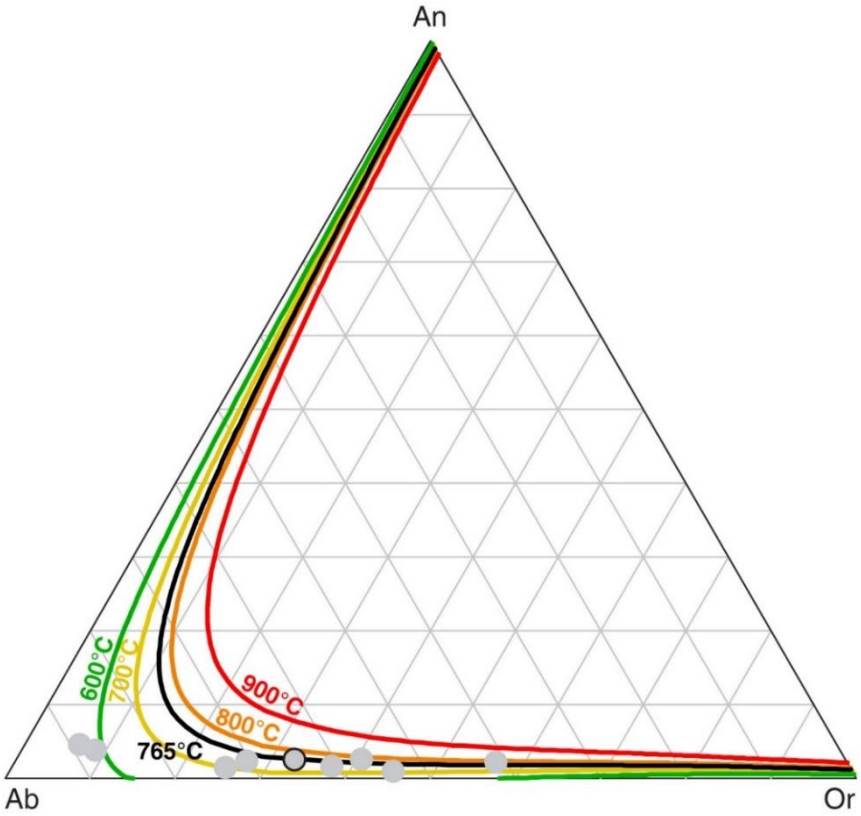

Figure 4.8. Feldspar ternary diagram with EPMA analyses (Lewis et al., in preparation) from Avanhandava chondrule 6 (Fig. 4.4) plotted on ternary solvi. 600-900 °C ternary solvi are generated in SOLVCALC (Wen and Nekvasil, 1994) using the calibration by Elkins and Grove (1990) at 1 bar pressure. Most points plot between the 700 and 800 °C solvi. The point outlined in black is the 5 μm spot analysis from Fig. 4.4d which closely matches the 765 °C solvus temperature.

4.2.2. Exsolution timescales and cooling rate

We used the method described by Parsons and Fitz Gerald (2011) to calculate the timescale over which the perthitic texture in Avanhandava chondrule 6 developed. They state that the diffusion length of the exsolution lamellae, *x*, is a function of the rate constant, *k*, and the time, *t*:

$$x^2 = kt, \tag{4.1}$$

where the diffusion length, *x*, can be taken as half the exsolution wavelength, λ:

$$x = \frac{\lambda}{2}, \tag{4.2}$$

and is easily measured as an average over multiple lamellae in reasonably homogeneous texture like those observed in Avanhandava chondrule 6 (Figs. 4.4 and 4.5). The rate constant, *k*, is then expressed as the Arrhenius relationship:

$$k = \frac{A}{e^{E_a/RT}}, \tag{4.3}$$

where *A* is the pre-exponential term, E_a is the activation energy, *R* is the gas constant, and *T* is the exsolution temperature. Substituting Equations 4.2 and 4.3 into Equation 4.1 and solving for time, *t*, as a function of temperature, *T* results in the final equation:

$$t = \frac{\lambda^2 e^{E_a/RT}}{4A}. \tag{4.4}$$

Values of A, Ea and R for perthite were calculated by Brady (1987), using the experimental results of Yund and Davidson (1978), and are given in Table 4.2. Yund and Davidson (1978) used a composition of Or_{35}, very similar to the composition we are considering, Or_{34}. Using the parameters in Table 4.2, we can generate a set of time-temperature curves based on exsolution wavelength. These curves are useful for

illustrating how temperature and exsolution wavelength each influence the interpreted timescale over which exsolution develops.

Table 4.2. Parameters governing the exsolution rate constant.

	A (m^2/s)	E_a (J/mol)	R (J/K mol)	reference
perthite	2.076×10^{-14}	139825	8.314	Brady (1987), Yund and Davidson (1978)
peristerite	3×10^{-8}	303000	8.314	Liu and Yund (1992)
peristerite	9×10^{-12}	220000	8.314	Parsons and Fitz Gerald (2011)

In Fig. 4.9, we plot the time-temperature curves for various exsolution wavelengths between 100-1000 nm. The measured average wavelength for Avanhandava chondrule 6, taken from the TEM image of the FIB section in Fig. 4.5a, is 650 nm. While this is not the precise location that the bulk composition was measured, the SEM images show reasonable textural similarity and we assume that the bulk composition is similar. Measuring wavelength via TEM is more precise than making the same measurement using lower resolution SEM images in which the exsolution lamellae are at an unknown angle to the surface, and where resolution of individual lamellae may not be possible. While there are also regions within chondrule 6 that clearly have varying wavelengths (Fig. 4.5c), the range of wavelengths gives cooling time scales that do not change significantly and are within a factor of about two. The variable wavelengths within the chondrule, and in adjacent grains, may have resulted from heterogeneous distribution of alkalis within each grain prior to cooling.

The two solvus temperatures we calculated above, 700 °C and 765 °C, for Ca-free alkali feldspar and ternary feldspar compositions, respectively, are plotted as dashed lines on Fig. 4.9 along with lines 30 °C below the solvus temperatures at 670 °C and 735 °C. Parsons and Fitz Gerald (2011) argued that because diffusion slows rapidly with

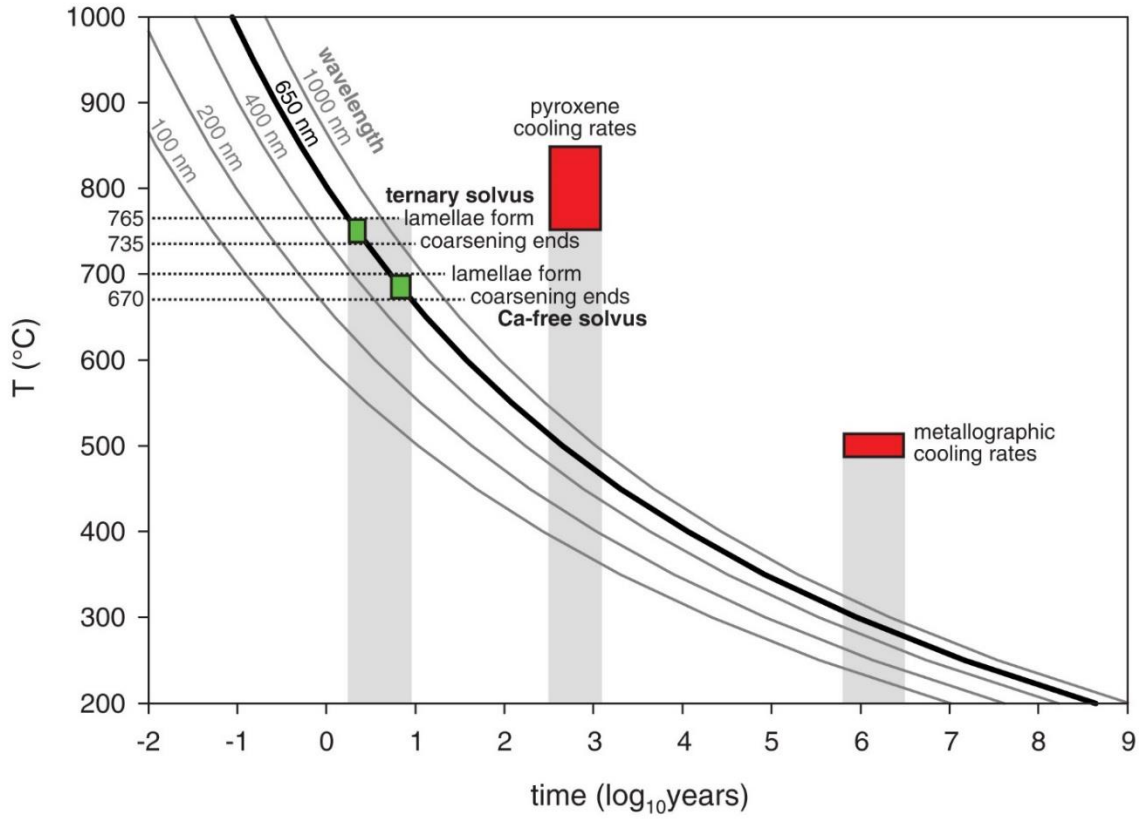

Figure 4.9. Alkali feldspar exsolution coarsening kinetics. Curves based on temperature and exsolution coarsening time are generated based on the method described by Parsons and Fitz Gerald (2011) using the calibration of Brady (1987) and Yund and Davidson (1978). The curve for exsolution wavelength determined from Fig. 4.5a, 650 nm, is highlighted in black. The two solvus temperatures determined for the Ca-free alkali solvus and the ternary solvus are denoted at 700 °C and 765 °C, respectively. Coarsening is expected to be completed within ~30 °C of the solvus (Abart et al., 2009), indicated with the 670 °C and 735 °C lines. Coarsening is calculated to occur between 1 and 3 years for the ternary solvus temperature and between 5 and 10 years for the Ca-free solvus temperature. For comparison, over the equivalent time period, cooling rates in H chondrites from pyroxene diffusion are 100 to 1000 years at ~800 °C (Ganguly et al., 2013) and metallographic cooling rates are between ~10^6-10^7 years at ~500 °C (Scott et al., 2014).

temperature, and because the majority of the lamellar coarsening was observed within 30 °C of the spinodal in a study by Abart et al. (2009), it was reasonable to extend that observation to the exsolution kinetics in their study. Following that argument, we use the same temperature range here as a first order approximation of the exsolution interval. In Fig. 4.9, the two rectangles plotted along the 650 nm wavelength line represent the two estimated timescale windows in which we calculate exsolution could have occurred.

The exsolution timescale is 5-10 years for the Ca-free alkali feldspar solvus temperature and 2-3 years for the ternary solvus temperature. The corresponding cooling rates are ~1 °C per 2-4 months from 670-700 °C and ~1 °C per month from 735-765 °C. For comparison, the equivalent 30 °C cooling period at the appropriate temperature using the metallographic and pyroxene diffusion rates mentioned above are also plotted of Fig. 4.9.

4.2.3. Peristerite coarsening timescale and cooling rate

Like the coarsening timescales that we determined for the perthite texture above, the peristerite intergrowth we illustrate in Fig. 4.5 can also provide a coarsening timescale. However, peristerite exsolution begins at a lower temperature than perthite (Carpenter, 1994) and there is evidence for a peristerite spinodal below the solvus temperature that may further affect the nucleation temperature (Carpenter, 1981). For the peristerite bulk composition, we use one of the Na-rich compositions measured in Avanhandava chondrule 6, $An_{8.7}Ab_{87.5}Or_{3.8}$ (Lewis et al. [in preparation], Appendix 1: Table A1.26, analysis #69). $An_{8.7}$ is close to the composition measured by Parsons and Fitz Gerald (2011), An_8 for the peristerite sample they studied from the Klokken intrusion. They determined the peristerite solvus and spinodal temperatures to be 570 °C and 450 °C, respectively, from Carpenter (1981, 1994).

We can use the same formalism as the perthite coarsening kinetics described above (Eq. 4.4) but with a pre-exponential term, A, and an activation energy, E_a, calibrated for peristerite. Parsons and Fitz Gerald (2011) used the calibration of Liu and Yund (1992) but also calculated a modified calibration for use with the peristerite textures observed in their sample from the Klokken pluton. The difference between the

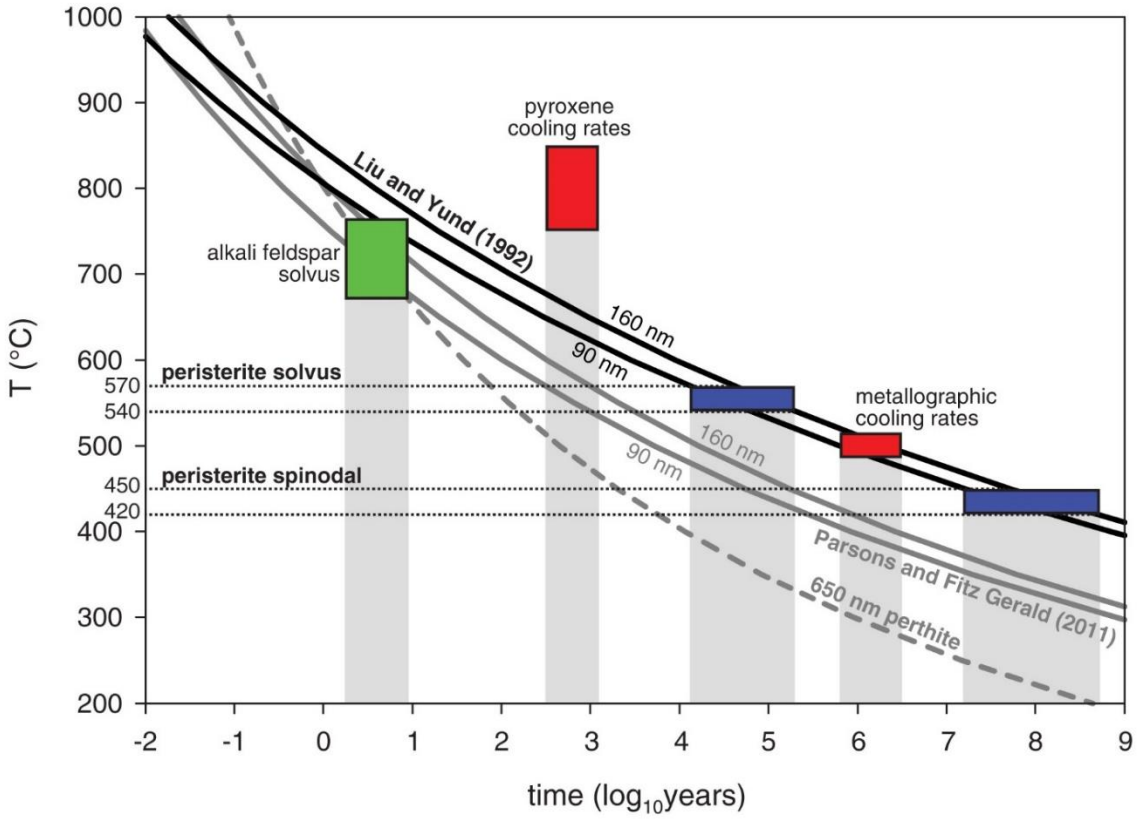

Figure 4.10. Peristerite coarsening kinetics. Curves based on temperature and exsolution coarsening time are generated based on the method described by Parsons and Fitz Gerald (2011) using the calibrations of Liu and Yund (1992), black lines, and Parsons and Fitz Gerald (2011), grey lines. Two lines were generated for each model with wavelengths of 90 nm and 160 nm, encompassing the range in wavelengths we measured in Fig. 4.5a. The peristerite solvus temperature, 570 °C, and spinodal temperature, 450 °C, are from Carpenter (1994) and Carpenter (1981), respectively. The timescale for peristerite coarsening via exsolution is 10^4-10^6 years and via spinodal decomposition is 10^7-10^9 years. The perthite timescales from Fig. 4.9 are shown in green along the 650 nm wavelength perthite curve (grey dashed line). The pyroxene and metallographic cooling timescales are shown in red for comparison.

two calibrations, they argue, is due to fluid mediation in the Klokken resulting in more rapid coarsening than is expected under dry conditions. Because retrograde metamorphism in OCs is dry (Lewis et al., in preparation), we utilize the calibration of Liu and Yund (1992).

In Fig. 4.10, we plot the peristerite time-temperature curves for 90 nm and 160 nm wavelengths, the range measured from the FIB section in Fig. 4.5a, using the Liu and

Yund (1992) calibration (black lines). The Parsons and Fitz Gerald (2011) calibration is also plotted for reference (grey lines). Like the perthite discussion above, we use a 30 °C coarsening interval for both the solvus and the spinodal, i.e., 570-540 °C and 450-420 °C, respectively. At these temperatures, the coarsening timescales are ~10^4-10^5 years for the solvus and 10^7-10^9 years for the spinodal (Fig. 4.10, blue rectangles). These correspond to cooling rates of 1 °C in 10^3-10^4 years and 1 °C in 10^6-10^7 years for the solvus and spinodal, respectively. For comparison, the exsolution timescales we calculated for perthite are shown in green with the 650 nm wavelength curve (grey dashed line). Pyroxene and metallographic cooling timescales are shown in red.

4.3. Cooling rate comparison and implications for asteroid evolution models

Figure 4.11 illustrates the cooling rates calculated above, as well as the cooling rates calculated for H chondrites using pyroxene (Ganguly et al., 2013) and metallographic (Scott et al., 2014) methods. Because the peristerite solvus is better characterized than the spinodal (Carpenter, 1981, 1994), we will focus on the cooling rate measured using the peristerite solvus temperature, in addition to the two perthite solvus temperatures. Taken together, the cooling rate data from feldspars, pyroxenes, and metal show a general trend of fast cooling at high temperature and slow cooling at low temperature. The fastest rates span a temperature range of 670-850 °C and consist of cooling rates of 1 °C per 0.1-100 years, determined by perthite (this study) and pyroxene diffusion rates (Ganguly et al., 2013). Slower cooling rates span the temperature range of about 500-600 °C with cooling rates of 1 °C between 10^3-10^5 years, determined by peristerite (this study) and metallographic measurements (Scott et al., 2014). Jones and Brearley (2011) also estimated an exsolution interval of 500-600 °C for the perthite they

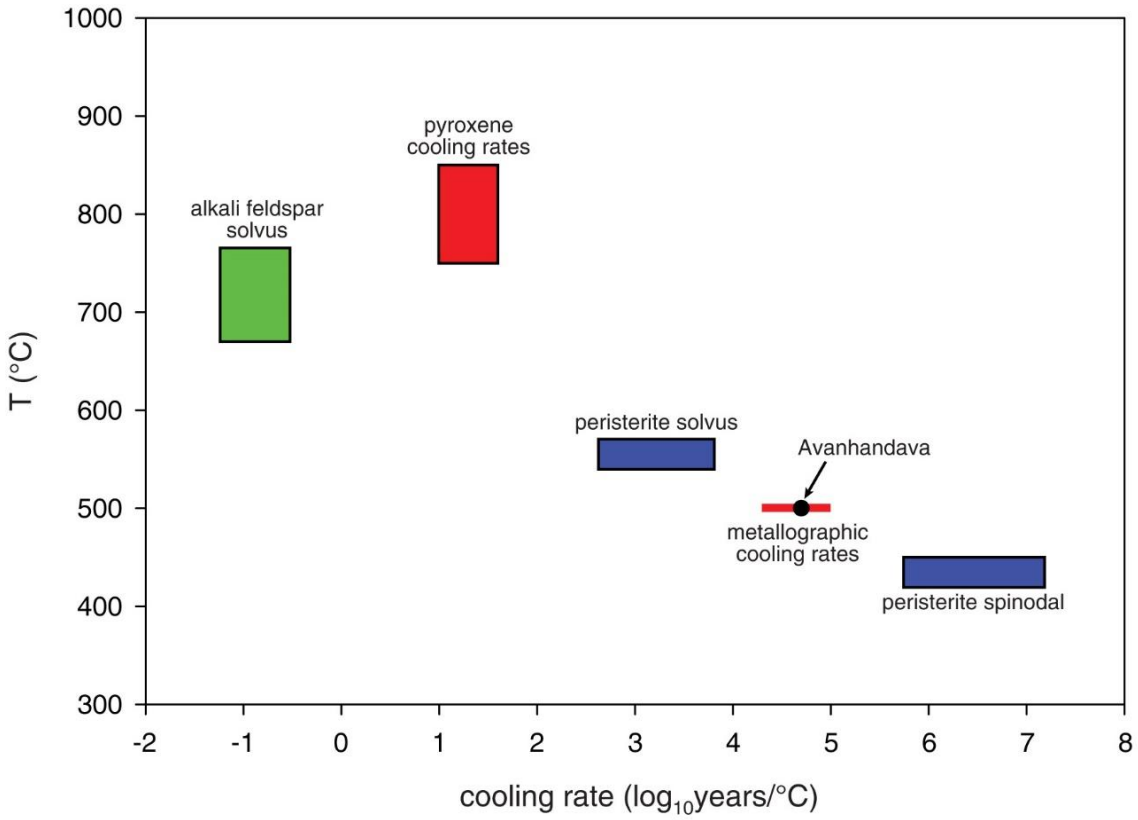

Figure 4.11. Comparison of feldspar, pyroxene, and metallographic cooling rates for H chondrites. Cooling rates for alkali feldspar solvus combine estimates from both the ternary feldspar solvus and the Ca-free solvus. Cooling rates determined from the peristerite spinodal are in grey because they are not considered as representative of the compositions and textures we observe. Pyroxene (Ganguly et al., 2013) and metallographic (Scott et al., 2014) cooling rates consist of all H chondrites, not just H4 chondrites. The black point within the range of metallographic cooling rates is the cooling rate measured specifically for Avanhandava (H4).

observe in Tuxtuac based on similarity to textures described in the Klokken intrusion (Brown and Parsons, 1988).

Despite the ambiguity in the peristerite measurements, the rough correlation between cooling rates determined from feldspar and from other methods is important for understanding the long-term evolution of OC-like asteroids. As Ganguly et al. (2013, 2016) point out, the fast cooling rates are inconsistent with the cooling rates predicted by an onion-shell model and suggest disruption after peak metamorphism in the rubble-pile scenario of Scott and Rajan (1981). A rubble-pile model is also suggested by Scott et al.

(2014) to explain a lack of trend in metallographic cooling rates with the petrologic type. We argue in Lewis et al. (in preparation) for high temperature, low duration bursts from internal degassing, or from impacts, to explain the heterogeneous incorporation of K and the rapid cooling rates inferred from fine-scale K-feldspar exsolution. While internal degassing is consistent with slow metallographic cooling rates, it cannot explain the rapid cooling rates determined from pyroxene.

The relatively consistent range of K-feldspar lamellae widths indicate consistently fast cooling rates at high temperatures in different chondrules in the same chondrite, among chondrites of different petrologic types, and among the different OC groups. The cooling rates determined based on pyroxene diffusion are also consistently fast for H4-6 chondrites (Ganguly et al., 2013). The metallographic measurements record consistently low cooling rates for lower temperatures over a range of petrologic types, but like the pyroxene-based cooling, are only measured in H chondrites (Scott et al., 2014). Clearly, cooling rates in any system are not correlated with petrologic type in the equilibrated H chondrites and the perthite textures may indicate no difference between the OC groups.

However, there does not appear to be consistency within a single group and petrologic type either. Telus et al. (2014) measured Al-Mg systematics in plagioclase of four H4 chondrites and found evidence for live ^{26}Al in three of the chondrites: Ste. Marguerite, Forest Vale, and Beaver Creek. They suggest these chondrites cooled rapidly below the Al-Mg closure temperature of ~450 °C. These three chondrites also had anomalously fast metallographic cooling rates of >1 °C per 200 years, at 500 °C, compared to 1 °C per 10^4-10^5 years for most H chondrites (Scott et al., 2014). The fourth H4 chondrite, Sena, did not have evidence for live ^{26}Al and had a typical, slow,

metallographic cooling rate (Telus et al., 2014; Scott et al., 2014). In Avanhandava, we measure a fast cooling rate at high temperature, >1 °C per year and Scott et al. (2014) measured a slow metallographic cooling rate at lower temperatures of 1 °C per $10^{4.7}$ years that is roughly consistent with our peristerite measurement of 1 °C in 10^3-10^4 years, at slightly higher temperatures (Fig. 4.11).

Ganguly et al. (2013) suggest a staged cooling model for H chondrites where petrologic types 4-6 initially cool quickly from high temperatures due to excavation by an impactor after peak metamorphism. Cooling rates at lower temperatures then decrease with increasing petrologic type due to reaccretion and burial in a way that allows type 4 to cool faster than type 6. Ganguly et al. (2013) based part of their low-temperature staged cooling rates on the Ar-Ar ages of Trieloff et al. (2003). However, the old Ar-Ar ages Trieloff et al. (2003) measured were in Ste Marguerite and Forest Vale, two chondrites found subsequently to have anomalously fast metallographic cooling rates (Scott et al., 2014) and evidence for live ^{26}Al that also indicate fast cooling rates (Telus et al., 2014). These new measurements suggest that OC cooling is more complex than the staged cooling model of Ganguly et al. (2013). Blackburn et al. (2017) suggest fast cooling rates in H4 chondrites are due to erosional impacting before 6 Myr.

We can say a few things given the observations discussed above. First, all OCs appear to have cooled rapidly (>1 °C per 100 years) at high temperature (>670 °C). Second, petrologic types 5 and 6 H chondrites cooled slowly (1 °C per 10^3-10^5 years) at lower temperature (500-600 °C). Third, type 4 H chondrites have low temperature cooling rates that vary from the slow rates experienced by type 5 and 6, to much faster cooling rates. Finally, none of these observations are consistent with simple onion-shell

cooling. While disruption after peak metamorphism (i.e., the rubble-pile model) does provide a framework for semi-chaotic cooling rates, the abundance of fine-scale K-feldspar exsolution lamellae in H, L, and LL OCs would imply multiple parent bodies underwent disruption at a similar point in their metamorphic history. It also implies that type 5 and 6 material were reaccreted such that they experienced the same range in metallographic cooling rates whereas type 4 material was exposed to a wide range of cooling rates at lower temperatures, presumably at burial depths of varying distance from the surface. Overall, our observations argue against rubble-pile cooling as well.

In Lewis et al. (in preparation), we suggest that interior degassing, in the form of high-temperature, short-duration bursts, as a mechanism for heterogeneous incorporation of K into plagioclase after peak metamorphism. While this provides a parent-body-independent model for K incorporation, and the presence of fine-scale K-feldspar exsolution, it does not provide an explanation for all the cooling rate measurements, particularly those made using pyroxene diffusion. Blackburn et al. (2017) attempt to reconcile seemingly contradictory observations through modeling and suggest that there was collisional erosion before 6 Myr for the H4 and L4 chondrites and full disruption at about 60 Myr followed by reaccretion.

Overall, K-feldspar exsolution textures have the potential to provide further constraints on OC cooling rates at high temperatures. Because we only present one cooling rate measured in one chondrite, many more cooling rates will need to be measured in order to provide a better understanding of feldspar-based cooling rates and cooling rate variability. Furthermore, because there appears to be significant variability in cooling paths among different OCs, particularly the type 4s, coordinated studies of

cooling rates using different methods (e.g., K-feldspar, pyroxene, and metallographic) on the same samples may be fruitful in discerning typical parent body processes from sample heterogeneity.

5. Summary and conclusions

We conducted a thorough examination of K-feldspar occurrences and textures, within chondrules, in petrologic type 3.6-6 H, L, and LL ordinary chondrites as an extension of our study on plagioclase alteration and equilibration (Lewis et al., in preparation). K-feldspar is a secondary mineral present in primary and secondary albite as fine-scale exsolution lamellae, 0.1-1.5 μm wide, in textures resembling perthite seen in terrestrial alkali feldspars. Larger patches of K-feldspar, up to 50 μm in size, are also present. Exsolution is observed in all OC groups but it is more common in petrologic type 4 than in types 5 and 6, rare in types 3.6-3.9, and absent in types <3.6. In the H4 Avanhandava, we also identified a peristerite intergrowth in the plagioclase.

We estimated cooling rates from the perthite and peristerite exsolution textures. For perthite, we determined cooling occurred at a rate of 1 °C per 1-4 months over a temperature interval of 670-765 °C. For peristerite, we estimated cooling occurred at a rate of 1 °C in 10^3-10^4 years from 570-540 °C. However, a lower temperature interval, 450-420 °C, corresponding to the peristerite spinodal, yields 1 °C per 10^6-10^7 years. In general, the fast, high temperature cooling rate determined by perthite is similar to cooling rates determined by pyroxene diffusion (Ganguly et al., 2013, 2016), while the peristerite cooling rate is closer to slow, low temperature, metallographic cooling rates (Scott et al., 2014). Because K-feldspar exsolution is present in similar fine-scale lamellae in all OC groups, we suggest that all OC parent bodies experienced the same

cooling history at high temperatures. These observations appear to be inconsistent with cooling models in both onion-shell and rubble-pile scenarios.

Acknowledgements

We would like to thank Elena Dobrică for her assistance with TEM operation and sample preparation. Work was carried out at the Electron Microbeam Analysis Facility, Department of Earth and Planetary Sciences and Institute of Meteoritics, University of New Mexico. J. Lewis acknowledges support from the Kelley-Silver Foundation, University of New Mexico and the New Mexico Space Grant Consortium. The work was partially funded by NASA grant NNX12AH61G (P.I. R. Jones).

References

Abart R., Petrishcheva E., Wirth R. and Rhede D. (2009) Exsolution by spinodal decomposition II: Perthite formation during slow cooling of anatexites from Ngoronghoro, Tanzania. *American Journal of Science* **309**, 450–475.

Akridge G., Benoit P. H. and Sears D. W. G. (1998) Regolith and megaregolith formation of H-chondrites: Thermal constraints on the parent body. *Icarus* **132**, 185–195.

Blackburn T., Alexander C. M. O'D., Carlson R. and Elkins-Tanton L. T. (2017) The accretion and impact history of the ordinary chondrite parent bodies. *Geochimica et Cosmochimica Acta* **200**, 201–217.

Brady J. B. (1987) Coarsening of fine-scale exsolution lamellae. *American Mineralogist* **72**, 697.

Brown W. L. and Parsons I. (1984) Exsolution and coarsening mechanisms and kinetics in an ordered cryptoperthite series. *Contributions to Mineralogy and Petrology* **86**, 3–18.

Brown W. L. and Parsons I. (1988) Zoned ternary feldspars in the Klokken intrusion: exsolution microtextures and mechanisms. *Contributions to Mineralogy and Petrology* **98**, 444–454.

Carpenter M. A. (1981) A "conditional spinodal" within the peristerite miscibility gap of plagioclase feldspars. *American Mineralogist* **66**, 553–560.

Carpenter M. A. (1994) Subsolidus phase relations of the plagioclase feldspar solid solution. In *Feldspars and Their Reactions* (ed. I. Parsons). Springer Netherlands, Dordrecht. pp. 221–269.

Elkins L. T. and Grove T. L. (1990) Ternary feldspar experiments and thermodynamic models. *American Mineralogist* **75**, 544–559.

Elkins-Tanton L. T., Weiss B. P. and Zuber M. T. (2011) Chondrites as samples of differentiated planetesimals. *Earth and Planetary Science Letters* **305**, 1–10.

Friedrich J. M., Bridges J. C., Wang M.-S. and Lipschutz M. E. (2004) Chemical studies of L chondrites. VI: Variations with petrographic type and shock-loading among equilibrated falls. *Geochimica et Cosmochimica Acta* **68**, 2889–2904.

Ganguly J., Tirone M., Chakraborty S. and Domanik K. (2013) H-chondrite parent asteroid: A multistage cooling, fragmentation and re-accretion history constrained by thermometric studies, diffusion kinetic modeling and geochronological data. *Geochimica et Cosmochimica Acta* **105**, 206–220.

Ganguly J., Tirone M. and Domanik K. (2016) Cooling rates of LL, L and H chondrites and constraints on the duration of peak thermal conditions: Diffusion kinetic modeling and implications for fragmentation of asteroids and impact resetting of petrologic types. *Geochimica et Cosmochimica Acta* **192**, 135–148.

Gattacceca J., Rochette P., Denise M., Consolmagno G. and Folco L. (2005) An impact origin for the foliation of chondrites. *Earth and Planetary Science Letters* **234**, 351–368.

Huss G. R., Rubin A. E. and Grossman J. N. (2006) Thermal metamorphism in chondrites. In *Meteorites and the Early Solar System II* (eds. D. S. Lauretta and H. Y. McSween Jr.). The University of Arizona Press, Tucson, AZ. pp. 567–586.

Jones R. H. and Brearley A. J. (2011) Exsolution in Feldspar in the Tuxtuac (LL5) Chondrite: A New Perspective on Cooling Rates for Metamorphosed Chondrites. *74rd Annual Meeting of the Meteoritical Society*, Abstract #5475.

Kovach H. A. and Jones R. H. (2010) Feldspar in type 4–6 ordinary chondrites: Metamorphic processing on the H and LL chondrite parent bodies. *Meteoritics & Planetary Science* **45**, 246–264.

Lewis J. A. and Jones R. H. (2016) Phosphate and feldspar mineralogy of equilibrated L chondrites: The record of metasomatism during metamorphism in ordinary chondrite parent bodies. *Meteoritics & Planetary Science* **51**, 1886–1913.

Lewis J. A. and Jones R. H. (in review) Primary feldspar in the Semarkona LL3.00 chondrite: Constraints on chondrule formation and secondary alteration. *Meteoritics & Planetary Science*.

Lewis J. A., Jones R. H. and Brearley A. J. (in preparation) Plagioclase alteration and equilibration in ordinary chondrites: Evidence for three stages of metasomatism during thermal metamorphism.

Lewis J. A., Jones R. H. and Garcea S. C. (in review) Chondrule porosity in the L4 chondrite Saratov: Dissolution, chemical transport, and fluid flow. *Geochimica et Cosmochimica Acta*.

Li C., Bridges J. C., Hutchison R., Franchi I. A., Sexton A. S., Ouyang Z. and Pillinger C. T. (2000) Bo Xian (LL3.9): Oxygen-isotopic and mineralogical characterisation of separated chondrules. *Meteoritics & Planetary Science* **35**, 561–568.

Liu M. and Yund R. A. (1992) NaSi-CaAl interdiffusion in plagioclase. *American Mineralogist* **77**, 275–283.

Macke R. J. (2010) Survey of meteorite physical properties: Density, porosity and magnetic susceptibility. Ph.D. thesis, University of Central Florida.

McSween H. Y., Ghosh A., Grimm R. E., Wilson L. and Young E. D. (2002) Thermal evolution models of asteroids. In *Asteroids III* (eds. W. F. Bottke, A. Cellino, P. Paolicchi, and R. P. Binzel). The University of Arizona Press, Tucson, AZ. pp. 559–571.

Nakamura T., Noguchi T., Tanaka M., Zolensky M. E., Kimura M., Tsuchiyama A., Nakato A., Ogami T., Ishida H., Uesugi M., Yada T., Shirai K., Fujimura A., Okazaki R., Sandford S. A., Ishibashi Y., Abe M., Okada T., Ueno M., Mukai T., Yoshikawa M. and Kawaguchi J. (2011) Itokawa dust particles: A direct link between S-Type asteroids and ordinary chondrites. *Science* **333**, 1113–1116.

Nekvasil H. (1994) Ternary feldspar/melt equilibria: A review. In *Feldspars and Their Reactions* (ed. I. Parsons). Springer Netherlands, Dordrecht. pp. 195–219.

Parsons I. (2010) Feldspars defined and described: A pair of posters published by the Mineralogical Society. Sources and supporting information. *Mineralogical Magazine* **74**, 529–551.

Parsons I. and Fitz Gerald J. D. (2011) Coarsening kinetics of coexisting peristerite and film microperthite over 10^4 to 10^5 years. *American Mineralogist* **96**, 1575.

Parsons I. and Lee M. R. (2009) Mutual replacement reactions in alkali feldspars I: Microtextures and mechanisms. *Contributions to Mineralogy and Petrology* **157**, 641–661.

Pellas P. and Storzer D. (1981) ^{244}Pu fission track thermometry and its application to stony meteorites. *Proceedings of the Royal Society of London. Series A, Mathematical and Physical Sciences* **374**, 253–270.

Rubin A. E. (1999) Formation of large metal nodules in ordinary chondrites. *Journal of Geophysical Research: Planets* **104**, 30799–30804.

Rubin A. E. (1994) Metallic copper in ordinary chondrites. *Meteoritics* **29**, 93–98.

Rubin A. E. (2004) Postshock annealing and postannealing shock in equilibrated ordinary chondrites: Implications for the thermal and shock histories of chondritic asteroids. *Geochimica et Cosmochimica Acta* **68**, 673–689.

Scott E. R. D., Krot T. V., Goldstein J. I. and Wakita S. (2014) Thermal and impact history of the H chondrite parent asteroid during metamorphism: Constraints from metallic Fe–Ni. *Geochimica et Cosmochimica Acta* **136**, 13–37.

Scott E. R. D. and Rajan R. S. (1981) Metallic minerals, thermal histories and parent bodies of some xenolithic, ordinary chondrite meteorites. *Geochimica et Cosmochimica Acta* **45**, 53–67.

Sipling P. J. and Yund R. A. (1976) Experimental determination of the coherent solvus for sanidine-high albite. *American Mineralogist* **61**, 897.

Stöffler D., Keil K. and Edward R.D S. (1991) Shock metamorphism of ordinary chondrites. *Geochimica et Cosmochimica Acta* **55**, 3845–3867.

Taylor L. A., Liu Y., Guan Y., Day J. M. D., Ma C., Hiroi T., Corder C. A., Assayag N., Rumble D., Cartigny P., Chen Y., Hand K. P., Pieters C. M., Eiler J. M., Pokhilenko N. P. and Podgornykh N. M. (2014) Metamorphism in the Chelyabinsk meteorite. *45th Lunar and Planetary Science Conference*, Abstract #2346.

Telus M., Huss G. R., Nagashima K. and Ogliore R. C. (2014) Revisiting Al-26-Mg-26 systematics of plagioclase in H4 chondrites. *Meteoritics & Planetary Science* **49**, 929–945.

Trieloff M., Jessberger E. K., Herrwerth I., Hopp J., Fieni C., Ghelis M., Bourot-Denise M. and Pellas P. (2003) Structure and thermal history of the H-chondrite parent asteroid revealed by thermochronometry. *Nature* **422**, 502–506.

Van Schmus W. R. and Wood J. A. (1967) A chemical-petrologic classification for the chondritic meteorites. *Geochimica et Cosmochimica Acta* **31**, 747–765.

Weisberg M. K., Smith C., Benedix G., Herd C. D. K., Righter K., Haack H., Yamaguchi A., Aoudjehane H. C. and Grossman J. N. (2009) The meteoritical bulletin, no. 96, September 2009. *Meteoritics & Planetary Science* **44**, 1355–1397.

Wen S. and Nekvasil H. (1994) SOLVCALC: An interactive graphics program package for calculating the ternary feldspar solvus and for two-feldspar geothermometry. *Computers & Geosciences* **20**, 1025–1040.

Yund R. A. (1974) Coherent exsolution in the alkali feldspars. In *Geochemical Transport and Kinetics* (eds. A. W. Hofmann, B. J. Giletti, H. S. Yoder Jr., and R. A. Yund). Carnegie Institution of Washington Publication. pp. 173–184.

Yund R. A. and Davidson P. (1978) Kinetics of lamellar coarsening in cryptoperthites. *American Mineralogist* **63**, 470–477.

CHAPTER 5

Chondrule porosity in the L4 chondrite Saratov: Dissolution, chemical transport, and fluid flow

In collaboration with:
Rhian H. Jones
Serafina C. Garcea

Submitted for publication to:
Geochimica et Cosmochimica Acta

Abstract

Porosity is an important physical property of meteorites and asteroids that affects density, material strength, and thermal diffusivity. Porosity can also promote chemical exchange by facilitating the transport of fluids and dissolved ions. We measured the porosity of individual chondrules from the L4 ordinary chondrite Saratov, using X-ray microtomography (μCT) and scanning electron microscopy, to examine the abundance and distribution of porosity in chondrules, and to understand how porosity relates to chemical exchange during parent body processes. Porosity was 1-2% by volume in the chondrules that we measured and maximum pore sizes were ~300 μm. Porosity distribution and morphology indicate that porosity is a secondary feature and most pores >1 μm were formed from the dissolution of chondrule mesostasis glass. Iron and K are preferentially enriched in phases adjacent to the most porous regions: Fe is enriched in pyroxene, and K is enriched in mesostasis where it is observed as either the silica alteration phase merrihueite, or fine-scale, K-feldspar exsolution in albitic feldspar. Some pores can be described as vugs, as they contain euhedral olivine and chromite, with textures indicating vapor deposition. Knowing the chondrule porosity, we estimate the matrix porosity in Saratov to be very high, 40-60%. We suggest that during prograde

metamorphism, an aqueous fluid originating from the matrix dissolved chondrule mesostasis glass, producing the observed porosity, and introducing FeO into the pyroxene phenocrysts. Fluids were less abundant through peak metamorphism, and chondrule mesostasis glass crystallized to fine-grained albite. During retrograde metamorphism, high temperature, short duration bursts of a dry, alkali-bearing fluid from the asteroid interior infiltrated the pore network, formed the vug phases, altered silica to merrihueite, and introduced K to the secondary albite. Fine-scale K-feldspar then exsolved from albite during rapid cooling to the ambient temperature. Overall, development of porosity during metamorphism on the L chondrite parent body contributed to the chemical evolution of its components, as well as affecting the physical properties of the parent asteroid.

1. Introduction

Porosity has significant effects on the physical properties of meteorites and asteroids, including density, material strength, and thermal diffusivity. An increasing number of density measurements have found that many asteroids are underdense when compared to the grain densities of their inferred meteorite analogs (Carry, 2012). Low asteroid densities are attributed to a combination of low density phases in the interior, such as volatile ices, small-scale microporosity that is observed in meteorites, and large-scale macroporosity that reflects the internal structure of the asteroid itself (Scheeres et al., 2015). For example, the S-type asteroid 25143 Itokawa, visited by the Hayabusa spacecraft, has an ordinary chondrite (OC) composition (Nakamura et al., 2011). It has a porosity of 41%, greater than most OCs, suggesting high macroporosity and possibly a rubble-pile-like interior structure (Fujiwara et al., 2006).

Density and porosity are important for understanding how asteroids respond to impact and other dynamical events. During an impact, compaction of porous material can help absorb the impact energy, reduce the likelihood of fragmentation, and increase the probability of survival of the body (Holsapple, 2009). Conversely, porosity can also lower the strength of an asteroid, leaving it more susceptible to disruption from dynamical forces, including tidal forces and YORP spin-up (Sánchez and Scheeres, 2014). In addition, the thermal evolution of an asteroid is strongly influenced by its porosity. Incorporation of energetic radioisotopes, such as short-lived ^{26}Al, into planetesimals during accretion heats up and thermally metamorphoses the surrounding material. Numerical models find that the insulating effects of porosity, when applied globally (Bennett and McSween, 1996) or in a surface regolith (Akridge et al., 1998; Harrison and Grimm, 2010), greatly affect the intensity and duration of thermal metamorphism. This is because thermal diffusivity is directly related to the material properties and porosity of the heated material (Opeil et al., 2012).

The presence of porosity also has important implications for chemical changes in asteroidal materials. In chondrites, porosity can facilitate the transport of fluids during aqueous alteration and during metasomatism that accompanies thermal metamorphism. Fluids carry elements into and out of various chondrite components, resulting in changes to primary mineralogy and the formation of secondary minerals. In carbonaceous chondrites, fluids alter primary phases and form phyllosilicates, carbonates, and other secondary minerals (Brearley, 2006). In OCs, porosity is seen in association with the development, and subsequent alteration, of the secondary minerals apatite, merrillite, and feldspar, during thermal metamorphism (Kovach and Jones, 2010; Jones et al., 2014;

Jones et al., 2016; Lewis and Jones, 2016b). In petrologic type 3 and 4 OCs, the development of porosity within chondrules provides evidence for aqueous alteration (Lewis and Jones, in review; Dobrică and Brearley, 2014; Lewis and Jones, 2014, 2015, 2016a) and dissolution of chondrule mesostasis in so-called "bleached chondrules" (Grossman et al., 2000). However, our understanding of the development and characteristics of porosity in OCs is limited.

Bulk porosity is currently measured in meteorites using two methods: glass bead volumetry with ideal-gas pycnometry (Macke, 2010) or X-ray microtomography (μCT: Almeida et al., 2014). Ideal-gas pycnometry uses an ideal gas (typically He) to penetrate the network of pores and to measure the volume of the solid material. While useful for interconnected pore networks, regardless of pore size, isolated pores are not included using this method. In contrast, μCT uses X-rays to successively image a rotating object and mathematically reconstruct the internal structure. Hence, this technique can measure porosity regardless of degree of interconnectivity. However, the voxel size of the scan, which is directly connected with the resolution, dictates the size of the smallest pores that can be measured. Therefore, only pores above a certain size (typically 2-3 times the voxel size: Maire and Withers, 2014) are included in these porosity measurements. In effect, both methods can lead to an underestimate of the bulk porosity. Almeida et al. (2014) calculated that bulk porosity measurements on chondrites made with μCT (using a resolution of 5-10 μm/voxel) were lower than, but within 15-20%, of those reported for ideal-gas pycnometry. They attributed these differences to the resolution limits of the μCT measurements and heterogeneity between different samples of the same meteorite.

Macke (2010) measured the bulk porosity of a wide variety of meteorite samples using ideal-gas pycnometry, including OCs. He found that OC falls had an average bulk porosity of ~10% but with a considerable range that extends up to 25% porosity for some samples. He also found that petrologic type 4 OCs have the highest average bulk porosity out of all the petrologic types. Macke (2010) noted an increase in porosity with increase in matrix abundance for all the chondrite groups, implying that the majority of the porosity is contained within the matrix. Almeida et al. (2014) made similar observations, but noted that the OCs with the highest bulk porosity also tended to have pores within chondrules in addition to the matrix. Ebel and Rivers (2007) used synchrotron-based μCT to characterize porosity in two chondrules separated from the CV3 chondrite, Allende. They measured the bulk porosity of the chondrules to be 0.1-0.6%, but did not suggest an origin for the pores.

Chondrules are igneous objects formed from the flash heating, and rapid cooling, of nebular material. Primary pores in igneous rocks are often formed by exsolution of gaseous species from a melt (i.e., vesicles) due to changes in physical environment like a reduction in pressure or temperature. However, secondary processes that cause in the dissolution and transport of primary phases can also result in the development of porosity. To better understand the abundance and distribution of pores within chondrules, the processes responsible for porosity development, as well as the nature and extent of chemical exchange between chondrules and matrix, we measured the porosity of individual chondrules from the L4 chondrite Saratov using laboratory μCT and scanning electron microscopy (SEM).

μCT-based porosity measurements allow for 3D porosity characterization that has several advantages over porosity characterization made on 2D polished sections. First, viewing porosity in 3D allows for a better understanding of pore connectivity throughout the sample. Second, 3D pore sizes can be measured directly so stereological corrections of 2D measurements are not needed. Third, heterogeneous distributions of porosity can be seen directly and do not need to be inferred though studies of multiple thin sections. Finally, and most importantly, there is no artificial increase in porosity due to mechanical removal of material during sample preparation.

Saratov has been the subject of a number of studies including investigations into shock (Rubin, 1994; Friedrich et al., 2004), thermal equilibration (Kessel et al., 2007), metasomatism (Lewis and Jones, 2015; Lewis and Jones, 2016a), and porosity (Alexeyva, 1958; Semenenko et al., 1992; Flynn et al., 1999; Girich and Semenenko, 2003; Macke, 2010). Saratov has experienced light to moderate shock and has been assigned shock stages of S2 (Rubin, 1994) and S3 (Friedrich et al., 2004). Bulk porosities were measured using He-pycnometry resulting in average porosities of 13% (Flynn et al., 1999) and 12.5% (Macke, 2010). Alexeyva (1958) reported bulk porosity of 18.2% using a mercury-based method. These porosity measurements are far higher than the average porosity for L chondrite falls of 8.0% (Macke, 2010). Saratov also contains highly porous fragments with porosities up to 65% (Semenenko et al., 1992; Girich and Semenenko, 2003). Lewis and Jones (2016a) noted a range of textures in chondrule plagioclase that indicate alteration by a metasomatic fluid, including the presence of pores that ranged from sub-μm to tens of μm in size. Because of the high bulk porosity and evidence for metasomatism, Saratov is a good candidate to investigate chondrule porosity.

In this paper, we present μCT measurements of chondrules and correlated 2D scanning electron microscope (SEM) observations to address the origins of chondrule porosity and to test the hypothesis that chondrule porosity is a secondary feature produced by metasomatic processes. We use measurements of chondrule porosity to understand the relative distribution of porosity between chondrules and matrix in Saratov, with implications for the physical properties of OC-like asteroids. We also discuss the role of porosity in providing pathways for fluid flow and facilitating the chemical evolution of chondrules and chondrites during thermal metamorphism.

2. Methods

2.1. μCT analysis

We separated chondrules from a Saratov hand sample through gentle crushing in an agate mortar and pestle. Saratov is very friable, so we could easily separate the chondrules from the matrix without fracturing the chondrules. We selected two large chondrules (Ch1, 3.7 mm and Ch7, 2.0 mm diameter) and 30 small chondrules (0.5-1.2 mm) for analysis by μCT. We used the Zeiss Xradia Versa 520 XCT at the Henry Moseley X-ray Imaging Facility, University of Manchester. The scans were conducted using an energy of 80 kV, 1600 projections, and an exposure time of 4 seconds. The large chondrules were scanned individually with voxel sizes of 3.7 μm and 1.3 μm for Ch1 and Ch7, respectively. The small chondrules were placed together in a pipette tip, packed with plastic wrap, and scanned using a voxel size of 1.8 μm. Porosity was calculated as the percentage void space within the solid material using the Avizo software package. Initially, an automatic threshold was applied and the results obtained were then refined using sophisticated segmentation methods to achieve more accurate estimates.

2.2. SEM analysis

Following µCT analysis, the two large chondrules were cut in half using a 0.15 mm wide diamond wafering blade. One half of each chondrule was mounted in epoxy and polished for electron beam analysis. The other half of each chondrule was left unpolished and used to image vugs. Backscattered electron (BSE) images were acquired at 10 kV and 16 nA on an FEI Quanta 3D Dualbeam® field emission gun scanning electron microscope (FEG-SEM) at the University of New Mexico. We made high-resolution (0.35 µm/px) BSE maps of each chondrule for 2D porosity analysis to estimate the percentage of bulk porosity at resolutions higher than allowed by the µCT measurements. Thresholding and particle analysis was performed in ImageJ, and we included all pores that were ≥1 µm in diameter using the measured pore area equivalent to the circular diameter (i.e., 7 total pixels). In addition to the chondrule maps, BSE maps were made of two full Saratov thin sections, UNM 1145 and USNM 1423-3. The maps consist of individual 1024x800 pixel images, captured at 1 µm/px, and stitched together in ImageJ (Preibisch et al., 2009).

2.3. TEM analysis

Two focused ion beam (FIB) sections were made, one in each of the large chondrules, using the FEI Quanta 3D Dualbeam® FEG-SEM/FIB to investigate the sub-µm porosity within the crystallized mesostasis. The FIB sections were imaged at 200 kV on a JEOL 2010F field emission gun scanning transmission electron microscope (STEM) using high-angle annular dark-field (HAADF) imaging and selected area electron diffraction (SAED). FIB/TEM work was performed at the University of New Mexico.

2.4. Quantitative EPMA maps

Quantitative wavelength-dispersive spectroscopic (WDS) maps of the two chondrules were acquired on a JEOL 8200 Electron Probe Microanalyzer (EPMA) at the University of New Mexico operated at 15 kV and 20 nA. Maps were made with Probe Software's Probe for EPMA in two passes using 100 ms/px dwell times with dimensions of 501x483 px and 467x433 px and 6 μm and 4 μm spot size for Ch1 and Ch7, respectively. The resulting intensity maps were quantified in CalcImage using ZAF corrections combined with mean atomic number (MAN) background corrections. MAN curves were generated using the following Taylor standards: olivine, albite, orthoclase, chromite, spessartine, MgO, hematite, and nickel and additional standards: doped diopside, labradorite, and sodalite.

The quantitative maps were then masked in Adobe Photoshop and the bulk silicate compositions of the chondrules calculated using a custom MATLAB script to identify chondrule pixels with oxide sums greater than 95%. In addition, pixels with SiO_2 contents of less than 20% were omitted to eliminate Fe-Ni metal and sulfides. Densities were determined for each pixel based on the assigned mineral phases, and the bulk silicate composition of each chondrule was calculated as the mean of the density-weighted compositions of accepted pixels. This method for determining the bulk compositions of multimineralic assemblages is similar to the method described by Carpenter et al. (2013, 2017). A detailed description of this process is presented in Appendix 2.

3. Results

It is worth considering the terminology surrounding porosity so that we may provide a self-consistent description of the chondrule porosities that we present here in comparison to literature studies. For our purposes, we use the term *pore* to refer to a volume that is absent of material within a sample. The term *pore* does not imply a specific process or morphology, but it does carry with it the connotation of being original to the sample (i.e., not the result of sample preparation). The *bulk porosity* of a sample is defined as the volume ratio of the sum of all pores to the total volume of the sample. This definition includes cracks and fractures that can be important for the bulk porosity of chondritic material.

Two important process-related terms for *pore* that are used consistently in the literature are v*esicle* and *vug*. Vesicles formed by the exsolution of gaseous species from a melt and are preserved during solidification. Vugs refer to pores that contain euhedral crystalline phases that have grown into the pore space by liquid or vapor depositional processes. It is important to note that the term *vug* does not imply an origin for the pore itself and only describes the presence of crystalline phases within it. Like *pore*, the terms *void* and *hole* are commonly used in the literature when referring to the absence of material in a sample. However, *void* and *hole* are often used in a broader context than *pore* and used in thin section studies where the effects of sample preparation are unknown. We will avoid the terms *void* and *hole* and will only use the terms *pore*, *vesicle*, and *vug* within their appropriate context.

3.1. Chondrule textures

Figure 5.1 shows μCT cross-sections and 3D porosity renderings for Ch1 (Fig. 5.1a,b) and Ch7 (Fig. 5.1c,d). Both are porphyritic pyroxene (PP) chondrules. Both are roughly radially zoned, with higher contrast (bright regions on the edge) indicating FeO enrichment in the outer zones of the chondrules (Fig. 5.1a,c). We interpret this to indicate that the chondrules were originally FeO-rich (Type II) and the outer zones were further enriched in FeO during parent body processing. This will be described in more detail below. The small chondrules that were scanned together (Fig. 5.2a) include a variety of textural types, including: porphyritic olivine (PO, Figs. 5.2b,c), porphyritic pyroxene (PP, Fig. 5.2d), porphyritic olivine and pyroxene (POP, Figs. 5.2e,f), barred olivine (BO, Fig. 5.2g), radiating pyroxene (RP, Fig. 5.2h), and cryptocrystalline (CC, Fig. 5.2i).

3.2. 3D porosity characterization

The 3D distribution of porosity within the two large chondrules is rendered in Figs. 5.1b and 5.1d. We measured the bulk porosity of Ch1 and Ch7 to be 0.8% and 1.0%, respectively (Table 5.1). We scanned and measured the bulk porosity of the 30 small chondrules together and determined an average porosity of 0.8%. Because the resolution of the scan dictates the smallest pores that can be resolved, it is important to consider the range of pores accounted for in each scan. Ch1 was scanned using a voxel size of 3.7 μm and, based on visual inspection of threshold data, it was estimated that at least 5 voxels are needed to resolve a pore. We used the spherical equivalent diameter, defined as the diameter of a sphere that has the same volume as the measured pore, regardless of morphology. Therefore, each voxel has a volume of ~ 51 μm^3, and 5 voxels have a combined volume of 253 μm^3 that has a spherical equivalent diameter of 8 μm.

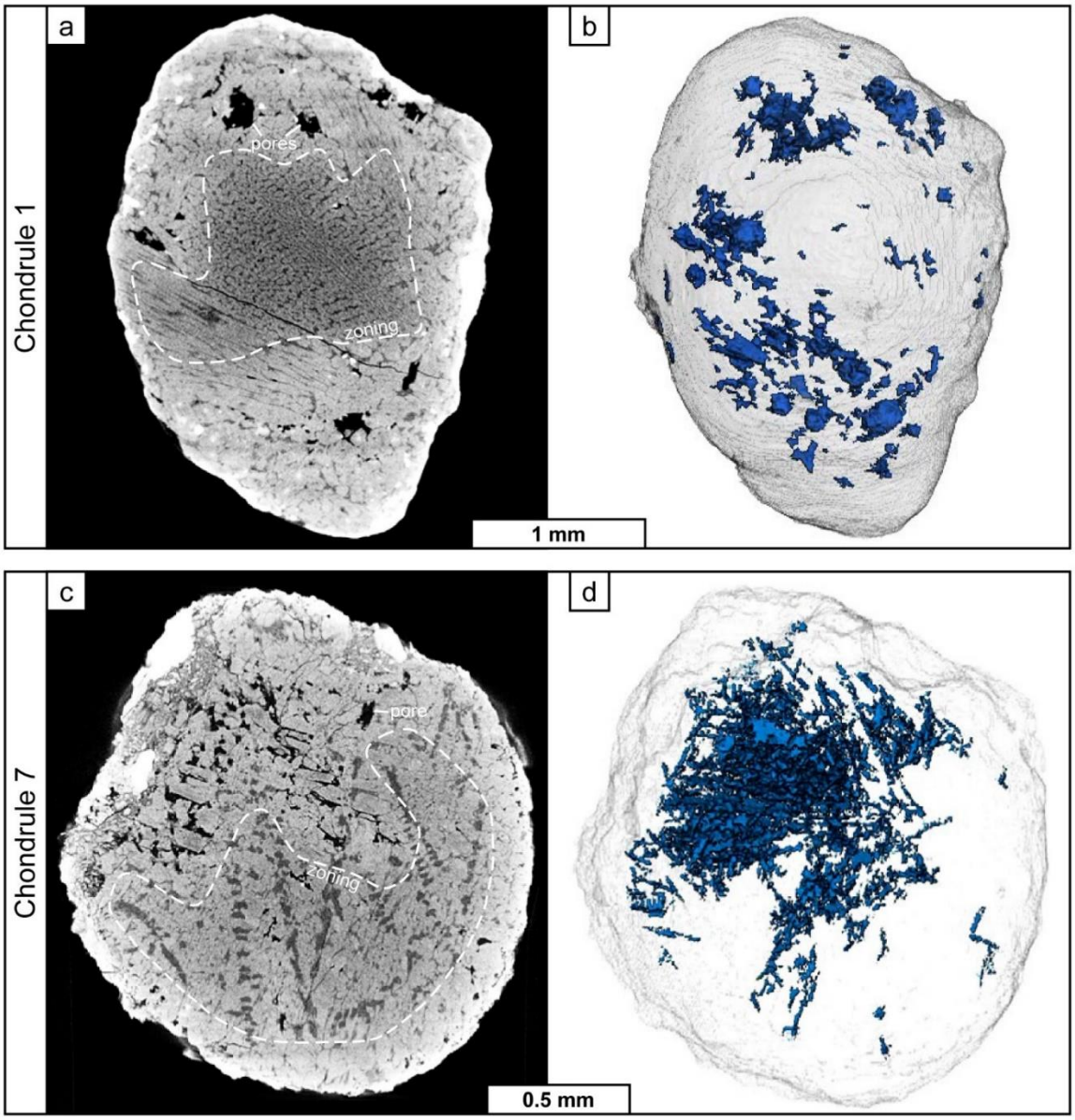

Figure 5.1. µCT cross-sections and 3D porosity renderings of the two large chondrules. A representative cross-section of Ch1 (a) shows round pores near the outer rim and distinct zoning (dashed line) with darkening toward the interior of the chondrule. The 3D rendering of the pore space in Ch1 (b) shows all the large pores (blue) are concentrated near the exterior of the chondrule (grey) and are not interconnected based on the observations obtained by the resolution of the scan (voxel size of 3.7 µm). The cross-section of Ch7 (c) shows elongate porosity in the upper left, near an area of remnant matrix, and zoning (dashed line) similar to Ch1 with darkening in the chondrule interior. The 3D porosity rendering (d) shows most of the porosity is interconnected and concentrated in the upper left. The use of higher resolution (voxel size of 1.3 µm) in this latter case allowed for the detection of interconnectivity between pores.

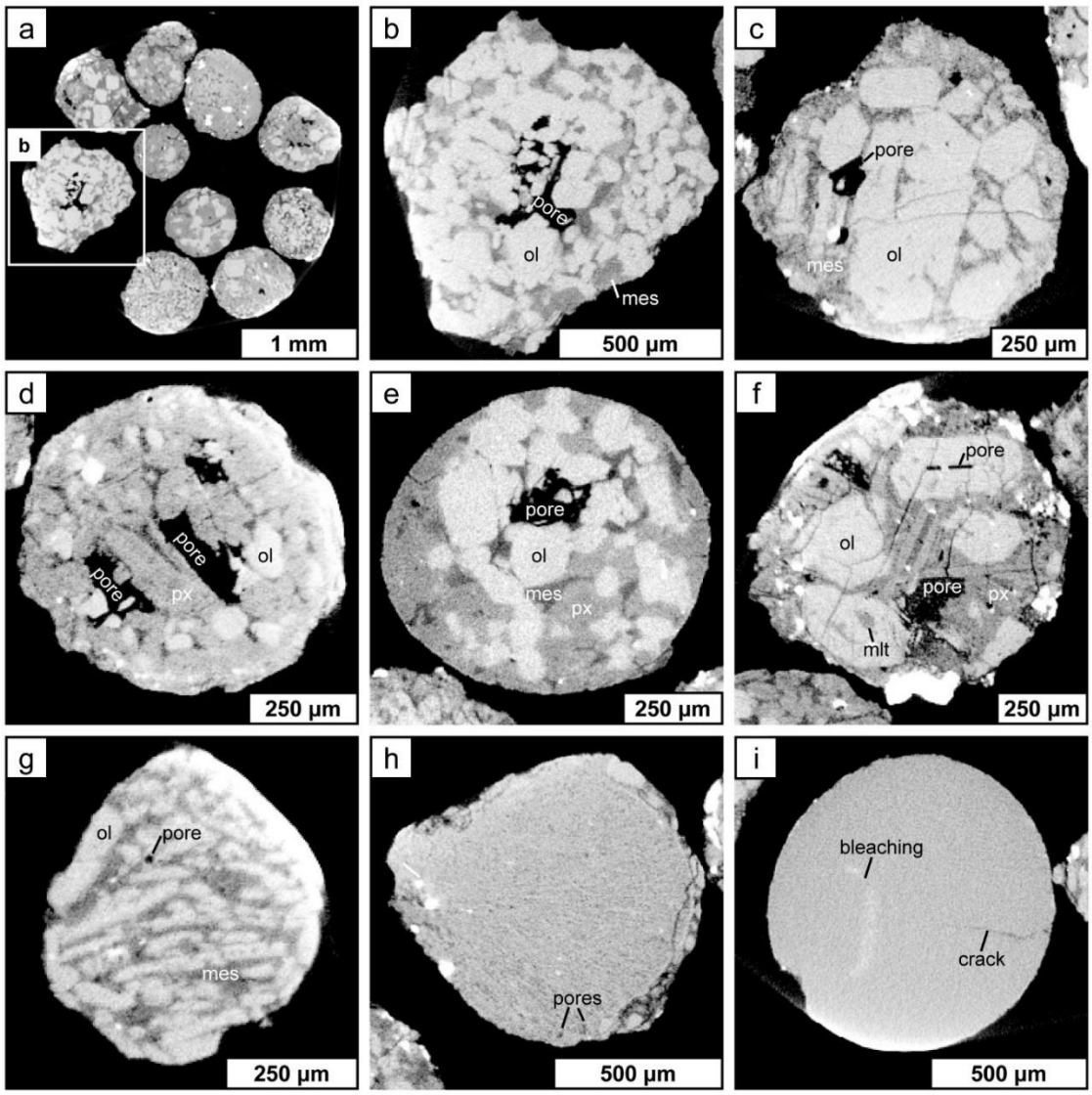

Figure 5.2. (a) µCT cross-sections of the small chondrules scanned together showing the dominant phases: olivine (ol), pyroxene (px), and mesostasis (mes). These include a variety of textural types including porphyritic olivine (b,c), porphyritic pyroxene (d), porphyritic olivine and pyroxene (e,f), barred olivine (g), radiating pyroxene (h), and a bleached, cryptocrystalline chondrule (i). All these chondrules contain pores including one within an olivine phenocryst (f), possibly through the dissolution of a melt inclusion (mlt).

Thus, the porosity measurement of Ch1 accounts for pores ≥8 μm in diameter. In addition, following the common rule that the resolution is equal to 2-3 times the voxel size considered (Maire and Withers, 2014), we achieve the same threshold value of ≥8 μm, when we are considering the voxel size of 3.7 μm. However, the approach based on the spherical equivalent diameter has the advantage that it can be used in comparing results obtained in 3D with those associated with the 2D analysis described below. Using this method, the porosity of Ch7 and the small chondrules are for pores ≥3 μm and ≥4 μm in diameter respectively.

Table 5.1. Porosity and other physical properties.

		Ch1	Ch7	small chondrules
3D bulk porosity (%)				
≥8 μm		0.8		
≥3 μm			1.0	
≥4 μm				0.8[1]
adjusted porosity ≥ 1 μm[2]		1.6	1.1	1.1
2D bulk porosity (%)				
≥8 μm		1.3		
≥3 μm			7.7	
≥1 μm		2.6	8.7	
% 2D bulk porosity ≥1 μm by pore diameter	1-3 μm	33	11	
	1-4 μm	39	14	26[3]
	3-8 μm	15	10	
	8-25 μm	11	13	
	25-100 μm	18	23	
	>100 μm	22	43	
volume (mm^3)		11.3	2.7	
mass (mg)		36.2	7.8	
bulk density (g/cm^3)		3.2	2.9	
major diameter (mm)		3.7	2.0	0.5-1.2

[1] average of 30 small chondrules scanned together
[2] estimated from 2D porosity analysis
[3] averaged from Ch1 and Ch7 estimate

Ch1 has several large, nearly spherical pores (~250 μm, Figs. 5.1a,b) in the outer few hundred μm of its volume, rendered in blue in Fig. 5.1b. It also has smaller porous regions that follow the morphology of intercrystalline mesostasis. Porosity in Ch1 is not connected as far as can be determined at the resolution used (with pores ≥8 μm), but it is possible that interconnected porosity could be detected if analyzed at finer scales. In contrast, most pores in Ch7 (Fig. 5.1d) are elongated, following the mesostasis morphology. They cluster in one region of the chondrule that is adjacent to the edge of the chondrule (Fig. 5.1c,d). Pores in this chondrule are largely interconnected at the resolution of the scan (pores ≥3 μm). Pores in the small chondrules also follow the morphology of the intercrystalline mesostasis (Fig. 5.2) and some are concentrated in the central regions of the chondrules (Figs. 5.2b-e). In other chondrules, pores are located closer to the chondrule exterior like in Ch1 (Fig. 5.2f). Chondrules with small phenocrysts and low mesostasis abundances only have small pores (<10 μm, Figs. 5.2g-i). The largest pores we observe are ~300 μm.

3.3. 2D pore size distribution

We have previously shown that Saratov chondrules contain a wide range of pore sizes from sub-μm to hundreds of μm (Lewis and Jones, 2016a). To understand the distribution of chondrule porosity at sizes below the resolution provided by the 3D scans, we estimated the size distribution of pores using high-resolution 2D BSE maps of cut and polished sections of Ch1 and Ch7 (Fig. 5.3). Like the 3D case considered above, the 2D diameter measurement used is a circular area equivalent diameter: the diameter of a circle that has the same area as the measured pore, regardless of its morphology. The maps have a resolution of 0.35 μm/px that allowed us to confidently resolve pores ≥1 μm in

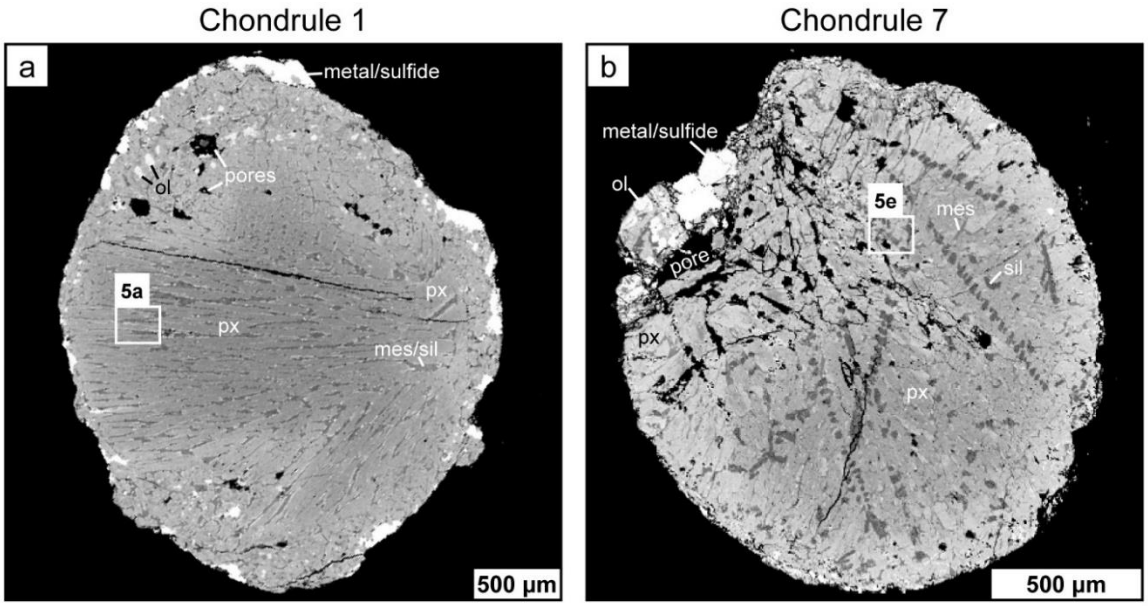

Figure 5.3. BSE images of the cut and polished faces of Ch1 (a) and Ch7 (b). White squares indicate areas represented in Fig. 5.5. White phases are metal and sulfides, the small, light gray grains are olivine (ol), the large region of zoned, medium grey is pyroxene (px), dark grey regions are silica (sil) and crystallized mesostasis glass (mes), and black regions are pores.

diameter (≥7 px). The results are presented graphically in Fig. 5.4 as the percentage of the total calculated porosity accounted for by pores within a given size range.

The porosity in Ch1 is dominated by small pores in the 1-3 μm range, whereas the porosity in Ch7 is dominated by the largest pores (>100 μm). This difference in porosity distribution between the two chondrules makes it difficult to ascribe a single pore size distribution to all chondrules. However, we can use the chondrule-specific curves to normalize the two large chondrules to pore sizes ≥1 μm, the results of which are presented in Table 5.1. The measured 3D porosity of Ch1, 0.8%, accounts for pores ≥8 μm. This is equivalent to 52% of the 2D pore distribution. Adding in the 1-8 μm pore range increases the porosity of Ch1 to 1.6%, defined as "adjusted porosity." Similarly, the measured 3D porosity of Ch7 is 1.0% and includes pores ≥3 μm, or 89% of the 2D

pore distribution. The porosity of Ch7 increases to 1.1% by including the 1-3 μm range of pore sizes.

The porosity of the small chondrules is 0.8% and includes pores ≥4 μm. The porosity accounted for by pores ≥4 μm in the two large chondrules is 61% and 86% for Ch1 and Ch7, respectively (Table 5.1). Hence, the average porosity of the large chondrules accounted for by pores in this size range is 74%. We can use this as a very rough estimate of the pore size distribution of the small chondrules and correct the porosity to 1.1% for pores ≥ 1 μm. However, as mentioned above, each chondrule has its own characteristic pore size distribution that may be significantly different from the distributions of the two chondrules we describe in detail here.

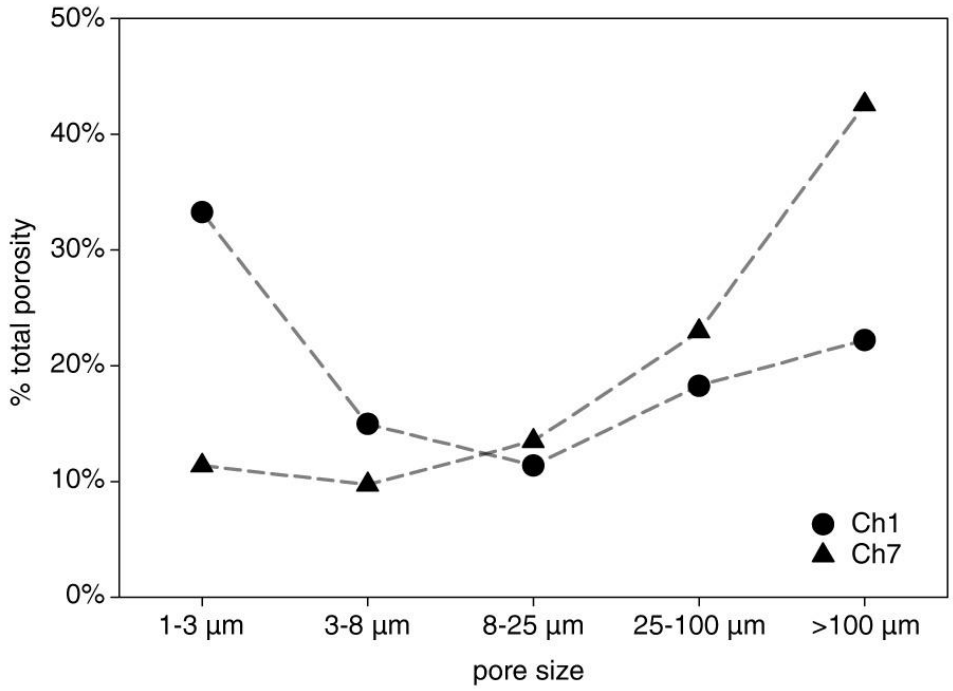

Figure 5.4. Porosity distribution calculated from 2D cut faces of Ch1 (circles) and Ch7 (triangles). Ch1 has a greater abundance of smaller pores, due to the greater abundance of chondrule mesostasis glass than Ch7 which has a greater abundance of large pores.

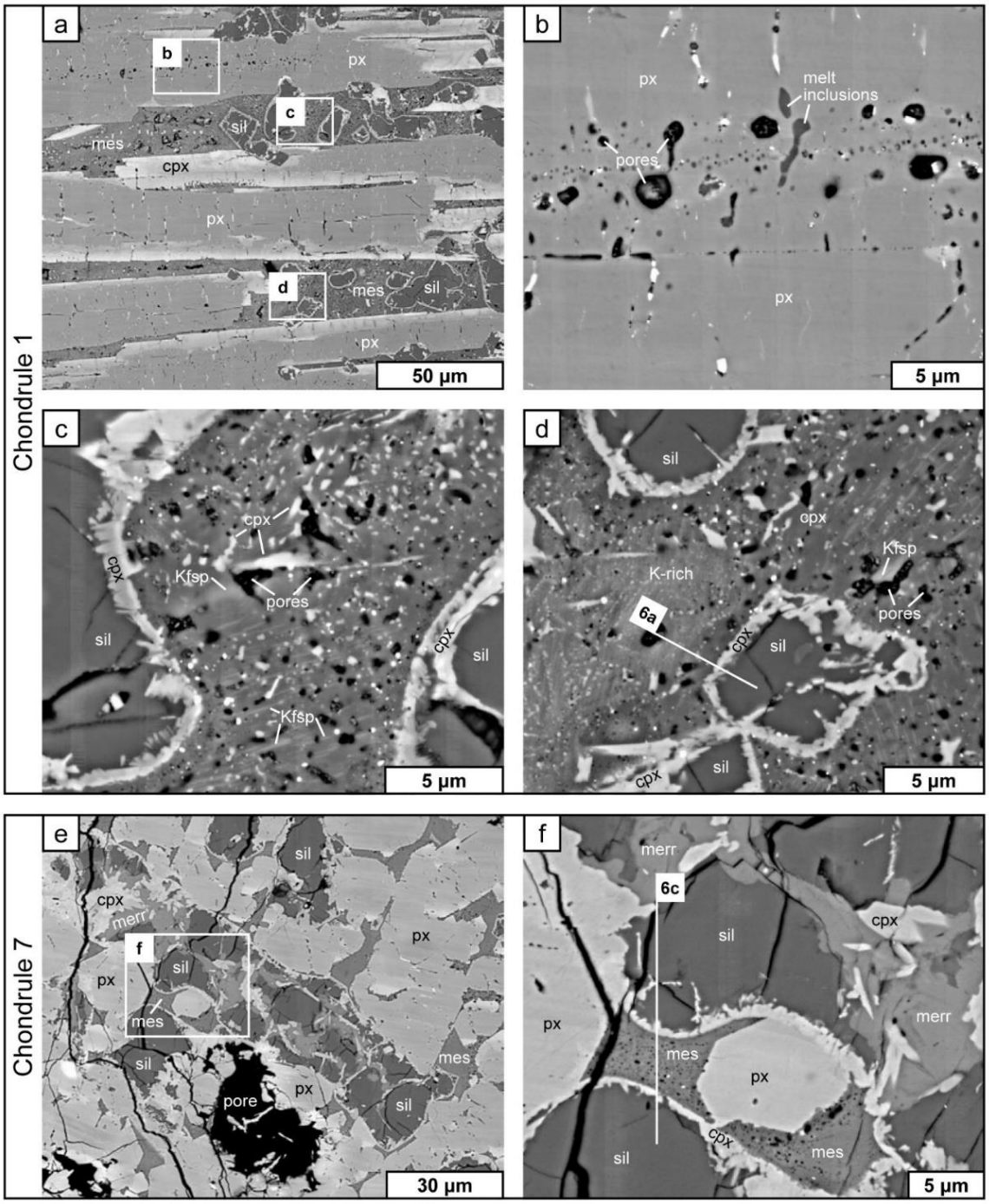

Figure 5.5. Detailed BSE images of Ch1 (a-d) and Ch7 (e-f), from regions highlighted in Fig. 5.3. (a) Shows the K-enriched border between the Fe-rich outer zone and the silica-bearing core of Ch1. The region contains low-Ca pyroxene (px), Ca-rich pyroxene (cpx), silica (sil), and crystallized mesostasis glass (mes). Three sub-regions are highlighted (b-d). (b) Shows pores and melt inclusions within the pyroxene phenocryst. (c) Illustrates porosity within the crystallized mesostasis glass dominated by albite exsolving K-feldspar (Kfsp) and adjacent to Ca-rich pyroxene rimmed silica. *(Caption continues on the following page).*

Figure 5.5. *(Caption continued from the previous page).* (d) Shows two different regions of crystallized mesostasis glass: the left side is enriched in K relative to the right side. Potassium is also preferentially enriched near the larger pores. The line in (d) shows the region in which a FIB section was extracted, illustrated in Fig. 5.6a. (e) A region of K enrichment in Ch7 in which silica has been altered to merrihueite (merr). (f) Close-up of a region in (e) illustrating the textural relationship between the silica and merrihueite and the porosity in the isolated patches of crystallized mesostasis glass. The line in (f) shows the FIB section extracted for Fig. 5.6c.

It is worth noting that the cumulative porosity measured in 2D is greater than that measured in 3D, even when measured over the same range. For Ch1, the measured porosity (≥8 μm) is 1.3% and 0.8% for 2D and 3D, respectively. Similarly, the measured 2D and 3D porosity for Ch7 (≥3 μm) is 7.7% and 1.0%, respectively. There are several reasons for this difference. First, we cut the chondrules roughly through the center along the long axis, where most of the porosity was observed in the μCT images. Second, removal of grains during polishing might have increased the observed porosity of the 2D sections, particularly in Ch7's highly porous region. Third, there may be differences in the results of porosity segmentation in 2D versus 3D. Overall, the 3D porosity measurements are likely more robust than the 2D measurements over the equivalent pore size range. We use an average chondrule porosity of 1-2% for the discussion below.

3.4. Chondrule mineralogy

2D BSE images (Figs. 5.3 and 5.5) reveal more detailed mineralogy in the two larger chondrules (Ch1 and Ch7) than can be seen in the μCT cross-sections. In both chondrules, the major phenocrysts are low-Ca pyroxene, commonly with rims of Ca-rich pyroxene (Fig. 5.5a,b,e). Interstitial to the large pyroxene phenocrysts, and what was referred to above as intercrystalline mesostasis, are grains of silica, isolated grains of Ca-rich pyroxene, and patches of crystallized mesostasis glass (Fig. 5.5a,c-f). Crystallized mesostasis glass is a fine-grained assemblage typically consisting of albitic plagioclase,

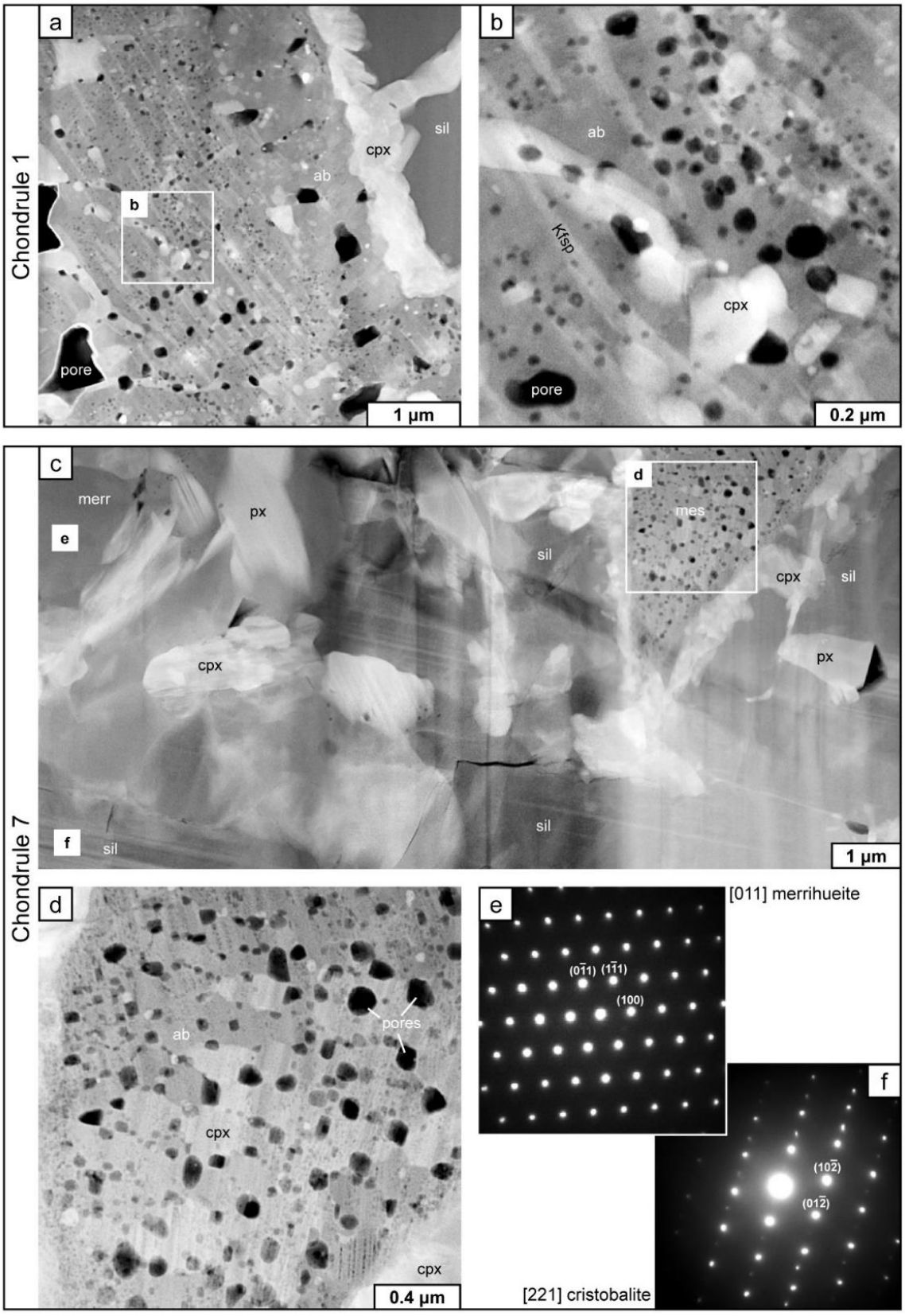
Chondrule 1
a
b
cpx
sil
ab
pore
1 µm
ab
Kfsp
cpx
pore
0.2 µm
Chondrule 7
c
merr
px
e
sil
d
mes
cpx
sil
cpx
px
f
sil
sil
1 µm
d
ab
pores
cpx
cpx
0.4 µm
e
[011] merrihueite
(0$\bar{1}$1) (1$\bar{1}$1)
(100)
f
(10$\bar{2}$)
(01$\bar{2}$)
[221] cristobalite

Figure 5.6. *(On previous page).* HAADF STEM images of FIB sections extracted from Ch1 (a-b) and Ch7 (c-d). (a) FIB section of Ch1 from Fig. 5.5d with porous crystallized mesostasis glass containing albite (ab) with K-feldspar exsolution (Kfsp), Ca-rich pyroxene (cpx), and silica (sil). (b) A close-up of (a) illustrating the extremely fine scale of the porosity. (c) FIB section of Ch7 from Fig. 5.5f with porous crystallized mesostasis glass, Ca-rich pyroxene, low-Ca pyroxene (px), twinned silica, and merrihueite (merr). (d) Close-up of crystallized mesostasis glass from (c) showing fine scale of porosity and the presence of pores predominantly along grain boundaries. Two SAD diffraction patterns from regions in (c) index as [011] merrihueite (e), and [221] cristobalite (f).

Ca-rich pyroxene, and oxides that form from devitrification of chondrule glass during thermal metamorphism. Merrihueite, $(K,Na)_2(Fe,Mg)_5Si_{12}O_{30}$, is also present in Ch7 (Fig. 5.5e,f), interstitial to the pyroxene phenocrysts, in a texture indicating replacement of silica. Merrihueite, and its Na-rich endmember roedderite, are known silica alteration phases in ordinary chondrites (Krot and Wasson, 1994; Wood and Holmberg, 1994). The texture we observe in Ch7 is similar to the textures observed by Krot and Wasson (1994) and Wood and Holmberg (1994).

3.5. 2D pore morphology

A closer look at 2D pore morphology below the resolution of the μCT scans (Fig. 5.5) reveals that porosity is present in low-Ca pyroxene, silica, and crystallized mesostasis in Ch1 (Figs. 5.5a-d). The cores of the pyroxene grains have circular pores several μm in size as well as cracks throughout (Figs. 5.5a,b). Porosity in the silica grains is only present as cracks (Fig. 5.5c). Most of the small-scale porosity is present in the crystallized mesostasis glass, which in Ch1 consists of albite with K-feldspar exsolution lamellae, Ca-rich pyroxene, oxides, and pores with a range of sizes up to ~1 μm in diameter (Figs. 5.5c,d). Coarser K-feldspar exsolution lamellae are present in the material directly adjacent to the larger pores (Figs. 5.5c,d). The abundance of K-feldspar lamellae

is heterogeneous in the crystallized mesostasis glass with some areas notably enriched in K (Fig. 5d).

The small-scale porosity in Ch7 (Figs. 5.5e,f) is almost entirely concentrated in the crystallized mesostasis glass, although minor porosity is seen in the low-Ca pyroxene, silica, and merrihueite. Fractures are present throughout all the phases. The crystallized mesostasis glass consists of albite, Ca-rich pyroxene, and pores up to ~1 μm in diameter. Unlike Ch1, oxides are rare and K-feldspar exsolution is absent. Crystallized mesostasis glass is also much less abundant in Ch7 relative to Ch1 as will be discussed further below.

FIB sections, labelled as 6a and 6c in Figs. 5.5d and 5.5f, respectively, were extracted from representative regions of crystallized mesostasis glass in the two chondrules considered and were imaged using HAADF STEM. These reveal a range of pore sizes and crystal morphologies (Fig. 5.6). Crystallized mesostasis glass in Ch1 includes 100-200 nm Ca-rich pyroxene grains and 50 nm wide sub-parallel K-feldspar exsolution lamellae in albite (Figs. 5.6a,b). Pore sizes generally range from ~10-100 nm, although μm-scale pores are also present. In Ch7, crystallized mesostasis glass has 100-300 nm grains of intergrown albite and Ca-rich pyroxene with triple junctions and ~10-100 nm diameter pores along grain boundaries (Figs. 5.6c,d). Parallel tracks of nm-scale pores are present within some of the albite grains (Fig. 5.6d). Both FIB sections include silica grains with polycrystalline Ca-rich pyroxene rims. The SAD patterns taken in the FIB section of Ch7 index to [011] merrihueite (Fig. 5.6e) and [221] cristobalite (Fig. 5.6f) for the silica phase.

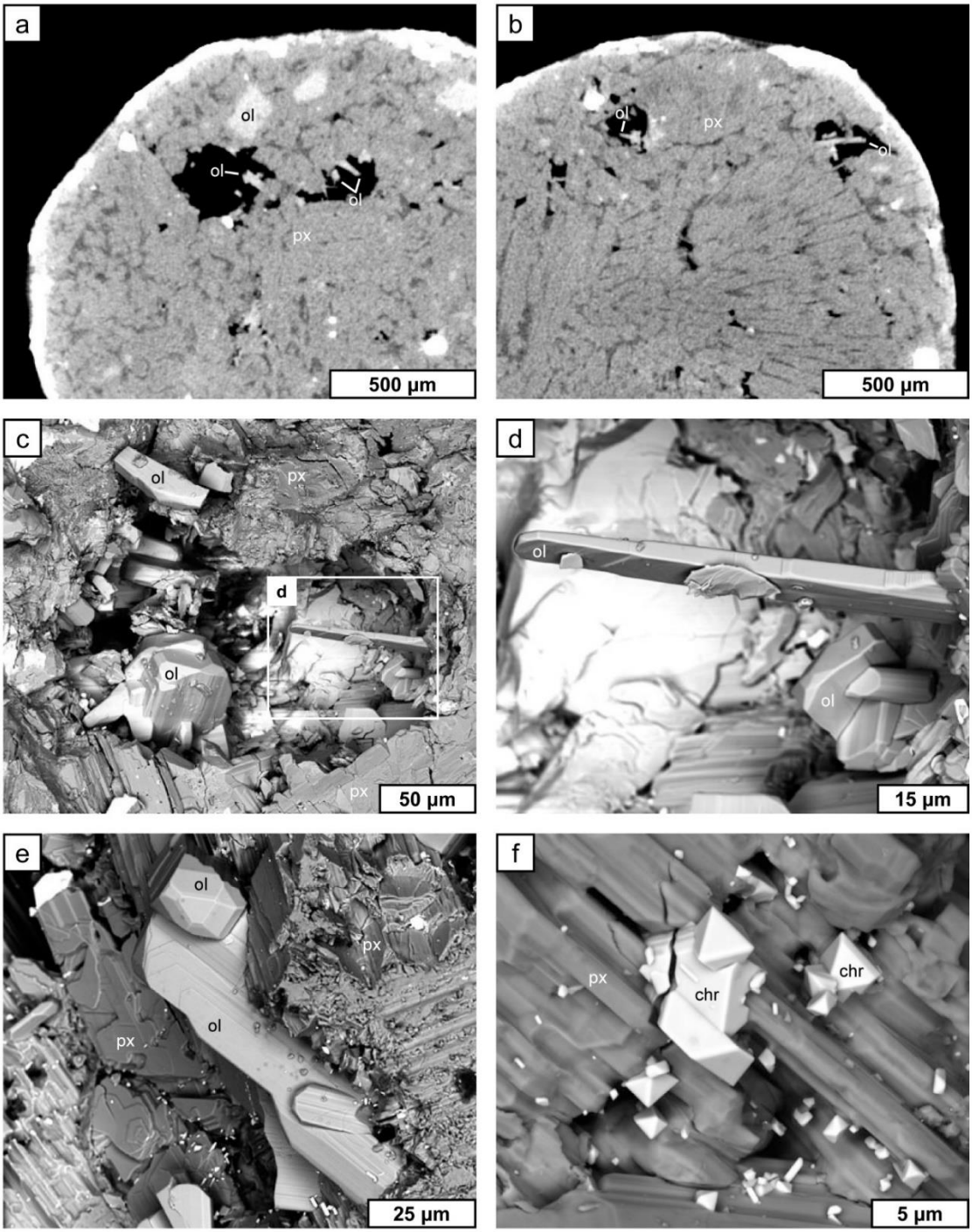

Figure 5.7. (a-b) µCT cross-sections of Ch1 showing vugs with acicular olivine crystals. (c-f) BSE images of phases in vugs from the unpolished cut half of Ch1. (c) A vug with euhedral olivine crystals including an acicular olivine illustrated in (d). (e) Vug with bladed and rounded olivine growing on low-Ca pyroxene. (f) Vug with euhedral chromite growing on low-Ca pyroxene.

3.6. Chondrule vugs

The large, spheroidal pores in Ch1 contain euhedral phases protruding from the pore boundary into the pore space (Fig. 5.7), which suggests that we should consider these objects to be vugs. In μCT slices (Fig. 5.7a,b), the phases growing into the vugs are brighter (greater attenuation, higher atomic number) than the surrounding low-Ca pyroxene, similar to the rare grains of olivine found along the outer edge of the chondrule (Fig. 5.7a). We also examined vugs in the unpolished half of Ch1 in the SEM. A few large, 200-250 μm diameter, pores are present at the surface and nearly all contain euhedral grains growing into them (Fig. 5.7c-f). Most of these grains are olivine of blocky or bladed morphologies with a similar composition to the surrounding material, approximately Fo_{80}, estimated using quantitative EDS. Nearly all the olivine showed growth bands on all or nearly all the observed faces (Fig. 5.7d,e).

Chromite, identified by EDS, was also observed growing as near perfect tetrahedra in many of the pores (Fig. 5.7f). The presence of chromite is not correlated with the presence of olivine as it appears in pores on its own or with olivine. Both olivine and chromite appear to have grown out of the pores using the abundant low-Ca pyroxene as a substrate. The pore surfaces are rough, and the orientation of low-Ca pyroxene substrate does not appear to correlate with the orientation of the vug crystals.

3.7. Quantitative element maps

Quantitative element maps and phase abundance maps for the two large chondrules are presented in Fig. 5.8, and the modal phase abundances are tabulated in Table 5.2. Ch1 is dominated by low-Ca pyroxene (65%) which is evident in the BSE image (Fig. 5.3a) and the phase abundance map (Fig. 5.8a). Other phases included Ca-

rich pyroxene (18%), olivine (1%), silica (3%) and crystallized mesostasis glass (13%). Metals and sulfides are present around the exterior of the chondrule (Fig. 5.8a). The pyroxene zoning noted in the μCT image (Fig. 5.1a) and visible as gray zoning in the BSE image (Fig. 5.3a) is very pronounced in the Mg# map in Fig. 5.8b, where Mg# is defined as Mg/(Mg+Fe)×100. Mg# is higher in the core with an average Mg# (atomic) of 90 and lower in the outer zone with an Mg# of 81. The pattern of zoning is not perfectly concentric but rather traces the positions of the large pores. In addition to zoning in FeO and MgO, zoning is present in SiO_2 and K_2O, as illustrated in the three element RGB (FeKSi) map shown in Fig. 5.8c. Zoning in SiO_2 reflects the higher abundance of silica, which is concentrated in the center of the chondrule. The crystallized mesostasis glass is enriched in K, as K-feldspar, along the border between the Fe-rich outer zone and silica-bearing core but is absent from the outer zone of the chondrule.

Table 5.2. Modal phase abundances.

	Ch1	Ch7
low-Ca pyx	65%	61%
Ca-pyx	18%	20%
olivine	1%	3%
silica	3%	7%
merrihueite		1%
mesostasis[1]	13%	8%

[1] crystallized mesostasis glass, a fine-grained assemblage of feldspar, Ca-rich pyroxene, and oxides

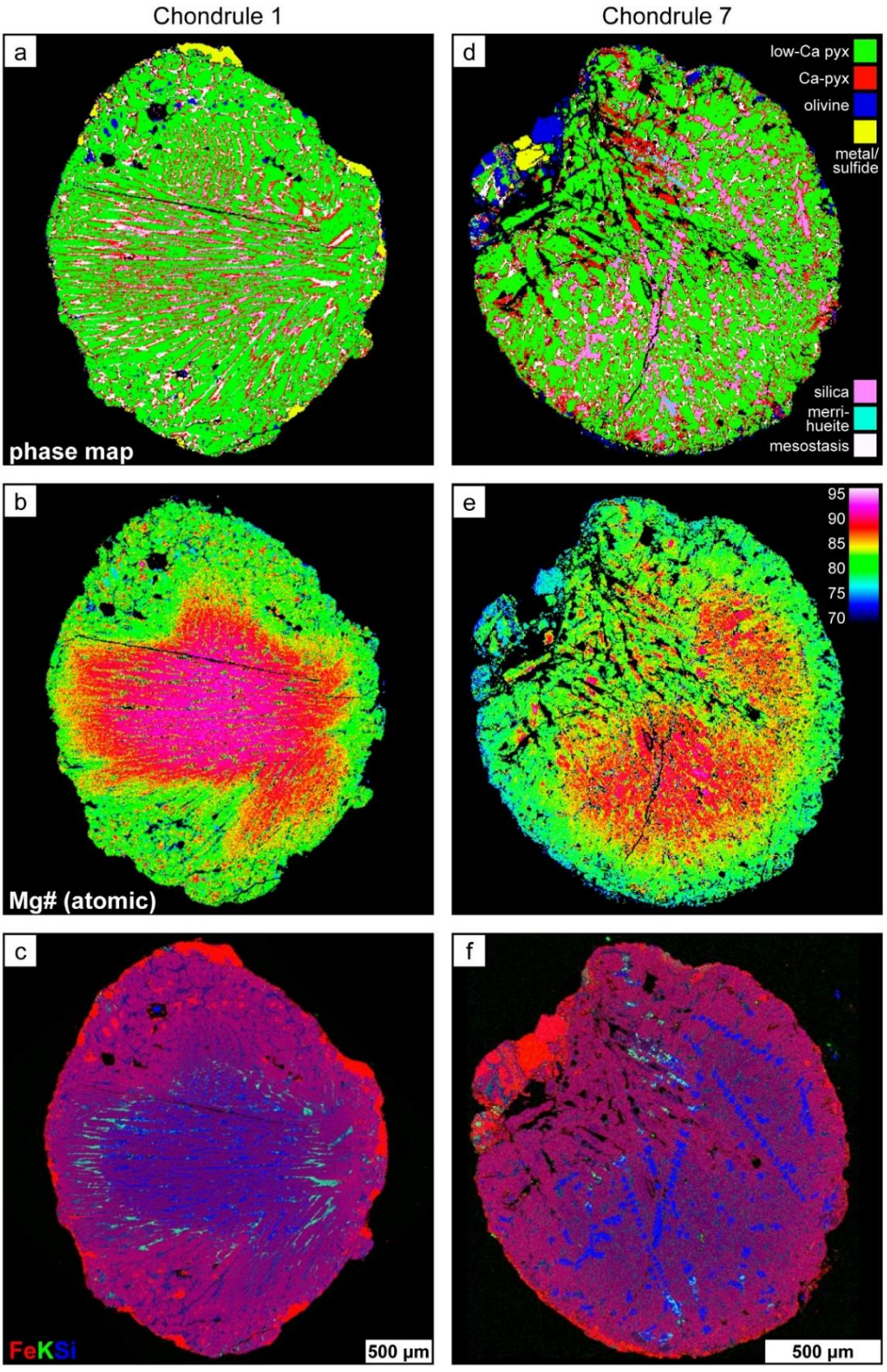
Chondrule 1
Chondrule 7
a
d
low-Ca pyx
Ca-pyx
olivine
metal/
sulfide
silica
merri-
hueite
mesostasis
phase map
b
e
95
90
85
80
75
70
Mg# (atomic)
c
f
FeKSi
500 µm
500 µm

Figure 5.8. *(On previous page).* EPMA maps of Ch1 (a-c) and Ch7 (d-f). Phase maps are shown in (a,d) and quantified in Table 5.2. Atomic Mg# (Mg/(Mg+Fe) × 100) is visualized in (b,e) to emphasize the Fe-enrichment in the outer zone. FeKSi RGB maps are shown in (c,f) to illustrate the correlation between the abundance of silica and K-enrichment with Fe-enriched outer zones.

As we have already shown, there are many similarities between Ch1 and Ch7. The latter is also dominated by low-Ca pyroxene (61%) with accessory Ca-rich pyroxene (20%), olivine (3%), silica (7%), merrihueite (1%), and crystallized mesostasis glass (8%) as shown in Figs. 5.8d. A few metals and sulfides are present along the chondrule exterior and are mostly concentrated in the region with the greatest porosity (Fig. 5.8d). Ch7 is also zoned with a higher Mg# core (atomic Mg# = 87) and lower Mg# outer zone (Mg# = 80), Fig 5.8e. Like Ch1, the degree of zoning follows the morphology of the porous regions, with the FeO rich region being the most porous. However, unlike Ch1, silica is not concentrated in the center but is evenly distributed throughout (Fig. 5.8d,f). Also, while there is some K enrichment in the boundary between the porous region and unaltered interior (Fig. 5.8f) like Ch1 (Fig. 5.8c), K is present in the K-bearing phase, merrihueite, and not as K-feldspar-bearing crystallized mesostasis glass.

3.8. Bulk silicate composition

The bulk silicate compositions for Ch1 and Ch7 are tabulated in Table 5.3. These were calculated using the quantitative element maps, as described in the methods section above. Phases were assigned to each pixel based on compositions (Figs. 5.8a,d) so that mineral densities could be used to produce accurate estimates of the bulk silicate compositions. Metals and sulfides are highlighted in the phase maps to illustrate their distributions but are not included in the silicate-only bulk compositions. As would be expected from their mineralogical similarity, the bulk compositions of the two chondrules are alike (Table 5.3). The overall Mg# (atomic) for the two chondrules are 84.3 and 82.5

Table 5.3. Bulk silicate compositions of large chondrules.

	Chondrule 1			Chondrule 7			Type IIB[1]	
	bulk	inner	outer	bulk	inner	outer	bulk	mesostasis
SiO_2	58.2	62.2	55.7	57.7	60.3	55.2	55.1	65.0
Al_2O_3	2.78	2.41	2.79	2.34	2.95	2.11	3.55	13.4
Cr_2O_3	0.55	0.55	0.53	0.48	0.50	0.49	0.54	0.12
FeO	8.77	5.23	11.3	9.95	6.93	11.8	10.2	10.4
MgO	26.5	26.2	26.8	26.3	26.4	27.0	26.9	1.46
CaO	1.93	2.19	1.71	2.33	1.86	2.65	2.18	4.68
Na_2O	1.16	1.19	1.04	0.80	0.98	0.75	1.33	4.27
K_2O	0.17	0.11	0.10	0.08	0.08	0.08	0.19	0.62
Total	100.0	100.0	100.0	100.0	100.0	100.0	100.0	100.0
Mg#[2]	75.1	83.3	70.5	72.6	79.2	69.6	72.4	12.3
Mg#[3]	84.3	89.9	81.0	82.5	87.2	80.3	82.4	20.0

[1] chondrules in Semarkona (LL3.00) from Jones (1996)
[2] MgO/(MgO+FeO)×100, wt.%
[3] Mg/(Mg+Fe)×100, atomic

for Ch1 and Ch7, respectively. The biggest differences are that Ch7 has ~1 wt.% more FeO and 50% less alkalis than Ch1.

Bulk compositions for the core and outer zones of the two chondrules, calculated for approximately the inner and outer third of the chondrule, respectively, are also tabulated in Table 5.3. For both chondrules, the cores have higher SiO_2 and Na_2O and outer zones have higher FeO. Cr_2O_3 and MgO do not show differences in concentration between core and outer zone for both chondrules. K_2O is also not zoned between the core and outer zones, but there is K_2O enrichment in the regions between the cores and outer zones (Figs. 5.8c,f) that is not captured in the core/outer zone measurements. CaO is higher in the core of Ch1 and Al_2O_3 is higher in the outer zone. The opposite is true for Ch7 with higher CaO in the outer zone and higher Al_2O_3 in the core. Zoning in the bulk SiO_2, Na_2O, Al_2O_3, and CaO content likely relates to the development of porosity through the removal of a mesostasis rich in these components. In contrast, zoning in K_2O likely

reflects the introduction of K and formation of the K-bearing phases K-feldspar and merrihueite.

3.9. Matrix porosity

We made additional observations of two Saratov thin sections (UNM 1145 and USNM 1423-3) to gain insight into porosity within the matrix. We estimate the chondrule abundance to be 70-80% in the two thin sections. Porosity is common in chondrules and in the matrix of both thin sections (Fig. 5.9a), but is generally more abundant in USNM 1423-3 (Fig. 5.9b) than UNM 1145 (Fig. 5.9c). In both cases, pores are more abundant in the matrix than in the chondrules but because Saratov is friable, matrix porosity may have been introduced by mechanical plucking of grains during thin section production. However, friability also implies low material strength that could be an indication of high matrix porosity. We will present a more detailed discussion of matrix porosity and its implications below.

4. Discussion

For OCs, bulk porosities are well characterized, due to the large number of samples available for study and extensive surveys of these samples (Macke, 2010). However, the distribution of porosities between the chondrite components, particularly between chondrules and matrix, is largely unexplored. Because chondrules compose such a large fraction of the bulk volume in OCs (60-80%: Scott and Krot, 2014), any variation of the amount of porosity within chondrules has a large effect on the calculated distribution of porosity in the matrix. It is also important to understand the origins of the pores within chondrules as it is fundamental to understand the effects of porosity on the physical properties of the whole chondrite. The development of chondrule porosity has

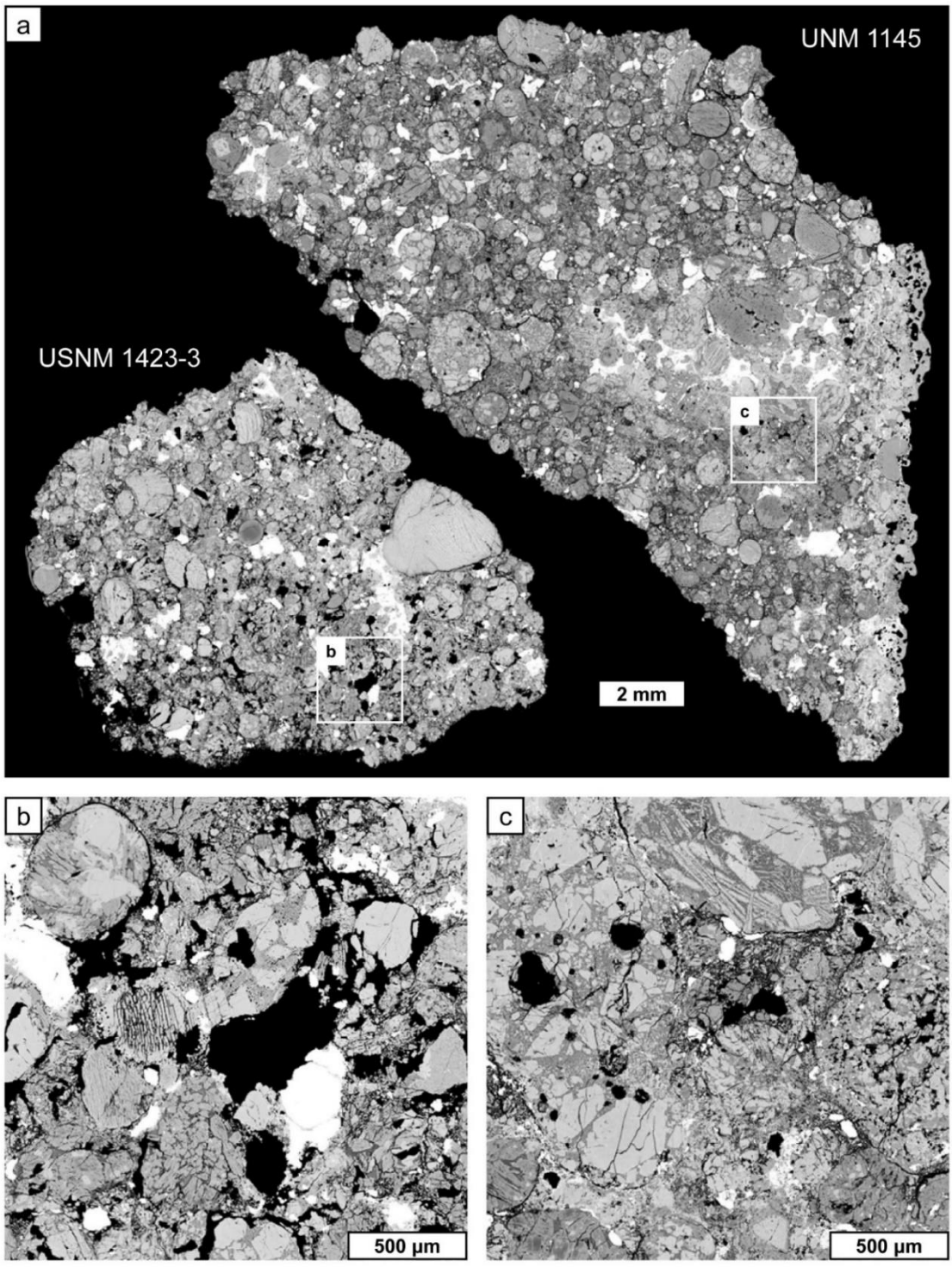

Figure 5.9. (a) A collage of BSE mosaics of two Saratov thin section, UNM 1145 and USNM 1423-3, illustrating thin-section-scale porosity. (b) Close-up of highly porous region from USNM 1423-3. (c) Close-up of porous region in UNM 1145 in which there are large pores within a porphyritic olivine chondrule.

important implications for the chemical evolution of chondrites during metamorphism. The abundance and interconnectivity of pores affects the open or closed system behavior of chondrules when interacting with metasomatic fluids, thus influencing the degree of chemical exchange between chondrules and the matrix and the chemical composition of fluids.

In the discussion that follows, we consider the possible origins of chondrule porosity, whether nebular (primary), parent body (secondary), or as the products of processes occurring on Earth (tertiary). We estimate the relative distribution of bulk porosity between chondrules and the matrix and discuss the physical implications. We discuss the presence of the vapor-deposited phases within the pores in context with other studies of vugs in OCs. Finally, we describe the overall effect of the development of porosity on the bulk chondrule composition in relation to secondary processes on the OC parent body.

4.1. Origin of chondrule porosity

In the chondrules we measured, porosity was found to be 1-2% by volume. This is similar to the bulk porosity measured by Ebel and Rivers (2007) in Allende (CV3) chondrules using μCT. Based on our results, pore sizes vary by 4-5 orders of magnitude (from nm to hundreds of μm) and the largest pores have morphologies indicating that they formed from the dissolution of chondrule mesostasis. Smaller pores are also present in the crystallized mesostasis, within phenocrysts, and as cracks found throughout. We now consider the origin of this porosity.

Many different processes can contribute to chondrule porosity and we broadly group these into primary, secondary and tertiary processes. What we refer to as primary

porosity, involves processes related to chondrule formation that took place in the solar nebula before accretion onto the parent asteroid. Porosity that develops in the parent body during secondary processing, such as aqueous alteration, thermal metamorphism, and shock, is what we refer to as secondary porosity. Tertiary porosity, involves processes that occur during the meteorite's residence on Earth such as weathering and sample preparation.

Pore forming processes include: degassing of chondrule melt (i.e., formation of vesicles), removal of mineral or amorphous phases through dissolution and chemical transport either on the parent asteroid or during weathering reactions on Earth, volume changes during primary or secondary crystallization, and mechanical processing such as impact or compaction. In addition, sample preparation, such as cutting and polishing, can loosen and remove mineral grains resulting in what is effectively a form of tertiary porosity. The study of porosity from thin sections and surficial studies of fragments leads to questions about whether the observed porosity is inherent to the sample or the result of sample preparation (Zbik and Lang, 1983). Using μCT allows us to avoid sample preparation issues in considering the nature and origins of chondrule porosity.

Primary chondrule porosity would form in the solar nebula, prior to accretion to the OC parent body. The most obvious possible source of primary porosity is gas entrained in chondrule melt, which could exsolve and form vesicles during chondrule cooling. Volatile species in the form of ices or hydrated mineral phases may also have been present in the precursor materials (e.g., Maharaj and Hewins, 1998). During the chondrule forming event, ices, as well as volatile species adsorbed onto precursor material, will become trapped in the molten droplets. If cooled rapidly, these volatiles

could possibly be retained within the chondrules, resulting in vesicles. Experimental studies of chondrule formation often result in vesicle-bearing charges whether from intentionally incorporated hydrous phases (Wdowiak, 1983; Maharaj and Hewins, 1998) or not (Maharaj and Hewins, 1994; Cohen and Hewins, 2004). However, there are no convincing reports of vesicles in natural chondrules, an important observation that Maharaj and Hewins (1998) use to argue against the incorporation of hydrous phases during chondrule formation. A study by Zbik and Lang (1983) did describe a subset of chondrule pores as vesicles, but these observations were made in chondrites that had undergone significant parent body processing and, as we will discuss further below, are likely secondary in origin. Similarly, a possible interpretation of the spheroidal pores in Ch1 is that they could have originally been vesicles, but without well-documented vesicles in unaltered chondrites we consider this interpretation unlikely.

Primary porosity that is not vesicular in nature is possible through the volume change that accompanies rapid crystallization. An experimental study by Connolly and Hewins (1995), in which dust was puffed onto molten chondrules to induce nucleation, produced intercrystalline pores, often connected to the chondrule surface, that they attribute to contraction of the remaining liquid during crystallization. The pore space in Ch7 resembles this texture to the extent that the pores are intercrystalline with some connection to the chondrule surface. However, the surface morphology and crystal growth patterns seen by Connolly and Hewins (1995) are significantly different from those we observe in Ch7. Also, the porosity described in their experimental study could have derived from volatile loss like the studies described above. While intercrystalline porosity has been noted within chondrules in low petrologic type OCs, it is attributed to

leaching of chondrule mesostasis during low temperature aqueous alteration (Lewis and Jones, in review; Grossman et al., 2000). Overall, without documented evidence of primary porosity observed in chondrules that have not undergone secondary processing, we cannot attribute the porosity we observe in these chondrules to primary processes.

Secondary porosity forms on the parent body during or after accretion and can be physical or chemical in nature. Bulk porosity that forms during accretion due to chondrule stacking or incomplete compaction of fluffy matrix particles is unlikely to affect chondrule porosity directly. However, physical processes such as compaction from impacts can cause fractures within chondrules. The large fracture in Ch1 (Figs. 5.1a, 5.3a) was likely formed by a physical process.

Two major chemical processes can cause chondrule porosity: volume changes associated with phase changes such as the crystallization of chondrule mesostasis glass, and the dissolution and removal of phases in a fluid. A combination of these two processes appears to be the major source of porosity in the two large chondrules we studied. The mesostasis in Ch1 (Fig. 5.5c,d, 5.6a,b) and Ch7 (Fig. 5.5f, 5.6c,d) contains abundant μm to sub-μm pores, fine-grained albitic plagioclase, Ca-rich pyroxene, and oxides consistent with crystallization of chondrule mesostasis glass during chondrule metamorphism. The greater abundance of 1-3 μm pores in Ch1 versus Ch7 (Fig. 5.4) is simply due to the greater abundance of crystallized mesostasis glass (Table 5.2) in which the fine-scale pores can form.

However, as we noted in the results, the expression of fine-scale porosity in the mesostasis of these two chondrules is different. The Ch7 pores are mainly found along grain boundaries (Fig. 5.6d), whereas the Ch1 pores are within phases (Fig. 5.6b). The

pores in Ch1 may have been formed, or at least modified, during the fluid infiltration that brought K into the chondrule to form the abundant K-feldspar exsolution we observe. The pores in Ch7 may have been formed by a solid-state crystallization process leaving pores on grain boundaries due to volume reduction. The K-bearing fluid that altered Ch1 may not have been able to penetrate the mesostasis glass in Ch7, but K is enriched in Ch7 in the silica alteration phase merrihueite. The fine-scale pores in Ch7 may not necessarily be interconnected, and hence may not be measured by He-pycnometry. However, as discussed above, they are also too small (<3 μm) to be adequately resolved by our μCT measurements.

Large-scale porosity, on a scale of tens of μm or greater, is likely too big to have been formed by phase change alone. For this reason, we consider that it must be the product of leaching. In Ch7, the pore morphology (Figs. 5.1c,d, 5.3b, 5.8d-f) is consistent with removal of chondrule mesostasis for several reasons. First, the pore structure mimics the elongated morphology of the mesostasis (Fig. 5.3b). Second, unlike the fine-scale porosity, the large-scale porosity is highly interconnected implying progressive removal and transport of material, not just localized contraction. Finally, the pore network is in direct contact with the edge of the chondrule.

Compared with Ch7, many large pores in Ch1 are more rounded (Figs. 5.1a,b, 5.3a, 5.8a-c). While we cannot rule out the possibility that these pores were originally metal/sulfide grains, several lines of evidence would suggest that they also formed by the removal of mesostasis. First, dissolution of large metal/sulfide grains without more pervasively dissolved mesostasis is difficult to reconcile considering the presence of intact metal/sulfide grains on the chondrule exterior (Fig. 5.8a). Second, some of the

smaller pores in Ch1 do follow the mesostasis morphology (Fig. 5.3a: top right and bottom), so the large pores could have originally been large regions of intercrystalline mesostasis. Finally, pervasive porosity at the μm to sub-μm scale could lead to the interconnectivity required to move material into and out of the chondrule. Further evidence for this is seen in Figs. 5.5c,d in which the material immediately surrounding μm-size pores is preferentially enriched in K (as K-feldspar) suggesting incorporation of K from a fluid that flowed through that pore.

Most pores present within the small chondrules also exhibit morphologies that indicate the dissolution of chondrule mesostasis (Fig. 5.2). Some of these pores can be very large (up to 300 μm long) relative to the size of the porphyritic chondrules (700-1000 μm in diameter) in which they are present (Figs. 5.2d-f). Large pores occur preferentially in porphyritic chondrules because of the relatively large regions of mesostasis found in these chondrules compared to finer-grained chondrule textures such as barred olivine, radiating pyroxene, and cryptocrystalline (Figs. 5.2g-i). Porosity is also present in the non-porphyritic chondrules, but is generally smaller and more difficult to resolve at the μCT scan resolution we used. The chondrule in Fig. 5.2f appears to have a pore within an olivine phenocryst. The presence of melt inclusions in the other olivine phenocrysts in this chondrule indicates that the olivine-bearing pore may have been produced by leaching of a melt inclusion, possibly connected to the grain edge through a crack.

Tertiary processes, those that have affected porosity since the meteorite has been on Earth, are unlikely to have had a significant impact on μCT-based chondrule porosity measurements of Saratov. The primary reason for this is that because Saratov is a fall, the

time this meteorite has spent outside of curation, and exposed to terrestrial weather, is minimal. Also, terrestrial weathering of ordinary chondrites is known to decrease porosity through the expansion of oxidation products into the pore space (Bland et al., 1998). We have not observed any of these weathering products within the chondrules in this study. While removal of grains during the cutting and polishing procedure may cause an increase in the 2D porosity measurements of Ch1 and Ch7 as discussed above, the 3D measurements are unaffected by sample preparation.

Overall, our observations of the porosity within these chondrules indicate a secondary, parent-body origin. The absence of observed primary porosity in unaltered chondrules renders the possibility of major primary porosity in these chondrules unlikely. Tertiary porosity is also unlikely because Saratov was not subject to terrestrial weathering and the μCT porosity measurements preclude the possibility of sample-preparation-induced porosity through mechanical removal of chondrule material. We suggest that the porosity in these chondrules is predominantly the result of mesostasis leaching. In addition, volume change during mesostasis crystallization may be responsible for some of the sub-μm porosity.

4.2. Porosity distribution and implications for asteroid physical properties

Generally speaking, the OCs are chondrule-rich assemblages (up to 80% chondrules in primitive OCs: Scott and Krot, 2014) and the chondrules are cemented together by a fine-grained matrix that coarsens with increasing petrologic type. Macke (2010) compared bulk porosity, averaged for each chondrite group, with the average chondrite matrix abundances of those groups from Brearley and Jones (1998). He noted a general trend toward increasing bulk porosity with increasing matrix abundance and

inferred that most of the porosity was contained within the matrix. This makes intuitive sense because chondrules are igneous objects and are expected to be relatively dense while the matrix largely consists of a fine-grained assemblage of crystalline and amorphous silicates, metals, and sulfides. We can evaluate this quantitatively using our observations: we can estimate matrix porosity in Saratov using the chondrule porosities we measured (1-2%), the bulk chondrite porosities measured by other studies, and an estimate of the chondrule abundance.

The bulk porosity of Saratov has been measured as 13% (Flynn et al., 1999), 14.1%, and 11.3% (Macke, 2010) using He-pycnometry. Alexeyva (1958) measured the bulk porosity of Saratov as 18.2% using a Hg-based technique. However, because we consider the He-pycnometry values to be more robust, we use the mass-weighted average porosity of the recent studies, 13%, for this discussion. A mass-weighted average is used under the assumption that larger samples will yield more representative bulk porosity measurements. Using the estimated chondrule abundance in Saratov, 70-80%, the average bulk porosity, and our adjusted chondrule porosity measurement of 1-2%, we estimate that the matrix porosity is 40-60%, the highest value being for an 80% chondrule abundance with a 1% chondrule porosity.

Examining the matrix directly in thin section it is easy to see that matrix porosity is highly variable (Fig. 5.9a). USNM 1423-3 (Fig. 5.9b) is much more porous than UNM 1145 (Fig. 5.9c), although both may fall within our 40-60% estimate. In addition, high porosity fragments (or aggregates), with porosities estimated to be up to 65%, were noted in Saratov by Semenenko et al. (1992) and Girich and Semenenko (2003) and fall near the upper range of our matrix porosity estimates. Because of the extremely friable nature

of Saratov, determining matrix porosity directly from thin section is not reliable due to the possibility of removing material during the sample preparation process. However, it is apparent from both our estimate above and the fragility of Saratov that matrix porosity is substantial.

A highly porous matrix has important implications for the physical properties of the parent asteroid, particularly material strength, thermal diffusivity, and fluid permeability. The friable nature of Saratov is likely due to low material strength in the matrix resulting from high porosity. Early numerical thermal models of OC onion-shell-like metamorphism effectively assigned a single porosity value to the whole asteroid, incorporated into the average thermal properties measured for porous OCs (Miyamoto et al., 1981). Bennett and McSween (1996) used thermal properties for both high (9-10%) and low (3-5%) porosity OCs to explore the differences between compacted and uncompacted asteroids. More recent models have recognized the importance of regolith insulation and include highly porous (up to 50%) outer layers into their models (Akridge et al., 1998; Harrison and Grimm, 2010).

For these onion-shell models, the extent of thermal metamorphism decreases from the core to the surface, resulting in successive layers that are represented by petrologic type 6 (core) to 3 (surface). Because the bulk porosity of OCs varies with petrologic type (Macke, 2010), the thermal properties of each layer are likely dependent on the degree of metamorphism experienced and thus evolve over the thermal history of the asteroid. For example, petrologic type 4 could represent an insulating layer at depth, below the regolith, that has not been considered. This is because petrologic type 4 represents the material where evidence for fluid activity is extensive, but the effects have not been

annealed out by progressive heating such as has been experienced by petrologic types 5 and 6. Average OC porosity decreases from type 4 to type 6 (Macke, 2010), so the thermal diffusivity of the asteroid should also increase with depth, and time, during the metamorphic process. Because bulk chondrule porosity is small compared to matrix porosity, the evolution of porosity with petrologic type is tied to processes that affect matrix, most likely recrystallization during thermal metamorphism. However, this simple picture is complicated by the fact that decreasing bulk porosity is also correlated with increasing shock stage (Macke, 2010) so that the porosity produced during thermal evolution of an asteroid can be subsequently altered by compaction and annealing during impact processing.

Porosity is also important because it controls permeability, and hence fluid flow, during aqueous alteration and during metasomatism associated with thermal metamorphism. The effects of aqueous alteration have been noted in Type 3 OCs (Alexander et al., 1989; Grossman et al., 2000; Grossman et al., 2002) and metasomatism is prevalent in petrologic types 4 and 5, including Saratov (Lewis and Jones, 2016a). Permeability requires interconnected porosity and the high porosity of OC matrix, at least in Saratov, implies a relatively high bulk permeability. However, the permeability of chondrules themselves is considerably lower.

We can estimate the difference in permeability between chondrules and matrix from the porosity estimates above, using the porosity-permeability relationship of Costa (2006). This relationship applies to non-granular porous media with fractal pore space geometry, like chondrules, unlike the classic Kozeny–Carman relation which is more appropriate for permeability in porous granular media, such as sand. In the absence of fit

parameters measured for chondrites, we used a variety of fit parameters determined by Costa (2006) for different studies of natural eruptive material (basalts and pumice) to provide estimates on the differences in permeability between chondrules and the matrix. Using this method, the estimated permeabilities of the chondrules that we measured are between 10^{-3}-10^{0} mdarcy (1-2% porosity, measured) and the permeability of the matrix between 10^{1}-10^{3} mdarcy (40-60% porosity, calculated), a difference of four orders of magnitude.

Extending this estimation to the bulk porosity of Saratov, 13%, yields a permeability of 10^{0}-10^{2} mdarcy. However, Corrigan et al. (1997) measured the permeability of chondrites to be lower: 10^{-2} mdarcy for Julesburg (L3.6, 5% porosity), 10^{-2}-10^{-1} mdarcy for Bali (CV3, 10% porosity), and 10^{-1}-10^{0} mdarcy for Murchison (CM2, 23% porosity). The difference between their measurements and our estimates is due to a lack of chondrite-appropriate fit parameters for the porosity-permeability relation. While the shape of the relation curve is reasonable, as is the 10^{4} mdarcy difference in permeability between chondrules and matrix, the absolute permeability values are clearly too high.

Additionally, the permeability of the chondrules is complicated in detail. Ch1 has large pores that, based on the resolution of the μCT scan used, are not interconnected; however, it is likely that they are connected at smaller scales. In contrast, Ch7 has interconnected porosity through one end of the chondrule that is easily visible in the μCT scan. In both cases, the total porosity is low and BSE images suggest that not all the pores are interconnected at smaller scales with respect to the resolution of the μCT scans, such as the pores internal to the pyroxene phenocrysts in Ch1 (Fig. 5.5b) or the matrix pores in

Ch7 (Fig. 5.6d). Permeability in chondrules is largely facilitated by leached and highly porous mesostasis in addition to cracks. It is likely that the high permeability of the matrix has allowed fluid flow, resulting in the dissolution and removal of chondrule mesostasis, which in turn led to the development of chondrule porosity.

4.3. Vugs and vapor deposited minerals

Euhedral crystals of olivine and chromite protruding into vugs, like those in Ch1 (Fig. 5.7), have been reported in several equilibrated OCs. Vugs have been described primarily, but not exclusively, in petrologic type 5 L and H chondrites. The crystals have been interpreted as the products of vapor deposition, and two mechanisms for their formation have been proposed: the fluids from which the crystals are deposited may be derived from shock volatilization or by parent body degassing during thermal metamorphism.

Olsen (1981) described large vugs (as big as 10 x 10 mm) in Farmington (L5), Oryinio (H5), and Tadjera (L5) and noted vugs in Lubock (L5), Arapahoe (L5) and Wickenburg (L6), all chondrites which were studied for extensive shock features by Smith and Goldstein (1977). In addition, vugs have been described in the heavily shocked meteorites Chelyabinsk (LL5), Shaw (L5), Rose City (H5), Jinju (H5), and Yanzhuang (H6) (Fruland, 1975; Taylor et al., 1979; Xie and Chen, 1997; Choi et al., 2015; Sharygin et al., 2015). The shock mechanism invokes the heterogeneous nature of shock propagation to vaporize small amounts of material during high energy shock events. The vaporized material then condenses into nearby pore spaces producing euhedral minerals. These minerals are typically common chondrite-forming minerals and include olivine, pyroxene, plagioclase, and chromite. The composition of these phases is often the same,

or similar, to the corresponding phases in the rest of the chondrite apart from albite: (Olsen, 1981) noted near endmember albite growing into pores in Farmington.

Vugs are also reported in the L5 chondrites Baszowka and Mt. Tazerzait (Wlotzka and Otto, 2001) and the H4 chondrite Sena (Christophe-Michel-Lévy, 1979), meteorites that do not have indications of high degrees of shock. Wlotzka and Otto (2001) differentiate vugs in these low-shock meteorites from vugs in meteorites that show evidence for high degrees of shock. They attribute the growth of olivine and pyroxene into pores of low-shock samples to vapor deposition during thermal metamorphism. Saratov also has a low degree of shock with an assigned shock stage of S2 (Rubin, 1994) or S3 (Friedrich et al., 2004). Since we have also shown that there is independent evidence for metasomatism in Saratov (Lewis and Jones, 2016b), we conclude that the vugs we observe in Saratov chondrules are more likely formed during thermal metamorphism via parent body degassing than from vapors produced during shock events.

Vugs within chondrules have only been reported specifically by Choi et al. (2015) in Jinju. It is likely that vugs are present in chondrules within other meteorites mentioned above, but the relatively large sizes of the vugs in the bulk meteorite relative to the chondrule sizes makes them less likely to be observed and reported. While the vugs within the matrix can be caused by pore spaces produced in the voids between chondrule components (e.g., pores between packed chondrules), vugs within chondrules require at least two events to produce them: removal of material to form the pore and addition of vapor to deposit the minerals.

The presence of vugs predominantly in type 5 OCs is instructive as to the processes involved in their formation. Although there is a large degree of heterogeneity between samples, type 4 OCs have, on average, the highest porosity of OC falls (Macke, 2010). This could be due to a combination of the crystallization of matrix and the removal of material via metasomatic fluids during thermal metamorphism. Thermal metamorphism is also characterized by the progressive chemical and textural equilibration of OC mineralogy through petrologic type 6. The temperatures experienced by type 5s may lead to deposition of minerals into the pores developed during metamorphic/metasomatic processing in type 4s. Porosity decreases in type 6 OCs relative to lower petrologic types with the completion of textural equilibration (Macke, 2010).

In summary, the mineral grains in vugs that we observe in Saratov chondrules were most likely formed by vapor deposition during thermal metamorphism. Large scale porosity, developed in the chondrules largely by dissolution and transport of chondrule mesostasis, was followed by a period of vapor transport and deposition.

4.4. Changes in bulk chondrule chemistry driven by porosity

Porosity affects bulk chondrule chemistry in two ways: through the removal of material during pore development and from metasomatic reactions that utilize pore networks. The development of porosity through dissolution of chondrule mesostasis glass, and transport of dissolved species out of the chondrule, removes elements enriched in the mesostasis like Si, Al, Na, and K. We estimate 20-30% loss of mesostasis in the two large chondrules based on the porosity and mesostasis abundance measurements made from the 2D chondrule maps (Fig. 5.3, Table 5.2). We can use the bulk and

mesostasis compositions of Type IIB chondrules (Table 5.3), measured in minimally metamorphosed, petrologic type 3.00 chondrite Semarkona (Jones, 1996), as an approximate analog for the pre-alteration composition of the Saratov chondrules. Removal of 25% of the mesostasis, with an average mesostasis abundance of 10% (Table 5.2), corresponds to a 21% loss of Al_2O_3 and 15% loss of alkalis from the bulk chondrule composition, in addition to minor losses of SiO_2 and CaO. From the μCT scans of the smaller chondrules (Figs. 5.2d-f) and the BSE maps of Saratov in thin sections (Fig. 5.9), it is evident that some chondrules have experienced an even greater degree of mesostasis loss.

Porosity also provides a transportation network for fluids that can engage in metasomatic exchange reactions with olivine and pyroxene phenocrysts in addition to crystallized feldspathic mesostasis and other phases. Ch1 and Ch7 have pronounced zoning in Mg# (Figs. 5.8b, 5.8e) with an average chondrule core Mg# (atomic) of 87-90 in both chondrules, surrounded by outer zones with an average Mg# of 80-81 (Table 5.3). In both chondrules, the locations of Fe-rich zones are directly correlated with the location of the highly porous regions. This implies the introduction of Fe into the chondrule through a mechanism related to the porosity. However, it is not clear whether the Fe was introduced during the mesostasis leaching event, by Fe-bearing fluids, or whether mesostasis leaching was later followed by infiltration of Fe-bearing fluids that utilized the existent porosity network. As discussed further below, introduction of Fe is usually thought to result from solid-state Fe-Mg diffusional exchange.

Like Fe, K appears to have been introduced through the pore network, either during or after mesostasis leaching. Potassium is enriched in the mesostasis along the

boundary between the core and outer zone in Ch1 and, to a lesser extent Ch7. However, the expression of K enrichment is very different between the two chondrules. Ch1 has K-feldspar exsolution from albite in the crystallized chondrule mesostasis (Fig. 5.5c,d). The presence of albite might also be evidence for the introduction of Na in addition to K. Albitization of Ca-bearing plagioclase is known to affect type 4 OCs (Kovach and Jones, 2010; Lewis and Jones, 2016b) and Saratov in particular (Lewis and Jones, 2016a). Although there is no evidence that Ca-plagioclase was present in these chondrules, the albitization in other chondrules requires the involvement of a Na-rich fluid. K-feldspar exsolution is coarser near the larger pores and generally heterogeneous throughout the boundary zone, indicating infiltration of an alkali-bearing fluid through the pore network.

The presence of exsolution in what may be generally described as an antiperthite texture, K-feldspar lamellae in an albite host, implies that the K was added at a temperature above the alkali-feldspar solvus, ~600 °C (Brown and Parsons, 1989), followed by cooling and exsolution. The fluids could have acted during metamorphism with exsolution taking place during retrograde metamorphism. However, the fine scale of the exsolution lamellae implies rapid cooling, ~1 °C per 10^1-10^3 year (Brown et al., 1983; Brown and Parsons, 1989; Lewis et al., 2016), much faster than is typically measured for retrograde metamorphism of ~1 °C per 10^4-10^6 years (Scott et al., 2014). Alternatively, late stage, high-temperature fluids moving through the asteroid during, or after, retrograde metamorphism could act in discrete bursts followed by rapid cooling to the ambient temperature, producing the textures we observe.

In contrast to Ch1, Ch7 contains merrihueite, an alkali-bearing phase, intergrown with the silica, and no K-feldspar in the crystallized mesostasis (Fig. 5.5f). The formation

of merrihueite in silica-merrihueite-bearing pyroxene chondrules has been attributed to a reaction of silica with an alkali-rich vapor on the parent body (Krot and Wasson, 1994) or in the solar nebula (Wood and Holmberg, 1994). Seifert and Schreyer (1969) studied the formation conditions of merrihueite and found that it formed in hydrous conditions at temperatures >560 °C at 0.5 kb fluid pressure. This is in line with the temperatures expected for incorporation of K into alkali feldspar in Ch1. Interestingly, while both chondrules were only a few mm apart in the hand sample, and both are silica-bearing, only Ch7 shows silica alteration to merrihueite.

There are two possible explanations for the difference in alteration features between the two chondrules. First, alteration of silica to merrihueite could have occurred in the solar nebula as was suggested by Wood and Holmberg (1994). Differences in the formation regions could then explain the differences in alteration between the two chondrules prior to their accretion near to each other on the parent body. However, one would expect parent body alteration by a K-bearing fluid to have then affected both chondrules equally and produce K-feldspar exsolution in both. Also, Krot and Wasson (1994) point out that merrihueite has only been seen in type 3 chondrites >3.7, implying a relationship with mild metamorphism.

A second, more likely, possibility is that the mode of alteration (K-feldspar vs merrihueite) is related to the abundance and distribution of the altered phase. Ch1 has over four times the abundance of crystallized mesostasis glass than silica (Table 5.2) and the silica is concentrated in the core (Figs. 5.5a, 5.8a,c), interior to a large portion of crystallized mesostasis. Ch7 has a more equal abundance and distribution of silica (plus merrihueite) and crystallized mesostasis glass (Table 5.2, Figs. 5.5e, 5.8d,f). The

crystallized mesostasis in Ch7 is also present in small, disconnected patches. K-bearing fluid infiltration from the chondrule exterior, through the pore network, is more likely to encounter mesostasis glass in Ch1 and silica in Ch7.

We suggest that a hot, >600 °C, anhydrous, K-bearing fluid infiltrated both chondrules during retrograde metamorphism, altering the major primary mesostasis phase, silica or glass/albite and that the system then cooled rapidly to ambient temperature. While Krot and Wasson (1994) did not consider hydrous alteration of silica to merrihueite, Seifert and Schreyer (1969) show that it is a viable mechanism. However, late-stage fluids are suggested to be anhydrous by the lack of OH in OC apatite (Jones et al., 2014; Jones et al., 2016; Lewis and Jones, 2016b). Krot and Wasson (1994) also suggest that merrihueite formation occurs during impact events that produced hot, alkali-bearing vapor alteration. This would explain the high-temperature incorporation of K into alkali feldspar following by rapid cooling to produce fine-scale antiperthite. It is also in line with the suggestion by Olsen (1981) that vugs are produced during impact events. However, the associated indicators for shock processing, such as high shock stage or brecciation, are absent in Saratov. Instead, we suggest that outgassing events from the asteroid core could also produce similar signatures in all cases. In an onion-shell asteroid model, the asteroid interior can still be at high temperatures, and may even be partially molten, while the exterior layers are undergoing retrograde metamorphism.

Overall, a complicated picture of secondary processing is painted by the development of porosity and the signature of chemical exchange revealed by these chondrules. OC chondrules clearly behaved as open systems during metamorphic processing. The development of chondrule porosity implies transport of Si, Al, Na, and K

out of the chondrules, largely through the dissolution of chondrule mesostasis. Pores created during mesostasis leaching serve as conduits for further metasomatic processing. The reduction of Mg# in the outer zone and near pores, and the presence of K-rich alteration of mesostasis and silica, implies the transport of Fe and K into the chondrules. We have previously observed that both K and Na are introduced into chondrules by fluids during thermal metasomatism and that alkali metasomatism of anorthitic feldspar is likely the major driver of plagioclase equilibration in type 3 and 4 OCs (Lewis and Jones, 2014; Lewis and Jones, 2016b). It is possible that Fe is incorporated during retrograde metamorphism along with Na and K, but this seems unlikely given the consistency with which Fe incorporation dictates the petrologic sequence.

Iron-Mg exchange between chondrules and the matrix is not often considered to be the result of fluid activity in OCs. It is treated as a solid state diffusional process in which olivine and pyroxene equilibrate chemically, as well as texturally, during thermal metamorphism. If this is the case here, then the Fe-Mg exchange must have postdated the formation of the porosity to achieve the pattern of Fe-enrichment we observe. However, fluid infiltration of Fe could produce the same effect. We propose the following sequence of events. During prograde metamorphism, aqueous fluids, derived from ices incorporated during accretion, leach away chondrule mesostasis glass, producing porosity, incorporating Fe into olivine and pyroxene, and transporting dissolved ions into the matrix. The fluid then runs out and the mesostasis continues to crystalize through peak metamorphism. During retrograde metamorphism, high temperature outgassing from the asteroid interior alters silica to merrihueite, incorporates Na and K into alkali feldspar, and crystalizes the vug phases, olivine and chromite, into the larger pores. The

temperature drops rapidly to the ambient temperature producing fine-scale K-feldspar exsolution.

The scale to which the system can be considered open beyond the chondrule scale is ambiguous. Concentrations of the elements lost during mesostasis leaching (Si, Al, Na, and K) do not show appreciable differences in bulk OCs between individual samples or petrologic types (Kallemeyn et al., 1989), suggesting closed system behavior on cm length scales. If this is the case, then the fluid carrying mesostasis-derived ions must have precipitated its salt ions nearby. One possibility is that they were precipitated into the matrix as an alkali-rich phase such as feldspar. In addition, this alkali-rich fluid could have altered phases within other chondrules, such as the albitization reactions seen in anorthitic plagioclase (Lewis and Jones, 2016a).

However, the lack of evidence for hydrated minerals in metamorphosed OCs implies that water itself must have acted in an open system manner on kilometer length scales. Dehydration of any hydrated phases through increasing metamorphic temperatures would have driven water into the outer layers of the asteroid. Large scale flow without long distance transport of ions could be facilitated by a low water-rock ratio. Leaching and transport of mesostasis ions would closely be followed by alteration of nearby material and ultimately precipitation of salt ions during evaporation.

5. Conclusions

We measured porosity in Saratov chondrules, using three-dimensional μCT and two-dimensional SEM observations, to characterize the abundance and distribution of pores within chondrules and to help understand how porosity facilitates chemical exchange during metamorphism. Bulk porosity in the chondrules we measured is 1-2%

by volume. We argue that chondrule porosity is a secondary, parent body feature. Pores form through the dissolution of chondrule mesostasis by an aqueous fluid during the metasomatism that accompanies thermal metamorphism. Because chondrule porosity is far less than the bulk chondrite porosity measured for Saratov, ~13%, and because chondrules comprise 70-80% of the volume, we estimate a highly porous matrix of 40-60%. This is consistent with thin section observations and the extremely friable nature of Saratov in hand sample.

Fluid-mediated chemical exchange utilizing pore networks is suggested through two observations. The first is through the presence of vugs, i.e., pores in which euhedral olivine and chromite crystals are present. We suggest that the vugs formed from vapor deposition during thermal metamorphism after the formation of large scale porosity. The second observation is the enrichment of Fe and K correlating with the pore network in chondrules. Pyroxene is enriched in Fe in the outer zones of chondrules and adjacent to the major pores, implying transport of Fe from the matrix through the pore network. K-enrichment, as K-feldspar exsolution in the crystallized mesostasis glass of Ch1, preferentially occurs near the Fe-enriched regions. In Ch7, K-enrichment occurs as the silica alteration phase merrihueite. We suggest that K-alteration of the two phases occurred during the same event(s) during retrograde metamorphism. Overall, the development of porosity during thermal metamorphism of the L chondrite parent body altered its physical properties and contributed to its chemical evolution.

Acknowledgements

We would like to thank Elena Dobrică for her assistance with the TEM and Adrian Brearley for useful discussions. Thin sections were provided by the Smithsonian

Institution's National Museum of Natural History and by the Institute of Meteoritics at the University of New Mexico. Electron microprobe, SEM, FIB, and TEM work were carried out in the Electron Microbeam Analysis Facility, Department of Earth and Planetary Sciences and Institute of Meteoritics, University of New Mexico. We would like to acknowledge the assistance provided by the Manchester X-ray Imaging Facility, which was funded in part by the EPSRC (grants EP/F007906/1, EP/F001452/1 and EP/I02249X/1). J. Lewis acknowledges support from the Kelley-Silver Foundation, University of New Mexico, the New Mexico Space Grant Consortium, and is grateful to the University of Manchester for sponsoring his visit to the School of Earth and Environmental Sciences. The work was partially funded by NASA grant NNX12AH61G (P.I. R. Jones) and by the Science and Technology Facilities Council (STFC), UK, grant ST/M001253/1.

References

Akridge G., Benoit P. H. and Sears D. W. G. (1998) Regolith and megaregolith formation of H-chondrites: Thermal constraints on the parent body. *Icarus* **132**, 185–195.

Alexander C. M. O'D., Barber D. J. and Hutchison R. (1989) The microstructure of Semarkona and Bishunpur. *Geochimica et Cosmochimica Acta* **53**, 3045–3057.

Alexeyva K. N. (1958) Physical properties of stony meteorites and their interpretation based on the hypothesis on the origin of meteorites. *Meteoritika* **16**, 67–77.

Almeida N. V., Smith C. L., Sykes D., Downes H., Ahmed F. and Russell S. S. (2014) Locating porosity in chondrites with X-ray micro-computed tomography (μCT). *77th Annual Meeting of the Meteoritical Society*, Abstract #5032.

Bennett M. E. and McSween H. Y. (1996) Revised model calculations for the thermal histories of ordinary chondrite parent bodies. *Meteoritics & Planetary Science* **31**, 783–792.

Bland P. A., Sexton A. S., Jull A. J. T., Bevan A. W. R., Berry F. J., Thornley D. M., Astin T. R., Britt D. T. and Pillinger C. T. (1998) Climate and rock weathering: A study of terrestrial age dated ordinary chondritic meteorites from hot desert regions. *Geochimica et Cosmochimica Acta* **62**, 3169–3184.

Brearley A. J. (2006) The action of water. In *Meteorites and the Early Solar System II* (eds. D. S. Lauretta and H. Y. McSween). The University of Arizona Press, Tucson, AZ. pp. 587–624.

Brearley A. J. and Jones R. H. (1998) Chondritic meteorites. In *Planetary Materials* (ed. J. J. Papike). Reviews in Mineralogy and Geochemistry, vol. 36. p. 3.1-3.398.

Brown W. L., Becker S. M. and Parsons I. (1983) Cryptoperthites and cooling rate in a layered syenite pluton: A chemical and TEM study. *Contributions to Mineralogy and Petrology* **82**, 13–25.

Brown W. L. and Parsons I. (1989) Alkali feldspars: Ordering rates, phase transformations and behaviour diagrams for igneous rocks. *Mineralogical Magazine* **53**, 25–42.

Carpenter P. K., Hahn T. M., Korotev R. L., Zeigler R. A. and Jolliff B. L. (2017) Quantitative EPMA compositional mapping of NWA 2995: Characterization and petrologic interpretation of mafic clasts. *48th Lunar and Planetary Science Conference*, Abstract #2607.

Carpenter P. K., North S. N., Jolliff B. L. and Donovan J. J. (2013) EPMA quantitative compositional mapping and analysis of lunar samples. *44th Lunar and Planetary Science Conference*, Abstract #1827.

Carry B. (2012) Density of asteroids. *Planetary and Space Science* **73**, 98–118.

Choi B.-G., Kim H., Kim H., Lee J. I., Kim T. H., Ahn I., Yi K. and Hong T. E. (2015) Jinju H5 chondrite: A new fall in Korea having numerous vugs filled with vapor-phase crystallized minerals. *78th Annual Meeting of the Meteoritical Society*, Abstract #5091.

Christophe-Michel-Lévy M. (1979) La pierre de Sena: Des informations sur les conditions de formation de chondrites a bronzite. *Bulletin de Minéralogie* **102**, 410–414.

Cohen B. A. and Hewins R. H. (2004) An experimental study of the formation of metallic iron in chondrules. *Geochimica et Cosmochimica Acta* **68**, 1677–1689.

Connolly H. C. and Hewins R. H. (1995) Chondrules as products of dust collisions with totally molten droplets within a dust-rich nebular environment: An experimental investigation. *Geochimica et Cosmochimica Acta* **59**, 3231–3246.

Corrigan C. M., Zolensky M. E., Dahl J., Long M., Weir J., Sapp C. and Burkett P. J. (1997) The porosity and permeability of chondritic meteorites and interplanetary dust particles. *Meteoritics and Planetary Science* **32**.

Costa A. (2006) Permeability-porosity relationship: A reexamination of the Kozeny-Carman equation based on a fractal pore-space geometry assumption. *Geophysical Research Letters* **33**, 1–5.

Dobrică E. and Brearley A. J. (2014) Widespread hydrothermal alteration minerals in the fine-grained matrices of the Tieschitz unequilibrated ordinary chondrite. *Meteoritics & Planetary Science* **49**, 1323–1349.

Ebel D. S. and Rivers M. L. (2007) Meteorite 3-D synchrotron microtomography: Methods and applications. *Meteoritics & Planetary Science* **42**, 1627–1646.

Flynn G. J., Moore L. B. and Klöck W. (1999) Density and porosity of stone meteorites: Implications for the density, porosity, cratering, and collisional disruption of asteroids. *Icarus* **142**, 97–105.

Friedrich J. M., Bridges J. C., Wang M.-S. and Lipschutz M. E. (2004) Chemical studies of L chondrites. VI: Variations with petrographic type and shock-loading among equilibrated falls. *Geochimica et Cosmochimica Acta* **68**, 2889–2904.

Fruland R. M. (1975) Volatile movement in Rose City meteorite, and implications concerning the impact and late thermal history of ordinary chondrites. *Meteoritics* **10**, 403.

Fujiwara A., Kawaguchi J., Yeomans D. K., Abe M., Mukai T., Okada T., Saito J., Yano H., Yoshikawa M., Scheeres D. J., Barnouin-Jha O., Cheng A. F., Demura H., Gaskell R. W., Hirata N., Ikeda H., Kominato T., Miyamoto H., Nakamura A. M., Nakamura R., Sasaki S. and Uesugi K. (2006) The rubble-pile asteroid Itokawa as observed by Hayabusa. *Science* **312**, 1330–1334.

Girich A. L. and Semenenko V. P. (2003) Highly porous aggregates within the Saratov (L4) and Galkiv (H4) chondrites. *66th Annual Meeting of the Meteoritical Society*, Abstract #5006.

Grossman J. N., Alexander C. M. O'D., Wang J. and Brearley A. J. (2000) Bleached chondrules: Evidence for widespread aqueous processes on the parent asteroids of ordinary chondrites. *Meteoritics & Planetary Science* **35**, 467–486.

Grossman J. N., Alexander C. M. O'D., Wang J. and Brearley A. J. (2002) Zoned chondrules in Semarkona: Evidence for high- and low-temperature processing. *Meteoritics & Planetary Science* **37**, 49–73.

Harrison K. P. and Grimm R. E. (2010) Thermal constraints on the early history of the H-chondrite parent body reconsidered. *Geochimica et Cosmochimica Acta* **74**, 5410–5423.

Holsapple K. A. (2009) On the "strength" of the small bodies of the solar system: A review of strength theories and their implementation for analyses of impact disruptions. *Planetary and Space Science* **57**, 127–141.

Jones R. H. (1996) FeO-rich, porphyritic pyroxene chondrules in unequilibrated ordinary chondrites. *Geochimica et Cosmochimica Acta* **60**, 3115–3138.

Jones R. H., McCubbin F. M., Dreeland L., Guan Y., Burger P. V. and Shearer C. K. (2014) Phosphate minerals in LL chondrites: A record of the action of fluids during metamorphism on ordinary chondrite parent bodies. *Geochimica et Cosmochimica Acta* **132**, 120–140.

Jones R. H., McCubbin F. M. and Guan Y. (2016) Phosphate minerals in the H group of ordinary chondrites, and fluid activity recorded by apatite heterogeneity in the Zag H3-6 regolith breccia. *American Mineralogist* **101**, 2452–2467.

Kallemeyn G. W., Rubin A. E., Wang D. and Wasson J. T. (1989) Ordinary chondrites: Bulk compositions, classification, lithophile-element fractionations and composition-petrographic type relationships. *Geochimica et Cosmochimica Acta* **53**, 2747–2767.

Kessel R., Beckett J. R. and Stolper E. M. (2007) The thermal history of equilibrated ordinary chondrites and the relationship between textural maturity and temperature. *Geochimica et Cosmochimica Acta* **71**, 1855–1881.

Kovach H. A. and Jones R. H. (2010) Feldspar in type 4–6 ordinary chondrites: Metamorphic processing on the H and LL chondrite parent bodies. *Meteoritics & Planetary Science* **45**, 246–264.

Krot A. N. and Wasson J. T. (1994) Silica-merrihueite/roedderite-bearing chondrules and clasts in ordinary chondrites: New occurrences and possible origin. *Meteoritics* **29**, 707–718.

Lewis J. A. and Jones R. H. (2016a) Feldspar in the L4 chondrite Saratov: The history and timing of metasomatism. *79th Annual Meeting of the Meteoritical Society*, Abstract #6121.

Lewis J. A. and Jones R. H. (2014) Microtextural study of feldspar in petrologic type 3 LL ordinary chondrites: A record of parent body metasomatism. *77th Annual Meeting of the Meteoritical Society*, Abstract #5176.

Lewis J. A. and Jones R. H. (2015) Microtextural study of feldspar in petrologic type 4 ordinary chondrites: Contrasting records of parent body metasomatism. *78th Annual Meeting of the Meteoritical Society*, Abstract #5119.

Lewis J. A. and Jones R. H. (2016b) Phosphate and feldspar mineralogy of equilibrated L chondrites: The record of metasomatism during metamorphism in ordinary chondrite parent bodies. *Meteoritics & Planetary Science* **51**, 1886–1913.

Lewis J. A. and Jones R. H. (in review) Primary feldspar in the Semarkona LL3.00 chondrite: Constraints on chondrule formation and secondary alteration. *Meteoritics & Planetary Science*.

Lewis J. A., Jones R. H. and Brearley A. J. (2016) Alkali feldspar exsolution in ordinary chondrites: Alkali metasomatism, metamorphism, and cooling rates. *47th Lunar and Planetary Science Conference*, Abstract #2559.

Macke R. J. (2010) Survey of meteorite physical properties: Density, porosity and magnetic susceptibility. Ph.D. thesis, University of Central Florida.

Maharaj S. V. and Hewins R. H. (1998) Chondrule precursor minerals as anhydrous phases. *Meteoritics & Planetary Science* **33**, 881–887.

Maharaj S. V. and Hewins R. H. (1994) Clues to chondrule precursors: An investigation of vesicle formation in experimental chondrules. *Geochimica et Cosmochimica Acta* **58**, 1335–1342.

Maire E. and Withers P. J. (2014) Quantitative X-ray tomography. *International Materials Reviews* **59**, 1–43.

Miyamoto M., Fujii N. and Takeda H. (1981) Ordinary chondrite parent body: An internal heating model. *Lunar and Planetary Science Conference Proceedings* **12B**, 1145–1152.

Nakamura T., Noguchi T., Tanaka M., Zolensky M. E., Kimura M., Tsuchiyama A., Nakato A., Ogami T., Ishida H., Uesugi M., Yada T., Shirai K., Fujimura A., Okazaki R., Sandford S. A., Ishibashi Y., Abe M., Okada T., Ueno M., Mukai T., Yoshikawa M. and Kawaguchi J. (2011) Itokawa dust particles: A direct link between S-Type asteroids and ordinary chondrites. *Science* **333**, 1113–1116.

Olsen E. (1981) Vugs in ordinary chondrites. *Meteoritics* **16**, 45–59.

Opeil C. P., Consolmagno G. J., Safarik D. J. and Britt D. T. (2012) Stony meteorite thermal properties and their relationship with meteorite chemical and physical states. *Meteoritics & Planetary Science* **47**, 319–329.

Preibisch S., Saalfeld S. and Tomancak P. (2009) Globally optimal stitching of tiled 3D microscopic image acquisitions. *Bioinformatics* **25**, 1463–1465.

Rubin A. E. (1994) Metallic copper in ordinary chondrites. *Meteoritics* **29**, 93–98.

Sánchez P. and Scheeres D. J. (2014) The strength of regolith and rubble pile asteroids. *Meteoritics & Planetary Science* **49**, 788–811.

Scheeres D. J., Britt D., Carry B. and Holsapple K. A. (2015) Asteroid interiors and morphology. In *Asteroids IV* (eds. P. Michel, F. E. DeMeo, and W. F. Bottke). pp. 745–766.

Scott E. R. D. and Krot A. N. (2014) Chondrites and their components. In *Treatise on Geochemistry (Second Edition), Volume 1: Meteorites and Cosmochemical Processes* (ed. Davis A. M.). Elsevier, Oxford. pp. 65–137.

Scott E. R. D., Krot T. V., Goldstein J. I. and Wakita S. (2014) Thermal and impact history of the H chondrite parent asteroid during metamorphism: Constraints from metallic Fe–Ni. *Geochimica et Cosmochimica Acta* **136**, 13–37.

Seifert F. and Schreyer W. (1969) Stability relations of $K_2Mg_5Si_{12}O_{30}$, and end member of the merrihueite-roedderite group of meteoritic minerals. *Contributions to Mineralogy and Petrology* **22**, 190–207.

Semenenko V. P., Girich A. L. and Sharkin O. P. (1992) Highly porous fragments in Saratov (L4) ordinary chondrite. *Lunar and Planetary Science Conference Proceedings*, 1261–1262.

Sharygin V. V., Grokhovsky V. I. and Yakovlev G. A. (2015) Mineral condensates in black lithology of Chelyabinsk chondrite. *78th Annual Meeting of the Meteoritical Society*, Abstract #5274.

Smith B. A. and Goldstein J. I. (1977) The metallic microstructures and thermal histories of severely reheated chondrites. *Geochimica et Cosmochimica Acta* **41**, 1061–1072.

Taylor G. J., Keil K., Berkley J. L., Lange D. E., Fodor R. V. and Fruland R. M. (1979) The Shaw meteorite: History of a chondrite consisting of impact-melted and metamorphic lithologies. *Geochimica et Cosmochimica Acta* **43**, 323–337.

Wdowiak T. J. (1983) Experimental investigation of electrical discharge formation of chondrules. In *Chondrules and their Origins* (ed. E. A. King). pp. 279–283.

Wlotzka F. and Otto J. (2001) Euhedral crystals in interstitial pores of the Baszkówka and Mt. Tazerzait L5 chondrites. *Geological Quarterly* **45**, 257–262.

Wood J. A. and Holmberg B. B. (1994) Constraints placed on the chondrule-forming process by merrihueite in the Mezö-Madaras chondrite. *Icarus* **108**, 309–324.

Xie X. and Chen M. (1997) Shock-produced vapor-grown crystals in the Yanzhuang meteorite. *Science in China Series D: Earth Sciences* **40**, 113–119.

Zbik M. and Lang B. (1983) Morphological features of pore spaces in chondrules. In *Chondrules and their Origins* (ed. E. A. King). pp. 319–329.

APPENDICES

APPENDIX 1

Individual EPMA analyses

1. Individual EPMA analyses of apatite in L chondrites (chapter 1)

Table A1.1. Individual EPMA analyses of apatite in Santa Barbara (L4), n=18

analysis #	13	14	15	18	19	20	21	22	23	27	32	35	36	37	38	39	40	41	*mean*	*1-sig*
P_2O_5	40.5	40.7	41.2	41.0	41.1	40.6	40.5	40.1	41.2	40.0	41.3	39.8	39.8	40.1	40.0	40.1	40.4	41.2	*40.5*	*0.5*
Y_2O_3	<0.04	<0.04	<0.04	<0.04	<0.04	<0.04	<0.04	<0.04	<0.04	<0.04	<0.04	<0.04	<0.04	<0.04	<0.04	<0.04	<0.04	<0.04	*<0.04*	*0.00*
Ce_2O_3	<0.05	<0.05	<0.05	<0.05	<0.05	<0.05	<0.05	<0.05	<0.05	<0.05	<0.05	<0.05	<0.05	<0.05	<0.05	<0.05	<0.05	<0.05	*<0.05*	*0.00*
FeO	0.34	0.33	0.42	0.18	0.42	1.23	0.79	1.86	0.51	0.94	0.98	0.44	0.76	0.34	1.80	1.55	1.57	0.75	*0.84*	*0.54*
MgO	<0.02	<0.02	0.21	<0.02	<0.02	0.03	0.02	0.05	<0.02	0.06	0.02	0.04	0.07	0.03	0.20	0.10	0.05	0.03	*0.05*	*0.06*
CaO	52.6	53.3	53.1	53.5	53.6	52.5	52.6	52.1	53.0	52.4	52.7	52.0	51.9	52.0	51.5	52.2	52.7	53.3	*52.6*	*0.6*
Na_2O	0.37	0.34	0.49	0.37	0.36	0.35	0.34	0.34	0.37	0.36	0.37	0.34	0.33	0.38	0.37	0.36	0.37	0.38	*0.37*	*0.03*
F	0.45	0.47	0.38	0.38	0.44	0.47	0.40	0.35	0.44	0.44	0.51	0.54	0.48	0.44	0.38	0.36	0.47	0.42	*0.43*	*0.05*
Cl	5.16	5.27	4.74	5.50	5.38	5.31	5.44	5.52	5.54	5.28	5.17	5.39	5.19	5.50	4.88	5.22	5.25	5.47	*5.29*	*0.22*
F = -O	0.19	0.20	0.16	0.16	0.19	0.20	0.17	0.15	0.18	0.18	0.21	0.23	0.20	0.18	0.16	0.15	0.20	0.18	*0.18*	*0.02*
Cl = -O	1.16	1.19	1.07	1.24	1.21	1.20	1.23	1.25	1.25	1.19	1.17	1.22	1.17	1.24	1.10	1.18	1.18	1.23	*1.19*	*0.05*
total	98.1	99.0	99.4	99.6	99.9	99.1	98.7	98.9	99.6	98.1	99.7	97.1	97.2	97.4	97.9	98.6	99.4	100.2	*98.8*	*1.0*
Cl/F (wt)	11.6	11.3	12.6	14.7	12.2	11.3	13.7	16.0	12.7	12.0	10.2	10.0	10.7	12.5	12.8	14.6	11.3	13.0	*12.4*	*1.6*
								formula based on 13 anions												
P	3.00	3.00	3.00	3.00	3.00	2.99	2.99	2.97	3.01	2.98	3.01	2.99	2.99	3.00	2.98	2.98	2.98	3.00	*2.99*	*0.01*
Ce	0.00	0.00	0.00	0.00	0.00	0.00	0.00	0.00	0.00	0.00	0.00	0.00	0.00	0.00	0.00	0.00	0.00	0.00	*0.00*	*0.00*
Y	0.00	0.00	0.00	0.00	0.00	0.00	0.00	0.00	0.00	0.00	0.00	0.00	0.00	0.00	0.00	0.00	0.00	0.00	*0.00*	*0.00*
Fe	0.02	0.02	0.03	0.01	0.03	0.09	0.06	0.14	0.04	0.07	0.07	0.03	0.06	0.03	0.13	0.11	0.11	0.05	*0.06*	*0.04*
Mg	0.00	0.00	0.03	0.00	0.00	0.00	0.00	0.01	0.00	0.01	0.00	0.00	0.01	0.00	0.03	0.01	0.01	0.00	*0.01*	*0.01*
Ca	4.94	4.96	4.90	4.95	4.95	4.90	4.93	4.89	4.90	4.94	4.87	4.95	4.93	4.93	4.86	4.90	4.91	4.91	*4.92*	*0.03*
Na	0.06	0.06	0.08	0.06	0.06	0.06	0.06	0.06	0.06	0.06	0.06	0.06	0.06	0.06	0.06	0.06	0.06	0.06	*0.06*	*0.01*
F	0.12	0.13	0.10	0.10	0.12	0.13	0.11	0.10	0.12	0.12	0.14	0.15	0.14	0.12	0.11	0.10	0.13	0.11	*0.12*	*0.01*
Cl	0.77	0.78	0.69	0.81	0.79	0.78	0.81	0.82	0.81	0.79	0.75	0.81	0.78	0.82	0.73	0.77	0.77	0.80	*0.78*	*0.03*
total	8.92	8.94	8.83	8.94	8.94	8.95	8.95	8.98	8.95	8.97	8.91	9.00	8.96	8.97	8.89	8.94	8.97	8.94	*8.94*	*0.04*
cation total	8.03	8.04	8.04	8.03	8.04	8.04	8.04	8.07	8.01	8.06	8.01	8.04	8.04	8.03	8.06	8.06	8.07	8.03	*8.04*	*0.02*
X site anion total	0.89	0.90	0.79	0.91	0.91	0.91	0.92	0.92	0.93	0.91	0.89	0.96	0.91	0.95	0.83	0.87	0.90	0.91	*0.90*	*0.04*
missing component	0.11	0.10	0.21	0.09	0.09	0.09	0.08	0.08	0.07	0.09	0.11	0.04	0.09	0.05	0.17	0.13	0.10	0.09	*0.10*	*0.04*
tetrahedral total	3.00	3.00	3.00	3.00	3.00	2.99	2.99	2.97	3.01	2.98	3.01	2.99	2.99	3.00	2.98	2.98	2.98	3.00	*2.99*	*0.01*
octahedral total	5.03	5.04	5.03	5.03	5.04	5.05	5.05	5.09	5.00	5.07	5.00	5.05	5.05	5.02	5.08	5.09	5.09	5.03	*5.05*	*0.03*
Cl/F (atomic)	6.20	6.05	6.73	7.86	6.54	6.08	7.33	8.58	6.78	6.45	5.47	5.36	5.74	6.71	6.84	7.83	6.05	6.94	*6.64*	*0.85*
Cl/(Cl+F)×100	86.1	85.8	87.1	88.7	86.7	85.9	88.0	89.6	87.2	86.6	84.5	84.3	85.2	87.0	87.2	88.7	85.8	87.4	*86.8*	*1.4*

Table A1.2. Individual EPMA analyses of apatite in Elenovka (L5), n=18

analysis #	1	2	6	7	8	9	13	14	15	17	18	25	26	27	28	29	30	31	*mean*	*1-sig*
P_2O_5	41.1	40.9	41.2	40.7	41.0	41.1	40.7	40.9	41.0	41.2	40.7	40.6	40.8	40.5	40.7	41.0	40.7	39.7	*40.8*	*0.3*
Y_2O_3	<0.04	<0.04	<0.04	<0.04	<0.04	<0.04	<0.04	<0.04	<0.04	<0.04	<0.04	<0.04	0.04	<0.04	<0.04	<0.04	<0.04	<0.04	*<0.04*	*0.01*
Ce_2O_3	<0.05	<0.05	<0.05	0.05	<0.05	<0.05	<0.05	<0.05	<0.05	<0.05	<0.05	0.07	<0.05	<0.05	0.07	0.07	0.06	<0.05	*<0.05*	*0.03*
FeO	0.15	<0.10	0.10	0.13	0.19	0.19	0.33	0.53	0.53	0.28	0.21	0.15	0.32	0.37	0.26	0.21	0.15	0.13	*0.24*	*0.13*
MgO	<0.02	<0.02	<0.02	<0.02	<0.02	<0.02	<0.02	<0.02	<0.02	<0.02	<0.02	0.06	<0.02	0.02	0.02	0.02	<0.02	<0.02	*<0.02*	*0.01*
CaO	53.5	53.5	53.4	53.7	53.7	53.5	53.3	53.2	53.4	53.6	52.9	52.9	53.2	53.0	53.3	53.1	53.3	52.4	*53.3*	*0.3*
Na_2O	0.38	0.37	0.36	0.37	0.38	0.37	0.39	0.40	0.40	0.39	0.36	0.44	0.39	0.39	0.41	0.45	0.39	0.40	*0.39*	*0.02*
F	0.69	0.61	0.43	0.44	0.56	0.52	0.51	0.66	0.61	0.51	0.68	0.31	0.49	0.62	0.33	0.41	0.26	0.53	*0.51*	*0.13*
Cl	5.15	5.30	5.59	5.51	5.18	5.29	5.43	5.07	5.13	5.51	5.25	5.43	5.09	5.04	5.49	5.32	5.68	5.31	*5.32*	*0.19*
F = -O	0.16	0.16	0.15	0.16	0.16	0.16	0.17	0.17	0.17	0.17	0.15	0.18	0.16	0.17	0.17	0.19	0.16	0.17	*0.16*	*0.01*
Cl = -O	0.16	0.14	0.10	0.10	0.13	0.12	0.11	0.15	0.14	0.12	0.15	0.07	0.11	0.14	0.07	0.09	0.06	0.12	*0.11*	*0.03*
total	99.5	99.4	99.6	99.5	99.6	99.6	99.2	99.3	99.7	100.1	98.6	98.5	99.1	98.6	99.2	99.2	99.2	97.1	*99.2*	*0.7*
Cl/F (wt)	7.4	8.7	13.1	12.6	9.3	10.2	10.8	7.7	8.4	10.8	7.7	17.6	10.4	8.1	16.6	13.0	21.9	10.0	*11.3*	*3.9*
								formula based on 13 anions												
P	3.00	3.00	3.01	2.99	2.99	3.00	2.99	3.00	2.99	3.00	3.01	3.00	3.00	2.99	2.99	3.00	2.99	2.99	*3.00*	*0.01*
Ce	0.00	0.00	0.00	0.00	0.00	0.00	0.00	0.00	0.00	0.00	0.00	0.00	0.00	0.00	0.00	0.00	0.00	0.00	*0.00*	*0.00*
Y	0.00	0.00	0.00	0.00	0.00	0.00	0.00	0.00	0.00	0.00	0.00	0.00	0.00	0.00	0.00	0.00	0.00	0.00	*0.00*	*0.00*
Fe	0.01	0.01	0.01	0.01	0.01	0.01	0.02	0.04	0.04	0.02	0.02	0.01	0.02	0.03	0.02	0.02	0.01	0.01	*0.02*	*0.01*
Mg	0.00	0.00	0.00	0.00	0.00	0.00	0.00	0.00	0.00	0.00	0.00	0.01	0.00	0.00	0.00	0.00	0.00	0.00	*0.00*	*0.00*
Ca	4.95	4.96	4.94	4.99	4.97	4.95	4.96	4.93	4.94	4.94	4.94	4.95	4.95	4.96	4.96	4.93	4.97	4.99	*4.95*	*0.02*
Na	0.06	0.06	0.06	0.06	0.06	0.06	0.07	0.07	0.07	0.07	0.06	0.07	0.07	0.07	0.07	0.07	0.06	0.07	*0.07*	*0.00*
F	0.19	0.17	0.12	0.12	0.15	0.14	0.14	0.18	0.17	0.14	0.19	0.09	0.13	0.17	0.09	0.11	0.07	0.15	*0.14*	*0.03*
Cl	0.75	0.78	0.82	0.81	0.76	0.77	0.80	0.74	0.75	0.80	0.78	0.80	0.75	0.75	0.81	0.78	0.84	0.80	*0.78*	*0.03*
total	8.97	8.98	8.95	8.98	8.95	8.95	8.98	8.96	8.96	8.97	8.98	8.93	8.92	8.96	8.94	8.92	8.95	9.00	*8.96*	*0.02*
cation total	8.03	8.03	8.02	8.05	8.04	8.03	8.05	8.03	8.04	8.03	8.02	8.04	8.04	8.05	8.04	8.03	8.04	8.05	*8.04*	*0.01*
X site anion total	0.94	0.94	0.93	0.93	0.91	0.92	0.94	0.92	0.92	0.94	0.96	0.89	0.88	0.92	0.90	0.89	0.91	0.95	*0.92*	*0.02*
missing component	0.06	0.06	0.07	0.07	0.09	0.08	0.06	0.08	0.08	0.06	0.04	0.11	0.12	0.08	0.10	0.11	0.09	0.05	*0.08*	*0.02*
tetrahedral total	3.00	3.00	3.01	2.99	2.99	3.00	2.99	3.00	2.99	3.00	3.01	3.00	3.00	2.99	2.99	3.00	2.99	2.99	*3.00*	*0.01*
octahedral total	5.02	5.03	5.01	5.06	5.05	5.03	5.05	5.04	5.05	5.03	5.02	5.04	5.04	5.06	5.05	5.03	5.05	5.07	*5.04*	*0.02*
Cl/F (atomic)	3.98	4.65	7.00	6.78	4.99	5.46	5.77	4.14	4.51	5.78	4.15	9.42	5.58	4.34	8.89	6.95	11.71	5.37	*6.08*	*2.10*
Cl/(Cl+F)×100	79.9	82.3	87.5	87.1	83.3	84.5	85.2	80.6	81.9	85.2	80.6	90.4	84.8	81.3	89.9	87.4	92.1	84.3	*84.9*	*3.6*

Table A1.3. Individual EPMA analyses of apatite in Bruderheim (L6), n=16

analysis #	7	8	9	10	11	12	17	18	19	20	21	28	34	35	36	37	*mean*	*1-sig*
P_2O_5	40.6	40.2	40.4	41.1	40.7	40.4	40.8	41.0	41.0	40.8	40.7	41.0	40.8	40.8	40.9	40.6	*40.8*	*0.2*
Y_2O_3	<0.04	<0.04	<0.04	<0.04	<0.04	<0.04	<0.04	<0.04	<0.04	<0.04	<0.04	<0.04	<0.04	<0.04	<0.04	<0.04	*<0.04*	*0.00*
Ce_2O_3	<0.05	<0.05	<0.05	0.06	<0.05	0.05	0.06	0.10	0.06	0.07	<0.05	0.05	0.05	0.05	<0.05	0.08	*0.05*	*0.02*
FeO	0.16	0.24	0.56	0.25	0.40	0.26	0.35	0.39	0.15	0.23	0.23	0.32	0.28	0.33	0.42	0.43	*0.31*	*0.11*
MgO	<0.02	<0.02	0.03	0.02	0.04	0.04	0.09	0.09	<0.02	0.04	0.04	0.04	0.03	<0.02	0.03	0.05	*0.04*	*0.02*
CaO	53.3	53.4	53.1	53.6	52.9	52.5	53.2	53.4	53.9	53.6	53.5	53.4	53.3	53.6	53.5	53.4	*53.4*	*0.3*
Na_2O	0.34	0.35	0.41	0.36	0.38	0.41	0.36	0.40	0.39	0.42	0.41	0.36	0.36	0.36	0.34	0.35	*0.37*	*0.03*
F	0.41	0.40	0.48	0.64	0.60	0.51	0.74	0.80	0.56	0.55	0.51	0.34	0.81	0.78	0.63	0.56	*0.58*	*0.14*
Cl	5.44	5.28	5.16	4.88	4.98	5.32	4.92	4.43	5.16	5.17	5.15	5.33	5.14	5.03	5.00	5.06	*5.09*	*0.23*
F = -O	0.17	0.17	0.20	0.27	0.25	0.21	0.31	0.34	0.23	0.23	0.22	0.14	0.34	0.33	0.27	0.23	*0.24*	*0.06*
Cl = -O	1.23	1.19	1.16	1.10	1.12	1.20	1.11	1.00	1.16	1.17	1.16	1.20	1.16	1.14	1.13	1.14	*1.15*	*0.05*
total	98.9	98.6	98.8	99.5	98.6	98.1	99.1	99.3	99.8	99.4	99.3	99.5	99.3	99.6	99.5	99.2	*99.2*	*0.4*
Cl/F (wt)	13.3	13.4	10.9	7.6	8.3	10.5	6.7	5.6	9.3	9.4	10.0	15.6	6.4	6.5	7.9	9.1	*9.4*	*2.8*
							formula based on 13 anions											
P	2.99	2.98	2.98	3.00	3.00	3.00	2.99	2.99	2.99	2.99	2.99	3.00	3.00	2.99	2.99	2.99	*2.99*	*0.01*
Ce	0.00	0.00	0.00	0.00	0.00	0.00	0.00	0.00	0.00	0.00	0.00	0.00	0.00	0.00	0.00	0.00	*0.00*	*0.00*
Y	0.00	0.00	0.00	0.00	0.00	0.00	0.00	0.00	0.00	0.00	0.00	0.00	0.00	0.00	0.00	0.00	*0.00*	*0.00*
Fe	0.01	0.02	0.04	0.02	0.03	0.02	0.03	0.03	0.01	0.02	0.02	0.02	0.02	0.02	0.03	0.03	*0.02*	*0.01*
Mg	0.00	0.00	0.00	0.00	0.00	0.00	0.01	0.01	0.00	0.00	0.01	0.00	0.00	0.00	0.00	0.01	*0.00*	*0.00*
Ca	4.97	5.00	4.96	4.95	4.93	4.94	4.94	4.94	4.97	4.97	4.97	4.94	4.95	4.97	4.95	4.96	*4.96*	*0.02*
Na	0.06	0.06	0.07	0.06	0.06	0.07	0.06	0.07	0.07	0.07	0.07	0.06	0.06	0.06	0.06	0.06	*0.06*	*0.00*
F	0.11	0.11	0.13	0.18	0.16	0.14	0.20	0.22	0.15	0.15	0.14	0.09	0.22	0.21	0.17	0.15	*0.16*	*0.04*
Cl	0.80	0.78	0.76	0.71	0.74	0.79	0.72	0.65	0.75	0.76	0.76	0.78	0.75	0.74	0.73	0.74	*0.75*	*0.04*
total	8.95	8.95	8.95	8.92	8.93	8.96	8.96	8.91	8.95	8.96	8.95	8.90	9.01	9.00	8.94	8.95	*8.95*	*0.03*
cation total	8.04	8.06	8.06	8.03	8.03	8.03	8.04	8.04	8.04	8.05	8.05	8.03	8.03	8.05	8.04	8.05	*8.04*	*0.01*
X site anion total	0.92	0.89	0.89	0.89	0.90	0.93	0.92	0.87	0.90	0.91	0.90	0.87	0.98	0.95	0.90	0.90	*0.91*	*0.03*
missing component	0.08	0.11	0.11	0.11	0.10	0.07	0.08	0.13	0.10	0.09	0.10	0.13	0.02	0.05	0.10	0.10	*0.09*	*0.03*
tetrahedral total	2.99	2.98	2.98	3.00	3.00	3.00	2.99	2.99	2.99	2.99	2.99	3.00	3.00	2.99	2.99	2.99	*2.99*	*0.01*
octahedral total	5.04	5.08	5.08	5.03	5.03	5.03	5.04	5.05	5.05	5.06	5.06	5.03	5.04	5.06	5.05	5.06	*5.05*	*0.02*
Cl/F (atomic)	7.11	7.16	5.82	4.06	4.46	5.61	3.58	2.98	4.98	5.03	5.37	8.38	3.41	3.46	4.26	4.87	*5.03*	*1.52*
Cl/(Cl+F)×100	87.7	87.7	85.3	80.3	81.7	84.9	78.2	74.8	83.3	83.4	84.3	89.3	77.3	77.6	81.0	83.0	*82.5*	*4.1*

Table A1.4. Individual EPMA analyses of apatite in Kendleton (L3 clast), n=6

analysis #	55	56	57	58	59	60	*mean*	*1-sig*
P_2O_5	41.2	41.5	41.1	40.6	40.5	39.8	*40.8*	*0.6*
Y_2O_3	<0.04	<0.04	<0.04	<0.04	<0.04	<0.04	*<0.04*	*0.00*
Ce_2O_3	<0.05	<0.05	<0.05	<0.05	0.06	<0.05	*<0.05*	*0.02*
FeO	0.17	0.17	0.16	0.17	0.31	0.60	*0.26*	*0.17*
MgO	<0.02	0.02	0.03	0.05	0.06	0.05	*0.04*	*0.02*
CaO	55.0	55.4	54.5	53.3	52.9	52.8	*54.0*	*1.1*
Na_2O	0.39	0.41	0.40	0.38	0.36	0.42	*0.39*	*0.02*
F	0.58	0.67	0.61	0.38	0.39	0.47	*0.52*	*0.12*
Cl	4.83	4.74	4.63	5.38	5.35	5.17	*5.02*	*0.33*
F = -O	0.24	0.28	0.26	0.16	0.16	0.20	*0.22*	*0.05*
Cl = -O	1.09	1.07	1.04	1.21	1.21	1.17	*1.13*	*0.07*
total	100.9	101.6	100.2	99.0	98.6	97.9	*99.7*	*1.4*
Cl/F (wt)	8.4	7.1	7.6	14.3	13.7	11.1	*10.3*	*3.1*
	formula based on 13 anions							
P	2.97	2.97	2.98	2.99	2.99	2.97	*2.98*	*0.01*
Ce	0.00	0.00	0.00	0.00	0.00	0.00	*0.00*	*0.00*
Y	0.00	0.00	0.00	0.00	0.00	0.00	*0.00*	*0.00*
Fe	0.01	0.01	0.01	0.01	0.02	0.04	*0.02*	*0.01*
Mg	0.00	0.00	0.00	0.01	0.01	0.01	*0.00*	*0.00*
Ca	5.03	5.02	5.00	4.97	4.95	4.98	*4.99*	*0.03*
Na	0.06	0.07	0.07	0.06	0.06	0.07	*0.07*	*0.00*
F	0.16	0.18	0.17	0.10	0.11	0.13	*0.14*	*0.03*
Cl	0.70	0.68	0.67	0.79	0.79	0.77	*0.73*	*0.06*
total	8.93	8.94	8.90	8.94	8.94	8.98	*8.94*	*0.03*
cation total	8.08	8.08	8.06	8.05	8.04	8.08	*8.06*	*0.02*
X site anion total	0.85	0.86	0.84	0.90	0.90	0.90	*0.87*	*0.03*
missing component	0.15	0.14	0.16	0.10	0.10	0.10	*0.13*	*0.03*
tetrahedral total	2.97	2.97	2.98	2.99	2.99	2.97	*2.98*	*0.01*
octahedral total	5.11	5.10	5.08	5.06	5.05	5.11	*5.08*	*0.03*
Cl/F (atomic)	4.48	3.80	4.05	7.64	7.35	5.94	*5.54*	*1.69*
Cl/(Cl+F)×100	81.8	79.2	80.2	88.4	88.0	85.6	*83.9*	*4.0*

Table A1.5. Individual EPMA analyses of apatite in Kendleton (L4 host), n=17

analysis #	2	3	9	10	11	12	13	19	20	21	22	25	26	27	28	29	31	*mean*	*1-sig*
P_2O_5	40.8	40.9	41.3	40.4	41.0	40.5	40.7	41.1	41.0	41.4	40.4	41.5	41.3	41.6	40.4	40.7	41.4	*41.0*	*0.4*
Y_2O_3	<0.04	<0.04	0.05	<0.04	<0.04	<0.04	<0.04	<0.04	<0.04	<0.04	<0.04	0.07	0.04	<0.04	<0.04	<0.04	0.04	*<0.04*	*0.02*
Ce_2O_3	0.06	0.10	0.06	0.06	<0.05	<0.05	<0.05	<0.05	0.06	<0.05	<0.05	<0.05	<0.05	<0.05	<0.05	0.07	<0.05	*<0.05*	*0.03*
FeO	0.28	0.61	0.38	1.92	0.61	0.61	0.46	0.18	0.28	0.23	0.44	0.62	0.31	0.33	0.90	0.84	0.29	*0.55*	*0.41*
MgO	0.12	0.09	0.10	0.36	0.19	0.19	0.12	0.11	0.06	0.57	0.06	0.06	0.05	0.13	0.11	0.54	0.31	*0.18*	*0.16*
CaO	53.1	52.8	53.5	51.8	53.4	52.6	53.6	53.0	53.3	51.8	52.7	53.6	54.0	53.7	52.7	51.9	52.7	*53.0*	*0.7*
Na_2O	0.34	0.36	0.34	0.37	0.34	0.33	0.32	0.37	0.34	0.71	0.34	0.34	0.35	0.36	0.32	0.54	0.47	*0.38*	*0.10*
F	1.22	0.94	1.09	1.19	1.17	1.22	1.16	1.24	1.28	1.10	1.41	1.11	1.32	1.25	1.03	0.84	0.86	*1.14*	*0.15*
Cl	4.05	4.13	3.97	3.67	4.09	3.88	4.09	3.95	3.93	3.58	3.86	4.15	3.78	3.91	4.07	3.70	3.60	*3.91*	*0.19*
F = -O	0.51	0.40	0.46	0.50	0.49	0.51	0.49	0.52	0.54	0.46	0.59	0.47	0.55	0.53	0.44	0.35	0.36	*0.48*	*0.07*
Cl = -O	0.91	0.93	0.90	0.83	0.92	0.87	0.92	0.89	0.89	0.81	0.87	0.94	0.85	0.88	0.92	0.84	0.81	*0.88*	*0.04*
total	98.5	98.7	99.5	98.4	99.5	98.0	99.0	98.6	98.7	98.2	97.7	100.0	99.7	99.9	98.2	97.9	98.5	*98.8*	*0.7*
Cl/F (wt)	3.33	4.40	3.63	3.10	3.50	3.17	3.54	3.20	3.07	3.24	2.75	3.75	2.87	3.12	3.94	4.39	4.21	*3.48*	*0.51*
								formula based on 13 anions											
P	3.00	3.00	3.00	2.98	2.99	2.99	2.98	3.01	3.00	3.02	3.00	3.00	2.99	3.01	2.98	2.99	3.01	*3.00*	*0.01*
Ce	0.00	0.00	0.00	0.00	0.00	0.00	0.00	0.00	0.00	0.00	0.00	0.00	0.00	0.00	0.00	0.00	0.00	*0.00*	*0.00*
Y	0.00	0.00	0.00	0.00	0.00	0.00	0.00	0.00	0.00	0.00	0.00	0.00	0.00	0.00	0.00	0.00	0.00	*0.00*	*0.00*
Fe	0.02	0.04	0.03	0.14	0.04	0.04	0.03	0.01	0.02	0.02	0.03	0.04	0.02	0.02	0.07	0.06	0.02	*0.04*	*0.03*
Mg	0.02	0.01	0.01	0.05	0.02	0.02	0.02	0.01	0.01	0.07	0.01	0.01	0.01	0.02	0.01	0.07	0.04	*0.02*	*0.02*
Ca	4.94	4.91	4.92	4.84	4.93	4.91	4.97	4.92	4.94	4.79	4.94	4.91	4.95	4.91	4.93	4.84	4.86	*4.91*	*0.05*
Na	0.06	0.06	0.06	0.06	0.06	0.06	0.05	0.06	0.06	0.12	0.06	0.06	0.06	0.06	0.05	0.09	0.08	*0.06*	*0.02*
F	0.33	0.26	0.30	0.33	0.32	0.34	0.32	0.34	0.35	0.30	0.39	0.30	0.36	0.34	0.29	0.23	0.23	*0.31*	*0.04*
Cl	0.60	0.61	0.58	0.54	0.60	0.57	0.60	0.58	0.58	0.52	0.57	0.60	0.55	0.57	0.60	0.55	0.53	*0.57*	*0.03*
total	8.96	8.89	8.90	8.93	8.96	8.95	8.97	8.93	8.95	8.85	9.00	8.92	8.94	8.92	8.94	8.83	8.78	*8.92*	*0.06*
cation total	8.03	8.03	8.02	8.06	8.04	8.04	8.06	8.02	8.03	8.02	8.03	8.02	8.04	8.02	8.05	8.05	8.02	*8.03*	*0.01*
X site anion total	0.93	0.86	0.87	0.87	0.91	0.91	0.92	0.92	0.93	0.82	0.96	0.90	0.90	0.90	0.89	0.78	0.76	*0.88*	*0.05*
missing component	0.07	0.14	0.13	0.13	0.09	0.09	0.08	0.08	0.07	0.18	0.04	0.10	0.10	0.10	0.11	0.22	0.24	*0.12*	*0.05*
tetrahedral total	3.00	3.00	3.00	2.98	2.99	2.99	2.98	3.01	3.00	3.02	3.00	3.00	2.99	3.01	2.98	2.99	3.01	*3.00*	*0.01*
octahedral total	5.03	5.02	5.02	5.09	5.05	5.04	5.08	5.01	5.03	5.00	5.04	5.02	5.04	5.01	5.07	5.06	5.00	*5.04*	*0.03*
Cl/F (atomic)	1.78	2.36	1.95	1.66	1.88	1.70	1.90	1.71	1.65	1.74	1.47	2.01	1.54	1.67	2.11	2.35	2.25	*1.87*	*0.27*
Cl/(Cl+F)×100	64.1	70.2	66.1	62.4	65.2	63.0	65.5	63.2	62.2	63.5	59.6	66.8	60.6	62.6	67.8	70.2	69.3	*64.8*	*3.2*

Table A1.6. Individual EPMA analyses of apatite in Kendleton (L5 clast), n=20 (1-15)

analysis #	94	102	109	110	111	112	118	125	126	127	128	129	130	131	132
P_2O_5	41.1	41.3	40.2	40.8	40.8	40.9	41.2	40.5	41.4	41.2	41.7	40.7	40.8	40.9	41.6
Y_2O_3	<0.04	0.04	<0.04	<0.04	<0.04	<0.04	<0.04	<0.04	<0.04	<0.04	<0.04	<0.04	<0.04	<0.04	<0.04
Ce_2O_3	0.05	<0.05	<0.05	<0.05	<0.05	0.08	0.08	<0.05	<0.05	0.05	<0.05	<0.05	<0.05	0.05	0.06
FeO	0.20	0.25	0.26	0.17	0.48	0.18	0.36	0.19	0.14	0.11	0.11	0.18	0.15	0.33	0.14
MgO	0.04	0.03	0.03	<0.02	0.04	0.02	0.03	0.04	<0.02	0.02	0.04	<0.02	0.05	0.08	0.03
CaO	53.7	54.7	53.1	53.3	53.2	52.9	54.5	52.6	54.9	53.5	54.9	53.3	53.8	52.6	54.3
Na_2O	0.43	0.44	0.39	0.39	0.43	0.44	0.38	0.41	0.40	0.45	0.38	0.40	0.40	0.40	0.42
F	0.59	0.70	0.56	0.50	0.50	0.60	0.67	0.60	0.79	0.61	0.67	0.62	0.73	0.69	0.71
Cl	5.06	4.90	5.14	5.14	5.11	5.13	4.85	5.17	4.60	5.30	4.68	5.18	4.86	5.19	4.80
F = -O	0.25	0.29	0.24	0.21	0.21	0.25	0.28	0.25	0.33	0.26	0.28	0.26	0.31	0.29	0.30
Cl = -O	1.14	1.10	1.16	1.16	1.15	1.16	1.09	1.17	1.04	1.20	1.06	1.17	1.10	1.17	1.08
total	99.8	101.0	98.4	99.0	99.2	98.9	100.7	98.1	100.8	99.7	101.2	98.9	99.5	98.8	100.7
Cl/F (wt)	8.5	7.0	9.2	10.2	10.2	8.6	7.2	8.6	5.8	8.7	7.0	8.4	6.7	7.5	6.7
	formula based on 13 anions														
P	3.00	2.98	2.98	3.00	2.99	3.01	2.98	3.00	2.98	3.00	2.99	3.00	2.99	3.01	3.00
Ce	0.00	0.00	0.00	0.00	0.00	0.00	0.00	0.00	0.00	0.00	0.00	0.00	0.00	0.00	0.00
Y	0.00	0.00	0.00	0.00	0.00	0.00	0.00	0.00	0.00	0.00	0.00	0.00	0.00	0.00	0.00
Fe	0.01	0.02	0.02	0.01	0.03	0.01	0.03	0.01	0.01	0.01	0.01	0.01	0.01	0.02	0.01
Mg	0.00	0.00	0.00	0.00	0.00	0.00	0.00	0.01	0.00	0.00	0.00	0.00	0.01	0.01	0.00
Ca	4.95	4.99	4.99	4.95	4.94	4.93	4.99	4.94	5.00	4.94	4.98	4.96	4.98	4.90	4.95
Na	0.07	0.07	0.07	0.07	0.07	0.07	0.06	0.07	0.07	0.07	0.06	0.07	0.07	0.07	0.07
F	0.16	0.19	0.15	0.14	0.14	0.16	0.18	0.17	0.21	0.17	0.18	0.17	0.20	0.19	0.19
Cl	0.74	0.71	0.76	0.76	0.75	0.75	0.70	0.77	0.66	0.77	0.67	0.76	0.71	0.76	0.69
total	8.94	8.96	8.98	8.93	8.93	8.94	8.94	8.97	8.94	8.97	8.90	8.97	8.96	8.97	8.92
cation total	8.04	8.07	8.06	8.03	8.04	8.03	8.06	8.03	8.06	8.03	8.05	8.04	8.05	8.02	8.03
X site anion total	0.90	0.90	0.92	0.89	0.89	0.92	0.88	0.93	0.87	0.94	0.85	0.93	0.91	0.96	0.88
missing component	0.10	0.10	0.08	0.11	0.11	0.08	0.12	0.07	0.13	0.06	0.15	0.07	0.09	0.04	0.12
tetrahedral total	3.00	2.98	2.98	3.00	2.99	3.01	2.98	3.00	2.98	3.00	2.99	3.00	2.99	3.01	3.00
octahedral total	5.04	5.09	5.08	5.03	5.05	5.02	5.08	5.03	5.08	5.03	5.06	5.05	5.07	5.01	5.03
Cl/F (atomic)	4.57	3.75	4.93	5.47	5.45	4.59	3.87	4.59	3.13	4.64	3.73	4.48	3.56	4.02	3.61
Cl/(Cl+F)×100	82.1	78.9	83.1	84.5	84.5	82.1	79.5	82.1	75.8	82.3	78.9	81.8	78.1	80.1	78.3

Table A1.6. *(Continued).* Individual EPMA analyses of apatite in Kendleton (L5 clast), n=20 (16-20)

analysis #	133	134	135	136	137	*mean*	*1-sig*
P_2O_5	41.0	40.6	41.2	41.3	41.0	*41.0*	*0.4*
Y_2O_3	<0.04	<0.04	<0.04	<0.04	<0.04	*<0.04*	*0.01*
Ce_2O_3	<0.05	<0.05	<0.05	0.08	0.05	*<0.05*	*0.03*
FeO	0.40	0.88	0.50	0.20	0.19	*0.27*	*0.18*
MgO	<0.02	<0.02	<0.02	<0.02	<0.02	*0.02*	*0.02*
CaO	53.9	52.6	53.4	54.3	54.4	*53.7*	*0.8*
Na_2O	0.41	0.39	0.38	0.39	0.40	*0.41*	*0.02*
F	0.49	0.41	0.53	0.44	0.49	*0.60*	*0.10*
Cl	5.19	5.22	5.12	5.20	5.08	*5.05*	*0.19*
F = -O	0.20	0.17	0.22	0.19	0.21	*0.25*	*0.04*
Cl = -O	1.17	1.18	1.16	1.17	1.15	*1.14*	*0.04*
total	100.0	98.8	99.7	100.6	100.2	*99.7*	*0.9*
Cl/F (wt)	10.7	12.8	9.7	11.7	10.3	*8.8*	*1.8*
	formula based on 13 anions						
P	2.99	3.00	3.00	2.99	2.98	*2.99*	*0.01*
Ce	0.00	0.00	0.00	0.00	0.00	*0.00*	*0.00*
Y	0.00	0.00	0.00	0.00	0.00	*0.00*	*0.00*
Fe	0.03	0.06	0.04	0.01	0.01	*0.02*	*0.01*
Mg	0.00	0.00	0.00	0.00	0.00	*0.00*	*0.00*
Ca	4.97	4.91	4.92	4.98	5.00	*4.96*	*0.03*
Na	0.07	0.07	0.06	0.06	0.07	*0.07*	*0.00*
F	0.13	0.11	0.14	0.12	0.13	*0.16*	*0.03*
Cl	0.76	0.77	0.75	0.75	0.74	*0.74*	*0.03*
total	8.94	8.92	8.92	8.92	8.94	*8.94*	*0.02*
cation total	8.05	8.04	8.03	8.05	8.06	*8.04*	*0.01*
X site anion total	0.89	0.88	0.89	0.87	0.87	*0.90*	*0.03*
missing component	0.11	0.12	0.11	0.13	0.13	*0.10*	*0.03*
tetrahedral total	2.99	3.00	3.00	2.99	2.98	*2.99*	*0.01*
octahedral total	5.07	5.04	5.03	5.06	5.09	*5.05*	*0.02*
Cl/F (atomic)	5.71	6.88	5.21	6.29	5.54	*4.70*	*0.99*
Cl/(Cl+F)×100	85.1	87.3	83.9	86.3	84.7	*82.0*	*3.1*

2. Individual EPMA analyses of merrillite in L chondrites (chapter 1)

Table A1.7. Individual EPMA analyses of merrillite in Santa Barbara (L4), n=22

analysis #	P_2O_5	Y_2O_3	Ce_2O_3	CaO	MgO	FeO	Na_2O	total		P	Y	Ce	Ca	Mg	Fe	Na	total	Mg#
1	45.5	<0.04	<0.05	46.3	3.50	1.26	2.70	99.3		13.9	0.00	0.00	18.0	1.89	0.38	1.89	36.1	83.2
2	45.1	0.04	0.07	44.5	3.41	2.77	2.72	98.6		14.0	0.01	0.01	17.4	1.86	0.85	1.93	36.0	68.7
3	46.3	<0.04	0.05	47.2	3.42	0.40	2.66	100.1		14.0	0.00	0.01	18.1	1.82	0.12	1.84	35.9	93.8
4	46.5	<0.04	0.07	46.8	3.46	0.40	2.68	99.9		14.1	0.00	0.01	17.9	1.84	0.12	1.86	35.8	94.0
5	46.3	0.06	<0.05	47.1	3.46	0.36	2.70	99.9		14.0	0.01	0.00	18.0	1.85	0.11	1.87	35.9	94.6
6	46.3	0.04	<0.05	47.0	3.47	0.33	2.67	99.8		14.0	0.01	0.00	18.0	1.85	0.10	1.85	35.9	95.0
7	46.4	0.05	<0.05	47.1	3.49	0.50	2.72	100.3		14.0	0.01	0.01	18.0	1.85	0.15	1.88	35.9	92.6
8	45.8	0.07	<0.05	46.7	3.58	0.68	2.59	99.4		14.0	0.01	0.00	18.0	1.92	0.20	1.81	35.9	90.4
9	45.8	0.06	<0.05	46.8	3.46	0.66	2.26	99.0		14.0	0.01	0.00	18.1	1.87	0.20	1.59	35.8	90.4
10	46.1	<0.04	0.05	46.6	3.42	0.64	2.63	99.4		14.0	0.01	0.01	18.0	1.83	0.19	1.83	35.9	90.6
11	45.3	0.07	<0.05	46.4	3.42	2.01	1.74	99.0		13.9	0.01	0.00	18.1	1.85	0.61	1.23	35.7	75.2
12	45.5	0.07	<0.05	46.0	3.36	1.84	2.30	99.1		14.0	0.01	0.01	17.9	1.82	0.56	1.61	35.9	76.5
16	45.3	<0.04	0.06	46.3	3.42	0.77	2.58	98.4		14.0	0.00	0.01	18.0	1.86	0.24	1.82	35.9	88.8
24	44.3	0.05	<0.05	44.9	3.69	1.88	2.55	97.3		13.9	0.01	0.00	17.8	2.04	0.58	1.83	36.1	77.8
25	45.0	0.06	<0.05	45.8	3.39	1.04	2.58	97.9		14.0	0.01	0.00	18.0	1.85	0.32	1.83	36.0	85.3
26	45.7	<0.04	<0.05	46.2	3.38	0.62	2.69	98.6		14.0	0.01	0.00	17.9	1.83	0.19	1.89	35.9	90.7
42	44.7	0.06	<0.05	46.0	3.24	1.25	2.48	97.7		13.9	0.01	0.00	18.1	1.77	0.39	1.77	36.0	82.2
43	44.4	<0.04	0.06	45.3	3.39	1.74	2.54	97.5		13.9	0.00	0.01	18.0	1.87	0.54	1.82	36.1	77.7
45	45.4	0.06	<0.05	46.3	3.40	1.25	2.67	99.1		13.9	0.01	0.00	18.0	1.84	0.38	1.87	36.0	82.9
46	46.1	0.04	<0.05	47.1	3.42	0.44	2.66	99.8		14.0	0.01	0.00	18.1	1.83	0.13	1.85	35.9	93.2
47	45.6	<0.04	<0.05	46.3	3.40	1.04	2.73	99.1		14.0	0.00	0.01	17.9	1.83	0.32	1.92	36.0	85.3
48	45.5	0.06	<0.05	46.4	3.43	1.23	2.68	99.4		13.9	0.01	0.00	18.0	1.85	0.37	1.88	36.0	83.2
mean	*45.6*	*0.04*	*<0.05*	*46.3*	*3.44*	*1.05*	*2.57*	*99.0*		*14.0*	*0.01*	*0.00*	*18.0*	*1.86*	*0.32*	*1.80*	*35.9*	*86.0*
1-sig	*0.6*	*0.02*	*0.02*	*0.7*	*0.09*	*0.66*	*0.22*	*0.9*		*0.1*	*0.00*	*0.00*	*0.1*	*0.05*	*0.20*	*0.15*	*0.1*	*7.4*

formula based on 56 oxygens

Table A1.8. Individual EPMA analyses of merrillite in Elenovka (L5), n=12

analysis #	P_2O_5	Y_2O_3	Ce_2O_3	CaO	MgO	FeO	Na_2O	total		P	Y	Ce	Ca	Mg	Fe	Na	total	Mg#
3	45.4	<0.04	<0.05	47.0	3.39	0.34	2.64	98.8		13.9	0.01	0.00	18.3	1.83	0.10	1.85	36.0	94.7
4	46.1	0.07	<0.05	46.8	3.43	0.42	2.65	99.5		14.0	0.01	0.00	18.0	1.84	0.13	1.84	35.9	93.6
5	45.4	0.04	<0.05	47.0	3.40	0.45	2.66	98.9		13.9	0.01	0.00	18.2	1.84	0.14	1.87	36.0	93.1
19	45.8	0.04	<0.05	46.7	3.38	0.70	2.62	99.4		14.0	0.01	0.01	18.1	1.82	0.21	1.83	35.9	89.6
20	45.7	0.04	0.06	46.7	3.37	0.66	2.59	99.1		14.0	0.01	0.01	18.1	1.81	0.20	1.82	35.9	90.1
21	45.9	<0.04	0.06	46.7	3.41	0.67	2.67	99.3		14.0	0.00	0.01	18.0	1.83	0.20	1.87	35.9	90.1
22	44.6	<0.04	<0.05	45.8	3.83	0.88	2.60	97.8		13.9	0.00	0.00	18.0	2.09	0.27	1.85	36.1	88.5
23	44.9	<0.04	<0.05	46.1	3.54	0.80	2.61	98.0		13.9	0.00	0.01	18.1	1.93	0.24	1.85	36.0	88.8
32	45.8	<0.04	0.05	46.7	3.47	0.40	2.68	99.1		14.0	0.00	0.01	18.1	1.87	0.12	1.88	35.9	93.9
33	45.6	<0.04	0.06	46.4	3.36	0.43	2.59	98.5		14.0	0.00	0.01	18.1	1.82	0.13	1.82	35.9	93.4
35	45.4	<0.04	<0.05	46.4	3.38	0.59	2.62	98.4		14.0	0.00	0.01	18.1	1.83	0.18	1.85	36.0	91.1
36	45.8	<0.04	0.06	46.2	3.69	0.44	3.03	99.3		14.0	0.00	0.01	17.8	1.98	0.13	2.12	36.1	93.7
mean	*45.5*	*<0.04*	*<0.05*	*46.5*	*3.47*	*0.56*	*2.66*	*98.8*		*14.0*	*0.00*	*0.01*	*18.1*	*1.87*	*0.17*	*1.87*	*36.0*	*91.7*
1-sig	*0.4*	*0.02*	*0.02*	*0.4*	*0.15*	*0.18*	*0.12*	*0.6*		*0.0*	*0.00*	*0.00*	*0.1*	*0.09*	*0.05*	*0.08*	*0.1*	*2.2*

formula based on 56 oxygens

Table A1.9. Individual EPMA analyses of merrillite in Bruderheim (L6), n=15

analysis #	P_2O_5	Y_2O_3	Ce_2O_3	CaO	MgO	FeO	Na_2O	total		P	Y	Ce	Ca	Mg	Fe	Na	total	Mg#
4	45.4	0.05	0.05	46.4	3.45	1.16	2.65	99.2		13.9	0.01	0.01	18.0	1.86	0.35	1.86	36.0	84.2
6	45.6	0.04	0.08	46.6	3.47	0.77	2.66	99.2		14.0	0.01	0.01	18.0	1.87	0.23	1.86	36.0	89.0
13	45.5	0.04	<0.05	46.5	3.41	0.38	2.65	98.5		14.0	0.01	0.00	18.1	1.85	0.12	1.87	35.9	94.0
14	45.5	<0.04	0.05	46.6	3.39	0.41	2.61	98.6		14.0	0.01	0.01	18.1	1.83	0.12	1.84	35.9	93.6
15	45.5	<0.04	0.06	46.6	3.44	0.41	2.70	98.8		14.0	0.01	0.01	18.1	1.86	0.12	1.90	36.0	93.7
16	45.3	<0.04	0.08	46.5	3.51	0.48	2.72	98.6		13.9	0.00	0.01	18.1	1.90	0.14	1.92	36.0	92.9
22	45.5	<0.04	<0.05	46.6	3.46	0.43	2.69	98.7		14.0	0.00	0.00	18.1	1.87	0.13	1.89	36.0	93.5
23	45.6	<0.04	0.08	46.7	3.50	0.55	2.68	99.1		14.0	0.01	0.01	18.1	1.89	0.16	1.88	36.0	92.0
24	45.4	0.08	<0.05	46.9	3.47	0.43	2.72	99.0		13.9	0.01	0.00	18.2	1.87	0.13	1.91	36.0	93.5
25	45.4	0.07	0.06	46.5	3.51	0.43	2.70	98.7		14.0	0.01	0.01	18.1	1.90	0.13	1.90	36.0	93.6
26	45.1	0.06	0.06	46.6	3.44	0.40	2.63	98.3		13.9	0.01	0.01	18.2	1.87	0.12	1.86	36.0	93.8
27	45.4	0.04	0.07	46.4	3.52	0.76	2.67	98.9		14.0	0.01	0.01	18.0	1.90	0.23	1.88	36.0	89.2
31	45.7	0.07	<0.05	46.4	3.48	1.00	2.68	99.4		14.0	0.01	0.00	17.9	1.87	0.30	1.87	36.0	86.1
32	45.9	<0.04	<0.05	46.7	3.49	0.57	2.71	99.4		14.0	0.00	0.00	18.0	1.87	0.17	1.89	35.9	91.6
33	46.2	<0.04	<0.05	46.8	3.45	0.41	2.63	99.6		14.0	0.01	0.01	18.0	1.85	0.12	1.83	35.9	93.7
mean	*45.6*	*0.04*	*0.05*	*46.6*	*3.46*	*0.57*	*2.67*	*98.9*		*14.0*	*0.01*	*0.01*	*18.1*	*1.87*	*0.17*	*1.88*	*36.0*	*91.6*
1-sig	*0.2*	*0.02*	*0.02*	*0.1*	*0.04*	*0.24*	*0.03*	*0.4*		*0.0*	*0.00*	*0.00*	*0.1*	*0.02*	*0.07*	*0.02*	*0.0*	*3.1*

formula based on 56 oxygens

Table A1.10. Individual EPMA analyses of merrillite in Kendleton (L3 clast), n=6

analysis #	P_2O_5	Y_2O_3	Ce_2O_3	CaO	MgO	FeO	Na_2O	total		P	Y	Ce	Ca	Mg	Fe	Na	total	Mg#
84	46.4	<0.04	0.09	46.5	3.51	0.47	2.86	99.8	*formula based on 56 oxygens*	14.1	0.00	0.01	17.8	1.87	0.14	1.99	35.9	93.0
85	46.0	<0.04	0.06	46.5	3.50	0.53	2.84	99.5		14.0	0.01	0.01	17.9	1.88	0.16	1.98	35.9	92.2
86	45.3	0.06	0.06	46.3	3.52	0.38	2.83	98.4		13.9	0.01	0.01	18.0	1.91	0.12	1.99	36.0	94.3
87	45.7	<0.04	<0.05	46.4	3.53	0.35	2.84	98.8		14.0	0.00	0.00	18.0	1.90	0.10	1.99	35.9	94.8
88	45.4	0.07	<0.05	46.2	3.51	0.37	2.82	98.4		14.0	0.01	0.00	18.0	1.90	0.11	1.99	36.0	94.4
89	45.7	0.07	<0.05	46.5	3.42	0.59	2.80	99.1		14.0	0.01	0.00	18.0	1.84	0.18	1.96	36.0	91.2
mean	*45.8*	*0.04*	*<0.05*	*46.4*	*3.50*	*0.45*	*2.83*	*99.0*		*14.0*	*0.01*	*0.01*	*18.0*	*1.88*	*0.14*	*1.98*	*36.0*	*93.3*
1-sig	*0.4*	*0.03*	*0.03*	*0.1*	*0.04*	*0.10*	*0.02*	*0.6*		*0.0*	*0.01*	*0.00*	*0.1*	*0.03*	*0.03*	*0.01*	*0.0*	*1.4*

Table A1.11. Individual EPMA analyses of merrillite in Kendleton (L4 host), n=14

analysis #	P_2O_5	Y_2O_3	Ce_2O_3	CaO	MgO	FeO	Na_2O	total		P	Y	Ce	Ca	Mg	Fe	Na	total	Mg#
1	45.3	0.07	<0.05	45.5	3.41	0.45	2.60	97.3	*formula based on 56 oxygens*	14.1	0.01	0.01	17.9	1.87	0.14	1.85	35.8	93.1
4	45.6	<0.04	<0.05	45.7	3.50	1.34	2.67	98.8		14.0	0.00	0.00	17.8	1.89	0.41	1.88	35.9	82.3
5	45.5	<0.04	0.11	46.1	3.51	1.05	2.65	98.9		14.0	0.01	0.01	17.9	1.90	0.32	1.87	36.0	85.7
6	45.2	0.04	<0.05	45.8	3.46	1.57	2.58	98.7		13.9	0.01	0.01	17.9	1.88	0.48	1.82	36.0	79.8
7	46.0	0.06	0.07	46.1	3.50	0.62	2.54	98.9		14.1	0.01	0.01	17.9	1.89	0.19	1.78	35.8	91.0
8	45.6	0.04	0.05	46.2	3.53	0.69	2.66	98.7		14.0	0.01	0.01	17.9	1.91	0.21	1.87	35.9	90.1
14	45.7	<0.04	<0.05	46.3	3.46	0.69	2.59	98.8		14.0	0.00	0.00	18.0	1.87	0.21	1.82	35.9	89.9
15	45.7	<0.04	0.05	46.5	3.49	1.02	2.71	99.5		14.0	0.00	0.01	18.0	1.88	0.31	1.89	36.0	86.0
16	45.8	<0.04	<0.05	46.6	3.43	0.70	2.61	99.1		14.0	0.00	0.00	18.0	1.85	0.21	1.82	35.9	89.8
23	45.4	<0.04	0.07	46.3	3.47	0.57	2.60	98.4		14.0	0.00	0.01	18.0	1.88	0.17	1.83	35.9	91.6
24	45.5	0.05	<0.05	46.2	3.54	0.58	2.67	98.6		14.0	0.01	0.01	18.0	1.91	0.18	1.88	36.0	91.6
33	45.7	<0.04	<0.05	46.7	3.42	0.38	2.65	98.9		14.0	0.00	0.00	18.1	1.85	0.11	1.86	35.9	94.2
34	45.6	<0.04	<0.05	45.9	3.47	0.34	2.71	98.0		14.1	0.00	0.00	17.9	1.88	0.10	1.91	35.9	94.8
35	45.7	<0.04	<0.05	46.0	3.51	0.36	2.64	98.3		14.1	0.00	0.01	17.9	1.90	0.11	1.86	35.8	94.6
mean	*45.6*	*<0.04*	*<0.05*	*46.1*	*3.48*	*0.74*	*2.63*	*98.7*		*14.0*	*0.01*	*0.01*	*17.9*	*1.88*	*0.22*	*1.85*	*35.9*	*89.6*
1-sig	*0.2*	*0.02*	*0.03*	*0.3*	*0.04*	*0.37*	*0.05*	*0.5*		*0.0*	*0.00*	*0.00*	*0.1*	*0.02*	*0.11*	*0.04*	*0.1*	*4.6*

Table A1.12. Individual EPMA analyses of merrillite in Kendleton (L5 clast), n=23

analysis #	P_2O_5	Y_2O_3	Ce_2O_3	CaO	MgO	FeO	Na_2O	total		P	Y	Ce	Ca	Mg	Fe	Na	total	Mg#
90	45.8	<0.04	<0.05	46.4	3.48	0.70	2.86	99.3		14.0	0.00	0.00	17.9	1.87	0.21	2.00	36.0	89.9
91	45.9	<0.04	0.05	46.4	3.48	0.70	2.87	99.4		14.0	0.00	0.01	17.9	1.87	0.21	2.00	36.0	89.9
92	45.8	<0.04	0.05	46.3	3.48	1.09	2.80	99.6		14.0	0.00	0.01	17.9	1.87	0.33	1.96	36.0	85.0
93	45.5	<0.04	<0.05	46.3	3.59	1.61	2.84	99.9		13.9	0.00	0.00	17.9	1.93	0.48	1.98	36.2	79.9
96	46.1	0.05	<0.05	46.4	3.58	0.32	2.82	99.3		14.0	0.01	0.01	17.9	1.91	0.10	1.96	35.9	95.2
97	45.8	<0.04	<0.05	46.6	3.61	0.34	2.87	99.3		14.0	0.00	0.00	18.0	1.94	0.10	2.01	36.0	95.0
98	45.8	0.05	<0.05	46.7	3.62	0.50	2.87	99.5		13.9	0.01	0.00	18.0	1.94	0.15	2.00	36.0	92.8
99	46.3	0.05	0.07	46.7	3.60	0.50	2.90	100.2		14.0	0.01	0.01	17.9	1.92	0.15	2.01	36.0	92.8
100	45.8	0.06	0.05	46.7	3.56	0.37	2.83	99.3		14.0	0.01	0.01	18.0	1.91	0.11	1.98	36.0	94.5
104	46.0	0.07	<0.05	46.7	3.63	0.53	2.89	99.9		14.0	0.01	0.00	17.9	1.94	0.16	2.01	36.0	92.5
105	46.3	<0.04	<0.05	46.5	3.56	0.42	2.87	99.6		14.0	0.00	0.01	17.8	1.90	0.13	1.99	35.9	93.8
106	45.5	0.04	0.06	46.5	3.57	0.64	2.83	99.1		13.9	0.01	0.01	18.0	1.92	0.19	1.99	36.1	90.8
107	45.7	<0.04	<0.05	46.6	3.54	0.67	2.82	99.4		13.9	0.01	0.00	18.0	1.90	0.20	1.97	36.0	90.4
108	46.0	<0.04	<0.05	46.7	3.53	0.56	2.79	99.6		14.0	0.00	0.00	18.0	1.89	0.17	1.94	36.0	91.8
113	45.8	0.04	0.08	46.7	3.58	0.38	2.80	99.4		14.0	0.01	0.01	18.0	1.92	0.11	1.95	36.0	94.4
114	45.7	<0.04	0.08	46.6	3.57	0.37	2.83	99.2		14.0	0.00	0.01	18.0	1.92	0.11	1.98	36.0	94.6
115	45.8	<0.04	<0.05	46.3	3.61	0.81	2.88	99.4		14.0	0.01	0.00	17.9	1.94	0.24	2.01	36.0	88.9
119	45.6	0.05	<0.05	46.8	3.65	0.66	2.76	99.6		13.9	0.01	0.00	18.0	1.96	0.20	1.93	36.0	90.8
120	46.0	0.05	<0.05	46.6	3.64	0.54	2.81	99.7		14.0	0.01	0.00	17.9	1.95	0.16	1.95	35.9	92.4
121	45.6	<0.04	0.10	46.3	3.58	0.31	2.72	98.7		14.0	0.00	0.01	18.0	1.93	0.09	1.91	35.9	95.3
122	46.1	<0.04	<0.05	46.7	3.66	0.43	2.94	99.8		14.0	0.01	0.00	17.9	1.96	0.13	2.04	36.0	93.9
123	45.3	<0.04	0.06	46.4	3.57	0.55	2.77	98.7		13.9	0.00	0.01	18.0	1.93	0.17	1.95	36.0	92.1
124	45.7	0.06	<0.05	47.0	3.59	0.42	2.76	99.6		13.9	0.01	0.00	18.1	1.93	0.13	1.92	36.0	93.8
mean	*45.8*	*<0.04*	*<0.05*	*46.6*	*3.58*	*0.58*	*2.83*	*99.5*		*14.0*	*0.01*	*0.01*	*18.0*	*1.92*	*0.18*	*1.98*	*36.0*	*91.8*
1-sig	*0.2*	*0.02*	*0.03*	*0.2*	*0.05*	*0.29*	*0.05*	*0.3*		*0.0*	*0.00*	*0.00*	*0.1*	*0.03*	*0.09*	*0.03*	*0.1*	*3.5*

formula based on 56 oxygens

3. Individual EPMA analyses of feldspar in L chondrites (chapter 1)

Table A1.13. Individual EPMA analyses of feldspar in Santa Barbara (L4), n=43 (1-15)

analysis #	33	35	36	37	43	44	45	47	48	56	58	61	62	63	64
chondrule	1	1	1	1	2	2	2	2	2	3	3	4	4	4	4
SiO_2	63.7	64.8	64.4	64.6	66.3	66.7	66.4	65.7	66.1	63.9	65.2	47.3	46.9	47.0	46.6
Al_2O_3	20.6	21.5	20.5	19.5	21.4	20.6	20.6	21.6	21.7	21.6	21.1	34.2	34.0	33.6	31.5
Cr_2O_3	0.07	<0.07	<0.07	<0.07	0.10	0.09	0.08	<0.07	<0.07	1.03	0.08	<0.07	0.70	0.94	1.92
FeO	2.67	1.65	1.94	1.92	0.48	0.96	0.86	0.59	0.31	1.22	0.59	0.38	0.84	0.77	1.07
MgO	0.12	0.11	0.57	0.71	0.02	0.04	0.04	0.04	<0.02	0.15	0.33	0.06	0.07	0.12	0.19
CaO	1.8	2.2	2.0	2.1	2.0	1.2	1.0	2.1	2.0	2.2	2.4	17.0	16.6	16.2	14.8
Na_2O	10.1	10.2	9.8	8.3	10.6	9.4	9.6	10.5	10.5	9.9	10.0	2.0	2.2	2.3	3.0
K_2O	0.77	0.80	1.67	3.80	0.84	2.87	2.18	0.90	0.82	0.83	0.93	0.04	0.07	0.07	0.09
total	99.8	101.3	100.8	101.1	101.7	101.9	100.8	101.4	101.4	100.9	100.6	101.1	101.4	101.0	99.2
	formula based on 8 oxygens														
Si	2.86	2.85	2.86	2.88	2.88	2.91	2.92	2.87	2.88	2.82	2.87	2.15	2.14	2.15	2.18
Al	1.09	1.11	1.07	1.03	1.10	1.06	1.07	1.11	1.11	1.13	1.10	1.84	1.83	1.81	1.73
Cr	0.00	0.00	0.00	0.00	0.00	0.00	0.00	0.00	0.00	0.04	0.00	0.00	0.03	0.03	0.07
Fe	0.10	0.06	0.07	0.07	0.02	0.04	0.03	0.02	0.01	0.05	0.02	0.01	0.03	0.03	0.04
Mg	0.01	0.01	0.04	0.05	0.00	0.00	0.00	0.00	0.00	0.01	0.02	0.00	0.01	0.01	0.01
Ca	0.09	0.10	0.10	0.10	0.09	0.05	0.05	0.10	0.09	0.11	0.11	0.83	0.81	0.79	0.74
Na	0.88	0.87	0.84	0.72	0.89	0.80	0.82	0.89	0.89	0.85	0.86	0.18	0.19	0.20	0.27
K	0.04	0.04	0.09	0.22	0.05	0.16	0.12	0.05	0.05	0.05	0.05	0.00	0.00	0.00	0.01
total	5.06	5.05	5.07	5.07	5.04	5.03	5.01	5.05	5.03	5.04	5.03	5.02	5.03	5.03	5.06
An	8.5	10.0	9.2	9.8	8.9	5.3	4.8	9.3	9.0	10.6	10.9	82.0	80.7	79.1	72.8
Ab	87.1	85.6	81.6	69.4	86.5	78.9	82.9	85.8	86.5	84.7	84.0	17.8	18.9	20.5	26.7
Or	4.4	4.4	9.1	20.8	4.5	15.8	12.4	4.8	4.4	4.7	5.1	0.2	0.4	0.4	0.5

Table A1.13. *(Continued).* Individual EPMA analyses of feldspar in Santa Barbara (L4), n=43 (16-30)

analysis #	65	66	67	68	69	70	71	73	75	78	79	80	81	82	83
chondrule	4	4	4	4	4	4	4	4	5	5	5	5	6	6	6
SiO_2	47.0	63.3	63.6	65.3	64.3	52.2	66.0	66.1	62.7	65.1	65.5	65.0	64.2	63.2	50.5
Al_2O_3	33.0	22.1	22.1	21.1	21.3	29.0	21.0	21.6	23.2	21.1	22.1	22.0	20.7	22.0	29.4
Cr_2O_3	1.67	<0.07	<0.07	<0.07	<0.07	0.76	<0.07	<0.07	0.16	0.09	<0.07	0.07	0.08	<0.07	1.83
FeO	1.43	0.62	0.55	0.44	0.62	0.82	0.73	0.59	0.71	0.67	0.44	0.67	2.62	1.87	2.18
MgO	0.20	0.06	0.14	0.03	0.03	0.10	0.04	<0.02	0.04	1.14	<0.02	0.15	0.08	0.05	0.28
CaO	15.4	2.9	3.0	2.0	2.1	11.1	1.4	2.0	4.2	2.2	2.3	2.4	1.9	3.0	11.5
Na_2O	2.6	9.9	9.9	10.5	10.5	5.1	8.3	10.4	9.5	10.2	10.2	8.5	10.0	9.7	4.6
K_2O	0.07	0.68	0.70	0.85	0.77	0.17	4.21	1.14	0.42	0.78	1.20	2.96	0.61	0.60	0.18
total	101.4	99.6	100.0	100.2	99.6	99.3	101.8	101.8	101.0	101.4	101.8	101.8	100.3	100.5	100.5
							formula based on 8 oxygens								
Si	2.15	2.82	2.82	2.88	2.86	2.39	2.90	2.88	2.77	2.85	2.85	2.85	2.86	2.81	2.32
Al	1.78	1.16	1.16	1.10	1.12	1.57	1.09	1.11	1.21	1.09	1.14	1.14	1.09	1.15	1.59
Cr	0.06	0.00	0.00	0.00	0.00	0.03	0.00	0.00	0.01	0.00	0.00	0.00	0.00	0.00	0.07
Fe	0.05	0.02	0.02	0.02	0.02	0.03	0.03	0.02	0.03	0.02	0.02	0.02	0.10	0.07	0.08
Mg	0.01	0.00	0.01	0.00	0.00	0.01	0.00	0.00	0.00	0.07	0.00	0.01	0.01	0.00	0.02
Ca	0.76	0.14	0.14	0.09	0.10	0.55	0.07	0.09	0.20	0.10	0.11	0.11	0.09	0.14	0.57
Na	0.23	0.86	0.85	0.90	0.91	0.46	0.71	0.88	0.82	0.87	0.86	0.73	0.86	0.84	0.41
K	0.00	0.04	0.04	0.05	0.04	0.01	0.24	0.06	0.02	0.04	0.07	0.17	0.03	0.03	0.01
total	5.05	5.05	5.04	5.04	5.06	5.04	5.03	5.04	5.05	5.06	5.04	5.03	5.04	5.05	5.07
An	76.4	13.4	14.0	9.0	9.3	54.0	6.7	9.0	19.3	10.2	10.4	11.3	9.1	14.0	57.3
Ab	23.2	82.9	82.1	86.3	86.5	45.0	70.0	84.9	78.4	85.5	83.1	72.3	87.4	82.7	41.6
Or	0.4	3.7	3.9	4.6	4.2	1.0	23.3	6.1	2.3	4.3	6.4	16.5	3.5	3.4	1.0

Table A1.13. *(Continued).* Individual EPMA analyses of feldspar in Santa Barbara (L4), n=43 (31-43)

analysis #	86	89	90	91	93	94	95	97	102	114	116	118	119		
chondrule	6	7	7	7	7	7	7	8	8	9	9	10	10	*mean*	*1-sig*
SiO_2	57.3	66.2	65.9	66.0	65.5	64.6	66.3	66.9	66.5	65.0	64.4	60.5	59.2	*62.0*	*6.5*
Al_2O_3	22.7	21.6	21.6	21.5	21.9	22.4	21.3	21.3	20.5	21.3	21.1	24.2	24.4	*23.3*	*4.1*
Cr_2O_3	2.72	<0.07	0.16	<0.07	<0.07	0.08	<0.07	<0.07	<0.07	<0.07	<0.07	0.12	<0.07	*0.30*	*0.63*
FeO	3.00	0.61	0.73	0.61	0.64	0.84	0.75	0.28	0.42	2.13	2.09	0.41	0.71	*1.03*	*0.72*
MgO	0.90	0.02	<0.02	0.07	0.03	0.12	0.26	<0.02	<0.02	0.06	0.11	0.07	0.08	*0.16*	*0.24*
CaO	4.5	2.0	2.0	1.9	2.3	2.5	1.8	1.5	0.9	2.0	2.0	5.5	6.2	*4.4*	*4.8*
Na_2O	8.2	10.2	10.5	10.8	10.4	10.2	10.6	10.7	9.4	10.3	10.2	8.3	7.9	*8.8*	*2.7*
K_2O	0.51	1.05	0.86	0.82	0.63	0.56	0.85	1.05	3.39	0.85	1.04	0.29	0.31	*1.03*	*0.99*
total	99.8	101.7	101.7	101.7	101.4	101.3	101.9	101.7	101.1	101.6	101.0	99.4	98.9	*100.9*	*0.9*
						formula based on 8 oxygens									
Si	2.62	2.88	2.87	2.87	2.86	2.83	2.88	2.90	2.93	2.85	2.85	2.71	2.68	*2.74*	*0.25*
Al	1.22	1.11	1.11	1.10	1.12	1.16	1.09	1.09	1.06	1.10	1.10	1.28	1.30	*1.22*	*0.24*
Cr	0.10	0.00	0.01	0.00	0.00	0.00	0.00	0.00	0.00	0.00	0.00	0.00	0.00	*0.01*	*0.02*
Fe	0.11	0.02	0.03	0.02	0.02	0.03	0.03	0.01	0.02	0.08	0.08	0.02	0.03	*0.04*	*0.03*
Mg	0.06	0.00	0.00	0.00	0.00	0.01	0.02	0.00	0.00	0.00	0.01	0.00	0.01	*0.01*	*0.02*
Ca	0.22	0.09	0.10	0.09	0.11	0.12	0.09	0.07	0.04	0.09	0.10	0.27	0.30	*0.21*	*0.24*
Na	0.72	0.86	0.88	0.91	0.88	0.87	0.89	0.90	0.80	0.87	0.88	0.72	0.70	*0.75*	*0.22*
K	0.03	0.06	0.05	0.05	0.04	0.03	0.05	0.06	0.19	0.05	0.06	0.02	0.02	*0.06*	*0.06*
total	5.09	5.03	5.04	5.05	5.04	5.04	5.04	5.03	5.04	5.05	5.07	5.02	5.03	*5.04*	*0.02*
An	22.8	9.1	9.3	8.6	10.3	11.4	8.3	6.8	4.2	9.2	9.2	26.5	29.7	*20.9*	*23.6*
Ab	74.2	85.1	86.0	87.0	86.2	85.5	87.1	87.6	77.4	86.1	85.1	71.9	68.6	*73.4*	*21.5*
Or	3.0	5.7	4.7	4.3	3.5	3.1	4.6	5.7	18.5	4.7	5.7	1.7	1.8	*5.7*	*5.5*

Table A1.14. Individual EPMA analyses of feldspar in Kramer Creek (L4), n=41 (1-15)

analysis #	3	4	5	6	9	11	12	13	14	15	16	17	21	22	44
chondrule	1	1	1	1	1	2	2	2	2	2	2	2	5	5	5
SiO_2	47.3	46.5	46.5	46.0	46.0	66.7	46.7	45.7	46.8	46.7	46.3	46.2	67.7	67.9	68.0
Al_2O_3	33.8	33.8	33.7	33.9	33.9	20.4	34.0	34.3	33.9	33.1	33.9	33.7	20.2	20.2	20.1
Cr_2O_3	<0.07	0.12	0.11	0.21	0.35	<0.07	<0.07	0.12	<0.07	0.19	0.19	<0.07	<0.07	<0.07	0.09
FeO	0.20	0.27	0.46	0.55	0.38	0.30	0.27	0.59	0.43	0.45	0.47	0.68	0.57	0.36	0.56
MgO	<0.02	0.03	0.03	0.05	0.07	<0.02	<0.02	0.04	0.02	0.04	0.04	0.06	<0.02	<0.02	<0.02
CaO	16.7	16.9	16.6	16.6	16.7	1.1	16.8	17.2	16.6	15.8	16.7	16.7	0.7	0.6	0.6
Na_2O	2.2	2.0	2.1	2.0	2.2	11.1	2.3	1.8	2.0	2.2	2.0	1.8	11.2	11.4	11.6
K_2O	0.02	0.02	0.03	0.03	0.03	0.44	0.03	0.02	0.03	0.04	0.03	0.03	0.30	0.35	0.33
total	100.2	99.7	99.5	99.3	99.6	100.0	100.1	99.8	99.8	98.5	99.6	99.2	100.8	100.8	101.3
							formula based on 8 oxygens								
Si	2.17	2.15	2.15	2.13	2.13	2.93	2.15	2.11	2.16	2.18	2.14	2.14	2.95	2.96	2.95
Al	1.82	1.84	1.84	1.85	1.85	1.06	1.84	1.87	1.84	1.82	1.85	1.84	1.04	1.03	1.03
Cr	0.00	0.00	0.00	0.01	0.01	0.00	0.00	0.00	0.00	0.01	0.01	0.00	0.00	0.00	0.00
Fe	0.01	0.01	0.02	0.02	0.01	0.01	0.01	0.02	0.02	0.02	0.02	0.03	0.02	0.01	0.02
Mg	0.00	0.00	0.00	0.00	0.00	0.00	0.00	0.00	0.00	0.00	0.00	0.00	0.00	0.00	0.00
Ca	0.82	0.84	0.82	0.83	0.83	0.05	0.83	0.85	0.82	0.79	0.83	0.83	0.03	0.03	0.03
Na	0.20	0.18	0.19	0.18	0.20	0.95	0.20	0.16	0.18	0.20	0.18	0.16	0.95	0.96	0.98
K	0.00	0.00	0.00	0.00	0.00	0.02	0.00	0.00	0.00	0.00	0.00	0.00	0.02	0.02	0.02
total	5.02	5.02	5.02	5.03	5.04	5.02	5.03	5.03	5.01	5.01	5.03	5.02	5.01	5.02	5.03
An	80.6	82.1	81.3	82.2	80.8	5.0	80.2	84.0	82.2	79.6	81.7	83.5	3.4	2.9	2.6
Ab	19.3	17.7	18.5	17.7	19.1	92.6	19.6	15.9	17.6	20.2	18.1	16.3	94.9	95.2	95.6
Or	0.1	0.1	0.1	0.2	0.1	2.4	0.2	0.1	0.2	0.2	0.2	0.2	1.7	1.9	1.8

Table A1.14. *(Continued).* Individual EPMA analyses of feldspar in Kramer Creek (L4), n=41 (16-30)

analysis #	45	46	29	30	31	32	33	35	36	37	38	39	40	41	42
chondrule	5	5	6	6	6	6	6	6	13	13	13	13	13	13	13
SiO_2	67.4	66.4	46.9	46.9	46.8	46.9	46.6	46.8	45.5	46.4	46.5	46.7	46.3	46.1	46.4
Al_2O_3	20.3	20.0	33.9	33.8	33.8	33.8	34.0	33.8	34.8	34.3	34.2	34.3	34.7	34.9	34.4
Cr_2O_3	<0.07	<0.07	<0.07	0.08	<0.07	<0.07	<0.07	0.08	0.33	0.25	0.25	0.23	<0.07	0.11	0.18
FeO	0.41	0.78	0.26	0.51	0.41	0.29	0.29	0.40	0.34	0.26	0.30	0.35	0.18	0.48	0.24
MgO	0.03	0.06	0.04	0.08	0.05	0.03	<0.02	0.03	0.04	0.03	0.03	0.04	<0.02	<0.02	0.02
CaO	0.9	0.9	16.9	16.4	16.8	16.5	17.2	16.7	17.7	17.2	17.1	17.0	17.5	17.7	17.3
Na_2O	11.3	11.0	1.9	2.0	1.9	2.3	1.8	2.0	1.5	1.8	1.8	1.9	1.6	1.4	1.8
K_2O	0.40	0.34	0.03	0.03	0.03	0.03	0.03	0.02	0.02	0.04	0.04	0.03	0.01	0.01	0.02
total	100.8	99.5	100.0	99.8	99.9	99.9	99.9	99.9	100.2	100.2	100.2	100.6	100.4	100.7	100.4
							formula based on 8 oxygens								
Si	2.94	2.94	2.16	2.16	2.16	2.16	2.14	2.16	2.10	2.13	2.14	2.14	2.12	2.11	2.13
Al	1.04	1.04	1.84	1.84	1.83	1.83	1.85	1.83	1.89	1.85	1.85	1.85	1.88	1.88	1.86
Cr	0.00	0.00	0.00	0.00	0.00	0.00	0.00	0.00	0.01	0.01	0.01	0.01	0.00	0.00	0.01
Fe	0.01	0.03	0.01	0.02	0.02	0.01	0.01	0.02	0.01	0.01	0.01	0.01	0.01	0.02	0.01
Mg	0.00	0.00	0.00	0.01	0.00	0.00	0.00	0.00	0.00	0.00	0.00	0.00	0.00	0.00	0.00
Ca	0.04	0.04	0.83	0.81	0.83	0.81	0.85	0.82	0.88	0.84	0.84	0.83	0.86	0.87	0.85
Na	0.96	0.94	0.17	0.18	0.17	0.20	0.16	0.18	0.13	0.16	0.16	0.17	0.14	0.12	0.16
K	0.02	0.02	0.00	0.00	0.00	0.00	0.00	0.00	0.00	0.00	0.00	0.00	0.00	0.00	0.00
total	5.03	5.02	5.01	5.01	5.01	5.03	5.01	5.02	5.02	5.02	5.01	5.02	5.01	5.01	5.02
An	4.1	4.2	82.9	81.7	82.9	79.9	83.9	81.7	86.9	83.8	84.0	82.9	85.9	87.7	84.2
Ab	93.7	93.9	17.0	18.1	16.9	19.9	15.9	18.2	13.0	16.0	15.8	16.9	14.0	12.2	15.7
Or	2.2	1.9	0.2	0.2	0.2	0.2	0.2	0.1	0.1	0.2	0.2	0.2	0.1	0.1	0.1

Table A1.14. *(Continued).* Individual EPMA analyses of feldspar in Kramer Creek (L4), n=41 (31-41)

analysis #	64	23	24	25	26	27	28	71	72	78	79		
chondrule	13	23	23	23	23	23	23	23	23	23	23	*mean*	*1-sig*
SiO_2	67.5	64.0	62.3	63.1	62.0	63.3	63.1	62.6	61.7	66.2	67.6	*54.2*	*9.4*
Al_2O_3	19.8	21.7	22.9	21.5	22.0	21.9	22.0	21.4	22.3	19.8	19.6	*28.6*	*6.6*
Cr_2O_3	<0.07	0.25	0.37	0.73	1.19	0.44	0.55	0.82	0.84	<0.07	<0.07	*0.21*	*0.27*
FeO	0.58	0.62	0.81	1.02	1.15	1.02	0.93	1.15	1.00	1.40	0.72	*0.55*	*0.30*
MgO	<0.02	0.05	0.06	0.08	0.16	0.07	0.08	0.05	0.06	<0.02	<0.02	*0.04*	*0.03*
CaO	0.3	2.8	4.2	2.9	3.5	3.1	3.2	2.9	3.7	0.8	0.4	*10.7*	*7.5*
Na_2O	11.5	10.1	9.1	9.8	9.4	9.9	9.7	9.7	9.3	11.1	11.3	*5.5*	*4.3*
K_2O	0.48	0.24	0.22	0.26	0.21	0.25	0.21	0.25	0.21	0.30	0.45	*0.14*	*0.15*
total	100.1	99.7	99.9	99.4	99.6	99.9	99.7	98.9	99.1	99.7	100.1	*99.9*	*0.5*
					formula based on 8 oxygens								
Si	2.96	2.84	2.77	2.82	2.78	2.82	2.81	2.82	2.77	2.93	2.97	*2.45*	*0.37*
Al	1.02	1.14	1.20	1.13	1.16	1.15	1.15	1.14	1.18	1.04	1.01	*1.53*	*0.38*
Cr	0.00	0.01	0.01	0.03	0.04	0.02	0.02	0.03	0.03	0.00	0.00	*0.01*	*0.01*
Fe	0.02	0.02	0.03	0.04	0.04	0.04	0.03	0.04	0.04	0.05	0.03	*0.02*	*0.01*
Mg	0.00	0.00	0.00	0.01	0.01	0.00	0.01	0.00	0.00	0.00	0.00	*0.00*	*0.00*
Ca	0.02	0.13	0.20	0.14	0.17	0.15	0.15	0.14	0.18	0.04	0.02	*0.53*	*0.37*
Na	0.98	0.87	0.79	0.85	0.82	0.85	0.84	0.84	0.81	0.96	0.97	*0.47*	*0.37*
K	0.03	0.01	0.01	0.01	0.01	0.01	0.01	0.01	0.01	0.02	0.02	*0.01*	*0.01*
total	5.03	5.03	5.02	5.03	5.03	5.03	5.03	5.03	5.03	5.03	5.02	*5.02*	*0.01*
An	1.5	13.0	19.9	13.9	16.8	14.4	15.0	13.9	17.7	3.7	2.0	*52.2*	*37.0*
Ab	95.8	85.7	78.9	84.7	82.0	84.2	83.8	84.6	81.1	94.6	95.6	*47.0*	*36.2*
Or	2.7	1.3	1.2	1.5	1.2	1.4	1.2	1.4	1.2	1.7	2.5	*0.8*	*0.8*

Table A1.15. Individual EPMA analyses of feldspar in Elenovka (L5), n=81 (1-20)

analysis #	22	23	24	25	27	28	29	30	31	32	33	35	36	37	38	39	41	43	44	45
chondrule	1	1	1	1	1	1	1	2	2	2	2	3	3	3	3	4	4	4	4	4
SiO_2	66.2	66.1	66.7	66.3	66.2	66.3	66.8	66.0	66.4	65.7	66.3	66.3	66.7	66.3	66.2	66.2	66.6	66.5	66.3	66.4
Al_2O_3	21.2	21.3	21.3	21.4	20.7	21.5	21.5	21.1	21.4	21.2	21.1	21.3	21.1	21.1	21.4	21.3	21.2	21.3	21.3	21.4
Cr_2O_3	<0.07	<0.07	<0.07	<0.07	<0.07	<0.07	<0.07	<0.07	<0.07	<0.07	<0.07	<0.07	<0.07	<0.07	<0.07	<0.07	<0.07	<0.07	<0.07	<0.07
FeO	0.25	0.43	0.41	0.34	0.81	0.55	0.47	0.56	0.43	0.76	0.30	0.21	0.22	0.28	0.61	0.26	0.45	0.33	0.30	0.33
MgO	<0.02	<0.02	<0.02	<0.02	1.19	0.02	<0.02	<0.02	<0.02	<0.02	<0.02	<0.02	<0.02	<0.02	<0.02	<0.02	0.04	0.02	0.03	0.03
CaO	2.15	2.14	2.15	2.20	2.06	2.14	2.10	2.00	2.13	2.16	2.07	2.24	2.01	2.07	2.16	2.22	2.16	2.23	2.16	2.19
Na_2O	10.1	10.1	9.9	10.1	9.8	9.8	10.0	10.1	10.1	9.8	10.1	9.8	10.0	10.1	10.1	10.0	10.2	10.1	10.1	10.1
K_2O	0.99	0.89	1.14	0.92	0.93	1.33	1.26	0.71	0.86	1.19	1.03	1.33	1.01	1.01	1.16	1.12	0.81	0.92	1.05	0.97
total	100.9	101.0	101.7	101.3	101.7	101.6	102.1	100.5	101.3	100.8	100.9	101.3	101.1	100.9	101.6	101.1	101.5	101.4	101.2	101.5
									formula based on 8 oxygens											
Si	2.90	2.89	2.90	2.89	2.88	2.89	2.89	2.90	2.89	2.89	2.90	2.89	2.91	2.90	2.88	2.89	2.90	2.90	2.89	2.89
Al	1.09	1.10	1.09	1.10	1.06	1.10	1.10	1.09	1.10	1.10	1.09	1.10	1.09	1.09	1.10	1.10	1.09	1.09	1.09	1.10
Cr	0.00	0.00	0.00	0.00	0.00	0.00	0.00	0.00	0.00	0.00	0.00	0.00	0.00	0.00	0.00	0.00	0.00	0.00	0.00	0.00
Fe	0.01	0.02	0.01	0.01	0.03	0.02	0.02	0.02	0.02	0.03	0.01	0.01	0.01	0.01	0.02	0.01	0.02	0.01	0.01	0.01
Mg	0.00	0.00	0.00	0.00	0.08	0.00	0.00	0.00	0.00	0.00	0.00	0.00	0.00	0.00	0.00	0.00	0.00	0.00	0.00	0.00
Ca	0.10	0.10	0.10	0.10	0.10	0.10	0.10	0.09	0.10	0.10	0.10	0.10	0.09	0.10	0.10	0.10	0.10	0.10	0.10	0.10
Na	0.85	0.86	0.84	0.85	0.83	0.83	0.84	0.86	0.85	0.84	0.86	0.83	0.85	0.86	0.85	0.85	0.86	0.85	0.85	0.85
K	0.06	0.05	0.06	0.05	0.05	0.07	0.07	0.04	0.05	0.07	0.06	0.07	0.06	0.06	0.06	0.06	0.05	0.05	0.06	0.05
total	5.01	5.01	5.01	5.01	5.03	5.01	5.01	5.01	5.01	5.02	5.01	5.01	5.00	5.01	5.03	5.01	5.01	5.01	5.01	5.01
An	10.0	10.0	10.0	10.2	9.8	9.9	9.7	9.5	10.0	10.1	9.6	10.4	9.4	9.6	9.9	10.3	10.0	10.3	10.0	10.1
Ab	84.5	85.1	83.7	84.7	84.9	82.7	83.4	86.5	85.2	83.3	84.7	82.3	85.0	84.8	83.7	83.5	85.6	84.6	84.3	84.5
Or	5.5	4.9	6.3	5.1	5.3	7.3	6.9	4.0	4.8	6.6	5.7	7.3	5.6	5.6	6.3	6.2	4.5	5.1	5.8	5.4

Table A1.15. *(Continued).* Individual EPMA analyses of feldspar in Elenovka (L5), n=81 (21-40)

analysis #	46	47	48	49	50	51	52	53	54	55	56	57	58	59	60	61	62	63	64	65
chondrule	4	5	5	5	5	5	5	5	5	5	6	6	6	6	6	6	6	6	6	7
SiO_2	65.9	66.0	66.5	66.3	65.8	66.3	66.6	66.5	66.5	65.7	66.3	65.9	66.7	66.5	66.4	66.1	66.4	66.3	66.4	66.3
Al_2O_3	21.0	21.1	21.0	21.2	21.2	21.3	21.1	21.1	21.1	20.8	21.0	21.1	20.9	21.1	20.9	21.0	20.6	21.0	20.9	21.1
Cr_2O_3	<0.07	<0.07	<0.07	0.28	<0.07	<0.07	<0.07	<0.07	<0.07	<0.07	<0.07	<0.07	<0.07	<0.07	<0.07	<0.07	<0.07	<0.07	<0.07	<0.07
FeO	0.34	0.48	0.45	0.52	0.58	0.61	0.41	0.44	0.58	0.56	0.33	0.43	0.45	0.58	0.51	0.49	0.48	0.47	0.49	0.51
MgO	0.13	<0.02	<0.02	0.02	<0.02	<0.02	<0.02	<0.02	<0.02	<0.02	<0.02	<0.02	<0.02	<0.02	<0.02	<0.02	<0.02	<0.02	<0.02	<0.02
CaO	2.16	2.10	1.89	2.05	2.17	2.17	2.06	2.07	2.12	2.11	2.12	2.18	2.09	2.14	2.13	2.16	2.09	2.13	2.13	2.11
Na_2O	10.1	10.1	10.1	10.0	9.9	10.0	10.0	9.9	9.6	9.7	10.0	10.0	10.0	10.2	10.1	10.1	10.1	9.9	10.1	10.0
K_2O	0.92	0.99	1.03	0.90	1.04	0.96	0.99	1.15	1.57	1.48	1.10	0.92	1.06	0.85	1.06	0.95	0.99	1.28	1.02	1.03
total	100.7	100.8	101.0	101.3	100.8	101.3	101.3	101.2	101.4	100.4	100.8	100.6	101.2	101.3	101.0	100.9	100.6	101.1	101.0	101.1
									formula based on 8 oxygens											
Si	2.89	2.89	2.91	2.89	2.89	2.89	2.90	2.90	2.90	2.90	2.90	2.89	2.91	2.90	2.90	2.90	2.91	2.90	2.91	2.90
Al	1.09	1.09	1.08	1.09	1.09	1.09	1.09	1.09	1.08	1.08	1.09	1.09	1.07	1.08	1.08	1.08	1.07	1.08	1.08	1.09
Cr	0.00	0.00	0.00	0.01	0.00	0.00	0.00	0.00	0.00	0.00	0.00	0.00	0.00	0.00	0.00	0.00	0.00	0.00	0.00	0.00
Fe	0.01	0.02	0.02	0.02	0.02	0.02	0.01	0.02	0.02	0.02	0.01	0.02	0.02	0.02	0.02	0.02	0.02	0.02	0.02	0.02
Mg	0.01	0.00	0.00	0.00	0.00	0.00	0.00	0.00	0.00	0.00	0.00	0.00	0.00	0.00	0.00	0.00	0.00	0.00	0.00	0.00
Ca	0.10	0.10	0.09	0.10	0.10	0.10	0.10	0.10	0.10	0.10	0.10	0.10	0.10	0.10	0.10	0.10	0.10	0.10	0.10	0.10
Na	0.86	0.86	0.86	0.85	0.85	0.85	0.85	0.84	0.81	0.83	0.85	0.85	0.85	0.86	0.86	0.86	0.86	0.84	0.85	0.84
K	0.05	0.06	0.06	0.05	0.06	0.05	0.06	0.06	0.09	0.08	0.06	0.05	0.06	0.05	0.06	0.05	0.06	0.07	0.06	0.06
total	5.02	5.02	5.01	5.00	5.01	5.01	5.00	5.00	5.01	5.01	5.01	5.01	5.01	5.01	5.01	5.02	5.01	5.01	5.01	5.01
An	10.0	9.7	8.8	9.7	10.1	10.1	9.6	9.7	9.9	9.9	9.9	10.2	9.7	9.9	9.8	10.0	9.7	9.9	9.9	9.9
Ab	84.9	84.8	85.5	85.3	84.1	84.6	84.8	83.8	81.3	81.9	84.1	84.7	84.5	85.4	84.3	84.8	84.9	83.1	84.4	84.4
Or	5.1	5.5	5.7	5.1	5.8	5.3	5.5	6.4	8.7	8.2	6.1	5.1	5.9	4.7	5.8	5.2	5.5	7.1	5.6	5.8

Table A1.15. *(Continued).* Individual EPMA analyses of feldspar in Elenovka (L5), n=81 (41-60)

analysis #	66	67	68	69	70	71	73	74	75	76	77	78	79	80	81	82	83	84	85	86
chondrule	7	7	7	7	7	8	8	8	8	8	8	8	8	9	9	9	9	9	9	9
SiO_2	66.4	66.7	66.4	66.6	66.9	66.4	66.4	66.1	66.3	66.3	65.6	66.2	65.7	65.5	65.6	65.8	65.8	65.8	65.8	64.4
Al_2O_3	21.4	21.2	21.3	21.3	21.3	21.3	21.3	21.4	21.4	21.2	21.1	21.1	20.8	21.0	21.3	21.2	20.9	20.9	21.0	20.6
Cr_2O_3	<0.07	<0.07	<0.07	<0.07	<0.07	<0.07	<0.07	<0.07	<0.07	<0.07	<0.07	<0.07	<0.07	<0.07	<0.07	<0.07	<0.07	<0.07	<0.07	<0.07
FeO	0.42	0.37	0.57	0.39	0.72	0.43	0.48	0.49	0.39	0.18	0.22	0.27	0.23	0.64	0.63	0.52	0.63	0.29	0.28	0.38
MgO	0.03	<0.02	0.07	<0.02	0.14	<0.02	0.02	0.02	<0.02	<0.02	<0.02	<0.02	0.06	0.02	<0.02	<0.02	<0.02	<0.02	<0.02	<0.02
CaO	2.15	2.11	2.14	2.14	2.10	2.21	2.18	2.18	2.16	2.23	2.23	2.18	2.17	2.13	2.08	2.10	2.06	2.13	2.11	2.18
Na_2O	9.9	9.9	10.0	10.2	10.2	10.2	10.1	9.8	10.2	9.9	10.0	10.3	9.7	10.0	10.0	9.5	10.0	10.1	9.8	9.9
K_2O	1.23	1.12	1.02	0.95	0.85	0.74	0.91	1.20	0.87	0.94	0.93	0.60	1.15	1.10	1.06	1.72	1.01	0.85	1.41	0.81
total	101.5	101.4	101.5	101.6	102.2	101.3	101.4	101.2	101.3	100.7	100.1	100.7	99.7	100.4	100.7	100.8	100.3	100.1	100.5	98.2
									formula based on 8 oxygens											
Si	2.89	2.90	2.89	2.90	2.89	2.89	2.89	2.89	2.89	2.90	2.89	2.90	2.91	2.89	2.88	2.89	2.90	2.90	2.90	2.89
Al	1.10	1.09	1.09	1.09	1.09	1.09	1.09	1.10	1.10	1.09	1.10	1.09	1.08	1.09	1.11	1.10	1.09	1.09	1.09	1.09
Cr	0.00	0.00	0.00	0.00	0.00	0.00	0.00	0.00	0.00	0.00	0.00	0.00	0.00	0.00	0.00	0.00	0.00	0.00	0.00	0.00
Fe	0.02	0.01	0.02	0.01	0.03	0.02	0.02	0.02	0.01	0.01	0.01	0.01	0.01	0.02	0.02	0.02	0.02	0.01	0.01	0.01
Mg	0.00	0.00	0.00	0.00	0.01	0.00	0.00	0.00	0.00	0.00	0.00	0.00	0.00	0.00	0.00	0.00	0.00	0.00	0.00	0.00
Ca	0.10	0.10	0.10	0.10	0.10	0.10	0.10	0.10	0.10	0.10	0.11	0.10	0.10	0.10	0.10	0.10	0.10	0.10	0.10	0.11
Na	0.83	0.84	0.85	0.86	0.85	0.86	0.85	0.83	0.86	0.84	0.85	0.88	0.83	0.85	0.85	0.81	0.85	0.86	0.84	0.86
K	0.07	0.06	0.06	0.05	0.05	0.04	0.05	0.07	0.05	0.05	0.05	0.03	0.06	0.06	0.06	0.10	0.06	0.05	0.08	0.05
total	5.01	5.00	5.01	5.02	5.01	5.01	5.01	5.01	5.01	5.00	5.01	5.01	5.00	5.02	5.02	5.01	5.01	5.01	5.02	5.01
An	10.0	9.9	10.0	9.8	9.8	10.3	10.1	10.2	10.0	10.5	10.4	10.1	10.3	9.9	9.7	9.8	9.7	10.0	9.8	10.4
Ab	83.2	83.9	84.4	85.0	85.5	85.6	84.9	83.2	85.2	84.2	84.4	86.6	83.2	84.0	84.4	80.6	84.7	85.3	82.4	85.0
Or	6.8	6.2	5.7	5.2	4.7	4.1	5.0	6.7	4.8	5.3	5.2	3.3	6.5	6.1	5.9	9.6	5.6	4.7	7.8	4.6

Table A1.15. *(Continued).* Individual EPMA analyses of feldspar in Elenovka (L5), n=81 (61-75)

analysis #	87	88	2	3	4	5	6	7	8	9	10	11	12	13	14
chondrule	9	9	11	11	11	11	11	12	12	12	12	12	12	12	12
SiO_2	65.8	65.8	65.9	66.3	66.5	66.0	66.4	66.6	66.8	66.5	66.5	66.4	66.2	66.6	66.4
Al_2O_3	20.8	21.1	21.2	21.5	21.3	21.1	21.3	21.6	21.4	21.4	21.3	21.3	21.0	21.1	21.2
Cr_2O_3	<0.07	<0.07	<0.07	<0.07	<0.07	<0.07	<0.07	<0.07	<0.07	<0.07	<0.07	<0.07	<0.07	<0.07	<0.07
FeO	0.47	0.96	0.58	0.51	0.40	0.46	0.40	0.41	0.47	0.57	0.48	0.26	0.43	0.42	0.45
MgO	<0.02	<0.02	0.20	<0.02	<0.02	<0.02	<0.02	<0.02	<0.02	0.07	0.02	0.02	<0.02	0.03	<0.02
CaO	2.14	2.15	2.13	2.20	2.18	2.13	2.17	2.21	2.20	2.29	2.15	2.12	2.15	1.95	2.12
Na_2O	10.0	10.2	9.9	10.1	10.0	10.0	10.2	10.0	10.1	10.2	10.0	9.8	10.1	10.0	10.2
K_2O	1.02	1.00	1.17	0.84	0.90	0.86	0.80	1.02	0.93	0.89	1.01	1.35	1.01	1.06	0.96
total	100.3	101.3	101.1	101.5	101.4	100.6	101.3	101.8	101.9	101.9	101.5	101.2	100.9	101.2	101.3
							formula based on 8 oxygens								
Si	2.90	2.88	2.88	2.89	2.90	2.90	2.90	2.89	2.90	2.89	2.89	2.90	2.90	2.91	2.89
Al	1.08	1.09	1.10	1.10	1.09	1.09	1.09	1.10	1.09	1.09	1.09	1.09	1.09	1.08	1.09
Cr	0.00	0.00	0.00	0.00	0.00	0.00	0.00	0.00	0.00	0.00	0.00	0.00	0.00	0.00	0.00
Fe	0.02	0.04	0.02	0.02	0.01	0.02	0.01	0.01	0.02	0.02	0.02	0.01	0.02	0.02	0.02
Mg	0.00	0.00	0.01	0.00	0.00	0.00	0.00	0.00	0.00	0.00	0.00	0.00	0.00	0.00	0.00
Ca	0.10	0.10	0.10	0.10	0.10	0.10	0.10	0.10	0.10	0.11	0.10	0.10	0.10	0.09	0.10
Na	0.86	0.87	0.84	0.86	0.85	0.85	0.86	0.84	0.84	0.86	0.85	0.83	0.85	0.85	0.86
K	0.06	0.06	0.07	0.05	0.05	0.05	0.04	0.06	0.05	0.05	0.06	0.08	0.06	0.06	0.05
total	5.01	5.03	5.02	5.01	5.01	5.01	5.01	5.01	5.01	5.02	5.01	5.01	5.01	5.01	5.02
An	10.0	9.8	9.9	10.2	10.2	10.0	10.1	10.3	10.2	10.5	10.0	9.9	10.0	9.1	9.8
Ab	84.4	84.7	83.6	85.2	84.8	85.2	85.5	84.1	84.6	84.6	84.4	82.6	84.4	85.0	84.9
Or	5.6	5.4	6.5	4.6	5.0	4.8	4.4	5.6	5.2	4.9	5.6	7.5	5.6	5.9	5.3

Table A1.15. *(Continued).* Individual EPMA analyses of feldspar in Elenovka (L5), n=81 (76-81)

analysis #	15	16	17	18	19	21		
chondrule	12	13	13	13	13	13	*mean*	*1-sig*
SiO_2	66.4	66.3	65.8	66.0	66.1	66.0	*66.2*	*0.4*
Al_2O_3	21.2	21.4	20.3	21.3	21.1	21.2	*21.2*	*0.2*
Cr_2O_3	<0.07	<0.07	<0.07	<0.07	<0.07	<0.07	*<0.07*	*0.03*
FeO	0.53	0.59	0.66	0.64	0.62	0.58	*0.46*	*0.14*
MgO	0.03	0.03	0.80	<0.02	0.05	0.03	*0.04*	*0.16*
CaO	2.20	2.16	3.26	2.18	2.16	2.12	*2.15*	*0.14*
Na_2O	10.2	9.7	9.8	10.1	9.9	9.6	*10.0*	*0.2*
K_2O	0.77	1.47	0.95	1.10	1.18	1.46	*1.04*	*0.20*
total	101.4	101.6	101.6	101.4	101.2	101.0	*101.1*	*0.6*
	formula based on 8 oxygens							
Si	2.89	2.89	2.88	2.88	2.89	2.89	*2.90*	*0.01*
Al	1.09	1.10	1.05	1.10	1.09	1.10	*1.09*	*0.01*
Cr	0.00	0.00	0.00	0.00	0.00	0.00	*0.00*	*0.00*
Fe	0.02	0.02	0.02	0.02	0.02	0.02	*0.02*	*0.01*
Mg	0.00	0.00	0.05	0.00	0.00	0.00	*0.00*	*0.01*
Ca	0.10	0.10	0.15	0.10	0.10	0.10	*0.10*	*0.01*
Na	0.86	0.82	0.83	0.85	0.84	0.81	*0.85*	*0.01*
K	0.04	0.08	0.05	0.06	0.07	0.08	*0.06*	*0.01*
total	5.02	5.01	5.04	5.02	5.01	5.01	*5.01*	*0.01*
An	10.2	10.0	14.8	10.0	10.0	10.0	*10.0*	*0.6*
Ab	85.6	81.8	80.1	83.9	83.4	81.8	*84.2*	*1.2*
Or	4.3	8.2	5.1	6.0	6.5	8.2	*5.8*	*1.1*

Table A1.16. Individual EPMA analyses of feldspar in Roy (1933) (L5), n=38 (1-20)

analysis #	8	9	10	11	12	28	29	31	35	13	14	15	16	17	18	19	20	21	26	27
chondrule	1	1	1	1	1	1	1	1	5	6	6	6	6	6	6	7	7	7	7	7
SiO_2	63.6	64.0	62.5	64.3	65.7	66.7	66.3	65.7	64.4	66.1	66.3	66.1	66.9	66.6	66.7	64.3	64.6	66.1	66.6	66.5
Al_2O_3	22.5	21.2	21.7	22.1	20.6	21.0	21.4	21.2	21.1	21.2	21.3	20.8	20.9	21.3	20.5	19.4	19.6	21.3	20.3	20.9
Cr_2O_3	<0.07	<0.07	<0.07	0.17	<0.07	<0.07	<0.07	<0.07	<0.07	<0.07	<0.07	<0.07	<0.07	<0.07	<0.07	<0.07	<0.07	<0.07	<0.07	<0.07
FeO	0.53	0.65	1.17	0.50	0.49	0.78	0.67	0.30	0.51	0.31	0.30	0.78	0.37	0.49	0.90	1.23	0.40	0.26	0.39	0.47
MgO	0.03	0.31	0.35	<0.02	0.05	0.02	<0.02	<0.02	<0.02	<0.02	<0.02	0.05	<0.02	<0.02	<0.02	0.07	0.02	<0.02	<0.02	0.09
CaO	3.65	3.17	3.32	3.27	1.78	1.69	1.97	2.05	2.09	2.17	2.15	1.77	1.70	2.12	1.47	0.83	1.23	2.09	1.28	1.84
Na_2O	9.4	9.6	9.3	9.5	10.0	10.0	10.3	10.0	10.1	10.1	10.0	9.9	10.1	10.0	10.2	3.5	3.3	10.0	8.9	9.9
K_2O	0.48	0.61	0.46	0.58	1.16	0.70	0.72	0.77	0.80	0.58	0.58	0.88	0.92	0.58	1.01	10.83	11.14	0.68	2.55	1.17
total	100.2	99.6	98.8	100.5	99.9	100.9	101.5	100.1	99.1	100.5	100.6	100.3	100.9	101.2	100.8	100.1	100.3	100.4	100.1	100.9
									formula based on 8 oxygens											
Si	2.82	2.85	2.81	2.84	2.91	2.91	2.89	2.89	2.88	2.90	2.90	2.91	2.92	2.90	2.92	2.94	2.94	2.90	2.94	2.91
Al	1.17	1.11	1.15	1.15	1.08	1.08	1.10	1.10	1.11	1.10	1.10	1.08	1.08	1.09	1.06	1.04	1.05	1.10	1.06	1.08
Cr	0.00	0.00	0.00	0.01	0.00	0.00	0.00	0.00	0.00	0.00	0.00	0.00	0.00	0.00	0.00	0.00	0.00	0.00	0.00	0.00
Fe	0.02	0.02	0.04	0.02	0.02	0.03	0.02	0.01	0.02	0.01	0.01	0.03	0.01	0.02	0.03	0.05	0.02	0.01	0.01	0.02
Mg	0.00	0.02	0.02	0.00	0.00	0.00	0.00	0.00	0.00	0.00	0.00	0.00	0.00	0.00	0.00	0.00	0.00	0.00	0.00	0.01
Ca	0.17	0.15	0.16	0.15	0.08	0.08	0.09	0.10	0.10	0.10	0.10	0.08	0.08	0.10	0.07	0.04	0.06	0.10	0.06	0.09
Na	0.81	0.83	0.81	0.81	0.86	0.85	0.87	0.86	0.87	0.86	0.85	0.85	0.86	0.85	0.86	0.31	0.30	0.85	0.77	0.84
K	0.03	0.03	0.03	0.03	0.07	0.04	0.04	0.04	0.05	0.03	0.03	0.05	0.05	0.03	0.06	0.63	0.65	0.04	0.14	0.07
total	5.02	5.02	5.03	5.01	5.02	4.99	5.02	5.00	5.03	5.00	4.99	5.00	5.00	4.99	5.01	5.01	5.01	5.00	4.98	5.00
An	17.2	14.9	16.0	15.4	8.4	8.2	9.2	9.7	9.8	10.2	10.3	8.5	8.1	10.1	7.0	4.1	6.0	9.9	6.2	8.7
Ab	80.1	81.7	81.4	81.3	85.1	87.8	86.8	86.0	85.7	86.5	86.4	86.5	86.8	86.6	87.3	31.6	29.5	86.2	78.9	84.8
Or	2.7	3.4	2.6	3.3	6.5	4.0	4.0	4.3	4.5	3.3	3.3	5.0	5.2	3.3	5.7	64.3	64.6	3.8	14.8	6.6

Table A1.16. *(Continued).* Individual EPMA analyses of feldspar in Roy (1933) (L5), n=38 (21-38)

analysis #	22	24	25	37	39	41	42	43	4	5	6	45	50	51	53	59	60	61		
chondrule	10	10	10	10	10	11	11	11	13	13	13	18	20	20	20	29	29	29	*mean*	*1-sig*
SiO_2	66.5	65.2	65.3	64.5	65.2	66.7	64.6	65.7	65.3	65.5	65.4	65.0	64.3	66.5	65.0	65.4	65.9	65.8	*65.5*	*1.0*
Al_2O_3	21.0	20.5	20.9	20.9	20.7	20.7	21.9	21.0	21.4	21.0	21.1	20.8	22.1	20.8	21.0	21.0	21.1	21.0	*21.0*	*0.6*
Cr_2O_3	<0.07	<0.07	<0.07	<0.07	<0.07	<0.07	0.08	<0.07	<0.07	<0.07	<0.07	<0.07	<0.07	<0.07	<0.07	<0.07	<0.07	<0.07	*<0.07*	*0.03*
FeO	0.42	0.46	0.35	0.28	0.28	0.14	0.18	0.21	0.28	0.23	0.30	0.20	0.18	0.10	0.40	0.26	0.23	0.19	*0.42*	*0.26*
MgO	<0.02	0.29	0.03	<0.02	<0.02	<0.02	<0.02	0.05	0.05	<0.02	<0.02	<0.02	<0.02	<0.02	0.04	<0.02	<0.02	<0.02	*0.05*	*0.08*
CaO	1.94	2.47	1.94	2.01	1.81	1.61	3.02	2.04	2.26	1.90	2.03	2.16	3.23	1.59	2.07	1.96	1.95	1.89	*2.09*	*0.61*
Na_2O	10.1	9.7	10.0	10.2	10.3	10.2	9.6	10.0	10.1	10.1	9.9	9.9	9.3	10.2	9.8	10.1	10.1	10.1	*9.6*	*1.5*
K_2O	0.85	0.83	0.52	0.82	1.03	1.04	0.53	0.86	0.63	0.94	1.03	1.08	0.50	1.00	1.00	0.85	0.99	0.89	*1.38*	*2.32*
total	100.8	99.5	99.1	98.8	99.4	100.4	100.0	99.8	100.0	99.7	99.7	99.1	99.7	100.2	99.3	99.5	100.2	99.8	*100.1*	*0.7*
									formula based on 8 oxygens											
Si	2.91	2.90	2.90	2.88	2.90	2.92	2.85	2.90	2.88	2.90	2.89	2.90	2.85	2.92	2.89	2.90	2.90	2.90	*2.89*	*0.03*
Al	1.08	1.07	1.09	1.10	1.09	1.07	1.14	1.10	1.11	1.10	1.10	1.09	1.15	1.08	1.10	1.10	1.09	1.09	*1.10*	*0.03*
Cr	0.00	0.00	0.00	0.00	0.00	0.00	0.00	0.00	0.00	0.00	0.00	0.00	0.00	0.00	0.00	0.00	0.00	0.00	*0.00*	*0.00*
Fe	0.02	0.02	0.01	0.01	0.01	0.01	0.01	0.01	0.01	0.01	0.01	0.01	0.01	0.00	0.01	0.01	0.01	0.01	*0.02*	*0.01*
Mg	0.00	0.02	0.00	0.00	0.00	0.00	0.00	0.00	0.00	0.00	0.00	0.00	0.00	0.00	0.00	0.00	0.00	0.00	*0.00*	*0.01*
Ca	0.09	0.12	0.09	0.10	0.09	0.08	0.14	0.10	0.11	0.09	0.10	0.10	0.15	0.07	0.10	0.09	0.09	0.09	*0.10*	*0.03*
Na	0.86	0.84	0.87	0.88	0.88	0.87	0.82	0.85	0.86	0.87	0.85	0.85	0.80	0.87	0.85	0.87	0.86	0.86	*0.82*	*0.13*
K	0.05	0.05	0.03	0.05	0.06	0.06	0.03	0.05	0.04	0.05	0.06	0.06	0.03	0.06	0.06	0.05	0.06	0.05	*0.08*	*0.14*
total	5.00	5.01	5.00	5.03	5.03	5.00	5.00	5.00	5.01	5.02	5.01	5.01	4.99	5.00	5.01	5.01	5.01	5.01	*5.01*	*0.01*
An	9.1	11.7	9.4	9.4	8.4	7.5	14.3	9.7	10.6	8.9	9.6	10.2	15.6	7.5	9.8	9.2	9.1	8.9	*9.9*	*2.9*
Ab	86.1	83.6	87.7	86.1	85.9	86.6	82.7	85.5	85.8	85.9	84.6	83.8	81.5	86.9	84.5	86.0	85.4	86.1	*82.1*	*12.5*
Or	4.8	4.7	3.0	4.5	5.7	5.8	3.0	4.9	3.5	5.2	5.8	6.0	2.9	5.6	5.7	4.7	5.5	5.0	*7.9*	*13.6*

Table A1.17. Individual EPMA analyses of feldspar in Bruderheim (L6), n=25 (1-15)

analysis #	143	144	145	146	147	148	149	135	139	140	129	130	121	122	103
chondrule	4	4	4	4	4	4	4	7	7	7	8	8	9	9	10
SiO_2	66.2	66.2	66.4	66.4	65.8	65.4	66.0	66.0	66.5	65.9	65.6	65.7	66.5	65.0	66.2
Al_2O_3	21.4	21.3	21.2	21.5	21.0	21.1	21.6	21.3	21.4	21.2	21.1	21.1	21.2	21.7	21.3
Cr_2O_3	<0.07	<0.07	0.13	<0.07	<0.07	<0.07	<0.07	<0.07	<0.07	<0.07	<0.07	0.08	<0.07	<0.07	<0.07
FeO	0.65	0.60	0.54	0.56	0.66	0.59	0.64	0.29	0.34	0.72	0.31	0.56	0.24	0.28	0.45
MgO	0.03	0.02	<0.02	<0.02	0.03	0.02	0.02	<0.02	0.04	<0.02	<0.02	<0.02	<0.02	<0.02	<0.02
CaO	2.12	2.16	2.14	2.07	2.09	2.14	2.15	2.19	2.27	2.24	2.15	2.21	2.08	2.41	2.16
Na_2O	9.5	9.9	10.0	9.9	10.1	9.3	9.4	9.9	9.8	10.1	10.0	10.0	10.1	9.9	10.0
K_2O	0.99	0.90	1.13	1.17	0.93	1.03	1.07	0.81	1.11	0.99	1.02	1.00	0.98	0.68	1.02
total	100.9	101.1	101.5	101.6	100.6	99.6	100.9	100.5	101.4	101.1	100.1	100.6	101.2	100.0	101.2
							formula based on 8 oxygens								
Si	2.89	2.89	2.89	2.89	2.89	2.89	2.89	2.90	2.90	2.89	2.89	2.89	2.90	2.87	2.89
Al	1.10	1.10	1.09	1.10	1.09	1.10	1.11	1.10	1.10	1.09	1.10	1.09	1.09	1.13	1.10
Cr	0.00	0.00	0.00	0.00	0.00	0.00	0.00	0.00	0.00	0.00	0.00	0.00	0.00	0.00	0.00
Fe	0.02	0.02	0.02	0.02	0.02	0.02	0.02	0.01	0.01	0.03	0.01	0.02	0.01	0.01	0.02
Mg	0.00	0.00	0.00	0.00	0.00	0.00	0.00	0.00	0.00	0.00	0.00	0.00	0.00	0.00	0.00
Ca	0.10	0.10	0.10	0.10	0.10	0.10	0.10	0.10	0.11	0.11	0.10	0.10	0.10	0.11	0.10
Na	0.81	0.84	0.84	0.84	0.86	0.80	0.80	0.84	0.83	0.86	0.85	0.85	0.86	0.85	0.84
K	0.06	0.05	0.06	0.06	0.05	0.06	0.06	0.05	0.06	0.06	0.06	0.06	0.05	0.04	0.06
total	4.99	5.01	5.01	5.01	5.02	4.98	4.98	5.00	5.00	5.02	5.01	5.02	5.01	5.01	5.01
An	10.3	10.2	10.0	9.7	9.8	10.6	10.5	10.4	10.6	10.4	10.1	10.3	9.6	11.4	10.1
Ab	84.0	84.8	83.8	83.9	85.1	83.3	83.3	85.0	83.2	84.2	84.3	84.1	85.0	84.7	84.3
Or	5.7	5.0	6.2	6.5	5.2	6.1	6.2	4.6	6.2	5.4	5.7	5.5	5.4	3.8	5.7

Table A1.17. *(Continued).* Individual EPMA analyses of feldspar in Bruderheim (L6), n=25 (16-25)

analysis #	106	107	110	111	112	113	114	116	118	119		
chondrule	10	10	10	11	11	11	11	11	11	11	*mean*	*1-sig*
SiO_2	65.1	66.6	66.6	66.1	66.7	65.9	65.9	66.0	65.8	66.8	*66.0*	*0.5*
Al_2O_3	20.9	21.4	21.4	21.0	21.4	21.4	20.8	20.5	21.9	21.7	*21.3*	*0.3*
Cr_2O_3	<0.07	<0.07	<0.07	<0.07	<0.07	<0.07	<0.07	<0.07	<0.07	<0.07	*<0.07*	*0.03*
FeO	0.45	0.55	0.42	0.41	0.50	0.61	0.88	0.65	0.78	0.37	*0.52*	*0.16*
MgO	0.04	<0.02	<0.02	<0.02	0.03	0.03	0.03	0.20	0.04	<0.02	*0.02*	*0.04*
CaO	2.11	2.12	2.16	2.16	2.23	2.13	2.11	2.36	2.40	2.32	*2.19*	*0.10*
Na_2O	10.0	9.9	10.0	10.0	9.6	9.2	10.4	9.9	9.3	8.8	*9.8*	*0.4*
K_2O	0.91	1.32	1.09	0.85	0.86	1.34	0.70	0.98	0.95	1.19	*1.00*	*0.16*
total	99.5	101.8	101.7	100.5	101.3	100.6	100.8	100.7	101.2	101.2	*100.9*	*0.6*
					formula based on 8 oxygens							
Si	2.89	2.89	2.89	2.90	2.90	2.89	2.89	2.90	2.87	2.90	*2.89*	*0.01*
Al	1.10	1.10	1.10	1.09	1.10	1.11	1.08	1.06	1.12	1.11	*1.10*	*0.01*
Cr	0.00	0.00	0.00	0.00	0.00	0.00	0.00	0.00	0.00	0.00	*0.00*	*0.00*
Fe	0.02	0.02	0.02	0.01	0.02	0.02	0.03	0.02	0.03	0.01	*0.02*	*0.01*
Mg	0.00	0.00	0.00	0.00	0.00	0.00	0.00	0.01	0.00	0.00	*0.00*	*0.00*
Ca	0.10	0.10	0.10	0.10	0.10	0.10	0.10	0.11	0.11	0.11	*0.10*	*0.00*
Na	0.86	0.83	0.85	0.85	0.81	0.78	0.88	0.85	0.79	0.74	*0.83*	*0.03*
K	0.05	0.07	0.06	0.05	0.05	0.07	0.04	0.06	0.05	0.07	*0.06*	*0.01*
total	5.02	5.01	5.01	5.01	4.98	4.98	5.03	5.02	4.98	4.94	*5.00*	*0.02*
An	9.9	9.9	10.0	10.1	10.8	10.5	9.7	11.0	11.8	11.8	*10.4*	*0.6*
Ab	85.0	82.9	84.0	85.1	84.3	81.7	86.4	83.6	82.7	81.0	*84.0*	*1.1*
Or	5.1	7.3	6.0	4.8	4.9	7.8	3.9	5.4	5.5	7.2	*5.6*	*1.0*

4. Individual EPMA analyses of feldspar in Semarkona (chapter 2)

Table A1.18. Individual EPMA analyses of feldspar in Semarkona (LL3.00), chondrule 3, n=4

analysis #	36	37	38	40	mean	1-sig
SiO_2	69.61	68.21	69.18	70.50	69.38	0.95
Al_2O_3	18.09	17.55	18.52	19.07	18.31	0.64
Cr_2O_3	0.03	0.00	0.02	0.00	0.01	0.01
FeO	1.54	1.92	1.00	0.68	1.29	0.55
MnO	0.03	0.07	0.03	0.02	0.04	0.02
MgO	0.22	0.31	0.22	0.16	0.23	0.06
CaO	0.59	0.42	0.44	0.19	0.41	0.17
Na_2O	11.73	10.47	11.30	11.59	11.27	0.56
K_2O	0.38	0.51	0.32	0.53	0.43	0.10
total	102.22	99.46	101.03	102.74	101.36	1.46
	formula based on 8 oxygens					
Si	3.01	3.02	3.01	3.01	3.01	0.01
Al	0.92	0.92	0.95	0.96	0.94	0.02
Cr	0.00	0.00	0.00	0.00	0.00	0.00
Fe	0.06	0.07	0.04	0.02	0.05	0.02
Mn	0.00	0.00	0.00	0.00	0.00	0.00
Mg	0.01	0.02	0.01	0.01	0.01	0.00
Ca	0.03	0.02	0.02	0.01	0.02	0.01
Na	0.98	0.90	0.95	0.96	0.95	0.03
K	0.02	0.03	0.02	0.03	0.02	0.01
total	5.03	4.98	5.00	5.00	5.01	0.02
An	2.7	2.1	2.0	0.9	1.9	0.8
Ab	95.3	94.9	96.2	96.3	95.7	0.7
Or	2.0	3.0	1.8	2.9	2.4	0.6

Table A1.18. *(Continued).* Individual EPMA analyses of feldspar in Semarkona (LL3.00), chondrule 28, n=11

analysis #	104	106	108	109	110	111	112	113	114	115	116	mean	1-sig
SiO_2	65.39	64.31	70.08	66.12	65.13	68.04	64.61	63.43	64.10	67.96	64.67	65.80	2.05
Al_2O_3	20.47	21.67	19.17	20.42	21.39	19.63	21.20	20.34	20.70	19.88	20.02	20.44	0.76
Cr_2O_3	0.02	0.02	0.00	0.01	0.02	0.00	0.01	0.04	0.04	0.01	0.01	0.02	0.01
FeO	1.68	0.74	1.05	0.75	0.99	0.69	0.88	3.00	1.83	0.94	2.12	1.33	0.74
MnO	0.04	0.01	0.05	0.02	0.05	0.04	0.04	0.04	0.08	0.04	0.03	0.04	0.02
MgO	0.44	0.12	0.13	0.16	0.11	0.05	0.21	0.36	1.45	0.06	0.26	0.31	0.40
CaO	2.46	3.04	0.14	1.83	2.58	0.99	2.64	2.79	4.09	0.66	2.44	2.15	1.15
Na_2O	10.18	9.94	11.60	10.53	10.08	10.85	10.13	9.58	9.51	11.37	10.01	10.34	0.68
K_2O	0.27	0.32	0.56	0.33	0.27	0.37	0.27	0.52	0.17	0.37	0.32	0.34	0.11
total	100.95	100.15	102.78	100.16	100.62	100.65	99.99	100.11	101.97	101.29	99.88	100.78	0.92
					formula based on 8 oxygens								
Si	2.88	2.84	3.00	2.91	2.87	2.97	2.86	2.84	2.81	2.96	2.88	2.89	0.06
Al	1.06	1.13	0.97	1.06	1.11	1.01	1.11	1.07	1.07	1.02	1.05	1.06	0.05
Cr	0.00	0.00	0.00	0.00	0.00	0.00	0.00	0.00	0.00	0.00	0.00	0.00	0.00
Fe	0.06	0.03	0.04	0.03	0.04	0.03	0.03	0.11	0.07	0.03	0.08	0.05	0.03
Mn	0.00	0.00	0.00	0.00	0.00	0.00	0.00	0.00	0.00	0.00	0.00	0.00	0.00
Mg	0.03	0.01	0.01	0.01	0.01	0.00	0.01	0.02	0.09	0.00	0.02	0.02	0.03
Ca	0.12	0.14	0.01	0.09	0.12	0.05	0.13	0.13	0.19	0.03	0.12	0.10	0.05
Na	0.87	0.85	0.96	0.90	0.86	0.92	0.87	0.83	0.81	0.96	0.87	0.88	0.05
K	0.02	0.02	0.03	0.02	0.02	0.02	0.02	0.03	0.01	0.02	0.02	0.02	0.01
total	5.03	5.03	5.01	5.02	5.02	4.99	5.03	5.05	5.06	5.02	5.03	5.03	0.02
An	11.6	14.2	0.6	8.6	12.2	4.7	12.4	13.5	19.0	3.0	11.7	10.1	5.4
Ab	86.9	84.0	96.3	89.6	86.3	93.2	86.1	83.6	80.0	94.9	86.5	88.0	5.1
Or	1.5	1.8	3.1	1.8	1.5	2.1	1.5	3.0	1.0	2.0	1.8	1.9	0.6

Table A1.18. *(Continued).* Individual EPMA analyses of feldspar in Semarkona (LL3.00), chondrules 10 and 33

	chondrule 10, n=3				
analysis #	28	30	34	mean	1-sig
SiO_2	59.52	64.43	62.53	62.16	2.47
Al_2O_3	22.42	19.83	18.92	20.39	1.82
Cr_2O_3	0.02	0.03	0.06	0.04	0.02
FeO	2.29	2.01	2.08	2.13	0.15
MnO	0.04	0.04	0.02	0.03	0.01
MgO	1.05	1.02	1.15	1.07	0.06
CaO	7.53	4.99	4.60	5.71	1.59
Na_2O	7.18	8.78	9.53	8.50	1.20
K_2O	0.16	0.18	0.21	0.19	0.03
total	100.23	101.32	99.10	100.21	1.11
	formula based on 8 oxygens				
Si	2.68	2.84	2.84	2.79	0.09
Al	1.19	1.03	1.01	1.08	0.10
Cr	0.00	0.00	0.00	0.00	0.00
Fe	0.09	0.07	0.08	0.08	0.01
Mn	0.00	0.00	0.00	0.00	0.00
Mg	0.07	0.07	0.08	0.07	0.01
Ca	0.36	0.24	0.22	0.27	0.08
Na	0.63	0.75	0.84	0.74	0.11
K	0.01	0.01	0.01	0.01	0.00
total	5.04	5.02	5.08	5.05	0.03
An	36.3	23.6	20.8	26.9	8.3
Ab	62.7	75.3	78.0	72.0	8.2
Or	0.9	1.0	1.1	1.0	0.1

	chondrule 33, n=8									
analysis #	118	121	122	123	124	125	126	127	mean	1-sig
SiO_2	60.97	60.39	60.84	60.25	60.56	58.83	60.34	61.14	60.41	0.71
Al_2O_3	21.01	23.10	24.13	23.83	22.10	22.54	24.02	23.53	23.03	1.09
Cr_2O_3	0.03	0.01	0.01	0.04	0.03	0.02	0.02	0.00	0.02	0.01
FeO	3.38	1.28	0.97	0.89	2.77	3.43	1.32	1.34	1.92	1.08
MnO	0.13	0.05	0.01	0.02	0.07	0.09	0.02	0.06	0.06	0.04
MgO	0.86	0.16	0.17	0.17	0.83	0.20	0.15	0.13	0.33	0.32
CaO	5.97	6.45	6.91	6.84	6.38	6.70	7.08	6.56	6.61	0.35
Na_2O	7.96	7.58	7.65	7.48	7.13	7.06	7.61	7.55	7.50	0.29
K_2O	0.27	0.28	0.15	0.19	0.32	0.31	0.27	0.26	0.26	0.06
total	100.58	99.29	100.85	99.70	100.20	99.19	100.83	100.58	100.15	0.67
	formula based on 8 oxygens									
Si	2.75	2.72	2.70	2.70	2.72	2.69	2.69	2.72	2.71	0.02
Al	1.12	1.23	1.26	1.26	1.17	1.21	1.26	1.23	1.22	0.05
Cr	0.00	0.00	0.00	0.00	0.00	0.00	0.00	0.00	0.00	0.00
Fe	0.13	0.05	0.04	0.03	0.10	0.13	0.05	0.05	0.07	0.04
Mn	0.00	0.00	0.00	0.00	0.00	0.00	0.00	0.00	0.00	0.00
Mg	0.06	0.01	0.01	0.01	0.06	0.01	0.01	0.01	0.02	0.02
Ca	0.29	0.31	0.33	0.33	0.31	0.33	0.34	0.31	0.32	0.02
Na	0.70	0.66	0.66	0.65	0.62	0.63	0.66	0.65	0.65	0.02
K	0.02	0.02	0.01	0.01	0.02	0.02	0.02	0.01	0.01	0.00
total	5.05	5.00	5.00	5.00	5.01	5.03	5.02	5.00	5.01	0.02
An	28.8	31.5	33.0	33.2	32.4	33.8	33.4	32.0	32.3	1.6
Ab	69.6	66.9	66.1	65.7	65.6	64.4	65.0	66.5	66.2	1.6
Or	1.6	1.6	0.9	1.1	2.0	1.9	1.5	1.5	1.5	0.4

Table A1.18. *(Continued).* Individual EPMA analyses of feldspar in Semarkona (LL3.00), chondrules 23 and 47

	chondrule 23, n=3				
analysis #	70	71	74	mean	1-sig
SiO_2	62.73	62.07	60.36	61.72	1.22
Al_2O_3	21.80	22.73	22.82	22.45	0.57
Cr_2O_3	0.07	0.04	0.14	0.08	0.05
FeO	1.54	1.14	1.34	1.34	0.20
MnO	0.19	0.10	0.25	0.18	0.07
MgO	1.50	0.67	2.08	1.42	0.71
CaO	6.71	6.43	7.96	7.03	0.82
Na_2O	6.08	6.87	6.48	6.48	0.40
K_2O	0.37	0.33	0.29	0.33	0.04
total	100.99	100.39	101.73	101.03	0.67
	formula based on 8 oxygens				
Si	2.77	2.76	2.67	2.73	0.05
Al	1.14	1.19	1.19	1.17	0.03
Cr	0.00	0.00	0.00	0.00	0.00
Fe	0.06	0.04	0.05	0.05	0.01
Mn	0.01	0.00	0.01	0.01	0.00
Mg	0.10	0.04	0.14	0.09	0.05
Ca	0.32	0.31	0.38	0.33	0.04
Na	0.52	0.59	0.56	0.56	0.04
K	0.02	0.02	0.02	0.02	0.00
total	4.93	4.95	5.02	4.97	0.04
An	37.0	33.4	39.7	36.7	3.2
Ab	60.6	64.6	58.5	61.2	3.1
Or	2.5	2.0	1.7	2.1	0.4

	chondrule 47, n=8									
analysis #	63	64	65	66	67	68	69	70	mean	1-sig
SiO_2	58.87	57.49	58.28	56.08	56.36	56.29	56.40	57.89	57.21	1.07
Al_2O_3	25.23	25.23	25.35	27.59	27.63	25.47	27.08	25.86	26.18	1.07
Cr_2O_3	0.07	0.00	0.11	0.05	0.00	0.02	0.02	0.06	0.04	0.04
FeO	0.43	0.99	0.51	0.39	0.38	0.88	0.41	0.66	0.58	0.24
MnO	0.06	0.00	0.05	0.13	0.00	0.02	0.11	0.17	0.07	0.06
MgO	0.51	0.75	0.57	0.37	0.35	0.57	0.44	0.51	0.51	0.13
CaO	8.76	8.79	8.99	10.54	10.38	8.79	10.46	9.29	9.50	0.82
Na_2O	6.62	6.36	6.33	5.82	5.73	6.36	5.76	5.74	6.09	0.36
K_2O	0.19	0.17	0.18	0.13	0.11	0.12	0.10	0.23	0.15	0.04
total	100.74	99.78	100.37	101.10	100.94	98.53	100.78	100.40	100.33	0.84
	formula based on 8 oxygens									
Si	2.62	2.60	2.61	2.51	2.52	2.57	2.53	2.59	2.57	0.05
Al	1.33	1.34	1.34	1.45	1.45	1.37	1.43	1.36	1.38	0.05
Cr	0.00	0.00	0.00	0.00	0.00	0.00	0.00	0.00	0.00	0.00
Fe	0.02	0.04	0.02	0.01	0.01	0.03	0.02	0.02	0.02	0.01
Mn	0.00	0.00	0.00	0.00	0.00	0.00	0.00	0.01	0.00	0.00
Mg	0.03	0.05	0.04	0.02	0.02	0.04	0.03	0.03	0.03	0.01
Ca	0.42	0.43	0.43	0.50	0.50	0.43	0.50	0.45	0.46	0.04
Na	0.57	0.56	0.55	0.50	0.50	0.56	0.50	0.50	0.53	0.03
K	0.01	0.01	0.01	0.01	0.01	0.01	0.01	0.01	0.01	0.00
total	5.00	5.02	5.00	5.02	5.01	5.02	5.01	4.98	5.01	0.01
An	41.8	42.9	43.5	49.6	49.7	43.0	49.8	46.6	45.9	3.5
Ab	57.1	56.1	55.5	49.6	49.7	56.3	49.6	52.1	53.3	3.3
Or	1.1	1.0	1.0	0.7	0.6	0.7	0.6	1.3	0.9	0.3

Table A1.18. *(Continued).* Individual EPMA analyses of feldspar in Semarkona (LL3.00), chondrules 20 and 41

	chondrule 20, n=5						
analysis #	45	46	47	48	49	mean	1-sig
SiO_2	52.04	53.54	54.23	53.27	52.53	53.12	0.86
Al_2O_3	28.09	28.62	26.03	27.43	27.92	27.62	0.98
Cr_2O_3	0.01	0.06	0.04	0.10	0.04	0.05	0.03
FeO	0.37	0.52	0.96	0.25	0.41	0.50	0.27
MnO	0.07	0.13	0.15	0.19	0.17	0.14	0.04
MgO	0.92	0.97	1.68	1.98	0.99	1.31	0.49
CaO	13.69	13.38	12.00	13.22	13.63	13.18	0.69
Na_2O	3.68	4.11	3.79	3.59	3.50	3.73	0.24
K_2O	0.07	0.07	0.14	0.08	0.05	0.08	0.03
total	98.96	101.39	99.00	100.11	99.24	99.74	1.03
	formula based on 8 oxygens						
Si	2.40	2.40	2.49	2.42	2.41	2.42	0.04
Al	1.52	1.52	1.41	1.47	1.51	1.48	0.05
Cr	0.00	0.00	0.00	0.00	0.00	0.00	0.00
Fe	0.01	0.02	0.04	0.01	0.02	0.02	0.01
Mn	0.00	0.01	0.01	0.01	0.01	0.01	0.00
Mg	0.06	0.06	0.11	0.13	0.07	0.09	0.03
Ca	0.68	0.64	0.59	0.64	0.67	0.64	0.03
Na	0.33	0.36	0.34	0.32	0.31	0.33	0.02
K	0.00	0.00	0.01	0.00	0.00	0.00	0.00
total	5.01	5.02	4.98	5.01	4.99	5.00	0.01
An	67.0	64.0	63.1	66.7	68.1	65.8	2.1
Ab	32.6	35.6	36.0	32.8	31.6	33.7	2.0
Or	0.4	0.4	0.8	0.5	0.3	0.5	0.2

	chondrule 41, n=3				
analysis #	78	79	80	mean	1-sig
SiO_2	52.78	51.25	53.79	52.61	1.28
Al_2O_3	29.44	28.67	27.37	28.50	1.05
Cr_2O_3	0.03	0.06	0.02	0.04	0.02
FeO	0.53	0.88	1.69	1.03	0.59
MnO	0.09	0.17	0.05	0.10	0.06
MgO	0.90	1.39	0.67	0.99	0.37
CaO	13.99	13.72	12.15	13.28	0.99
Na_2O	3.43	3.38	4.02	3.61	0.36
K_2O	0.07	0.07	0.13	0.09	0.03
total	101.25	99.59	99.90	100.25	0.88
	formula based on 8 oxygens				
Si	2.37	2.35	2.45	2.39	0.05
Al	1.56	1.55	1.47	1.53	0.05
Cr	0.00	0.00	0.00	0.00	0.00
Fe	0.02	0.03	0.06	0.04	0.02
Mn	0.00	0.01	0.00	0.00	0.00
Mg	0.06	0.10	0.05	0.07	0.03
Ca	0.67	0.67	0.59	0.65	0.05
Na	0.30	0.30	0.36	0.32	0.03
K	0.00	0.00	0.01	0.01	0.00
total	5.00	5.02	4.99	5.00	0.02
An	69.0	68.9	62.0	66.6	4.0
Ab	30.6	30.7	37.2	32.8	3.8
Or	0.4	0.4	0.8	0.6	0.2

Table A1.18. *(Continued).* Individual EPMA analyses of feldspar in Semarkona (LL3.00), chondrules 26 and 30

	chondrule 26, n=5						
analysis #	84	86	89	90	91	mean	1-sig
SiO_2	47.88	45.44	46.36	46.61	44.93	46.24	1.14
Al_2O_3	30.42	31.73	31.08	35.01	34.81	32.61	2.15
Cr_2O_3	0.00	0.05	0.06	0.02	0.03	0.03	0.02
FeO	0.96	2.46	0.56	0.18	0.32	0.90	0.92
MnO	0.07	0.12	0.05	0.05	0.02	0.06	0.04
MgO	2.39	1.00	3.34	0.78	0.71	1.64	1.17
CaO	17.48	16.29	17.07	18.98	19.28	17.82	1.27
Na_2O	1.13	1.44	0.67	0.45	0.53	0.84	0.42
K_2O	0.05	0.14	0.08	0.03	0.03	0.07	0.04
total	100.36	98.67	99.27	102.10	100.67	100.22	1.33
	formula based on 8 oxygens						
Si	2.20	2.14	2.15	2.10	2.07	2.13	0.05
Al	1.65	1.76	1.70	1.86	1.89	1.77	0.10
Cr	0.00	0.00	0.00	0.00	0.00	0.00	0.00
Fe	0.04	0.10	0.02	0.01	0.01	0.03	0.04
Mn	0.00	0.00	0.00	0.00	0.00	0.00	0.00
Mg	0.16	0.07	0.23	0.05	0.05	0.11	0.08
Ca	0.86	0.82	0.85	0.92	0.95	0.88	0.05
Na	0.10	0.13	0.06	0.04	0.05	0.08	0.04
K	0.00	0.01	0.00	0.00	0.00	0.00	0.00
total	5.02	5.04	5.03	4.99	5.01	5.02	0.02
An	89.3	85.5	92.9	95.7	95.1	91.7	4.3
Ab	10.4	13.7	6.6	4.1	4.7	7.9	4.1
Or	0.3	0.9	0.5	0.2	0.2	0.4	0.3

	chondrule 30, n=6							
analysis #	93	94	95	97	98	100	mean	1-sig
SiO_2	48.77	49.60	49.13	48.07	49.71	47.60	48.81	0.84
Al_2O_3	28.55	29.67	29.35	31.72	30.58	32.48	30.39	1.49
Cr_2O_3	0.08	0.11	0.04	0.07	0.03	0.03	0.06	0.03
FeO	0.40	0.74	0.79	0.24	0.22	0.56	0.49	0.25
MnO	0.03	0.14	0.04	0.00	0.02	0.05	0.05	0.05
MgO	3.94	1.87	1.64	1.15	1.38	1.00	1.83	1.08
CaO	17.46	17.09	16.83	18.09	17.66	18.22	17.56	0.55
Na_2O	0.44	0.69	0.58	0.42	0.57	0.88	0.60	0.17
K_2O	0.03	0.15	0.13	0.02	0.03	0.04	0.07	0.06
total	99.69	100.05	98.54	99.77	100.21	100.87	99.86	0.77
	formula based on 8 oxygens							
Si	2.25	2.28	2.28	2.21	2.27	2.18	2.24	0.04
Al	1.55	1.60	1.61	1.72	1.65	1.75	1.65	0.07
Cr	0.00	0.00	0.00	0.00	0.00	0.00	0.00	0.00
Fe	0.02	0.03	0.03	0.01	0.01	0.02	0.02	0.01
Mn	0.00	0.01	0.00	0.00	0.00	0.00	0.00	0.00
Mg	0.27	0.13	0.11	0.08	0.09	0.07	0.13	0.07
Ca	0.86	0.84	0.84	0.89	0.86	0.89	0.86	0.02
Na	0.04	0.06	0.05	0.04	0.05	0.08	0.05	0.02
K	0.00	0.01	0.01	0.00	0.00	0.00	0.00	0.00
total	4.99	4.96	4.94	4.95	4.93	4.99	4.96	0.03
An	95.5	92.3	93.3	95.9	94.3	91.7	93.8	1.7
Ab	4.4	6.7	5.8	4.0	5.5	8.0	5.7	1.5
Or	0.2	1.0	0.9	0.1	0.2	0.2	0.4	0.4

Table A1.18. *(Continued).* Individual EPMA analyses of feldspar in Semarkona (LL3.00), chondrule 1, n=16

analysis #	45	46	47	48	49	50	51	52	53	54	55	30	31	32	33	34	mean	1-sig
SiO_2	49.68	49.65	49.46	51.16	50.44	49.10	50.63	50.01	49.62	49.83	49.63	49.29	49.39	50.08	50.67	49.43	49.88	0.58
Al_2O_3	31.60	31.84	30.68	29.67	30.86	31.30	31.36	30.96	32.51	29.75	30.55	31.13	30.70	30.73	29.77	31.05	30.90	0.76
Cr_2O_3	0.03	0.03	0.05	0.05	0.00	0.02	0.01	0.03	0.01	0.11	0.05	0.00	0.03	0.00	0.00	0.04	0.03	0.03
FeO	0.39	0.49	0.39	0.33	0.66	0.95	0.17	0.29	0.26	0.39	0.64	0.29	0.57	0.28	0.45	0.26	0.43	0.20
MnO	0.00	0.01	0.03	0.04	0.06	0.02	0.02	0.02	0.01	0.06	0.02	0.00	0.03	0.05	0.03	0.00	0.02	0.02
MgO	1.47	1.51	1.83	3.23	1.60	1.54	1.39	1.42	1.20	2.59	3.38	1.41	1.53	1.45	2.28	1.25	1.82	0.68
CaO	18.46	18.62	18.30	18.31	18.25	18.12	18.30	18.29	18.56	18.30	17.66	18.91	18.54	18.28	18.35	18.25	18.34	0.26
Na_2O	0.26	0.28	0.19	0.14	0.13	0.23	0.19	0.14	0.16	0.23	0.51	0.23	0.23	0.22	0.20	0.19	0.22	0.09
K_2O	0.03	0.04	0.01	0.02	0.04	0.03	0.05	0.03	0.03	0.02	0.02	0.04	0.03	0.04	0.05	0.02	0.03	0.01
total	101.93	102.48	100.93	102.94	102.04	101.31	102.12	101.21	102.37	101.29	102.47	101.31	101.06	101.15	101.80	100.49	101.68	0.68
							formula based on 8 oxygens											
Si	2.23	2.22	2.25	2.28	2.27	2.23	2.27	2.26	2.22	2.26	2.23	2.23	2.24	2.27	2.28	2.25	2.25	0.02
Al	1.68	1.68	1.64	1.56	1.63	1.67	1.65	1.65	1.71	1.59	1.62	1.66	1.65	1.64	1.58	1.67	1.64	0.04
Cr	0.00	0.00	0.00	0.00	0.00	0.00	0.00	0.00	0.00	0.00	0.00	0.00	0.00	0.00	0.00	0.00	0.00	0.00
Fe	0.01	0.02	0.01	0.01	0.02	0.04	0.01	0.01	0.01	0.01	0.02	0.01	0.02	0.01	0.02	0.01	0.02	0.01
Mn	0.00	0.00	0.00	0.00	0.00	0.00	0.00	0.00	0.00	0.00	0.00	0.00	0.00	0.00	0.00	0.00	0.00	0.00
Mg	0.10	0.10	0.12	0.21	0.11	0.10	0.09	0.10	0.08	0.18	0.23	0.10	0.10	0.10	0.15	0.08	0.12	0.05
Ca	0.89	0.89	0.89	0.87	0.88	0.88	0.88	0.89	0.89	0.89	0.85	0.92	0.90	0.89	0.89	0.89	0.89	0.01
Na	0.02	0.02	0.02	0.01	0.01	0.02	0.02	0.01	0.01	0.02	0.04	0.02	0.02	0.02	0.02	0.02	0.02	0.01
K	0.00	0.00	0.00	0.00	0.00	0.00	0.00	0.00	0.00	0.00	0.00	0.00	0.00	0.00	0.00	0.00	0.00	0.00
total	4.94	4.95	4.94	4.95	4.92	4.95	4.92	4.92	4.93	4.96	4.99	4.95	4.94	4.93	4.94	4.92	4.94	0.02
An	97.3	97.1	98.1	98.5	98.4	97.6	97.8	98.4	98.2	97.6	94.9	97.6	97.6	97.6	97.8	98.0	97.7	0.8
Ab	2.5	2.7	1.9	1.3	1.3	2.2	1.9	1.4	1.6	2.3	4.9	2.2	2.2	2.2	1.9	1.9	2.1	0.8
Or	0.2	0.2	0.1	0.1	0.2	0.2	0.3	0.2	0.2	0.1	0.2	0.2	0.2	0.3	0.3	0.1	0.2	0.1

Table A1.18. *(Continued).* Individual EPMA analyses of feldspar in Semarkona (LL3.00), chondrule 68, n=7

analysis #	50	51	52	53	54	55	57	mean	1-sig
SiO_2	45.70	43.37	43.20	43.65	43.50	45.95	44.38	44.25	1.14
Al_2O_3	33.20	35.28	34.99	34.51	35.09	30.04	34.71	33.98	1.87
Cr_2O_3	0.02	0.07	0.07	0.00	0.00	0.16	0.00	0.05	0.06
FeO	0.17	0.19	0.08	0.18	0.11	0.46	0.00	0.17	0.14
MnO	0.04	0.00	0.00	0.00	0.02	0.07	0.07	0.03	0.03
MgO	0.81	0.55	0.58	0.68	0.61	4.02	1.18	1.20	1.26
CaO	19.04	19.65	19.84	19.39	19.45	18.99	19.91	19.47	0.36
Na_2O	0.32	0.24	0.16	0.21	0.13	0.30	0.17	0.22	0.07
K_2O	0.04	0.03	0.03	0.04	0.03	0.08	0.04	0.04	0.02
total	99.33	99.39	98.96	98.66	98.94	100.07	100.46	99.40	0.65
			formula based on 8 oxygens						
Si	2.12	2.02	2.02	2.05	2.03	2.13	2.05	2.06	0.05
Al	1.82	1.94	1.93	1.91	1.93	1.64	1.89	1.87	0.11
Cr	0.00	0.00	0.00	0.00	0.00	0.01	0.00	0.00	0.00
Fe	0.01	0.01	0.00	0.01	0.00	0.02	0.00	0.01	0.01
Mn	0.00	0.00	0.00	0.00	0.00	0.00	0.00	0.00	0.00
Mg	0.06	0.04	0.04	0.05	0.04	0.28	0.08	0.08	0.09
Ca	0.95	0.98	1.00	0.97	0.97	0.94	0.98	0.97	0.02
Na	0.03	0.02	0.01	0.02	0.01	0.03	0.01	0.02	0.01
K	0.00	0.00	0.00	0.00	0.00	0.00	0.00	0.00	0.00
total	4.98	5.02	5.02	5.01	5.00	5.06	5.02	5.02	0.02
An	96.8	97.7	98.4	97.8	98.7	96.8	98.3	97.8	0.8
Ab	3.0	2.2	1.4	1.9	1.2	2.8	1.5	2.0	0.7
Or	0.3	0.2	0.2	0.3	0.2	0.5	0.2	0.2	0.1

Table A1.18. *(Continued).* Individual EPMA analyses of feldspar in Semarkona (LL3.00), chondrule 36, n=15

analysis #	138	139	140	141	142	143	144	145	146	147	148	149	150	151	152	mean	1-sig
SiO_2	47.81	48.70	47.46	48.28	47.89	49.71	48.89	49.63	47.59	47.51	48.46	48.08	48.37	48.45	48.10	48.33	0.69
Al_2O_3	30.11	28.22	31.26	30.06	30.88	28.06	28.28	28.10	31.25	30.96	29.65	31.50	30.30	30.89	30.54	30.00	1.25
Cr_2O_3	0.05	0.02	0.01	0.03	0.00	0.06	0.01	0.03	0.02	0.03	0.01	0.01	0.01	0.01	0.05	0.02	0.02
FeO	0.14	0.14	0.13	0.14	0.20	0.16	0.16	0.17	0.12	0.19	0.74	0.18	0.11	0.24	0.21	0.20	0.15
MnO	0.00	0.02	0.03	0.00	0.01	0.00	0.00	0.02	0.01	0.00	0.00	0.02	0.00	0.01	0.01	0.01	0.01
MgO	2.08	2.80	1.78	2.51	1.81	2.69	2.34	2.44	1.80	1.86	2.52	1.89	1.89	1.88	2.59	2.19	0.37
CaO	19.58	19.33	19.59	19.32	19.69	19.41	19.01	19.06	19.83	19.55	19.13	19.59	19.21	19.35	19.74	19.43	0.25
Na_2O	0.09	0.07	0.03	0.10	0.04	0.12	0.17	0.21	0.01	0.08	0.21	0.07	0.22	0.04	0.11	0.10	0.07
K_2O	0.02	0.01	0.01	0.04	0.04	0.01	0.04	0.04	0.02	0.04	0.07	0.00	0.03	0.02	0.01	0.03	0.02
total	99.89	99.32	100.30	100.47	100.56	100.23	98.91	99.69	100.65	100.22	100.78	101.35	100.14	100.88	101.37	100.32	0.68
							formula based on 8 oxygens										
Si	2.21	2.26	2.18	2.21	2.20	2.28	2.27	2.29	2.18	2.19	2.22	2.19	2.22	2.21	2.19	2.22	0.04
Al	1.64	1.54	1.69	1.63	1.67	1.52	1.55	1.53	1.69	1.68	1.60	1.69	1.64	1.66	1.64	1.62	0.06
Cr	0.00	0.00	0.00	0.00	0.00	0.00	0.00	0.00	0.00	0.00	0.00	0.00	0.00	0.00	0.00	0.00	0.00
Fe	0.01	0.01	0.00	0.01	0.01	0.01	0.01	0.01	0.00	0.01	0.03	0.01	0.00	0.01	0.01	0.01	0.01
Mn	0.00	0.00	0.00	0.00	0.00	0.00	0.00	0.00	0.00	0.00	0.00	0.00	0.00	0.00	0.00	0.00	0.00
Mg	0.14	0.19	0.12	0.17	0.12	0.18	0.16	0.17	0.12	0.13	0.17	0.13	0.13	0.13	0.18	0.15	0.03
Ca	0.97	0.96	0.96	0.95	0.97	0.96	0.95	0.94	0.97	0.96	0.94	0.95	0.95	0.95	0.96	0.96	0.01
Na	0.01	0.01	0.00	0.01	0.00	0.01	0.01	0.02	0.00	0.01	0.02	0.01	0.02	0.00	0.01	0.01	0.01
K	0.00	0.00	0.00	0.00	0.00	0.00	0.00	0.00	0.00	0.00	0.00	0.00	0.00	0.00	0.00	0.00	0.00
total	4.98	4.97	4.97	4.98	4.97	4.96	4.96	4.96	4.98	4.98	4.99	4.97	4.97	4.96	4.99	4.97	0.01
An	99.1	99.3	99.7	98.9	99.4	98.8	98.2	97.9	99.7	99.1	97.6	99.3	97.8	99.5	98.9	98.9	0.7
Ab	0.8	0.6	0.2	0.9	0.3	1.1	1.5	1.9	0.1	0.7	1.9	0.7	2.0	0.3	1.0	1.0	0.6
Or	0.1	0.1	0.1	0.2	0.2	0.1	0.3	0.2	0.1	0.2	0.4	0.0	0.2	0.1	0.1	0.2	0.1

Table A1.18. *(Continued).* Individual EPMA analyses of feldspar in Semarkona (LL3.00), chondrule 22, n=4

analysis #	56	57	58	59	mean	1-sig
SiO_2	44.56	44.16	45.37	45.29	44.84	0.58
Al_2O_3	35.78	36.30	35.05	34.98	35.53	0.63
Cr_2O_3	0.01	0.00	0.05	0.00	0.02	0.02
FeO	1.19	1.12	1.07	0.75	1.03	0.19
MnO	0.02	0.04	0.01	0.05	0.03	0.02
MgO	0.54	0.66	0.71	1.02	0.73	0.20
CaO	19.99	19.87	19.92	19.45	19.81	0.25
Na_2O	0.08	0.03	0.04	0.00	0.04	0.03
K_2O	0.03	0.04	0.03	0.04	0.04	0.01
total	102.19	102.21	102.26	101.57	102.06	0.32
	formula based on 8 oxygens					
Si	2.03	2.01	2.06	2.06	2.04	0.03
Al	1.92	1.95	1.88	1.88	1.91	0.03
Cr	0.00	0.00	0.00	0.00	0.00	0.00
Fe	0.05	0.04	0.04	0.03	0.04	0.01
Mn	0.00	0.00	0.00	0.00	0.00	0.00
Mg	0.04	0.05	0.05	0.07	0.05	0.01
Ca	0.97	0.97	0.97	0.95	0.97	0.01
Na	0.01	0.00	0.00	0.00	0.00	0.00
K	0.00	0.00	0.00	0.00	0.00	0.00
total	5.02	5.02	5.00	5.00	5.01	0.01
An	99.1	99.5	99.4	99.7	99.5	0.2
Ab	0.7	0.2	0.4	0.0	0.3	0.3
Or	0.2	0.2	0.2	0.3	0.2	0.0

5. Individual EPMA analyses of feldspar in ordinary chondrites (chapter 3)

Table A1.19. Individual EPMA analyses of feldspar in Bishunpur (LL3.15), chondrule 7, n=12

analysis #	30	31	32	33	34	35	36	40	41	42	43	44	mean	1-sig
SiO_2	43.6	43.1	43.2	44.0	43.5	43.7	46.4	43.4	42.8	42.9	43.2	41.8	43.5	1.1
Al_2O_3	36.5	36.7	37.2	36.6	36.5	35.6	34.8	36.9	36.2	36.8	36.2	35.4	36.3	0.7
Cr_2O_3	<0.07	<0.07	<0.07	<0.07	0.09	<0.07	0.14	<0.07	<0.07	<0.07	<0.07	<0.07	<0.07	0.05
FeO	0.49	0.45	0.38	0.44	0.53	0.70	0.45	0.52	0.44	0.36	1.22	0.57	0.55	0.23
MnO	0.10	0.10	<0.08	<0.08	<0.08	0.13	0.10	<0.08	<0.08	<0.08	<0.08	<0.08	<0.08	0.05
MgO	0.43	0.29	0.19	0.36	0.39	0.68	0.28	0.34	0.24	0.19	0.28	0.33	0.33	0.13
CaO	20.7	20.5	20.6	20.3	20.8	20.4	19.4	20.6	20.1	20.6	20.3	20.1	20.4	0.4
Na_2O	0.03	0.06	0.04	0.09	0.03	0.13	0.09	0.03	0.18	0.39	0.06	0.15	0.11	0.10
K_2O	0.05	0.03	0.05	0.04	0.05	0.04	0.05	0.05	<0.02	0.03	0.05	0.05	0.04	0.01
total	101.8	101.2	101.8	101.9	101.8	101.3	101.6	101.9	99.9	101.2	101.2	98.4	101.2	1.0
	formula based on 8 oxygens													
Si	1.99	1.98	1.97	2.01	1.99	2.01	2.11	1.98	1.99	1.97	1.99	1.98	2.00	0.04
Al	1.97	1.99	2.01	1.97	1.97	1.93	1.86	1.99	1.98	1.99	1.97	1.98	1.97	0.04
Cr	0.00	0.00	0.00	0.00	0.00	0.00	0.01	0.00	0.00	0.00	0.00	0.00	0.00	0.00
Fe	0.02	0.02	0.01	0.02	0.02	0.03	0.02	0.02	0.02	0.01	0.05	0.02	0.02	0.01
Mn	0.00	0.00	0.00	0.00	0.00	0.01	0.00	0.00	0.00	0.00	0.00	0.00	0.00	0.00
Mg	0.03	0.02	0.01	0.02	0.03	0.05	0.02	0.02	0.02	0.01	0.02	0.02	0.02	0.01
Ca	1.02	1.01	1.01	0.99	1.02	1.01	0.94	1.01	1.00	1.02	1.00	1.02	1.00	0.02
Na	0.00	0.01	0.00	0.01	0.00	0.01	0.01	0.00	0.02	0.03	0.01	0.01	0.01	0.01
K	0.00	0.00	0.00	0.00	0.00	0.00	0.00	0.00	0.00	0.00	0.00	0.00	0.00	0.00
total	5.03	5.03	5.03	5.01	5.03	5.04	4.97	5.03	5.03	5.05	5.03	5.04	5.02	0.02
An	99.5	99.3	99.4	99.0	99.5	98.6	98.9	99.4	98.4	96.5	99.2	98.4	98.8	0.8
Ab	0.2	0.5	0.4	0.8	0.3	1.2	0.8	0.3	1.6	3.3	0.5	1.3	0.9	0.9
Or	0.3	0.2	0.3	0.2	0.3	0.3	0.3	0.3	0.0	0.2	0.3	0.3	0.2	0.1

Table A1.19. *(Continued).* Individual EPMA analyses of feldspar in Bishunpur (LL3.15), chondrules 2 and 1

	chondrule 2, n=4						**chondrule 1, n=2**				
analysis #	73	74	76	77	mean	1-sig	analysis #	63	65	mean	1-sig
SiO_2	49.8	49.3	49.4	51.7	50.0	1.1	SiO_2	55.3	55.8	55.6	0.4
Al_2O_3	28.1	27.9	30.1	28.8	28.7	1.0	Al_2O_3	27.0	27.1	27.0	0.1
Cr_2O_3	0.24	0.22	<0.07	0.10	0.14	0.11	Cr_2O_3	0.09	0.13	0.11	0.03
FeO	0.43	0.86	0.55	0.75	0.64	0.19	FeO	0.59	0.84	0.71	0.18
MnO	<0.08	<0.08	0.14	<0.08	<0.08	0.07	MnO	<0.08	0.13	<0.08	0.09
MgO	1.77	2.23	0.95	0.65	1.40	0.73	MgO	1.18	0.97	1.08	0.15
CaO	14.8	14.3	15.5	13.3	14.5	0.9	CaO	11.3	10.6	11.0	0.5
Na_2O	3.51	3.30	3.28	4.67	3.69	0.66	Na_2O	5.91	6.30	6.11	0.28
K_2O	0.03	0.03	0.03	0.04	0.03	0.01	K_2O	0.04	0.05	0.05	0.01
total	98.7	98.2	99.9	100.0	99.2	0.9	total	101.4	102.0	101.7	0.5
	formula based on 8 oxygens							*formula based on 8 oxygens*			
Si	2.32	2.31	2.27	2.37	2.32	0.04	Si	2.48	2.49	2.48	0.01
Al	1.54	1.54	1.63	1.55	1.57	0.04	Al	1.42	1.42	1.42	0.00
Cr	0.01	0.01	0.00	0.00	0.01	0.00	Cr	0.00	0.00	0.00	0.00
Fe	0.02	0.03	0.02	0.03	0.02	0.01	Fe	0.02	0.03	0.03	0.01
Mn	0.00	0.00	0.01	0.00	0.00	0.00	Mn	0.00	0.00	0.00	0.00
Mg	0.12	0.16	0.07	0.04	0.10	0.05	Mg	0.08	0.06	0.07	0.01
Ca	0.74	0.72	0.76	0.65	0.72	0.05	Ca	0.54	0.51	0.53	0.03
Na	0.32	0.30	0.29	0.41	0.33	0.06	Na	0.51	0.54	0.53	0.02
K	0.00	0.00	0.00	0.00	0.00	0.00	K	0.00	0.00	0.00	0.00
total	5.06	5.07	5.06	5.06	5.06	0.00	total	5.07	5.07	5.07	0.00
An	69.7	70.4	72.2	61.0	68.3	5.0	An	51.3	48.1	49.7	2.3
Ab	30.1	29.4	27.6	38.7	31.5	5.0	Ab	48.5	51.6	50.0	2.2
Or	0.2	0.2	0.2	0.2	0.2	0.0	Or	0.2	0.3	0.2	0.1

Table A1.20. Individual EPMA analyses of feldspar in Chainpur (LL3.4), chondrules 16, 17, and 18

	chondrule 16, n=4					
analysis #	39	40	41	42	mean	1-sig
SiO_2	44.9	45.3	47.8	48.0	46.5	1.6
Al_2O_3	35.3	36.4	34.3	34.8	35.2	0.9
Cr_2O_3	<0.07	<0.07	<0.07	0.12	<0.07	0.06
FeO	0.61	0.59	0.79	0.73	0.68	0.10
MnO	<0.08	<0.08	<0.08	0.10	<0.08	0.05
MgO	0.09	0.05	0.15	0.13	0.10	0.04
CaO	15.9	18.2	17.4	17.0	17.1	0.9
Na_2O	1.68	1.71	1.55	1.65	1.65	0.07
K_2O	0.15	0.02	0.04	0.07	0.07	0.06
total	98.6	102.3	102.0	102.5	101.4	1.8
	formula based on 8 oxygens					
Si	2.09	2.05	2.16	2.15	2.11	0.05
Al	1.94	1.94	1.82	1.84	1.89	0.06
Cr	0.00	0.00	0.00	0.00	0.00	0.00
Fe	0.02	0.02	0.03	0.03	0.03	0.00
Mn	0.00	0.00	0.00	0.00	0.00	0.00
Mg	0.01	0.00	0.01	0.01	0.01	0.00
Ca	0.80	0.88	0.84	0.82	0.83	0.04
Na	0.15	0.15	0.14	0.14	0.15	0.01
K	0.01	0.00	0.00	0.00	0.00	0.00
total	5.02	5.05	5.00	5.00	5.02	0.02
An	83.2	85.3	85.9	84.7	84.8	1.2
Ab	15.9	14.5	13.8	14.9	14.8	0.9
Or	0.9	0.1	0.2	0.4	0.4	0.4

	chondrule 17, n-2			
analysis #	30	34	mean	1-sig
SiO_2	59.5	64.5	62.0	3.6
Al_2O_3	26.1	21.8	23.9	3.1
Cr_2O_3	<0.07	0.09	<0.07	0.07
FeO	0.67	1.13	0.90	0.32
MnO	0.16	0.31	0.23	0.11
MgO	0.53	1.98	1.26	1.03
CaO	8.7	8.1	8.4	0.4
Na_2O	6.24	7.82	7.03	1.11
K_2O	0.04	0.21	0.12	0.12
total	101.9	105.9	103.9	2.9
	formula based on 8 oxygens			
Si	2.62	2.74	2.68	0.09
Al	1.35	1.09	1.22	0.19
Cr	0.00	0.00	0.00	0.00
Fe	0.02	0.04	0.03	0.01
Mn	0.01	0.01	0.01	0.00
Mg	0.03	0.13	0.08	0.06
Ca	0.41	0.37	0.39	0.03
Na	0.53	0.64	0.59	0.08
K	0.00	0.01	0.01	0.01
total	4.98	5.04	5.01	0.04
An	43.3	36.0	39.7	5.1
Ab	56.5	62.8	59.7	4.5
Or	0.2	1.1	0.7	0.6

	chondrule 18, n=3				
analysis #	59	60	62	mean	1-sig
SiO_2	60.4	60.1	61.4	60.6	0.7
Al_2O_3	25.3	27.7	27.0	26.7	1.2
Cr_2O_3	<0.07	<0.07	<0.07	<0.07	0.00
FeO	1.23	0.76	0.74	0.91	0.28
MnO	<0.08	<0.08	<0.08	<0.08	0.00
MgO	1.86	0.29	0.27	0.81	0.91
CaO	8.9	9.3	8.4	8.9	0.5
Na_2O	7.80	7.41	8.19	7.80	0.39
K_2O	0.05	0.06	0.04	0.05	0.01
total	105.5	105.6	106.0	105.7	0.3
	formula based on 8 oxygens				
Si	2.59	2.57	2.60	2.59	0.02
Al	1.28	1.39	1.35	1.34	0.06
Cr	0.00	0.00	0.00	0.00	0.00
Fe	0.04	0.03	0.03	0.03	0.01
Mn	0.00	0.00	0.00	0.00	0.00
Mg	0.12	0.02	0.02	0.05	0.06
Ca	0.41	0.43	0.38	0.40	0.02
Na	0.65	0.61	0.67	0.65	0.03
K	0.00	0.00	0.00	0.00	0.00
total	5.09	5.05	5.06	5.07	0.03
An	38.5	40.8	36.0	38.5	2.4
Ab	61.2	58.9	63.8	61.3	2.5
Or	0.2	0.3	0.2	0.2	0.1

Table A1.21. Individual EPMA analyses of feldspar in Parnallee (LL3.6), chondrule 1, n=13

analysis #	36	37	40	41	42	43	44	46	47	48	49	51	52	mean	1-sig
SiO_2	45.7	46.2	45.7	46.2	46.1	46.4	47.2	45.4	45.3	46.5	46.5	46.3	45.3	46.1	0.6
Al_2O_3	35.7	35.9	35.6	35.9	36.0	35.7	36.1	36.1	35.7	36.1	35.8	35.6	34.7	35.8	0.4
Cr_2O_3	<0.03	<0.03	0.04	0.03	<0.03	<0.03	<0.03	<0.03	<0.03	<0.03	<0.03	<0.03	<0.03	<0.03	0.01
FeO	0.53	0.67	0.65	0.50	0.70	0.61	0.57	0.67	0.87	0.78	0.62	0.66	2.06	0.76	0.40
MnO	0.06	<0.03	0.04	<0.03	<0.03	<0.03	<0.03	0.03	<0.03	<0.03	<0.03	<0.03	<0.03	<0.03	0.02
MgO	0.05	0.08	0.31	0.13	0.06	0.15	0.08	0.03	0.05	0.25	0.04	0.11	0.16	0.12	0.08
CaO	17.3	17.5	17.2	15.4	17.4	16.1	15.5	17.9	17.5	16.0	17.8	16.8	16.8	16.9	0.8
Na_2O	1.95	1.83	2.02	2.47	1.81	2.86	3.20	1.65	1.73	1.78	1.79	2.69	1.65	2.11	0.52
K_2O	0.09	0.08	0.10	0.13	0.08	0.11	0.13	0.06	0.07	0.11	0.06	0.08	0.10	0.09	0.02
total	101.4	102.3	101.6	100.8	102.2	101.9	102.8	101.9	101.3	101.5	102.5	102.2	100.8	101.8	0.6
						formula based on 8 oxygens									
Si	2.08	2.09	2.08	2.11	2.08	2.10	2.12	2.06	2.07	2.11	2.09	2.09	2.09	2.09	0.01
Al	1.92	1.91	1.91	1.93	1.92	1.90	1.91	1.93	1.92	1.92	1.90	1.90	1.89	1.91	0.01
Cr	0.00	0.00	0.00	0.00	0.00	0.00	0.00	0.00	0.00	0.00	0.00	0.00	0.00	0.00	0.00
Fe	0.02	0.03	0.02	0.02	0.03	0.02	0.02	0.03	0.03	0.03	0.02	0.03	0.08	0.03	0.02
Mn	0.00	0.00	0.00	0.00	0.00	0.00	0.00	0.00	0.00	0.00	0.00	0.00	0.00	0.00	0.00
Mg	0.00	0.01	0.02	0.01	0.00	0.01	0.01	0.00	0.00	0.02	0.00	0.01	0.01	0.01	0.01
Ca	0.85	0.85	0.84	0.75	0.84	0.78	0.74	0.87	0.86	0.78	0.86	0.81	0.83	0.82	0.04
Na	0.17	0.16	0.18	0.22	0.16	0.25	0.28	0.14	0.15	0.16	0.16	0.24	0.15	0.19	0.04
K	0.01	0.00	0.01	0.01	0.00	0.01	0.01	0.00	0.00	0.01	0.00	0.00	0.01	0.01	0.00
total	5.05	5.04	5.06	5.04	5.04	5.08	5.07	5.04	5.05	5.01	5.04	5.08	5.05	5.05	0.02
An	82.6	83.7	82.0	76.9	83.8	75.2	72.3	85.4	84.5	82.7	84.3	77.1	84.5	81.2	4.3
Ab	16.8	15.9	17.5	22.3	15.8	24.2	27.0	14.2	15.1	16.6	15.3	22.4	14.9	18.3	4.2
Or	0.5	0.4	0.6	0.8	0.5	0.6	0.7	0.3	0.4	0.7	0.3	0.5	0.6	0.5	0.1

Table A1.21. *(Continued).* Individual EPMA analyses of feldspar in Parnallee (LL3.6), chondrules 3 and 7

	chondrule 3, n=6							
analysis #	79	81	93	94	96	99	mean	1-sig
SiO_2	48.1	45.6	44.8	45.3	45.2	45.5	45.8	1.2
Al_2O_3	34.9	35.5	35.2	35.2	35.2	35.2	35.2	0.2
Cr_2O_3	<0.03	0.05	0.07	<0.03	<0.03	<0.03	<0.03	0.03
FeO	0.11	0.20	0.36	0.37	0.40	0.26	0.28	0.11
MnO	<0.03	<0.03	<0.03	<0.03	0.04	<0.03	<0.03	0.02
MgO	0.07	0.08	0.35	0.30	0.40	0.23	0.24	0.14
CaO	16.2	16.3	17.6	17.4	17.4	17.3	17.0	0.6
Na_2O	2.94	3.12	1.65	1.73	2.03	1.85	2.22	0.64
K_2O	0.13	0.11	0.11	0.07	0.10	0.09	0.10	0.02
total	102.5	100.9	100.1	100.4	100.7	100.5	100.9	0.8
	formula based on 8 oxygens							
Si	2.16	2.09	2.07	2.08	2.07	2.09	2.09	0.03
Al	1.84	1.91	1.92	1.91	1.91	1.90	1.90	0.03
Cr	0.00	0.00	0.00	0.00	0.00	0.00	0.00	0.00
Fe	0.00	0.01	0.01	0.01	0.02	0.01	0.01	0.00
Mn	0.00	0.00	0.00	0.00	0.00	0.00	0.00	0.00
Mg	0.00	0.01	0.02	0.02	0.03	0.02	0.02	0.01
Ca	0.78	0.80	0.87	0.86	0.86	0.85	0.84	0.04
Na	0.26	0.28	0.15	0.15	0.18	0.16	0.20	0.06
K	0.01	0.01	0.01	0.00	0.01	0.01	0.01	0.00
total	5.05	5.10	5.05	5.04	5.07	5.04	5.06	0.02
An	74.7	73.9	85.0	84.4	82.1	83.4	80.6	5.0
Ab	24.5	25.6	14.4	15.2	17.3	16.1	18.9	4.9
Or	0.7	0.6	0.6	0.4	0.6	0.5	0.6	0.1

	chondrule 7, n=4					
analysis #	169	172	181	187	mean	1-sig
SiO_2	47.5	46.2	45.7	46.7	46.6	0.8
Al_2O_3	33.6	34.6	34.3	34.0	34.1	0.4
Cr_2O_3	<0.03	<0.03	<0.03	0.03	<0.03	0.01
FeO	0.19	0.16	0.17	0.74	0.31	0.28
MnO	<0.03	0.03	<0.03	<0.03	<0.03	0.01
MgO	0.15	0.12	0.07	0.37	0.18	0.13
CaO	16.2	17.1	16.7	17.1	16.8	0.4
Na_2O	2.59	2.38	2.39	1.90	2.31	0.29
K_2O	0.13	0.09	0.07	0.11	0.10	0.03
total	100.3	100.7	99.4	101.0	100.4	0.7
	formula based on 8 oxygens					
Si	2.18	2.12	2.12	2.14	2.14	0.03
Al	1.81	1.87	1.87	1.83	1.85	0.03
Cr	0.00	0.00	0.00	0.00	0.00	0.00
Fe	0.01	0.01	0.01	0.03	0.01	0.01
Mn	0.00	0.00	0.00	0.00	0.00	0.00
Mg	0.01	0.01	0.00	0.03	0.01	0.01
Ca	0.79	0.84	0.83	0.84	0.83	0.02
Na	0.23	0.21	0.21	0.17	0.21	0.03
K	0.01	0.01	0.00	0.01	0.01	0.00
total	5.04	5.06	5.05	5.03	5.05	0.01
An	77.0	79.5	79.2	82.7	79.6	2.3
Ab	22.3	20.0	20.5	16.6	19.8	2.3
Or	0.7	0.5	0.4	0.7	0.6	0.2

Table A1.21. *(Continued).* Individual EPMA analyses of feldspar in Parnallee (LL3.6), chondrules 8 and 2

	chondrule 8, n=7									chondrule 2, n=2				
analysis #	193	194	196	199	202	206	207	mean	1-sig	analysis #	62	68	mean	1-sig
SiO_2	47.0	47.3	47.6	46.8	47.4	47.3	46.7	47.1	0.3	SiO_2	65.0	67.1	66.1	1.5
Al_2O_3	34.0	33.5	33.4	33.3	33.4	33.7	33.2	33.5	0.3	Al_2O_3	21.1	21.2	21.2	0.1
Cr_2O_3	<0.03	<0.03	<0.03	<0.03	0.04	<0.03	<0.03	<0.03	0.02	Cr_2O_3	<0.03	0.04	<0.03	0.03
FeO	0.27	0.36	0.24	0.36	0.44	0.35	0.32	0.33	0.07	FeO	1.50	1.50	1.50	0.00
MnO	<0.03	<0.03	<0.03	<0.03	<0.03	<0.03	<0.03	<0.03	0.00	MnO	<0.03	0.03	<0.03	0.02
MgO	0.27	0.16	0.14	0.23	0.49	0.29	0.79	0.34	0.23	MgO	0.16	0.98	0.57	0.58
CaO	16.7	16.4	15.9	16.1	16.3	16.6	16.1	16.3	0.3	CaO	1.0	2.3	1.6	0.9
Na_2O	2.40	2.29	2.70	2.54	2.41	2.22	2.23	2.40	0.17	Na_2O	10.82	9.43	10.12	0.98
K_2O	0.10	0.10	0.09	0.20	0.06	0.09	0.12	0.11	0.04	K_2O	1.10	1.18	1.14	0.05
total	100.7	100.1	100.0	99.6	100.6	100.4	99.4	100.1	0.5	total	100.7	103.8	102.2	2.2
	formula based on 8 oxygens										*formula based on 8 oxygens*			
Si	2.15	2.17	2.18	2.17	2.17	2.16	2.16	2.17	0.01	Si	2.87	2.87	2.87	0.00
Al	1.83	1.82	1.81	1.81	1.80	1.82	1.81	1.81	0.01	Al	1.10	1.07	1.08	0.02
Cr	0.00	0.00	0.00	0.00	0.00	0.00	0.00	0.00	0.00	Cr	0.00	0.00	0.00	0.00
Fe	0.01	0.01	0.01	0.01	0.02	0.01	0.01	0.01	0.00	Fe	0.06	0.05	0.05	0.00
Mn	0.00	0.00	0.00	0.00	0.00	0.00	0.00	0.00	0.00	Mn	0.00	0.00	0.00	0.00
Mg	0.02	0.01	0.01	0.02	0.03	0.02	0.05	0.02	0.02	Mg	0.01	0.06	0.04	0.04
Ca	0.82	0.81	0.78	0.80	0.80	0.81	0.80	0.80	0.01	Ca	0.05	0.10	0.08	0.04
Na	0.21	0.20	0.24	0.23	0.21	0.20	0.20	0.21	0.02	Na	0.93	0.78	0.85	0.10
K	0.01	0.01	0.01	0.01	0.00	0.01	0.01	0.01	0.00	K	0.06	0.06	0.06	0.00
total	5.05	5.03	5.04	5.05	5.04	5.03	5.04	5.04	0.01	total	5.07	5.01	5.04	0.04
An	78.9	79.4	76.0	76.9	78.6	80.0	79.3	78.5	1.5	An	4.5	10.9	7.7	4.6
Ab	20.5	20.0	23.4	21.9	21.0	19.4	20.0	20.9	1.4	Ab	89.5	82.3	85.9	5.1
Or	0.5	0.6	0.5	1.1	0.3	0.5	0.7	0.6	0.2	Or	6.0	6.8	6.4	0.5

Table A1.21. *(Continued).* Individual EPMA analyses of feldspar in Parnallee (LL3.6), chondrule 9, n=9

analysis #	210	211	214	215	216	220	223	225	226	mean	1-sig
SiO_2	70.1	66.2	68.1	70.5	68.0	69.1	66.6	70.6	70.6	68.9	1.7
Al_2O_3	18.1	16.1	19.2	19.1	18.7	19.1	18.2	19.2	18.4	18.5	1.0
Cr_2O_3	<0.03	0.11	0.04	<0.03	<0.03	<0.03	<0.03	<0.03	<0.03	<0.03	0.04
FeO	0.92	2.75	0.57	0.63	1.51	1.28	0.71	0.50	0.53	1.04	0.73
MnO	<0.03	0.06	<0.03	0.05	<0.03	<0.03	<0.03	<0.03	<0.03	<0.03	0.02
MgO	0.69	1.80	0.19	0.19	0.33	0.91	0.30	0.21	0.33	0.55	0.53
CaO	1.1	3.0	0.2	0.1	0.4	0.6	0.5	0.1	0.2	0.7	0.9
Na_2O	10.99	9.53	11.08	11.54	11.26	11.04	9.89	11.71	11.36	10.93	0.74
K_2O	0.74	0.60	0.86	0.58	0.54	0.52	1.77	0.33	0.47	0.71	0.42
total	102.6	100.1	100.1	102.7	100.8	102.6	98.0	102.7	101.9	101.3	1.6
				formula based on 8 oxygens							
Si	3.01	2.96	2.99	3.01	2.98	2.97	3.00	3.01	3.03	3.00	0.02
Al	0.91	0.85	0.99	0.96	0.97	0.97	0.96	0.97	0.93	0.95	0.04
Cr	0.00	0.00	0.00	0.00	0.00	0.00	0.00	0.00	0.00	0.00	0.00
Fe	0.03	0.10	0.02	0.02	0.06	0.05	0.03	0.02	0.02	0.04	0.03
Mn	0.00	0.00	0.00	0.00	0.00	0.00	0.00	0.00	0.00	0.00	0.00
Mg	0.04	0.12	0.01	0.01	0.02	0.06	0.02	0.01	0.02	0.04	0.04
Ca	0.05	0.14	0.01	0.01	0.02	0.03	0.02	0.01	0.01	0.03	0.04
Na	0.92	0.83	0.94	0.96	0.96	0.92	0.86	0.97	0.95	0.92	0.05
K	0.04	0.03	0.05	0.03	0.03	0.03	0.10	0.02	0.03	0.04	0.02
total	5.01	5.04	5.01	5.00	5.03	5.02	5.00	5.00	4.99	5.01	0.02
An	4.9	14.1	0.8	0.6	1.8	2.9	2.5	0.5	1.0	3.2	4.3
Ab	91.1	82.5	94.4	96.2	95.2	94.2	87.2	97.7	96.3	92.8	5.0
Or	4.0	3.4	4.8	3.2	3.0	2.9	10.3	1.8	2.6	4.0	2.5

Table A1.22. Individual EPMA analyses of feldspar in Dhajala (H3.8), chondrules 2 and 1

	chondrule 2, n=6								chondrule 1, n=2				
analysis #	89	90	91	92	93	94	mean	1-sig	analysis #	86	87	mean	1-sig
SiO_2	50.4	49.7	49.7	49.7	49.4	49.8	49.8	0.3	SiO_2	47.1	51.1	49.1	2.8
Al_2O_3	33.5	34.1	34.2	34.2	34.3	34.5	34.1	0.3	Al_2O_3	35.2	32.8	34.0	1.8
Cr_2O_3	<0.07	<0.07	0.13	<0.07	<0.07	<0.07	<0.07	0.05	Cr_2O_3	<0.07	<0.07	<0.07	0.00
FeO	0.37	0.38	0.58	0.24	0.31	0.17	0.34	0.14	FeO	0.15	0.32	0.24	0.13
MnO	<0.09	<0.09	<0.09	<0.09	<0.09	0.12	<0.09	0.05	MnO	<0.09	<0.09	<0.09	0.00
MgO	0.03	0.08	0.06	0.05	0.05	0.03	0.05	0.02	MgO	0.18	0.26	0.22	0.06
CaO	16.2	17.2	16.8	16.3	17.3	16.9	16.8	0.4	CaO	18.5	15.5	17.0	2.1
Na_2O	2.83	2.40	2.52	2.67	2.31	2.44	2.53	0.19	Na_2O	1.46	3.68	2.57	1.56
K_2O	0.06	0.07	0.09	0.09	0.11	0.10	0.09	0.02	K_2O	0.07	0.17	0.12	0.07
total	103.4	103.9	104.1	103.3	103.7	104.1	103.7	0.3	total	102.7	103.7	103.2	0.8
	formula based on 8 oxygens									*formula based on 8 oxygens*			
Si	2.23	2.20	2.20	2.20	2.19	2.20	2.20	0.02	Si	2.11	2.26	2.19	0.10
Al	1.75	1.78	1.78	1.79	1.79	1.79	1.78	0.02	Al	1.87	1.71	1.79	0.11
Cr	0.00	0.00	0.00	0.00	0.00	0.00	0.00	0.00	Cr	0.00	0.00	0.00	0.00
Fe	0.01	0.01	0.02	0.01	0.01	0.01	0.01	0.01	Fe	0.01	0.01	0.01	0.00
Mn	0.00	0.00	0.00	0.00	0.00	0.00	0.00	0.00	Mn	0.00	0.00	0.00	0.00
Mg	0.00	0.01	0.00	0.00	0.00	0.00	0.00	0.00	Mg	0.01	0.02	0.01	0.00
Ca	0.77	0.81	0.80	0.78	0.82	0.80	0.80	0.02	Ca	0.89	0.73	0.81	0.11
Na	0.24	0.21	0.22	0.23	0.20	0.21	0.22	0.02	Na	0.13	0.32	0.22	0.13
K	0.00	0.00	0.00	0.00	0.01	0.01	0.00	0.00	K	0.00	0.01	0.01	0.00
total	5.01	5.02	5.02	5.02	5.02	5.01	5.02	0.00	total	5.02	5.05	5.04	0.02
An	75.7	79.5	78.3	76.8	80.0	78.9	78.2	1.7	An	87.1	69.3	78.2	12.6
Ab	24.0	20.1	21.2	22.7	19.4	20.6	21.3	1.7	Ab	12.5	29.8	21.1	12.2
Or	0.3	0.4	0.5	0.5	0.6	0.6	0.5	0.1	Or	0.4	0.9	0.6	0.4

Table A1.22. *(Continued).* Individual EPMA analyses of feldspar in Dhajala (H3.8), chondrules 11 and 5

	chondrule 11, n=8									
analysis #	105	106	107	108	109	110	111	112	mean	1-sig
SiO_2	60.9	60.1	60.3	65.3	57.9	60.8	56.9	61.1	60.4	2.5
Al_2O_3	27.2	28.0	28.1	25.2	28.9	26.8	29.5	23.3	27.1	2.0
Cr_2O_3	<0.07	<0.07	<0.07	0.08	<0.07	0.08	<0.07	0.12	<0.07	0.05
FeO	0.53	0.23	0.25	0.65	0.35	0.43	0.34	1.10	0.48	0.29
MnO	<0.09	0.09	0.09	0.15	<0.09	<0.09	<0.09	0.32	<0.09	0.11
MgO	0.84	0.05	0.08	0.58	0.07	0.51	0.06	2.86	0.63	0.95
CaO	9.7	10.1	9.8	7.0	10.6	8.8	11.4	9.7	9.6	1.3
Na_2O	7.14	6.90	6.82	8.67	6.34	7.26	5.78	6.67	6.95	0.84
K_2O	0.12	0.14	0.13	0.20	0.13	0.23	0.11	0.18	0.16	0.05
total	106.4	105.5	105.6	107.8	104.2	104.8	104.1	105.4	105.5	1.2
	formula based on 8 oxygens									
Si	2.58	2.56	2.57	2.71	2.51	2.60	2.47	2.63	2.58	0.07
Al	1.36	1.41	1.41	1.23	1.47	1.35	1.51	1.18	1.37	0.11
Cr	0.00	0.00	0.00	0.00	0.00	0.00	0.00	0.00	0.00	0.00
Fe	0.02	0.01	0.01	0.02	0.01	0.02	0.01	0.04	0.02	0.01
Mn	0.00	0.00	0.00	0.01	0.00	0.00	0.00	0.01	0.00	0.00
Mg	0.05	0.00	0.01	0.04	0.00	0.03	0.00	0.18	0.04	0.06
Ca	0.44	0.46	0.45	0.31	0.49	0.40	0.53	0.45	0.44	0.07
Na	0.59	0.57	0.56	0.70	0.53	0.60	0.49	0.56	0.57	0.06
K	0.01	0.01	0.01	0.01	0.01	0.01	0.01	0.01	0.01	0.00
total	5.04	5.02	5.01	5.03	5.03	5.03	5.02	5.06	5.03	0.01
An	42.6	44.3	43.9	30.4	47.7	39.6	51.9	44.0	43.1	6.3
Ab	56.8	54.9	55.4	68.6	51.6	59.2	47.5	55.0	56.1	6.1
Or	0.6	0.8	0.7	1.1	0.7	1.3	0.6	1.0	0.8	0.2

	chondrule 5, n=4					
analysis #	101	102	103	104	mean	1-sig
SiO_2	60.9	62.0	64.1	60.1	61.8	1.7
Al_2O_3	27.2	26.6	25.7	27.5	26.8	0.8
Cr_2O_3	<0.07	<0.07	<0.07	0.17	<0.07	0.08
FeO	0.53	0.61	0.63	0.82	0.65	0.12
MnO	<0.09	<0.09	<0.09	<0.09	<0.09	0.00
MgO	0.03	0.17	0.40	0.13	0.18	0.16
CaO	9.3	8.7	7.1	9.3	8.6	1.0
Na_2O	7.80	8.38	9.04	7.23	8.11	0.78
K_2O	0.16	0.20	0.16	0.16	0.17	0.02
total	105.9	106.7	107.1	105.4	106.3	0.7
	formula based on 8 oxygens					
Si	2.59	2.62	2.68	2.57	2.62	0.05
Al	1.36	1.33	1.27	1.39	1.34	0.05
Cr	0.00	0.00	0.00	0.01	0.00	0.00
Fe	0.02	0.02	0.02	0.03	0.02	0.00
Mn	0.00	0.00	0.00	0.00	0.00	0.00
Mg	0.00	0.01	0.02	0.01	0.01	0.01
Ca	0.42	0.39	0.32	0.42	0.39	0.05
Na	0.64	0.69	0.73	0.60	0.67	0.06
K	0.01	0.01	0.01	0.01	0.01	0.00
total	5.05	5.07	5.06	5.04	5.05	0.01
An	39.3	36.1	29.9	41.1	36.6	4.9
Ab	59.9	62.9	69.3	58.0	62.5	4.9
Or	0.8	1.0	0.8	0.8	0.9	0.1

Table A1.23. Individual EPMA analyses of feldspar in Bo Xian (LL3.9), chondrules 1 and 4

	chondrule 1, n=8									
analysis #	106	107	108	110	111	112	113	114	mean	1-sig
SiO_2	47.0	47.1	47.4	47.0	46.5	47.1	47.9	47.6	47.2	0.4
Al_2O_3	34.0	34.4	34.7	34.8	35.0	34.3	34.9	34.7	34.6	0.3
Cr_2O_3	0.09	<0.08	<0.08	<0.08	<0.08	<0.08	<0.08	0.10	<0.08	0.04
FeO	0.26	0.28	0.64	0.73	0.46	0.30	<0.10	0.21	0.36	0.24
MnO	0.10	<0.08	<0.08	<0.08	<0.08	<0.08	<0.08	<0.08	<0.08	0.04
MgO	<0.02	<0.02	0.04	0.03	<0.02	<0.02	<0.02	<0.02	<0.02	0.02
CaO	16.4	16.8	16.6	16.7	17.2	16.3	17.1	16.9	16.8	0.3
Na_2O	2.91	2.68	2.75	2.62	2.51	2.74	2.48	2.36	2.63	0.18
K_2O	0.06	0.06	0.08	0.09	0.07	0.08	0.06	0.06	0.07	0.01
total	100.8	101.3	102.2	101.9	101.8	100.9	102.5	101.9	101.7	0.6
	formula based on 8 oxygens									
Si	2.15	2.14	2.14	2.13	2.11	2.15	2.15	2.15	2.14	0.01
Al	1.83	1.84	1.85	1.86	1.87	1.85	1.85	1.85	1.85	0.01
Cr	0.00	0.00	0.00	0.00	0.00	0.00	0.00	0.00	0.00	0.00
Fe	0.01	0.01	0.02	0.03	0.02	0.01	0.00	0.01	0.01	0.01
Mn	0.00	0.00	0.00	0.00	0.00	0.00	0.00	0.00	0.00	0.00
Mg	0.00	0.00	0.00	0.00	0.00	0.00	0.00	0.00	0.00	0.00
Ca	0.80	0.82	0.81	0.81	0.84	0.80	0.82	0.82	0.81	0.01
Na	0.26	0.24	0.24	0.23	0.22	0.24	0.22	0.21	0.23	0.02
K	0.00	0.00	0.00	0.00	0.00	0.00	0.00	0.00	0.00	0.00
total	5.06	5.06	5.06	5.06	5.06	5.05	5.04	5.03	5.05	0.01
An	75.4	77.3	76.7	77.5	78.8	76.4	79.0	79.5	77.6	1.4
Ab	24.2	22.4	22.9	22.0	20.8	23.2	20.7	20.1	22.0	1.4
Or	0.3	0.3	0.4	0.5	0.4	0.5	0.3	0.3	0.4	0.1

	chondrule 4, n=5						
analysis #	78	79	80	81	82	mean	1-sig
SiO_2	45.3	46.2	47.6	47.4	46.5	46.6	0.9
Al_2O_3	35.2	34.5	34.1	33.7	34.2	34.3	0.6
Cr_2O_3	<0.08	<0.08	<0.08	<0.08	<0.08	<0.08	0.00
FeO	0.70	0.77	0.73	0.75	0.84	0.76	0.05
MnO	<0.08	<0.08	<0.08	<0.08	<0.08	<0.08	0.00
MgO	0.03	<0.02	<0.02	0.03	<0.02	<0.02	0.02
CaO	17.9	17.2	16.5	16.2	16.6	16.9	0.7
Na_2O	1.89	2.92	2.97	3.30	2.93	2.80	0.53
K_2O	0.06	0.09	0.05	0.08	0.09	0.07	0.02
total	101.1	101.7	101.9	101.5	101.2	101.5	0.4
	formula based on 8 oxygens						
Si	2.08	2.11	2.16	2.16	2.13	2.13	0.03
Al	1.90	1.85	1.82	1.81	1.84	1.85	0.04
Cr	0.00	0.00	0.00	0.00	0.00	0.00	0.00
Fe	0.03	0.03	0.03	0.03	0.03	0.03	0.00
Mn	0.00	0.00	0.00	0.00	0.00	0.00	0.00
Mg	0.00	0.00	0.00	0.00	0.00	0.00	0.00
Ca	0.88	0.84	0.80	0.79	0.81	0.83	0.04
Na	0.17	0.26	0.26	0.29	0.26	0.25	0.05
K	0.00	0.01	0.00	0.00	0.01	0.00	0.00
total	5.06	5.10	5.07	5.08	5.08	5.08	0.02
An	83.7	76.2	75.2	72.7	75.5	76.7	4.2
Ab	16.0	23.3	24.5	26.9	24.1	22.9	4.1
Or	0.3	0.5	0.3	0.4	0.5	0.4	0.1

Table A1.23. *(Continued).* Individual EPMA analyses of feldspar in Bo Xian (LL3.9), chondrule 5, n=4

analysis #	83	84	87	89	mean	1-sig
SiO_2	51.5	51.8	51.8	52.3	51.9	0.3
Al_2O_3	31.5	30.7	31.1	30.7	31.0	0.4
Cr_2O_3	<0.08	<0.08	<0.08	<0.08	<0.08	0.00
FeO	0.73	0.80	0.89	0.75	0.79	0.07
MnO	<0.08	<0.08	<0.08	<0.08	<0.08	0.00
MgO	0.02	<0.02	<0.02	0.08	0.02	0.04
CaO	13.4	12.9	12.6	12.5	12.9	0.4
Na_2O	5.10	5.44	5.38	5.41	5.33	0.16
K_2O	0.05	0.07	0.09	0.08	0.07	0.02
total	102.2	101.7	101.9	101.8	101.9	0.2
	formula based on 8 oxygens					
Si	2.31	2.33	2.33	2.35	2.33	0.02
Al	1.66	1.63	1.65	1.62	1.64	0.02
Cr	0.00	0.00	0.00	0.00	0.00	0.00
Fe	0.03	0.03	0.03	0.03	0.03	0.00
Mn	0.00	0.00	0.00	0.00	0.00	0.00
Mg	0.00	0.00	0.00	0.01	0.00	0.00
Ca	0.64	0.62	0.61	0.60	0.62	0.02
Na	0.44	0.47	0.47	0.47	0.46	0.01
K	0.00	0.00	0.00	0.00	0.00	0.00
total	5.09	5.09	5.09	5.08	5.09	0.01
An	59.1	56.5	56.2	55.9	56.9	1.4
Ab	40.7	43.2	43.3	43.7	42.7	1.4
Or	0.3	0.4	0.5	0.4	0.4	0.1

Table A1.24. Individual EPMA analyses of feldspar in Saratov (L4), chondrules 3, 5, and 26

	chondrule 3, n=2			
analysis #	32	33	mean	1-sig
SiO_2	47.9	48.0	48.0	0.0
Al_2O_3	35.9	35.7	35.8	0.2
Cr_2O_3	0.11	<0.07	<0.07	0.08
FeO	0.67	0.64	0.65	0.02
MnO	<0.08	<0.08	<0.08	0.00
MgO	<0.02	<0.02	<0.02	0.00
CaO	18.5	17.3	17.9	0.9
Na_2O	1.73	2.44	2.08	0.50
K_2O	0.05	0.18	0.12	0.10
total	104.9	104.2	104.5	0.5
	formula based on 8 oxygens			
Si	2.11	2.13	2.12	0.01
Al	1.87	1.86	1.86	0.00
Cr	0.00	0.00	0.00	0.00
Fe	0.02	0.02	0.02	0.00
Mn	0.00	0.00	0.00	0.00
Mg	0.00	0.00	0.00	0.00
Ca	0.87	0.82	0.85	0.04
Na	0.15	0.21	0.18	0.04
K	0.00	0.01	0.01	0.01
total	5.03	5.05	5.04	0.02
An	85.3	78.9	82.1	4.5
Ab	14.4	20.1	17.3	4.0
Or	0.3	1.0	0.6	0.5

	chondrule 5, n=5						
analysis #	38	39	40	41	42	mean	1-sig
SiO_2	48.5	49.1	48.6	49.0	48.1	48.7	0.4
Al_2O_3	35.7	34.7	35.5	35.3	34.2	35.1	0.6
Cr_2O_3	0.09	<0.07	<0.07	<0.07	<0.07	<0.07	0.04
FeO	0.52	0.31	0.55	0.59	0.63	0.52	0.13
MnO	<0.08	<0.08	<0.08	<0.08	<0.08	<0.08	0.00
MgO	<0.02	0.04	0.03	<0.02	0.03	<0.02	0.02
CaO	18.0	17.0	16.9	17.5	17.8	17.4	0.5
Na_2O	1.90	2.55	3.36	2.64	2.08	2.50	0.57
K_2O	0.08	0.12	0.11	0.15	0.08	0.11	0.03
total	104.8	103.8	105.0	105.1	102.9	104.3	1.0
	formula based on 8 oxygens						
Si	2.13	2.18	2.14	2.15	2.16	2.15	0.02
Al	1.85	1.81	1.84	1.83	1.81	1.83	0.02
Cr	0.00	0.00	0.00	0.00	0.00	0.00	0.00
Fe	0.02	0.01	0.02	0.02	0.02	0.02	0.00
Mn	0.00	0.00	0.00	0.00	0.00	0.00	0.00
Mg	0.00	0.00	0.00	0.00	0.00	0.00	0.00
Ca	0.85	0.80	0.79	0.82	0.86	0.83	0.03
Na	0.16	0.22	0.29	0.22	0.18	0.21	0.05
K	0.00	0.01	0.01	0.01	0.00	0.01	0.00
total	5.02	5.03	5.09	5.05	5.03	5.05	0.03
An	83.6	78.1	73.1	77.9	82.2	79.0	4.1
Ab	16.0	21.3	26.3	21.3	17.4	20.4	4.1
Or	0.4	0.7	0.5	0.8	0.4	0.6	0.2

	chondrule 26, n=3				
analysis #	82	84	85	mean	1-sig
SiO_2	47.9	47.5	47.2	47.6	0.4
Al_2O_3	34.6	34.7	35.0	34.8	0.2
Cr_2O_3	0.12	0.20	0.09	0.13	0.05
FeO	0.21	0.37	0.21	0.26	0.09
MnO	<0.08	<0.08	<0.08	<0.08	0.00
MgO	0.04	0.03	<0.02	0.02	0.02
CaO	17.0	18.2	18.0	17.7	0.6
Na_2O	3.05	2.27	2.17	2.50	0.48
K_2O	0.38	0.19	0.24	0.27	0.10
total	103.4	103.5	102.9	103.2	0.3
	formula based on 8 oxygens				
Si	2.14	2.13	2.12	2.13	0.01
Al	1.82	1.83	1.85	1.84	0.02
Cr	0.00	0.01	0.00	0.00	0.00
Fe	0.01	0.01	0.01	0.01	0.00
Mn	0.00	0.00	0.00	0.00	0.00
Mg	0.00	0.00	0.00	0.00	0.00
Ca	0.82	0.87	0.87	0.85	0.03
Na	0.26	0.20	0.19	0.22	0.04
K	0.02	0.01	0.01	0.02	0.01
total	5.08	5.06	5.05	5.07	0.02
An	74.0	80.7	81.0	78.6	3.9
Ab	24.0	18.3	17.7	20.0	3.5
Or	2.0	1.0	1.3	1.4	0.5

Table A1.24. *(Continued).* Individual EPMA analyses of feldspar in Saratov (L4), chondrules 8 and 9

	chondrule 8, n=4						**chondrule 9, n=3**					
analysis #	50	52	53	54	mean	1-sig	analysis #	56	57	58	mean	1-sig
SiO_2	49.8	50.4	49.3	50.4	50.0	0.5	SiO_2	50.8	51.2	55.8	52.6	2.8
Al_2O_3	33.4	31.9	32.8	32.0	32.5	0.7	Al_2O_3	32.4	32.2	29.6	31.4	1.6
Cr_2O_3	0.08	0.10	0.23	0.26	0.17	0.09	Cr_2O_3	0.09	0.15	0.08	0.11	0.04
FeO	0.90	1.04	0.73	1.08	0.94	0.16	FeO	0.72	0.82	0.71	0.75	0.06
MnO	<0.08	<0.08	<0.08	<0.08	<0.08	0.00	MnO	0.09	<0.08	<0.08	<0.08	0.05
MgO	0.04	0.11	0.06	0.07	0.07	0.03	MgO	0.05	0.39	0.11	0.18	0.18
CaO	16.1	15.2	15.5	15.1	15.5	0.4	CaO	15.4	15.0	11.7	14.0	2.1
Na_2O	3.46	3.65	3.61	3.42	3.53	0.11	Na_2O	3.62	3.88	5.44	4.31	0.98
K_2O	0.17	0.12	0.25	0.10	0.16	0.07	K_2O	0.21	0.17	0.22	0.20	0.02
total	104.0	102.5	102.5	102.5	102.9	0.7	total	103.4	103.8	103.6	103.6	0.2
	formula based on 8 oxygens							*formula based on 8 oxygens*				
Si	2.21	2.26	2.22	2.26	2.24	0.03	Si	2.26	2.27	2.44	2.32	0.10
Al	1.75	1.69	1.74	1.69	1.72	0.03	Al	1.70	1.68	1.53	1.63	0.09
Cr	0.00	0.00	0.01	0.01	0.01	0.00	Cr	0.00	0.01	0.00	0.00	0.00
Fe	0.03	0.04	0.03	0.04	0.04	0.01	Fe	0.03	0.03	0.03	0.03	0.00
Mn	0.00	0.00	0.00	0.00	0.00	0.00	Mn	0.00	0.00	0.00	0.00	0.00
Mg	0.00	0.01	0.00	0.00	0.00	0.00	Mg	0.00	0.03	0.01	0.01	0.01
Ca	0.76	0.73	0.75	0.73	0.74	0.02	Ca	0.73	0.71	0.55	0.66	0.10
Na	0.30	0.32	0.31	0.30	0.31	0.01	Na	0.31	0.33	0.46	0.37	0.08
K	0.01	0.01	0.01	0.01	0.01	0.00	K	0.01	0.01	0.01	0.01	0.00
total	5.07	5.05	5.07	5.04	5.06	0.02	total	5.05	5.06	5.03	5.05	0.02
An	71.3	69.2	69.4	70.6	70.1	1.0	An	69.4	67.5	53.6	63.5	8.6
Ab	27.8	30.2	29.2	28.9	29.0	1.0	Ab	29.5	31.6	45.2	35.4	8.5
Or	0.9	0.7	1.3	0.5	0.9	0.3	Or	1.1	0.9	1.2	1.1	0.1

Table A1.24. *(Continued).* Individual EPMA analyses of feldspar in Saratov (L4), chondrules 10 and 7

	chondrule 10, n=6							
analysis #	61	62	63	65	66	67	mean	1-sig
SiO_2	63.7	59.7	62.5	67.5	63.3	65.0	63.6	2.6
Al_2O_3	21.4	26.3	23.6	21.5	25.2	22.3	23.4	2.0
Cr_2O_3	0.77	0.09	0.17	0.13	<0.07	0.19	0.23	0.28
FeO	1.82	0.82	1.04	1.15	0.77	1.54	1.19	0.42
MnO	0.12	<0.08	<0.08	0.09	<0.08	<0.08	<0.08	0.05
MgO	1.14	0.85	1.49	2.55	0.10	2.00	1.36	0.87
CaO	4.9	10.0	8.9	6.7	7.5	6.5	7.4	1.8
Na_2O	9.20	6.94	8.11	6.83	8.49	9.22	8.13	1.06
K_2O	0.35	0.13	0.20	0.32	0.18	0.34	0.25	0.09
total	103.3	104.8	106.1	106.8	105.6	107.2	105.6	1.4
	formula based on 8 oxygens							
Si	2.77	2.58	2.67	2.81	2.69	2.74	2.71	0.08
Al	1.10	1.34	1.18	1.05	1.26	1.11	1.17	0.11
Cr	0.03	0.00	0.01	0.00	0.00	0.01	0.01	0.01
Fe	0.07	0.03	0.04	0.04	0.03	0.05	0.04	0.02
Mn	0.00	0.00	0.00	0.00	0.00	0.00	0.00	0.00
Mg	0.07	0.05	0.09	0.16	0.01	0.13	0.09	0.05
Ca	0.23	0.46	0.41	0.30	0.34	0.29	0.34	0.09
Na	0.78	0.58	0.67	0.55	0.70	0.75	0.67	0.09
K	0.02	0.01	0.01	0.02	0.01	0.02	0.01	0.01
total	5.06	5.05	5.08	4.94	5.04	5.09	5.04	0.05
An	22.2	44.0	37.5	34.5	32.6	27.6	33.1	7.6
Ab	75.9	55.3	61.5	63.6	66.4	70.7	65.6	7.2
Or	1.9	0.7	1.0	2.0	1.0	1.7	1.4	0.6

	chondrule 7, n=6							
analysis #	44	45	46	47	48	49	mean	1-sig
SiO_2	69.4	68.6	66.8	66.7	69.9	70.5	68.7	1.6
Al_2O_3	20.1	21.0	22.0	22.2	19.9	19.6	20.8	1.1
Cr_2O_3	0.11	<0.07	<0.07	<0.07	<0.07	<0.07	<0.07	0.04
FeO	0.68	0.71	0.63	0.59	0.67	0.60	0.65	0.05
MnO	<0.08	<0.08	<0.08	<0.08	<0.08	<0.08	<0.08	0.00
MgO	<0.02	0.03	<0.02	<0.02	0.13	0.21	0.06	0.09
CaO	1.2	2.0	3.0	3.3	0.7	0.6	1.8	1.1
Na_2O	11.48	11.27	10.71	10.52	11.79	11.57	11.22	0.50
K_2O	0.40	0.33	0.28	0.25	0.59	0.57	0.40	0.15
total	103.4	104.0	103.4	103.5	103.8	103.6	103.6	0.2
	formula based on 8 oxygens							
Si	2.96	2.92	2.86	2.85	2.97	2.99	2.92	0.06
Al	1.01	1.05	1.11	1.12	1.00	0.98	1.04	0.06
Cr	0.00	0.00	0.00	0.00	0.00	0.00	0.00	0.00
Fe	0.02	0.03	0.02	0.02	0.02	0.02	0.02	0.00
Mn	0.00	0.00	0.00	0.00	0.00	0.00	0.00	0.00
Mg	0.00	0.00	0.00	0.00	0.01	0.01	0.00	0.01
Ca	0.06	0.09	0.14	0.15	0.03	0.03	0.08	0.05
Na	0.95	0.93	0.89	0.87	0.97	0.95	0.93	0.04
K	0.02	0.02	0.02	0.01	0.03	0.03	0.02	0.01
total	5.02	5.03	5.04	5.03	5.03	5.01	5.03	0.01
An	5.5	8.9	13.1	14.6	3.2	2.6	8.0	5.1
Ab	92.4	89.4	85.5	84.1	93.7	94.4	89.9	4.3
Or	2.1	1.7	1.5	1.3	3.1	3.1	2.1	0.8

Table A1.24. *(Continued).* Individual EPMA analyses of feldspar in Saratov (L4), chondrule 15, n=4

analysis #	68	69	70	71	mean	1-sig
SiO_2	69.8	71.2	71.8	68.7	70.4	1.4
Al_2O_3	17.5	19.9	19.6	17.6	18.7	1.3
Cr_2O_3	0.12	<0.07	0.11	<0.07	<0.07	0.07
FeO	1.16	0.74	0.47	1.05	0.85	0.31
MnO	<0.08	0.09	<0.08	0.14	<0.08	0.07
MgO	1.97	0.15	0.15	1.92	1.05	1.04
CaO	2.5	0.3	0.6	2.4	1.4	1.2
Na_2O	10.59	12.18	11.86	10.57	11.30	0.84
K_2O	0.53	0.40	0.45	0.65	0.51	0.11
total	104.1	105.0	105.0	103.0	104.3	0.9
	formula based on 8 oxygens					
Si	2.97	2.98	3.00	2.96	2.98	0.02
Al	0.88	0.98	0.97	0.90	0.93	0.05
Cr	0.00	0.00	0.00	0.00	0.00	0.00
Fe	0.04	0.03	0.02	0.04	0.03	0.01
Mn	0.00	0.00	0.00	0.01	0.00	0.00
Mg	0.13	0.01	0.01	0.12	0.07	0.07
Ca	0.11	0.01	0.03	0.11	0.07	0.05
Na	0.87	0.99	0.96	0.88	0.93	0.06
K	0.03	0.02	0.02	0.04	0.03	0.01
total	5.04	5.03	5.01	5.05	5.03	0.02
An	11.1	1.3	2.6	10.8	6.4	5.2
Ab	86.1	96.6	95.0	85.8	90.9	5.8
Or	2.8	2.1	2.4	3.5	2.7	0.6

Table A1.25. Individual EPMA analyses of feldspar in Bjurböle (L/LL4), chondrules 15 and 14

	chondrule 15, n=3				
analysis #	107	109	110	mean	1-sig
SiO_2	52.6	50.1	50.0	50.9	1.5
Al_2O_3	32.1	34.0	33.9	33.4	1.0
Cr_2O_3	0.14	<0.06	0.10	0.08	0.07
FeO	0.86	0.82	0.68	0.79	0.10
MnO	0.11	<0.07	<0.07	<0.07	0.06
MgO	0.06	0.04	0.08	0.06	0.02
CaO	14.3	16.0	16.3	15.5	1.1
Na_2O	3.96	2.88	2.76	3.20	0.66
K_2O	0.17	0.12	0.12	0.14	0.03
total	104.4	103.9	103.9	104.1	0.3
	formula based on 8 oxygens				
Si	2.31	2.21	2.21	2.24	0.06
Al	1.66	1.77	1.77	1.73	0.06
Cr	0.00	0.00	0.00	0.00	0.00
Fe	0.03	0.03	0.03	0.03	0.00
Mn	0.00	0.00	0.00	0.00	0.00
Mg	0.00	0.00	0.01	0.00	0.00
Ca	0.67	0.76	0.77	0.73	0.05
Na	0.34	0.25	0.24	0.27	0.06
K	0.01	0.01	0.01	0.01	0.00
total	5.03	5.03	5.03	5.03	0.00
An	66.0	74.9	76.0	72.3	5.5
Ab	33.1	24.4	23.3	26.9	5.3
Or	0.9	0.7	0.6	0.7	0.1

	chondrule 14, n=6							
analysis #	101	102	103	104	105	106	mean	1-sig
SiO_2	47.7	51.5	47.0	64.5	68.4	51.0	55.0	9.1
Al_2O_3	34.7	31.7	35.5	19.6	21.5	31.5	29.1	6.8
Cr_2O_3	0.38	<0.06	0.13	<0.06	<0.06	1.47	0.33	0.58
FeO	0.41	0.77	0.25	3.49	0.59	1.40	1.15	1.21
MnO	<0.07	<0.07	<0.07	<0.07	<0.07	<0.07	<0.07	0.00
MgO	0.03	0.40	0.06	0.11	0.03	0.22	0.14	0.14
CaO	17.1	13.6	17.9	1.1	1.5	13.5	10.8	7.6
Na_2O	2.18	3.71	1.70	10.72	11.02	3.72	5.51	4.23
K_2O	0.06	0.16	0.06	0.59	0.60	0.13	0.27	0.26
total	102.7	101.9	102.6	100.2	103.7	103.0	102.3	1.2
	formula based on 8 oxygens							
Si	2.14	2.31	2.11	2.89	2.91	2.28	2.44	0.36
Al	1.84	1.67	1.88	1.03	1.08	1.66	1.53	0.38
Cr	0.01	0.00	0.00	0.00	0.00	0.05	0.01	0.02
Fe	0.02	0.03	0.01	0.13	0.02	0.05	0.04	0.05
Mn	0.00	0.00	0.00	0.00	0.00	0.00	0.00	0.00
Mg	0.00	0.03	0.00	0.01	0.00	0.01	0.01	0.01
Ca	0.82	0.65	0.86	0.05	0.07	0.65	0.52	0.36
Na	0.19	0.32	0.15	0.93	0.91	0.32	0.47	0.35
K	0.00	0.01	0.00	0.03	0.03	0.01	0.02	0.01
total	5.03	5.02	5.02	5.08	5.02	5.03	5.03	0.02
An	81.0	66.3	85.0	5.2	6.9	66.2	51.8	36.2
Ab	18.6	32.8	14.7	91.4	89.9	33.0	46.7	34.8
Or	0.4	0.9	0.3	3.3	3.2	0.8	1.5	1.4

Table A1.25. *(Continued).* Individual EPMA analyses of feldspar in Bjurböle (L/LL4), chondrules 6 and 8

	chondrule 6, n=3				
analysis #	89	90	91	mean	1-sig
SiO_2	60.0	61.9	55.2	59.0	3.5
Al_2O_3	27.5	26.0	30.7	28.1	2.4
Cr_2O_3	0.13	0.14	0.18	0.15	0.03
FeO	0.72	0.63	0.44	0.60	0.14
MnO	<0.07	<0.07	<0.07	<0.07	0.00
MgO	0.08	0.48	0.20	0.25	0.21
CaO	8.7	7.6	12.4	9.5	2.5
Na_2O	7.42	8.02	5.40	6.95	1.37
K_2O	0.20	0.20	0.12	0.17	0.04
total	104.7	105.0	104.6	104.7	0.2
	formula based on 8 oxygens				
Si	2.58	2.65	2.40	2.54	0.13
Al	1.40	1.31	1.57	1.43	0.13
Cr	0.00	0.00	0.01	0.01	0.00
Fe	0.03	0.02	0.02	0.02	0.01
Mn	0.00	0.00	0.00	0.00	0.00
Mg	0.00	0.03	0.01	0.02	0.01
Ca	0.40	0.35	0.58	0.44	0.12
Na	0.62	0.66	0.46	0.58	0.11
K	0.01	0.01	0.01	0.01	0.00
total	5.04	5.03	5.04	5.04	0.00
An	38.8	33.9	55.5	42.7	11.3
Ab	60.1	65.0	43.9	56.4	11.1
Or	1.1	1.0	0.6	0.9	0.2

	chondrule 8, n=8									
analysis #	92	93	95	96	97	98	99	100	mean	1-sig
SiO_2	71.4	72.6	68.8	68.7	68.3	69.3	68.7	68.6	69.6	1.5
Al_2O_3	20.4	20.2	19.9	19.9	19.6	20.2	19.9	19.8	20.0	0.3
Cr_2O_3	<0.06	<0.06	0.08	<0.06	<0.06	<0.06	0.10	0.10	<0.06	0.05
FeO	0.52	0.34	0.47	0.67	1.14	0.34	0.46	0.53	0.56	0.26
MnO	<0.07	<0.07	<0.07	<0.07	<0.07	0.08	<0.07	<0.07	<0.07	0.03
MgO	0.33	0.20	0.15	0.86	0.99	0.32	0.31	0.60	0.47	0.31
CaO	0.7	0.4	0.6	0.8	0.9	0.8	0.8	1.1	0.8	0.2
Na_2O	11.38	10.35	10.11	10.42	11.09	10.30	10.38	9.92	10.49	0.49
K_2O	1.43	3.36	3.06	1.68	1.12	2.47	2.40	2.78	2.29	0.80
total	106.2	107.5	103.2	103.1	103.1	103.8	103.1	103.5	104.2	1.7
	formula based on 8 oxygens									
Si	2.97	2.99	2.96	2.95	2.94	2.96	2.95	2.95	2.96	0.02
Al	1.00	0.98	1.01	1.01	0.99	1.01	1.01	1.00	1.00	0.01
Cr	0.00	0.00	0.00	0.00	0.00	0.00	0.00	0.00	0.00	0.00
Fe	0.02	0.01	0.02	0.02	0.04	0.01	0.02	0.02	0.02	0.01
Mn	0.00	0.00	0.00	0.00	0.00	0.00	0.00	0.00	0.00	0.00
Mg	0.02	0.01	0.01	0.06	0.06	0.02	0.02	0.04	0.03	0.02
Ca	0.03	0.02	0.03	0.04	0.04	0.04	0.04	0.05	0.04	0.01
Na	0.92	0.83	0.84	0.87	0.92	0.85	0.86	0.83	0.87	0.04
K	0.08	0.18	0.17	0.09	0.06	0.13	0.13	0.15	0.12	0.04
total	5.03	5.02	5.04	5.03	5.06	5.03	5.04	5.04	5.04	0.01
An	3.2	1.9	2.7	3.7	4.0	3.7	3.8	4.9	3.5	0.9
Ab	89.4	80.8	81.2	87.1	90.0	83.2	83.5	80.3	84.4	3.9
Or	7.4	17.3	16.1	9.2	6.0	13.1	12.7	14.8	12.1	4.1

Table A1.26. Individual EPMA analyses of feldspar in Avanhandava (H4), chondrules 4 and 5

	chondrule 4, n=6								chondrule 5, n=3					
analysis #	55	56	57	58	59	60	mean	1-sig	analysis #	61	62	63	mean	1-sig
SiO_2	60.9	61.9	61.0	64.7	65.6	64.8	63.2	2.1	SiO_2	65.5	66.6	55.7	62.6	6.0
Al_2O_3	26.6	26.2	26.4	25.2	24.8	24.8	25.7	0.8	Al_2O_3	23.3	22.7	29.2	25.0	3.6
Cr_2O_3	<0.07	<0.07	<0.07	<0.07	<0.07	<0.07	<0.07	0.00	Cr_2O_3	<0.07	<0.07	0.26	0.09	0.15
FeO	0.43	0.28	0.59	0.45	0.41	0.45	0.43	0.10	FeO	0.32	0.28	0.42	0.34	0.07
MnO	<0.08	<0.08	<0.08	<0.08	<0.08	<0.08	<0.08	0.00	MnO	<0.08	<0.08	<0.08	<0.08	0.00
MgO	0.05	0.04	<0.02	0.03	0.08	0.03	0.04	0.03	MgO	0.04	<0.02	0.04	0.03	0.02
CaO	7.4	6.7	7.1	6.0	5.3	5.5	6.4	0.9	CaO	3.5	2.4	10.6	5.5	4.5
Na_2O	7.01	7.24	7.52	9.16	9.21	8.90	8.17	1.02	Na_2O	9.61	9.77	5.72	8.37	2.29
K_2O	0.39	0.39	0.44	0.47	0.48	0.44	0.44	0.04	K_2O	0.76	1.13	0.21	0.70	0.46
total	102.9	102.8	103.1	106.0	105.9	105.0	104.3	1.5	total	103.0	102.8	102.1	102.6	0.4
	formula based on 8 oxygens									*formula based on 8 oxygens*				
Si	2.64	2.68	2.65	2.72	2.76	2.75	2.70	0.05	Si	2.82	2.86	2.46	2.71	0.22
Al	1.36	1.34	1.35	1.25	1.23	1.24	1.29	0.06	Al	1.18	1.15	1.52	1.28	0.21
Cr	0.00	0.00	0.00	0.00	0.00	0.00	0.00	0.00	Cr	0.00	0.00	0.01	0.00	0.01
Fe	0.02	0.01	0.02	0.02	0.01	0.02	0.02	0.00	Fe	0.01	0.01	0.02	0.01	0.00
Mn	0.00	0.00	0.00	0.00	0.00	0.00	0.00	0.00	Mn	0.00	0.00	0.00	0.00	0.00
Mg	0.00	0.00	0.00	0.00	0.00	0.00	0.00	0.00	Mg	0.00	0.00	0.00	0.00	0.00
Ca	0.35	0.31	0.33	0.27	0.24	0.25	0.29	0.04	Ca	0.16	0.11	0.50	0.26	0.21
Na	0.59	0.61	0.63	0.75	0.75	0.73	0.68	0.07	Na	0.80	0.81	0.49	0.70	0.18
K	0.02	0.02	0.02	0.03	0.03	0.02	0.02	0.00	K	0.04	0.06	0.01	0.04	0.03
total	4.98	4.97	5.01	5.04	5.02	5.01	5.00	0.03	total	5.02	5.00	5.02	5.01	0.01
An	36.2	33.1	33.5	26.1	23.6	24.8	29.5	5.3	An	16.1	11.2	50.0	25.8	21.1
Ab	61.6	64.6	64.0	71.5	73.9	72.9	68.1	5.3	Ab	79.8	82.5	48.8	70.4	18.7
Or	2.2	2.3	2.5	2.4	2.5	2.4	2.4	0.1	Or	4.1	6.3	1.2	3.9	2.6

Table A1.26. *(Continued).* Individual EPMA analyses of feldspar in Avanhandava (H4), chondrule 2, n=12

analysis #	35	36	37	38	39	40	41	42	43	44	45	46	mean	1-sig
SiO_2	66.7	67.2	70.3	66.1	66.8	70.2	71.7	68.3	69.0	67.1	67.1	67.9	68.2	1.7
Al_2O_3	19.9	20.2	22.2	19.3	19.9	21.9	22.5	19.9	22.4	22.4	22.5	22.7	21.3	1.3
Cr_2O_3	<0.07	<0.07	<0.07	<0.07	<0.07	<0.07	<0.07	<0.07	<0.07	<0.07	<0.07	<0.07	<0.07	0.00
FeO	0.29	0.27	0.34	0.19	0.13	0.27	0.22	0.57	0.62	0.23	0.23	0.44	0.32	0.15
MnO	<0.08	<0.08	<0.08	<0.08	<0.08	<0.08	<0.08	<0.08	<0.08	<0.08	<0.08	<0.08	<0.08	0.00
MgO	<0.02	<0.02	0.43	0.87	<0.02	0.03	0.09	1.92	<0.02	<0.02	0.05	0.03	0.28	0.58
CaO	0.9	1.0	3.0	0.9	0.9	1.9	2.4	5.2	2.5	2.6	2.4	2.7	2.2	1.2
Na_2O	0.50	2.84	10.69	0.91	1.34	10.86	8.96	9.36	10.08	10.03	9.79	9.92	7.11	4.28
K_2O	15.41	12.44	0.66	14.31	14.59	0.59	1.27	0.98	1.16	0.78	0.98	1.10	5.36	6.56
total	103.7	104.0	107.7	102.6	103.6	105.7	107.0	106.2	105.8	103.3	103.1	104.7	104.8	1.7
						formula based on 8 oxygens								
Si	2.96	2.95	2.89	2.96	2.96	2.92	2.93	2.87	2.89	2.87	2.87	2.87	2.91	0.04
Al	1.04	1.05	1.08	1.02	1.04	1.07	1.08	0.98	1.10	1.13	1.13	1.13	1.07	0.05
Cr	0.00	0.00	0.00	0.00	0.00	0.00	0.00	0.00	0.00	0.00	0.00	0.00	0.00	0.00
Fe	0.01	0.01	0.01	0.01	0.00	0.01	0.01	0.02	0.02	0.01	0.01	0.02	0.01	0.01
Mn	0.00	0.00	0.00	0.00	0.00	0.00	0.00	0.00	0.00	0.00	0.00	0.00	0.00	0.00
Mg	0.00	0.00	0.03	0.06	0.00	0.00	0.01	0.12	0.00	0.00	0.00	0.00	0.02	0.04
Ca	0.04	0.05	0.13	0.04	0.04	0.08	0.10	0.23	0.11	0.12	0.11	0.12	0.10	0.05
Na	0.04	0.24	0.85	0.08	0.12	0.88	0.71	0.76	0.82	0.83	0.81	0.81	0.58	0.35
K	0.87	0.70	0.03	0.82	0.82	0.03	0.07	0.05	0.06	0.04	0.05	0.06	0.30	0.37
total	4.97	4.99	5.02	4.98	4.99	5.00	4.91	5.04	5.00	5.00	4.99	5.01	4.99	0.03
An	4.6	4.6	13.1	4.6	4.2	8.4	11.7	22.2	11.3	12.2	11.4	12.2	10.1	5.2
Ab	4.4	24.6	83.5	8.4	11.8	88.5	80.8	72.8	82.4	83.5	83.1	81.8	58.8	34.8
Or	90.9	70.8	3.4	87.0	84.0	3.1	7.5	5.0	6.3	4.3	5.5	6.0	31.2	38.7

Table A1.26. *(Continued).* Individual EPMA analyses of feldspar in Avanhandava (H4), chondrules 3 and 7

	chondrule 3, n=8									
analysis #	47	48	49	50	51	52	53	54	mean	1-sig
SiO_2	67.1	66.8	67.0	68.3	66.1	65.8	66.7	66.1	66.7	0.8
Al_2O_3	22.0	21.0	21.8	21.4	22.5	22.4	21.9	22.4	21.9	0.5
Cr_2O_3	<0.07	<0.07	<0.07	<0.07	<0.07	<0.07	<0.07	<0.07	<0.07	0.00
FeO	0.25	0.41	0.35	0.30	0.28	0.41	0.23	0.32	0.32	0.07
MnO	<0.08	<0.08	<0.08	<0.08	<0.08	<0.08	<0.08	0.10	<0.08	0.03
MgO	0.04	0.02	0.15	0.03	<0.02	0.03	<0.02	<0.02	0.03	0.05
CaO	2.2	1.4	2.4	1.6	2.7	2.3	2.3	2.5	2.2	0.4
Na_2O	10.75	6.77	10.10	9.62	10.14	10.02	10.07	9.96	9.68	1.22
K_2O	0.80	6.96	1.28	2.37	0.73	0.75	0.99	0.90	1.85	2.14
total	103.1	103.3	103.1	103.7	102.4	101.8	102.2	102.3	102.7	0.7
	formula based on 8 oxygens									
Si	2.88	2.91	2.88	2.92	2.85	2.86	2.88	2.86	2.88	0.02
Al	1.11	1.08	1.11	1.08	1.15	1.15	1.12	1.14	1.12	0.03
Cr	0.00	0.00	0.00	0.00	0.00	0.00	0.00	0.00	0.00	0.00
Fe	0.01	0.01	0.01	0.01	0.01	0.01	0.01	0.01	0.01	0.00
Mn	0.00	0.00	0.00	0.00	0.00	0.00	0.00	0.00	0.00	0.00
Mg	0.00	0.00	0.01	0.00	0.00	0.00	0.00	0.00	0.00	0.00
Ca	0.10	0.06	0.11	0.07	0.12	0.11	0.11	0.12	0.10	0.02
Na	0.89	0.57	0.84	0.80	0.85	0.84	0.84	0.83	0.81	0.10
K	0.04	0.39	0.07	0.13	0.04	0.04	0.05	0.05	0.10	0.12
total	5.04	5.03	5.03	5.01	5.02	5.01	5.01	5.01	5.02	0.01
An	9.9	6.3	10.7	7.4	12.2	11.0	10.5	11.8	10.0	2.1
Ab	85.9	55.9	82.5	79.7	83.9	84.8	84.0	83.3	80.0	9.9
Or	4.2	37.8	6.9	12.9	4.0	4.2	5.4	4.9	10.0	11.6

	chondrule 7, n=4					
analysis #	77	80	81	82	mean	1-sig
SiO_2	64.6	66.4	66.8	66.7	66.1	1.0
Al_2O_3	20.4	22.0	22.3	22.5	21.8	1.0
Cr_2O_3	<0.07	<0.07	<0.07	<0.07	<0.07	0.00
FeO	0.18	0.17	0.36	0.48	0.30	0.15
MnO	<0.08	<0.08	<0.08	<0.08	<0.08	0.00
MgO	<0.02	<0.02	0.03	0.05	<0.02	0.03
CaO	1.1	1.2	2.5	2.5	1.8	0.8
Na_2O	1.09	10.27	10.04	9.63	7.76	4.45
K_2O	13.78	0.51	0.98	1.29	4.14	6.44
total	101.1	100.6	103.0	103.1	101.9	1.3
	formula based on 8 oxygens					
Si	2.93	2.90	2.87	2.86	2.89	0.03
Al	1.09	1.13	1.13	1.14	1.12	0.02
Cr	0.00	0.00	0.00	0.00	0.00	0.00
Fe	0.01	0.01	0.01	0.02	0.01	0.01
Mn	0.00	0.00	0.00	0.00	0.00	0.00
Mg	0.00	0.00	0.00	0.00	0.00	0.00
Ca	0.05	0.05	0.11	0.11	0.08	0.03
Na	0.10	0.87	0.84	0.80	0.65	0.37
K	0.80	0.03	0.05	0.07	0.24	0.37
total	4.97	4.99	5.01	5.01	4.99	0.02
An	5.5	5.8	11.3	11.6	8.5	3.4
Ab	10.1	91.3	83.4	81.2	66.5	37.8
Or	84.4	3.0	5.3	7.2	25.0	39.7

Table A1.26. *(Continued).* Individual EPMA analyses of feldspar in Avanhandava (H4), chondrule 6, n=9

analysis #	68	69	70	71	72	73	74	75	76	*mean*	*1-sig*
SiO_2	71.8	70.1	68.2	66.8	68.0	68.4	68.3	67.5	68.1	*68.6*	*1.5*
Al_2O_3	20.4	21.6	20.4	19.7	20.4	19.8	19.8	20.2	21.5	*20.4*	*0.7*
Cr_2O_3	<0.07	<0.07	<0.07	<0.07	<0.07	<0.07	<0.07	<0.07	<0.07	*<0.07*	*0.00*
FeO	0.32	0.54	0.63	0.44	0.38	0.57	0.51	0.40	0.39	*0.46*	*0.10*
MnO	<0.08	0.14	<0.08	<0.08	<0.08	<0.08	<0.08	0.10	<0.08	*<0.08*	*0.05*
MgO	0.03	<0.02	0.04	0.04	0.03	<0.02	<0.02	<0.02	<0.02	*<0.02*	*0.02*
CaO	0.4	2.0	0.5	0.5	0.5	0.2	0.3	0.6	1.4	*0.7*	*0.6*
Na_2O	7.75	11.07	8.56	4.87	7.80	6.48	8.77	6.74	10.85	*8.10*	*2.00*
K_2O	7.27	0.73	5.03	10.15	5.99	8.23	4.57	7.31	0.84	*5.57*	*3.19*
total	107.9	106.2	103.4	102.5	103.1	103.7	102.2	102.8	103.1	*103.9*	*1.9*
				formula based on 8 oxygens							
Si	2.98	2.92	2.95	2.96	2.95	2.97	2.97	2.95	2.91	*2.95*	*0.03*
Al	1.00	1.06	1.04	1.03	1.04	1.02	1.02	1.04	1.08	*1.04*	*0.03*
Cr	0.00	0.00	0.00	0.00	0.00	0.00	0.00	0.00	0.00	*0.00*	*0.00*
Fe	0.01	0.02	0.02	0.02	0.01	0.02	0.02	0.01	0.01	*0.02*	*0.00*
Mn	0.00	0.00	0.00	0.00	0.00	0.00	0.00	0.00	0.00	*0.00*	*0.00*
Mg	0.00	0.00	0.00	0.00	0.00	0.00	0.00	0.00	0.00	*0.00*	*0.00*
Ca	0.02	0.09	0.02	0.02	0.03	0.01	0.01	0.03	0.07	*0.03*	*0.03*
Na	0.62	0.89	0.72	0.42	0.66	0.55	0.74	0.57	0.90	*0.67*	*0.16*
K	0.39	0.04	0.28	0.57	0.33	0.46	0.25	0.41	0.05	*0.31*	*0.18*
total	5.02	5.02	5.03	5.02	5.02	5.02	5.02	5.02	5.02	*5.02*	*0.00*
An	1.7	8.7	2.3	2.1	2.5	0.9	1.4	2.6	6.5	*3.2*	*2.6*
Ab	60.8	87.5	70.5	41.3	64.8	54.0	73.4	56.9	89.0	*66.4*	*15.5*
Or	37.5	3.8	27.2	56.6	32.7	45.1	25.2	40.6	4.5	*30.4*	*17.6*

APPENDIX 2

Method for determining bulk chemical compositions from quantitative EPMA maps

1. Introduction

Determining bulk chemical compositions of geologic materials from polished mounts and thin sections is useful for answering a range of questions. In chondrites, the bulk compositions of chondrules can be used to understand their formation in the solar nebula (e.g., Fig. 2.6) and their alteration during parent body processing (e.g., Fig. 5.8). In achondrites, the bulk compositions of clasts (Carpenter et al., 2017) and symplectites (Carpenter et al., 2013) can be used to understand the origin and history of the host material. However, these samples can be complex and determining bulk compositions difficult. Some are characterized by fine-grained intergrowths and others exhibit pronounced compositional zoning.

Electron probe microanalysis (EPMA) is primary tool for making precise measurements of minerals and other phases in polished mounts or thin sections. There are two general methods for determining bulk compositions using EPMA: defocused beam analysis (DBA) and modal recombination analysis (MRA). DBA uses a broad beam, or scanned beam with continuous collection, to average the composition of the material over the area of interest. MRA uses modal phase abundances, determined from electron or element maps, combined with phase compositions and densities to determine an average composition.

Berlin (2009) illustrates that MRA is superior to DBA because the former suffers from compositional misrepresentation of phases that differ from the average density of

the analyzed material. That is, in DBA, high density phases such as metals and sulfides are underrepresented in the bulk composition whereas low density phases such as glasses are overrepresented. However, accurate MRA can be difficult to achieve using phase compositions from representative point analyses if individual mineral phases show pronounced zoning.

In this appendix, I will demonstrate a method of processing quantitative EPMA maps that results in density-corrected bulk chemical compositions. This method can be used in heavily zoned minerals even if the density varies with composition. I will also demonstrate its use in determining modal mineral abundances and in isolating and characterizing individual minerals. While I used MATLAB to implement this method, it is not specific to MATLAB and can be implemented in various analytical software packages and programming languages. For this example, I will use Semarkona (LL3.00) chondrule 23, a Type I POP chondrule from Lewis and Jones (in review) (Figs. 2.3c,d, 2.6). A backscattered electron (BSE) image and qualitative FeMgAl RGB image of chondrule 23 are shown in Fig. A2.1.

2. Data acquisition

For chondrule 23, I acquired 300x300 pixel maps for 10 elements in two passes on a JEOL 8200 EPMA using Probe for EPMA software. I used 80 ms/px dwell time and a 2 μm spot size producing 600x600 μm maps. The resulting intensity maps were processed using mean atomic number (MAN) background corrections to produce quantitative oxide maps using CalcImage. MAN background corrections are useful for estimating peak background intensities without having to produce off-peak maps.

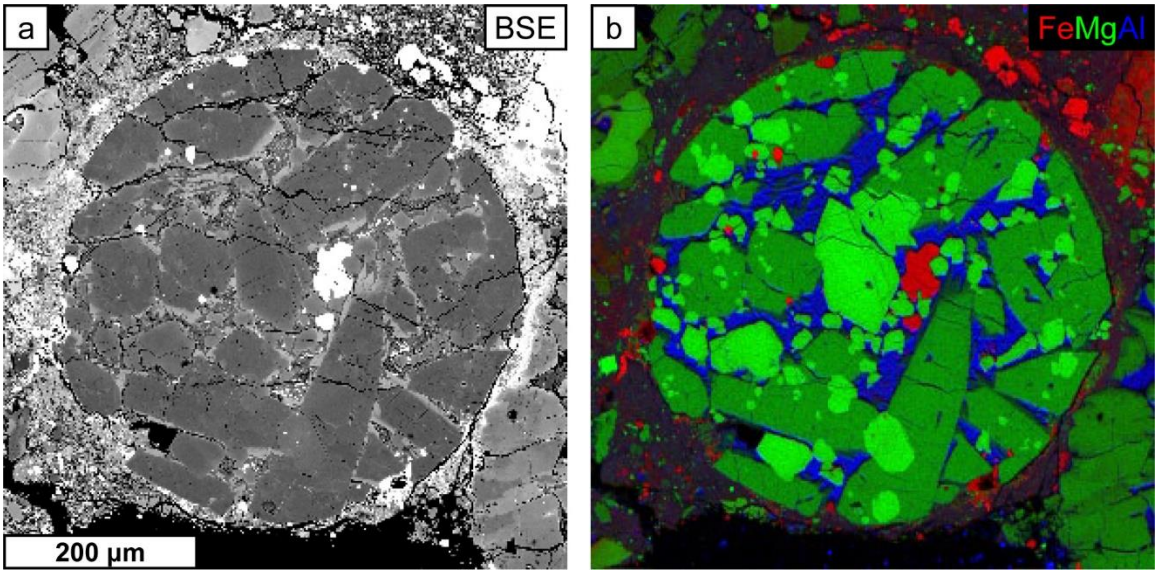

Figure A2.1. BSE image and RGB element map of Semarkona (LL3.00) chondrule 23. (a) BSE image illustrating Type I POP chondrule in Semarkona. (b) Qualitative FeMgAl RGB element map of chondrule 23 illustrating troilite (red), olivine (bright green), pyroxene (dark green), and feldspathic mesostasis (blue).

However, other background correction methods can also be used. The resulting full-frame quantitative oxide maps are shown in Fig. A2.2.

3. Masking and point selection

After data collection and processing to produce quantitative oxide maps, I use the BSE image (Fig. A2.1a) to produce a mask of the chondrule to remove matrix, and other external features, that are not wanted in the bulk composition. I typically do this in Adobe Photoshop with unwanted areas colored black and the chondrule colored white. The mask needs to contain only black and white pixels and be the same exact resolution as the maps. The BSE image generated during acquisition is perfect for this purpose.

I apply the chondrule mask to all oxide maps and then produce a histogram of oxide totals (Fig. A2.3a). There should be a peak near 100%. I then constrain totals to a symmetric window around the peak. In this example, the peak is at 98% and I use a broad

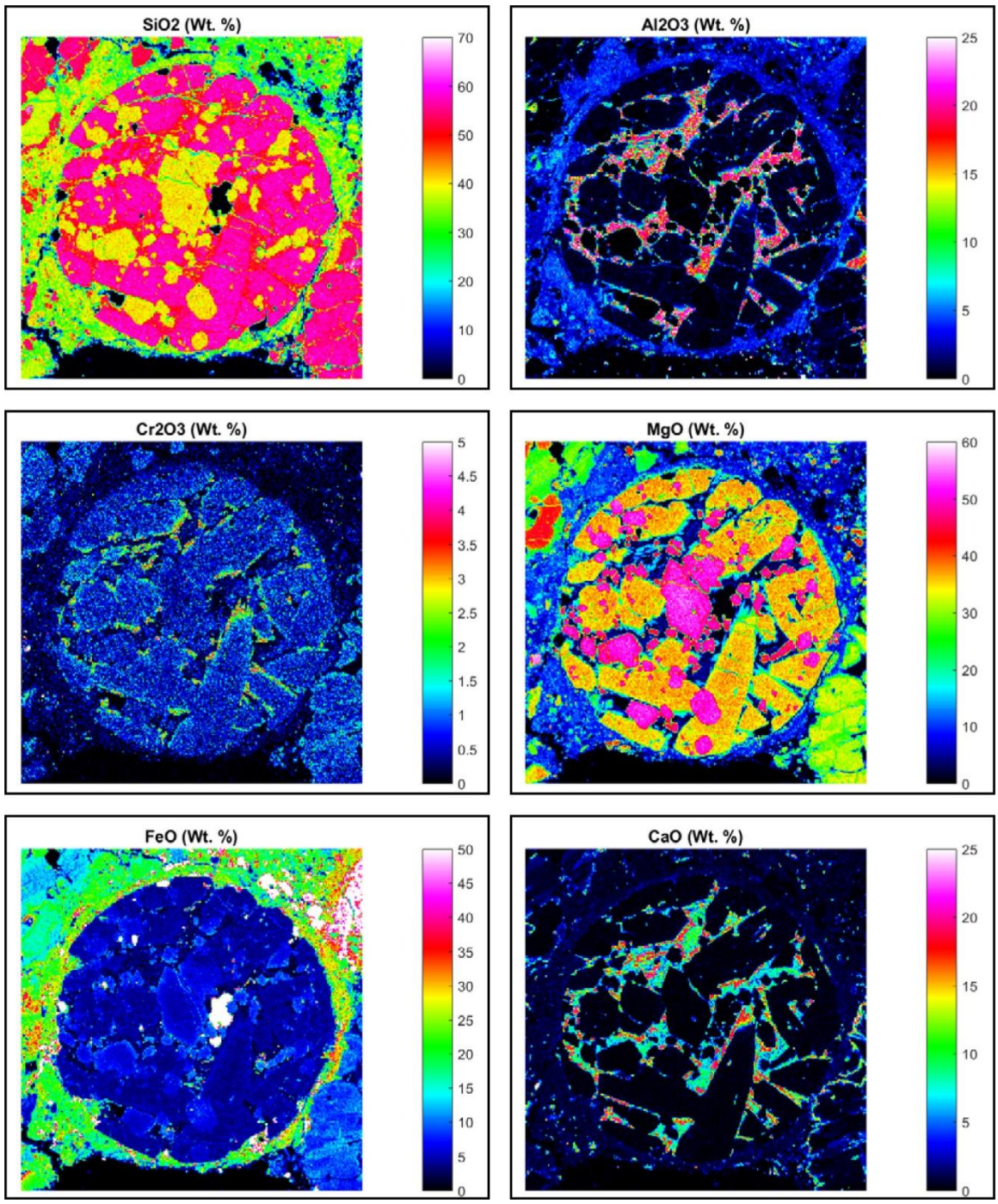

Figure A2.2. Quantitative EPMA oxide maps for SiO_2, Al_2O_3, Cr_2O_3, MgO, FeO, and CaO.

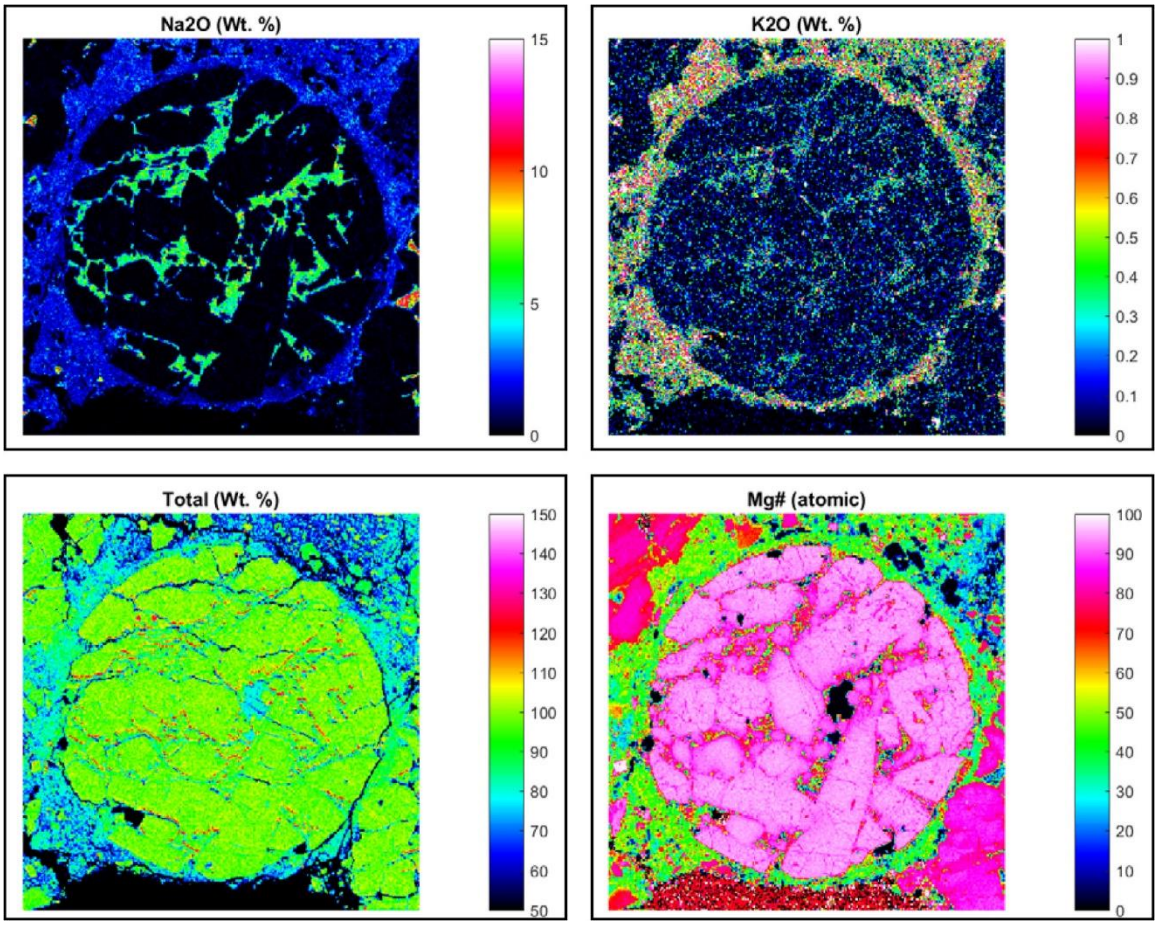

Figure A2.2. *(Continued).* Quantitative EPMA oxide maps for Na_2O, K_2O, total wt.% oxide, and atomic Mg# (Mg/(Mg+Fe)×100%).

window of 90-106% (Fig. A2.3b). Because of the low dwell time (80 ms/px), the precision of any given pixel is not as good as typical 30 second point analyses. As such a broad window that captures most of the peak will provide enough points to calculate a bulk composition. Furthermore, I eliminate pixels where the SiO_2 content is <20% because I am only interested in the bulk silicate composition of this chondrule, not the metals or sulfides. However, metals and sulfides can also be calculated with this method.

Figure A2.4 illustrates the masking process with the chondrule mask (Fig. A2.4a) and the accepted pixel mask (Fig. A2.4b) applied to the FeMgAl image (Figs. A2.4c,d).

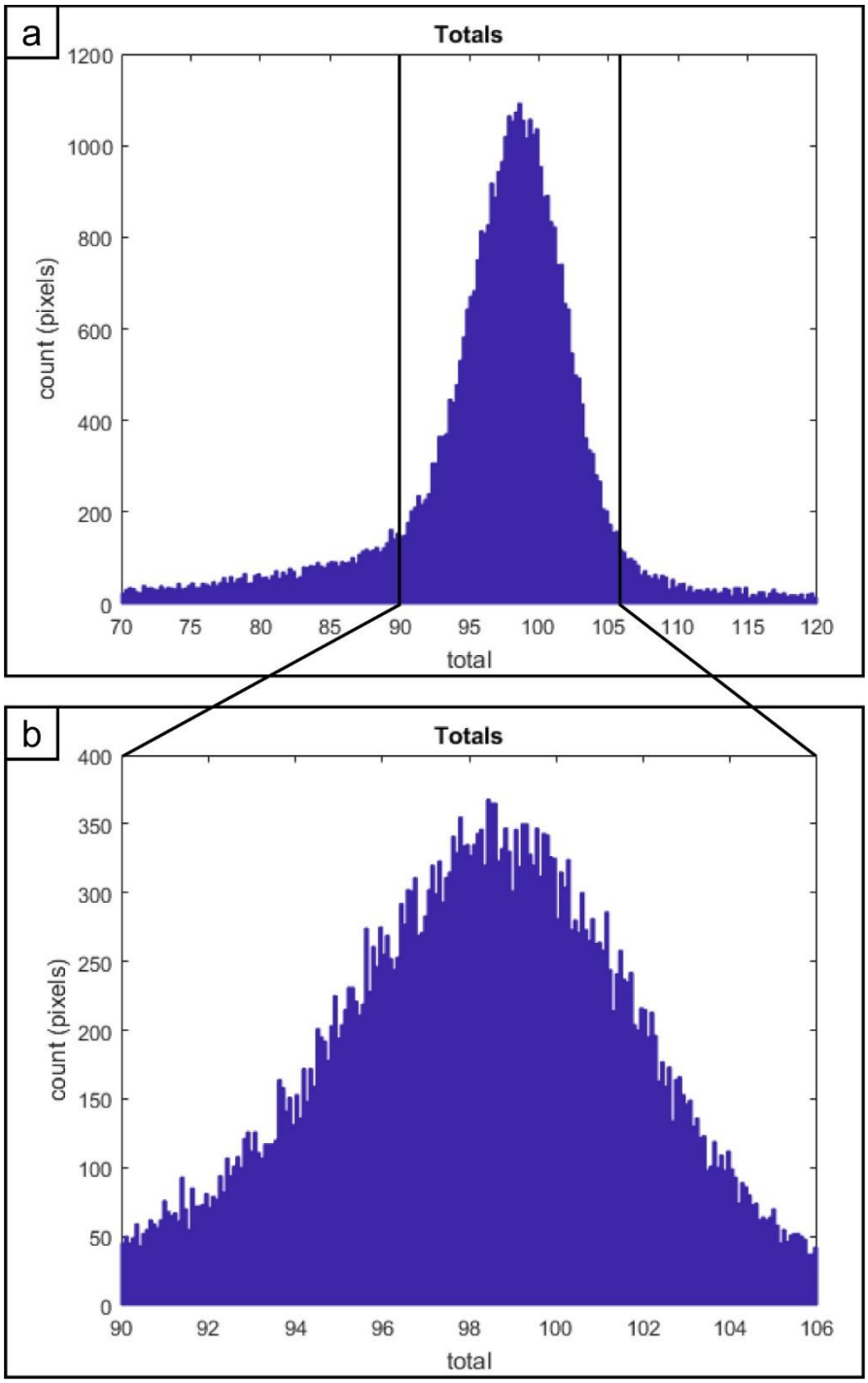

Figure A2.3. Histogram of oxide totals. (a) Broad histogram showing oxide totals from all masked pixels between 70 and 120 wt.% oxide totals. (b) Final selected window of 90-106 wt.% oxide totals, centered on the peak at 98%.

Notice the sulfides (red in Fig. A2.4c) are removed in the final set of accepted pixels (Fig. A2.4d). Also absent are pores, cracks, and many grain boundaries. These are regions in which the totals deviate from the accepted window (Fig. A2.3b).

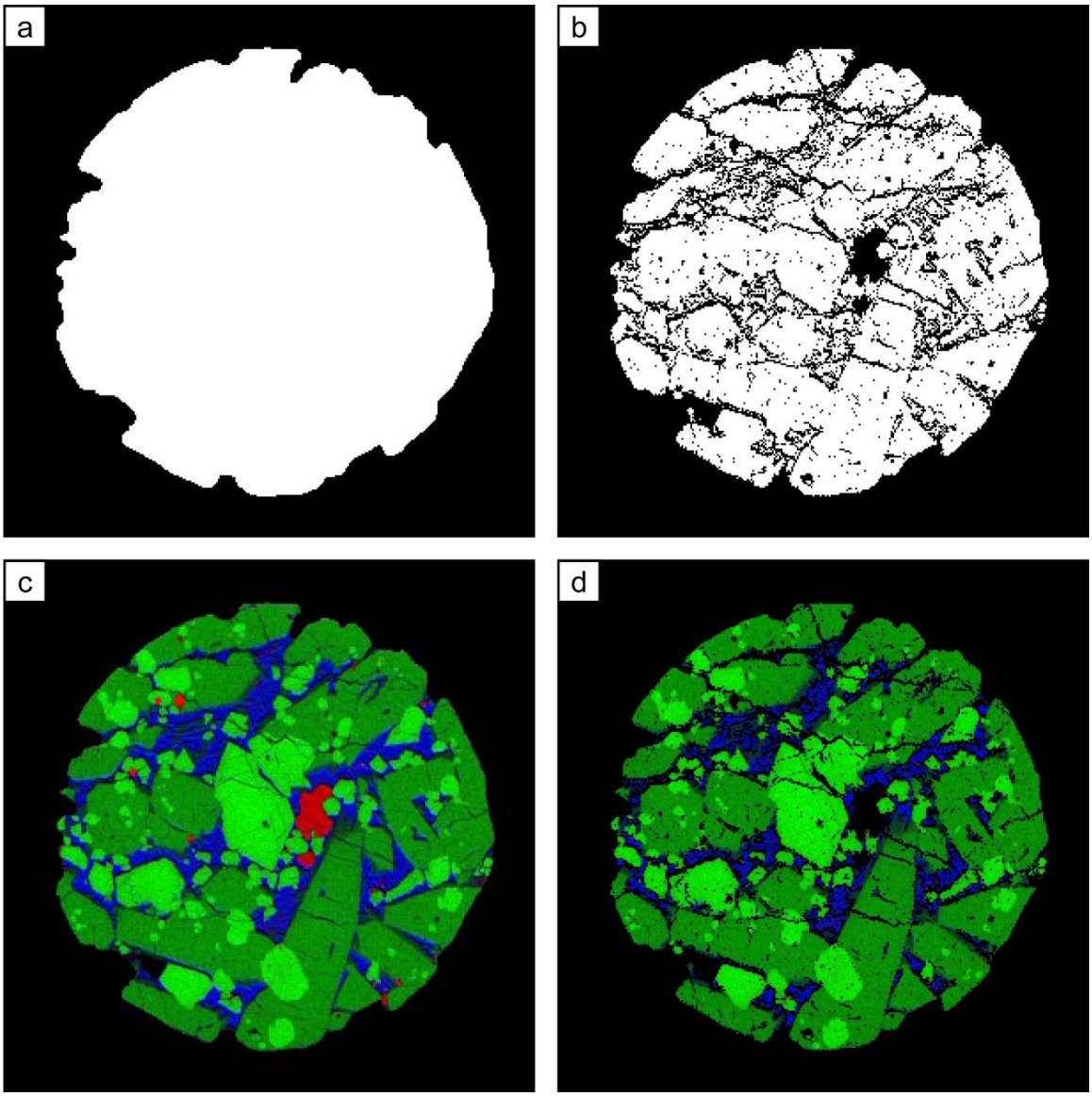

Figure A2.4. Illustration of masking. (a) Chondrule only mask and (b) chondrule mask with rejected pixels removed for violating totals restriction or SiO_2 content constraints. (c) FeMgAl RGB map with chondrule only mask applied. (d) FeMgAl RGB map with chondrule mask and accepted pixels mask applied.

4. Phase selection and abundance

Once a set of acceptable pixels are selected, the next step is to divide those pixels up into different phases. This is done through visualization in oxide-oxide plots (Fig. A2.5). This chondrule is simple in that it only contains four major phases: olivine, clinopyroxene (CPX), orthopyroxene (OPX), and mesostasis. Olivine is separated from the other phases based on its high MgO/SiO_2 ratio (blue pixels in Fig. A2.5a). Next, mesostasis is separated out based on its high Al_2O_3 content (purple pixels in Fig. A2.5b). Finally, CPX and OPX are separated based on CaO content (orange and yellow pixels in Fig. A2.5c).

There is considerable scatter in the individual points that can lead to difficulty discerning phase boundaries, particularly in zoned phases. However, heat maps can reveal compositional clustering and provide more easily visible boundaries between the phases. These heat maps are 2D histograms in which the count/bin is assigned a color value. In addition, the heat maps have been converted to $\log_{10}$(count) so that, in this case, the white pixels have nearly two orders of magnitude more counts than the green pixels. The resulting phase map is shown in Fig. A2.6 and can be compared to the BSE image to check for consistency and reliability. The phase map can also be used to determine the modal phase abundances by dividing the number of pixels assigned to a phase by the total number of good pixels. The modal phase abundances for chondrule 23 are listed in Table 2.2.

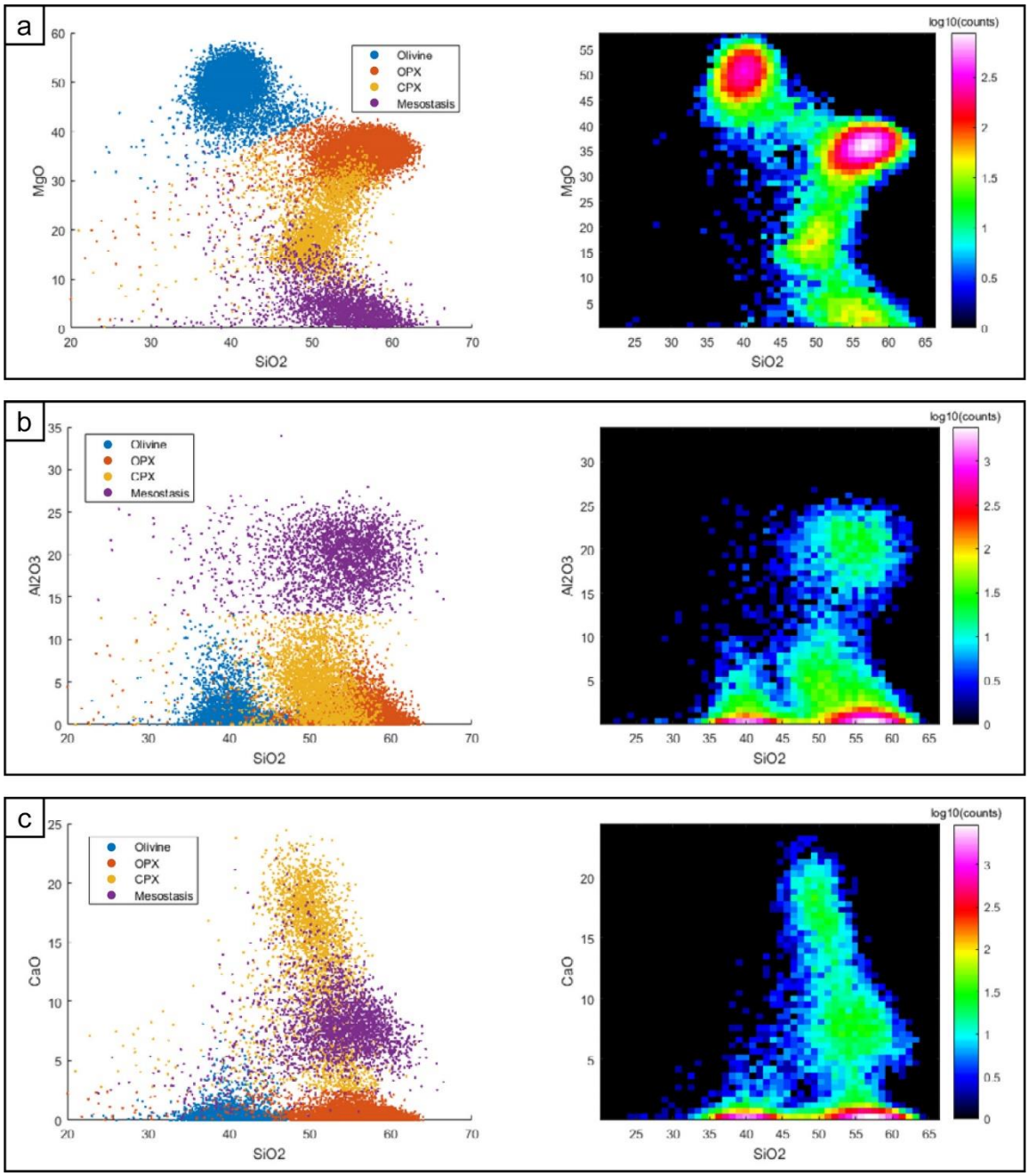

Figure A2.5. Oxide-oxide plots for phase discrimination. These are presented as point plots and as log-based heat maps. (a) SiO_2-MgO plot to distinguish olivine (blue). (b) SiO_2-Al_2O_3 plot to distinguish mesostasis (purple). (c) SiO_2-CaO to distinguish CPX (yellow) from OPX (orange).

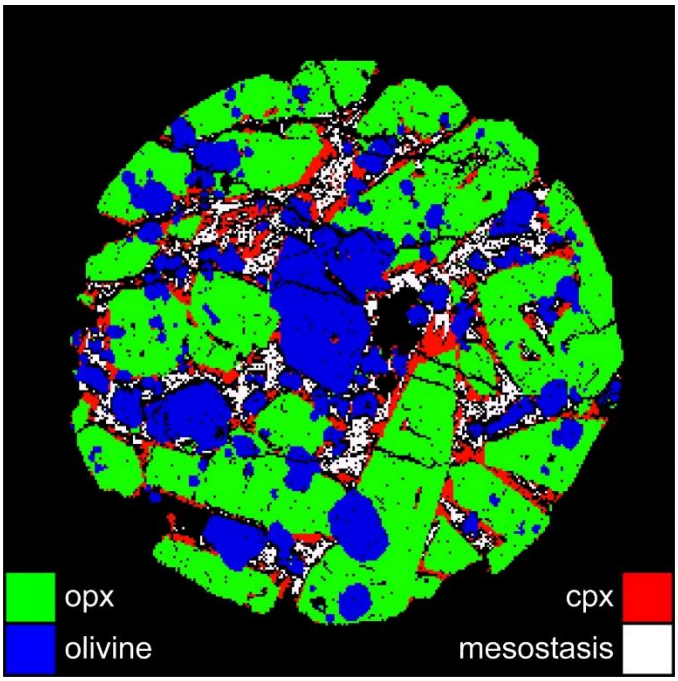

Figure A2.6. Chondrule phase map illustrating OPX (green), CPX (red), olivine (blue), and mesostasis (white).

5. Density mapping and bulk composition

The next step is to assign a density to each phase. This can be done simply, such as one density value per phase, or in a more complex manner involving solid solution. In this example we use a density of 2.6 g/cm^3 (average plagioclase) for the mesostasis. Olivine was assigned 3.2-4.4 g/cm^3 as a solid solution between forsterite and fayalite, based on atomic Mg# (Fig. A2.2). A similar process was done with OPX: 3.2-3.9 g/cm^3 for enstatite-ferrosilite and CPX: 3.3-3.6 g/cm^3 for diopside-hedenbergite. The density map for chondrule 23 is illustrated in Fig. A2.7. The bulk composition is then determined by taking a density-weighted mean of each oxide map. The bulk composition for chondrule 23 produced by this method is listed in Table 2.2.

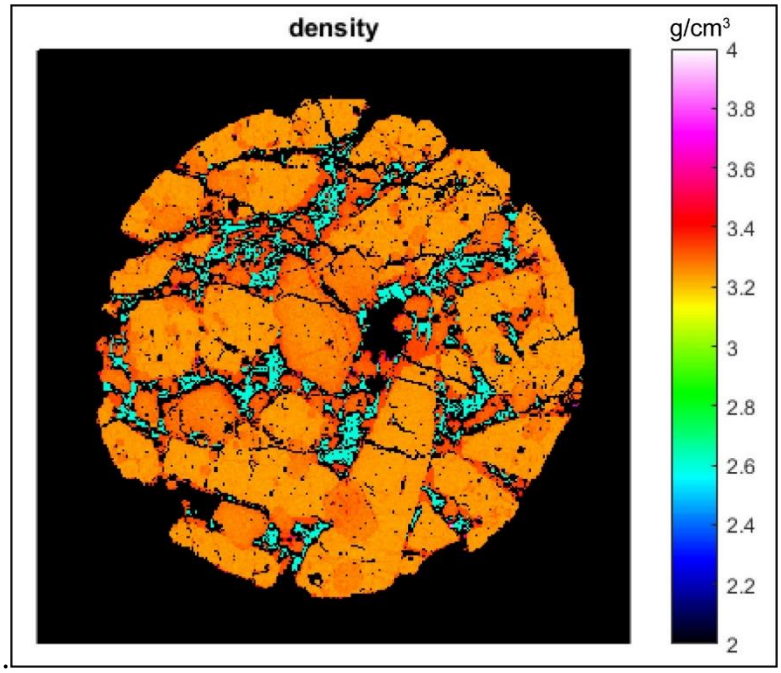

Figure A2.7. Phase density map for chondrule 23.

6. Additional uses and limitations

Figure A2.8 illustrates a simple application of this method to major mineralogy in chondrule 23. Atomic Mg# is being displayed for olivine, CPX, and OPX together in Fig. A2.8a and for each mineral separately in Figs. A2.8b-d. Any given phase can be extracted and displayed using any of the chemical information produced by the maps. This is particularly useful for zoned phases. Here, we can see OPX laths (Figure A2.8b) are not zoned whereas the olivine phenocrysts are zoned in Mg relative to Fe (Figure A2.8c) with the outer rim matching the Mg# of CPX (Figure A2.8d). Another potential use of these data is more statistically rigorous cluster analysis than the simple visual phase separation displayed in Fig. A2.5.

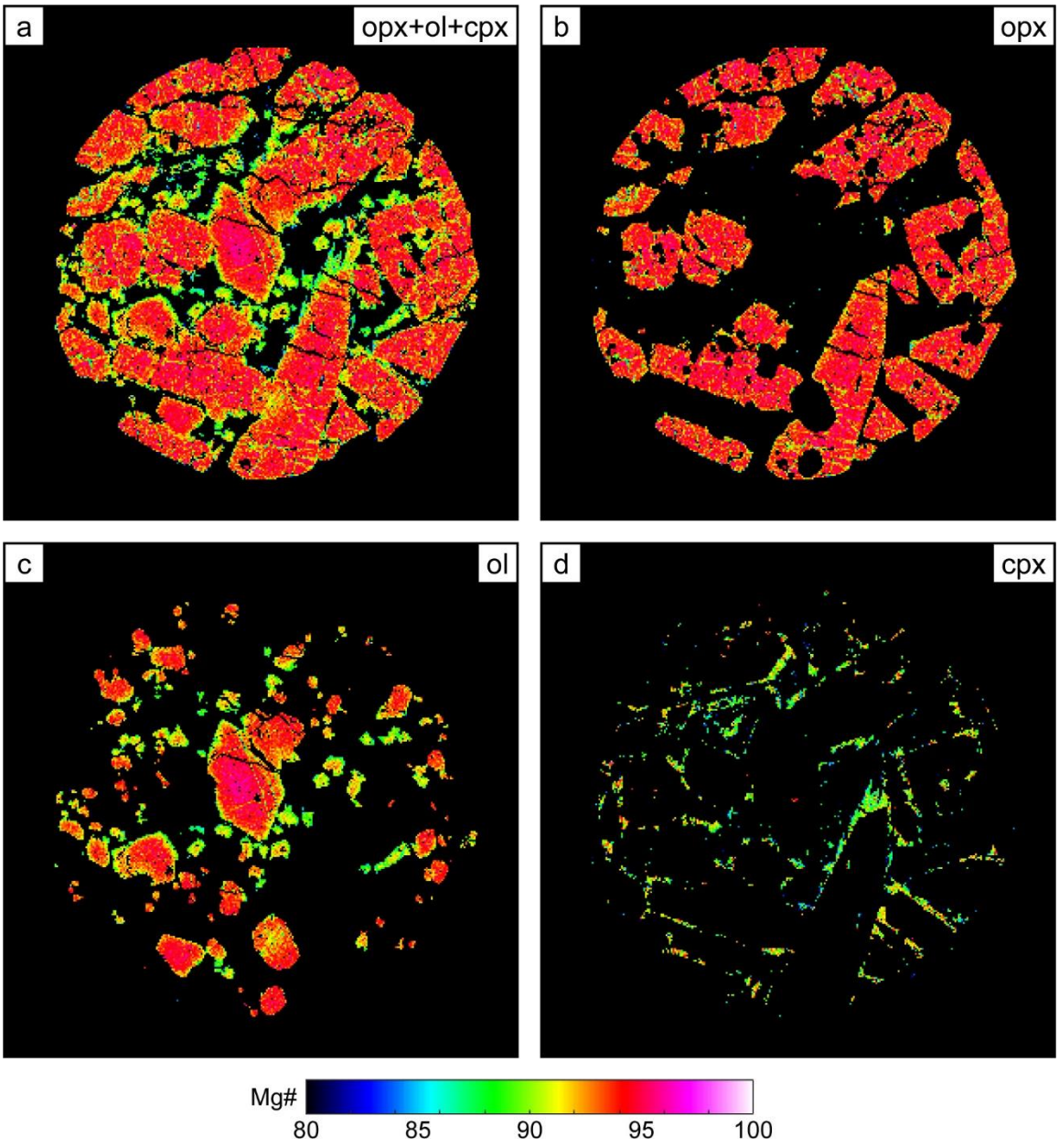

Figure A2.8. Atomic Mg# of major phenocrysts in chondrule 23. (a) Olivine, CPX, and OPX, (b) OPX only, (c) olivine only, and (d) CPX only.

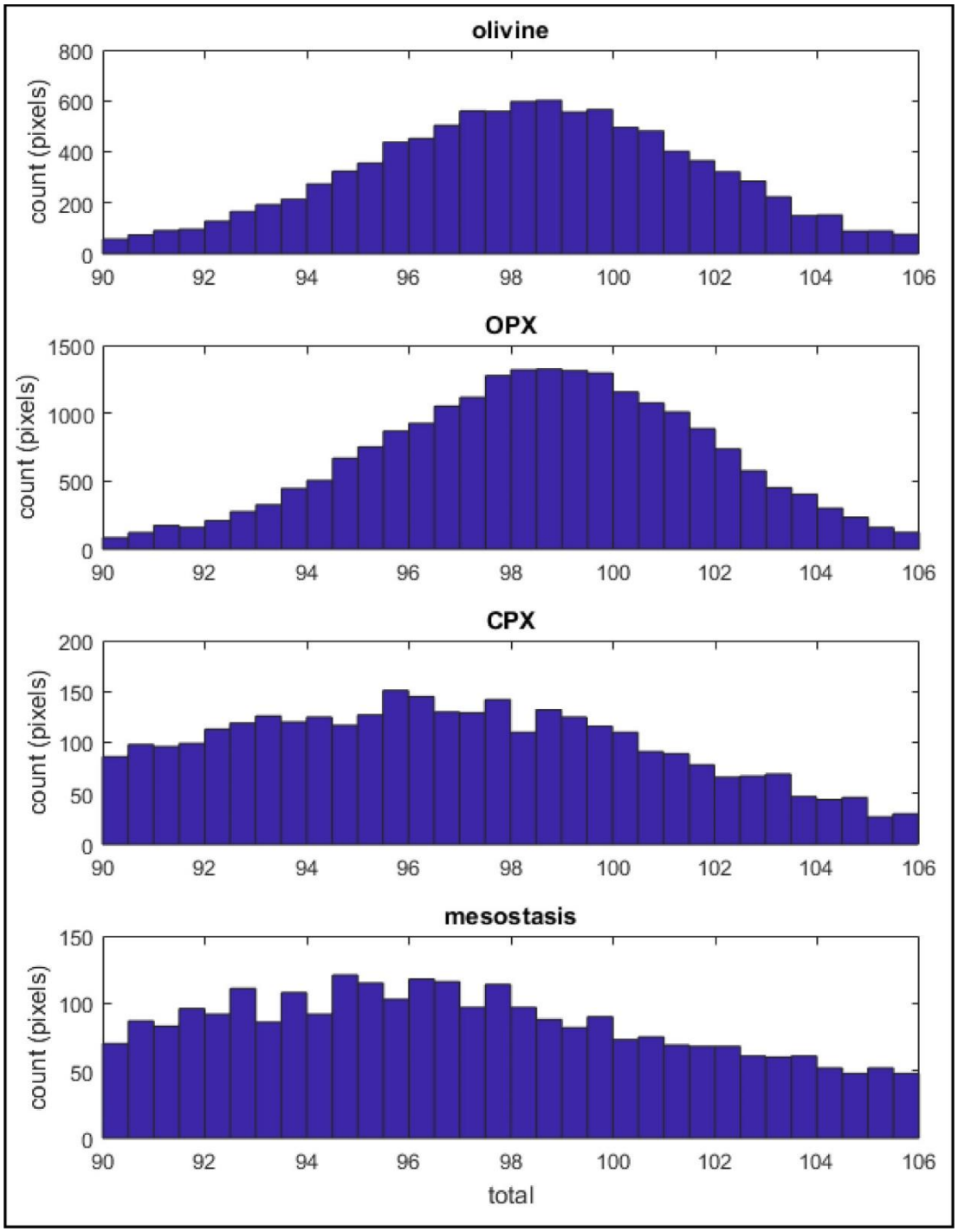

Figure A2.9. Histogram of wt.% oxide totals for each phase separately.

There are also limitations to the accuracy of the bulk composition generated using this method. First, removing low and high totals removes anomalous analyses, particularly those on grain boundaries (Fig. A2.6). Removal of pixels on grain boundaries leads to the loss of a greater percentage of low-abundance phases, such as mesostasis glass in this case. Second, not all phases have the same histogram peak seen in Fig. A2.3. In fact, each phase can have its own peak and the bulk peak is just a sum of the different phases. This is illustrated in Fig. A2.9 where olivine and OPX share one peak and CPX and mesostasis are close to another peak at lower Mg#. Thus, constraining all phases to the 90-106% window preferentially removes good pixels in some phases over others. Finally, the precision of the bulk composition is dependent upon on the precision of the original data. Despite these potential issues, this method provides a reasonable starting point for generating bulk chemical compositions using quantitative EPMA maps in complex samples.

References

Berlin J. (2009) Mineralogy and bulk chemistry of chondrules and matrix in petrologic type 3 chondrites: Implications for early solar system processes. Ph.D dissertation, University of New Mexico.

Carpenter P. K., Hahn T. M., Korotev R. L., Zeigler R. A. and Jolliff B. L. (2017) Quantitative EPMA compositional mapping of NWA 2995: Characterization and petrologic interpretation of mafic clasts. *48th Lunar and Planetary Science Conference*, Abstract #2607.

Carpenter P. K., North S. N., Jolliff B. L. and Donovan J. J. (2013) EPMA quantitative compositional mapping and analysis of lunar samples. *44th Lunar and Planetary Science Conference*, Abstract #1827.

Lewis J. A. and Jones R. H. (in review) Primary feldspar in the Semarkona LL3.00 chondrite: Constraints on chondrule formation and secondary alteration. *Meteoritics & Planetary Science*.

APPENDIX 3

Compilation of radiogenic ages from ordinary and carbonaceous chondrites

1. Introduction

The formation and early evolution of the solar system is tied to our understanding of primitive asteroids. Chondrites are samples of these primitive asteroids that have fallen to Earth as meteorites and are known to contain the first solids formed in the solar nebula: calcium-aluminum-rich inclusions (CAIs) and chondrules (Scott and Krot, 2005). In addition to their primitive constituents, chondrites retain records of some of the earliest chemical and physical processing in the forms of aqueous alteration (Brearley, 2006) and thermal metamorphism (Huss et al., 2006). Also, chondrites are nearly identical in composition to the bulk solar system (i.e., the Sun) so they are often taken to be the starting material for the terrestrial planets (Anders and Grevesse, 1989; McDonough and Sun, 1995). Since the earliest histories of Earth and the other terrestrial planets have largely been lost due to differentiation and extensive geologic processing, chondrites can be used as proxies for reconstructing the first few million years of solar system evolution.

Perhaps the most powerful tools for understanding the chronology of geologic processes are radioactive isotopes. Both long- and short-lived isotope systems are applicable to the study of chondrites and their components. The long-lived U-Pb system has proven useful for absolute dating of a variety of solar system materials. Due to its two simultaneous systems $^{238}U \rightarrow ^{206}Pb$ and $^{235}U \rightarrow ^{207}Pb$, only the Pb components typically need to be measured to provide useful (Pb-Pb) ages. Most importantly, Pb-Pb dating of CAIs, the first material to condense in the solar nebula, has set the formation age of the

solar system to 4567.30±0.16 Ma (Connelly et al., 2012). Lead-Pb can also be used to date chondrite metamorphism due to the development of phosphates which can contain relatively high concentrations of U (Göpel et al., 1994).

Short-lived radioisotope systems provide ages relative to an anchor sample. It is commonly thought that a supernova injected a variety of radioactive isotopes into the solar nebula shortly before the first materials started to form although other sources of short-lived radioisotopes are possible (Davis and McKeegan, 2014). These isotopes decay fairly quickly and can provide detailed chronology of the early solar system relative the anchor sample. In order to provide an absolute age, the absolute age for the anchor sample needs to be measured (e.g., Pb-Pb age).

Although they only provide relative ages, short-lived radioisotope systems have some advantages over long-lived systems. Their analytical procedures are easier than high-precision, long-lived isotope measurements and certain phases can be targeted due to their preference for the short-lived parent isotopes. For example, Al-Mg is used to date chondrule formation because chondrules often have Al-rich mesostasis glass and Mn-Cr is used to date aqueous alteration because Mn^{2+} easily substitutes for Ca^{2+} or Mg^{2+} in precipitating carbonates. However, these methods rely on an important assumption that the solar nebula was homogenous with respect to the isotope in question. So far, this assumption appears to hold, at least for the inner solar system materials for which we have samples (Villeneuve et al., 2009).

The purpose of this study was to use radioisotope ages to create a chronology for the assembly, aqueous alteration, and thermal metamorphism of chondritic asteroids. This

was done by compiling a wide range of ages from the literature pertaining to chondrite components and parent body processes.

2. Methods

An extensive search through the literature was required to create a coherent timeline for chondritic asteroids. However, constraints were made on the types of ages collected and a large percentage of the data required reprocessing in order to be internally consistent. These constraints and processes are described below.

2.1. Data acquisition

There were several considerations made when assembling this set of data. First, a limited number of isotopic systems were included: Pb-Pb, Al-Mg, Mn-Cr, and Hf-W. These systems are commonly applied to chondritic materials and cover the range of processes considered in this chronology with enough data points to provide representative durations for each process. Lead-Pb is the long-lived system primarily used to date the short-lived radioisotope anchors (CAIs and angrites) and thermal metamorphism from phosphates. Aluminum-Mg is often used to date chondrule formation from Al-rich mesostasis and thermal metamorphism from the development of feldspar. Manganese-Cr is used to date aqueous alteration due to the formation of the carbonate minerals calcite, dolomite, and breunnerite. Hafnium-W is used to date metamorphism in the metal-bearing ordinary chondrites. Argon-Ar ages have also been used to date late-stage metamorphism from feldspar due to relatively low closure temperatures but will not be included here because the system is easily disturbed by shock. In fact, Ar-Ar is also used to reveal impact histories of meteorite parent bodies though asteroid disruption is outside the scope of this study.

Second, relative ages were not included for objects acting as anchors. For example, Al-Mg ages were not included for CAIs because CAIs act as the anchor for the for the Al-Mg system. While it is important to consider Al-Mg for CAIs in terms of initial ratios, nebular homogeneity, and duration of CAI formation, the absolute ages produced from using these ratios acquire a degree of circularity and were not considered here. Relative ages for angrites were also not included because they act as the Mn-Cr and Hf-W anchor and there may be evidence for disturbance of the Al-Mg system (Kleine et al., 2012). Also, angrites are only presented as an anchor and not a major part of the chondrite timeline itself.

Third, spurious data were avoided. This was only a problem with Mn-Cr ages for which poor standards caused issues with early analyses resulting in alteration ages predating parent body assembly. Poor data were specifically called out in the literature and not included here. Data that have generated considerable literature discussion but have not been proven spurious (e.g., Pb-Pb ages of select CAIs) were still included.

Finally, anchors for the short-lived systems were chosen from the literature based on how commonly they have been used and how confidently the literature perceives in their reliability. CAIs are often used to anchor the Al-Mg system because if their high Al content. D'Orbigny is the oldest angrite sample and produces Mn-Cr and Hf-W values in the range needed for aqueous alteration and thermal metamorphism. Initial ratios and absolute ages were chosen from different literature sources as their values have been revised and updated over time. Decay constants were calculated from half-lives reported in the National Nuclear Data Center's NuDat 2 database (http://www.nndc.bnl.gov/nudat2/).

2.2. Standardization of short-lived radioisotope data

Measurement of short-lived radioisotopes consists of producing isochron diagrams from which the initial amount of radioactive material can be determined using the slope of a linear regression. The relative age of the sample is then calculated according to Equation A3.1 using the Al-Mg system as an example:

$$\Delta t = -\frac{1}{\lambda}\ln\left(\frac{\left(\frac{^{26}\mathrm{Al}}{^{27}\mathrm{Al}}\right)_{sample}}{\left(\frac{^{26}\mathrm{Al}}{^{27}\mathrm{Al}}\right)_{anchor}}\right) \quad \text{(A3.1)}$$

where Δt is the age relative to the anchor sample and λ is the decay constant. The absolute age is then calculated relative to the absolute age of the anchor.

Ages reported in the literature for short-lived radioisotope measurements used the best values for decay constants, anchor initial ratios, and anchor absolute ages at the time they were published. However, since the data acquired for this project were reported over a 25-year period, the values used to calculate their relative and absolute ages have changed over that time, sometimes considerably. For example, literature values for the half-life of ^{26}Al ranges from 7.00×10^5 y to 7.30×10^5 y with the current value being 7.17×10^5 y.

Because of these variations, short-lived radioisotope ages cannot be compared to each other using the values as they have been reported. However, the initial ratios can be used to recalculate an internally consistent set of ages using updated literature values and Equation A3.1. The constant and anchor values used to recalculated absolute ages in the three short-lived radioisotope systems are listed in Table A3.1. Errors (2σ) for the initial ratios were propagated using Equation A3.1 but the errors associated with the half-life

and anchor values were not included. Changes in the decay constants for long-lived radioisotopes were not considered.

Table A3.1. Values used for standardizing short-lived radioisotope ages.

		Al-Mg	Mn-Cr	Hf-W
Half-Life ($t_{½}$) [a]		7.17×10^{5} y	3.74×10^{6} y	8.90×10^{6} y
Decay Constant (λ) [b]		9.67×10^{-7} y^{-1}	1.85×10^{-7} y^{-1}	7.79×10^{-8} y^{-1}
Anchor	Sample	CAIs (Allende & Efremovka)	D'Orbigny (angrite)	D'Orbigny (angrite)
	Initial Ratio	$^{26}Al/^{27}Al = 5.23\times10^{-5}$ [c]	$^{53}Mn/^{55}Mn = 3.24\times10^{-6}$ [d]	$^{182}Hf/^{180}Hf = 7.15\times10^{-5}$ [e]
	Absolute Age	4567.30 Ma [f]	4563.37 Ma [g]	4563.37 Ma [g]

[a] Half-lives from National Nuclear Data Center, NuDat 2 database, http://www.nndc.bnl.gov/nudat2/; [b] calculated: $\lambda = \ln 2/t_{½}$; [c] Jacobsen et al. (2008); [d] Glavin et al. (2004); [e] Kleine et al. (2012); [f] Connelly et al. (2012); [g] Brennecka and Wadhwa (2012).

3. Results

A total of 220 radiogenic ages were assembled from the literature in order to construct the chondrite chronology. The distribution of these ages is summarized numerically by object and system in Table A3.2 and summarized visually by object and age in Figure A3.1. All data are plotted in Figures A3.2-A3.7 in the discussion and tabulated with references in Table A3.3. Each point is assigned a number which appears next to that point in each figure and corresponds to the row number in Table A3.3. These point numbers will be referred to in the text.

CAIs constitute the shortest formation interval of 3.18 Myr and range from 4568.50 Ma to 4565.32 Ma (points 1-13). The age of the solar system is taken to be 4567.30 Ma from Connelly et al. (2012) and the scatter about this age will be addressed in the discussion. Chondrule formation has a longer duration of 4.70 Myr and starts approximately with the start of the solar system (points 14-160). The assembly of the

various chondrite parent asteroids can then be assumed to have occurred after the last chondrule age for that group using the principal of inclusions. Possible exceptions to this are the CB chondrites (points 83 and 84) which will be addressed in the discussion. Aqueous alteration and thermal metamorphism are typically assumed to take place on the parent asteroids after assembly.

Table A3.2. Number of ages per object and isotopic system.

	Pb-Pb	Al-Mg	Mn-Cr	Hf-W	Total
CAIs	13				13
Chondrules	11	132	3	1	147
Aqueous Alteration			24		24
Thermal Metamorphism	21	2		4	27
Angrites	9				9
Total	54	134	27	5	220

Aqueous alteration spans 4.84 Myr and starting at 4565.92 Ma, 1.37 Myr after the formation of the solar system (points 161-184). The heavily aqueously altered meteorites (CIs and CMs) typically do not have any remaining chondrules with which to constrain asteroid assembly however chondrules in the weakly altered CM Paris were dated to 4566.47 Ma (point 75; Hewins et al., 2014) which is consistent with subsequent aqueous alteration. Thermal metamorphism appears to be a much longer process with ages ranging from 4562.70 Ma to 4504.40 Ma, a 58.30 Myr span (points 185-211). All metamorphic ages are older than the chondrule ages which is also consistent with thermal metamorphism post-dating assembly. Lead-Pb ages for angrites range 7.82 Myr from 4564.42 Ma to 4556.60 Ma (points 212-220), considerably shorter than the metamorphic history recorded in chondrites.

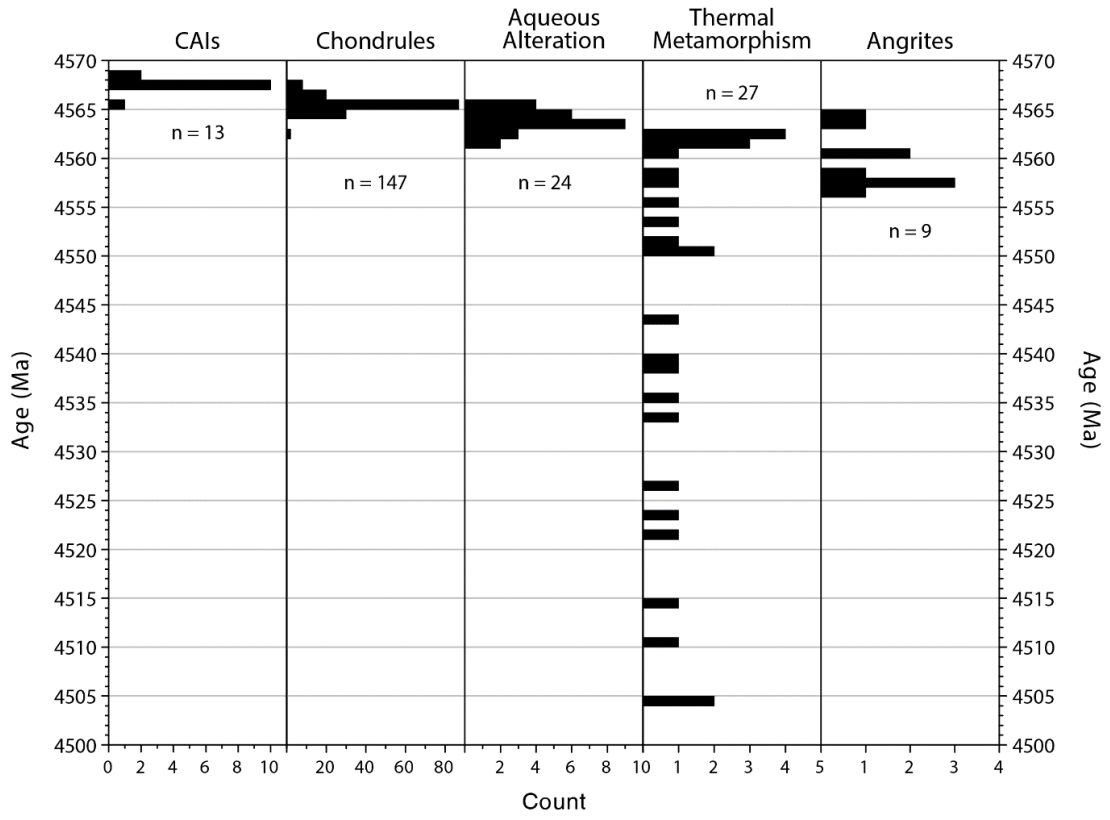

Figure A3.1. Distribution of ages for chondrite components and processes. All points are represented in 1 Myr bins.

4. Discussion

4.1. CAIs

CAIs (calcium-aluminum-rich inclusions) are refractory nebular condensates found within most chondrites in varying modal abundances. CAI mineralogy was thermodynamically predicted to condense out of a high temperature gas of solar composition and the first inclusions were described in the CV chondrite Allende shortly after it fell in 1969 (McSween and Huss, 2010). As such, these refractory inclusions are of great interest for understanding the high temperature environment surrounding the early Sun. Duration of formation is expected to be relatively short and roughly correspond to Type 0 young solar objects (YSOs). Astronomically, these objects are

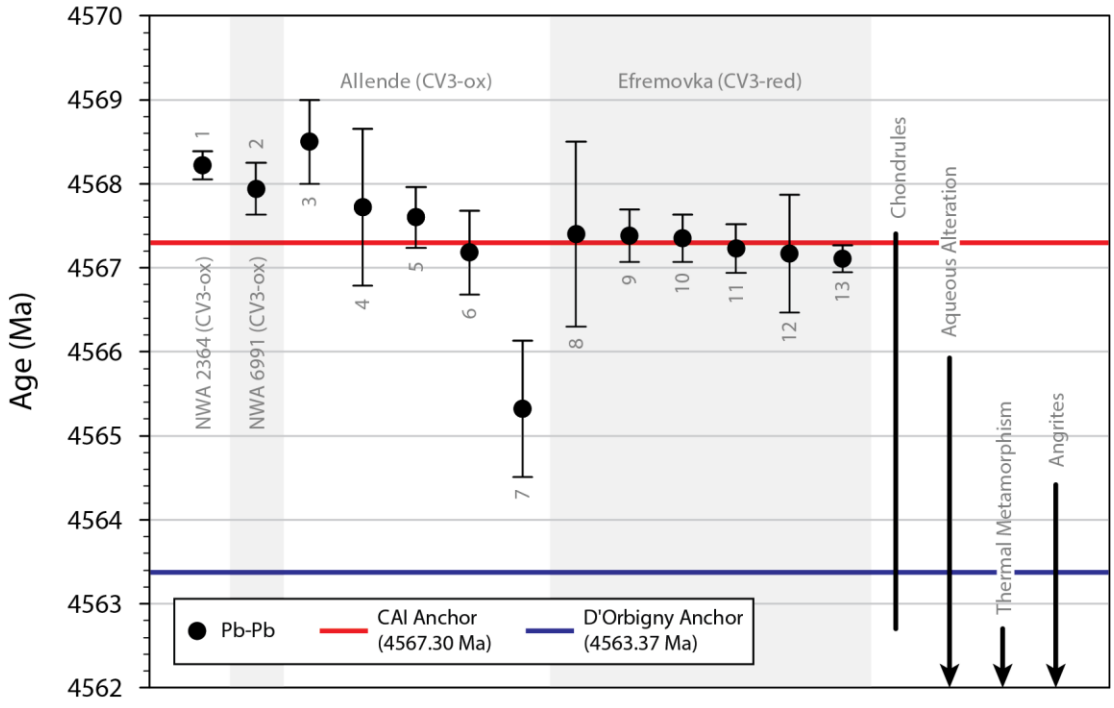

Figure A3.2. CAIs. Individual meteorites are grouped, red and blue lines represent the CAI and D'Orbigny anchors respectively. See text for details.

characterized by rapid accretion onto the young star from an envelope of gas and dust for less than a million years (Williams and Cieza, 2011). Figure A3.2 shows the literature values for absolute ages of CAIs which show a range of 3.18 Myr. Although this is a shorter duration than the other objects considered here, it is still considerably longer than the expected million-year timescale.

A possible explanation for this discrepancy lies in how the ages were calculated. Typically, the $^{238}U/^{235}U$ ratio is assumed to be fixed with a value of 137.88. This assumption simplifies the analysis as only Pb isotopic ratios need to be measured to in order to produce the final isochron. However, Amelin et al. (2010) pointed out that large variability in CAI ages may be due to $^{238}U/^{235}U$ ratios differing from the canonical value of 137.88 and showed that measured ratios indeed differ with values of 137.876 and

137.724 for Allende CAIs and chondrules respectively. Using the measured $^{238}U/^{235}U$ ratio, Amelin et al. (2010) produced an age of 4567.18 Ma for the Allende CAI (point 6). More recently, Connelly et al. (2012) produced three more CAI ages from the CV Efremovka ranging from 4567.23 Ma to 4567.38 Ma with measured $^{238}U/^{235}U$ ratios of 137.627 to 137.832 (points 9-11). The average of these last three points is 4567.30±0.16 Ma (implying a 0.16 Myr duration) and is the value adopted in this paper for CAI formation and the starting age of the solar system (Connelly et al., 2012).

While variable $^{238}U/^{235}U$ ratios may account for some scatter in the CAI ages (e.g., point 7), it does not make the issue disappear entirely. Points 1-3 hover around 4568 Ma and while point 3 was measured assuming constant $^{238}U/^{235}U$, points 1 and 2 were measured using the updated method (Bouvier and Wadhwa, 2010; Bouvier et al., 2011). This leaves two possibilities. First, that CAI ages are bimodal with one set forming around 4567 Ma and the other around 4568 Ma (at least within the scope of this limited data set). This may not be impossible as it is known that accretion onto a young star is not always a continuous process. FU Orionis has been observed to produce short, intense bursts which are attributed to surges of accretion (Williams and Cieza, 2011). However, these bursts occur on observational timescales much shorter than would be necessary to describe the million-year range shown in the data. Though in principal, discrete, high-energy bursts of accretion could create CAIs with discrete age populations. The other possibility to describe the remaining scatter in the data is that there are additional unsolved analytical issues.

4.2. Chondrules

Chondrules are millimeter sized igneous spherules that are common in most chondrites. They formed from flash heating of nebular material in the first few AU from the sun, further than the inferred formation environment of CAIs. While there is little agreement on the exact mechanism that causes the flash heating events (impacts, bow shocks, nebular lightning, magnetic reconnection events, etc.), it is generally accepted that chondrules mark a time characterized by high energy processing of material within the solar nebula (Scott and Krot, 2005). Chondrule formation roughly lasts through the Type III YSO phase and ends with dissipation of gas and dust in the protoplanetary disk leaving a bare scattered disk (Williams and Cieza, 2011). The duration of chondrule formation from literature ages is 4.70 Myr with a mean age 1.87 Myr after CAI formation (Figure A3.3).

The start of chondrule formation has been the source of considerable debate. Initially, the limited amount of chondrule data seemed to indicate a million-year gap between the formation of CAIs and chondrules. However, more recent data for the CV3 chondrite Allende show some chondrules are just as old as CAIs (points 14-19) and must have started forming at roughly the same time (Bizzarro et al., 2004; Connelly et al., 2012). These early ages are further enforced by observations of chondrules found within CAIs (Krot et al., 2005b). Interestingly, most meteorites do not show such primitive ages but instead have youngest reported ages of around 4566.5 Ma or less.

The duration of chondrule formation from the data presented in Figure A3.3 is 4.70 Myr. However, this includes two points for CB chondrites (points 83 and 84) which are noticeable outliers from the rest of the data. CB chondrites are also unusual in that

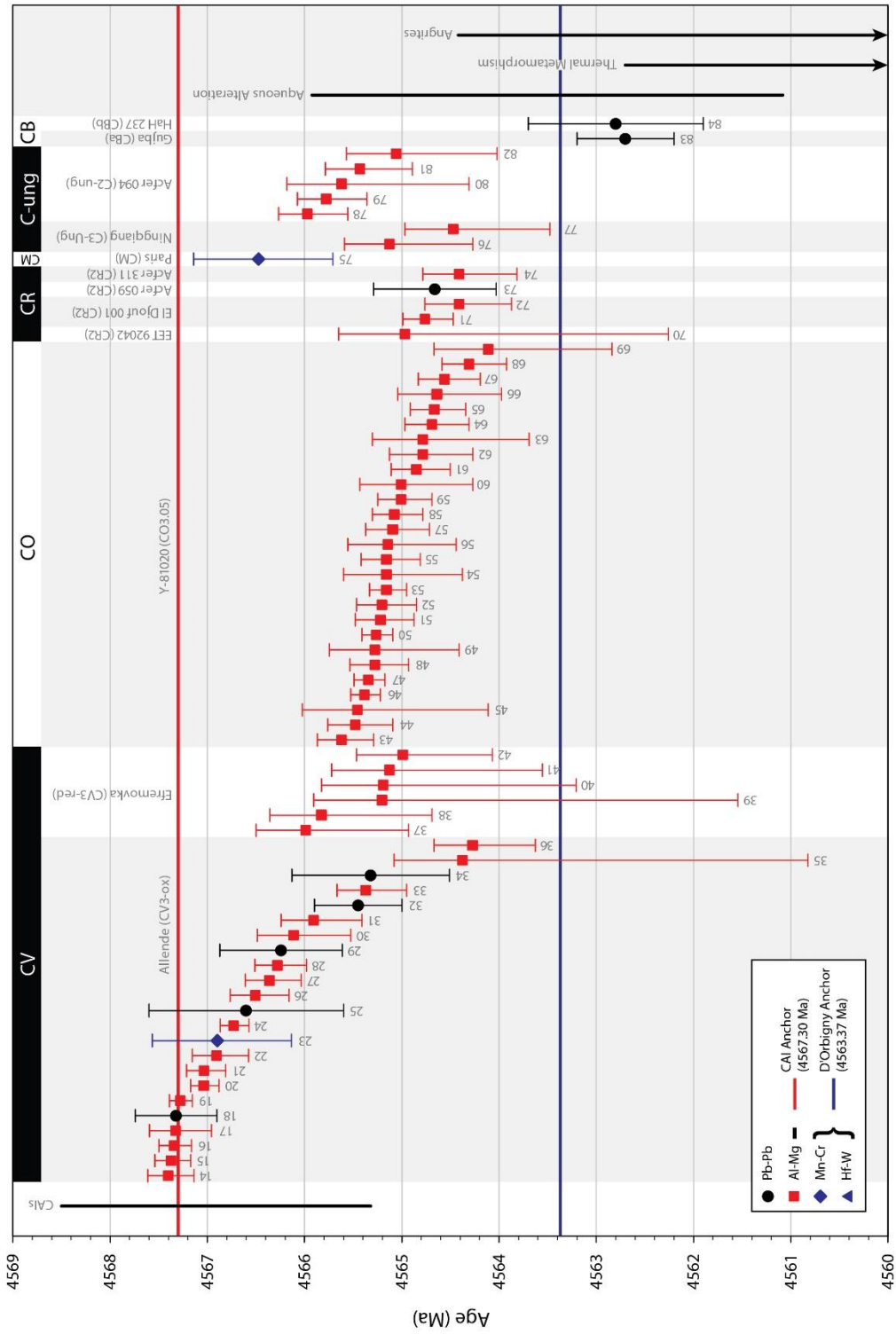

Figure A3.3. Chondrules in carbonaceous chondrites. Individual meteorites are grouped, red and blue lines represent the CAI and D'Orbigny anchors respectively. See text for details.

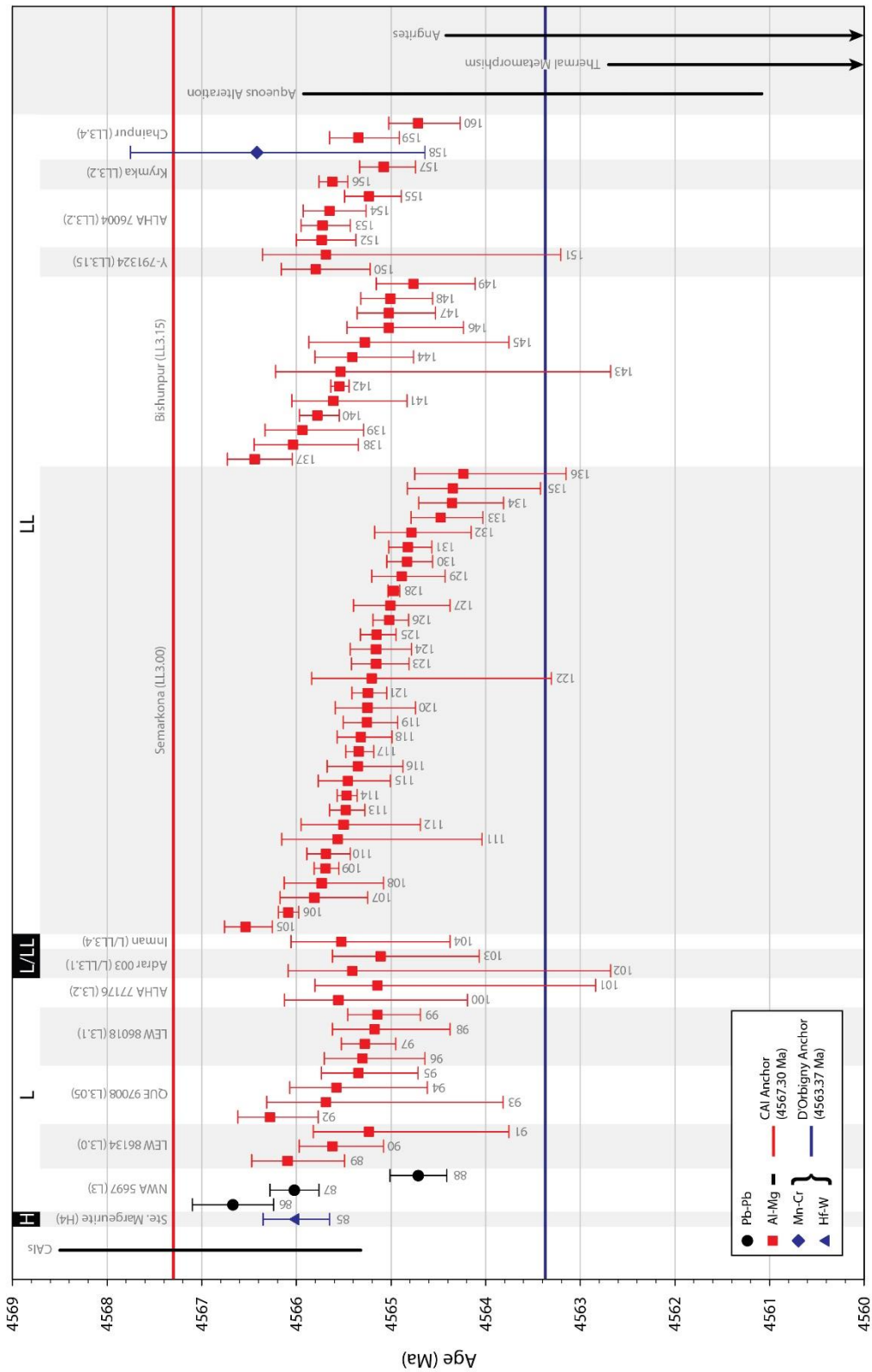

Figure A3.3. *(Continued)*. Chondrules in ordinary chondrites. Individual meteorites are grouped, red and blue lines represent the CAI and D'Orbigny anchors respectively. See text for details.

they contain up to 70% metal by volume, far greater than any other chondrite class. It is because of this, and other evidence, they are not considered to form in the same manner as other chondrites but instead formed as the product of an impact generated vapor-melt plume. As such, chondrules within CB chondrites likely date the impact event at ~4563 Ma (Krot et al., 2005a). Removing CB chondrites reduces the duration for chondrule formation by 30% to 3.29 Myr with no chondrules after 4564 Ma.

Figure A3.4 is a histogram illustrating the age distribution of chondrules in carbonaceous and ordinary chondrites. It also serves to highlight the above discussion concerning the ages of chondrules in Allende and the CB chondrites. Removing these two groups from consideration, the majority of chondrule formation occurs between 4567 Ma and 4564 Ma and averaging 4565.26 Ma with a single peak in both carbonaceous and ordinary chondrites. In fact, the averages for each of these groups considered separately only varies by 0.29 Ma. Since ordinary and carbonaceous chondrites originate from the inner and outer asteroid belt respectively, the similar age distributions seem to indicate that the chondrule formation interval was not radially dependent within the resolution of the data. The peak in the age distribution of chondrules may represent the peak in chondrule production within the disk. However, it is more likely this peak age represents the end of the high energy period in the nebula and a decrease in probability that a given chondrule will be reprocessed before accreting onto its parent asteroid.

4.3. Aqueous alteration

Most carbonaceous chondrites have experienced varying degrees of aqueous alteration (Brearley, 2006). Models of fluid flow and alteration in chondritic asteroids often assume small bodies ($\leq$ 50 km) which accretes with a fraction of ice that melts due

to heat from radioactive decay, typically ^{26}Al and ^{60}Fe (e.g., Palguta et al., 2010). The melted ice then moves through the asteroid due to pressure gradients or convective processes altering the primary mineralogy to phyllosilicates. Carbonates also form during this process and can be dated to provide an age of alteration. The duration of this alteration from CM and CI chondrites from the literature is 4.84 Myr starting 1.38 Myr after CAIs (Figure A3.5).

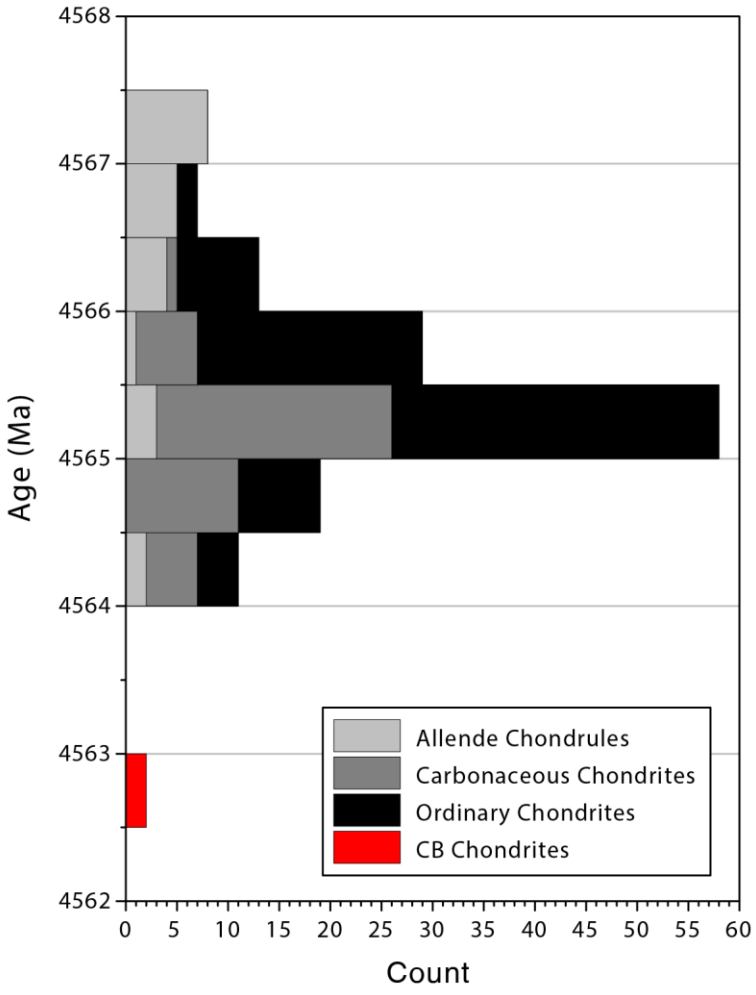

Figure A3.4. Distribution of chondrules ages. All chondrule ages are represented in 0.5 Myr bins.

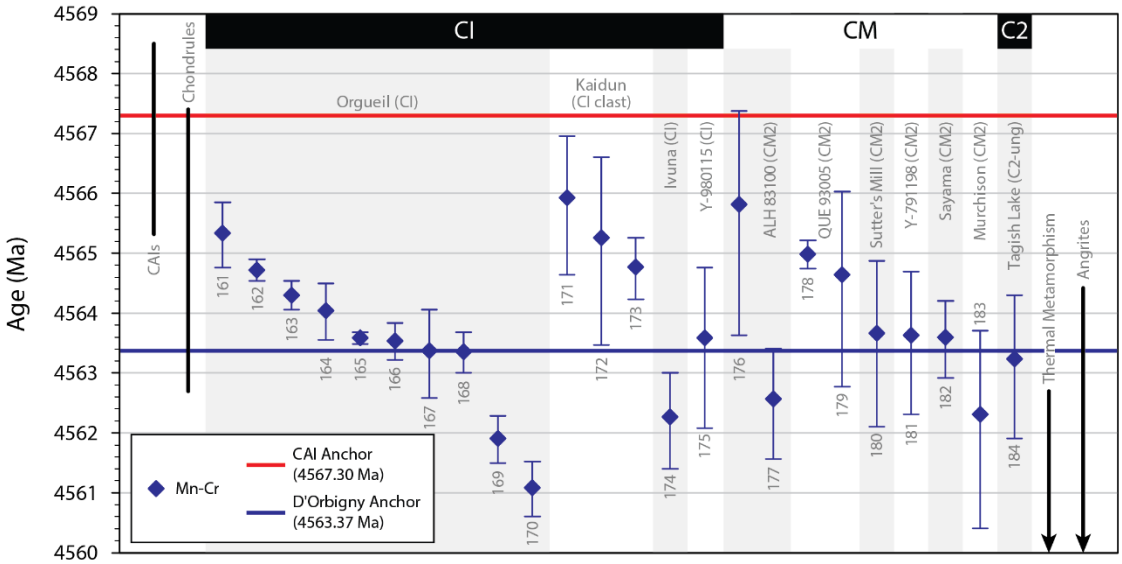

Figure A3.5. Aqueous alteration. Individual meteorites are grouped, red and blue lines represent the CAI and D'Orbigny anchors respectively. See text for details.

As mentioned in the results, chondrules for CIs and CMs do not typically survive the alteration process so only one measurement attributed to a chondrule is available for the CM chondrite Paris (point 75). As would be expected, this chondrule age which predates CM alteration although Hewins et al. (2014) attributes this measurement to chondrule formation purely because of its old age. As such, establishing the assembly-alteration timeline is not yet possible. What does seem apparent from the literature data is that carbonates were forming on asteroids while chondrules were still being formed though largely after the 4565.26 Ma peak in chondrule ages. This is possibly another indication that the dynamic environment in the solar nebula started to relax after that time.

However, Mn-Cr dating is not without its issues. As mentioned above, data from a couple studies were not included (e.g., Brearley and Hutcheon, 2000, 2002) because anomalously high initial ratios produced carbonate ages that predated CAI formation,

sometimes significantly. Fujiya et al. (2012) pointed out that differences in matrix effects between the carbonate samples and olivine standards could produce errors of over 2 Myr. Recent studies use synthetic standards and have produced more reasonable ages for carbonate formation but another problem may exist, that of the half-life measurement. As in this study, most reported ages do not propagate errors associated with half-lives and these errors can be quite substantial, 10% in the case of ^{53}Mn. In addition, the ^{53}Mn half-life has not been recalculated since 1974 during which the analytical precision of measurements requiring an accurate determination of the half-life have increased dramatically (Tyra, 2015).

4.4. Thermal metamorphism

While carbonaceous chondrites typically experience aqueous alteration, ordinary chondrites more commonly experience thermal metamorphism. Similar to aqueous alteration, thermal metamorphism is driven by the radioactive decay of short-lived radionuclides such as ^{26}Al and ^{60}Fe. However, ordinary chondrites seem to have accreted with little or no ice and to a size large enough that internal heating caused extensive thermal metamorphism not typically seen in carbonaceous chondrites. From the literature, the first metamorphic ages are from 4562.7 and span over 58 Myr (Figure A3.6). Since there are far more ordinary chondrite chondrule ages than for aqueously altered chondrite groups it is easy to say that metamorphism postdated assembly as is expected. However, these ages typically date retrograde metamorphism and provide little information about the period of onset.

Degree of thermal metamorphism is denoted by a numerical petrologic type between 4 and 6 where type 6 has seen the greatest amount of recrystallization (Huss et

al., 2006). Typically metamorphism modeled as an onion shell where the core of asteroid has the highest petrologic type (greatest degree of thermal metamorphism) and the outer layers show progressively fewer metamorphic effects closer to the cold surface (Harrison and Grimm, 2010). It is predicted that layers of lower petrologic type will cool sooner than the higher petrologic type layers which broadly appears to be true as can be seen in phosphate ages of H chondrites (e.g., points 189, 193, and 199).

The approximate closure temperatures for Pb-Pb are 725ºC in silicates and 450ºC in phosphates, for Hf-W in metal-silicate is 875ºC, and for Al-Mg in plagioclase is 450ºC so that the higher temperature chronometers should recorder older ages than those with lower closure temperatures (Kleine et al., 2008; Telus et al., 2014). Again, this is broadly true as exemplified by Richardton which shows younger silicate Pb-Pb and metal-silicate Hf-W ages (points 190 and 191) and older Pb-Pb phosphate ages (points 192 and 193). Unfortunately, while these data seem to indicate quiescent onion shell metamorphism for ordinary chondrite asteroids, metallographic cooling rates show a more turbulent history and suggest many of these meteorites were excavated by impact and cooled in an ejecta blanket (Scott et al., 2014).

Metamorphic ages may also be affected by a number of other processes. Lead-Pb ages were measured on phosphates which are known to alter in the presence of fluids from merrillite to apatite with considerably lower abundances of REEs (Jones et al., 2014). Aluminum-Mg ages conducted on plagioclase are subject to two potential issues: diffusion and alteration. Magnesium diffusion in albitic plagioclase is considerably faster (lower closure temperature) than anorthite so measurements of albite may report lower ^{26}Mg excess and subsequently older ages (Van Orman et al., 2014). This may also be a

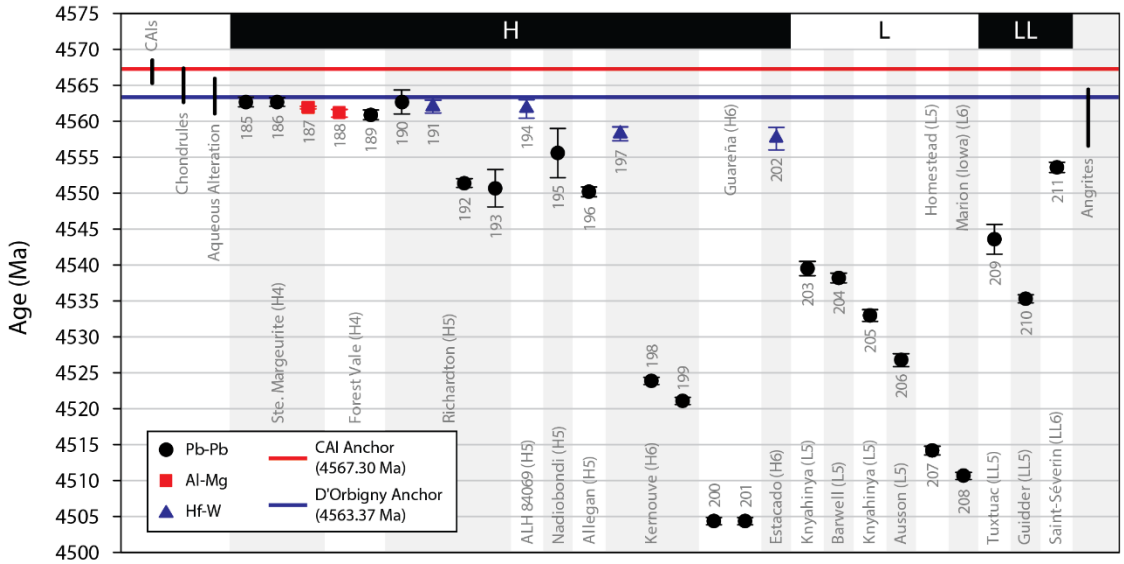

Figure A3.6. Thermal metamorphism. Individual meteorites are grouped, red and blue lines represent the CAI and D'Orbigny anchors respectively. See text for details.

problem for Al-Mg ages of albite-bearing chondrules. Anorthitic feldspar is also known to alter to anorthite, likely stripping its excess Mg (Kovach and Jones, 2010). Finally, Al-Mg and Hf-W are of limited use beyond a few half-lives of the beginning of the solar system (CAIs) and only provide information about the earliest parts of the metamorphic process. While initial $^{238}U/^{235}U$ ratios for the Pb-Pb ages may also stray from canonical, the shift in ages expected for variable U isotopes is minor compared to the large spread of metamorphic ages.

4.5. Angrites

Angrites are derived from an unknown differentiated asteroid (or possibly group of asteroids). This asteroid was large enough (or accreted early enough) for heat from radioactive decay to cause melting and differentiation. While angrites are only included here as the anchor for the Mn-Cr and Hf-W systems, the duration of geologic processing on the angrite parent body is of interest as a comparison to chondritic processes. Lead-Pb

ages for angrites are shown in Figure A3.7 and span 7.82 Myr from 4567.42 Ma to 4556.60 Ma.

The anchor for the two short-lived systems Mn-Cr and Hf-W was chosen to be D'Orbigny (point 213) because it is well characterized and the Pb-Pb age was recently redetermined using a measured $^{238}U/^{235}U$ ratio (Brennecka and Wadhwa, 2012). Though as is apparent from the figure, angrites as a whole do not represent a discrete point in time but instead record igneous activity over an approximately 8 Myr period. Depending on the validity of point 212 which assumed constant $^{238}U/^{235}U$ (Amelin, 2008), the earliest recorded angrite melts were produced after, or at least towards the end of, chondrule formation. This is consistent with the timing of CB chondrules which were likely formed in an impact event between large planetary embryos that were at least partially differentiated (Krot et al., 2005a).

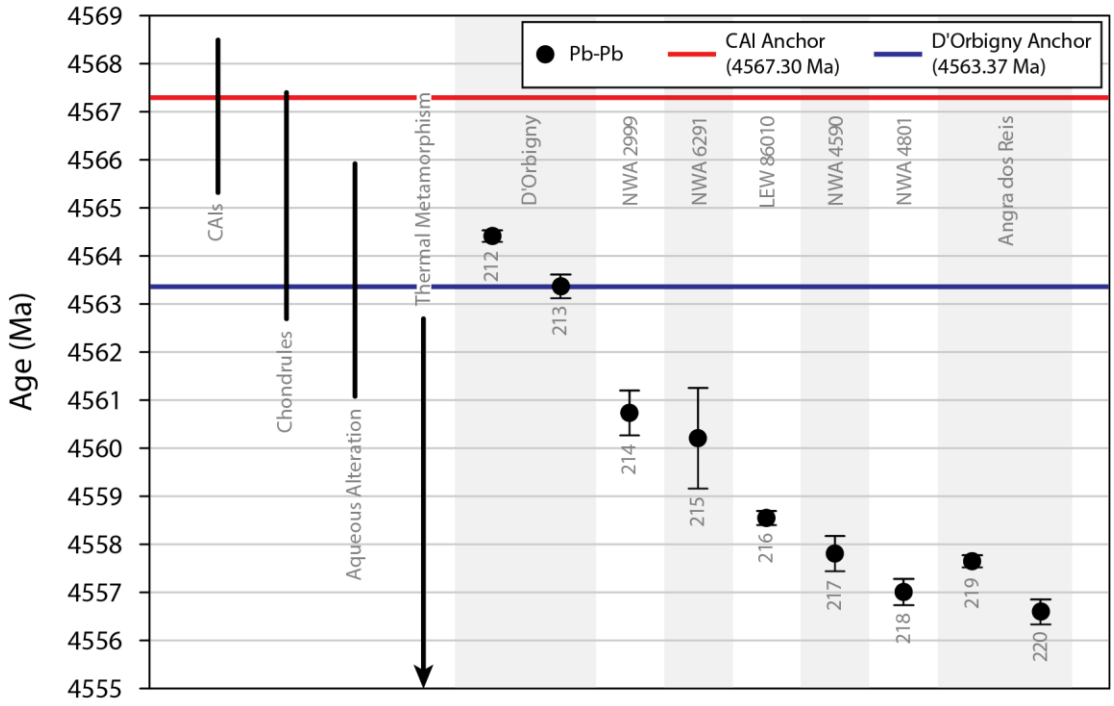

Figure A3.7. Angrites. Individual meteorites are grouped, red and blue lines represent the CAI and D'Orbigny anchors respectively. See text for details.

5. Summary and conclusions

CAIs show a wider range of ages than expected and this is likely, at least in part, due to the variability of $^{238}U/^{235}U$. The age of the solar system from CAIs is taken to be 4567.30 Ma. Chondrules appear to have started forming simultaneously with CAIs and lasted a little over 3 Myr. Ordinary and carbonaceous chondrites have similar age distributions though the CV3 Allende appears to have anomalously young chondrules. Chondrules in CB chondrites post-date all other chondrule forming events which is attributed to formation from the collisions of planetesimals. The peak in chondrule ages at 4565.26 Ma may signal a calming of the disk.

This period roughly corresponds to the start of aqueous alteration which progresses for less than 5 Myr. Though the Mn-Cr system used to date aqueous alteration may still be prone to significant analytical uncertainty. Thermal metamorphism postdates chondrule formation by 1 Myr and lasts over 58 Myr. Metamorphic ages of different phases are roughly consistent with their respective closure temperatures though the cooling environment may not be so simple. Angrites underwent geologic processing over an 8 Myr period starting at the end of chondrule formation which is consistent with formation of CB chondrites by collision of planetesimals and the start of thermal metamorphism.

This chronology of chondritic asteroids not only helps in understanding of the formation and evolution of material in the asteroid belt, it illuminates the dynamic environment in which the Earth was formed. Our planet likely went through many of the same stages and incorporated much of the same material as chondritic asteroids but on a

far larger scale. The diminutive size of chondritic asteroids allows for these early solar system processes to be preserved and studied 4.5 billion years later.

Table A3.3. Radiogenic age data.

CAIs

#	Meteorite	Class	Feature	Method	Age (Ma)	2σ (+/-)	Reference
1	NWA 2364	CV3-ox	CAIs	Pb-Pb	4568.22	0.17/0.17	Bouvier and Wadhwa (2010)
2	NWA 6991	CV3-ox	CAIs	Pb-Pb	4567.94	0.31/0.31	Bouvier et al. (2011)
3	Allende	CV3-ox	CAIs	Pb-Pb	4568.50	0.50/0.50	Bouvier et al. (2007)
4	Allende	CV3-ox	CAIs	Pb-Pb	4567.72	0.93/0.93	Connelly et al. (2008)
5	Allende	CV3-ox	CAIs	Pb-Pb	4567.60	0.36/0.36	Jacobsen et al. (2008)
6	Allende	CV3-ox	CAIs	Pb-Pb	4567.18	0.50/0.50	Amelin et al. (2010)
7	Allende	CV3-ox	CAIs	Pb-Pb	4565.32	0.81/0.81	Connelly and Bizzarro (2009)
8	Efremovka	CV3-red	CAIs	Pb-Pb	4567.40	1.10/1.10	Amelin et al. (2002)
9	Efremovka	CV3-red	CAIs	Pb-Pb	4567.38	0.31/0.31	Connelly et al. (2012)
10	Efremovka	CV3-red	CAIs	Pb-Pb	4567.35	0.28/0.28	Connelly et al. (2012)
11	Efremovka	CV3-red	CAIs	Pb-Pb	4567.23	0.29/0.29	Connelly et al. (2012)
12	Efremovka	CV3-red	CAIs	Pb-Pb	4567.17	0.70/0.70	Amelin et al. (2002)
13	Efremovka	CV3-red	CAIs	Pb-Pb	4567.11	0.16/0.16	Amelin et al. (2006)

Chondrules

#	Meteorite	Class	Feature	Method	Age (Ma)	2σ (+/-)	Reference
14	Allende	CV3-ox	chondrules	Al-Mg	4567.40	0.21/0.26	Bizzarro et al. (2004)
15	Allende	CV3-ox	chondrules	Al-Mg	4567.37	0.17/0.20	Bizzarro et al. (2004)
16	Allende	CV3-ox	chondrules	Al-Mg	4567.34	0.15/0.18	Bizzarro et al. (2004)
17	Allende	CV3-ox	chondrules	Al-Mg	4567.33	0.27/0.37	Bizzarro et al. (2004)
18	Allende	CV3-ox	chondrules	Pb-Pb	4567.32	0.42/0.42	Connelly et al. (2012)
19	Allende	CV3-ox	chondrules	Al-Mg	4567.28	0.11/0.12	Bizzarro et al. (2004)
20	Allende	CV3-ox	chondrules	Al-Mg	4567.04	0.14/0.16	Bizzarro et al. (2004)
21	Allende	CV3-ox	chondrules	Al-Mg	4567.03	0.18/0.22	Bizzarro et al. (2004)
22	Allende	CV3-ox	chondrules	Al-Mg	4566.91	0.25/0.33	Bizzarro et al. (2004)
23	Allende	CV3-ox	chondrules	Mn-Cr	4566.90	0.67/0.76	Yin et al. (2009)
24	Allende	CV3-ox	chondrules	Al-Mg	4566.73	0.14/0.16	Bizzarro et al. (2004)
25	Allende	CV3-ox	chondrules	Pb-Pb	4566.60	1.00/1.00	Amelin and Krot (2007)
26	Allende	CV3-ox	chondrules	Al-Mg	4566.51	0.26/0.35	Bizzarro et al. (2004)
27	Allende	CV3-ox	chondrules	Al-Mg	4566.36	0.25/0.33	Bizzarro et al. (2004)
28	Allende	CV3-ox	chondrules	Al-Mg	4566.28	0.23/0.30	Bizzarro et al. (2004)
29	Allende	CV3-ox	chondrules	Pb-Pb	4566.24	0.63/0.63	Connelly et al. (2012)
30	Allende	CV3-ox	chondrules	Al-Mg	4566.11	0.37/0.59	Bizzarro et al. (2004)
31	Allende	CV3-ox	chondrules	Al-Mg	4565.91	0.33/0.50	Bizzarro et al. (2004)
32	Allende	CV3-ox	chondrules	Pb-Pb	4565.45	0.45/0.45	Connelly et al. (2008)
33	Allende	CV3-ox	chondrules	Al-Mg	4565.37	0.30/0.42	Hutcheon et al. (2009)
34	Allende	CV3-ox	chondrules	Pb-Pb	4565.32	0.81/0.81	Connelly and Bizzarro (2009)
35	Allende	CV3-ox	chondrules	Al-Mg	4564.38	0.70/3.55	Hutcheon et al. (2009)
36	Allende	CV3-ox	chondrules	Al-Mg	4564.27	0.39/0.65	Hutcheon et al. (2009)
37	Efremovka	CV3-red	chondrules	Al-Mg	4565.99	0.51/1.06	Hutcheon et al. (2009)
38	Efremovka	CV3-red	chondrules	Al-Mg	4565.83	0.53/1.14	Hutcheon et al. (2009)
39	Efremovka	CV3-red	chondrules	Al-Mg	4565.20	0.70/3.66	Hutcheon et al. (2009)
40	Efremovka	CV3-red	chondrules	Al-Mg	4565.19	0.64/1.98	Hutcheon et al. (2009)
41	Efremovka	CV3-red	chondrules	Al-Mg	4565.13	0.60/1.57	Hutcheon et al. (2009)
42	Efremovka	CV3-red	chondrules	Al-Mg	4564.99	0.48/0.92	Hutcheon et al. (2000)

43	Y-81020	CO3.05	chondrules	Al-Mg	4565.62	0.25/0.33	Kurahashi et al. (2008)
44	Y-81020	CO3.05	chondrules	Al-Mg	4565.48	0.28/0.39	Kurahashi et al. (2008)
45	Y-81020	CO3.05	chondrules	Al-Mg	4565.46	0.57/1.34	Kurahashi et al. (2008)
46	Y-81020	CO3.05	chondrules	Al-Mg	4565.38	0.14/0.16	Kurahashi et al. (2008)
47	Y-81020	CO3.05	chondrules	Al-Mg	4565.34	0.15/0.17	Kurahashi et al. (2008)
48	Y-81020	CO3.05	chondrules	Al-Mg	4565.28	0.26/0.35	Kurahashi et al. (2008)
49	Y-81020	CO3.05	chondrules	Al-Mg	4565.28	0.46/0.87	Kurahashi et al. (2008)
50	Y-81020	CO3.05	chondrules	Al-Mg	4565.26	0.15/0.17	Kurahashi et al. (2008)
51	Y-81020	CO3.05	chondrules	Al-Mg	4565.22	0.26/0.35	Kurahashi et al. (2008)
52	Y-81020	CO3.05	chondrules	Al-Mg	4565.20	0.26/0.35	Kurahashi et al. (2008)
53	Y-81020	CO3.05	chondrules	Al-Mg	4565.16	0.17/0.21	Kurahashi et al. (2008)
54	Y-81020	CO3.05	chondrules	Al-Mg	4565.16	0.44/0.78	Kurahashi et al. (2008)
55	Y-81020	CO3.05	chondrules	Al-Mg	4565.16	0.26/0.35	Kurahashi et al. (2008)
56	Y-81020	CO3.05	chondrules	Al-Mg	4565.14	0.41/0.70	Kunihiro et al. (2004)
57	Y-81020	CO3.05	chondrules	Al-Mg	4565.09	0.28/0.38	Kurahashi et al. (2008)
58	Y-81020	CO3.05	chondrules	Al-Mg	4565.08	0.23/0.29	Kurahashi et al. (2008)
59	Y-81020	CO3.05	chondrules	Al-Mg	4565.01	0.24/0.32	Kurahashi et al. (2008)
60	Y-81020	CO3.05	chondrules	Al-Mg	4565.01	0.43/0.74	Kurahashi et al. (2008)
61	Y-81020	CO3.05	chondrules	Al-Mg	4564.85	0.26/0.35	Kurahashi et al. (2008)
62	Y-81020	CO3.05	chondrules	Al-Mg	4564.79	0.34/0.51	Kurahashi et al. (2008)
63	Y-81020	CO3.05	chondrules	Al-Mg	4564.79	0.52/1.09	Yurimoto and Wasson (2002)
64	Y-81020	CO3.05	chondrules	Al-Mg	4564.69	0.28/0.38	Kunihiro et al. (2004)
65	Y-81020	CO3.05	chondrules	Al-Mg	4564.67	0.25/0.32	Kurahashi et al. (2008)
66	Y-81020	CO3.05	chondrules	Al-Mg	4564.64	0.40/0.67	Kunihiro et al. (2004)
67	Y-81020	CO3.05	chondrules	Al-Mg	4564.56	0.27/0.36	Kunihiro et al. (2004)
68	Y-81020	CO3.05	chondrules	Al-Mg	4564.31	0.28/0.38	Kurahashi et al. (2008)
69	Y-81020	CO3.05	chondrules	Al-Mg	4564.11	0.55/1.27	Kunihiro et al. (2004)
70	EET 92042	CR2	chondrules	Al-Mg	4564.97	0.68/2.71	Hutcheon et al. (2009)
71	El Djouf 001	CR2	chondrules	Al-Mg	4564.76	0.23/0.29	Nagashima et al. (2008)
72	El Djouf 001	CR2	chondrules	Al-Mg	4564.41	0.35/0.54	Nagashima et al. (2008)
73	Acfer 059	CR2	chondrules	Pb-Pb	4564.66	0.63/0.63	Amelin et al. (2002)
74	Acfer 311	CR2	chondrules	Al-Mg	4564.41	0.38/0.60	Nagashima et al. (2008)
75	Paris	CM	chondrules	Mn-Cr	4566.47	0.67/0.76	Hewins et al. (2014)
76	Ningqiang	C3-Ung	chondrules	Al-Mg	4565.13	0.46/0.86	Hsu et al. (2003)
77	Ningqiang	C3-Ung	chondrules	Al-Mg	4564.47	0.50/0.99	Hsu et al. (2003)
78	Acfer 094	C2-ung	chondrules	Al-Mg	4565.97	0.30/0.42	Hutcheon et al. (2009)
79	Acfer 094	C2-ung	chondrules	Al-Mg	4565.78	0.30/0.42	Hutcheon et al. (2000)
80	Acfer 094	C2-ung	chondrules	Al-Mg	4565.62	0.56/1.31	Sugiura and Krot (2007)
81	Acfer 094	C2-ung	chondrules	Al-Mg	4565.43	0.35/0.54	Hutcheon et al. (2009)
82	Acfer 094	C2-ung	chondrules	Al-Mg	4565.06	0.51/1.04	Sugiura and Krot (2007)
83	Gujba	CBa	chondrules	Pb-Pb	4562.70	0.50/0.50	(Krot et al., 2005a)
84	HaH 237	CBb	chondrules	Pb-Pb	4562.80	0.90/0.90	(Krot et al., 2005a)
85	Ste. Margeurite	H4	chondrules	Hf-W	4566.01	0.35/0.36	Kleine et al. (2008)
86	NWA 5697	L3	chondrules	Pb-Pb	4566.67	0.43/0.43	Connelly et al. (2012)
87	NWA 5697	L3	chondrules	Pb-Pb	4566.02	0.26/0.26	Connelly et al. (2012)
88	NWA 5697	L3	chondrules	Pb-Pb	4564.71	0.30/0.30	Connelly et al. (2012)
89	LEW 86134	L3.0	chondrules	Al-Mg	4566.09	0.38/0.60	Rudraswami and Goswami (2007)
90	LEW 86134	L3.0	chondrules	Al-Mg	4565.62	0.35/0.54	Rudraswami and Goswami (2007)
91	LEW 86134	L3.0	chondrules	Al-Mg	4565.23	0.59/1.48	Rudraswami and Goswami (2007)
92	QUE 97008	L3.05	chondrules	Al-Mg	4566.28	0.34/0.51	Rudraswami and Goswami (2007)
93	QUE 97008	L3.05	chondrules	Al-Mg	4565.69	0.63/1.87	Rudraswami and Goswami (2007)
94	QUE 97008	L3.05	chondrules	Al-Mg	4565.58	0.49/0.96	Rudraswami and Goswami (2007)
95	QUE 97008	L3.05	chondrules	Al-Mg	4565.34	0.39/0.63	Rudraswami and Goswami (2007)
96	LEW 86018	L3.1	chondrules	Al-Mg	4565.30	0.40/0.66	Rudraswami and Goswami (2007)
97	LEW 86018	L3.1	chondrules	Al-Mg	4565.28	0.25/0.33	Rudraswami and Goswami (2007)
98	LEW 86018	L3.1	chondrules	Al-Mg	4565.17	0.44/0.80	Rudraswami and Goswami (2007)
99	LEW 86018	L3.1	chondrules	Al-Mg	4565.14	0.31/0.45	Rudraswami and Goswami (2007)
100	ALHA 77176	L3.2	chondrules	Al-Mg	4565.56	0.57/1.36	Rudraswami and Goswami (2007)
101	ALHA 77176	L3.2	chondrules	Al-Mg	4565.14	0.66/2.31	Rudraswami and Goswami (2007)

102	Adrar 003	L/LL3.1	chondrules	Al-Mg	4565.41	0.68/2.73	Rudraswami and Goswami (2007)
103	Adrar 003	L/LL3.1	chondrules	Al-Mg	4565.11	0.51/1.04	Rudraswami and Goswami (2007)
104	Inman	L/LL3.4	chondrules	Al-Mg	4565.52	0.53/1.15	Russell et al. (1996)
105	Semarkona	LL3.00	chondrules	Al-Mg	4566.54	0.22/0.28	Russell et al. (1997)
106	Semarkona	LL3.00	chondrules	Al-Mg	4566.09	0.10/0.11	Villeneuve et al. (2009)
107	Semarkona	LL3.00	chondrules	Al-Mg	4565.81	0.36/0.56	Rudraswami et al. (2008)
108	Semarkona	LL3.00	chondrules	Al-Mg	4565.73	0.40/0.66	Rudraswami et al. (2008)
109	Semarkona	LL3.00	chondrules	Al-Mg	4565.69	0.12/0.14	Villeneuve et al. (2009)
110	Semarkona	LL3.00	chondrules	Al-Mg	4565.69	0.20/0.25	Rudraswami et al. (2008)
111	Semarkona	LL3.00	chondrules	Al-Mg	4565.56	0.59/1.53	Mishra and Goswami (2014)
112	Semarkona	LL3.00	chondrules	Al-Mg	4565.50	0.45/0.81	Kita et al. (2000)
113	Semarkona	LL3.00	chondrules	Al-Mg	4565.48	0.17/0.20	Kita et al. (2000)
114	Semarkona	LL3.00	chondrules	Al-Mg	4565.47	0.10/0.11	Villeneuve et al. (2009)
115	Semarkona	LL3.00	chondrules	Al-Mg	4565.46	0.31/0.45	Kita et al. (2000)
116	Semarkona	LL3.00	chondrules	Al-Mg	4565.35	0.32/0.48	Villeneuve et al. (2009)
117	Semarkona	LL3.00	chondrules	Al-Mg	4565.34	0.14/0.16	Villeneuve et al. (2009)
118	Semarkona	LL3.00	chondrules	Al-Mg	4565.32	0.25/0.33	Hutcheon and Hutchison (1989)
119	Semarkona	LL3.00	chondrules	Al-Mg	4565.26	0.25/0.32	Villeneuve et al. (2009)
120	Semarkona	LL3.00	chondrules	Al-Mg	4565.25	0.34/0.51	Mishra et al. (2010)
121	Semarkona	LL3.00	chondrules	Al-Mg	4565.25	0.17/0.20	Villeneuve et al. (2009)
122	Semarkona	LL3.00	chondrules	Al-Mg	4565.20	0.63/1.90	Mishra et al. (2010)
123	Semarkona	LL3.00	chondrules	Al-Mg	4565.16	0.26/0.35	Kita et al. (2000)
124	Semarkona	LL3.00	chondrules	Al-Mg	4565.16	0.27/0.37	Mishra et al. (2010)
125	Semarkona	LL3.00	chondrules	Al-Mg	4565.15	0.17/0.21	Villeneuve et al. (2009)
126	Semarkona	LL3.00	chondrules	Al-Mg	4565.02	0.17/0.20	Villeneuve et al. (2009)
127	Semarkona	LL3.00	chondrules	Al-Mg	4565.01	0.39/0.63	Kita et al. (2000)
128	Semarkona	LL3.00	chondrules	Al-Mg	4564.97	0.06/0.06	Rudraswami et al. (2008)
129	Semarkona	LL3.00	chondrules	Al-Mg	4564.89	0.32/0.46	Villeneuve et al. (2009)
130	Semarkona	LL3.00	chondrules	Al-Mg	4564.83	0.21/0.27	Villeneuve et al. (2009)
131	Semarkona	LL3.00	chondrules	Al-Mg	4564.82	0.20/0.25	Villeneuve et al. (2009)
132	Semarkona	LL3.00	chondrules	Al-Mg	4564.79	0.39/0.63	Mostefaoui et al. (2002)
133	Semarkona	LL3.00	chondrules	Al-Mg	4564.48	0.31/0.45	Villeneuve et al. (2009)
134	Semarkona	LL3.00	chondrules	Al-Mg	4564.35	0.35/0.54	Villeneuve et al. (2009)
135	Semarkona	LL3.00	chondrules	Al-Mg	4564.35	0.48/0.93	Mishra and Goswami (2014)
136	Semarkona	LL3.00	chondrules	Al-Mg	4564.23	0.52/1.08	Mishra and Goswami (2014)
137	Bishunpur	LL3.15	chondrules	Al-Mg	4566.44	0.29/0.40	Mostefaoui et al. (2002)
138	Bishunpur	LL3.15	chondrules	Al-Mg	4566.04	0.41/0.69	Mostefaoui et al. (2002)
139	Bishunpur	LL3.15	chondrules	Al-Mg	4565.94	0.39/0.65	Mostefaoui et al. (2002)
140	Bishunpur	LL3.15	chondrules	Al-Mg	4565.78	0.19/0.23	Kita et al. (2005)
141	Bishunpur	LL3.15	chondrules	Al-Mg	4565.61	0.44/0.78	Mostefaoui et al. (2002)
142	Bishunpur	LL3.15	chondrules	Al-Mg	4565.55	0.09/0.10	Kita et al. (2005)
143	Bishunpur	LL3.15	chondrules	Al-Mg	4565.54	0.68/2.86	Mostefaoui et al. (2002)
144	Bishunpur	LL3.15	chondrules	Al-Mg	4565.41	0.39/0.65	Kita et al. (2005)
145	Bishunpur	LL3.15	chondrules	Al-Mg	4565.28	0.59/1.52	Mostefaoui et al. (2002)
146	Bishunpur	LL3.15	chondrules	Al-Mg	4565.03	0.44/0.79	Rudraswami et al. (2008)
147	Bishunpur	LL3.15	chondrules	Al-Mg	4565.03	0.33/0.49	Rudraswami et al. (2008)
148	Bishunpur	LL3.15	chondrules	Al-Mg	4565.01	0.31/0.45	Mostefaoui et al. (2002)
149	Bishunpur	LL3.15	chondrules	Al-Mg	4564.76	0.40/0.65	Mostefaoui et al. (2002)
150	Y-791324	LL3.15	chondrules	Al-Mg	4565.79	0.37/0.57	Rudraswami et al. (2008)
151	Y-791324	LL3.15	chondrules	Al-Mg	4565.69	0.67/2.48	Rudraswami et al. (2008)
152	ALHA 76004	LL3.2	chondrules	Al-Mg	4565.73	0.27/0.36	Rudraswami et al. (2008)
153	ALHA 76004	LL3.2	chondrules	Al-Mg	4565.72	0.23/0.29	Rudraswami et al. (2008)
154	ALHA 76004	LL3.2	chondrules	Al-Mg	4565.65	0.28/0.39	Rudraswami et al. (2008)
155	ALHA 76004	LL3.2	chondrules	Al-Mg	4565.23	0.26/0.34	Rudraswami et al. (2008)
156	Krymka	LL3.2	chondrules	Al-Mg	4565.62	0.14/0.16	Kita et al. (2005)
157	Krymka	LL3.2	chondrules	Al-Mg	4565.08	0.25/0.34	Kita et al. (2005)
158	Chainpur	LL3.4	chondrules	Mn-Cr	4566.42	1.33/1.78	Yin et al. (2007)
159	Chainpur	LL3.4	chondrules	Al-Mg	4565.34	0.30/0.43	Russell et al. (1996)
160	Chainpur	LL3.4	chondrules	Al-Mg	4564.72	0.31/0.44	Russell et al. (1997)

Aqueous alteration

#	Meteorite	Class	Feature	Method	Age (Ma)	2σ (+/-)	Reference
161	Orgueil	CI	dolomite	Mn-Cr	4565.33	0.52/0.57	Hoppe et al. (2007)
162	Orgueil	CI	dolomite	Mn-Cr	4564.72	0.18/0.18	Hoppe et al. (2007)
163	Orgueil	CI	dolomite	Mn-Cr	4564.30	0.23/0.24	Hoppe et al. (2007)
164	Orgueil	CI	dolomite	Mn-Cr	4564.04	0.45/0.49	Hoppe et al. (2007)
165	Orgueil	CI	breunnerite	Mn-Cr	4563.58	0.10/0.10	Hoppe et al. (2007)
166	Orgueil	CI	breunnerite	Mn-Cr	4563.53	0.30/0.32	Hoppe et al. (2007)
167	Orgueil	CI	dolomite	Mn-Cr	4563.37	0.69/0.79	Fujiya et al. (2013)
168	Orgueil	CI	breunnerite	Mn-Cr	4563.35	0.32/0.34	Hoppe et al. (2007)
169	Orgueil	CI	breunnerite	Mn-Cr	4561.91	0.38/0.41	Hoppe et al. (2007)
170	Orgueil	CI	breunnerite	Mn-Cr	4561.08	0.44/0.48	Hoppe et al. (2007)
171	Kaidun	CI (clast)	dolomite	Mn-Cr	4565.92	1.04/1.28	Petitat et al. (2011)
172	Kaidun	CI (clast)	dolomite	Mn-Cr	4565.26	1.34/1.79	Petitat et al. (2011)
173	Kaidun	CI (clast)	dolomite	Mn-Cr	4564.77	0.49/0.54	Petitat et al. (2011)
174	Ivuna	CI	dolomite	Mn-Cr	4562.26	0.74/0.86	Fujiya et al. (2013)
175	Y-980115	CI	dolomite	Mn-Cr	4563.58	1.18/1.50	Fujiya et al. (2013)
176	ALH 83100	CM2	carbonates	Mn-Cr	4565.82	1.55/2.19	de Leuw et al. (2009)
177	ALH 83100	CM2	dolomite	Mn-Cr	4562.56	0.84/1.00	Fujiya et al. (2012)
178	QUE 93005	CM2	dolomite	Mn-Cr	4564.98	0.23/0.24	Lee et al. (2012)
179	QUE 93005	CM2	dolomite	Mn-Cr	4564.64	1.39/1.87	de Leuw et al. (2009)
180	Sutter's Mill	CM2	dolomite	Mn-Cr	4563.66	1.21/1.56	Jilly et al. (2014)
181	Y-791198	CM2	calcite	Mn-Cr	4563.63	1.06/1.32	Fujiya et al. (2012)
182	Sayama	CM2	dolomite	Mn-Cr	4563.60	0.60/0.68	Fujiya et al. (2012)
183	Murchison	CM2	calcite	Mn-Cr	4562.31	1.40/1.90	Fujiya et al. (2012)
184	Tagish Lake	C2-ung	dolomite	Mn-Cr	4563.24	1.07/1.33	Fujiya et al. (2013)

Thermal metamorphism

#	Meteorite	Class	Feature	Method	Age (Ma)	2σ (+/-)	Reference
185	Ste. Margeurite	H4	phosphates	Pb-Pb	4562.70	0.70/0.70	Göpel et al. (1994)
186	Ste. Margeurite	H4	phosphates	Pb-Pb	4562.70	0.60/0.60	Göpel et al. (1994)
187	Ste. Margeurite	H4	feldspar	Al-Mg	4561.96	0.16/0.19	Telus et al. (2014)
188	Forest Vale	H4	feldspar	Al-Mg	4561.24	0.40/0.65	Telus et al. (2014)
189	Forest Vale	H4	phosphates	Pb-Pb	4560.90	0.70/0.70	Göpel et al. (1994)
190	Richardton	H5	silicate	Pb-Pb	4562.70	1.70/1.70	Amelin et al. (2005)
191	Richardton	H5	metal-silicate	Hf-W	4562.09	0.84/0.90	Kleine et al. (2008)
192	Richardton	H5	phosphates	Pb-Pb	4551.40	0.60/0.60	Göpel et al. (1994)
193	Richardton	H5	phosphates	Pb-Pb	4550.70	2.60/2.60	Amelin et al. (2005)
194	ALH 84069	H5	metal-silicate	Hf-W	4561.83	1.23/1.37	Kleine et al. (2008)
195	Nadiobondi	H5	phosphates	Pb-Pb	4555.60	3.40/3.40	Göpel et al. (1994)
196	Allegan	H5	phosphates	Pb-Pb	4550.20	0.70/0.70	Göpel et al. (1994)
197	Kernouve	H6	metal-silicate	Hf-W	4558.31	0.92/1.00	Kleine et al. (2008)
198	Kernouve	H6	phosphates	Pb-Pb	4523.90	0.50/0.50	Göpel et al. (1994)
199	Kernouve	H6	phosphates	Pb-Pb	4521.10	0.50/0.50	Göpel et al. (1994)
200	Guareña	H6	phosphates	Pb-Pb	4504.40	0.50/0.50	Göpel et al. (1994)
201	Guareña	H6	phosphates	Pb-Pb	4504.40	0.50/0.50	Göpel et al. (1994)
202	Estacado	H6	metal-silicate	Hf-W	4557.68	1.45/1.64	Kleine et al. (2008)
203	Knyahinya	L5	phosphates	Pb-Pb	4539.50	1.00/1.00	Göpel et al. (1994)
204	Barwell	L5	phosphates	Pb-Pb	4538.20	0.70/0.70	Göpel et al. (1994)
205	Knyahinya	L5	phosphates	Pb-Pb	4533.00	0.80/0.80	Göpel et al. (1994)
206	Ausson	L5	phosphates	Pb-Pb	4526.80	0.90/0.90	Göpel et al. (1994)
207	Homestead	L5	phosphates	Pb-Pb	4514.20	0.60/0.60	Göpel et al. (1994)
208	Marion (Iowa)	L6	phosphates	Pb-Pb	4510.70	0.50/0.50	Göpel et al. (1994)
209	Tuxtuac	LL5	phosphates	Pb-Pb	4543.60	2.10/2.10	Göpel et al. (1994)
210	Guidder	LL5	phosphates	Pb-Pb	4535.30	0.60/0.60	Göpel et al. (1994)
211	Saint-Séverin	LL6	phosphates	Pb-Pb	4553.60	0.70/0.70	Göpel et al. (1994)

Angrites

#	Meteorite	Class	Feature	Method	Age (Ma)	2σ (+/-)	Reference
212	D'Orbigny	angrite	bulk	Pb-Pb	4564.42	0.12/0.12	Amelin (2008)
213	D'Orbigny	angrite	bulk	Pb-Pb	4563.37	0.25/0.25	Brennecka and Wadhwa (2012)
214	NWA 2999	angrite	bulk	Pb-Pb	4560.74	0.47/0.47	Brennecka and Wadhwa (2012)
215	NWA 6291	angrite	bulk	Pb-Pb	4560.21	1.05/1.05	Brennecka and Wadhwa (2012)
216	LEW 86010	angrite	bulk	Pb-Pb	4558.55	0.15/0.15	Amelin (2008)
217	NWA 4590	angrite	bulk	Pb-Pb	4557.81	0.37/0.37	Brennecka and Wadhwa (2012)
218	NWA 4801	angrite	bulk	Pb-Pb	4557.01	0.27/0.27	Brennecka and Wadhwa (2012)
219	Angra dos Reis	angrite	bulk	Pb-Pb	4557.65	0.13/0.13	Amelin (2008)
220	Angra dos Reis	angrite	bulk	Pb-Pb	4556.60	0.26/0.26	Brennecka and Wadhwa (2012)

References

Amelin Y. (2008) U–Pb ages of angrites. *Geochimica et Cosmochimica Acta* **72**, 221–232.

Amelin Y., Ghosh A. and Rotenberg E. (2005) Unraveling the evolution of chondrite parent asteroids by precise U-Pb dating and thermal modeling. *Geochimica et Cosmochimica Acta* **69**, 505–518.

Amelin Y., Kaltenbach A., Iizuka T., Stirling C. H., Ireland T. R., Petaev M. and Jacobsen S. B. (2010) U–Pb chronology of the Solar System's oldest solids with variable 238U/235U. *Earth and Planetary Science Letters* **300**, 343–350.

Amelin Y. and Krot A. (2007) Pb isotopic age of the Allende chondrules. *Meteoritics & Planetary Science* **42**, 1321–1335.

Amelin Y., Krot A. N., Hutcheon I. D. and Ulyanov A. A. (2002) Lead isotopic ages of chondrules and calcium-aluminum-rich inclusions. *Science* **297**, 1678–1683.

Amelin Y., Wadhwa M. and Lugmair G. (2006) Pb-isotopic dating of meteorites using 202Pb-205Pb double-spike: Comparison with other high-resolution chronometers. *37th Lunar and Planetary Science Conference Proceedings*, Abstract #1970.

Anders E. and Grevesse N. (1989) Abundances of the elements: Meteoritic and solar. *Geochimica et Cosmochimica Acta* **53**, 197–214.

Bizzarro M., Baker J. A. and Haack H. (2004) Mg isotope evidence for contemporaneous formation of chondrules and refractory inclusions. *Nature* **431**, 275–278.

Bouvier A., Blichert-Toft J., Moynier F., Vervoort J. D. and Albarède F. (2007) Pb–Pb dating constraints on the accretion and cooling history of chondrites. *Geochimica et Cosmochimica Acta* **71**, 1583–1604.

Bouvier A., Brennecka G. A. and Wadhwa M. (2011) Absolute chronology of the first solids in the solar system. *LPI Contributions* **1639**, 9054.

Bouvier A. and Wadhwa M. (2010) The age of the Solar System redefined by the oldest Pb-Pb age of a meteoritic inclusion. *Nature Geoscience* **3**, 637–641.

Brearley A. J. (2006) The action of water. In *Meteorites and the Early Solar System II* (eds. D. S. Lauretta and H. Y. McSween). The University of Arizona Press, Tucson, AZ. pp. 587–624.

Brearley A. J. and Hutcheon I. D. (2000) Carbonates in the CM1 chondrite ALH84034: Mineral chemistry, zoning and Mn-Cr systematics. *31st Lunar and Planetary Science Conference*, Abstract #1407.

Brearley A. J. and Hutcheon I. D. (2002) Carbonates in the Y791198 CM2 Chondrite: Zoning and Mn-Cr Systematics. *Meteoritics & Planetary Science Supplement* **37**, A23.

Brennecka G. A. and Wadhwa M. (2012) Uranium isotope compositions of the basaltic angrite meteorites and the chronological implications for the early Solar System. *Proceedings of the National Academy of Sciences* **109**, 9299–9303.

Connelly J. N., Amelin Y., Krot A. N. and Bizzarro M. (2008) Chronology of the solar system's oldest solids. *The Astrophysical Journal Letters* **675**, L121–L124.

Connelly J. N. and Bizzarro M. (2009) Pb–Pb dating of chondrules from CV chondrites by progressive dissolution. *Chemical Geology* **259**, 143–151.

Connelly J. N., Bizzarro M., Krot A. N., Nordlund Å., Wielandt D. and Ivanova M. A. (2012) The absolute chronology and thermal processing of solids in the solar protoplanetary disk. *Science* **338**, 651–655.

Davis A. M. and McKeegan K. D. (2014) Short-lived radionuclides and early solar system chronology. In *Treatise on Geochemistry (Second Edition), Volume 1: Meteorites and Cosmochemical Processes* (ed. Davis A. M.). pp. 361–395.

Fujiya W., Sugiura N., Hotta H., Ichimura K. and Sano Y. (2012) Evidence for the late formation of hydrous asteroids from young meteoritic carbonates. *Nature Communications* **3**, 627.

Fujiya W., Sugiura N., Sano Y. and Hiyagon H. (2013) Mn–Cr ages of dolomites in CI chondrites and the Tagish Lake ungrouped carbonaceous chondrite. *Earth and Planetary Science Letters* **362**, 130–142.

Glavin D. P., Kubny A., Jagoutz E. and Lugmair G. W. (2004) Mn-Cr isotope systematics of the D'Orbigny angrite. *Meteoritics & Planetary Science* **39**, 693–700.

Göpel C., Manhès G. and Allègre C. J. (1994) U-Pb systematics of phosphates from equilibrated ordinary chondrites. *Earth and Planetary Science Letters* **121**, 153–171.

Harrison K. P. and Grimm R. E. (2010) Thermal constraints on the early history of the H-chondrite parent body reconsidered. *Geochimica et Cosmochimica Acta* **74**, 5410–5423.

Hewins R. H., Bourot-Denise M., Zanda B., Leroux H., Barrat J.-A., Humayun M., Goepel C., Greenwood R. C., Franchi I. A., Pont S., Lorand J.-P., Cournede C., Gattacceca J., Rochette P., Kuga M., Marrocchi Y. and Marty B. (2014) The Paris meteorite, the least altered CM chondrite so far. *Geochimica et Cosmochimica Acta* **124**, 190–222.

Hoppe P., MacDougall D. and Lugmair G. W. (2007) High spatial resolution ion microprobe measurements refine chronology of carbonate formation in Orgueil. *Meteoritics & Planetary Science* **42**, 1309–1320.

Hsu W., Huss G. R. and Wasserburg G. J. (2003) Al-Mg systematics of CAIs, POI, and ferromagnesian chondrules from Ningqiang. *Meteoritics & Planetary Science* **38**, 35–48.

Huss G. R., Rubin A. E. and Grossman J. N. (2006) Thermal metamorphism in chondrites. In *Meteorites and the Early Solar System II* (eds. D. S. Lauretta and H. Y. McSween Jr.). The University of Arizona Press, Tucson, AZ. pp. 567–586.

Hutcheon I. D. and Hutchison R. (1989) Evidence from the Semarkona ordinary chondrite for 26Al heating of small planets. *Nature* **337**, 238–241.

Hutcheon I. D., Krot A. N. and Ulyanov A. A. (2000) ^{26}Al in anorthite-rich chondrules in primitive carbonaceous chondrites: evidence chondrules postdate CAI. *31st Lunar and Planetary Science Conference Proceedings*, Abstract #1869.

Hutcheon I. D., Marhas K. K., Krot A. N., Goswami J. N. and Jones R. H. (2009) ^{26}Al in plagioclase-rich chondrules in carbonaceous chondrites: Evidence for an extended duration of chondrule formation. *Geochimica et Cosmochimica Acta* **73**, 5080–5099.

Jacobsen B., Yin Q., Moynier F., Amelin Y., Krot A. N., Nagashima K., Hutcheon I. D. and Palme H. (2008) ^{26}Al–^{26}Mg and ^{207}Pb–^{206}Pb systematics of Allende CAIs: Canonical solar initial ^{26}Al/^{27}Al ratio reinstated. *Earth and Planetary Science Letters* **272**, 353–364.

Jilly C. E., Huss G. R., Krot A. N., Nagashima K., Yin Q.-Z. and Sugiura N. (2014) Mn-53-Cr-53 dating of aqueously formed carbonates in the CM2 lithology of the Sutter's Mill carbonaceous chondrite. *Meteoritics & Planetary Science* **49**, 2104–2117.

Jones R. H., McCubbin F. M., Dreeland L., Guan Y., Burger P. V. and Shearer C. K. (2014) Phosphate minerals in LL chondrites: A record of the action of fluids during metamorphism on ordinary chondrite parent bodies. *Geochimica et Cosmochimica Acta* **132**, 120–140.

Kita N. T., Nagahara H., Togashi S. and Morishita Y. (2000) A short duration of chondrule formation in the solar nebula: Evidence from ^{26}Al in Semarkona ferromagnesian chondrules. *Geochimica et Cosmochimica Acta* **64**, 3913–3922.

Kita N. T., Tomomura S., Tachibana S., Nagahara H., Mostefaoui S. and Morishita Y. (2005) Correlation between aluminum-26 ages and bulk Si/Mg ratios for chondrules from LL3.0-3.1 chondrites. *36th Lunar and Planetary Science Conference*, Abstract #1750.

Kleine T., Hans U., Irving A. J. and Bourdon B. (2012) Chronology of the angrite parent body and implications for core formation in protoplanets. *Geochimica et Cosmochimica Acta* **84**, 186–203.

Kleine T., Touboul M., Van Orman J. A., Bourdon B., Maden C., Mezger K. and Halliday A. N. (2008) Hf–W thermochronometry: Closure temperature and constraints on the accretion and cooling history of the H chondrite parent body. *Earth and Planetary Science Letters* **270**, 106–118.

Kovach H. A. and Jones R. H. (2010) Feldspar in type 4–6 ordinary chondrites: Metamorphic processing on the H and LL chondrite parent bodies. *Meteoritics & Planetary Science* **45**, 246–264.

Krot A. N., Amelin Y., Cassen P. and Meibom A. (2005a) Young chondrules in CB chondrites from a giant impact in the early Solar System. *Nature* **436**, 989–992.

Krot A. N., Yurimoto H., Hutcheon I. D. and MacPherson G. J. (2005b) Chronology of the early Solar System from chondrule-bearing calcium-aluminium-rich inclusions. *Nature* **434**, 998–1001.

Kunihiro T., Rubin A. E., McKeegan K. D. and Wasson J. T. (2004) Initial ^{26}Al/^{27}Al in carbonaceous-chondrite chondrules: Too little ^{26}Al to melt asteroids. *Geochimica et Cosmochimica Acta* **68**, 2947–2957.

Kurahashi E., Kita N. T., Nagahara H. and Morishita Y. (2008) Al-26-Mg-26 systematics of chondrules in a primitive CO chondrite. *Geochimica et Cosmochimica Acta* **72**, 3865–3882.

Lee M. R., Lindgren P., Sofe M. R., Alexander C. M. O'D. and Wang J. (2012) Extended chronologies of aqueous alteration in the CM2 carbonaceous chondrites: Evidence from carbonates in Queen Alexandra Range 93005. *Geochimica et Cosmochimica Acta* **92**, 148–169.

de Leuw S., Rubin A. E., Schmitt A. K. and Wasson J. T. (2009) ^{53}Mn–^{53}Cr systematics of carbonates in CM chondrites: Implications for the timing and duration of aqueous alteration. *Geochimica et Cosmochimica Acta* **73**, 7433–7442.

McDonough W. F. and Sun S. -s. (1995) The composition of the Earth. *Chemical Geology* **120**, 223–253.

McSween H. Y. and Huss G. R. (2010) *Cosmochemistry*. Cambridge University Press.

Mishra R. K. and Goswami J. N. (2014) Fe–Ni and Al–Mg isotope records in UOC chondrules: Plausible stellar source of ^{60}Fe and other short-lived nuclides in the early Solar System. *Geochimica et Cosmochimica Acta* **132**, 440–457.

Mishra R. K., Goswami J. N., Tachibana S., Huss G. R. and Rudraswami N. G. (2010) ^{60}Fe and ^{26}Al in chondrules from unequilibrated chondrites: Implications for early solar system processes. *The Astrophysical Journal Letters* **714**, L217.

Mostefaoui S., Kita N. T., Togashi S., Tachibana S., Nagahara H. and Morishita Y. (2002) The relative formation ages of ferromagnesian chondrules inferred from their initial aluminum-26/aluminum-27 ratios. *Meteoritics & Planetary Science* **37**, 421–438.

Nagashima K., Krot A. N. and Huss G. R. (2008) ^{26}Al in chondrules from CR carbonaceous chondrites. *39th Lunar and Planetary Science Conference Proceedings*, Abstract #2224.

Palguta J., Schubert G. and Travis B. J. (2010) Fluid flow and chemical alteration in carbonaceous chondrite parent bodies. *Earth and Planetary Science Letters* **296**, 235–243.

Petitat M., Marrocchi Y., McKeegan K. D., Mostefaoui S., Meibom A., Zolensky M. E. and Gounelle M. (2011) ^{53}Mn-^{53}Cr ages of Kaidun carbonates. *Meteoritics & Planetary Science* **46**, 275–283.

Rudraswami N. G. and Goswami J. N. (2007) ^{26}Al in chondrules from unequilibrated L chondrites: Onset and duration of chondrule formation in the early solar system. *Earth and Planetary Science Letters* **257**, 231–244.

Rudraswami N. G., Goswami J. N., Chattopadhyay B., Sengupta S. K. and Thapliyal A. P. (2008) ^{26}Al records in chondrules from unequilibrated ordinary chondrites: II. Duration of chondrule formation and parent body thermal metamorphism. *Earth and Planetary Science Letters* **274**, 93–102.

Russell S. S., Huss G. R., MacPherson G. J. and Wasserburg G. J. (1997) Early and late chondrule formation: New constraints for solar nebula chronology from Al-26/Al-27 in unequilibrated ordinary chondrites. *28th Lunar and Planetary Science Conference*, Abstract #1209.

Russell S. S., Srinivasan G., Wasserburg G. J., MacPherson G. J. and Huss G. R. (1996) Evidence for widespread 26-Al in the solar nebula and constraints for nebula time scales. *Science* **273**, 757–762.

Scott E. R. D. and Krot A. N. (2005) Chondritic meteorites and the high-temperature nebular origins of their components. In *Chondrites and the Protoplanetary Disk* (eds. A. N. Krot, E. R. D. Scott, and B. Reipurth). Astronomical Society of the Pacific Conference Series. pp. 15–53.

Scott E. R. D., Krot T. V., Goldstein J. I. and Wakita S. (2014) Thermal and impact history of the H chondrite parent asteroid during metamorphism: Constraints from metallic Fe–Ni. *Geochimica et Cosmochimica Acta* **136**, 13–37.

Sugiura N. and Krot A. N. (2007) ^{26}Al-^{26}Mg systematics of Ca-Al-rich inclusions, amoeboid olivine aggregates, and chondrules from the ungrouped carbonaceous chondrite Acfer 094. *Meteoritics & Planetary Science* **42**, 1183–1195.

Telus M., Huss G. R., Nagashima K. and Ogliore R. C. (2014) Revisiting Al-26-Mg-26 systematics of plagioclase in H4 chondrites. *Meteoritics & Planetary Science* **49**, 929–945.

Tyra M. A. (2015) The forgotten uncertainties in using radiochronometry to date minerals that formed in the early solar system: The example of ^{53}Mn. *46th Lunar and Planetary Science Conference,* Abstract #2911.

Van Orman J. A., Cherniak D. J. and Kita N. T. (2014) Magnesium diffusion in plagioclase: Dependence on composition, and implications for thermal resetting of the 26Al–26Mg early solar system chronometer. *Earth and Planetary Science Letters* **385**, 79–88.

Villeneuve J., Chaussidon M. and Libourel G. (2009) Homogeneous distribution of ^{26}Al in the solar system from the Mg isotopic composition of chondrules. *Science* **325**, 985–988.

Williams J. P. and Cieza L. A. (2011) Protoplanetary disks and their evolution. *Annual Review of Astronomy and Astrophysics.* **49**, 67–117.

Yin Q.-Z., Jacobsen B., Moynier F. and Hutcheon I. D. (2007) Toward consistent chronology in the early solar system: High-resolution ^{53}Mn-^{53}Cr chronometry for chondrules. *The Astrophysical Journal Letters* **662**, L43.

Yin Q.-Z., Yamashita K., Yamakawa A., Tanaka R., Jacobsen B., Ebel D., Hutcheon I. D. and Nakamura E. (2009) ^{53}Mn-^{53}Cr systematics of Allende chondrules and ε54Cr–Δ17O correlation in bulk carbonaceous chondrites. *40th Lunar and Planetary Science Conference,* Abstract #2006.

Yurimoto H. and Wasson J. T. (2002) Extremely rapid cooling of a carbonaceous-chondrite chondrule containing very ^{16}O-rich olivine and a ^{26}Mg-excess. *Geochimica et Cosmochimica Acta* **66**, 4355–4363.

«Планета есть колыбель разума, но нельзя вечно жить в колыбели».
—Константин Циолковский

“A planet is the cradle of mind, but one cannot live in a cradle forever.”
—Konstantin Tsiolkovsky